

STRUCTURAL IMPLICATIONS OF ULTRA-HIGH PERFORMANCE FIBRE-REINFORCED CONCRETE IN BRIDGE DESIGN

THÈSE N° 4051 (2008)

PRÉSENTÉE LE 16 AVRIL 2008

À LA FACULTÉ DE L'ENVIRONNEMENT NATUREL, ARCHITECTURAL ET CONSTRUIT
LABORATOIRE DE CONSTRUCTION EN BÉTON
PROGRAMME DOCTORAL EN STRUCTURES

ÉCOLE POLYTECHNIQUE FÉDÉRALE DE LAUSANNE

POUR L'OBTENTION DU GRADE DE DOCTEUR ÈS SCIENCES

PAR

Ana SPASOJEVIĆ

ingénieur civil diplômée de l'Université de Niš, Serbie
et de nationalité serbe

acceptée sur proposition du jury:

Prof. E. Brühwiler, président du jury
Prof. A. Muttoni, directeur de thèse
Prof. T. Keller, rapporteur
Dr F. Toutlemonde, rapporteur
Prof. N. V. Tue, rapporteur



ÉCOLE POLYTECHNIQUE
FÉDÉRALE DE LAUSANNE

Suisse
2008

мојој породици,

Дарију

Préface

Le béton fibré à ultra-hautes performances (BFUHP) est un nouveau matériau dont les caractéristiques mécaniques sont très supérieures à celles du béton ordinaire : sa résistance à la compression est environ 6 fois plus élevée et se rapproche ainsi de celle de l'acier alors que sa résistance à la traction est environ 4 fois plus élevée que celle d'un béton ordinaire. Malgré ces caractéristiques, l'utilisation de ce matériau pour des structures nouvelles reste limitée. Ceci à cause du coût considérable du matériau, parce que les solutions structurales adaptées à ses caractéristiques spécifiques restent encore partiellement à développer et du fait que les méthodes de dimensionnement du béton armé ordinaire ne s'y appliquent pas nécessairement.

L'ajout d'une grande quantité de fibres, facteur important dans l'augmentation du coût, ne permet qu'une augmentation très limitée de la résistance à la traction. Il assure par contre une augmentation considérable de la capacité de déformation du matériau, qui peut devenir déterminante dans des structures hyperstatiques de faibles dimensions (aspect souvent évoqué, mais jusqu'ici peu considéré dans les travaux théoriques sur le comportement structural des éléments en BFULHP).

Dans la thèse de Mlle Spasojevic, le comportement des éléments minces non armés est étudié dans l'optique de la construction des ponts et des passerelles. Le choix de ces ouvrages d'art découle du fait que ce nouveau matériau performant semble surtout s'imposer pour des applications où les exigences tant mécaniques qu'en matière de durabilité sont élevées.

L'étude de Mlle Spasojevic se concentre sur le comportement et la résistance des éléments fléchis en BFULHP, isostatiques et hyperstatiques, ainsi que sur les dalles. Les résultats des approches analytiques de Mlle Spasojevic, vérifiés par deux séries expérimentales sur poutres et sur dallettes minces, permettent de comprendre l'influence de la taille des éléments sur leur résistance et leur capacité de déformation à la rupture. Sur cette base, l'applicabilité des méthodes de dimensionnement plastique aux éléments minces en BFULHP est analysée de façon rigoureuse, ce qui constitue une contribution significative vers un dimensionnement simple et sûr de tels éléments.

Le comportement des dalles de roulement est complété par l'étude de leur résistance au poinçonnement, un mode de rupture qui limite souvent la résistance des dalles de roulement des ponts en béton armé. Les résultats de l'étude, supportés par une série d'essais conduite dans le cadre de cette thèse, montrent une application prometteuse de la théorie de la fissure critique et peuvent servir pour l'estimation pratique de la résistance au poinçonnement des dalles en BFULHP.

Une synthèse des concepts développés pendant la thèse permettent finalement à Mlle Spasojevic d'envisager des applications possibles du BFULHP au domaine des ponts et passerelles.

Acknowledgements

I am very pleased to be able to thank a lot of nice people and important institutions for having helped me carry out this research and given me their support.

First I would like to thank Professor Dr Aurelio Muttoni, my Thesis Director and the Director of the Structural Concrete Laboratory (IS-Béton) at the Ecole Polytechnique Fédérale de Lausanne (EPFL), where this research was performed. I thank him for having given me the opportunity to undertake this work and learn lots of interesting new things, for the support and guidance during my research.

I wish to express my gratitude to the members of the jury, who generously gave their time to review my work and offered insightful and valuable comments: Prof. Dr T. Keller, Dr F. Toutlemonde and Prof. Dr N. V. Tue and Prof. Dr E. Brühwiler, President of the jury.

I would like to acknowledge the support of the Swiss Federal Roads Authority who funded and guided this research project. I thank the Eiffage Group for their technical support in the experimental part of this work, and their kindness and desire to share their experience and knowledge. I would like to express my appreciation to the EPFL for the grant I received for the first year of my doctoral schooling.

I am especially grateful to all my colleagues at the IS-Béton, and colleagues from related laboratories - their friendly presence and everyday support were important to me. My thanks to Dr Olivier Burdet and Dr Miguel Fernandez Ruiz for their professional help during these last years. Special thanks to Yvonne, for always being ready to help. I also wish to thank those who are no longer part of the IS-Béton team, but with whom I shared many pleasant moments. I sincerely thank all my students, in particular one of my Master students, now an engineer, Adrien Salvo, for his valuable participation in part of the experimental research carried out during this thesis.

Efficient help during the experimental work was also provided by the technical staff of the Structural Institute, to all of whom I wish to express deep gratitude.

I would like to express my sincere thanks to Ms Margaret Howett for her help with the writing of this document and valuable suggestions.

Thanks to my friends in Switzerland - both at and outside of the EPFL - for pleasant moments spent together over recent years. I owe particular thanks to all my wonderful friends back in Serbia, in Niš, with whom I grew up, learned to appreciate life, and who were always there for me. And my gratitude to my university colleagues in Niš, with whom I took my first professional steps, which, thanks to them, were enjoyable times.

There are surely much better ways to thank those I love the most, those with whom I sincerely share all the joy and happiness, and who were unselfishly always there for me; I want to dedicate this work to them. In this way I wish to thank my family, my mum and my dad, for the freedom and the unconditional support they have always given me and for the enthusiasm they continue to express. It is from them that I have learnt that a way to live a beautiful life is to design structures! Thanks to my beloved sister and her cheerful family, my adorable Sofija and Sava, for insisting on reminding me that life has other beautiful moments to offer.

My deepest gratitude I need to express to Dario, for unselfishly sharing with me his profound professional knowledge, for time and effort generously spent in correcting this document and most of all for his everyday support, for the smile always present on his face and all the beautiful moments we spend together.

Abstract

The present research represents a theoretical and experimental contribution to the understanding of the structural behaviour of elements made of ultra-high performance fibre-reinforced concrete (UHPFRC).

UHPFRC is investigated as an advanced cementitious material offering particular potential in innovative bridge design. The optimised material composition results in high compressive strength and non-negligible tensile strength and ductility, provided by multi-microcracking. This allows significant tensile forces to be sustained by elements in bending even without the use of ordinary reinforcement. Thanks also to the material's resistance to environmental degradation, very thin structural elements can be constructed.

This research focuses primarily on the bending behaviour and design of thin UHPFRC beams and slabs. Punching-shear is also investigated as a possible failure mode of thin UHPFRC slabs. One of the main differences between other concretes and UHPFRC is that the latter requires mechanical models capable of taking tensile behaviour into account for rational structural application. Analytical and numerical models are developed in this study to simulate the non-linear bending response of UHPFRC beams and slabs. This permits the assessment of element behaviour at service states and prediction of failure loads. Theoretical research on both bending and punching-shear failure is supported by experimental research on beams and slabs made of BSI® UHPFRC with 2.5 % volume of 20-mm long steel fibres.

The analytical model for beams in bending takes both material multi-microcracking and macrocrack propagation with tensile softening into consideration. Multi-microcracking is modelled as a pseudo-plastic tensile behaviour, while the macrocrack is simulated based on the assumptions of the fictitious crack model. The results are in good agreement with experimental data and simulations obtained from a developed finite element model. Using theoretical results and experimental data it is demonstrated that pre-peak behaviour and bending strength are mainly governed by multi-microcracking. The propagation of the macrocrack provides only a minor additional contribution to bending strength, but, in the case of thin beams, plays an important role in providing ductility in bending. Theoretical results demonstrate that, due to the presence of pronounced pseudo-plastic deformations, size effect on bending strength is much less significant for UHPFRC than for other quasi-brittle materials, which corresponds to experimental observations. It is however shown that, even if the pseudo-plastic phase is less pronounced, thin elements develop behaviour similar to that of elements with high pseudo-plastic tensile deformations, owing to the low stress decrease in tensile softening. Nonetheless, in the absence of pseudo-plastic tensile deformations, the behaviour of thick elements approaches that of typical quasi-brittle materials, with a more pronounced size effect.

In the case of thin statically indeterminate beams and slabs, it is shown that a high level of tensile ductility can allow sufficient internal force redistribution to occur, leading to a significant increase in load-bearing capacity. Moreover, high rotations can be sustained after cracking while almost constant bending strength is maintained, resulting in a plastic-like behaviour. It is demonstrated that the theory of plasticity can thus be applied: a formulation is proposed to predict the resistant plastic moment, enabling easy estimation of the bending failure load for thin elements. The analysis results show good agreement with test results for slabs of different thicknesses. However, due to the remarkable size effect on ductility in bending, the rotation capacity of UHPFRC elements thicker than approximately 100 mm is limited, and the theory of plasticity does not apply.

Experimental and theoretical research on the punching-shear failure of thin UHPFRC slabs demonstrates the influence of structural parameters on achieved shear resistance. A proposal is made for considering fibre contribution in shear resistance as a structure-dependent parameter, relating the critical shear crack opening to slab rotation. This approach results in more accurate predictions for thin elements with larger deformations as compared to current code predictions that overestimate resistances for such elements.

With a view to the structural application of UHPFRC in bridge design, the concept of ribbed deck slab is studied. Based on the theoretical and experimental results it is demonstrated that thin UHPFRC slabs (*40-60 mm*) without ordinary reinforcement can be effectively used in this concept: sufficient bending and punching-shear resistances to locally applied traffic loads can be ensured. With prestressed ribs, UHPFRC ribbed slabs attain high load-bearing capacity, while structural dead weight is significantly decreased. This concept could open up new vistas in the design of new structures and offers effective possibilities for the structural repair or widening of existing bridges.

Keywords: ultra-high performance fibre-reinforced concrete (UHPFRC), beam, slab, thin elements, structure, bridge, ribbed deck, bending, punching, design, plastic analysis, cracking, tensile hardening, tensile softening, bending strength, ductility, size effect

Résumé

La recherche théorique et expérimentale effectuée dans le cadre de cette thèse apporte une contribution à la compréhension du comportement structurel des éléments en béton fibré à ultra hautes performances (BFUHP/UHPFRC).

Le BFULHP est étudié en qualité de matériau cimentaire avancé, qui offre des possibilités spécifiques pour l'innovation dans le domaine de la conception des ponts. La composition optimale du matériau entraîne une haute résistance à la compression ainsi qu'une résistance et une ductilité non négligeables en traction, grâce à la microfissuration. Cela permet de reprendre des efforts de traction significatifs dans les éléments fléchis, même en absence d'armatures ordinaires. Grâce aussi à la durabilité du matériau vis-à-vis de la dégradation environnementale, des éléments de structures très minces peuvent être ainsi réalisés.

Cette recherche se concentre principalement sur le comportement et sur le dimensionnement en flexion de poutres et dalles en BFULHP sans armature ordinaire. Le poinçonnement est également investigué en tant que possible mode de rupture. Une différence importante par rapport aux autres types de béton réside dans le fait que, pour une utilisation structurale rationnelle du BFULHP, des modèles mécaniques qui tiennent compte de son comportement en traction sont nécessaires. Dans cette recherche, des modèles analytiques et numériques sont développés pour simuler la réponse non linéaire en flexion des poutres et dalles en BFULHP. Cela permet de décrire le comportement des éléments à l'état limite de service, mais aussi de prévoir leur charge de rupture. La recherche théorique, aussi bien pour la flexion que pour le poinçonnement, s'appuie sur les résultats d'essais en laboratoire sur poutres et dalles réalisées avec le BFULHP BSI®, contenant 2.5 % en volume de fibres métalliques, avec une longueur de 20 mm.

Le modèle analytique pour les poutres fléchies tient compte de la multi-microfissuration du matériau ainsi que de la propagation d'une macro-fissure avec un comportement adoucissant en traction. La multi-microfissuration est idéalisée avec un comportement pseudo-plastique en traction, alors que la macro-fissure est modélisée selon les hypothèses du modèle de la fissure fictive. Les résultats sont en bonne concordance avec les données expérimentales ainsi qu'avec les résultats des modélisations numériques effectués par la méthode des éléments finis. En se basant sur les résultats théoriques et expérimentaux, il a été possible de démontrer que la multi-microfissuration gouverne le comportement avant-pic et la résistance flexionnelle. La propagation de la macro-fissure n'apporte qu'une contribution mineure à la résistance flexionnelle mais, dans les éléments minces, elle joue un rôle important pour le développement d'un comportement ductile en flexion. Les résultats théoriques montrent que, grâce à la présence de déformations pseudo-plastiques significatives, l'effet d'échelle sur la résistance en flexion est beaucoup moins important pour le BFULHP que pour les autres matériaux quasi-fragiles, conformément aux résultats expérimentaux. Même si la phase pseudo-plastique est peu importante, les éléments minces peuvent développer une résistance et une ductilité similaires à celles développées par un matériau qui a de grandes déformations pseudo-plastiques. Cela est possible grâce à la diminution lente et progressive des contraintes dans la phase adoucissante. Néanmoins, en absence de déformations pseudo-plastiques, le comportement des éléments épais approche le comportement typique des matériaux quasi-fragiles, avec un effet d'échelle plus important.

Dans le cas de poutres hyperstatiques et de dalles, il est montré que la ductilité en traction peut permettre une redistribution significative des efforts internes dans les éléments minces, avec une augmentation importante de la résistance ultime et le développement d'un comportement similaire à un mécanisme plastique. De plus, de grandes rotations peuvent se développer après fissuration tout en gardant un moment résistant de flexion presque constant. La théorie de la plasticité peut ainsi être appliquée pour prédire la capacité portante des poutres et des dalles minces. La définition d'une approche pour prédire le moment résistant plastique permet d'estimer de manière aisée la charge de rupture en flexion. Les résultats de l'analyse concordent avec les résultats d'essais sur dalles de différentes épaisseurs. Cependant, à cause de l'effet d'échelle important qui existe sur la ductilité en

flexion, la capacité de rotation est limitée pour les éléments en BFUHP épais ($>100\text{ mm}$), et la théorie de la plasticité ne s'applique pas.

La recherche expérimentale et théorique sur la rupture au poinçonnement des dalles minces en BFUHP démontre l'influence des paramètres structuraux sur la résistance à l'effort tranchant. En reliant l'ouverture de la fissure critique pour l'effort tranchant à la rotation de la dalle, une proposition est faite pour permettre de tenir compte de la contribution des fibres à la résistance à l'effort tranchant en fonction de paramètres dépendant de la structure. Pour les éléments minces et très déformables, cette approche permet une prédiction plus précise et plus prudente que celle obtenue avec les normes existantes.

Dans le cadre d'une application structurale du BFUHP pour le dimensionnement des ponts, le concept de dalle nervurée est étudié. Sur la base des résultats théoriques et expérimentaux, il est démontré que des dalles minces en BFUHP ($40\text{-}60\text{ mm}$) sans armatures ordinaires peuvent être utilisées selon ce même concept structural, car elles fournissent une résistance à la flexion et au poinçonnement suffisante pour reprendre les charges de trafic appliqués localement et pour les transmettre aux porteurs principaux. Avec des nervures précontraintes, les dalles nervurées en BFUHP peuvent offrir une grande résistance tout en réduisant significativement le poids propre de la structure. Ce concept est intéressant pour la réalisation de nouvelles structures, mais aussi dans le cadre de la réhabilitation et de l'élargissement de structures existantes.

Mots-clefs: béton fibré à ultra-hautes performances (BFUHP), poutre, dalle, éléments minces, structure, pont, dalle nervurée, flexion, poinçonnement, dimensionnement, analyse plastique, fissuration, comportement durcissant en traction, comportement adoucissant en traction, résistance flexionnelle, ductilité, effet d'échelle

Riassunto

La ricerca teorica e sperimentale effettuata nell'ambito di questa tesi fornisce un contributo alla comprensione del comportamento strutturale degli elementi in calcestruzzo fibro-rinforzato ad altissime prestazioni (*ultra high performance fibre reinforced concrete*, UHPFRC).

L'UHPFRC è studiato in quanto materiale cementizio innovativo, capace di offrire possibilità di innovazione specifiche nell'ambito della concezione dei ponti. La composizione ottimale del materiale gli conferisce una resistenza alla compressione elevata e, allo stesso tempo, una resistenza ed una duttilità non trascurabili in trazione, grazie alla microfessurazione. Negli elementi inflessi ciò permette di riprendere sforzi di trazione considerevoli, anche in assenza di armature tradizionali. Grazie anche alla durabilità del materiale nei confronti dell'aggressività ambientale, è possibile realizzare elementi strutturali di spessore molto contenuto.

Questa ricerca si concentra principalmente sul comportamento e sul dimensionamento in flessione di travi e piastre in UHPFRC senza armature tradizionali. Il punzonamento è altresì analizzato, quale possibile modalità di rottura. Una differenza importante rispetto ad altri tipi di calcestruzzo risiede nel fatto che, per un uso strutturale efficace dell'UHPFRC, sono necessari modelli meccanici che tengano in considerazione il suo comportamento in trazione. Modelli di tipo analitico e numerico sono stati sviluppati nell'ambito di questa ricerca per simulare la risposta non lineare in flessione di travi e piastre in UHPFRC. Grazie a tali modelli è possibile descrivere il comportamento degli elementi in stato di servizio, ma anche prevederne il carico di rottura. Tanto per la flessione quanto per il punzonamento, la ricerca teorica è sostenuta dai risultati di prove di laboratorio su travi e piastre realizzate in BSI®, un particolare tipo di UHPFRC rinforzato con il 2.5 % in volume di fibre metalliche di lunghezza pari a 20 mm.

Il modello analitico di trave inflessa considera sia la fase di multi-microfessurazione in trazione del materiale sia la propagazione di una fessura macroscopica con comportamento tensione-apertura di fessura degradante (*softening*). La multi-microfessurazione è idealizzata con un comportamento pseudo-plastico in trazione, mentre l'analisi della macro-fessura si basa sulle ipotesi di un modello a fessura coesiva. I risultati concordano con i dati sperimentali e con i risultati di modellazioni numeriche effettuate con il metodo degli elementi finiti. Basandosi sui risultati teorici e sperimentali, si dimostra che la multi-microfessurazione controlla il comportamento pre-picco e la resistenza flessionale. La fase di propagazione della macro-fessura apporta soltanto un contributo marginale alla resistenza flessionale, ma svolge, negli elementi sottili, un ruolo di rilievo per lo sviluppo della duttilità in flessione. I risultati teorici mostrano che, in presenza di deformazioni importanti in fase pseudo-plastica, l'effetto di scala sulla resistenza in flessione è molto meno importante per un UHPFRC che per altri materiali quasi-fragili. Se la fase pseudo-plastica è poco estesa, gli elementi sottili possono sviluppare resistenza e duttilità simili a quelle sviluppate da un materiale con deformazioni in fase pseudo-plastica più importanti: ciò è reso possibile dalla diminuzione lenta e progressiva delle tensioni nella fase *softening*. Nel caso di elementi spessi ed in assenza di fase pseudo-plastica, tuttavia, il comportamento si avvicina al comportamento tipico dei materiali quasi-fragili, con effetto di scala importante.

Nel caso di travi staticamente determinate o di piastre, si dimostra che per elementi sottili (spessore inferiore a 100 mm) la duttilità in trazione permette una redistribuzione efficace degli sforzi interni, con aumento rilevante della resistenza ultima e sviluppo di un comportamento simile ad un meccanismo plastico. Inoltre, rotazioni di entità significativa possono svilupparsi nella fase post-fessurativa, pur mantenendo una resistenza flessionale quasi costante. La teoria della plasticità può pertanto essere applicata per il calcolo della capacità portante di travi e piastre sottili. La definizione di un approccio per predire il momento resistente plastico permette di stimare in modo semplice il carico di rottura di elementi staticamente determinati. I risultati dell'analisi concordano con i risultati di prove su piastre di diverso spessore. A causa dell'effetto di scala importante che interessa la duttilità in flessione, tuttavia, la capacità di rotazione di elementi in UHPFRC spessi (> 100 mm) è limitata, e la teoria della plasticità non può essere utilizzata.

La ricerca sperimentale e teorica sulla rottura per punzonamento di piastre sottili in UHPFRC evidenzia l'influenza dei parametri strutturali, quali geometria e condizioni d'appoggio, sulla resistenza al taglio. Da un punto di vista teorico, l'apertura della fessura critica per la resistenza al taglio é espressa in funzione della rotazione nella piastra. É così possibile formulare un modello di calcolo che permette di esprimere il contributo delle fibre alla resistenza al taglio in funzione dei parametri strutturali. Per elementi snelli, tale approccio permette una predizione più precisa e più prudente di quella ottenuta utilizzando le norme esistenti.

Nell'ambito di un'applicazione strutturale dell'UHPFRC nella concezione dei ponti, si considera il concetto di piastra nervata. Sulla base dei risultati teorici e sperimentali, si dimostra che piastre sottili in UHPFRC (40-60 mm) senza armature tradizionali possono essere utilizzate come parti di piastre nervate di ponte stradale, poiché forniscono una resistenza alla flessione ed al punzonamento sufficiente per riprendere i carichi di traffico applicati localmente e trasmetterli agli elementi portanti principali. Con nervature precomprese, le piastre nervate in UHPFRC possono offrire una grande resistenza riducendo al contempo, ed in modo considerevole, il peso proprio della struttura. Questo concetto é interessante per la realizzazione di nuove strutture, ma anche nell'ambito del ripristino o dell'ampliamento di strutture esistenti.

Parole chiave: calcestruzzo fibro-rinforzato ad altissime prestazioni, trave, piastra, elementi sottili, struttura, ponte, piastra nervata, flessione, punzonamento, dimensionamento, calcolo plastico, fessurazione, comportamento incrudente in trazione, comportamento softening in trazione, resistenza flessionale, duttilità, effetto di scala

Table of contents

Préface	i
Acknowledgements	iii
Summary, Résumé, Riassunto	v
Table of contents	xi
1. Introduction	1
1.1 Exposition of problem	1
1.2 Objectives	2
1.3 Thesis organisation	3
2. Possibilities for structural improvements in concrete bridges	5
2.1 Introduction	5
2.2 History of concrete bridges	5
2.2.1 Lessons from the history of bridges	5
2.2.2 Material and structural development in concrete bridges	6
2.3 Possible directions for improvement in concrete bridge design	7
2.3.1 Efficient structural shapes	7
2.3.2 Classic concrete solutions using more resistant concretes	9
2.4 Conclusions	10
3. UHPFRC: material properties	13
3.1 UHPFRC: definition, material development	13
3.2 Microstructure of the material	15
3.2.1 Ultra-high performance concrete matrix	15
3.2.2 Fibres in UHPFRC	18
3.2.3 Different types of UHPFRC	20
3.3 Mechanical properties of UHPFRC	21
3.3.1 Uniaxial Compression	22
3.3.2 Uniaxial Tension	29
3.4 Other material properties of UHPFRC	46
3.5 Conclusions	47
4. Analysis and design of UHPFRC structural elements in bending	49
4.1 UHPFRC elements in bending: problems involved	49
4.2 Fracture models for quasi-brittle materials	51
4.3 Proposed model for bending of UHPFRC elements	55
4.3.1 Approach	55
4.3.2 Hypotheses of the model	57
4.3.3 Linear-elastic behaviour	59
4.3.4 Non-linear behaviour due to multi-microcracking	59
4.3.5 Non-linear behaviour with macrocrack propagation	69
4.4 Application of the developed model	90
4.4.1 Validation of the model with experimental data: BSI-Céracem UHPFRC	90
4.4.2 Validation of the model with experimental data: other materials	94
4.4.3 Size effect of UHPFRC elements in bending	97
4.5 Conclusions	101
4.5.1 Developed analytical model	101
4.5.2 Behaviour and design of UHPFRC in bending	101

5.	Application of the theory of plasticity in the design of statically indeterminate UHPFRC beams	103
5.1	Introduction	103
5.2	Theory of plasticity in design of concrete structures	104
5.2.1	Fundamentals of the theory of plasticity applied to concrete	104
5.3	Non-linear analysis of statically indeterminate beams in bending	106
5.3.1	Analysis approach	106
5.3.2	Algorithm for the simulation of non-linear load-displacement behaviour	108
5.3.3	Results of analysis	110
5.4	Plastic solutions for a clamped beam	115
5.5	Comparison of results: non-linear and plastic analysis	118
5.6	Compressive membrane action	121
5.7	Conclusion	121
6.	Bending and punching behaviour of thin UHPFRC slabs	123
6.1	Thin UHPFRC slabs as structural elements	123
6.2	Bending behaviour of UHPFRC slabs	124
6.2.1	Bending theory of thin plates	124
6.2.2	Finite difference approach for non-linear behaviour of UHPFRC slabs	130
6.2.3	Results of the non-linear analysis	132
6.2.4	Comparison of theoretical and experimental results	135
6.2.5	Theory of plasticity in design of thin UHPFRC slabs	137
6.2.6	Softening hinge in UHPFRC	141
6.2.7	Conclusions	141
6.3	Punching shear strength of UHPFRC slabs	142
6.3.1	Resistance models	143
6.3.2	Punching shear resistance of thin slabs: experimental results	144
6.3.3	Relationship between slab rotation and punching shear strength	147
6.3.4	Punching shear in UHPFRC design recommendations	148
6.3.5	Fibre contribution to shear strength: a proposal	150
6.3.6	Practical aspects of size effect on punching shear strength	151
6.3.7	Conclusions	152
7.	Structural application of UHPFRC	153
7.1	Advantages and limitations of UHPFRC for structural application	153
7.2	Domains of application for UHPFRC	154
7.2.1	Applications of UHPFRC in road bridges	157
7.2.2	Conclusions	162
7.3	Case study: design of a UHPFRC ribbed deck slab	163
7.3.1	Structural concept	163
7.3.2	Design basis	164
7.3.3	Design procedure	166
7.3.4	Design for local failures	167
7.3.5	Design for global failure	169
7.3.6	Serviceability states	175
7.3.7	Conclusions	175
8.	Conclusions and prospects	177
8.1	Conclusions of the research	177
8.2	Prospects for further research	181

Bibliography	183
List of notations	199

Appendices:

Appendix M1

Behaviour of beam with pseudo-plastic tensile yielding: equation development

Appendix M2

Behaviour of beam with a fictitious crack: equation development

Appendix T1

Testing of thin UHPFRC elements

Curriculum Vitae

1. Introduction

1.1 Exposition of problem

The present research investigates possible structural applications of ultra-high performance fibre-reinforced concrete (UHPFRC) for advanced bridge design. The search for solutions in the design of more efficient bridges, in terms of material consumption, ease of construction, aesthetic appeal, durability etc., represents an unceasing engineering task.

There are many parameters influencing bridge design, and consequently many possible ways for its improvement. More efficient structural forms and more adapted materials and construction techniques are the major parameters leading to a successful structural concept. The application of advanced cementitious materials, such as UHPFRC, has been identified as one of the promising ways to innovate in bridge design. Cement-based materials, in general, are widely used building materials due to the availability of their components and low production energy. Ordinary reinforced concrete (OC) solutions are well accepted in design practice and optimised with respect to material consumption and construction process. It is acknowledged that the use of high-strength concretes (HSCs) leads to a certain decrease in material quantity, principally due to its increased compressive strengths, while all tensile forces continue to be borne by reinforcement and prestressing steel. This means that all constructive constraints linked with reinforcement placement, as in design with ordinary concrete, apply to HSCs, allowing no radical improvements. On the other hand, UHPFRCs are specifically tailored materials that, in addition to greatly increased compressive strength, are characterised by non-negligible strength and ductility in tension, allowing significant tensile forces to be sustained in bending even if passive reinforcement is not used. Due to the greatly improved material mechanical strengths and material compactness that provide a high degree of resistance to unfavourable environmental conditions, very thin structural elements can be considered. Material workability characterised by self-placing and self-compacting, in addition to the economy of labour in relation to the placement of ordinary reinforcement, increase production speed and make the material well suited for precasting. Light elements permit easy manipulation and rapid construction. Corrosion is almost completely avoided in dense UHPC matrix, significantly reducing maintenance costs and extending the service life of UHPFRC structures.

Despite its vastly improved material properties, the structural application of UHPFRC is still not widespread. To date, UHPFRC is successfully used mostly in cases where OC barely meets particular design requirements, principally with regard to lightness, mechanical resistances or resistances to aggressive environments. Apart from certain technical drawbacks and the actual cost of the material, the limited structural exploitation of UHPFRC may be partially explained by engineers' needs and habits concerning design with familiar materials and the lack of practical design approaches for UHPFRC.

Since its appearance on the market in 1995, UHPFRC has been an important subject of in-depth academic research, mostly focused on understanding the material microstructure and the principles of development of its improved material properties. However, for design purposes, its structural behaviour needs to be thoroughly understood to allow rational models assessing element resistances and appropriate analytic approaches to be defined.

The tensile behaviour characterised by a multi-microcracking phase and significant fractural toughness makes the response of UHPFRC elements quite different from that of OC or other fibre-reinforced concretes (FRCs). To enable the material to be fully exploited, tensile behaviour must be taken into account in design, meaning that the resistance models for OC, HSC or FRC elements cannot be directly applied. Knowledge of the behaviour of other concretes, which are typical quasi-brittle materials, influences to some extent considerations concerning the description of UHPFRC element behaviour. However, in thin structural elements, the tensile ductility of UHPFRC results in behaviour more similar to that of plastic-like materials.

Thus, a certain amount of effort is required to establish appropriate mechanical models that will provide a safe application of the knowledge acquired on the material level to structural analysis and design. This task must be supported by both theoretical and experimental studies. Most of the research in this domain deals with the performances of elements in simple bending, whereas the behaviour of UHPFRC elements in redundant systems has been insufficiently investigated. However, statically indeterminate elements, such as thin slabs without ordinary reinforcement, are assumed to be those that allow the material's potential to be best exploited: sufficient tensile ductility enables the redistribution of internal forces, resulting in increased flexural load-bearing capacity. In addition to bending, punching-shear failure must be assured in thin elements, a failure mode that has not been widely investigated in UHPFRC slabs. Finally, if the above mentioned resistances are assured, thin slabs can be used as local bearing elements in a structure, as in the case of ribbed elements, providing the system with high load-bearing capacity with a significant decrease in weight. The principal questions arising are: what is the actual load-bearing capacity of statically determinate and indeterminate UHPFRC elements, and which design approach is appropriate for assessing it? What are the most suitable structural forms for a successful application of UHPFRC in bridge design and are the shapes that are well suited for OC appropriate for the full exploitation of UHPFRC? What is the final benefit of employing UHPFRC rather than other concretes?

Assessing the effective potential of UHPFRC structural elements is of more global interest than just their application in improved bridge design. Interest already exists for other structures like footbridges, roofs, as well as for the upgrading or repair of existing structures. It is also important to allow structural engineers to become more familiar with the potential of UHPFRC, and, by providing practical design approaches, to introduce UHPFRC more into engineering practice instead of its current more academically oriented significance.

1.2 Objectives

With a view to the structural application of UHPFRC, the principal objectives of the work comprise the understanding and modelling of the mechanical behaviour of structural elements, with the possibility of predicting their response at service states and failure. The final aim is to present practical conclusions and proposals for the design of UHPFRC beams and thin slabs without ordinary reinforcement. This involves the following objectives:

- concerning simply supported beams:
 - study bending behaviour and develop a model enabling element response to be reproduced as a function of non-linear material laws known from uniaxial response and fractural properties; verify the model experimentally;
 - identify the influence of material tensile properties on bending behaviour, and the influence of size effect on bending strength and ductility;
- concerning statically indeterminate beams and slabs:
 - develop models enabling the bending behaviour of statically indeterminate elements (beams and slabs) to be reproduced based on known non-linear material laws; observe the influence of material ductility and system redundancy on element load-bearing capacity; verify the model experimentally;
 - investigate the possibility of applying more straightforward analysis than non-linear, e.g. plastic analysis, for failure load prediction;
 - identify the influence of size effect on the response of statically indeterminate elements and its consequences for practical design;
 - investigate experimentally and theoretically the punching-shear resistance of thin slabs.

Finally a UHPFRC deck slab, comprising thin unreinforced slab elements and prestressed ribs, is studied, with the aim of demonstrating the potential of UHPFRC for structural application.

1.3 Thesis organisation

The thesis consists of eight chapters, with the structure schematically represented in Figure 1.1. Generally, each chapter consists of a short literature overview for the domain considered, theoretical study and results with eventual comparison with experimental data, and concluding remarks.

In Chapter 2, possibilities for the improvement of concrete bridge design are discussed, with a review of significant events related to the evolution of concrete bridge design. The orientation of the research towards the application of UHPFRC for improved bridge design is justified.

In Chapter 3, the UHPFRC material properties important for structural application are presented. Although the characterisation of material properties is not the principal aim of this study, it was found important to recall the origin of the advanced properties based on the material microstructure and to propose rational analytical formulations describing material mechanical behaviour.

Chapters 4 to 6 deal with the structural behaviour of UHPFRC without ordinary reinforcement:

In Chapter 4, a model describing the non-linear bending behaviour of UHPFRC elements is developed. The model takes into account both the multi-microcracking characterising UHPFRC material as well as the propagation of a discrete crack with tensile softening. The influence of material tensile behaviour on element bending response is observed and sensitivity to size effect in bending is discussed in comparison to other concretes.

In Chapter 5, the non-linear behaviour of statically indeterminate beams is studied: based on the developed approach, the influence of size effect on the development of plastic-like behaviour is investigated. The possibility of applying the theory of plasticity for the prediction of failure load is discussed.

Chapter 6 is devoted to the analysis of thin UHPFRC slabs subjected to bending and punching-shear failure. The development of a non-linear bending response due to tensile ductility is modelled, and the possibility of exhibiting plastic-like response at failure is studied.

In Chapter 7, the structural application of UHPFRC is criticised, with a particular accent on application in bridge design. Existing UHPFRC systems are briefly reviewed, and a case study of the design of a UHPFRC ribbed deck slab is performed.

Chapter 8 presents conclusions and prospects for further research related to the problems dealt with in this thesis.

Three appendices are added to this document: Appendix M1 and M2, providing additional information on development of analytical expressions used for the bending model, and Appendix T1 presenting the results of the experimental research on beams subjected to bending and thin slabs subjected to bending and punching shear.

1. Introduction
2. Possibilities of structural improvement in concrete bridges <ul style="list-style-type: none">- brief review of evolution of concrete bridges- possible directions for advances in bridge design
3. UHPFRC : material properties <ul style="list-style-type: none">- advanced material properties as a function of enhanced material microstructure- material constitutive laws
4. Analysis and design of UHPFRC elements in bending <ul style="list-style-type: none">- development of a model for bending behaviour of quasi-brittle materials, taking into account multi-microcracking and a fictitious macrocrack- size effect in quasi-brittle materials and UHPFRC
5. Application of the theory of plasticity in design of statically indeterminate UHPFRC beams <ul style="list-style-type: none">- development of a procedure for non-linear analysis of statically indeterminate UHPFRC beams in bending- application of the theory of plasticity in prediction of failure loads
6. Bending and punching behaviour of thin UHPFRC slabs <ul style="list-style-type: none">- development of a procedure for non-linear analysis of axisymmetric slabs- application of the theory of plasticity in prediction of failure load- punching-shear resistance – influence of structural parameters
7. Structural applications of UHPFRC <ul style="list-style-type: none">- existing structural applications, with a focus on bridge design- case study: design of a UHPFRC ribbed bridge deck
8. Conclusions and prospects
Appendix M1 : development of relationships for bending in presence of pseudo-plastic tensile phase Appendix M2 : development of relationships for bending in presence of pseudo-plastic tensile phase and a fictitious crack Appendix T1 : testing of thin elements in bending and punching

Figure 1.1: Thesis structure

2. Possibilities for structural improvements in concrete bridges

2.1 Introduction

Improvement of the performance and efficiency of bridges is an ongoing task in engineering design. In the context of this research, efficient structures are defined as structures that satisfy design requirements with a minimum amount of materials, enabling easy and rational construction. The efficiency of a structure thus depends on a number of heterogeneous parameters. However, the major factor in improving structural performances is the appropriate use of building material in an adapted structural shape. For this purpose, topological optimisation is carried out to identify efficient structural shapes providing maximal structural stiffness for a given volume of material. An alternative approach consists of optimising the dimensions of predefined structural shapes, and using more resistant materials. As a case study for this approach, a continuous prestressed box-girder is considered, since it represents a classic structural concept well suited for reinforced concrete bridges both with respect to exploitation of material strength and construction process. The solution is controlled by the ultimate limit state, serviceability limit state requirements or constructive constraints, according to current structural design recommendations. A parametric analysis is performed by varying girder span-to-depth ratio and concrete grade, i.e. compressive strength, in order to demonstrate the contribution of improved material strengths to system efficiency.

2.2 History of concrete bridges

2.2.1 Lessons from the history of bridges

The study of existing and historical structural examples provides an important source of ideas for possibilities in the realm of bridge improvement. Throughout history, structural design has been based on the principles of strength, durability, functionality, economy, and aesthetics (“firmitas, utilitas, venustas”, M. Vitruvius in “De architectura”, 1st century BC). These basic design principles still apply today, thus allowing analogies between known ancient structures and contemporary ones to be made. It is also interesting to note some successful rediscoveries of ancient structural systems thanks to the availability of new building materials and development in design tools that have made the more accurate prediction of structural behaviour possible. This is the case for cable-stayed bridges, for example, applying the principles used for movable bridges back in 1617 (Fausat Verantius), or under-spanned bridges, developed at the beginning of the 19th century (Pont de la Caille, G. H. Dufour, 1824) and rediscovered over recent decades (Obere Argen Brücke, Schlaich, 1989). As a general conclusion, it can be said that the most significant progress in structure development concerns inventions in the materials field that allow the optimisation of existing structural concepts by reducing material consumption or the development of conceptually innovative structural systems. Reduced material consumption while maintaining sufficient strength and appropriate stiffness has been a constant driving force throughout this evolution. Being a multidisciplinary task, bridge design is also influenced by progress made in other domains, such as structural analysis, numerical methods and technological developments, notably in construction techniques. However, a substantial time lag is usually observed between the introduction of a new component and the moment when its relevant properties are fully exploited in design.

2.2.2 Material and structural development in concrete bridges

When it comes to concrete bridges, the previous conclusions also apply, although the history of concrete bridges is relatively recent: some basic principles of concrete-like materials have been known since the earliest building times, but the beginning of the modern era of concrete only dates back to the 19th century (Chapter 3, Figure 3.2). However, since then, there has been significant interest in its application, and, thanks to continuous improvements on the material level as well as in the knowledge of its structural behaviour, concrete has become the most widely used building material [Penttala 1997]. Moreover, concrete has low fabrication costs and energy consumption and is made of widely available materials that compose the Earth's crust [Scrivener 2005]. It thus meets the additional contemporary requirements related to environmental impact.

The major phases in the development of reinforced concrete bridges were the invention of voided section, specifically conceived for the material mechanical properties, and the invention of prestressing. In 1875 the first reinforced concrete bridge was designed by J. Monier in Chazelet, France, almost two decades after the first patent for reinforced elements was granted. The first structural concepts were strongly influenced by traditional massive masonry arches (Figure 2.1a)), which did not allow the advantages of reinforced concrete to be well appreciated. It was not until the beginning of the 20th century that R. Maillart designed the first structural shapes specifically conceived for reinforced concrete structures (Figure 2.1b)). The mechanical properties of concrete did not evolve significantly during that period. An important step forward in concrete structures was made in the 1920s with the invention of prestressing by Freyssinet in France and Dischinger in Germany. This concept enabled better material exploitation, and made it possible to significantly increase the span of concrete bridges. The first bridge using this technology was built in 1928 in Alsleben, Germany, with a span of 68 m. The widespread application of prestressing did not begin until after the Second World War however.

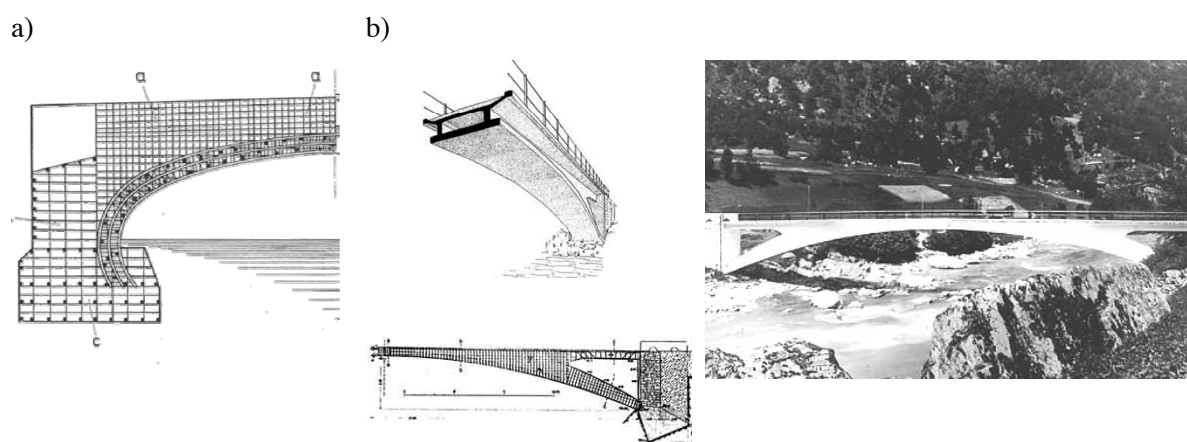


Figure 2.1: Steps in evolution of concrete bridges: a) the first patent for RC bridge, J. Monier, 1873, France; b) Tavanasa bridge, R. Maillart, 1905, Switzerland

A new concrete era started in the 1970s with the rapid development of material properties, introduction of fibre reinforcement, superplasticisers, and various pozzolanic additives, but no particular novelties in bridge design followed these innovations. Contemporary concrete bridges nonetheless still successfully combine the two above-mentioned principles of voided cross section and prestressing. However, the renewed idea of underspanned systems applied as hybrid (Figure 2.4 a)) or completely concrete structures (Figure 2.4 b)) can be considered as an interesting new point for medium-span bridges.

The most recent development in cement-based materials, dating back to 1995 (Figure 3.2), was ultra high-performance fibre-reinforced concrete, UHPFRC [Richard, Cheyrezy 1995]. This material possesses characteristics that are significantly superior compared with those of other concretes (Chapter 3). Thanks to its strength and ductility, structural elements can be made without the use of

passive reinforcement, thus offering a new challenge in concrete design and the opportunity to develop innovative structural concepts and shapes. Up until now, however, in design of road bridges UHPFRC has been mainly used to reduce sectional dimensions in traditionally designed structural elements [Park et al. 2003]. The first application of UHPFRC to road bridges in 2001, in France [Simon et al. 2002], exemplifies this trend: it consists of prestressed girders typically used for ordinary concrete, in which the use of UHPFRC has resulted in significantly reduced material consumption and the use of ordinary reinforcement only in joint areas (Chapter 7).

The properties of UHPFRC can be exploited in a more interesting way for renewing the concept of ribbed structures, introduced by Nervi in 1935 [Nervi 1997]. This concept can successfully benefit from material strengths and the possibility of avoiding passive reinforcement to significantly decrease element sizes while maintaining high strengths and structural stiffness. An application of ribbed slab for bridge deck is under investigation at the Laboratoire Central des Ponts et Chaussées (LCPC), within the scope of MIKTI French national project [Toutlemonde et al. 2005], (Chapter 7).

Another interesting possible application for UHPFRC is in composite structures, where a layer of UHPFRC is applied over an ordinary concrete girder [Habel 2004], resulting in improved service condition stiffness and ultimate load-bearing capacities. A further application of UHPFRC in composite bridge girders is developed as a part of the European project named New Road Construction Concept (NR2C): UHPFRC is applied as the upper compressive layer of a lightweight hybrid girder, comprising fibre-reinforced polymer as a tensile layer and a lightweight concrete core [Keller et al. 2007].

2.3 Possible directions for improvement in concrete bridge design

Based on the knowledge of historical and recent developments in material and bridge engineering, it can be concluded that optimisation in bridge design should be achieved either by conceiving more efficient structural shapes or exploiting higher performance materials to optimise already existing shapes. These two possibilities are numerically analysed in this section.

2.3.1 Efficient structural shapes

In a first approximation, efficient structural shapes can be defined as shapes requiring the use of the least amount of material for a given stiffness or strength or, conversely, providing the highest stiffness or strength for a given amount of material. In this case, stiffness is chosen as the controlling parameter for structural performance. If structural stiffness is expressed as a function of structural shape, stiffness can be optimised with the structural shape as a design variable. This approach is made possible by means of topological optimisation [Bendsoe 1995], [Sigmund 2001].

Topological optimisation and the application to the shape of bridge superstructure

The main advantage of topological optimisation in relation to other types of structural optimisation is that no structural shape is initially prescribed, which *a priori* allows more freedom in the search for the best suited shape. The principles of the theory are applied on a design continuum with boundary conditions corresponding to a bridge superstructure, enabling a number of efficient structural shapes to be identified [Spasojevic 2006], Figure 2.2.

The aim of the analysis is to find the material distribution providing the highest structural stiffness for a given amount of material, V , with given design domain and boundary conditions. The design domain is meshed in finite elements, and the portions that need to be kept intact for functional reasons are predefined (e.g. driving surface).

Based on the assumptions of linear elastic behaviour, the structural response must satisfy the equilibrium and compatibility conditions, $\mathbf{K} U = F$, where \mathbf{K} is the global stiffness matrix, and U and F the displacement and load vectors respectively. The global structural stiffness is considered in terms of strain energy and, consequently, the problem of stiffness maximisation is defined as:

$$\min C = \sum_{i=1}^N u_i^T k_i u_i \quad (2.1)$$

where C is the structural compliance, k_i and u_i are local stiffness matrices and displacement vectors and N is the number of elements. The stiffness of an element is represented as $k_i = \eta_i \cdot k_0$, where k_0 is the stiffness of the initial elastic solid and η_i is a relative density parameter (pseudodensity) ranging from zero to unit and assigned to each element. Finally, the objective function of the problem, C , is expressed as a function of design variables η_i as $C = f(\eta_i, k_0, u_i)$.

A set of design variables satisfying constraints, $0 \leq V \leq V_0 - V^*$, where V_0 is the initial volume and V^* is the volume to be removed, forms a feasible region in which the minimum of the objective function is found.

The formulated problem is treated by a finite element method using software package ANSYS. As a comparative solution, a procedure was developed for MatLab, based on the similar solutions proposed in [Sigmund 2001]. Figure 2.2 a) shows examples of design domains on which the topological optimisation was performed and the obtained results of density distribution plots, representing the optimised structural shapes (Figure 2.2 b)). Elements with a pseudodensity, η_i , close to 1 correspond to highly dense matter (grey colours), while those with η_i close to 0 correspond to the matter that can be removed, and is thus not visible in the figures. The examples of density distribution plots in Figure 2.2 b) comprise the same amount of material ($V = 0.27V_0$) for various boundary conditions. The results demonstrate that the same quantity of material is disposed in various efficient shapes, depending on the boundary conditions.

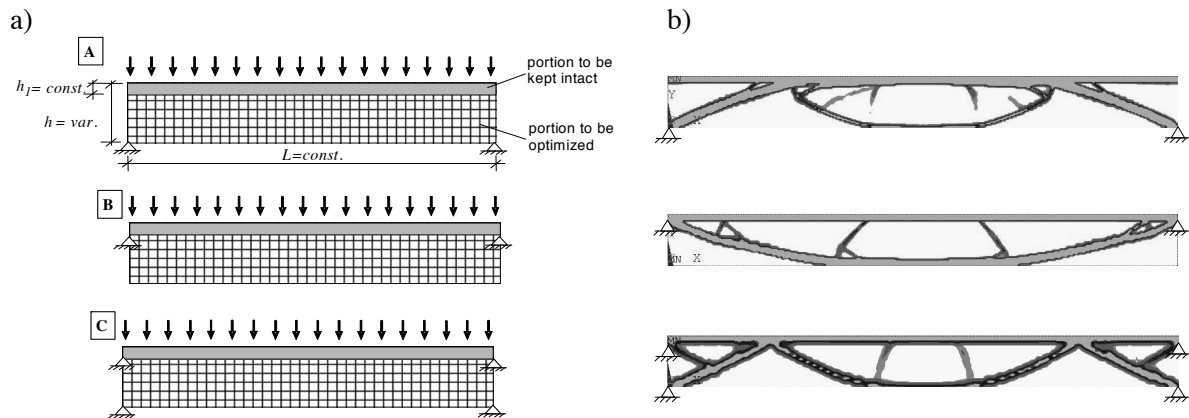


Figure 2.2: Topological optimisation: a) initial body - 2D continuum with portions to be kept intact for three sets of boundary conditions; b) optimised shapes for various boundary conditions, with $V = 0.27V_0$ and $L/h = 10$

The important conclusion that can be drawn from the results of the analysis (Figure 2.3) is that a well chosen topology provides a significant decrease in material volume, while maintaining a significant portion of the initial stiffness. Figure 2.3 a) shows the relationship between decrease in volume and decrease in stiffness of system A in Figure 2.2 a), with a slenderness $L/h = 10$. Change in stiffness is expressed here as a ratio between the mid-span vertical displacement of the initial system, w_0 , and displacement of the optimised system, w . In the initial part of the curve, a decrease in material volume causes almost no change in stiffness because material making a very small contribution to the stiffness is removed. After a certain level of volume reduction, the volume decreases due to diminution of the thickness of the members, while the shape remains the same. The decrease in stiffness then becomes much faster. It should be pointed out that in this example the initial volume

contains a portion which is not subjected to optimisation (representing driving surface, thus keeping a constant density over its thickness). The theoretical point for $w_0/w \rightarrow 0$ in Figure 2.3 a) corresponds to the case in which all matter except the deck would be removed ($V = 0.10 V_0$). Similar curves were obtained for other boundary conditions and for slenderness values L/h varying between 10 and 30.

The curves plotted in Figure 2.3 b) show the difference in global structural stiffness of optimised shapes (w/L) expressed as a function of slenderness and boundary conditions. A significant difference in stiffness is observed between the various shapes: the under-spanded structure obtained for boundary conditions B is much more flexible than the combination of the arch and under-spanded central span that result from boundary conditions A and C.

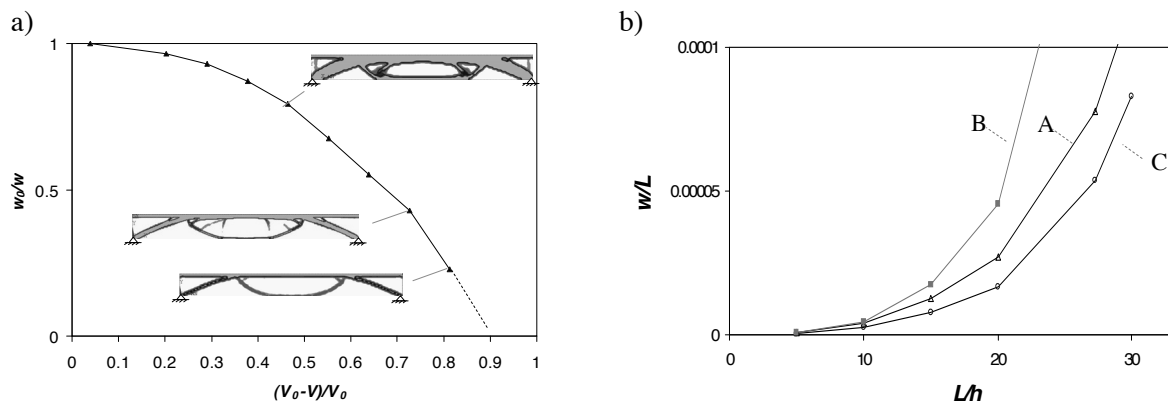


Figure 2.3: a) change in structural stiffness (w_0/w) as function of volume reduction for boundary conditions A in Figure 2.2 and $L/h = 10$ with corresponding optimised shapes; b) global structural stiffness as function of slenderness for boundary conditions A, B and C; $V = 0.43V_0$

Analogies can be found between the obtained topologically optimal shapes and actual concrete structures. This is clearly exemplified in Figure 2.4, which shows a striking resemblance between the optimisation results and a recently built structures.

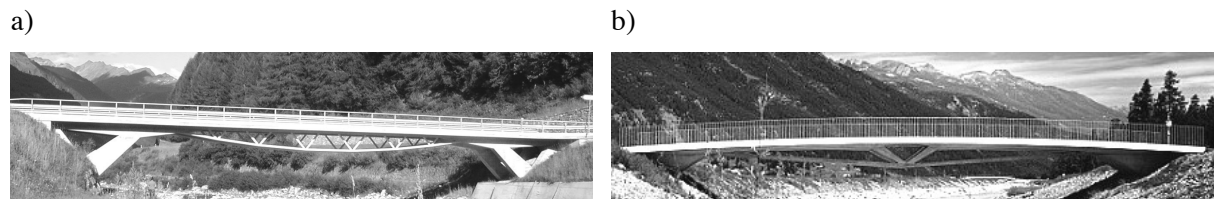


Figure 2.4: Recognition of numerically simulated optimal material distributions in real structures: a) Villa Bedretto Bridge, Switzerland [Muttoni 1999]; b) Flaz River Bridge, Switzerland [Pedrazzini, Pedrazzini 2006]

2.3.2 Classic concrete solutions using more resistant concretes

Another, more classic, approach in designing structures consists of sizing elements with predefined shapes and material strengths. The advantage of this approach is that additional design principles, such as constructability, aesthetic appeal etc., which cannot be included in topological optimisation for instance, are implicitly respected by the predefined shape.

A numerical model was developed to investigate the potential of predefined shapes of concrete bridges. In addition to static and geometric constraints (as in the previous case) the model includes design constraints related to ultimate limit states, serviceability limit states and constructive requirements for concrete structures. A continuous girder with a box-cross section of constant height and no transversal prestressing in the deck slab is studied as a well known case of an efficient

prestressed concrete bridge. The results are illustrated in Figure 2.5: figure a) presents the equivalent height of concrete cross section, h_{equiv} , which is the ratio of cross section area to deck width, needed for various slendernesses, L/h , and material strengths. The results are plotted against values corresponding to existing bridges in Switzerland, obtained from [Menn 1982]. Good correlation between simulated values and statistical data is observed. Figure 2.5 b) shows the influence of increased concrete strength, f_{ck} , on this system. As expected, this structural system is fairly insensitive to the compressive strength of concrete, in particular for smaller spans and structures with limited slenderness; higher concrete strengths are, however, beneficial in slender girders. This behaviour mainly results from the fact that a large part of the concrete cross section is constituted by the bridge deck and webs, whose dimensions are to some extent influenced by constructive constraints. The web dimensions are mostly governed by constraints related to cables and concrete placement, which suggests that the use of external prestressing could be a possible solution for better exploitation of this system [Naaman, Breen 1990], [Benouaich et al. 2000].

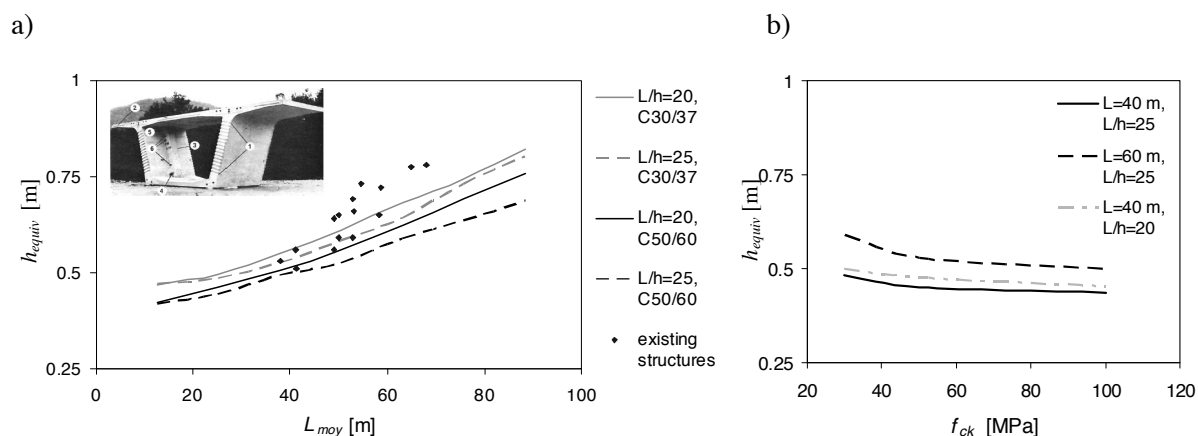


Figure 2.5: Parametric simulation of structural response: a) influence of span on amount of concrete, compared to existing structures; b) influence of concrete strength on amount of concrete

The application of high strength and high performance concretes can lead to some higher savings in concrete (up to approx. 30 %) and reinforcement, obtained by optimising the deck slab and varying girder height, as shown in [Toutlemonde et al. 2002], [Toutlemonde et al. 2003]. These solutions benefit also from other material properties of HPCs, such as easier casting, higher strengths at early age, improved durability etc.

However, the potential of UHPFRC, based on the material's mechanical performances and possibility to avoid the use of passive reinforcement, enables much more significant material savings and increase in slenderness of road bridge girders [Sorelli et al. 2007]. In the case of a girder with box-cross section, the application of UHPFRC for road bridge PS34 crossing highway A51, France, lead to more than two times decreased concrete quantity and a very fast construction [Bouteille, Resplendino 2005], Chapter 7.

2.4 Conclusions

A review of existing structures shows that bridge design relies significantly on traditional concepts, and innovations typically take a long time to be incorporated in design practice. A strong tendency towards structures with a small weight-to-stiffness-and-strength ratio can be identified as a driving force in innovations.

The application of topological optimisation enabled shapes with maximum structural stiffness for a given amount of material to be identified. It was shown that significant material savings could be obtained using an appropriate topology while a high portion of initial stiffness is maintained. An

example of a system combining an arch with an underspanned element was recognised as being very efficient in terms of weight-to-stiffness ratio. Concrete bridges have recently been constructed based on this concept.

The influence of compressive strength of ordinary concrete on required material amount is studied for the case of a typical continuous box-girder bridge with internal prestressing. Based on the results, it can be concluded that the application of improved concrete strength led to limited savings in material, which may be explained by constructive constraints.

The application of UHPFRC, however, can be considered as a promising way to provide innovative solutions for bridge design. UHPFRC is stronger than ordinary concrete, can replace passive reinforcement and is a self-placing and self-compacting material. It reduces the constructive constraints lined with the placement of reinforcement and allows a more effective distribution of the matter. Consequently, structural stiffness and structural strength can be assured, while structure weight is significantly reduced. The material's potential can be well exploited in thin-walled elements, consisting of slab without ordinary reinforcement and prestressed ribs.

3. UHPFRC: material properties

Ultra-high performance fibre-reinforced concrete (UHPFRC) is studied in this chapter as a material for structural application. Unlike conventional construction materials, high-performance concretes are the result of a so-called “integrated structural and material design” [Li, Fischer 2002]. According to this concept, the material composition is tailored to ensure specific structural performances. It is thus important to study UHPFRC at different levels in order to understand the origin of its particular structural behaviour.

The objectives of this chapter are to present the material’s properties of interest for advanced structural applications, and to present the models for mechanical behaviour needed for further structural analysis and design.

Structure of chapter

In Section 3.1 the material is defined from the structural engineering point of view, and the development of advanced cementitious materials is briefly reviewed.

Section 3.2 provides a basic insight into the microstructure of UHPFRC, considered as a composite material. This section explains how the concept of this material is developed and which principal features are enhanced in order to achieve the desired material properties. The main advances of UHPFRC composition with respect to other concrete materials are briefly discussed. The composition of the UHPFRC used in the present study is also given.

The material properties, relevant for the structural application, are divided into mechanical material properties (Section 3.3), and other material properties (Section 3.4).

Section 3.3 focuses on the material’s behaviour in uniaxial compression and in uniaxial tension. The behaviour is discussed by considering the material on a macroscopic scale, principally as a continuum. The mathematical formulation of mechanical behaviour provided in this section is of interest for this research, since it is the basic input for further analysis and design. Various constitutive material curves are studied and proposals are made for the description of both compressive and tensile behaviour.

Section 3.4 provides basic information on the time-dependent behaviour of UHPFRC (shrinkage, creep), durability, self-healing as well as resistance to impact load, energy dissipation, and fire resistance. This section is based on literature review.

In Section 3.5, conclusions with respect to the two principal contributions of the chapter are drawn:

- concerning material properties, detailing the advantages of the material that are promising for structural application;
- concerning proposed material constitutive laws for the requirements of analysis and design.

3.1 UHPFRC: definition, material development

Definitions

Ultra-high performance fibre-reinforced concrete (UHPFRC) is an advanced reinforced cementitious material. “Ultra-high performance” refers principally to improved mechanical strengths, fractural toughness, and durability. Typical behaviour of UHPFRC in a uniaxial state of stress in comparison to other concretes is shown schematically in Figure 3.1.

According to the French Interim Recommendations on UHPFRC [SETRA, AFGC 2002], UHPFRC is a material with a cement matrix of a characteristic compressive strength in excess of *150 MPa*, and with sufficient fibre content to achieve ductile behaviour under tension. These mechanical properties

enable UHPFRC to be clearly distinguished from other concretes (Figure 3.1). The Japanese recommendations [JSCE 2006] impose the same limits for strength and ductility, but also specify material composition by limiting maximal aggregate size, water-cement ratio, and fibre quantity and strength.

According to the classification of fibre-reinforced concretes (FRC) proposed in [Naaman, Reinhardt 2006] and [Stang, Li 2004], UHPFRC is distinguished between other FRCs as a material exhibiting strain hardening in tension (Figure 3.1), whereas other FRCs may exhibit a hardening behaviour in bending, but are characterised by strain softening in tension.

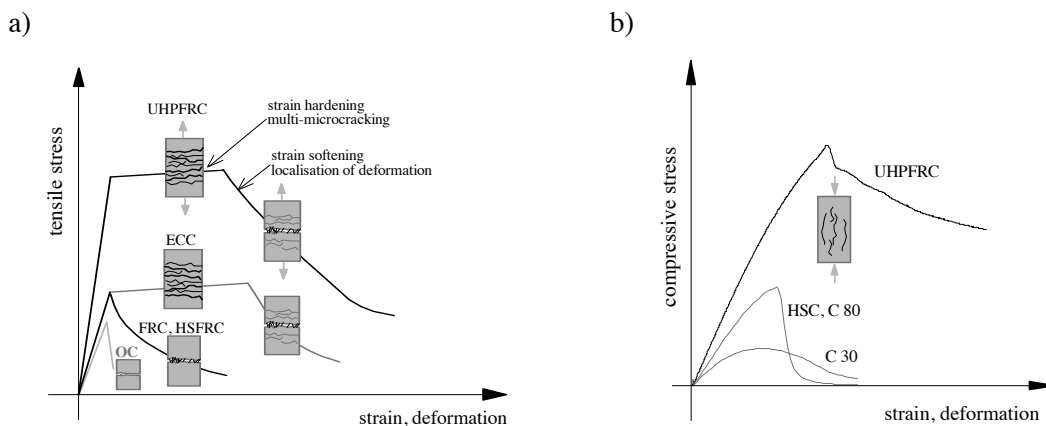


Figure 3.1: Typical response of UHPFRC in uniaxial stress state in comparison to ordinary (OC) and high-strength concrete (HSC), fibre-reinforced normal or high-strength concrete (FRC, HSFRC), and engineered cementitious composites (ECC): a) uniaxial tension, adapted from [Li, Fischer 2002]; b) uniaxial compression

Historical development

On the timescale of concrete development, UHPFRC can be considered as the latest innovation (Figure 3.2) originally developed by Bouygues SA, France, in 1995 [Richard, Cheyrezy 1995]. The origin of advanced concretes dates back to the 1960s and 1970s with the investigations on the strength improvement of the cement paste by heat-curing under pressure¹ [Roy et al. 1972], [Roy, Gouda 1973], or applying low water-cement ratios [Yudenfreund et al. 1972a], [Yudenfreund et al. 1972].

Development in material science provided a better insight into the material's microstructure, and made it possible to influence the target material properties more significantly. From the 1960s onwards, more elaborated material mixtures were obtained with the introduction of fillers and superplasticizers, as described in [Mielenz 1984], [ACI 1989]. The continually increased compactness of the matrices led to increased strength but also increased brittleness. The matrices were made more ductile by adding discontinuous fibres, an idea in evidence from the beginning of the construction era and applied to concrete since the 1960s [Romualdi, Mandel 1964].

In recent years the collaboration between structural and material engineering led to an integrated design, based on the tailoring of the material's composition to meet specific requirements for structural applications [Van Mier 1997], [Li, Fischer 2002]. UHPFRC can be considered as the advanced result of this collaboration. The material was optimised with respect to mechanical strengths, fractural toughness, durability, placing method and time, keeping mixing and casting procedures as close as possible to existing practice [Richard, Cheyrezy 1995], [Acker, Behloul 2004].

¹ In [Richard, Cheyrezy 1995] the work of Freyssinet in the 1930s on the application of pressure to concrete during setting is mentioned.

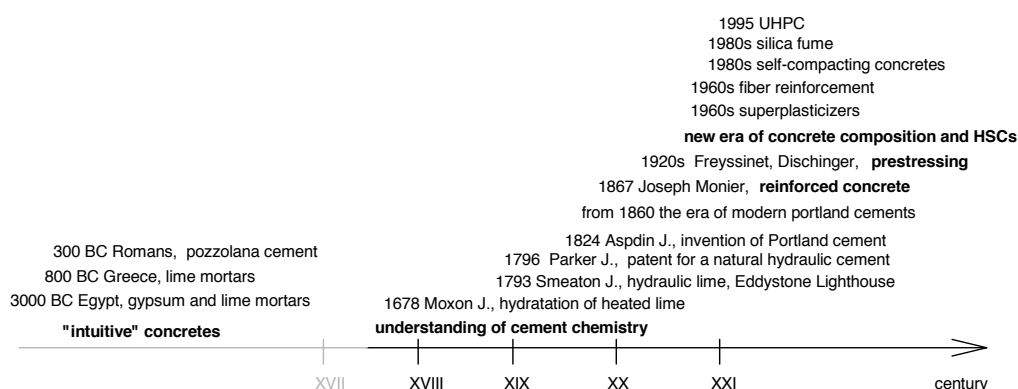


Figure 3.2: Brief history of cement and concrete, based on data from [Chamberlain et al. 1995], [Mielenz 1984], [Scrivener 2005]

3.2 Microstructure of the material

The structural performances of UHPFRC result from properties of its principal constituents – the cementitious matrix and the fibres, and their interaction. The conceptual bases of the advanced UHPC matrix are discussed in Section 3.2.1. The section aims to examine the relationship between the mechanical performance and microstructure of the material, but no in-depth explanations on concrete chemistry and formation of the microstructure are provided. Types of fibres used in UHPFRC and the role of matrix-fibres interaction are discussed in Section 3.2.2.

3.2.1 Ultra-high performance concrete matrix

In conventional structural design concrete is considered as a continuum. However, concrete is a material of a heterogeneous structure, with the heterogeneity and its effects on mechanical behaviour observable on different length scales [Van Mier 1997], [Ulm et al. 2004]. UHPC is typically characterised as the material with the microstructure that is significantly enhanced regarding homogeneity in comparison to ordinary and high-strength concretes. This is the principal argument in explaining the improved strengths and durability of UHPFRC.

Mechanical effects of heterogeneity

The distribution of different phases in the material and differences in their mechanical properties are the main reasons for the appearance of the stress concentration that imposes the material's strength limits. The phenomenon of stress concentration in materials was recognised by Griffith in the 1920s [Griffith 1921], and is nowadays widely accepted in fracture mechanics theories. Based on this, the relationship between improved mechanical properties and enhanced material homogeneity can be drawn.

Heterogeneity in concrete microstructure and possibilities for decreasing it

In mechanical terms, concrete can be defined as a complex, non-homogeneous system of solid phase, pores and water [Scrivener 1989]. Heterogeneity problems in concrete are caused primarily by the presence of pores and the differences in mechanical properties (stiffness and strength) of solid phases. Observing concrete on different length scales, different components can be distinguished (Table 3.1). Consequently, the conclusions regarding possibilities for the improvement of homogeneity can be drawn on different levels.

Table 3.1: Multiscale heterogeneous structure of concrete, adapted from [Ulm et al. 2004]

Length scale and representative system	composed of:
$> 10^{-3}$ m, Concrete	Cement paste, aggregates, interfacial transition zone
$< 10^{-4}$ m, Cement paste	C-S-H matrix, CH crystals, macro and capillary porosity
$< 10^{-6}$ m, C-S-H matrix	C-S-H matrix (C-S-H phases, capillary and gel porosity)
$10^{-9} - 10^{-10}$ m, nanoscale	C-S-H solid (cement hydration product)

On the length scale higher than the millimetre scale, chemically inert aggregates, hardened cement paste, and interfacial transition zone are distinguished in hardened concrete (Figure 3.3). Aggregates tend to form rigid inclusions in the paste. The different mechanical properties of aggregates, paste and the interfacial zone lead to the generation of cracks in the interfacial zone once the load is applied. The size of these cracks is directly proportional to aggregate diameter [Richard, Cheyrezy 1995], meaning that a significant reduction in microcrack size is achieved with reduction of aggregate size. The influence of the quality of aggregates on mechanical properties is also reported [Donza et al. 2002].

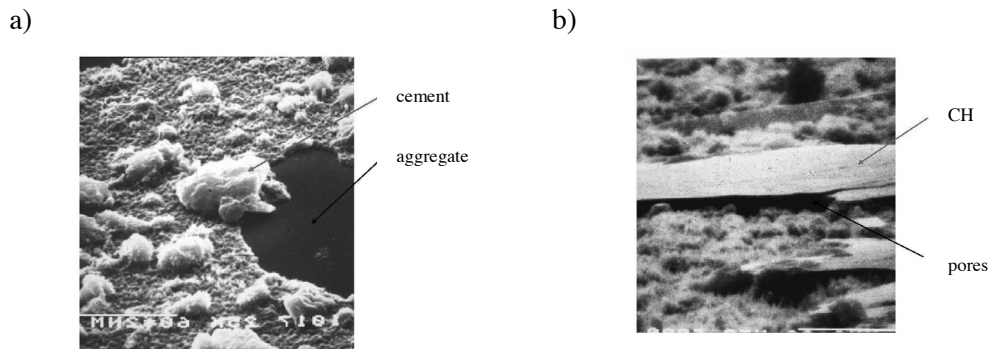


Figure 3.3: Hardened ordinary concrete on microstructural level, [Mehta, Monteiro 2005]: a) material heterogeneity; b) interfacial transition zone

On the length scale below 10^{-4} m, in an ordinary it is observed that the interfacial transition zone is the zone with significant heterogeneity, containing the highest percentage of the porosity and high content of large calcium hydroxide (CH) crystals, produced during hydration (Figure 3.3). The porosity at this level significantly influences the mechanical strengths (Figure 3.4 a)) since the stress concentrates around the pores, initialising microcracks.

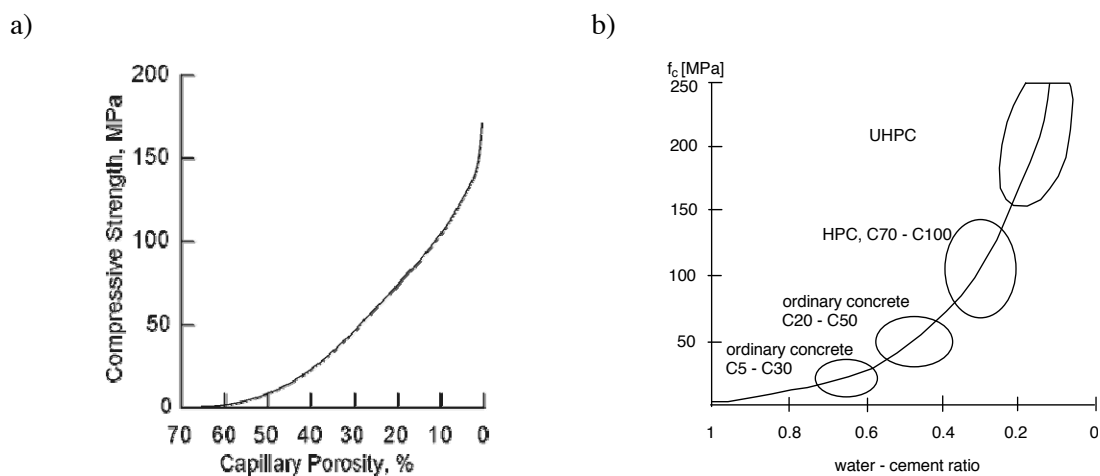


Figure 3.4: a) Effect of porosity on compressive strengths, according to Power's model [Mehta, Monteiro 2005]; b) Effect of water-cement ratio on compressive strengths, adapted from [König et al. 2001]

Apart from its structure, the volume of the formed interfacial zone has an important influence on material strengths. This volume can be related to aggregate size, density of granular compactness, and water-cement ratio. This causes the interaction with the microstructure at this level with the components observed at the previous one. To enhance density, tailoring of the granular mixture for optimal aggregate packing is a well recognised principle, known since roman road-making [Scrivener 2005], through to modern packing models [de Larrard, Sedran 1994], [Okamura, Ozawa 1995]. Granular mix is optimised with respect to relative density and quantity of water required. The quantity of water in the cement paste, as well as for hydration, is important for control of the spacing of cement grains. More spacing means more space for the interfacial zone to form, leading to increased porosity. The influence of the water-cement ratio on compressive strength is shown in Figure 3.4.

Principles of UHPC composition

Based on the previous observations, the principles applied in tailoring the UHPC matrix can be detailed:

- coarse aggregates are eliminated, decreasing the mechanical effects of heterogeneity (maximal aggregate size less than 7 mm, Table 3.2; according to the Japanese recommendations maximal aggregate size is even less than 2.5 mm);
- granular mix is optimised; for the composition of a fine-grained mixture, silica fume and/or silica flour are added. This component in particular improves the properties of the UHPC, acting both as filler and pozzolanic material [Grabowski, Gillott 1989]. The Figure 3.5 shows the physical effect of silica fume, as “micro-filler” of space, and also providing the lubrication effect. As a pozzolanic material, it reacts chemically with CH, forming compounds with cementitious properties (calcium silicate hydrate, C-S-H). Therefore, the addition of silica fume improves the paste on two levels: it reduces porosity mainly by reducing the space for growth of CH, and improves the mechanical properties of the cement paste by reacting with CH;

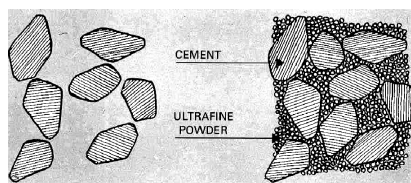


Figure 3.5: Silica fume acting as “micro-filler” of the space between cement grains. The specific surface area of silica fume is approximately $20\,000\text{ m}^2/\text{kg}$, 50 times greater than that of cement

- the paste volume is higher than the voids index; this means that the paste is less restrained by the granular skeleton and consequently fewer pores are formed during plastic shrinkage than in the case of ordinary concrete;
- a low water-cement ratio is applied; this maintains the small spacing of the cement grains, decreasing space for the formation of the interfacial zone;
- admixtures are included to achieve sufficient workability of the fresh paste, which otherwise decreases with a decrease in the water-cement ratio [Mielenz 1984];
- optionally, the microstructure can be further enhanced by a production process such as heat-curing or the application of pressure [Reda et al. 1999];

The resulting concrete matrix is very dense, with almost no capillary porosity, in comparison with 20 - 25 % of capillary pores present in ordinary concretes or 12 - 20 % in high-strength concretes [Vernet 2003]. The obtained interfacial transition zone is very thin in relation to that of ordinary or HSC, and no large CH crystals are present [Reda et al. 1999], indicating a well-developed bond between the improved cement paste and aggregates. The Young’s modulus of cement pastes is higher than 50 GPa [Richard, Cheyrezy 1995]. The less difference there is between the stiffness of

the cement paste and the stiffness of the aggregate, the lower the mechanical heterogeneity of the mix. Moreover, the viscosity of the fresh mix enables self-compacting, and thus no additional compacting treatment is necessary after casting.

Composition of UHPC

The typical compositions of ordinary concrete, HSC, and UHPC are listed in Table 3.2. UHPC is distinguished as a fine-grained concrete, with the special selection of aggregates, high binder content and low water-cement ratio.

Table 3.2: Examples of composition of ordinary, high-performance and ultra-high performance concrete and average material properties

		Ordinary concrete	HSC ¹	UHPC ²
matrix composition	Component:	[kg/m ³]	[kg/m ³]	[kg/m ³]
	Portland cement	< 400	410	700 - 1000
	Coarse aggregate	≈ 1000	920	0 - 200
	Fine aggregate, sand	≈ 700	620	1000 - 2000
	Silica fume	-	40	200 - 300
	Superplasticizers	-	5	10 - 40
	Water	> 200	100 - 150	110 - 200
Water-cement ratio		> 0.35	0.28 - 0.38	< 0.24
Water/binder ratio			< 0.38	< 0.22
Reinforcement / Fibres [kg/m ³]		designed	designed	> 150
properties	Density [kg/m ³]	2000 - 2800	2000 - 2800	> 2500
	Compressive strength [MPa]	< 60	60 - 100	> 150
	Tensile strength [MPa]	< 3	< 5	> 8
	Initial modulus of elasticity [GPa]	≈ 30	< 45	50 - 70
	Fracture energy [J/m ²]	30 - 200 ³	< 150 ⁴	< 90 without fibres ⁴ > 10 000 with fibres

¹ [Larrard, Sedran 2002], ² [Graybeal, Hartmann 2003], [Reda et al. 1999], [Graybeal 2006], ³ [CEB 1993], ⁴ [Wittmann 2002]

3.2.2 Fibres in UHPFRC

Fibres are incorporated in UHPC in order to enhance the fracture properties of the composite material. Since the pioneering work of Romualdi in the 1960s based on the idea on controlling cracking in concrete by fibre bridging [Romualdi, Mandel 1964], both fibre technology and knowledge of the interaction between fibres and matrix have constantly developed [Naaman 2007]. The present section deals only with the fibres as a component of the UHPFRC material. Mechanisms of fibre action in UHPFRC are discussed in more details in Section 3.3.2.

The additional role of fibres in UHPFRC, in comparison to the role of fibres in ordinary and in high-strength fibre-reinforced concrete, is to provide sufficient ductility of the material in tension without a decrease in stress. This is achieved by choosing the appropriate type and quantity of fibres.

Types of fibres

Fibres are characterised by the material and its mechanical properties, and by their geometry. In structural engineering, steel and synthetic fibres are mainly used, although a great variety of fibres made of other materials exists. This is related to the strength and stiffness that is required of the desired fibre contribution. In order to enable the transfer of force with a small crack opening and to

sustain tensile force without breaking, a high modulus of elasticity and high strengths are required. The modulus of elasticity of steel fibres is 200 GPa and strengths are in the range of $1\,000 - 3\,000 \text{ MPa}$, with a deformation at failure of $3 - 4 \%$ [Denarié 2005]. In Japanese recommendations for UHPFRC [JSCE 2006], minimal fibre strength is limited to $2\,000 \text{ MPa}$.

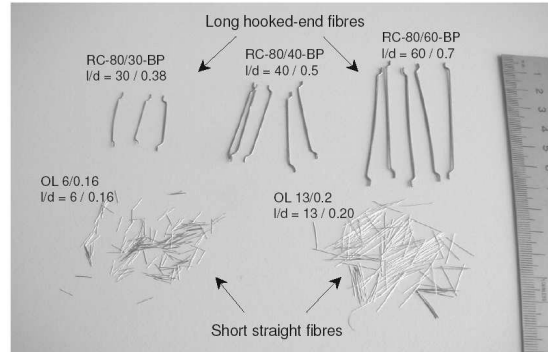


Figure 3.6: Example of types of steel fibres used in FRC and UHPFRC, from [Markovic 2006]

Fibres used in UHPFRC are typically short, smooth, and straight, while hooked fibres are more often used in high-strength or ordinary concretes (Figure 3.6). Fibre geometry is expressed in terms of aspect ratio, l_f/d_f , where l_f is the nominal fibre length and d_f the diameter of the fibre. Required fibre geometry can be estimated based on the relationship between pullout force and fibre-breaking force [Behloul 1996]:

$$l_{bf} \cdot \pi \cdot d_f \cdot \tau_f \leq \frac{d_f^2 \cdot \pi}{4} \cdot f_{s,f} \quad (3.1)$$

where the left side of the equation represents the force that can be transferred to the matrix over the maximal development length, l_{bf} , with an average shear stress, τ_f , acting on the fibre-matrix interface; the right side represents the maximal force that can be transferred by the axial deformation of the fibre, with $f_{s,f}$ the strength of the fibre. For a maximal development length assumed as $l_{bf} = l_f/2$, fibre geometry must satisfy the relationship

$$\frac{l_f}{d_f} \leq \frac{f_{s,f}}{2 \cdot \tau_f} \quad (3.2)$$

For approximated values of the interfacial shear $\tau_f = 5 \text{ MPa}$ [Tjiptobroto, Hansen 1993] and fibre strength $f_{s,f} = 1\,500 \text{ MPa}$, the value of the aspect ratio needs to be smaller than 150 . Some more detailed models on anchorage lengths and optimal fibre radius can be found in [Ulm 2002].

Fibre quantity

Fibre content is usually expressed in terms of fibre volume fraction, V_f , representing the ratio between the fibre volume and material volume (matrix and fibres).

Fibres quantity varies in different types of UHPFRC, § 3.2.3, usually in the range of $2 - 6 \%$ V_f . In some UHPFRCs it may be as high as 10% V_f [Rossi 2000], [Rossi et al. 2005].

An intuitive definition of minimal fibre quantity, which can be drawn from the analogy with ordinary reinforced concrete, is: fibre quantity must be sufficient to transfer tensile force greater than or equal to the force carried by the matrix prior to cracking. A detailed model for minimal fibre quantity prediction based on the fracture properties of materials is presented in § 3.3.2.4.

According to Japanese recommendations [JSCE 2006] minimal fibre quantity is limited to 2% V_f . In the French recommendations for UHPFRC Article 6.0,1 [SETRA, AFGC 2002], the minimal V_f is not defined, but verified indirectly by the tensile response of the material after the cracking of the matrix. The proposed relationship actually implies that the average stress, σ , that can be transferred

by the bridged crack up to an opening of 0.3 mm is equal to or greater than the matrix tensile strength, $f_{ct,m}$:

$$\frac{1}{3 \cdot 10^{-4}} \cdot \int_0^{3 \cdot 10^{-4}} \sigma(w) dw \geq f_{ct,m} \quad (3.3)$$

where $\sigma(w)$ is the measured stress as a function of the crack opening, starting at the first cracking of the matrix.

No limits for the maximal fibre quantity are defined in the current recommendations for FRC. However, fibre quantity must remain low to allow good workability of the fresh paste and prevent an anisotropic fibre distribution. A simplified relationship providing the maximal fibre quantity based on the volume associated to every fibre, $V_2 = \pi l_f^2 d_f / 4$, can be found in [Behloul 1996]. When the ratio of $V_f V_2 / v_f$, where v_f is the volume of a single fibre, is lower than one, the fibres can be oriented in all directions. A higher ratio indicates a tendency to local anisotropy. This model is actually inspired by a study on the orientation of stick-like viruses, by L. Onsager [Onsager 1949].

3.2.3 Different types of UHPFRC

Different types of UHPFRCs are currently available on the market. The principal differences lie in the composition of the mixture: water-cement ratio, water-to-fine¹ ratio, maximal aggregate size. The fiber volume fraction is also a variable.

Concerning the basic development principles, there are two main kinds of UHPFRC. Following the idea of improving the homogeneity of the row mix, a class of concretes known as densified small particle concrete (DSP) has been developed. The matrix of this concrete has a very compact granular packing, with high content of superplasticizers and silica fume, and hard aggregates [Richard, Cheyrezy 1995], [Rossi 2000]. Another approach was oriented towards improving the strength of the paste, based on the concept of the so called macro-defect-free concretes (MDF). This material comprises a paste that is modified by the addition of water-soluble polymers [Alford et al. 1982], and, from the manufacturing point of view, is highly demanding.

UHPFRC that are currently used in construction have been developed according to the concept of DSP concretes. In 1995 a UHPFRC known as reactive powder concrete, RPC, was launched by Bouygues SA, France. It contained fibres of 13 mm in length and 0.15 mm in diameter, with a 2 - 2.5 % fibre volume fraction. Further enhancements were more oriented towards different geometry of fibres added. Multi-scale fibre reinforced concert (MSFRC), with a high fibre volume fraction (11 %) and fibres of different sizes, was developed by the LCPC, France [Rossi 1997], [Tailhan et al. 2003]. By elaborating the compactness of the matrix and surface of fibres a UHPFRC known as DUCTAL was developed by the companies Lafarge, Bouygues and Rhodia [Acker, Behloul 2004], [Graybeal, Hartmann 2003]. The steel fibre content of this material is relatively low, 2 % V_f . UHPFRC developed in Germany contains 1.5 - 2.5 % of fibres in volume, and a decreased amount of cement [Fehling et al. 2005]. Compresit is the registered name of a UHPFRC patented in Denmark with a typical fibre volume fraction of 6 % [Nielsen 1995]. A multi-modal high-performance hybrid-fibre concrete with three types of short straight fibres was developed in the Netherlands [Sato et al. 2000], and a similar concepts High-performance hybrid-fibre concrete is under investigation at Delft University of Technology [Markovic 2006]. A class of UHPFRC patented in Great Britain under the name CARDIFR has been modelled at Cardiff University, containing 6 % of steel fibres of two different lengths [Stiel et al. 2004].

Another category of innovative concrete materials, known as engineered cementitious composites (ECC) [Li 1993], [Li, Fischer 2002], [Kabele 1995] is present on the market. These can be classed as advanced cementitious materials, in particular since they exhibits considerable strain hardening in

¹ fine is composed of cement and fillers (e.g. silica fume)

tension (Figure 3.1). They do not however meet UHPFRC requirements regarding compressive strength of the matrix.

UHPC used in the present study

In the present study the material used is BSI® UHPFRC. BSI (“Béton Special Industriel”) is UHPFRC developed by the company EIFFAGE in collaboration with cement manufacturer SIKA at the end of the 1990s [Maeder et al. 2004]. The composition of the material and average mechanical properties are listed in Table 3.3.

Table 3.3: Composition of BSI®

	Quantity	Unit
Component:		
Pre-mix ¹	2355	kg/m ³
Water	195	kg/m ³
Superplasticizers	44.6	kg/m ³
Fibres, $l_f = 20$ mm, $d_f = 0.3$ mm	195	kg/m ³
Total weight	2789.6	kg/m ³
Water-cement ratio	0.22	-
Water/binder ratio	0.19	-
Fibre quantity V_f	2.5	vol. %
Compressive strength f_c	≈ 190	MPa
Tensile strength f_{ct}	≈ 9	MPa
Modulus of elasticity	≈ 60	GPa
Fractural toughness	$> 15\ 000$	J/m ²

¹ Pre-mix includes: Portland cement (CEM 1), sand, fine aggregates of diameter 0 - 7 mm, and silica fume; [Maeder et al. 2004]

Fibres used are straight steel fibres, with the nominal diameter $d_f = 0.3$ mm and nominal length $l_f = 20$ mm. It should be noted that the fibre quantity in the material used is not very high in comparison to other UHPFRCs, while the material properties achieved are satisfactory (§ 3.3.2).

3.3 Mechanical properties of UHPFRC

For design purposes, the mechanical behaviour of the material has to be known and mathematically described by constitutive curves that are accurate and easily applicable.

Accuracy is achieved by relating the curves to parameters that are physically significant for the observed material behaviour (intrinsic material properties). For this reason the mechanics of the material must be understood. For applicability, the intrinsic parameters should be easily obtainable from a characterization test of the material, and the shape of the curves has to be sufficiently simple.

In the case of ordinary concrete, compressive strength is the principal parameter used in constitutive curves. For UHPFRC both compressive and tensile behaviours are relevant in the design, and, unlike in ordinary concrete, tensile behaviour is not directly related to compressive behaviour.

The general structure of Sections 3.3.1, dealing with behaviour in compression, and 3.3.2, dealing with tension, is as follows:

- material behaviour is described qualitatively, based on the experimental data
- analytical material models are presented and their applicability to the UHPFRC used in this study is investigated
- proposals for possible material models, well adapted for further structural analysis, are made
- design curves proposed by existing recommendations for UHPFRC are also included.

3.3.1 Uniaxial Compression

3.3.1.1 UHPC without fibres

UHPC matrix without fibres exhibits a compressive behaviour characterised by:

- high strength, $f_{cm} > 150 \text{ MPa}$,
- high modulus of elasticity, in the range of 50 GPa to 70 GPa , representing the linear part of the stress-strain curve,
- linearity limit of stress-strain curve corresponding to $70 - 80 \%$ of compressive strength,
- Poisson's ratio remaining constant up to $70 - 80 \%$ of compressive strength,
- extremely brittle failure.

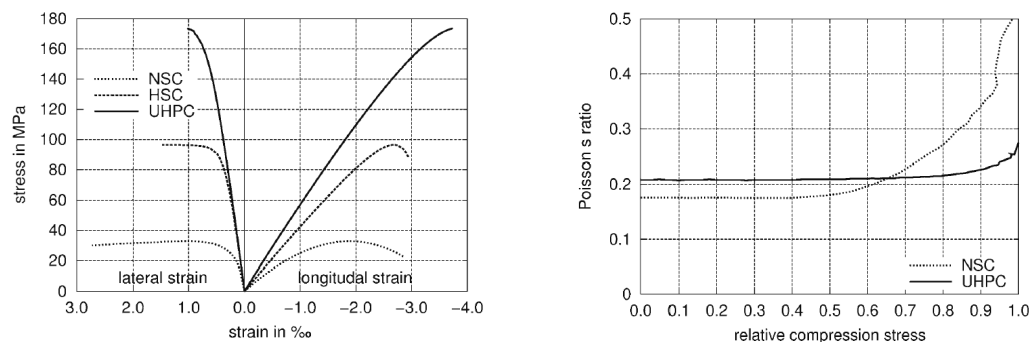


Figure 3.7: Behaviour of UHPC, high-strength and ordinary concrete (NSC) in compression, [Tue et al. 2004]: a) stress-strain relationship; b) Poisson's ratio development over compression stress

Figure 3.7 shows the behaviour of UHPC under static compressive load in comparison to the behaviour of ordinary and high-strength concrete. The failure is of an explosive nature, and the descending branch cannot be observed in the stress-strain curve. The increase in brittleness with the increase in compressive strength is a phenomenon already observed for ordinary and high-strength concretes. This tendency is also exhibited by UHPC. The typical fracture energy of UHPC fibre-free matrix is almost in the range of mortars ($50 - 90 \text{ J/m}^2$) [Wittmann 2002], while that of HPC is approximately 150 J/m^2 [CEB 1993].

The increase in the initial stiffness of UHPC in comparison to ordinary concrete is primarily related to the increase in the modulus of elasticity of the hardened cement paste. It has been reported that the Young's modulus of RPC paste can rise to 75 GPa for very high paste densities, in comparison to approximately 30 GPa achieved in ordinary cement pastes [Richard, Cheyrezy 1995].

The nonlinearity of the curve for higher levels of axial strains results from microcracking that starts at the aggregate and paste interface. The higher homogeneity of UHPC leads to the formation of macrocracks at a much higher average stress than is the case with ordinary and HSC. On the other hand, the effect of stress transfer by aggregate interlock is less pronounced because of smaller aggregate size and the cracks going through the aggregates, resulting in a less pronounced nonlinear phase and a much more brittle failure.

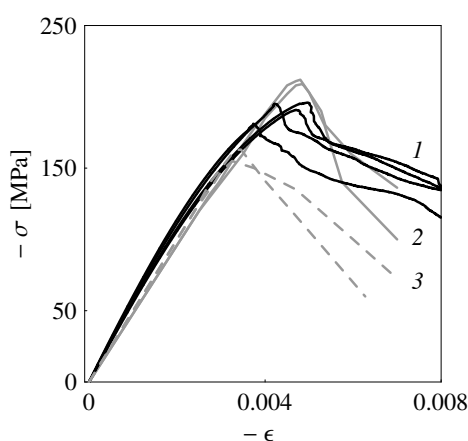
The strains corresponding to maximal stress are higher than those of ordinary concrete. This tendency was also recognised for high-strength concretes, and consequently included in design recommendations ([CEB 1995], Article 2.1.4.4).

3.3.1.2 UHPC with fibres

The addition of fibres to a UHPC matrix leads to less brittle compressive behaviour, with fibres having a similar effect from the mechanical point of view, to that produced by aggregates in ordinary concrete. Figure 3.8 a) shows the results of static uniaxial compression tests on elements made of different UHPFRCs, and of the UHPFRC used in this study [Jungwirth, Muttoni 2005]. The behaviour is characterised by the following regimes:

- linear elastic part guided by the behaviour of the cementitious matrix, with the modulus of elasticity, E_c , in the range of 50 - 70 GPa
- non-linear part prior to failure load
- post-peak softening behaviour¹

a)



b)

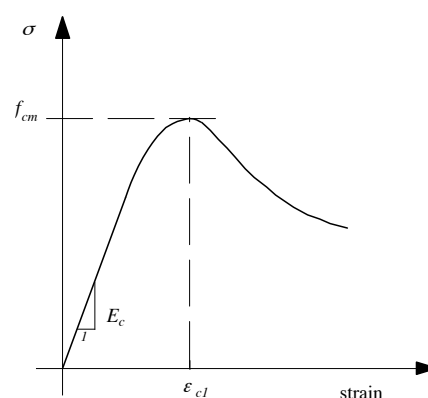


Figure 3.8: UHPFRC behaviour in compression: a) measured stress-strain relationship of different UHPFRCs in compression (tests on cylinders $D/L= 100/200$ mm), 1)[Jungwirth, Muttoni 2005], 2)[Fehling et al. 2005], 3)[Reineck, Greiner 2004]; b) characteristic parameters of stress-strain curve

The compressive strength is slightly improved by fibre addition. In [Nielsen 1995] and [Behloul 1996] an increase of 5 - 10 % in average compressive strength for fibre quantities of up to 4 % V_f is reported.

The non-linear part before failure load is more pronounced than with fibre-free matrix, due to the improved stress transfer mechanism through the microcracks, as mentioned in § 3.3.1.1. The compressive strength is reached at a strain in the range of 3.5 - 5 ‰. Apart from the effect of element size, the post-peak behaviour is influenced mainly by:

- fibre content, V_f ,
- fibre type (straight or hooked fibres, aspect ratio, l_f/d_f), and
- interaction of fibres and matrix (interfacial shear, fibre length to aggregate ratio).

¹ The post-peak correspond to a localisation of deformation, and as a consequence it is a structural property, affected by size and test conditions; extensive research in this field for ordinary concrete is carried out by RILEM Committee [Van Mier 1997a].

3.3.1.3 Constitutive and design stress-strain relationship in compression

No simple theory exists for the modelling of either concrete or fibre-reinforced concrete in compression, since this behaviour results from the complex mechanism developed in its micro-structure, § 3.2.1, § 3.3.2.3. Some models, based on micro-mechanical approaches are available in the literature [Li 1992a], [Nielsen 1995]. These models allow FRC behaviour to be estimated as a function of the strength of the plain matrix and action of the fibres.

The present study follows the approach that is closer to conventional structural design, where empirical models with simple analytical expressions are used to describe the concrete compressive behaviour. The characteristic points in these analytical expressions are related to the characteristic parameters of the composite material, such as average compressive strength, f_{cm} , corresponding strain, ε_{c1} , which represent the maximum point of the curve, and the modulus of elasticity, representing the slope of the initial part of the curve (Figure 3.8 b)). These data can be easily determined by uniaxial compression test.

In a more general way, the analytical expression for the post-peak behaviour should contain the parameters related to the fractural toughness of the material. Fractural toughness is associated with the action of fibres and can be expressed by the means of the fibre reinforcement index, $RI=V_f l_f/d_f$. The influence of this parameter in FRC is dealt with by many authors, such as Fanella and Naaman [Fanella, Naaman 1985]. In the present study, the reinforcement index is a constant, and consequently no conclusions with respect to its influence could have been drawn.

Stress-strain relationship in Design Recommendations for UHPFRC

According to the Interim Recommendations for UHPFRC, Article 1.3, [SETRA, AFGC 2002], behaviour in compression is defined by:

- the characteristic compressive strength, f_{ck} ,
- the Young's modulus of elasticity, E_c .

For design at ultimate limit states (ULS) and serviceability limit states (SLS), the use of a conventional linear constitutive law with yield plateau is suggested by French and Japanese recommendations, (Figure 3.9 a)). No detailed information on the shape of the softening part of the curve is given in this document. The German approach [Schmidt, Fehling 2005] suggests the use of a curve passing from the parabolic for $f_c = 110 \text{ MPa}$ to linear for $f_c = 210 \text{ MPa}$, followed by a plateau (Figure 3.9 b)). Design values are obtained from the characteristic values and safety factors, γ_c . The additional multiplication factor for the characteristic value of the compressive strength, 0.85, is introduced in the recommendations. The end of the plastic plateau is limited to 3.5 ‰ according to French and Japanese recommendations, while the German provisions state that this value, ε_{c3u} , should be assumed in order to take brittleness into account.

The advantage of the proposed curves lies in their easy application in the design, requiring only two parameters. Moreover, for the evaluation at SLS, both the French and the Japanese recommendations suggest that the material can be considered as linear-elastic.

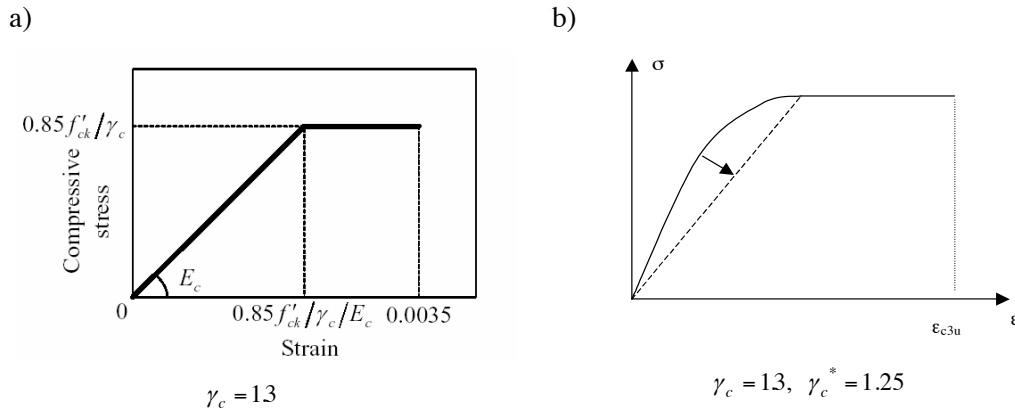


Figure 3.9: Design curve for compressive stress – strain relationship at ULS according to: a) [SETRA, AFGC 2002] and [JSCE 2006]; b) from [Schmidt, Fehling 2005] according to [DAfStB 2003]

It should be noted, however, that the current design recommendations seem too conservative with respect to the exploitation of material ductility in compression. Figure 3.10 a) shows the comparison of design curves at ULS according to [SETRA, AFGC 2002] and [JSCE 2004] with test results. The same Figure b) shows the design curves at ULS for ordinary and high-strength concrete, in comparison with the constitutive material curve, according to CEB-FIB Model Code 1990 [CEB 1993]. The main reason for this more conservative limitation of the ultimate strain in UHPFRC in comparison to other concretes may be explained by uncertainty regarding determination of the plateau and its only partial validation by tests.

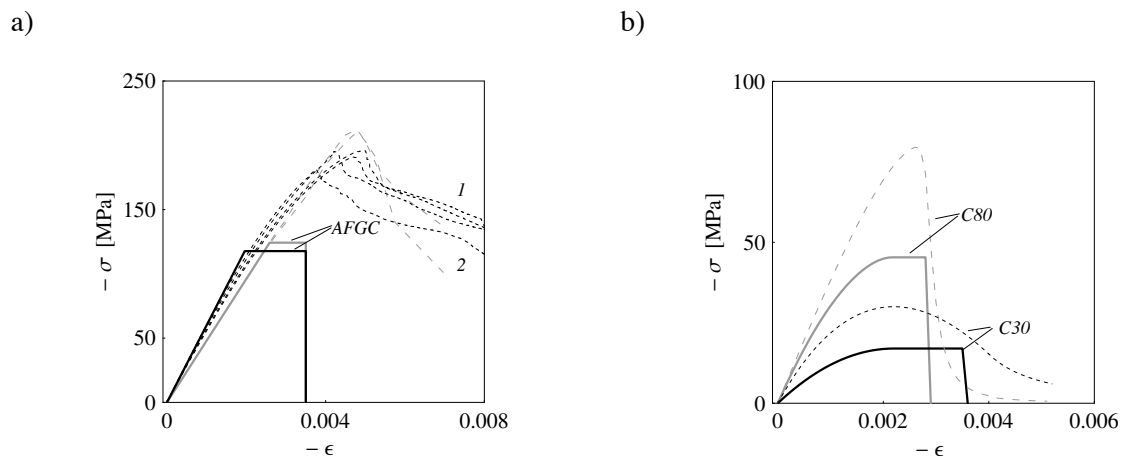


Figure 3.10: Comparison of measured or constitutive stress-strain response with design curves at ultimate limit states (ULS): a) UHPFRC: design curves according to [SETRA, AFGC 2002], tests: 1)[Jungwirth, Muttoni 2005], 2)[Fehling et al. 2005]; b) ordinary, C30, and high-strength concrete, C80; constitutive curves (dashed lines) and design curves at ULS (solid lines) according to [CEB 1993]

3.3.1.4 Investigation of appropriate constitutive compression curves

To define a material law that more accurately describes the behaviour of UHPFRC in compression, families of material curves that are well applicable to ordinary, HSC and FR concrete, are examined. The tendency is to formulate an analytical expression that can take into account the physical phenomenon of the progressive damage (due to microcracking) occurring with increased deformation ϵ ,

$$\sigma = E_c(1 - K_\sigma) \cdot \epsilon \quad (3.4)$$

where K_σ is a variable governed by the damage, yielding to 0 for $\varepsilon = 0$ to 1 for completely damaged material. Possibilities for extending some of the models to UHPFRC are proposed. The considered analytical curves and correcting parameters are summarised in Table 3.4, and plotted in Figure 3.11.

A) An important family of constitutive curves for concrete is based on the proposal of Sargin and Handa [Sargin, Handa 1969], Table 3.4. A large number of curves used for the design of ordinary and high-strength concretes is based on the relationship proposed by the CEB Model Code 90 [CEB 1993], Article 2.1.4.4.1, which is a simplified version of the expression proposed by Sargin, obtained for $D = 0$. For high-strength concretes (grades higher than C50) the extensions to Model Code 90 [CEB 1995] recommends that the strain at maximal stress, ε_{c1} , be a function of average concrete strength, f_{cm} , and the descending branch of the curve be replaced by a curve based on a model proposed by Van Gysel and Taerwe [Taerwe, Van Gysel 1996]. These expressions are calibrated for materials that are generally more fragile than a UHPFRC and can not be applied to UHPFRC in a straight forward way, also because of the significant variability in the post-peak behaviour for different UHPFRC (Figure 3.8). If the parameter ε_{c1} is introduced as the measured value for UHPFRC, and consequently the secant modulus is calculated as $E_{c1} = f_{cm} / \varepsilon_{c1}$, the expression proposed by Model Code 90 describes ascending part of the curve satisfactorily. However, this expression is incapable of approaching the complete descending branch, which can be explained by the difference in fractural toughness between UHPFRC and the concretes for which the expressions are calibrated.

B) Another group of curves proposed in the literature is based on the model of Carreira and Chu [Carreira, Chu 1985], Table 3.4. Ezeldin and Balaguru [Ezeldin, Balaguru 1992] used the analytical expression of Carreira and Chu to approximate the stress-strain behaviour of fibre-reinforced concrete by expressing β as a linear function of the reinforcement index, $RI = V_f \cdot l_f / d_f$. The values for β are based on tests with RI varying between 0.23 and 0.76, which is lower than in typical UHPFRC, and, like the proposal of Taerwe and Van Gyse, cannot be directly applied to UHPFRCs. Hsu and Hsu [Hsu, Hsu 1994] proposed replacing β by $n\beta$, with both parameters, n and β , depending on the matrix strength and fibre volume fraction.

C) A well accepted analytical formulation for describing the compressive behaviour of concrete is proposed by Thorenfeldt, Tomaszewicz and Jensen [Thorenfeldt et al. 1987], Table 3.4. For the ascending branch this curve coincides with the curve proposed by Carreira and Chu, while the descending part is calibrated with a single parameter that enables the measured curve to be approached. The formulation remains similar to that of Carreira and Chu however, and leads to similar results.

D) Various models proposing an exponential expression for the description of the descending branch of the stress-strain curve can be found in the literature [Cusson, Paultre 1995], [Apostolos, Shah 1985]. The shape of the exponential curve is generally appropriate for an analytical description of UHPFRC in compression softening.

Possibilities for extending existing models to UHPFRC in compression

Modified Sargin's curve for UHPFRC:

The general formulation of Sargin's curve (Table 3.4) is investigated in this section for the description of both the ascending and descending branches of UHPFRC. It was observed that the increase of parameter D chiefly increases the stresses in the descending branch; strains in the range $\varepsilon_c < 1.45 \varepsilon_{c1}$, and stress in the descending branch higher than $0.75 f_{cm}$, are well approximated with $0 < D < 0.4$, which is in accordance with the previous observation on the applicability of Model Code 90. The stress-strain relationship for higher strain levels is better approximated with values $0.6 < D < 1$. Consequently, parameter D is proposed as a function of strain level, in the following form:

$$D = a\eta + b\eta^2, \quad (3.5)$$

$$\eta = \frac{\varepsilon_c}{\varepsilon_{c1}}, \text{ with } a = 1.414 - 0.848 \cdot \frac{E_c}{E_{c1}}, b = -0.333 + 0.241 \cdot \frac{E_c}{E_{c1}}.$$

The curve respects the boundary conditions needed to correctly represent the physics of the material (Equation 3.6): the initial slope of the curve is equal to the material's initial tangential stiffness, E_c , and the maximum of the curve corresponds to deformation ε_{c1} .

$$\lim_{\varepsilon_c \rightarrow 0} \left(\frac{\partial \sigma_c}{\partial \varepsilon_c} \right) = E_c \quad \wedge \quad \lim_{\varepsilon_c \rightarrow \varepsilon_{c1}} \left(\frac{\partial \sigma_c}{\partial \varepsilon_c} \right) = 0 \quad (3.6)$$

Coefficients a and b are determined so that the surfaces of the areas under the simulated and the tested curves are equal (equality of toughness). The coefficient D defined in Equation 3.5 provides a smooth and continuous analytical expression that enables the curve to be followed integrally in the descending as well as ascending regimes, Figure 3.11 a).

Proposals for parameters for the application of other shapes of curves are given in the following table.

Table 3.4: Constitutive curves for UHPFRC in compression

Shape of curve: $y = \frac{\sigma_c}{f_{cm}}, \eta = \frac{\varepsilon_c}{\varepsilon_{c1}}$	Parameters	Proposal for UHPFRC (BSI)
A) Sargin ¹⁾ $y = \frac{A\eta + (D-1)\eta^2}{1 + (A-2)\eta + D\eta^2}$	$A = \frac{E_c}{E_{c1}}, E_{c1} = \frac{f_{cm}}{\varepsilon_{c1}}$ D to be calibrated for descending branch	$D=f(\varepsilon_c)$ Equ. 3.5
B) Carreira ²⁾ $y = \frac{\beta\eta}{\beta-1+\eta^\beta}$	$\beta = \frac{1}{1 - \frac{f_{cm}}{\varepsilon_{c1}E_c}} = \frac{1}{1-A^{-1}}$	$y = \frac{n\beta\eta}{n\beta-1+\eta^{n\beta}}$ $n=1.1$
C) TTJ ³⁾ $y = \frac{n \cdot \eta}{n-1+\eta^{n \cdot k}}$	$n = \frac{E_c}{E_c - E_{c1}} = \frac{1}{1 - \frac{f_{cm}}{\varepsilon_{c1}E_c}} = \frac{1}{1-A^{-1}} = \beta, k = \begin{cases} 1 \forall \frac{\varepsilon_c}{\varepsilon_{c1}} \leq 1 \\ > 1 \forall \frac{\varepsilon_c}{\varepsilon_{c1}} > 1 \end{cases}$	$k=1.05$
D) Exponential curve ⁴⁾ $\sigma_c = e^{k_1(\varepsilon_c - \varepsilon_{c1})^{k_2}} \cdot f_{cm},$ only for $\varepsilon_c > \varepsilon_{c1}$	k_1, k_2 , calibrated for descending branch	$k_1=175$ $k_2=1.05$

¹⁾ [Sargin, Handa 1969], ²⁾ [Carreira, Chu 1985], ³⁾ [Thorenfeldt et al. 1987], ⁴⁾ [Cusson, Paultre 1995]

In this table y is normalised stress and η is normalised strain, with σ_c compressive stress, f_{cm} average compressive strength, ε_c compressive strain and ε_{c1} the strain corresponding to compressive strength.

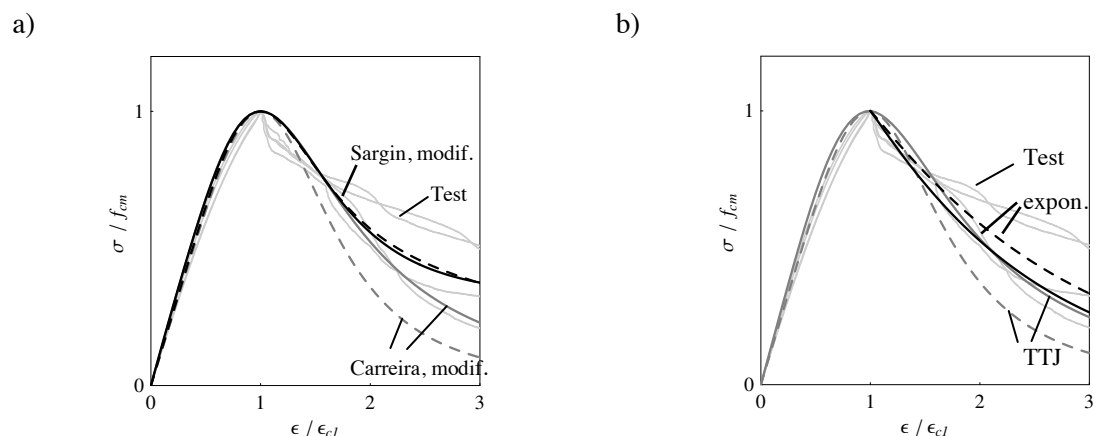


Figure 3.11: Comparison of the proposed material curves in compression and measured data (light grey, [Jungwirth, Muttoni 2005]); curves are plotted for two sets of parameters: $f_{cm} = -195 \text{ MPa}$, $\epsilon_{cl} = -4.85 \text{ ‰}$ (solid line) and $f_{cm} = -180 \text{ MPa}$, $\epsilon_{cl} = -4.0 \text{ ‰}$ (dashed line): a) Modified Sargin's curve (black) and Carreira's curve (grey); b) exponential (black) and TTJ (grey) curve

All investigated expressions give plausible results for the ascending part of the curve. The shapes of the modified Sargin's and exponential curve give satisfactory approximation of the descending branches for various strength levels, while the curves proposed by Carreira and TTJ are more sensitive to strength variation.

3.3.1.5 Material curves in the case study

When the continuous curve is necessary for analysis, the modified Sargin's curve is found to be appropriate for the description of compressive behaviour. For the analysis in which the ascending and descending branches can be separated, the Sargin's curve with coefficient $D \rightarrow 0$ can be used for the ascending part, and the exponential curve for the descending branch, which enables a simple integration of the stress. For numerical integration, both models are easily applicable. If compressive failure does not occur, a linear curve characterised with the modulus of elasticity $E_c = 60 \text{ GPa}$ (Appendix T1) provides sufficiently accurate results for the UHPFRC used in this study.

3.3.1.6 Conclusions

The behaviour of UHPFRC in compression is characterised by very high strength, greater than 150 MPa , a high strain at maximal stress (4-5 ‰ for the tested UHPFRC) and significant post-peak ductility.

No practical formulation of a general material model for UHPFRC behaviour in compression, taking matrix/fibre interaction into account, is available in the literature.

Constitutive curves used for ordinary, HSC and FRC can be used for describing the ascending part of UHPFRC in compression and the modifications of certain curves can also give a satisfactory approximation of the descending part. Proposals for the correcting parameters are given for the UHPFRC used in this study. More generally, these parameters are influenced by the fracture properties, associated to the fibre action. In the present study this influence could not be considered, since the material matrix and the reinforcement index were constant ($RI = 1.6$). However, the proposed curves show good plausibility with regard to other UHPFRCs containing similar fibre quantities.

Regarding design, current recommendations for UHPFRC impose a conservative limit for ultimate compressive strain. The possibility of using a less conservative ultimate strain limit needs to be further investigated.

3.3.2 Uniaxial Tension

3.3.2.1 Matrix in uniaxial traction

The tensile strength of UHPC matrix is in the range of 10 MPa , which is significantly higher than that of other concretes, and can be explained by the increased compactness of the matrix. As stated in § 3.2.1.1, the fibre-free matrix is extremely brittle (Table 3.2).

3.3.2.2 Matrix with fibres in uniaxial traction

The addition of fibres to UHPC matrix leads to a tensile behaviour that can be schematically presented as in Figure 3.12. The measured curves of UHPFRC members subjected to a uniaxial tensile test are plotted in Figure 3.20. The following regimes of behaviour are distinguished:

- linear-elastic behaviour up to the stress level corresponding to matrix tensile strength;
- pseudo strain hardening behaviour resulting from multi-microcracking;
- strain softening behaviour with localisation of deformation.

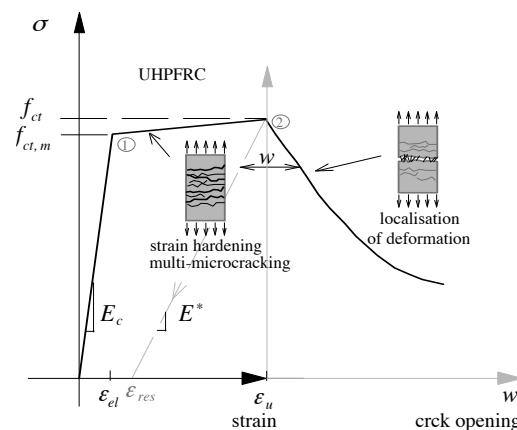


Figure 3.12: Uniaxial tensile response of UHPFRC element and notations for characteristic values

Linear-elastic behaviour

The maximal stress attained in this regime coincides with the tensile strength of the matrix, $f_{ct,m}$, and it is observed that the first cracking stress is scarcely influenced by the presence of fibres [Shah 1991]. The major part of maximal tensile strength is achieved in this regime, but with a very small part of corresponding deformations ($\epsilon_{el} \ll \epsilon_u$). No permanent microstructural changes take place during this deformation, and it can be considered as linear-elastic, with the modulus of elasticity E_c corresponding to the initial modulus of elasticity in compression, § 3.3.1.2.

Pseudo strain hardening behaviour

The end of the elastic regime corresponds to the occurrence of the first microcrack at the section with statistically the weakest matrix strength [Behloul 1996]. With the further increase of deformations beyond the elastic level, uniaxial tensile stress increases at a much lower rate than in the elastic regime, or remains constant ($f_{ct} \geq f_{ct,m}$). The high increase in deformations that characterises this phase is due to the formation of a large number of tiny cracks, of micron magnitude, termed multi-

microcracking. This continuous microcracking process, with well distributed, closely spaced openings bridged by the fibres, observed on the elements scale resembles a plastic or strain hardening behaviour. Owing to the fact that no true plastic microstructural changes take place a term “pseudo strain hardening” or “pseudo plastic” is used to describe this behaviour. The physical distinction between these deformations and those of a real plastic material can be seen during the unloading of a UHPFRC element, where the descending curve clearly shows the behaviour of a damaged (cracked) material (Figure 3.20 b)).

Pseudo strain hardening behaviour distinguishes UHPFRC from other FRCs [Naaman, Reinhardt 2006], (Figure 3.1). It is characterised by the maximal deformation that can be attained before strain softening begins, ε_u , and by the strength attained at that level of deformation, f_{ct} . For a typical UHPFRC, ε_u has a value in the range of 2 - 3 ‰. Both of these parameters (ε_u and f_{ct}) are functions of the quantity and properties of the fibres, and their interaction with the matrix. An increase in tensile and flexural strengths in relation to fibre volume quantity is demonstrated in a lot of research. Figure 3.13 shows an example of the effect of quantity and type of fibres on tensile strength. It should be noted that 2 ‰ fibre volume fracture content may be sufficient to considerably increase tensile strength.

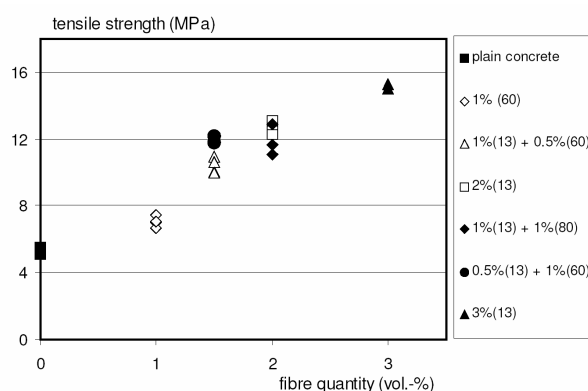


Figure 3.13: Uniaxial tensile strengths of a UHPC with different types and quantities of fibres, hybrid-fibre concrete [Markovic 2006]

In order to treat pseudo strain hardening as a material property, it is essential to assess the conditions for stable multi-microcracking, studied in § 3.3.2.4.

Strain softening behaviour

The end of strain hardening phase coincides with the moment when, for the increase in deformation, the transfer of the same (nor higher) intensity of average stress in one of the sections can no longer be assured. This can be expressed as the moment when the strain hardening capacity of the material is exhausted. When stress starts to decrease, the sections other than the weakest one start to unload decreasing the deformation, and the deformation localises in the weakest section¹, developing a so-called “macrocrack”. The energetic conditions that must be fulfilled to ensure the stability of macrocrack growth are discussed in § 4.3.5.3.

Similarly to the previous one, this phase remains governed by fibre action, but, unlike to the previous phase, observed on the element scale, it is influenced by specimen size. For this reason, for it to be considered as a material property [Hillerborg 1985], the strain softening behaviour can no longer be expressed as a function of average deformation, but of localised deformation, i.e. crack opening. The deformation capacity during strain softening is very pronounced for UHPFRC and the limiting value is typically related to half the length of the longest fibre.

¹ Various positions of localised crack in UHPFRC tie elements can be seen in [Reineck, Greiner 2004a].

Strain softening behaviour remains qualitatively the same as that of FRCs, investigated experimentally and analytically by many authors [Naaman et al. 1974], [Nammur, Naaman 1989], [Morrison et al. 1988].

3.3.2.3 Mechanism of fibre action and multi-microcracking principle

When the first microcrack occurs in the matrix, the opening of the crack is restricted by the presence of fibres if their resistance is sufficiently high. If a single fibre crossing the crack is considered, as the crack opening increases, the stress transferred by the fibre between the crack faces changes due to several phenomena. This crack-bridging mechanism is a possible combination of the following actions (Figure 3.14):

- fibre deformation,
- fibre pullout: cracking of the interface between fibre and matrix (debonding), and frictional slip,
- deformation of pulled-out fibre, and
- fibre rupture.

Depending on a dominant crack-bridging mechanism and its capacity to dissipate energy, different types of failures can occur:

- fibre break or pullout during crack initiation so that the load borne after formation of the crack decrease; strain softening occurs thus with the formation of a single crack which governs ultimate strength and further deformation;
- fibre is capable of sustaining a greater load after the initiation of the first crack by deforming and pulling-out, allowing the formation of new cracks; this results in pseudo strain hardening behaviour, and an increase in overall deformation.

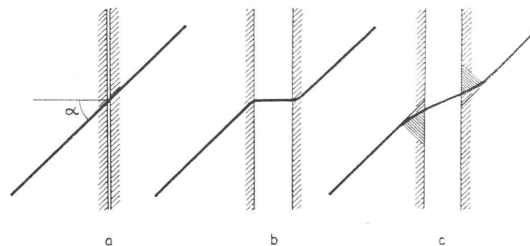


Figure 3.14: Behaviour of a fibre bridging the crack [Hillerborg 1980]

Physical parameters that interfere with the complex mechanism of crack-bridging by fibres determine whether the material can exhibit pseudo strain hardening and with which deformational capacity. Some researchers have dealt with the analytical formulation of this problem [Aveston et al. 1971], [Naaman et al. 1991], [Li 1993], based on description of the behaviour of a single fibre in the matrix.

To ensure that pseudo strain hardening behaviour occurs, the pullout of the fibres is the desirable energy dissipation mechanism of crack-bridging. To achieve this, it must be ensured that the matrix strength and fibre-matrix interface can provide the adequate bond and further frictional resistance during pullout mechanism. However the created resistances (due primarily to the bond) should not be sufficiently high to provoke failure of fibres with the matrix cracking instead of pullout development. The pseudo strain hardening behaviour thus depends greatly on matrix-fibre interaction and fibre geometry [Bartos 1981], [Brandt 1985], [Casanova 1996].

UHPFRC are conceptually developed to meet those conditions. As it will be shown in this thesis, the pseudo strain hardening behaviour of UHPFRC has important implications for structural application. For that reason, it is necessary to demonstrate that it is a stable process, with a strong likelihood of occurrence.

3.3.2.4 Conditions for a stable developpement of multi-microcrack

The condition for stable first cracking can be simplified in a similar manner to that used in the case of reinforced concrete elements (Equation 3.7): when the matrix fails, at stress $f_{ct,m}$, the load borne by the unit area of the matrix is then transferred to the fibres; if the fibre strength is $f_{s,f}$, the following inequality must be respected:

$$f_{s,f} \cdot V_f \geq f_{ct,m} \cdot V_m + \sigma' \cdot V_f \quad (3.7)$$

where σ' is the stress borne by the fibres prior to matrix cracking, $\sigma' = E_f \cdot \epsilon_{cm}$, and V_m is matrix volume fraction, $V_m = 1 - V_f$. This gives approximate information concerning the fibre strength needed for stable first cracking. The further cracking condition requires more thorough models.

One of the earliest models used to describe multi-microcracking based on energy equilibrium was proposed by Aveston, Cooper and Kelly, known as the ACK model [Aveston et al. 1971], [Aveston, Kelly 1973]. Principles of the ACK models are used in further study in order to demonstrate the potential of the material for developing multi-microcracking. Another formulation that can be used for the same purpose is proposed by Li, [Li 1993], and Li, Mishra and Wu [Li et al. 1995], also based on the fracture energy.

Multi-microcracking criteria based on the ACK model

The ACK model explains the phenomenon of multi-microcracking based on comparison of the energies that are dissipated during this process. The multi-microcracking principle can be summarised as follows: at the formation of the first matrix crack, the energy required to grow the crack is greater than the energy required for the formation of a new crack. A practical formulation of this condition in terms of fibre volume fraction is derived in [Tjiptobroto, Hansen 1993] and graphically shown in Figure 3.15 b).

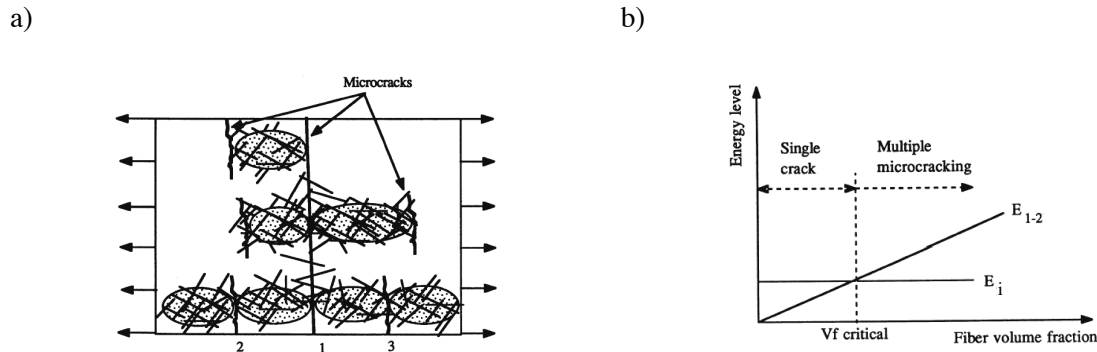


Figure 3.15: a) Multi-microcracking in fibre-reinforced material; b) determination of critical fibre volume fraction in HPFRC, according to [Tjiptobroto, Hansen 1993]: E_i is the energy of the formation of new cracks, E_{1-2} the energy needed to grow the crack

According to the ACK model, the following work is assumed to take place during crack opening:

- destruction of the interface bond between fibres and matrix,
- extension of fibres with increase in elastic strain, ΔU_f ,
- loss of strain energy by matrix due to zero stress at the crack face, ΔU_m ,
- increase in fibre and decrease in matrix deformation, resulting in matrix sliding over the fibres, causing frictional work, ΔU_{fr} ,
- work done for the formation of the new crack surface, corresponding to the fracture energy of the matrix, $G_{F,m}$.

The energy required for the opening of the first microcrack sufficiently to reach the softening region (energy for passing from point 1 to point 2, Figure 3.12) is denoted by E_{1-2} and, according to [Tjiptobroto, Hansen 1993], can be obtained by adding together the increase in fibre strain energy, ΔU_{f-mc} , debonding, U_{db} and frictional energy, ΔU_{fr} :

$$E_{1,2} = \Delta U_{f,mc} + U_{db} + \Delta U_{fr}. \quad (3.8)$$

The energy required for the creation of a new microcrack (crack 1, 2, 3 etc, Figure 3.15a)), is denoted by E_i , and can be assumed as being equal to the fracture energy of the matrix, $G_{F,m} V_m$, increase in fibre strain energy, $\Delta U_{f,mu}$, and decrease in matrix strain energy, ΔU_m :

$$E_i = G_{F,m} V_m + \Delta U_{f,mu} - \Delta U_m \quad (3.9)$$

As long as the value of E_i is lower than the value of $E_{1,2}$, multi-cracking can occur, Figure 3.15 b). Tjiptobroto and Hansen have developed the expressions for the energy terms in Equations 3.8 and 3.9 as a function of the effective fibre volume fraction, V_{ef} , that is related to actual fibre volume fraction, V_f , using a reduction factor η :

$$V_{ef} = \eta V_f, \quad 0 < \eta < 1. \quad (3.10)$$

From the limiting condition $E_{1,2} = E_i$, the critical fibre volume fraction, V_{cr} , is determined as the minimal fibre volume fraction, V_f , required to enable multi-cracking to occur.

Multi-microcracking of the UHPFRC used in this study

For the material used in the present study, results for the frictional stress, τ_f , and debonding energy (the fracture energy of the second failure mode, $G_{F,II}$) are accepted from the tests on similar fibre type and concrete matrices, such as DSP concrete [Tjiptobroto, Hansen 1993], and high-performance hybrid-fibre concrete [Markovic 2006].

In Figure 3.16 the comparison between the energy required to open a crack ($E_{1,2}$, grey line) and the energy required for creation of new cracks (E_i , black line) is shown. The curves in Figure 3.16 are plotted for $\tau_f = 3.7 \text{ MPa}$, $G_{F,II} = 46 \text{ J/m}^2$ and $G_{F,m} = 110 \text{ J/m}^2$, while the other data are given in Table 3.3. These values are accepted on the safety side: for τ_f the value of 5 MPa and $G_{F,II} = 120 \text{ J/m}^2$ can be accepted according to [Tjiptobroto, Hansen 1993]; in [Wittmann 2002] values $G_{F,m} = 40 - 90 \text{ J/m}^2$, is reported for high-performance matrixes.

In Figure 3.16 a) the results are also plotted for the decreased values of τ_f and $G_{F,II}$ and the increased value of $G_{F,m}$, which is an even more conservative combination of parameters, an obviously leads to an increased critical value of the volume fraction (intersection of dashed lines). The decrease in interfacial shear strength, τ_f and the decrease in fracture energy $G_{F,II}$ lead to a decrease in the energy that is dissipated with the opening of the first crack ($E_{1,2}$); the increased fracture energy of the matrix, $G_{F,m}$, increases the energy for the formation of new cracks, E_i , which eventually leads to an increase in the minimal quantity of fibre needed for the development of multi-microcracking. The energy curves in Figure 3.16 a) are plotted for reduction factor $\eta = 0.5$.

The influence of the reduction factor, η , on critical fibre volume fraction, V_{cr} , is presented in Figure 3.16 b). This plot shows the increase of V_{cr} with the decrease of parameter η (the decrease in effective fibre volume), meaning that with a decrease in effective fibre volume, the material rapidly approaches the limiting condition for hardening (V_{cr} approaches or exceeds V_f).

It can be concluded that for the UHPFRC used in this study, assuming that an effective fibre volume fraction of $0.5 V_f$ is assured, the multi-microcracking can occur, since the material's fibre volume fraction ($V_f = 2.5\%$) is slightly higher than the obtained critical fibre volume fraction. The variation in effective fibre volume is principally related to fibre orientation. The effects of fibre orientation on both flexural and tensile strengths and on the fracture energy of UHPFRC are also observed experimentally [Stiel et al. 2004], [Behloul 1996]. Since fibre orientation is strongly influenced by the casting procedure, care should be taken to place the fresh concrete in such a way as to ensure pseudo strain hardening in materials with a low fibre-reinforcement index.

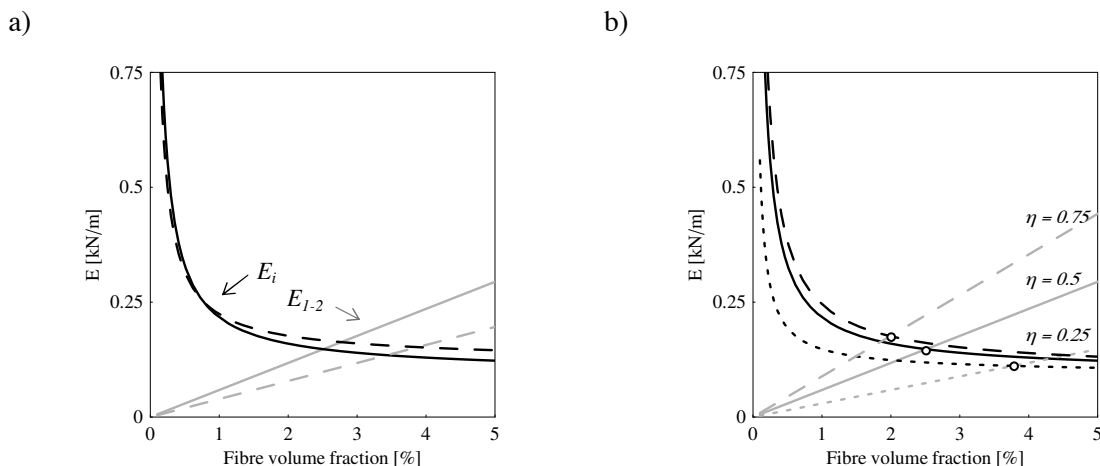


Figure 3.16: Fracture energies as a function of fibre volume fraction: a) $\eta = const = 0.5$, with $\tau_f = 3.7 \text{ MPa}$, $G_{F, II} = 46 \text{ J/m}^2$ and $G_{F, m} = 110 \text{ J/m}^2$ (plane line) and with the critical combination of decreased τ_f and $G_{F, II}$ values (30% decrease) and 30% increased value of $G_{F, m}$; b) with average values of τ_f , $G_{F, m}$ and $G_{F, II}$ and $\eta = var$.

In [Li 1993] an expression for critical fibre volume fraction was formulated based on the steady state cracking condition and with the introduction of the probability density functions for the orientation and position of the fibre's centroid from the crack. This model will not be discussed here. The conclusions from the developed relationship will be given however, since they are of interest in understanding the concept of UHPFRCs: the low toughness of the matrix, strong interfacial bond and friction, and high aspect ratio of fibres (l_f/d_f) can lead to pseudo strain hardening with even a small fibre volume fraction. This is plausible with the results obtained from the AVK model (Figure 3.16).

3.3.2.5 Modelling of material behaviour in tension: $\sigma(\epsilon)$ and $\alpha(w)$ curves

According to § 3.3.2.2, the behaviour of UHPFRC in tension has to be described by means of two relationships: stress-strain $\sigma(\epsilon)$ up to the point when strain softening occurs, and stress-crack opening $\alpha(w)$ describing the localised deformation, Figure 3.12.

Two families of models are used for describing tensile behaviour: micromechanical and macromechanical models. The first family includes models based on the behaviour of a single fibre in the matrix, as mentioned in § 3.3.2.3, with two possible ways of describing the system's equilibrium: using the energy balance approach, or the force equilibrium, [Stang, Shah 1990]. Some of these models are presented in closed analytical forms ([Aveston, Kelly 1973], [Li 1992], [Ouyang et al. 1999] etc.), while some are better adapted for numerical implementation ([Kabele 2000], [Ulm 2002]).

Macromechanical models observe the integral response of the material as a continuum. The formulation is based on the affinity of analytically defined shapes with the experimentally observed behaviour. This is a widely accepted approach, well suited to design needs, as already explained for compressive behaviour, § 3.3.1.3.

Micromechanical models for FRC behaviour

Micromechanical models generally comprise a two-stage procedure: firstly, the pullout behaviour of a single fibre is modelled, usually by assuming that the fibre is at right angles to the crack direction and that the embedded length of the fibre is known. For the known mechanical and geometrical properties of the fibre, matrix and interface, the force-pullout relationship, $\alpha(\delta)$, for one fibre can be derived. This has been done by several authors on the basis of energy as well as equilibrium

approaches, with similar results [Stang, Shah 1990]. The influence of the inclination of the fibre with respect to the crack direction as well as other phenomena such as the bending and failure of the fibre, or the local failure of embedding concrete, can also be considered at this stage [Pfyf 2003]. The second stage passes from describing the behaviour of a single fibre to the behaviour of the fibred material. The problem is principally related to the distribution and orientation of fibres, which are finitely long and randomly placed, and their interaction. From the known behaviour of a single fibre, $\alpha(\delta, \phi, z)$, as a function of its orientation, ϕ , and its position with respect to the crack, z , the effect of several fibres crossing a crack can be determined by integrating the $\alpha(\delta, \phi, z)$ relationship. The integration is performed over possible range of fibre orientation and position, with fibre disposition based on statistical assumptions (Equation 3.16). A considerable amount of experimental and theoretical work on fibre distribution is carried out [Li et al. 1996], [Behloul 1996], [Akkaya et al. 2001]. In addition, the effect of the interaction of randomly oriented fibres can be either positive (local confinement due to surrounding fibres) or negative (surrounding fibres causing microcracking weakening the matrix)¹.

A general formulation of material mechanical response during microcracking with the presence of fibres can thus be as follows:

$$\sigma(\delta) = V_f \int_{\phi=0}^{\pi/2} \int_{z=0}^{(l_f/2)\cos\phi} \sigma(\delta, \phi, z) p(\phi) p(z) dz d\phi \quad (3.11)$$

where $\alpha(\delta, \phi, z)$ is the stress-displacement (pullout) response of a single fibre in the matrix, and $p(\phi)$ and $p(z)$ are probability density functions for the orientation and position of fibres centroid from the crack.

In [Li et al. 1991] and [Li 1992] a formulation of probability functions $p(\phi)$ and $p(z)$ is given, and the relationship of the remote stress-crack opening, $\alpha(\delta)$ can be expressed in a simplified manner [Li et al. 1996]:

$$\sigma(\delta) = \begin{cases} \sigma_{cu} \cdot \left(2 \cdot \left(\frac{\delta}{\delta_p} \right)^{1/2} - \frac{\delta}{\delta_p} \right) & \forall \delta \leq \delta_p \\ \sigma_{cu} \cdot \left(1 - 2 \cdot \frac{\delta}{l_f} \right)^2 & \forall \delta_p \leq \delta \leq l_f/2 \\ 0 & \forall \delta > l_f/2 \end{cases} \quad (3.12)$$

where

$$\sigma_{cu} = \frac{1}{2} \cdot g \cdot \tau_f \cdot V_f \frac{l_f}{d_f}, \quad (3.13)$$

with factor g including parameters related to fibre-matrix interaction, and δ_p the opening corresponding to maximum bridging stress

$$\delta_p = \frac{\tau_f \cdot l_f^2}{E_f \cdot d_f \cdot (1 + \eta)}. \quad (3.14)$$

¹ In [Behloul 1996] it was experimentally observed that residual stress (in softening) is proportional to V_f for 2.4 and 4 % of fibres, but residual stresses for 1 and 2.4 % of fibres are almost identical, indicating the influence of more damage caused by the higher fibre content in the cracked region.

Behloul [Behloul 1996] has developed a similar model that enables the variability of the number of fibres in a section and variability in matrix resistance with respect to fibre quantity and type of solicitation to be taken into account. The mean value of the stress sustained by the cracked section as a function of the normalised crack opening r , $r = 2w / l_f$, is expressed as:

$$\bar{\sigma}(r) = \alpha \cdot V_f \cdot \frac{l_f}{d_f} \cdot \tau_f \cdot g(\alpha, f) \cdot F(\alpha, r) \quad (3.15)$$

and the expression for the stress variation coefficient is:

$$CV(\sigma(r)) = 2.1 \cdot \frac{d_f}{(\alpha \cdot V_f \cdot S_{rep})^{1/2}} \cdot \quad (3.16)$$

In Equations 3.15 and 3.16 α is the fibre orientation factor, f is the representative coefficient of fibre inclination with respect to direction of solicitation, and $g(\alpha, f)$ represents the function of the combined influence of the two parameters on strength. Function $F(\alpha, r)$ represents the influence of the orientation factor on the shape of the post-peak curve. An advantage of adopting statistical approach is that the upper and lower limits of material strength can be determined, and crack development can also be explained.

Similar developments relating to multiple cracking with short aligned fibres, based on fracture mechanics approaches, can be found in [Stang, Shah 1986], [Ouyang et al. 1999]. Simplified models that take into account fibre-matrix interaction using average interfacial shear, τ_f , and introduce the efficiency factor η (Equation 3.10), enabling problems caused by finite fibre length and random orientation to be dealt with, have a practical significance particularly for the determination of average composite cracking strength [Naaman et al. 1974], [Naaman, Reinhardt 2006], [Swamy, Mangat 1974], [Behloul 1996].

Micromechanical approaches were used to describe the behaviour of UHPFRC materials [Jungwirth 2006]. Moreover, these approaches can be useful for the development of UHPFRC, in that they allow the fibre and fibre-matrix interface properties to be tailored to meet specific requirements. However, the chief problems related to the application of micromechanical models are their complexity and the need for parameters usually not easily available in design. For practical reasons, engineers are more interested in the behaviour of composite material, that can be determined from the experimental data at the structural level, as explained in the next section.

Macro-mechanical models based on the measured curves

Tensile tests

The use of experimental data to establish the stress-strain and stress-crack opening relationship in tension also gives rise to certain problems, mainly related to:

- the appropriate test method
- methods for deriving the pure material curves from test data, without the influence of test method and specimen geometry.

A great deal of research in this field has been done by the RILEM committee since steel fibre-reinforced concrete (SFRC) has been more intensively used in design. Recommendations for SFRC and UHPFRC propose that either the direct tensile or flexural test be performed for material characterisation [SETRA, AFGC 2002], [RILEM 2003]. Both tests can be performed on notched or unnotched specimens. Direct tensile testing is more difficult to perform, but provides more reliable results. According to some authors [Hillerborg 1980], the tensile test is the only accurate way to determine the tensile behaviour of FRC materials. It should be pointed out that there is a problem in distinguishing between tensile strain hardening and tensile softening during the hardening in bending. Consequently the determination of tensile hardening from the bending test, if no additional information on tensile response is available, is uncertain. The problems concerning the relationship

between tensile and bending behaviour in the case of strain-hardening materials are again referred to in Chapter 4.

Derivation of material curve form the uniaxial tensile test

Here the material's tensile behaviour is derived from uniaxial tensile tests on unnotched specimen (Figure 3.20). Deriving the stress-strain part of the curve from the force-elongation curve (Figure 3.17) is a straightforward task while the softening part of the curve requires some additional considerations: the stress–crack opening curve, $\sigma(w)$, characterises the material at the fracture zone only, signifying that, during strain softening, deformations increase only in the localised section, while the rest of the specimen exhibits deformation decrease following the unloading part of the $\sigma(\varepsilon)$ curve (Figure 3.17). Thus, for derivation of the stress–crack opening it is essential to know the unloading modulus of the damaged (microcracked) material, E^* .

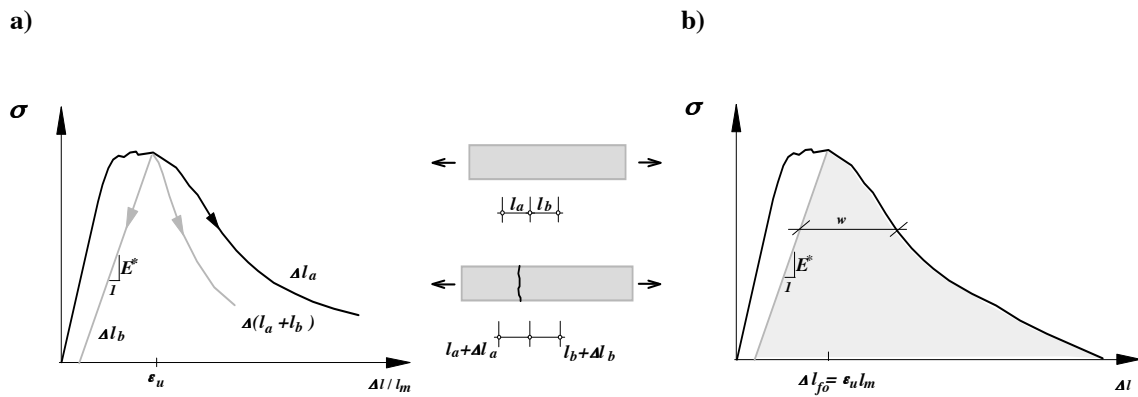


Figure 3.17: Stress-elongation curves, according to [Hillerborg 1980]: a) stress-average deformation for different measurement bases; b) stress-elongation and crack opening

The measured data in the direct tensile test is the elongation of the measurement base, Δl , of the initial length of l_m . If the elongation of the measurement base at the formation of the macrocrack is Δl_{fo} , the further increase in deformation is actually the increase in crack opening, w , and the decrease in deformation of the surrounding material, as a function of average stress. The surrounding material is considered to have a linear stress–strain relationship for stress decrease, characterised by an unloading modulus, E^* (Figure 3.17). Thus, assuming that unloading occurs in a homogeneous manner along the whole measurement base, for elongations greater than Δl_{fo} :

$$\Delta l = \Delta l_{fo} + w + \frac{\Delta \sigma}{E^*} \cdot l_m, \quad (3.17)$$

where $\Delta \sigma < 0$, and $\frac{\Delta \sigma}{E^*}(\Delta l - w)$ is disregarded for a small l_m . The crack opening w is obtained as

$$w = \Delta l - \Delta l_{fo} - \frac{\Delta \sigma}{E^*} l_m = \Delta l - l_m \cdot \varepsilon_u - \frac{\Delta \sigma}{E^*} l_m. \quad (3.18)$$

Analytical expressions for the $\sigma(w)$ curve

Analytical curves describing the behaviour of FRC in tensile strain softening can be found in the literature ([Stang et al. 1995], [Behloul 1996], [Kosa, Naaman 1990], [Shah 1987]), and in general can be grouped into several families. Some of these curves are considered for the description of the strain softening behaviour of the tested UHPFRC. Analytical expressions and plots against the measured data are given in Section 3.3.2.8.

3.3.2.6 Concept of fracture energy in FRC and UHPFRC

The relationship between average stress and crack opening provides information concerning the amount of energy required for the opening of the crack up to the maximal value, w_c , (grey surface in Figure 3.17 b)). This energy is traditionally defined as the fracture energy of concrete and fibre-reinforced concrete material, G_F ,

$$G_F = \int_0^{w_c} \sigma(w)dw, \quad (3.19)$$

and was introduced in this concept for ordinary concrete by Hillerborg, Mod er and Petersson, via the fictitious crack model [Hillerborg et al. 1976]. The principles of this model are given in § 4.2, but only the definition 3.19 is included here, as a means of distinguishing between the nature of fracture energy as defined in linear elastic fracture mechanics theories and the energy consumed for the opening of the bridged crack. The latter is actually dissipated throughout the crack-bridging actions, which for an FRC include debonding, friction, deformation and possible fibre failure, as explained in § 3.3.2.3 and § 3.3.2.4.

There is also a significant difference in the definition of the crack, which is, in fracture mechanics terms, a stress-free surface, while the crack in FRC materials transfers a considerable amount of stress, and the term “fictitious” is found more appropriate to designate such material discontinuity. However, on the macroscopic (structure-relevant) scale, the fictitious crack is the representative crack in fibre-reinforced concretes, while the stress free-microcracks in the matrix are insignificant on this scale. This justifies the concept of fracture energy as defined in Equation 3.19.

The fracture energy values of typical UHPFRC are in a range higher than $10\,000\text{ J/m}^2$, while for ordinary concrete, fracture energy is of the magnitude of 100 J/m^2 , Table 3.2. It should be noted that the significance of the total fracture energy, G_F , of UHPFRC is less important than that of brittle materials or even ordinary concrete. The initial rate of change in fracture energy for crack growth becomes more significant, as explained in the case of stable crack propagation, § 4.3.5.3.

3.3.2.7 Constitutive and design material curves in tension

Constitutive curves in recommendations for UHPFRC

Present recommendations for UHPFRC suggest the use of tests (tensile or bending) for characterization of tensile behaviour. Transfer factor is proposed in order to derive intrinsic curves from different test procedures [SETRA, AFGC 2002]. Figure 3.18 a) shows a proposal for constitutive curves in tension according to French recommendations, while a simplified stress-crack opening relationship, suggested by Japanese recommendations, is shown in the same figure b).

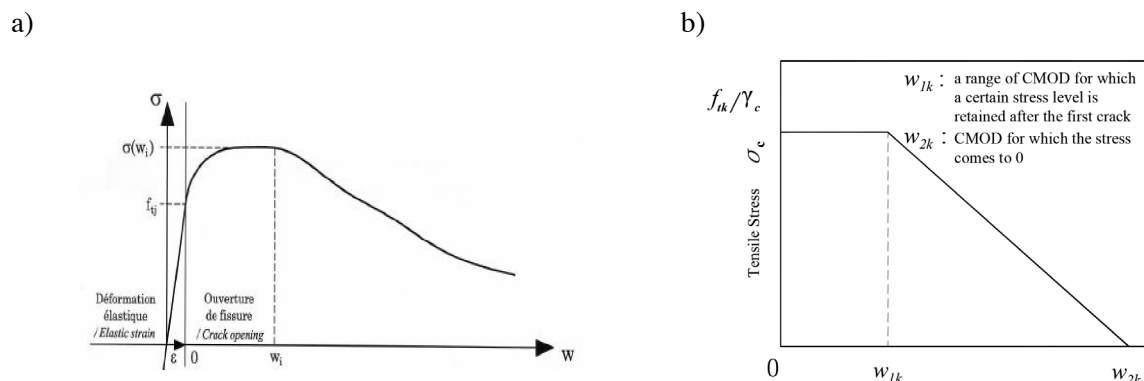


Figure 3.18: Characteristic tensile curves: a) stress-strain and crack opening according to [SETRA, AFGC 2002]; b) idealised stress-crack opening according to [JSCE 2006]

Design curves in recommendations for UHPFRC

In order to simplify computations, current recommendations propose the use of a continuous stress-strain curve including the softening part. It should be remembered that “a complete stress-strain curve does not exist as a material property; in case where such curves are shown, they have to be referred to a certain length over which the additional deformation within the fracture zone has been averaged”, [Hillerborg 1991].

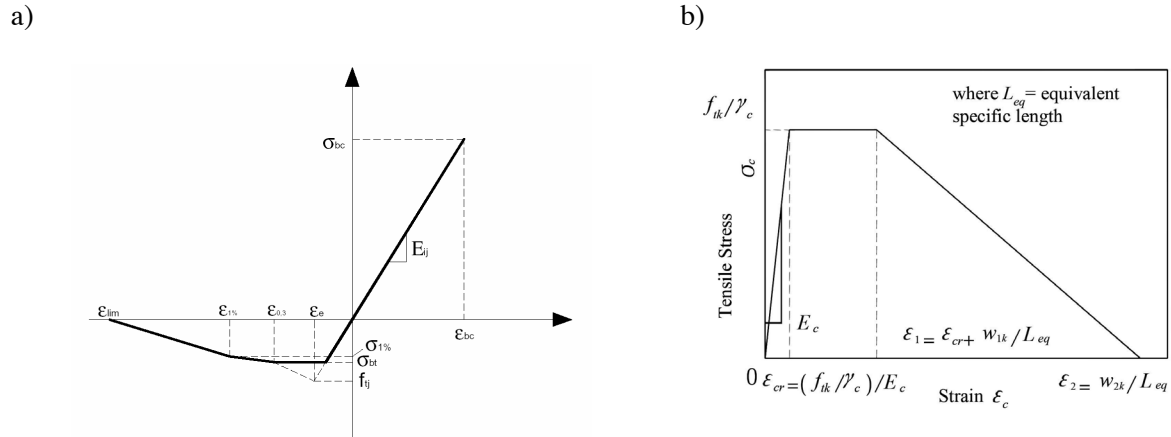


Figure 3.19: Design curves: a) by [SETRA, AFGC 2002]; b) by [JSCE 2006]

French recommendations [SETRA, AFGC 2002] introduce a quantity termed the characteristic length, l_c , for transforming $\sigma(w)$ (Figure 3.18 a)) into the $\sigma(\varepsilon)$ curve (Figure 3.19 a)). The characteristic length is dependent on sectional dimensions, and for rectangular and T cross-sections, a value $l_c=2/3 h$ is proposed by these regulations, with h being the depth of the section. The transformation is based on the relationship

$$\varepsilon = \frac{w}{l_c} + \frac{f_{ct}}{\gamma_c \cdot E_c} \quad (3.20)$$

where γ_c is the appropriate design safety factor.

In Japanese recommendations, the equivalent specific length, L_{eq} , is used to transform the $\sigma(w)$ (Figure 3.18 b)) into the $\sigma(\varepsilon)$ curve (Figure 3.19 b)). This value is calculated using numerical simulations, and is reported as being dependent on section height and shape. The expression for L_{eq} is based on the assumption that the flexural strengths, obtained by the FEM analysis using $\sigma(w)$, is equal to the flexural strength obtained from the section equilibrium using the $\sigma(\varepsilon)$ curve. The following relationship is derived from this numerical analysis:

$$L_{eq} = h \cdot 0.8 \cdot \left(1 - \frac{1}{(1.05 + 6 \cdot h/l_{ch})^4} \right) \quad (3.21)$$

where

$$l_{ch} = \frac{G_F \cdot E_c}{f_{ct}^2} \quad (3.22)$$

For the sake of comparison with the l_c , for a typical UHPFRC with 2% V_f , the value of the equivalent specific length L_{eq} is obtained in the range of $0.16 h - 0.35 h$ for thin elements (10 - 200 mm), that is smaller value, leading to higher tensile deformations, in comparison to $l_c=2/3 h$ proposed by the French recommendations. For more thick elements the difference between L_{eq} and l_c becomes less significant.

Further comments concerning the characteristic length used to transform the $\sigma(w)$ into the $\sigma(\varepsilon)$ can be found in Chapter 4.

3.3.2.8 Tensile behaviour of UHPFRC used in present study; proposed material curves

For the UHPFRC used in this study (Table 3.3) the data are provided from direct tensile tests. Tests were performed at the EPFL Structural Concrete Laboratory. Two types of test specimens were considered: unnotched (Figure 3.20 a)) and notched (Figure 3.20 b)). More information about these tests can be found in [Jungwirth 2006]. Unnotched specimens show lower tensile strength, coinciding with the strength of the statistically least resistant section.

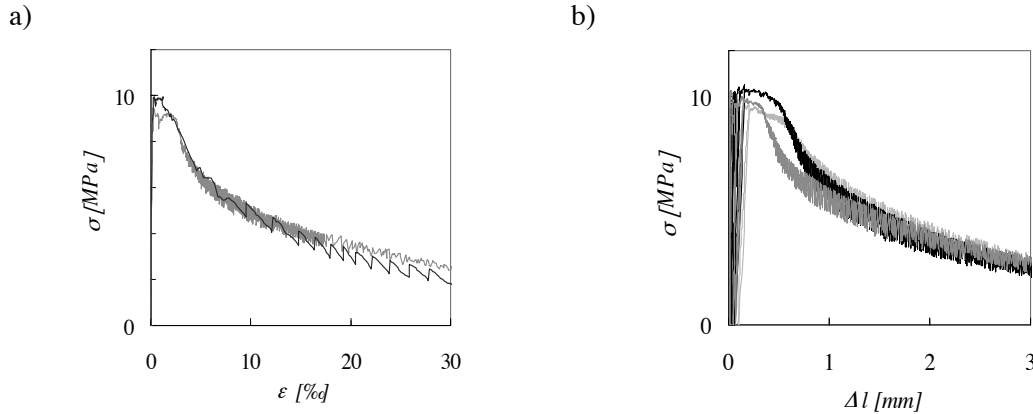


Figure 3.20: Measured response of UHPFRC specimen in uniaxial tension: a) average deformation over measurement base $l_m = 100 \text{ mm}$ of unnotched specimens (G14T1, G14T3); b) elongation of measurement base $l_m = 100 \text{ mm}$ of notched specimens (G15F1, G15F2, G15F); more detailed data are presented in [Jungwirth 2006]

Stress- strain curve

Based on the experimental data (Figure 3.20) and in accordance with the previous analytical considerations (§ 3.3.2.4) the multi-microcracking takes place throughout the volume of the element up to a certain deformation. Microcracks are spaced closely together, with small openings, invisible to the naked eye. For a representative volume relevant for the structural scale, the integral of localised deformations can be considered as a state of uniform change in the material's structure, thus giving a homogeneous continuous behaviour, as if no localisation took place. From the bulk strain and stress increases, the average uniaxial values can be obtained as follows:

$$\sigma_{xx} = \frac{1}{A} \int_A \sigma_{i,xx} dA, \quad (3.23)$$

$$\varepsilon_{xx} = \frac{1}{L} \int_L \varepsilon_{i,xx}(x) dx, \quad (3.24)$$

where x is direction of tensile force, and A is cross-section of the element.

For the studied UHPFRC, the tensile behaviour before localisation of deformations is represented by a bilinear $\sigma(\varepsilon)$ curve (Figure 3.21). This curve is obtained respecting the integral of the force, based on the following assumptions:

- the elastic part is characterised by $f_{ct} = 9 \text{ MPa}$ and $E_c = 60 \text{ GPa}$, (Appendix T1),
- multi-microcracking is represented by a hardening with zero slope, designated the pseudo-plastic plateau
- the pseudo-plastic plateau is limited to $\varepsilon_u = 2.5 \text{ ‰}$, also according to [Jungwirth 2006].

The stress-strain relationship in unloading, E_d , is considered to be constant for a pseudo-plastic deformation attained (Figure 3.21 b)). For the tested material, the value of the unloading slope for the

maximal pseudo-plastic deformation attained, ε_u , is $E^* = 5.8 \text{ GPa}$, based on data from [Jungwirth 2006].

The advantage of a bilinear material model with zero hardening slope is that it enables the simple development of analytical expressions for prediction of element resistances. Moreover, it is shown in Chapter 4 that this model is appropriate for simulation of the behaviour of elements made of other UHPFRCs, and materials that exhibit slight strain hardening. Significant pseudo strain hardening slopes are very rarely observed in UHPFRC.

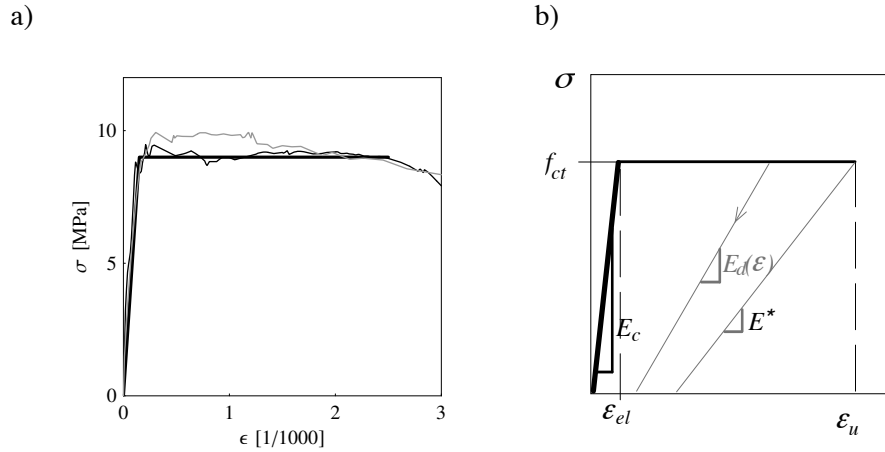


Figure 3.21: a) Measured and assumed constitutive stress-strain relationship (up to ultimate homogenous deformation) for BSI UHPFRC; b) characteristic points of the $\sigma(\varepsilon)$ curve (notations)

Stress-crack opening

The stress–crack opening, $\alpha(w)$, curve characterises the material at the fracture zone. The analytical expression for design relevant $\alpha(w)$ relationship can be formulated providing that the portions of fracture energies required for small crack openings are maintained. This yields the shape of the curve with the initial slope corresponding to the slope of the measured curve. The importance of this criterion is explained in Chapter 4.

According to § 3.3.2.6, the energy required to open the crack of a unit area from crack opening level w_i to w_{i+1} , is

$$\Delta G_{F_i} = \int_{w_i}^{w_{i+1}} \sigma(w) dw. \quad (3.25)$$

If an interpolation function is found over the measured data, $\{\{\sigma, w\}\}$, an approximate $\alpha(w)$ function is sought, verifying the accuracy of the approximate function using the equality of the energy portions (Equation 3.25) as follows:

$$\int_{w_i}^{w_{i+1}} \sigma_{\text{interpolation}}(w) dw = \int_{w_i}^{w_{i+1}} \sigma_{\text{approximate}}(w) dw \quad (3.26)$$

For further analytical implementation in design, the additional criterion was the simplicity of the form of the approximate function, and its integrability.

It is found that the stress-crack opening relationship is satisfactorily approximated either by the multi-linear curve (Figure 3.22 b), Equation 3.32), or the curve of the following analytical shape (Figure 3.22 a)):

$$\sigma(w) = f_{ct} \cdot \frac{1}{\left(1 + \frac{w}{w_{n,w}}\right)^p} \quad (3.27)$$

where both the parameters, $w_{n,w}$ and p , are determined from data fitting. Good correlation with test results was found for parameter $p=1.2$. The parameter $w_{n,w}$ corresponds to the crack opening at which stress decreases to the value of $2^{-p} f_{ct}$. In the case of the measured curves, with $p=1.2$, $w_{n,w}$ yields $w_{n,w} = 1 \text{ mm}$.

This curve is similar to the curve proposed by the empirical model of Stang [Stang et al. 1995], [Li 1993Li et al. 1993]:

$$\sigma(w) = f_{ct} \cdot \frac{1}{1 + \left(\frac{w}{w_{1/2}}\right)^p} \quad (3.28)$$

where p and $w_{1/2}$ are also the parameters to be obtained from experimental data, and, similarly to the previous curve, $w_{1/2}$ corresponds to the crack opening when stress decreases to $0.5 f_{ct}$.

The advantage of the curve proposed in Equation 3.27 is that the initial slope is a determined value:

$$\lim_{w \rightarrow 0} \frac{d\sigma(w)}{dw} = -\frac{f_{ct} \cdot p}{w_{n,w}} \quad (3.29)$$

since

$$\frac{d\sigma(w)}{dw} = -\frac{f_{ct}}{w_{n,w}} \cdot p \cdot \left(1 + \frac{w}{w_{n,w}}\right)^{-(p+1)} \quad (3.30)$$

while, for $p \neq 1$, it is indeterminate for Equation 3.28. Both curves exhibit the similar inaccuracy for stress at higher crack openings: neither the stress nor the slope of the curves at $w = w_{cr}$ yields zero, Figure 3.22 a). However, this inaccuracy occurs for large crack openings ($> 6 \text{ mm}$), which, as shown in Chapter 4, are of no practical interest in the major part of the analysis (bending, bending with N force).

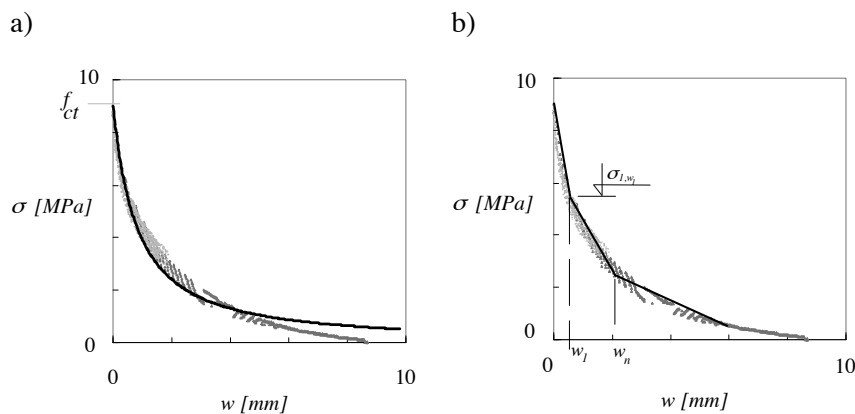


Figure 3.22: Material constitutive law for stress-crack opening relationship and measured data: a) curve resulting from Equation 3.27; b) multilinear curve.

An additional advantage of Expression 3.27 is that it is an integrable function for $w > 0$:

$$\int_w \sigma(w)dw = f_{ct} \frac{-\left(1 + \frac{w}{w_{n,w}}\right)^{-p} \cdot \left(w + w_{n,w} - w_{n,w} \left(1 + \frac{w}{w_{n,w}}\right)^p\right)}{p-1}. \quad (3.31)$$

For the development of analytical expressions for further elements analysis, it was found more suitable and equally accurate to use a multilinear curve to describe the stress-crack opening relationship¹:

$$\begin{aligned} \sigma_w(w) &= C_1 - C_2 w = f_{ct} - \frac{f_{ct} - \sigma_{w1}}{w_1} w \quad \forall 0 \leq w \leq w_1 \\ \sigma_w(w) &= C_3 - C_4 w = \sigma_{w1} - \frac{\sigma_{w1} - \sigma_{w2}}{w_1 - w_2} (w - w_1) \quad \forall w_1 \leq w \leq w_2, C_3 = \sigma_{w1} + \frac{\sigma_{w1} - \sigma_{w2}}{w_1 - w_2} w_1, C_4 = \frac{\sigma_{w1} - \sigma_{w2}}{w_1 - w_2}, \\ &\text{etc.} \end{aligned} \quad (3.32)$$

where the inflection points, $\{\{w_i, \alpha(w_i)\}\}$, can be found using the curve proposed in Equation 3.27 and condition 3.26. For the first part of the linear curve, the equality of the slopes (Equation 3.29) can also be used as a criterion for definition of the parameters in Equation 3.32. For the given data, the first inflection point is set at $w_1 = 0.5 \text{ mm}$.

Furthermore, considering that for the most frequent design needs (e.g. bending resistance), only the small crack openings range is attained, the first linear part of the $\alpha(w)$ is typically sufficient.

Consideration of some other $\alpha(w)$ curves

The curve proposed by Behloul's model [Behloul 1996] (Equation 3.15) with approximation of the function $F(\alpha, r)$ by a polynomial curve $(1-r)^\gamma$ yields the shape

$$\sigma(w) = f_{ct} (1-r)^\gamma = f_{ct} \left(1 - \frac{w}{w_{cr}}\right)^\gamma \quad (3.33)$$

where $\gamma = 2 / \alpha$. For an isotropic case ($\alpha = 0.5$), for example, the function $F(\alpha, r)$ yields $(1-r)^4$. A similar curve shape is proposed by Kosa and Naaman [Kosa, Naaman 1990] with $\gamma = 3$. The initial slope of this curve is influenced by the ratio between tensile strength and critical crack opening (w_{cr} , which is typically assumed as $l_f/2$), and the parameter γ :

$$\text{Lim}_{w \rightarrow 0} \frac{d\sigma(w)}{dw} = -\frac{f_{ct} \cdot \gamma}{w_{cr}} \quad (3.34)$$

since

$$\frac{d\sigma(w)}{dw} = -\frac{f_{ct}}{w_{cr}} \cdot \gamma \cdot \left(1 - \frac{2w}{l_f}\right)^{\gamma-1}. \quad (3.35)$$

This curve was found suitable for different materials [Marti et al. 1999], including ordinary concrete [Kenel 2002] where γ is found by the least-squares fit, as a value ranging between 4 and 6. However the initial slope with the mentioned range of γ is found unsatisfactory for describing the behaviour of the tested UHPFRC (Figure 3.23 a)). The reason is the difference in ratio between f_{ct} and w_{cr} , (as parameters influencing the initial slope, Equation 3.34). Consequently, higher γ values enable a

¹ Bilinear curves are commonly used for modelling of softening behaviour of ordinary and SFRCs [RILEM 2002];

better fitting of the first part of the curve, but in this case the rest of the curve is not well followed (Figure 3.23 b)). Additionally, it should be stated that, using a standard procedure for fitting the parameters (e.g. least-squares fit) over the whole set of data, the obtained curves may respect the integral

$$\int_0^{w_{cr}} \sigma_{approximate}(w)dw = G_F ,$$

but stress values in the initial part of the curve are overestimated, which can lead to unreliable predictions of the element's resistances (Figure 3.23 b)).

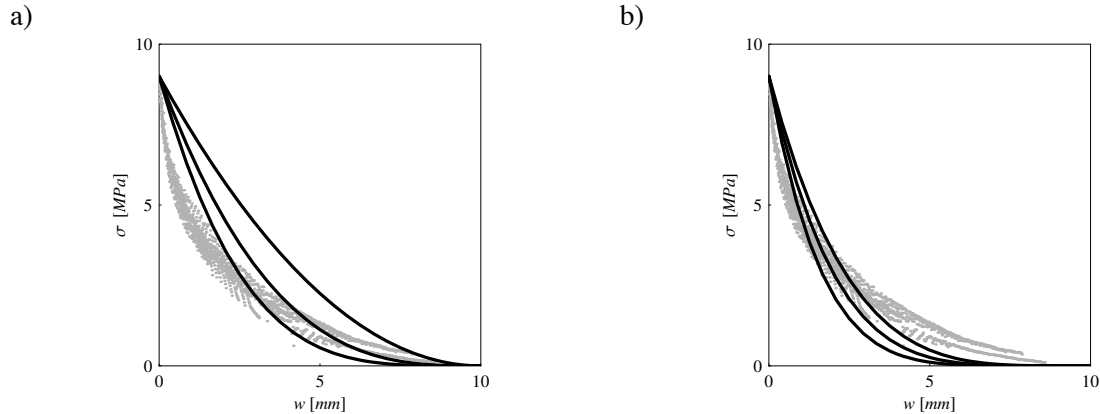


Figure 3.23: Modelling of tensile strain softening according to Equation 3.33: a) with $w_{cr}=l_f / 2$ and $\gamma = 2, 3$ and 4 ; b) with $w_{cr}=l_f / 2$ and parameter γ obtained by fitting for three sets of measured data ($\gamma = 4.2, 5.1$ and 6.3)

Another family of curves is based on the shape proposed by Shah [Shah 1987] :

$$\sigma(w) = f_{ct} \cdot e^{-q \cdot w^p} \tag{3.36}$$

with q and p being fitting parameters. A plot of such a shape against the measured data is shown in Figure 3.24. This expression enables material behaviour to be represented with sufficient precision. It is found less attractive for analytical application in the design of elements however. In cases where numerical integration is applicable, this form of curve can be well applied.

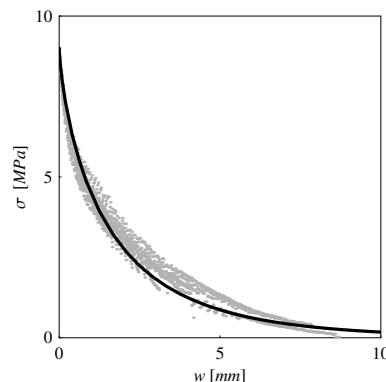


Figure 3.24: Fitted exponential curve (Equation 3.36) with obtained parameters $q = 0.7$ and $p = 0.75$

3.3.2.9 Concluding remarks

UHPFRC is a material that exhibit high tensile strengths, in the range of 10 MPa , but especially high tensile strains ($2\text{--}3\text{ ‰}$), achieved with no decrease in stress (Figure 3.25). This behaviour, governed by the presence of short fibre reinforcement with random distribution, must be able to develop in the structural element, for it to be implemented as a material property in the design. To this end, a minimal quantity of fibres and their effectiveness need to be assured. It is shown both experimentally and analytically that in a UHPC matrix, providing that the casting procedure is correct, strain hardening behaviour can be achieved as from a fibre volume fraction of 2 ‰ .

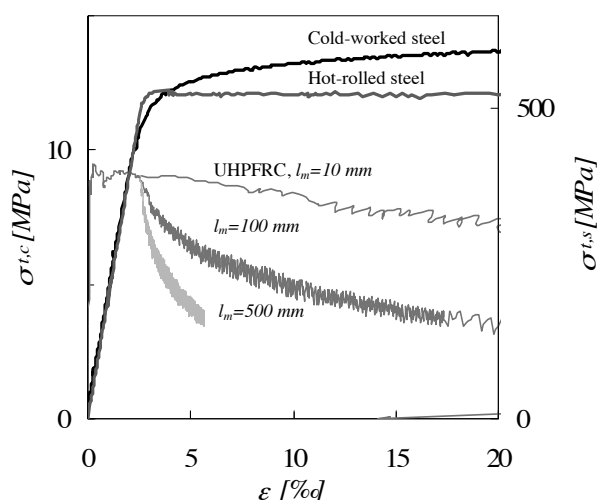


Figure 3.25: Comparison of tensile capacities of UHPFRC and reinforcing steel bars: for the softening part of stress-deformation curve of UHPFRC, deformations of the element are averaged over different lengths, l_m ; deformations of the steel bars are provided by tests [Redaelli 2006], and values are in agreement with the code [CEB 1993]

The UHPFRC used in this study, containing a 2.5 ‰ steel fibre volume fraction, is characterised by a tensile strength of 9 MPa with a plateau in tension reaching 2.5 ‰ (Figure 3.25).

The structure-relevant crack is considered to develop with tensile strain softening. This crack transfers a significant part of the tensile stress (a “fictitious crack”), resulting in a high fracture energy value in comparison to other concretes (higher than 10 KJ/m^2 compared to approx. 100 J/m^2 , Figure 3.26).

Models for the description of strain-softening behaviour are investigated and a simple analytical formulation is proposed. For design needs only the small crack opening range is of interest, and it is sufficient to apply the linear stress-crack opening relationship, respecting the slope of the softening curve rather than the integral up to maximal crack opening (G_F). Continuous curves may be of more interest for numerical application.

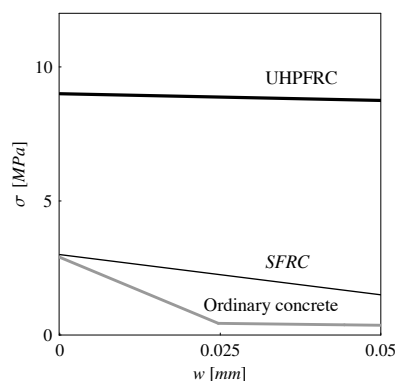


Figure 3.26: Comparison of slopes of softening curves of UHPFRC, SFRC and ordinary concrete

3.4 Other material properties of UHPFRC

The material properties referred to in the following sections, although important in providing correct structural performance, are not the subject of the present research. For this reason only the principal points and relevant references are summarised.

3.4.1 Long term behaviour: shrinkage, creep, self-healing

According to some authors, creep and shrinkage are “the most outstanding characteristics” of UHPC [Acker, Behloul 2004], since the effect of both phenomena is significantly decreased.

Shrinkage is a process primarily caused by the self-dessication, and due to the low water-cement ratio in UHPFRC, it is reported that the major part of shrinkage occurs immediately after settling, while practically no shrinkage occurs after early age. A difference in behaviour is reported between thermally treated and non-treated UHPC. According to French recommendations [SETRA, AFGC 2002], autogenous shrinkage is defined as a function of the water-cement ratio, and for thermally non-treated material with a water-cement ratio of $0.17 - 0.20$, for time $t \rightarrow \infty$, the shrinkage value is $550 \mu\text{m}/\text{m}$. For thermally treated material no shrinkage develops according to these recommendations. Certain manufacturers of UHPFRC give similar values: zero to $10 \mu\text{m}/\text{m}$ post-cure shrinkage and $550 \mu\text{m}/\text{m}$ for thermally non-treated material characterises Ductal, the UHPFRC manufactured by Lafarge [Graybeal 2006].

Creep is closely related to shrinkage behaviour from the microstructural point of view, [Acker 2004a], and it is observed that thermal treatment significantly reduces creep [SETRA, AFGC 2002]. The evolution of creep function depends on the age of the material at loading. For example, a creep coefficient of $0.2-0.8$ is suggested for Ductal, with the lower values corresponding to thermally treated material and the higher to non-treated material. In normal concrete, the creep coefficient can reach the value of 3 to 4. Low creep values are of particular interest for the application of prestressing (reduction of prestress losses).

More details concerning the creep and shrinkage of UHPC, HPC, and ordinary concrete, based on the description of microstructural changes, can be found in [Acker 2004], [Acker 2004a] and [Kamen 2007].

Another positive consequence of a low water-cement ratio and the fact that a considerable percentage of the cement paste remains unhydrated, is that, in the presence of humidity, further hydration can take place in microcracks. This is known as the self-healing effect. The results of an experimental programme conducted in order to quantify the self-healing of UHPC materials are reported in [Granger et al. 2007], [Hearn, Morley 1997]. Both the recovery of global stiffness and the improvement in strength of initially cracked specimens are reported, as a function of the time of healing. The stiffness recovery is due to the formation of new crystals with a stiffness close to that of the C-S-H crystals that were initially formed.

3.4.2 Porosity, durability

As already mentioned in relation to the conception principles of UHPC, the matrix is tailored in order to decrease porosity on different scales, resulting in hardly any capillary porosity in comparison with other concrete materials [Vernet 2003], [Schmidt, Fehling 2005], Figure 3.27.

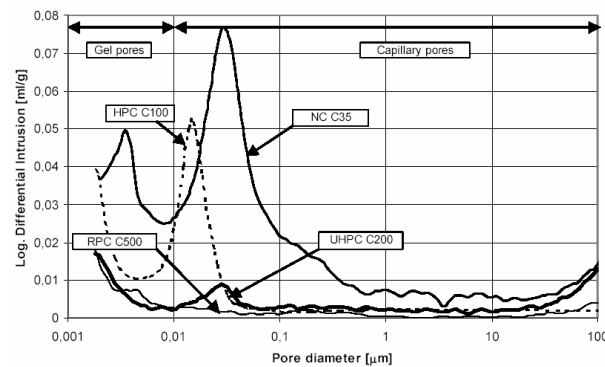


Figure 3.27: Distribution of pores of different size in UHPC, HPC and ordinary concrete, from [Schmidt, Fehling 2005]

The durability of UHPFRC is related to this impressively decreased porosity, and to generally improved material homogeneity. This results in highly improved resistance to the penetration of chlorides, frost and freezing attack, etc. Various laboratories are investigating these issues worldwide. More detailed information on these properties and characteristic durability values can be found in [Vernet 2003], [Schmidt, Fehling 2005].

Microcracking, characterised by small crack openings, has been proved to have only a small impact on permeability, and consequently durability [Aldea et al. 1999].

3.4.3 Energy-dissipation capacity, impact resistance

UHPFRC has a high energy-dissipation capacity, which ensures cracking stability even in the case of relatively strong impact. For typical rates of impact loading on civil engineering structures, it is demonstrated that tensile strength increases up to two times, and compressive strengths up to 1.5 times according to [SETRA, AFGC 2002] and based on research on RPC, e.g. [Toutlemonde et al. 1998].

3.4.4 Fire resistance

UHPFRC reinforced with steel fibres only exhibits relatively unfavourable behaviour. Due to the low content of connected pores, and higher enclosed porosity, steam cannot escape, resulting in an increase in internal stresses in the presence of high temperatures. Fire resistance problems can be avoided by the use of organic fibres, [Acker, Behloul 2004], which, in melting, create communication between the pores. The addition of approximately 0.7 % in volume of polypropylene fibres provides sufficient fire resistance [Heinz et al. 2004].

3.5 Conclusions

UHPFRC is a new, advanced concrete material of elaborated composition, with remarkably superior mechanical strengths and durability in comparison to other concretes.

As a result of material optimization on different scales, the obtained UHPC microstructure is very homogeneous and compact, with almost no capillary porosity. The developed microstructure explains the significantly improved mechanical properties. Ductility is achieved by the addition of short fibres, in an optimal quantity that also maintains the workability of the fresh mixture.

The compressive strength of UHPFRC is higher than 150 MPa; tensile strength, in the range of 10 MPa, is characterised by significant ultimate strain (approx. 2-3 ‰), and the cracking behaviour of the composite is characterised by a fracture energy higher than 10 kJ/m².

From a qualitative point of view, the compressive behaviour of UHPFRC does not differ substantially from the behaviour of ordinary concrete, and it is possible to model it with a slight adaptation of material laws used for ordinary concretes. More detailed conclusions on the behaviour in compression and modelling are given in § 3.3.1.6.

The tensile behaviour of UHPFRC is characterised by the strain-hardening phase, often with a small slope, that distinguishes it from other concretes and FRCs. The potential of the material to develop strain-hardening phase depends on the quantity of fibres and their orientation, the latter being strongly influenced by the casting procedure. Details of this behaviour and modelling possibilities for further design needs are discussed in § 3.3.2, and conclusions are given in § 3.3.2.9.

In addition to mechanical strengths, the properties of interest for structural application such as creep and shrinkage, durability, and impact strengths are also impressively improved due to the material microstructure.

The combination of these properties postulates more advanced structural application:

- high strengths and ductility, combined with material durability, suggest that applications without passive reinforcement, and with a decrease in element size, may be possible;
- the plasticity of the fresh material allows easy placement in a variety of formworks, without additional vibrating; combined with the fact that the ordinary reinforcement can be excluded, a gain in production time and a greater freedom of form are possible.

4. Analysis and design of UHPFRC structural elements in bending

The objective in this chapter is to study bending behaviour of UHPFRC elements and develop a practical procedure for their analysis and design. Elements without conventional reinforcement are considered.

The specific mechanical properties of the material lead to an element bending response with a pronounced non-linear part, governed by multi-microcracking in the tensile region and the propagation of a localised macrocrack. For this reason fracture mechanics theories are required for understanding UHPFRC element response in bending. An analytical model describing the behaviour of elements in the presence of pseudo-plastic tensile strain (representing multi-microcracking) and the localised crack is developed in this study. The results are compared with the experimental results obtained in a test programme on thin UHPFRC elements in bending (Appendix T1). The results of the analytical model are also compared with the results of a developed numerical model for finite element analysis. The plausibility of analytical results is also demonstrated for elements made of other quasi-brittle materials, with and without the multi-microcracking phase. A simplified version of the model is proposed for design purposes.

The influence of the specific tensile properties of UHPFRC on bending strengths and ductility are studied by means of parametric analysis, with the major parameters for the analysis being the maximal deformation achieved during the microcracking phase and the slope of tensile softening law. Based on these results, the size effect in relation to strength and to the deformational capacity of elements made of UHPFRC and other quasi-brittle materials is discussed. Conclusions regarding practical design procedures for UHPFRC thin elements without ordinary reinforcement are drawn.

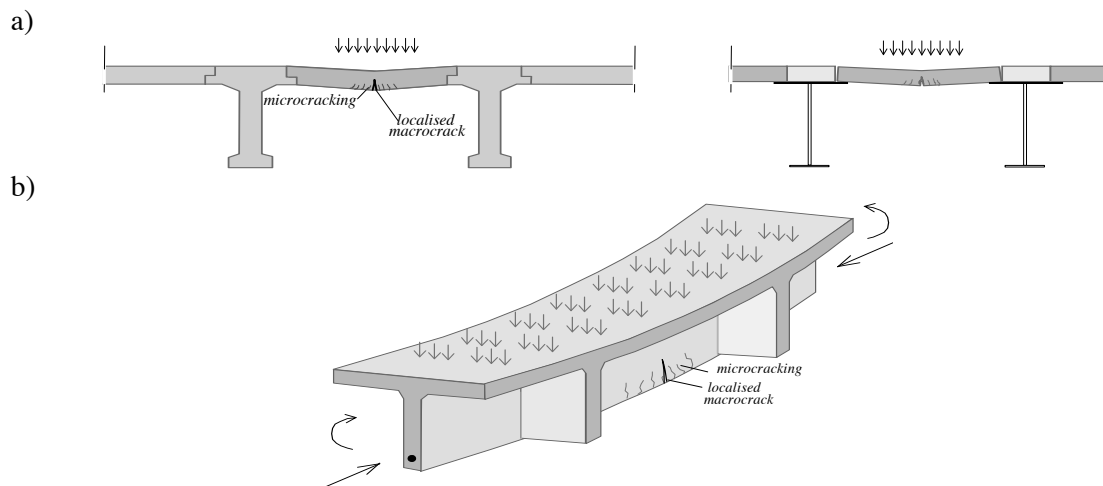


Figure 4.1: UHPFRC structural elements failing in bending, without the possibility of redistributing internal force; thus the resistance of the element corresponds to the resistance of a critical section; a) thin elements without ordinary reinforcement; b) deep elements, with prestressing reinforcement

4.1 UHPFRC elements in bending: problems involved

Models that describe the bending behaviour of UHPFRC in a physically realistic way and allow prediction of resistance to bending failure are required for structural design. The principal difference between the behaviour of UHPFRC elements and those made of ordinary RC and FRC is that a significant tensile force is sustained by the material itself, primarily due to significant ductility in tension. These mechanical properties change both the design approach and the structural concept for

an appropriate application of UHPFRC, allowing ordinary reinforcement to be excluded in some structural elements.

UHPFRC elements of interest for structural application are thin slabs without ordinary reinforcement, with a short span (Figure 4.1 a)), or deeper prestressed beams with a longer span (Figure 4.1 b)). In statically determinate systems failing in bending, the resistance of the element is governed by the resistance of a critical section. In statically indeterminate systems (Figure 4.2) the rotational capacities of the first cracked sections may provide a certain amount of force redistribution, enabling further increase in load. These systems are studied in Chapters 5 and 6, while the present chapter deals with the bending of statically determinate systems.

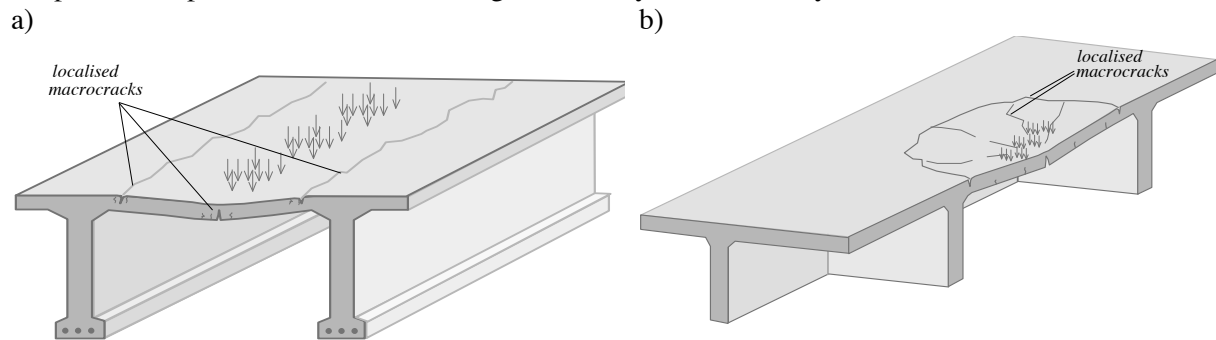


Figure 4.2: UHPFRC structural elements failing in bending with the possibility of redistributing internal force; the resistance of the element is higher than that of the first cracked section, a) thin slab with two line supports (in I-shaped girder); b) thin slab with four line supports (in ribbed slab)

Design recommendations for UHPFRC structures

Intensive work has been carried out on developing design recommendations for UHPFRC in recent years by different national and international research committees. These efforts have focused on material characterisation, formulation of material constitutive laws, and resistance models. Current documents remain at the level of provisions:

- Interim Recommendations by the UHPFRC working group of the French Association of Civil Engineers, AFGC, and the Technical Department for Transport, Roads and Bridges Engineering and Road Safety within the French Ministry for Transport, SETRA, chaired by B. Lecinq and J. Resplendino [SETRA, AFGC 2002]; the document is based mostly on the recommendations for steel-fibre reinforced concrete by AFREM;
- The Draft Recommendations for UHPFRC of the Japanese Society of Civil Engineers, JSCE, published on September 2006 [JSCE 2006];
- A State-of-the-art Report on UHPC by the German Association for Reinforced Concrete, published in 2003 [DAfStB 2003];
- Material Property Characterisation of Ultra-High Performance Concrete, a report published by the U.S. Department of Transportation [Graybeal 2006].

The documentation published by the RILEM technical committee 162 on fibre-reinforced concretes may also provide useful information for the design of UHPFRC elements [RILEM 2002].

Considering the design in bending, a transition from knowledge gained at the material level to safe application in structural elements becomes a delicate task, owing to the fact that the bending resistance of a UHPFRC member is associated to cracking behaviour which is affected by size effect. This phenomenon characterises all quasi-brittle material, and is also well recognised for ordinary concrete ([CEB 1993], [Bazant, Cedolin 1991]), although the fracture properties of concrete elements reinforced with ordinary bars are not normally included in design. Moreover, the bending resistance of an RC element is determined according to the theory of plasticity [SIA 2003b], with no tensile forces being sustained by the concrete. When it comes to materials with a significant tensile

strain hardening and tensile softening capacity, such as UHPFRC, the material's capability to sustain tensile forces is of interest in design.

4.2 Fracture models for quasi-brittle materials

Since crack formation and propagation play an important role in both ordinary and fibre-reinforced concrete structures, fracture mechanics (FM) theories can be applied in assessing their behaviour at failure [Bazant 1976]. The characteristics of cracks in concretes, being quasi-brittle materials, make the use of non-linear FM theories obligatory. Among existing approaches, the most widely accepted are the fictitious crack model, (FCM) proposed by Hillerborg, Modéer and Petersson [Hillerborg et al. 1976], and the crack band model proposed by Bazant [Bazant 1976], [Bazant, Oh 1983]. The two models differ mainly in the concept of the crack zone (Figure 4.3). Some other approaches to modelling cracks in concrete can be found in literature [Carpinteri, Massabò 1997], [Li et al. 1996].

Fictitious crack model

The FCM is an application of the Dugdale-Barenblatt strip yield model, with the assumption of a non-constant intensity of the stress transferred at the crack tip (Figure 4.3 a)). It is also known as the “cohesive zone model” [Hillerborg 1991]. Most of the models describing the behaviour of concrete structures in the presence of a localised crack apply the principal hypotheses of the FCM. In the present thesis the FCM is also used for the development of an analytical bending model (§4.3.5) and for a numerical, finite element model (Appendix M2). For this reason the hypotheses of the FCM are detailed:

- the intensity of the stress transferred over the crack (fracture mode I) is a monotonically decreasing function of the separation of crack surfaces (henceforth referred to as crack opening in further text), $\sigma = \sigma(w)$; the stress-crack opening relationship is a material property defining the fracture zone, which replaces conventional fracture mechanics material properties, such as K_I , G , J , COD [Hillerborg 1980];
- the fracture process zone is the fictitious crack itself [Hillerborg 1980], and the total energy dissipated in the crack is dissipated for the crack opening;
- the crack forms when the tensile strength, f_{ct} , is reached at the crack tip, and propagates with the same value of tensile stress at this point (Figure 4.3 a)). For this reason the stress intensity factor loses its significance in the FCM.

The FCM is suitable for implementation in a structural model analysed by a finite element method. The model enables the stability of crack growth for any $\sigma(w)$ relationship to be observed in a realistic way. The size effect can also be predicted by this model.

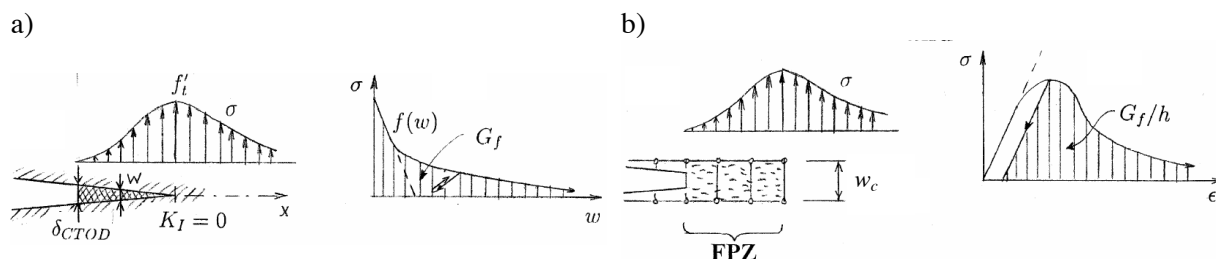


Figure 4.3: Crack models for quasi-brittle materials: a) fictitious (cohesive) crack model; b) crack band model; from [Bazant 2002]

Crack band model

Similarly to the FCM, the crack band model, proposed by Bazant, enables the formation and propagation of a crack transferring tensile force to be described accurately, and the size effect to be

observed. The principal difference is that the line crack is replaced by a band, of width w_c , in which the non-linear deformations near the crack are uniformly smeared (Figure 4.3 b)). This approach may be more appropriate for finite element analysis, but it is essentially equivalent to the line crack approach if the mean strain across the crack band corresponds to the ratio of the crack opening over the w_c [Bazant, Cedolin 1991].

4.2.1 Existing models for bending in quasi-brittle materials

The bending behaviour of quasi-brittle materials can be described by models that take into account the development and propagation of a discrete crack transferring tensile force. Particularly since the first developments in fibre-reinforced concretes (FRC), characterised by significant tensile force transfer over the crack, numerous models for describing bending response have been proposed in the literature. According to the approach used to describe the crack, two groups of bending models can be distinguished:

- continuous models, and
- discrete crack models.

In continuous models the influence of crack opening is smeared over a certain distance, usually as a function of element depth and the correlated stress-strain, σ - ε , relationship is used to characterise the crack¹. The development of some of the continuous approaches for bending can be found in [Naaman et al. 1993], [Behloul 1996] etc. In the year 2000, the RILEM committee for FRC published the Recommendations for σ - ε design method for SFRC elements [RILEM 2000].

The major difference between continuous and discrete crack bending models is that in the latter the stress transferred by a crack is expressed as a function of crack opening, based on the assumptions of the FCM, [Ulfkjær et al. 1995], [Armelin, Banthia 97], [Stang, Olesen 1998], [Olesen 2001]. Various approaches for analysing structural response in the presence of a discrete crack are proposed, differing principally in the way in which the crack-surrounding region is modelled:

- the crack implemented in a linear continuum; in this case the disturbance of the stress field due to stress decrease in the crack is taken into account by finite element method (FEM) analysis;
- the crack modelled as a non-linear hinge; in this case kinematic assumptions are made enabling the region surrounding the crack to be taken into account regardless of the real state of stress.

The possibilities and limits concerning the application of discrete crack models in analysing UHPFRC in bending were investigated in the present research and thus the main assumptions of some of these models are detailed. The comparison between the results from existing discrete models and results from the model developed in this thesis are given in Section 4.4.

4.2.1.1 Models for non-linear hinge

The hypotheses applied in non-linear hinge models, summarised below, enable the presence of a discrete crack in a bending element to be taken into account without the need for FEM analysis:

- the non-linear behaviour of the element is concentrated in the zone of the hinge, of length s , whose endfaces are assumed to remain plane, providing continuity with the rest of the element (Figure 4.4);
- mechanical equilibrium in the cracked section is established using the tensile softening stress-crack opening relationship in the cracked part, while the rest of the section follows the linear-elastic material law (e.g. Figure 4.5 a));
- kinematic assumptions are introduced to describe the hinge zone (Figure 4.4), while the rest of the structure behaves linear-elastically. The classic non-linear hinge approach gives an average curvature that corresponds to a given crack opening, while some other models (e.g [Casanova, Rossi 1996]) enable the curvature in the very cracked section to be distinguished.

¹ In some of the earliest works on the bending of SFRC, [Swamy, Mangat 1974], bending resistance was considered only as a characteristic of the composite material.

A state-of-the-art document on non-linear hinge models for bending of SFRC is published by [RILEM 2002].

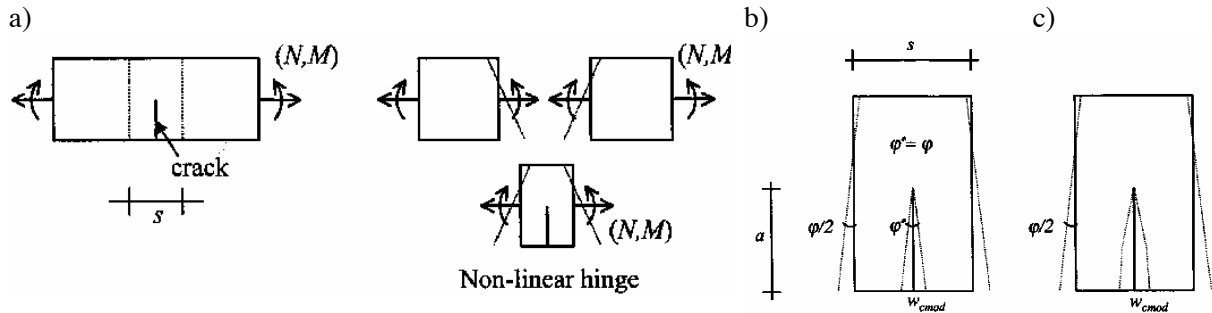


Figure 4.4: a) Concept of the non-linear hinge; b) and c) different kinematic assumptions; from [RILEM 2002]

In the non-linear hinge model proposed by Pedersen [Pedersen 1996], the kinematic hypothesis assumes that the fictitious crack surfaces are plane, and that the crack opening angle is equal to the overall rotation (angular deformation) of the non-linear hinge (Figure 4.4 b)). The crack propagates when maximal tensile strength is attained at the crack tip (Figure 4.5 a)). The non-linear hinge is related to the crack mouth opening displacement, w_{CMOD} , as follows:

$$h - x_0 = \frac{1}{\varphi} \cdot \left(\frac{f_{ct}}{E_c} \cdot s + w_{CMOD} \right) \quad (4.1)$$

for a constant distribution of the curvature, $\chi = f_{ct} / E_c / (h - x_0 - a)$, along the length s of the non-linear hinge. In this formulation h is the section height, x_0 the position of the neutral axis, a crack length, φ rotation (Figure 4.5 a)), and f_{ct} and E_c are tensile strength and modulus of elasticity. By defining a value for parameter s , the relationship between bending moment and rotation (or the averaged curvature) can be found based on the equilibrium of sectional forces (Figure 4.5 b)).

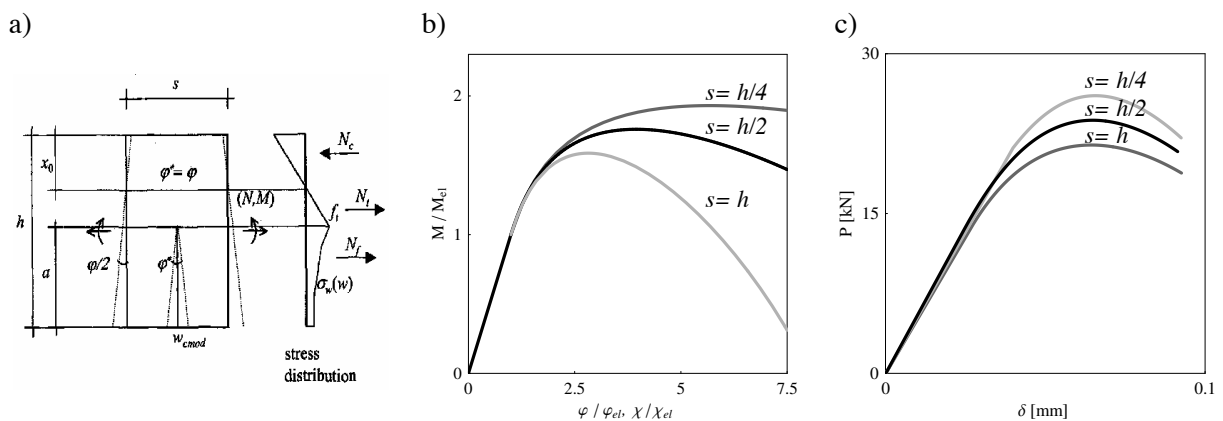


Figure 4.5: Non-linear hinge model proposed by Pedersen: a) kinematic and force equilibrium of non-linear hinge; b) simulated moment-rotation (or average curvature) relationship with variation of the non-linear hinge length (parameter s); c) simulated force-displacement response of a beam in three-point bending

For application in structural analysis, the length of the non-linear hinge, s , is considered a fitting parameter. According to the author and others [Ulfkjaer et al. 1995], [RILEM 2002], it has been shown that reasonable results are obtained with $s = h/2$ for plane concrete and FRC. The model is used to simulate moment-rotation relationships for a FRC beam and the results are plotted in Figure 4.5 b) for different values of parameter s ($s = 1/4 h$, $1/2 h$ and h). The geometry of the beam and material properties are assumed as in the case study presented in [RILEM 2002]: beam of span $L = 500$ mm, and constant cross section 150×150 mm, subjected to three-point bending; modulus of elasticity $E_c = 35$ GPa, tensile strength $f_{ct} = 3$ MPa, and the initial slope of the strain softening curve of

30 MPa/mm up to crack opening $w = 0.05 \text{ mm}$ and zero stress at $w = 10 \text{ mm}$. It can be seen that varying parameter s results in a significant change in maximal bending resistance, and above all a change in deformational capacity of the non-linear hinge. More ductility is obtained with non-linear hinges of shorter lengths. Considering the simulated force-displacement response as a function of parameter s , the influence on resistant moment remains, while the effect on deformation lessens (Figure 4.5 c)). For the given boundary conditions, force-displacement relationship is found in a closed form, as a function of s . Otherwise, displacements can be obtained by curvature integration along beam length (Equation 4.20).

Another non-linear hinge model is presented by **Casanova and Rossi** in [Casanova, Rossi 1996], [Casanova, Rossi 1997]. The assumptions of this model regarding the kinematics of the non-linear hinge are similar to those of the model proposed by Pedersen (Figure 4.4 b)) - the angle between the fictitious crack faces remains proportional to the angular rotation, $\varphi = w_{CMOD} / a$. But two curvatures are considered in this model: the curvature in the cracked section, χ_c , and the elastic curvature at the edge of the non-linear hinge, χ_{el} . Assuming a parabolic variation of the curvature along the non-linear hinge, an average value can be obtained ($\chi_m = (2\chi_{el} + \chi_c)/3$). The length of the non-linear hinge varies with the crack length as $\Delta f = 2a$. Examples of application of the model to simulate behaviour of a cracked section in FRC subjected to bending are plotted in Figure 4.6 b) and c). The same beam and material properties used to illustrate the model of Pedersen are applied for this analysis.

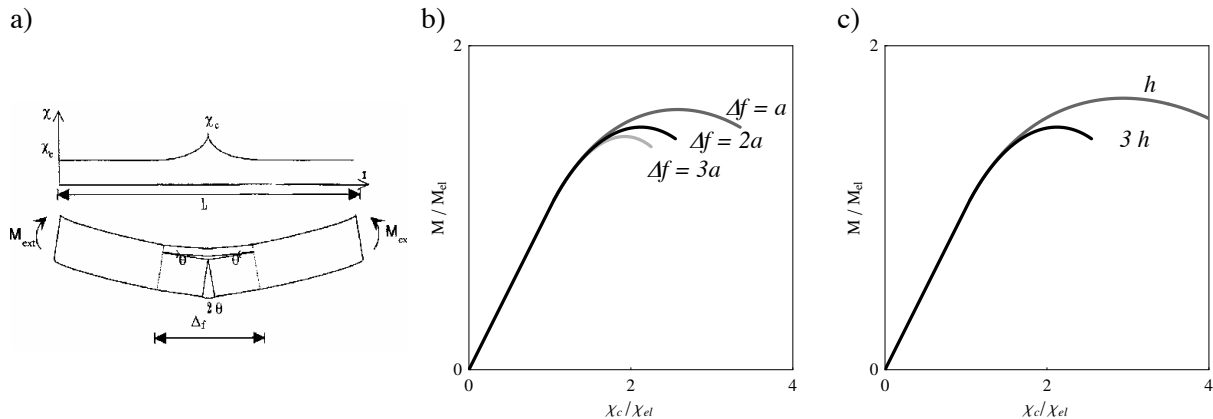


Figure 4.6: Non-linear hinge model proposed by Casanova and Rossi: a) kinematic hypothesis; b) simulated $M-\chi_c$ response of the cracked section, with variation of non-linear hinge length; c) possibility to predict size effect with respect to bending strength and ductility ($\Delta f/a = 2a$)

The model of **Maalej and Li** [Maalej, Li 1994], [Li et al. 1996] applies the concept of the fictitious crack model, FCM, using an iterative procedure to resolve the problem of crack mouth opening displacement w (CMOD), based on the idea of superposition (Figure 4.7): the CMOD w is the sum of the CMOD w_1 of a real (stress-free) crack of crack length a , caused by applied bending moment M (Figure 4.7 b)) and of the closing CMOD w_2 , caused by cohesive stress $\alpha(x)$ (Figure 4.7 c)). The components of crack opening, w_1 and w_2 , are calculated using expressions provided by Tada, Paris and Irwin in [Tada et al. 1985].

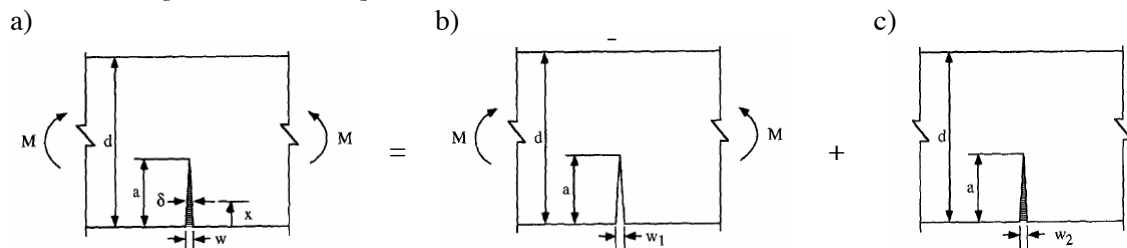


Figure 4.7: Superposition of CMODs in model proposed by Maalej and Li [Maalej, Li 1994]

Other approaches to non-linear hinge modelling (e.g. Figure 4.4 c)) can be found in literature.

The force-displacement (P - δ) response of a beam in bending can be obtained by applying the presented non-linear hinge models, by either integrating the curvature, or superposing the elastic displacement of uncracked beam and the displacement due to the non-linear hinge rotation with the rest of the body assumed as being rigid body. A closed form solution (as a function of s) can be found for the model proposed by Pedersen when a simple tensile softening law is applied. The model of Casanova and Rossi and that of Maalej and Li both require an iterative resolution for M - χ and P - δ relationships.

The models presented above are developed for elements made of materials characterised by tensile softening, for which the deformation localises in a single crack while the rest of the element behaves as a linear-elastic continuum. In the case of UHPFRC, characterised by tensile hardening, the localisation of deformation occurs after the development of a non-linear multi-microcracking phase that extends over a larger part of the beam. This additional non linear contribution is not taken into account by the previously presented models.

4.3 Proposed model for bending of UHPFRC elements

An analytical model for describing the non-linear inelastic bending response of a UHPFRC member is developed in this section. The model enables the resistance and deformability of bending elements required for structural design to be assessed. An element made of UHPFRC attains bending resistance during the cracking phase. For this reason the reliable introduction of the multi-microcracking phase and a localised macrocrack constitute the principal issues of the model.

4.3.1 Approach

The studied structural member is assumed to be of sufficient length in relation to its thickness, and subjected to transversal load, allowing the hypotheses of the classic beam theory to be applied. This enables the analysis and design procedure to be maintained similar to the practical design performed for ordinary civil engineering structures, studying the distribution of stresses and strains in the element via the stress-strain distribution at the cross-sectional level. The mechanical properties of the material in tension result in different states of deformation and correlated stress distribution over the section height. As previously mentioned, in a statically determinate system bending failure is governed by the failure of the most loaded section, termed the critical section.

Based on the deformation states of the critical section, different behaviour regimes of an element in bending are distinguished (Figure 4.8):

- A) Linear-elastic behaviour
- B) Non-linear inelastic behaviour before macrocrack opening
- C) Non-linear behaviour with macrocrack opening, and increase in load-bearing capacity of the element (resistance increase with local tensile softening in the crack)
- D) Post-peak behaviour (resistance decrease)

The study is performed regime by regime, on a beam element subjected to three-point bending (Figure 4.8 c)). The beam has a rectangular cross-section of width b and height h , and the span of the beam is L .

The non-linear phase before macrocrack opening (regime B) is characterised by the presence of multi-microcracking, which is considered a homogeneous material property (§ 3.3.2.8) and is represented by pseudo-plastic yielding in tension (Figure 4.10 b)). This enables the formulation of close form solutions describing the force-displacement relationship for the element before tension softening occurs. Similar approaches to modelling the multi-microcracking phase, applying numerical analysis, are presented in [Casanova 1996], [Kabele 2000], [Kunieda et al. 2002], [Tailhan et al. 2003]. For typical UHPFRC material properties, it is shown that the non-linear behaviour

before the macrocrack starts to propagate is the regime in which the element response during service life is situated. For this reason, it was also important to develop an analytical formulation defining the stiffness of a member in the presence of damaged (microcracked) regions.

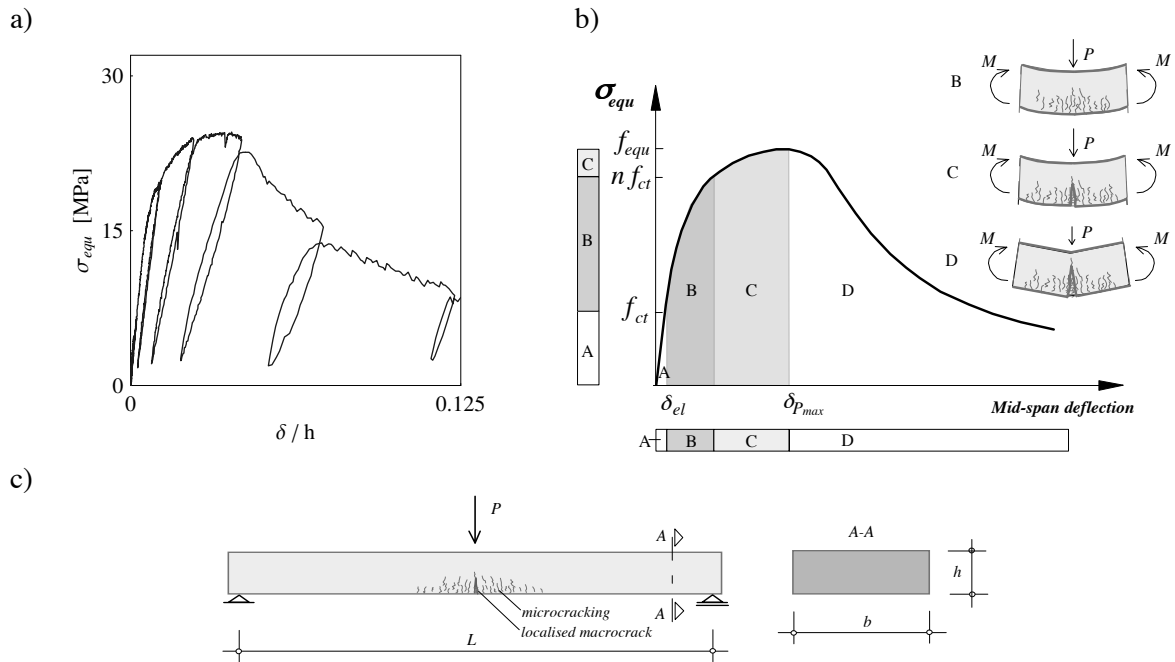


Figure 4.8: UHPFRC beam in three-point bending: a) an example of normalised force-displacement response of a tested element (Appendix T1); b) schematic force-displacement response with distinction of behaviour regimes; c) geometry and boundary conditions of case study with schematic representation of cracked region

The ultimate limit states of the studied member (end of the regime C) are attained with macrocrack opening, and both the strength and deformability in this regime are of interest. The macrocrack is modelled using the assumptions of the fictitious crack model [Hillerborg et al. 1976] (§ 4.2) and the propagation of the fictitious crack in the member is governed by energy equilibrium, based on fracture mechanics theories. Using the results of the model, an approach providing the analytical relationship between the force and deformation of a cracked section is also proposed.

As in any structural analysis, three groups of equations must be satisfied for each of the mentioned behaviour regimes:

- equations of equilibrium (static equations)
- equations of continuity (kinematic equations)
- constitutive equations (material behaviour).

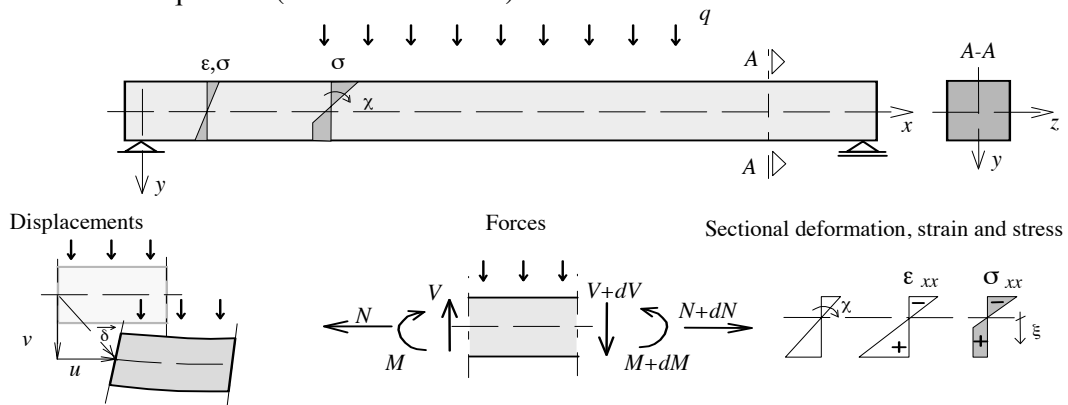


Figure 4.9: Positive orientation of axes, positive signs for internal forces, stresses and strains

4.3.2 Hypotheses of the model

The following hypotheses are applied in the developed model:

- Element is not subjected to normal force ($N=0$);
- Small displacements are assumed: the equilibrium of internal and external forces is established on the undeformed system, enabling linearisation of the equilibrium differential equations (First Order Theory);
- The theory of small deformations is respected: higher degrees of deformational values are disregarded in the calculation of componential displacements, providing linearisation of the relationship between deformations and displacements;
- The Navier-Bernoulli hypothesis for deformations of uncracked and microcracked section is assumed: plane sections remain plane and perpendicular to mid-plane after deformation; compatibility conditions are then provided by the following linear relationship

$$\varepsilon_{xx}(y) = \chi \cdot y = \frac{1}{\rho_{xx}} \cdot y \quad (4.2)$$

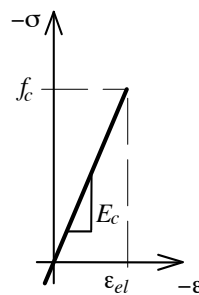
where

$$\chi = \frac{1}{\rho_{xx}} \approx \frac{d^2v}{dx^2} \quad (4.3)$$

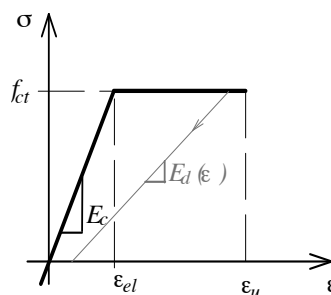
is the curvature of the mid-plane, corresponding to radius ρ_{xx} , and v is the vertical displacement of the beam's mid-plane. (Positive orientation of element axes, positive signs for internal forces, stresses and strains are indicated in Figure 4.9.) The right side of Equation 4.3 is obtained by disregarding $(dv/dx)^2$, which is much smaller than 1. All other deformations $\varepsilon_{xy}, \varepsilon_{xz}, \varepsilon_{yz}, \varepsilon_{zz}$ are negligible;

- In order to develop analytical expressions, material behaviour is represented by simplified relationships: a linear elastic stress-strain relationship $\sigma(\varepsilon)$ is used in compression¹, elastic-plastic (bilinear) stress-strain relationship with constant-stress plateau and limited strain is used in tension, and a linear stress-crack opening relationship $\sigma(w)$ is used for tension softening curve² (Figure 4.10);

a) Compression



b) Tension: stress-strain,



stress-crack opening

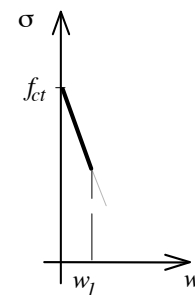


Figure 4.10: Material constitutive laws used for development of the analytical model; numerical values used in the present study for UHPFRC are given in § 3.3.1 and § 3.3.2

- Plastic yielding in tension occurs for $\sigma_{xx} = f_{ct}$. (The applied yielding criteria is justified for bending failure, where shear stress remains sufficiently low and the maximal principal tensile stress σ_1 does not exceed maximal normal tensile stress σ_{xx});

¹ For modelling of bending in elements without ordinary reinforcement and with $N=0$, compressive strains remain in the linear-elastic range

² Only the initial part of softening curve is relevant in providing bending strength of UHPFRC elements

- Hypotheses related to the development and propagation of the fictitious crack, based on fracture mechanics theories, are presented in § 4.2; some additional hypothesis will be introduced in § 4.3.5.

Based on the previous hypotheses, sectional equilibrium is assured by respecting the following equations:

$$M(x) = \iint y \cdot \sigma_{xx}(x, y) dy dz, \quad N(x) = \iint \sigma_{xx}(x, y) dy dz, \quad (4.4)$$

where $M(x)$ and $N(x)$ are bending moment and normal force along the length of the element, x . The internal forces must satisfy the following relationships:

$$\frac{dM(x)}{dx} = V, \quad \frac{dV(x)}{dx} = -q, \quad (4.5)$$

where $V(x)$ is shear force along the length of the element and q is the load acting on the system (Figure 4.9).

Disregarding the contribution of shear deformations, the deflection of the beam is represented by the deflection of the beam's mid-plane, v , as a function of x only, with the governing equation for the mid-plane deflection

$$\frac{d^2}{dx^2} \left(\iint y \cdot \sigma_{xx}(x, y) dy dz \right) = -q. \quad (4.6)$$

For a general stress-strain relationship $\sigma_{xx}(\varepsilon)$, Equation 4.6 cannot be solved by algebraic methods. If the distribution of the curvature χ along x is known however, the displacement can be obtained from the integration of Equation 4.3 with two known boundary conditions. Alternatively, the force-displacement relationship can be obtained by the second moment of area theory. Thus, the displacement at each point of the member can be determined if the function of the curvature along x is known. For this reason, the derivation of the continuous function of the curvature for a non-linear material behaviour is of interest in the present study.

The force-displacement response of the element in bending will often be presented in a normalised form, by means of equivalent bending stress, σ_{equ} , and equivalent bending strength, f_{equ} . Equivalent bending stress (or simply bending stress) is defined as

$$\sigma_{equ} = \frac{M(q, x)}{I_{z,el}} \cdot y_{hl,el}, \quad (4.7)$$

where $I_{z,el}$ is the moment of inertia of the elastic uncracked section with respect to axis z , passing through the section centroid (Figure 4.9), and $y_{hl,el}$ is the distance of the outermost tensile fibre from the centroid. The equivalent bending strength (or simply bending strength) represents the maximal value of bending stress, obtained for $M = M_{max}$, where M_{max} is the maximal moment sustained by the critical section. For the geometry and boundary conditions of the case study (Figure 4.8 c)), the reference bending stress is defined as

$$\sigma_{equ} = \frac{M(P, L/2)}{b \cdot h^2 / 6} = \frac{P \cdot L}{4 \cdot b \cdot h^2 / 6}, \quad (4.8)$$

where P is the mid-span point load, L is the element span, and b and h are the width and height of the section respectively. Bending strength is obtained for $P = P_{max}$, where P_{max} is the maximal force sustained by the element.

4.3.3 Linear-elastic behaviour

Linear-elastic behaviour characterises the element as long as the maximal tensile strain in the critical section is smaller than the elastic strain ϵ_{el} . Only a small part of the bending strength ($0.35 - 0.4 f_{equ}$) and a very small part of the corresponding deformations of a UHPFRC beam ($1/10 \delta_{pmax}$) are achieved in this regime (Figure 4.8 b)). This behaviour is accurately described with known equations of linear-elastic beam analysis, enabling the maximal force $P_{el,max}$ sustained by the system in this regime, and the corresponding deformation δ_{el} to be determined.

4.3.4 Non-linear behaviour due to multi-microcracking

If the deformation or force in the system increases beyond the elastic regime, the force-displacement response becomes non-linear (Figure 4.11 a)). Pseudo-plastic yielding occurs in sections in which tensile strains exceed the elastic limit. Unlike typical plastic yielding, e.g. in metals, which is isotropic regarding compressive and tensile behaviours, the pseudo-plastic yielding considered here appears only in the tension region. This results in an asymmetric distribution of stresses over the section, with displacement of the neutral axis from the centroid of the cross-section towards the compressed zone, as shown in Figure 4.11 c) and 4.12.

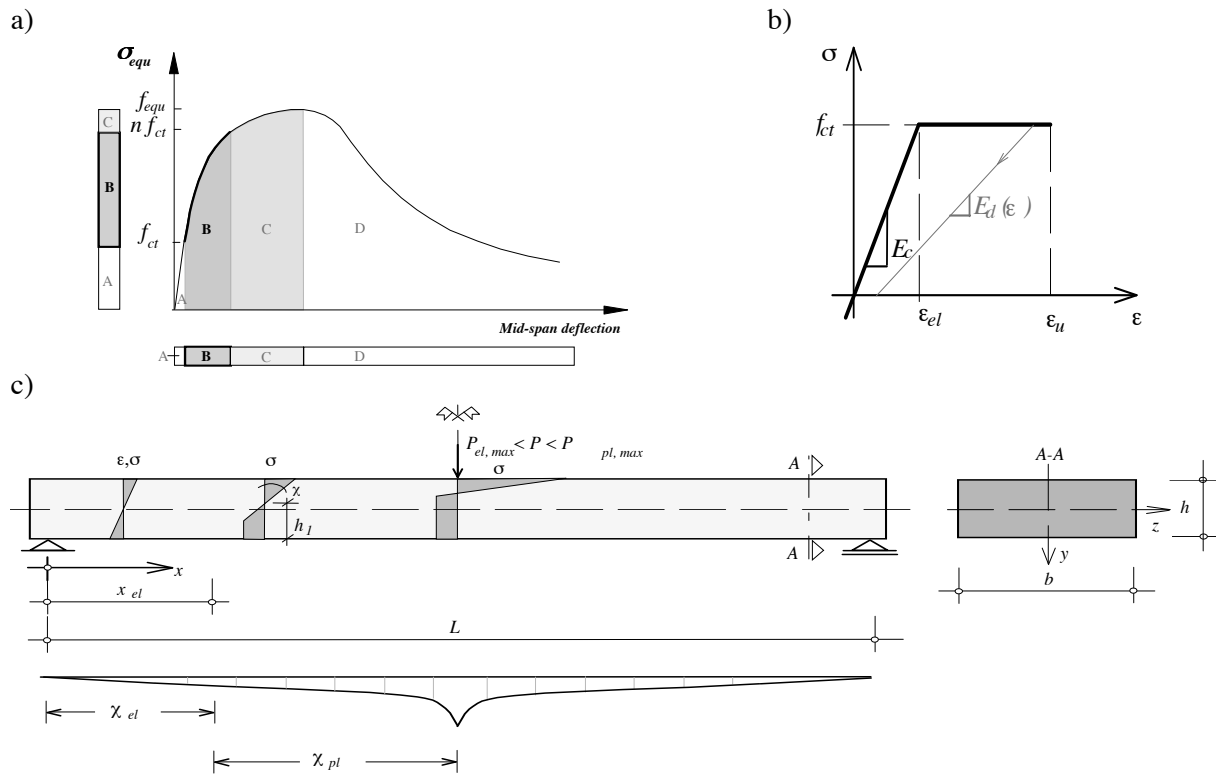


Figure 4.11: a) Position of multi-microcracking regime (B) in whole force-displacement response in bending, b) material behaviour in tension, c) distribution of curvature along element's axis

This phase ends when the maximal tensile strain in the critical section attains the value of uniaxial tensile strain prior to strain softening, ϵ_u , (Figure 4.11 b)). The coinciding force P and the corresponding moment at the critical section are designated $P_{pl,max}$ and $M_{pl,max}$, respectively. Bending stress (Equation 4.7) at the end of the multi-microcracking regime is

$$\sigma_{equ}(M_{pl,max}) = n_{fct} f_{ct}, \quad (4.9)$$

where n_{fct} is a coefficient to be developed (Equation 4.16).

Considering the entire element, there are the parts that are still in the linear-elastic phase (for $x \leq x_{el}$), and the parts with different levels of quasi-plastic yielding in tension ($x_{el} \leq x \leq L/2$, in symmetric boundary conditions), Figure 4.11 c). The position x_{el} varies as a function of load level P .

Respecting the hypotheses given in § 4.3.2, the relationship between the deformation and the sectional force, i.e. moment-curvature relationship, and the force-displacement relationship for the member are found in a closed form (Equations 4.10, 4.11, and 4.22). An analytical development of these relationships is presented in Appendix M1. Only the final expressions are given in the following sections.

4.3.4.1 Cross-section with pseudo-plastic yielding in tension

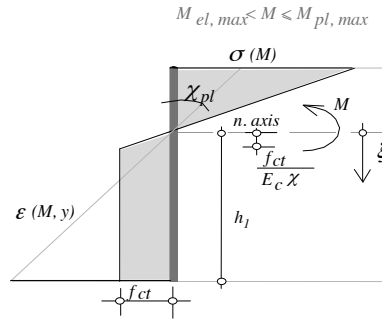


Figure 4.12: Stress and strain distribution in the section with pseudo-plastic yielding in tension

The moment-curvature relationship of the rectangular section is governed by the following equations:

$$M(\chi_{pl}) = b \left(\frac{f_{ct} h^2}{2} - \frac{\sqrt{2} f_{ct}^{3/2} h^{3/2}}{3\sqrt{E_c} \sqrt{\chi_{pl}}} \right) \quad \text{for } \chi_{el,max} \leq \chi_{pl} \leq \chi_{pl,max} \quad (4.10)$$

or

$$\chi_{pl}(M) = \frac{8b^2 f_{ct}^3 h^3}{9E_c (bf_{ct} h^2 - 2M)^2} \quad \text{for } M_{el,max} \leq M \leq M_{pl,max}^1 \quad (4.11)$$

where $\chi_{el,max}$ and $\chi_{pl,max}$ are the curvatures at the first cracking and at the end of the pseudo-plastic regime respectively, defined as

$$\chi_{el,max} = \frac{f_{ct} \cdot 2}{E_c h} \quad (4.12)$$

$$\chi_{pl,max} = \chi_{pl}(\epsilon_u) = \frac{E_c \epsilon_u + \sqrt{f_{ct} (2E_c \epsilon_u - f_{ct})}}{E_c h} \quad (4.13)$$

Moments $M_{el,max}$ and $M_{pl,max}$ are the maximal moments that can be borne by the section, with $N=0$, in elastic and pseudo-plastic regimes respectively, defined as

$$M_{el,max} = f_{ct} \frac{bh^2}{6} \quad (4.14)$$

¹ For $\chi < \chi_{el,max}$ and $M < M_{el,max}$, expressions $M(\chi)$ and $\chi(M)$ are well known from linear-elastic analysis.

$$M_{pl,max} = M(\chi_{pl,max}) = f_{ct} \frac{bh^2}{6} \left(3 - \frac{2\sqrt{2}f_{ct}}{\sqrt{f_{ct}(E_c\varepsilon_u + \sqrt{f_{ct}(2E_c\varepsilon_u - f_{ct})})}} \right). \quad (4.15)$$

The maximal bending stress before the macrocrack occurs, termed pseudo-plastic bending strength, can then be expressed, according to Equation 4.8, as

$$\sigma_{equ}(M_{pl,max}) = \frac{M_{pl,max} 6}{bh^2} = n_{f_{ct}} \cdot f_{ct} \quad (4.16)$$

where

$$n_{f_{ct}} = \left(3 - \frac{2\sqrt{2}f_{ct}}{\sqrt{f_{ct}(E_c\varepsilon_u + \sqrt{f_{ct}(2E_c\varepsilon_u - f_{ct})})}} \right). \quad (4.17)$$

The moment-curvature relationship (Equation 4.10) for the critical section, before the macrocrack starts to propagate, is plotted in Figure 4.13. Here, bending moment value is normalised by maximal elastic moment, $M_{el,max}$, and curvature is multiplied by section thickness. It should be noted that, for a constant value of ε_u , the maximal normalised moment achieved at the end of this regime is a size-independent value. This can equally be concluded from Equation 4.17 that is a function of material intrinsic properties and, consequently, pseudo-plastic bending strength is a function of material properties only. Maximal curvature (Equation 4.13) remains inversely proportional to element height, as in the linear-elastic regime, and thus the thinner elements are characterised by a higher curvature at the end of the pseudo-plastic region.

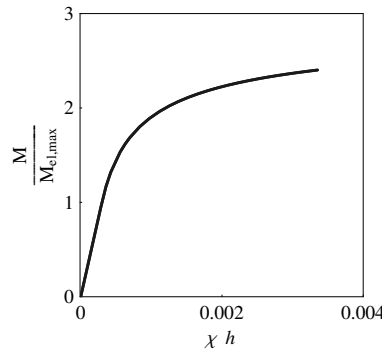


Figure 4.13: Normalised moment-curvature relationship for rectangular sections in pseudo-plastic tensile yielding

Figure 4.14 shows the ratio of pseudo-plastic bending to tensile strength, $n_{f_{ct}}$, as a function of maximal tensile strain ε_u at the end of the pseudo-plastic tensile plateau. For the UHPFRC used in this study, with $\varepsilon_u = 2.5 \text{ ‰}$, $f_{ct} = 9 \text{ MPa}$ and $E_c = 60 \text{ GPa}$, the pseudo-plastic bending strength is 2.4 times the tensile strength. Studying the rate of $n_{f_{ct}}$ as function of ε_u , it can be seen that, for an ε_u higher than approximately 1 ‰, the pseudo-plastic bending strength increases much more slowly (Figure 4.14). For $\varepsilon_u = 1 \text{ ‰}$ the $n_{f_{ct}}$ already has a value of 2.1, while for $\varepsilon_u = 5 \text{ ‰}$ the $n_{f_{ct}} = 2.56$. It is also important to note that for a typical value of ε_u (2-3 ‰), the small variation in strain (e.g. $\pm 0.5 \text{ ‰}$ due to dispersion of material resistance) causes a change in $n_{f_{ct}}$ that is never higher than 3 ‰ (Figure 4.14 b)).

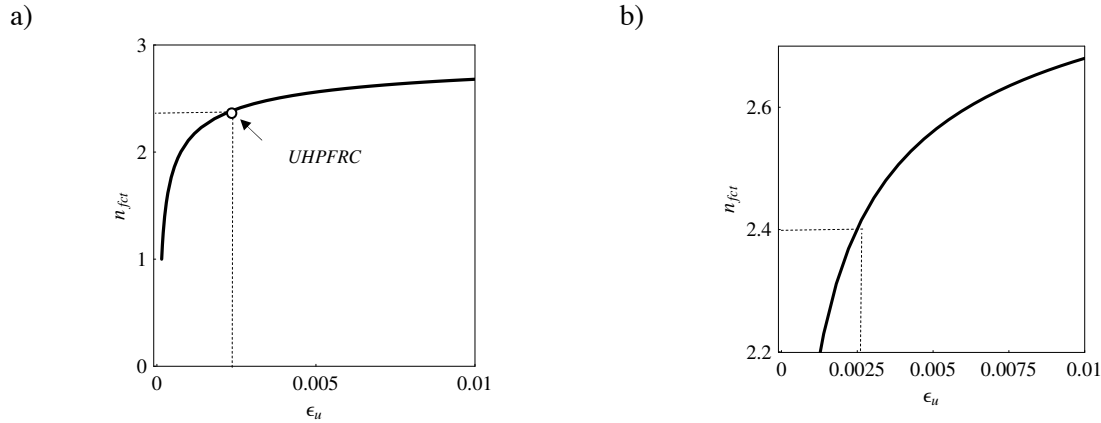


Figure 4.14: a) Ratio between equivalent bending strength prior to macrocrack opening and tensile strength as a function of maximal tensile strain; plots for $f_{ct} = 9 \text{ MPa}$ and $E_c = 60 \text{ GPa}$; b) zoom of plot a)

The influence of tensile strength, f_{ct} , on the increase in pseudo-plastic bending strength is shown in Figure 4.15. Pseudo-plastic bending strength as a function of ϵ_u increases slightly faster for lower tensile strengths. In Figure 4.15 the increase in flexural strength is plotted for $f_{ct} = 3 \text{ MPa}$ (tensile strength of an ordinary concrete), $f_{ct} = 10 \text{ MPa}$ (a typical value for UHPFRC) and $f_{ct} = 25 \text{ MPa}$ (a very high tensile strength, possible for some UHPFRCs, § 4.4.2). From these plots, it can be concluded that the relative increase in pseudo-plastic bending strength is much less sensitive to tensile strength than to maximal tensile strain, ϵ_u .

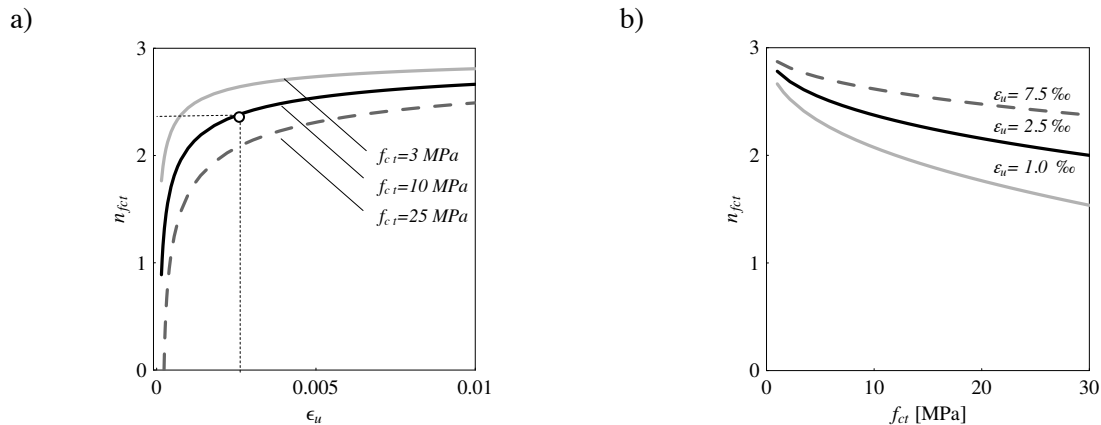


Figure 4.15: Pseudo-plastic bending strength for various material properties in tension: a) as a function of maximal tensile strain, for different tensile strengths; b) as a function of tensile strengths, for different maximal tensile strains; E_c , is kept constant in these plots

The increase in pseudo-plastic bending strength thus depends primarily on maximal tensile strain, ϵ_u , and it can be demonstrated that for $\epsilon_u \rightarrow \infty$, the right side of Equation 4.16 yields $3 f_{ct}$, which is the theoretical limit for rigid-perfectly plastic bending strength, comprising infinite compressive strength. For realistic material properties, however, this limit cannot be attained, since failure in compression occurs once a certain level of deformation is reached.

Verification of compression capacity

The expression for pseudo-plastic bending strength (Equation 4.16) assumes that the corresponding compressive stresses are linear-elastic. It can be easily concluded that, since $f_{ct} \ll |f_{cm}|$, where f_{cm} is compressive strength, the depth of the section part in tension (h_t , Figure 4.12) is higher than $h/2$, meaning that the strain attained at the outermost tensile fibre, ϵ_u , is higher than the strain attained at

the outermost compressive fibre, ε_c , ($\varepsilon_u > |\varepsilon_c|$). For a typical UHPFRC, the ε_u has a value in the range of 2-3 ‰, and the ε_c remains in the linear-elastic regime within that range of values (§ 3.3.1), and thus the assumptions of Equation 4.16 are respected.

More precisely, the maximal compressive stress attained at the end of pseudo-plastic phase, $\sigma_{c,pl}$, can be expressed by Equations 4.18 or 4.19. This actually represents the minimal elastic compressive stress required to enable maximal tensile strain to be developed:

$$|\sigma_{c,pl}| = -f_{ct} + \sqrt{2} \sqrt{f_{ct} \left(E_c \varepsilon_u + \sqrt{f_{ct} (2E_c \varepsilon_u - f_{ct})} \right)}. \quad (4.18)$$

The minimal required ratio between compressive stress and tensile strength is

$$n_{ct} = \frac{|\sigma_{c,pl}|}{f_{ct}} = -1 + \frac{1}{f_{ct}} \sqrt{2} \sqrt{f_{ct} \left(E_c \varepsilon_u + \sqrt{f_{ct} (2E_c \varepsilon_u - f_{ct})} \right)}. \quad (4.19)$$

The plots of the expression 4.19, as a function of ε_u , for different levels of tensile strengths are given in Figure 4.16. The values obtained for n_{ct} justify the interest in providing sufficient compressive strength in order to exploit the tensile capacities of UHPFRC, considering in addition that the deformation, and thus maximal compressive stress, will continue to increase in the following regime (regime C). For a typical UHPFRC, the compressive stress required at the end of the pseudo-plastic phase is 5-6 times tensile strength, which is largely satisfied. This also allows Equations 4.10 to 4.15 to be applied in further analysis. Plots in Figure 4.16 show an increasing requirement for compressive stress as a function of ε_u , and a decreasing requirement as a function of tensile strength.

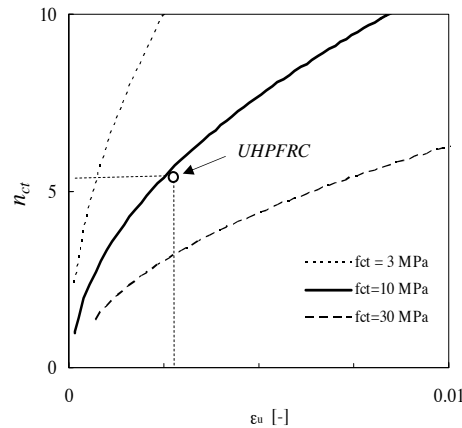


Figure 4.16: Minimal ratio of compressive stress to tensile strengths required to enable exploitation of maximal tensile strain ε_u

4.3.4.2 Element behaviour in presence of pseudo-plastic yielding

For the given boundary conditions (Figure 4.11 c)) the function of curvature $\chi(M)$, Equation 4.11, can be expressed as a continuous function along the length of the element, with $M = M(P, x)$ being the continuous function of the moment along x . Plots in Figure 4.17 a) represent the distribution of curvature along the element length (up to mid-span) for different load levels.

It can be noted that for load levels of up to approx. 70-80 % of maximal load in the pseudo-plastic phase $P_{pl,max}$ curvatures deviate slightly from the elastic curvatures. The significant increase in curvature occurs when the load approaches the level of $P_{pl,max}$ (see also Figure 4.13), causing a considerable local increase in deformations in the vicinity of the most loaded section. Thus, multi-microcracking, which in a uniaxial stress state prevents strain localisation, causes the concentration of deformations in the case of a non-constant tensile force along the element. Similar conclusions can be drawn regarding the deformations of a member subjected to a uniformly distributed load (Figure 4.17 b)).

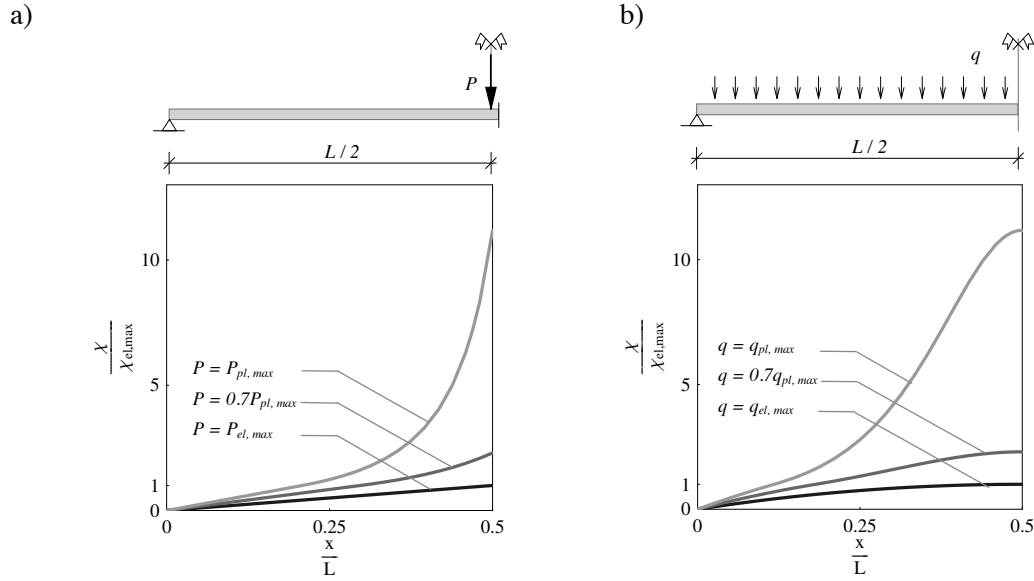


Figure 4.17: Distribution of curvature along length of beam at various load levels, for boundary conditions of : a) three-point bending; b) uniformly distributed load along a simple beam

The force-displacement relationship for the beam can finally be obtained e.g. by the integration of curvature. For simple symmetric load cases, closed form solutions can be established from the following

$$\delta_x(P) = 2 \cdot \int_0^{L/2} \chi(x, P) \cdot \bar{M}(x) \cdot dx \quad (4.20)$$

where $\bar{M}(x)$ is defined as

$$\begin{cases} \bar{M} = \left(1 - \frac{x}{L}\right) \cdot m & \forall m \leq x \\ \bar{M} = \left(1 - \frac{x}{L}\right) \cdot m - (m - x) = x - \frac{x}{L}m & \forall m > x \end{cases} \quad (4.21)$$

The solution for the mid-span deflection of a beam subjected to three-point bending is obtained in the following form:

$$\begin{aligned} \delta_{L/2}(P) &= 2 \left[\int_0^{x_{el}} \frac{M(x, P)}{E_c I} \cdot \bar{M}(x) \cdot dx + \int_{x_{el}}^{L/2} \chi_{pl}(x, P) \cdot \bar{M}(x) \cdot dx \right] = \\ &= 2 \left[\int_0^{\frac{f_{ct} b h^2}{3P}} \frac{P \cdot x}{2E_c I} \cdot \frac{1}{2} x \cdot dx + \int_{\frac{f_{ct} b h^2}{3P}}^{L/2} \chi_{pl}(x, P) \cdot \frac{1}{2} x \cdot dx \right] = \\ &= \frac{2b^2 f_{ct}^3 \cdot h^3}{27E_c P^2} + \frac{8b^2 f_{ct}^3 \cdot h^3 \left(-\frac{3}{2} + \frac{2bf_{ct}h^2}{2bf_{ct}h^2 - LP} - \text{Log} \left(\frac{2}{3} bf_{ct}h^2 \right) + \text{Log} \left(bf_{ct}h^2 - \frac{LP}{2} \right) \right)}{9E_c P^2} \quad \forall P_{el, \max} \leq P \leq P_{pl, \max} \end{aligned} \quad (4.22)$$

Otherwise, for an arbitrary monotonic function of the bending moment, performing a numerical integration applying any standard integration procedure gives satisfactory results.

The force-displacement relationships for UHPFRC beams of different heights are plotted in Figure 4.18. In Figure 4.18 b) the simulated curves are plotted against the measured data of beams of 25, 40 and 60 mm height, in constant span $L = 420$ mm, subjected to a three-point bending test (Appendix T1). The analytical results show very good agreement with experimental results. As previously stated, the bending strength attained prior to the development of macrocracking is size-independent, and it can be seen that a high proportion of bending strength (more than 85%) is achieved in this regime. Regarding the deformational capacity of the elements, it is evident that the thinner elements are more deformable which is further discussed in § 4.4.3.

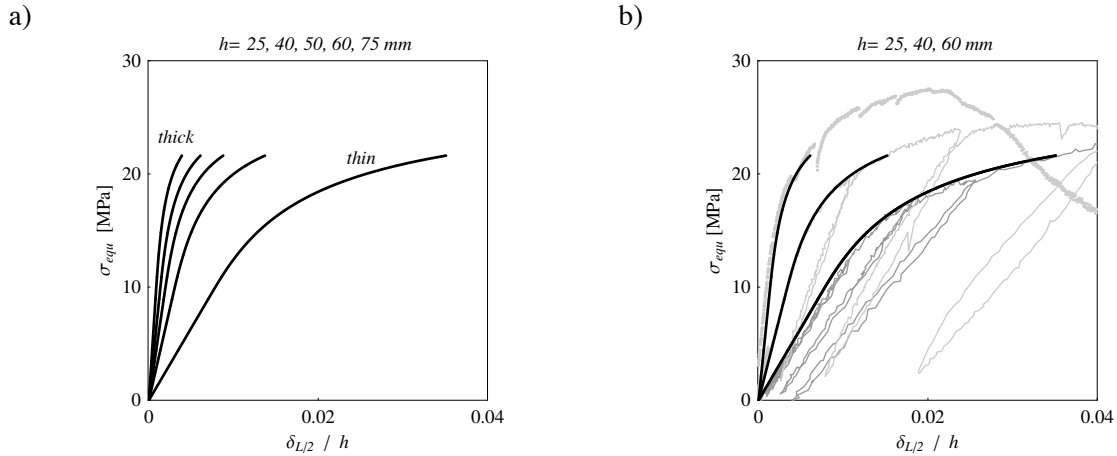


Figure 4.18: Bending stress over mid-span displacement for beams of various heights, h , subjected to three-point bending, with 420 mm span: a) simulations with $f_{ct} = 9$ MPa, $\epsilon_u = 2.5$ ‰ and $E_c = 60$ GPa, b) simulations and measured response of UHPFRC beams (Appendix T1)

In addition, longitudinal deformations along the length of the beam can also be predicted by applying the developed equations. Let us observe the elongation of two points on the tensile (lower) side of the element. For the sake of comparison with experimental data, let us consider the two points at the position $x = L/2 - l_m/2$ and $L/2 + l_m/2$, $L/2$ being the point of introduction of the force (Figure 4.19).

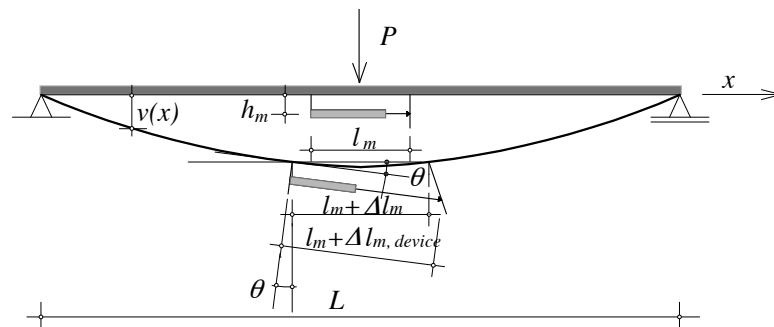


Figure 4.19: Measurement of non-linear tensile deformations: initial position and rotation of measurement points caused by rotation of beam

The elongation of the two points, using symmetry with respect to mid-point, is determined by the following expression:

$$\Delta l_m(P) = \int_{L/2-l_m/2}^{L/2+l_m/2} \varepsilon_{xx, y=-\frac{h}{2}}(x, P) \cdot dx = 2 \cdot \int_{L/2-l_m/2}^{L/2} \chi(x, P) \cdot h_l(\chi(x, P)) \cdot dx \quad (4.23)$$

where both of the functions $\chi(x)$ and $h_l(\chi)$ are analytically defined (Appendix M1), and the integration can be performed. The calculated elongation, Δl_m , is plotted in Figure 4.20 against the measured data as a grey line. Owing to the geometry of the measurement device (Figure 4.19), the experimentally captured deformations are higher than the beam deformations, due to the rotation of the measurement base. The error is more pronounced for slender beams because of their higher deformability (Figure 4.20 a)).

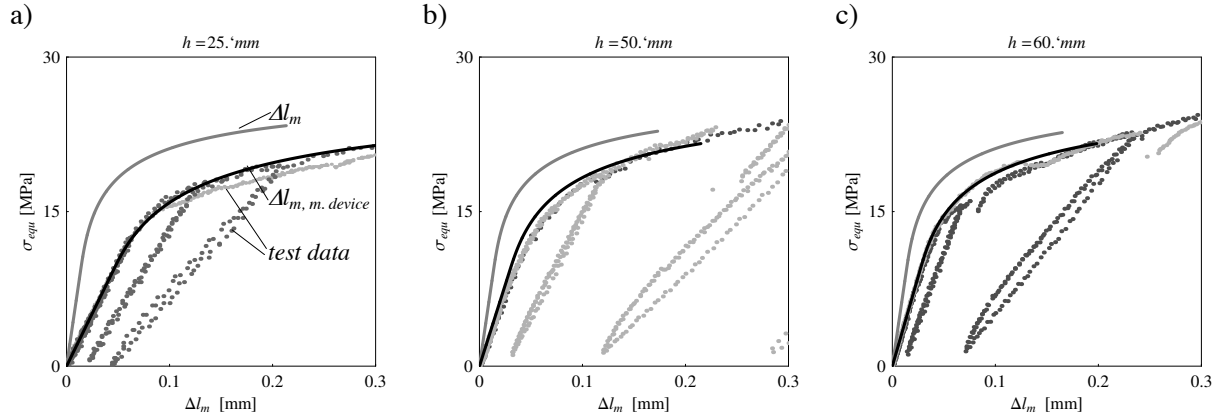


Figure 4.20: Calculated and measured elongations of the measurement base during the elastic-pseudo-plastic phase, for beams of various depths; continuous grey lines denote actual elongation, while the black lines denote calculated elongation of the same measurement base but captured at the position of the measurement device

The relationship between measured elongation, $\Delta l_{m, device}$, and actual elongation, Δl_m , can be obtained from the geometry of the device (Figure 4.19) if the rotation θ of the member at the position of the measurement device is known:

$$\Delta l_{m, device} = \frac{\Delta l_m + 2 \cdot h_m \cdot \tan(\theta)}{\cos(\theta)} + (l_m + \Delta l_m) \cdot \tan(\theta)^2 - \left(1 - \frac{1}{\cos(\theta)}\right) \cdot l_m \quad (4.24)$$

The rotation θ can be obtained from integration of the curvature function, respecting the boundary conditions:

$$\theta(x) = \frac{dv(x)}{dx} = \int_x \chi(M(x, P)) \cdot dx + C_1 \quad (4.25)$$

For three-point bending:

$$\theta(x = L/2) = 0 \Rightarrow C_1 = - \int_0^{L/2} \chi(M(x, P)) \cdot dx \quad (4.26)$$

Using Equation 4.11, rotation θ at the position $x = L/2 - l_m/2$ is then calculated as

$$\theta(x = L/2 - l_m/2) = \int_0^{L/2-l_m/2} \chi(M(x, P)) \cdot dx - \int_0^{L/2} \chi(M(x, P)) \cdot dx = - \int_{L/2-l_m/2}^{L/2} \chi(M(x, P)) \cdot dx \quad (4.27)$$

for each level of load P . The obtained measured elongation (Equations 4.24 and 4.27) shows good agreement with experimental data (Figure 4.20, black line).

These results, together with results obtained from the photogrammetry analysis (Figure 4.28 showing no localisation of deformation in one crack prior to $P_{pl,max}$), confirm¹ that the multi-microcracking observed in uniaxial tension also develops in bending and can be well modelled using pseudo-plastic material properties in tension.

4.3.4.3 Inelastic unloading and actual element stiffness in multi-microcracking regime

The multi-microcracking causes damage in the material (§3.3.2) that results in inelastic behaviour, which is also different from real plastic behaviour. This can be observed experimentally, during the unloading of the element that had previously exhibited deformations beyond the elastic limit (Figure 4.22). The unloading curve shows a decreased stiffness that is the actual stiffness of the element once microcracking occurs, and this is of interest for design. The relationships developed for determining unloading stiffness, based on the stiffness of the damaged material E_d are given in more detail in (Appendix M1). Only the final expressions and principal results are given in the following.

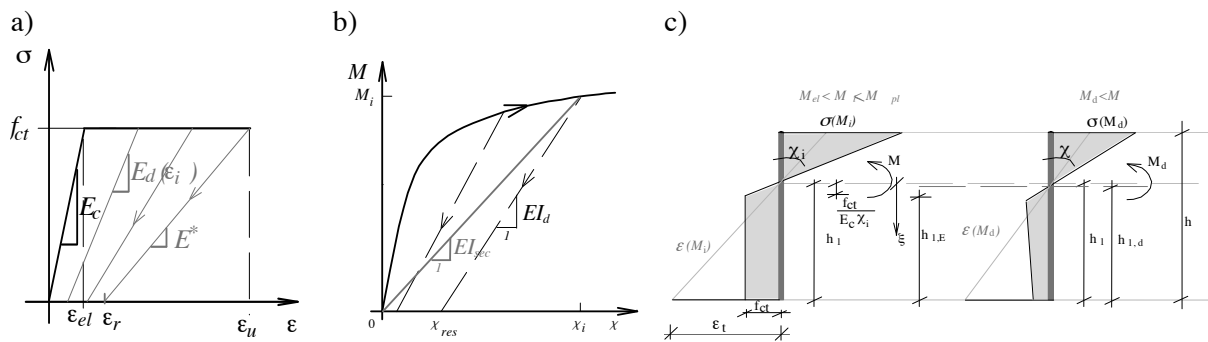


Figure 4.21: Inelastic behaviour due to multi-microcracking of UHPFRC: a) loss in stiffness in uniaxial tension; b) loss of bending stiffness; c) distribution of sectional forces due to change of modulus of elasticity in cracked part

The variation in stiffness of a damaged section is schematically shown in Figure 4.21 a) and b) for uniaxial tensile and bending state respectively, and a distribution of stresses in the section during the unloading phase is shown in c). The bending stiffness of tested elements is shown in Figure 4.22, and it can be noted that bending stiffness is a function of previously achieved deformation. The bending stiffness of a section that has reached maximal curvature χ_i can be calculated using the following expression:

$$EI_d = b \cdot \left(\frac{(f_{ct} + \sigma_{rf}) \cdot (E_c \cdot h_1 \cdot \chi_i - f_{ct}) \cdot (f_{ct} - 2 \cdot E_c \cdot \varepsilon_{rf} + E_c \cdot h_1 \cdot \chi_i) - 2 \cdot E_c^2 \cdot \varepsilon_{rf}^2 \cdot K_1}{2 \cdot E_c^2 \cdot \chi_i^3} + \frac{1}{3} \cdot E_c \cdot \left((h - h_1)^3 + \frac{f_{ct}^3}{E_c^3 \cdot \chi_i^3} \right) \right) \quad (4.28)$$

where the newly introduced coefficients are given in Appendix M1. This enables the curvature at unloading, χ_{unload} , of any section along the element that was loaded with maximal force P_i , and also the relationship between force and displacement to be calculated:

¹ If only the force-load point deflection (P - δ) relationship is verified, the conclusions may be misleading, since similar P - δ relationships may result from the opening of a localised crack without development of pseudo-plastic deformations (§ 4.4).

$$\delta(P, P_i) = 2 \left[\int_0^{x_{el}} \frac{M(x, P)}{E_c I} \cdot \bar{M}(x) \cdot dx + \int_{x_{el}}^{L/2} \chi_{unload}(x, P, P_i) \cdot \bar{M}(x) \cdot dx \right]. \quad (4.29)$$

The predicted unloading paths for tested UHPFRC elements are plotted against measured data in Figure 4.22, showing good agreement.

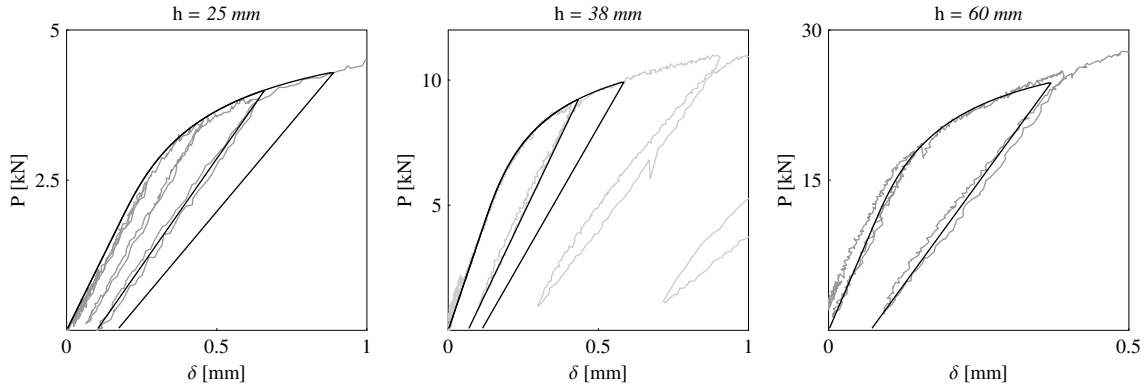


Figure 4.22: Measured and simulated stiffness of microcracked element

This approach enabled the actual element stiffness, K_d , to be predicted as a function of the maximal load sustained by the element, P_i . Figure 4.23 a) shows the ratio of the sectional bending stiffness, EI_d , to initial elastic stiffness, EI , as a function of the maximal curvature achieved in the section. On the same plot it can be seen that this relationship is similar to the relationship between the relative curvature and the ratio of secant, EI_{sec} , to elastic stiffness. This implies that, for a practical estimation, the secant stiffness can be used, giving results on the safety side. Similar observations can be made regarding the element stiffness, K . For an element in three-point bending, the loss of element stiffness as a function of maximal load P_i is plotted in Figure 4.23 b). It is interesting to note that, for these boundary conditions, the unloading stiffness for $P_i = 0.8 P_{pl,max}$ is almost 85 % of initial stiffness. As will be shown, the service load range of a statically determinate element is below this limit, which gives the information on the error produced by calculating element deformations by applying the initial elastic stiffness. Similar conclusions for a beam under uniformly distributed load are given in Appendix M1.

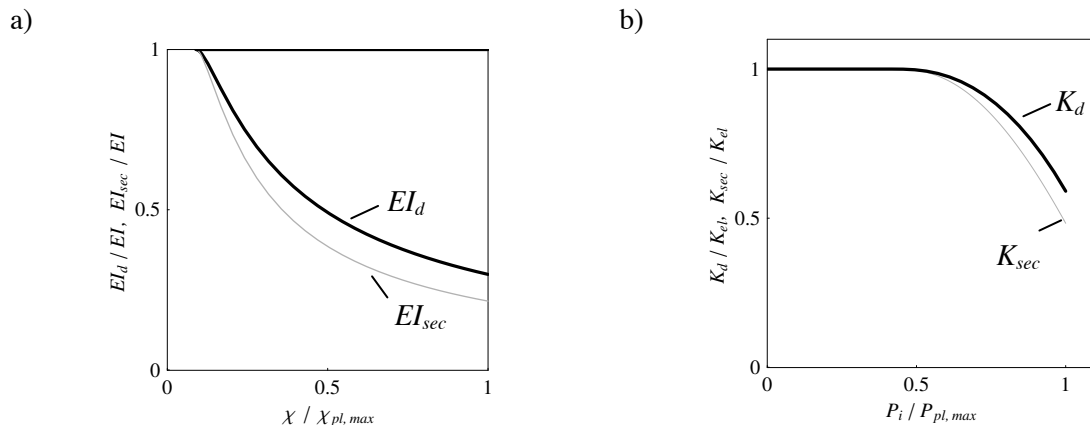


Figure 4.23: Relative decrease in bending stiffness due to multi-microcracking: a) sectional stiffness, EI_d ; b) stiffness of a beam in three-point bending, K_d .

4.3.5 Non-linear behaviour with macrocrack propagation

A macrocrack is assumed to start propagating when the maximal pseudo-plastic strain ε_u is reached in the critical section (Figure 4.24). In reality, the location of the first macrocrack is influenced by the distribution of material resistance, which in the case of fibre-reinforced materials, is influenced by the variability in fibre effectiveness along the element's length [Behloul 1996], causing that the crack may appear in a less loaded section with lower resistance. The deviation of the position of the crack from the most loaded section can also be seen in specimens tested during the present research (Appendix T1). However, it is assumed that the macrocrack is located at mid-span and that material behaviour is homogeneous all along the element. The macrocrack in the element will be modelled using the hypotheses of the fictitious crack model (FCM, § 4.2).

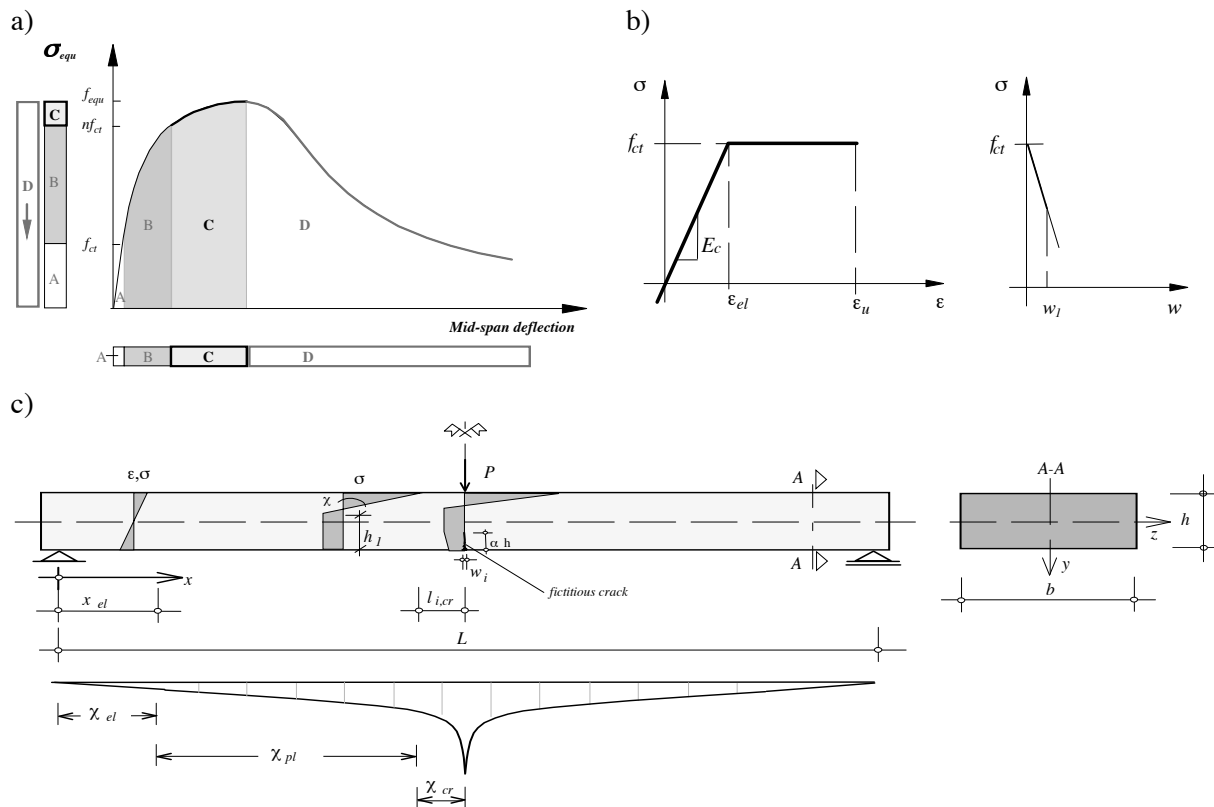


Figure 4.24: UHPFRC beam in bending: a) position of regime with macrocrack opening in whole normalised force-displacement response; b) material laws in tension; c) geometry and boundary conditions of case study, with distribution of curvature along element's axis

Since the macrocrack is capable of transferring significant stress for small crack openings, the force in the system can continue to increase as deformations increase (Figure 4.24 a)). Prior to peak force, the sections in the vicinity of the crack are subjected to local unloading, due to stress decrease in the macrocrack (Figure 4.24 d)), while the rest of the member behaves in the same way as during phase "B".

4.3.5.1 Cross-section with pseudo-plastic yielding and fictitious crack propagation

The equilibrium of a cracked section with one part in pseudo-plastic yielding in tension is studied as the first step of the analysis. The parameters describing the state of stress and strain of the cracked section are shown in Figure 4.25. The uncracked part of the section is characterised by curvature χ ($\chi < \chi_{pl,max}$), whereas the fictitious crack is characterised by its length αh and the crack mouth

opening displacement (CMOD) w_i . The latter two are new parameters in the equilibrium equations of internal forces that did not exist in the equations describing the uncracked state.

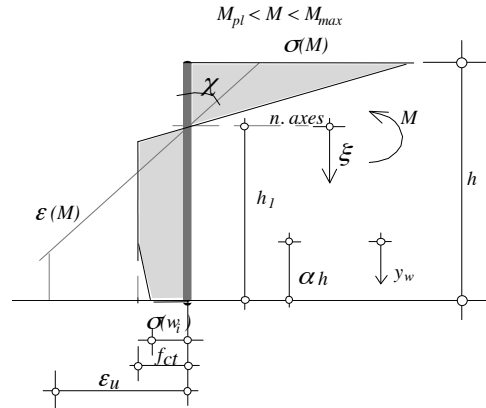


Figure 4.25: Assumed distribution of stress and strain in a cracked section

The following assumptions are made:

- the fictitious crack starts to propagate when the tensile strain at the crack tip reaches ϵ_{ii} ;
- the Navier-Bernoulli hypothesis of plane sectional deformations is valid for the uncracked part of the section;
- the crack pattern is known: a linear relationship for crack opening along the length of the crack $w(y_w)$ is assumed (as in the models of [Maalej, Li 1994], [Casanova, Rossi 1996]):

$$w(y_w) = \frac{w_i}{\alpha \cdot h} \cdot y_w \quad (4.30)$$

In the non-cracked zone, the stress at any point is related to deformations by the $\sigma(\epsilon)$ relationships. In the zone of the fictitious crack, the stress is related to crack opening w . The bending moment sustained by the section is obtained using Equation 4.4:

$$M = \int_A \sigma_{xx} \xi dA = f(\chi, h_1, \alpha, w_i).$$

With the assumed crack pattern i.e. the relationship between parameters α and w_i , and the equilibrium condition $\Sigma N = 0$, bending moment is expressed as a function of two parameters:

$$M = M(\chi, \alpha) \vee M = M(w_i, \alpha) \vee M = M(\chi, w_i). \quad (4.31)$$

Since the two parameters are independent, the equilibrium of a cracked section has an infinite number of solutions for an imposed curvature, or for an imposed crack length or crack opening. Analytical expressions for the relationships 4.31 are given in Appendix M2.

Figure 4.26 shows a field of bending moments that can be sustained by a cracked section, as a function of curvature, χ , and CMOD, w_i . Every line plotted in Figure 4.26 a) represents normalised values of bending moment $M = M(\chi, w_i)$ (Equation A 2.12) for a constant curvature $i: \chi_{pl, max}$, $i=1, 2, \dots$, with w_i being variable. The moment is normalised with the maximal value of the moment achieved prior to crack opening $M_{pl, max}$. The curves are plotted for a typical UHPFRC ($f_{ct} = 9MPa$, $\epsilon_u = 2.5 \text{‰}$, $f_c = 180 MPa$, $d\alpha(w)/dw = 6.8 MPa/mm$). Similarly, in Figure 4.27 normalised values of possible bending moments are plotted as a function of w_i and normalised crack length, α . By normalising the moment value, $M / M_{pl, max}$, the obtained analytical expressions are functions of material properties only, independent of section dimensions, so the plotted fields therefore apply to all specimen sizes.

It can be seen that for any imposed curvature, $i \cdot \chi_{pl,max}$ in Figure 4.26, or any imposed crack length, αh , in Figure 4.27, there is an infinite number of equilibrated solutions as a function of crack opening. However, for an equilibrated bending member with a given geometry, only one moment corresponds to any imposed deformation and, for an increasing deformation, only one possible equilibrium path exists. Due to the fact that all the values of χ , α and w_i increase for a monotonic increase in deformation, the shape of the equilibrium paths will be as schematically shown in Figure 4.26 b). Considering the possible field of solutions again, it is important to note that, for given material properties, there is an upper bound for the maximal moment¹. Moreover, the moment can be higher than the maximal moment prior to crack propagation, $M_{pl,max}$, for only a limited range of crack openings.

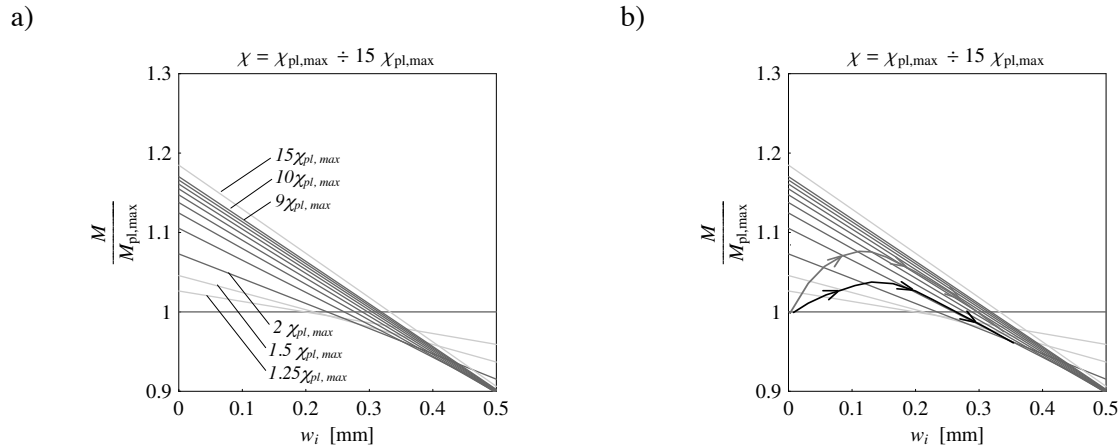


Figure 4.26: a) Possible field of bending moment of a cracked section as a function of CMOD, w_i , and curvature in non-cracked part of section, χ ; b) the same plot as in a) with two of an infinite number of possible moment-curvature relationships; material properties used: $f_{ct} = 9\text{MPa}$, $\epsilon_u = 2.5 \text{‰}$, $f_c = 180\text{MPa}$, $d\alpha(w)/dw = 6.8\text{MPa/mm}$

For the UHPFRC used, some important conclusions can be drawn from the plotted curves:

- maximal moment is attained with small fictitious crack openings (smaller than 0.35 mm), regardless of beam size;
- maximal moment is less than 20 % higher than the maximal moment reached prior to the fictitious crack opening;
- the deformations (e.g. curvature) may increase significantly with even small crack openings, while $M > M_{pl,max}$; this suggests the potential of this regime in providing element ductility.

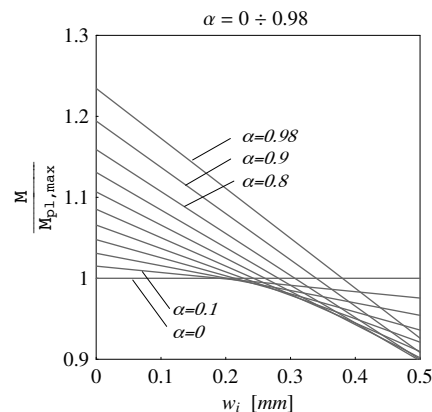


Figure 4.27: Possible field of bending moments of a cracked section as a function of CMOD, w_i , for a crack length αh

¹ Note that for a greater increase in curvature, softening in compression may take place, decreasing the section's bearing capacity.

The first conclusion justifies the use of the linear stress-crack opening relationship in the equilibrium equations describing behaviour up to maximal force, and in the bending softening regime, at least while $M \geq M_{pl\ max}$. Small crack openings are also observed both experimentally, by means of photogrammetry data, and numerically. Figure 4.28, shows the relative horizontal displacements Δx , of two points between which a crack is detected by means of photogrammetric analysis. Since the chosen points are spaced close together, at a distance of approximately $1.5\ mm$ (Appendix T1), their relative displacement is practically identical to that of crack opening. Examples of crack openings for two beams of different heights, $h = 25\ mm$ and $h = 60\ mm$, are plotted against bending stress. It can be seen that maximal force is reached for crack openings smaller than $0.2\ mm$. Similar experimental observations are reported in [Graybeal 2006]. In addition, from the plotted diagrams it can be seen that no crack opening occurs until a significantly high level of bending stress is reached, justifying the applied hypothesis that the high percentage of bending stress is achieved with a homogeneous (pseudo-plastic) material behaviour, with no localisation of deformation in a single crack.

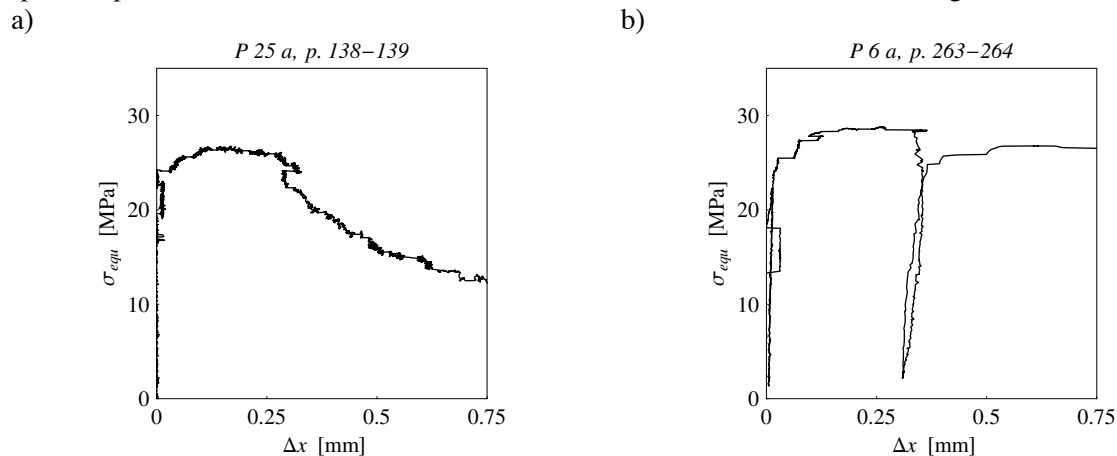


Figure 4.28: Force-“crack mouth opening” relationship; data obtained by photogrammetric analysis of beams in three-point bending; Δx represents the relative displacement of two points at approx. $1.5\ mm$ from the CMOD: a) beam of height $h = 25\ mm$, (P 25a, Appendix T1); b) beam of $h = 60\ mm$ (P 6a)

4.3.5.2 Force-displacement relationship for a cracked member

The above analysis of cracked section equilibrium shows that for a UHPFRC element with typical material properties, the major part of bending strength is achieved before propagation of the fictitious crack. However, as already mentioned, the cracked regime is relevant since it can allow high deformations to develop without a decrease in force. In order to obtain a unique relationship between forces and deformations, one additional condition is needed to relate the two parameters describing the fictitious crack. Two approaches are developed and discussed in the following sections. The first approach is based on energy balance in the systems, while the second approach introduces a parameter relating the cracked and uncracked parts of the section. The latter leads to an explicit analytical formulation for the moment-curvature relationship, which is convenient for practical application.

4.3.5.2.1 Energy balance in a cracked member

The balance between the energy brought into the system and the energy consumed for the deformation and fictitious crack opening is used to predict the bending response of a cracked element. In the case of FRC materials, in which significant strain softening is present, the application of fracture mechanics (FM) theories based on energy criteria rather than application of strength criteria is suggested by many authors [Hillerborg 1980], [Van Mier 1997], [Bazant, Oh 1983], [Li 2006]. This also applies to UHPFRC. The fundamental principles of the energy balance approach are briefly reviewed in the following.

Energy release rate, G , and fracture energy, G_F

The principal assumption in the energy balance approach is that a certain amount of energy is required for the formation of a unit area of crack surface. The energy required for crack growth is considered to be a material property, known as fracture energy, G_F , (also fracture toughness). When a crack grows, a certain amount of energy is released from the system to the crack, at a rate of $G [J/m^2]$. The available energy release rate, G , depends on element geometry, applied load, and crack length.

Energy balance approach

In 1920 Griffith proposed an energy balance approach, based on the first law of thermodynamics, to describe the formation of a crack: a crack forms and grows only if this process causes the total energy E of the system to remain constant or to decrease. This indicates that the critical condition for a crack to form and grow in equilibrium is that there is no net change in total energy [Anderson 1995]. The total energy of the system is defined as

$$E = \Pi + W_s \tag{4.32}$$

where Π is the potential energy and W_s is the work required to create new crack surface. The potential energy, Π , corresponds to the difference between the internal strain energy, U , and the work of external load, F :

$$\Pi = U - F \tag{4.33}$$

The strain energy in an elastic body can be obtained as follows:

$$U = \int_{\delta} P(\delta) d\delta \tag{4.34}$$

If pseudo-plastic deformations occur in a body, as in the case of UHPFRC elements, only a part of the integral on the right side of Equation 4.34 is reversible energy stored in the system, while a part is spent for damage, U_D (Figures 4.29 and 4.32). The work of external forces is $F = P \cdot \delta$.

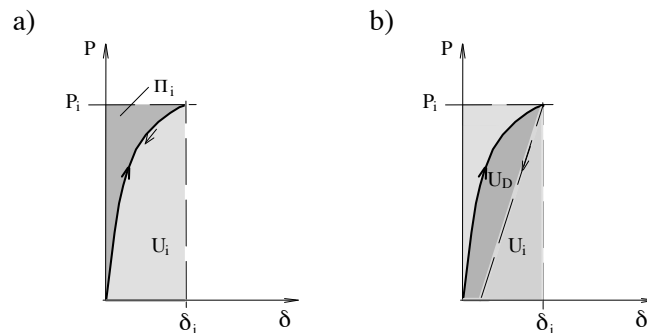


Figure 4.29: Energy of the system subjected to loading P , with corresponding load point displacement δ : a) in a non-linear elastic material, b) in a non-linear damaged material

For an increment in crack area, dA , the energy balance can then be formulated as follows:

$$\frac{dE}{dA} = \frac{d\Pi}{dA} + \frac{dW_s}{dA} \tag{4.35}$$

and as a limit case:

$$\frac{dE}{dA} = 0 \Rightarrow \frac{d\Pi}{dA} = -\frac{dW_s}{dA} . \quad (4.36)$$

According to Irwin [Irwin 1956], the opposite of the ratio $d\Pi/dA$ is defined as energy release rate G :

$$G = -\frac{d\Pi}{dA} , \quad (4.37)$$

whereas dW_s/dA is the already introduced fracture energy G_F . Thus, the energy balance (Equation 4.36) can be rewritten as

$$\frac{d(P \cdot \delta - U)}{dA} = \frac{dW_s}{dA} , \quad (4.38)$$

or, more compactly $G = G_F$.

Conditions for stable crack growth

Based on the principle of energy balance the conditions for stable crack propagation can be formulated as follows: if the proportion of energy that can be released from the system is smaller than the energy required for crack growth, the crack remains unchanged. Additional energy is needed (e.g. brought by force of displacement load) in order to allow crack growth. If, with crack propagation, the energy available for crack growth becomes greater than the fracture energy, the crack becomes unstable. These conditions can be formulated as:

$$G \leq G_F \quad (4.39)$$

$$\wedge \frac{dG}{dA} \leq \frac{dG_F}{dA} , \quad dA = b \cdot da , \quad (4.40)$$

with a being crack length, b being constant width of the crack. According to 4.40, a crack of length a will propagate in a stable way if the variation of the energy release rate for an incremental crack opening dA is lower than the variation in the fracture energy for the same dA . The first criterion is generally less demanding than the second one, as it will be shown with an example in the following paragraph.

It is not useless to recall here that, according to Definition 4.33, the potential energy Π of the system is composed of two contributions: the work $P\delta$ done by the applied loads and the strain energy U . In a structural system, two cases must be distinguished with respect to the second term, U (Equation 4.38): in case of unloading in the system ($dP/dA < 0$), the strain energy decreases ($dU/dA < 0$), whereas in case of increasing load ($dP/dA > 0$) there will generally be some parts of the system, typically those located around the crack, that experience unloading, but the rest of the material will experience an increase in the stress and strain conditions. In the first case, a limit condition for crack stability occurs when the rate of releasing the strain energy stored in the system is equal or higher than the fracture energy G_F : in this case, the crack propagates in an unstable way even if no work of applied load is provided. On the contrary, an additional energy should be supplied by the load in order to make the crack propagate.

Fracture energy for UHPFRC

In the case of quasi-brittle materials, like concrete, FRC and UHPFRC, the classic definition of fracture energy should be reconsidered (§ 3.3.2.6). For elastic brittle materials, cracks are assumed to be stress-free, and in this context, G_F is the energy required to create a new stress-free crack surface in a previously uncracked material. In the case of quasi brittle materials, a part of the crack close to the tip is assumed to be able to bear some tensile stress (fictitious crack), whereas the rest of the crack behaves like the real stress-free crack (Figure 4.30 a). In this case, the energy required for crack propagation comprises the energy spent on fracturing the uncracked material and the energy

required for separation of the crack faces up to the point where no more stress can be transferred. In the case of UHPFRC (Figure 4.30 b)), the matrix is very brittle, whereas the stress bearing capacity of the fibres is very high: thus, the fracture energy represents the energy required for crack opening (§ 3.3.2.6), while the energy required for crack formation is negligible. According to the modelling approach adopted in this work, the energy associated to the multi-microcracking that occurs before the tensile softening, is related to deformational dissipation and is included in the surface covered by the tensile stress-strain relationship of UHPFRC.

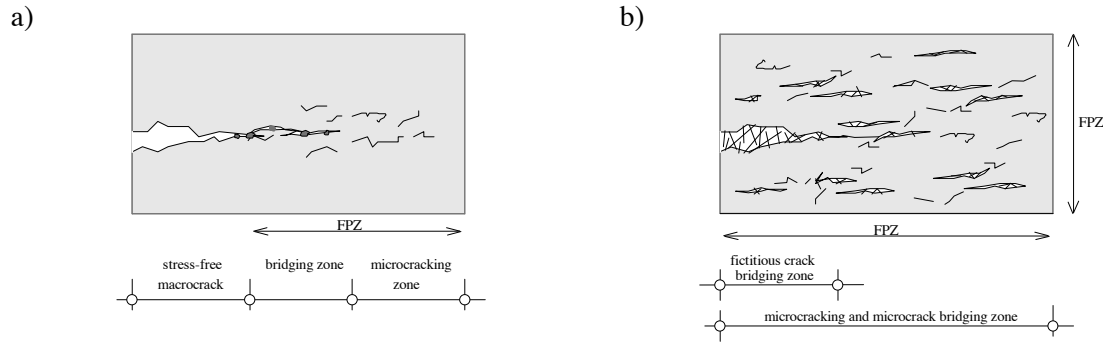


Figure 4.30: a) Schematic illustration of crack growth and representation of fracture process zone (FPZ) in ordinary concrete, adapted from [Van Mier 1997]; b) fracture proces zone in UHPFRC, adapted from [Kabele 2000]; according to the FCM the FPZ is the fictitious crack itself

Conditions for stable crack growth in a UHPFRC member in tension

Before considering the general conditions for stable crack growth in a UHPFRC member in bending, the stability conditions in uniaxial tensile state are investigated. It is assumed that a monotonously increasing displacement is imposed to a member, that the maximal tensile strain ϵ_u was attained and that the force in the system starts to decrease. Assuming that the crack has developed through the whole cross-section, crack energy and consequently the criteria for crack stability become functions of crack opening w_i .

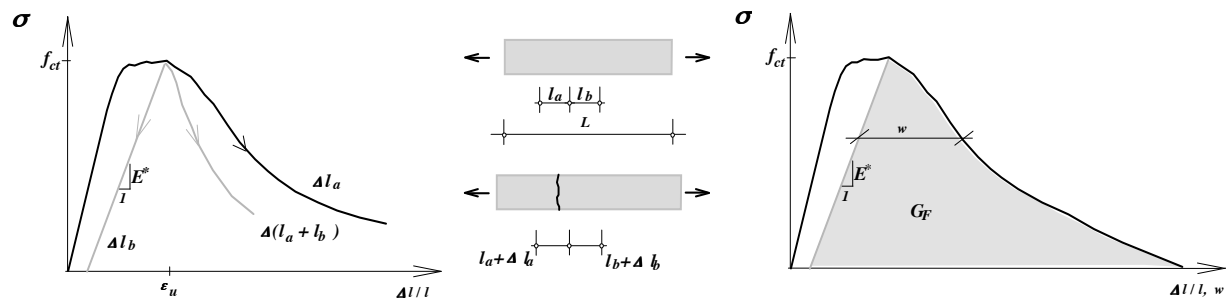


Figure 4.31: Member in uniaxial tension, definition of fracture energy, adapted from [Hillerborg 1980]

We will first consider the stability criterion 4.40. At a certain point in the descending branch, the energy per unit surface that can be released by the microcracked system is a function of the stress variation, the length of the specimen and the unloading stiffness E^* of the material:

$$G = f(\Delta\sigma, L, E^*) = f(w_i, L, E^*) . \tag{4.41}$$

G can be expressed as a function of crack opening w_i :

$$G = \frac{\Delta\sigma(w_i)}{E^*} \cdot (L + \Delta L - w_i) \cdot \frac{f_{ct} + \sigma(w_i)}{2} + \int_{\Delta L_{w_0}}^{\Delta L} \sigma(w_i) d\Delta L \quad (4.42)$$

while the energy required to open the crack up to crack opening w_i is

$$G_{F,w_i} = \int_0^{w_i} \sigma(w_i) dw_i . \quad (4.43)$$

The rate of change in the released energy and the corresponding rate of the energy consumed by the fictitious crack opening are then related as functions of crack opening:

$$\frac{\partial G}{\partial w_i} \leq \frac{\partial G_{F,w_i}}{\partial w_i} \quad (4.44)$$

For a $\sigma(w)$ law typically used for concretes, the maximal value of the right side of the Inequality 4.44 is obtained for $w \rightarrow 0$, thus the most critical point for stability is at the beginning of the softening branch. With the assumed linear stress-crack opening relationship defined in § 3.3.2.8, the previous condition becomes:

$$\Leftrightarrow \frac{C_2(f_{ct} - C_2 w_i)}{E^*} L \leq f_{ct} - C_2 w_i, \quad C_2 = \frac{\partial \sigma(w_i)}{\partial w_i} \quad (4.45)$$

thus:

$$C_2 L \leq E^* \quad (4.46)$$

where C_2 is the initial slope of the stress-crack opening relationship (§ 3.3.2.8). Equation 4.46 indicates that the crack stability is governed by the length of the specimen and by two material properties, namely the slope of the $\sigma-w$ relationship and the slope of the unloading stress-strain behaviour. Equation 4.46 enables the *critical length* l_{cr} , as the maximal length of a specimen for which the crack can propagate in a stable way, to be defined:

$$l_{cr} \leq \frac{E^*}{C_2} . \quad (4.47)$$

For a member in tension, the stability condition defined by Equation 4.39 gives:

$$G \leq G_F \Leftrightarrow \frac{f_{ct}^2}{2E^*} L \leq G_F . \quad (4.48)$$

In the case of a linear stress-crack opening relationship:

$$G_F = \frac{f_{ct}^2}{2 \cdot C_2} \quad (4.49)$$

and the two conditions given by Equations 4.46 and 4.48 give the same result in terms of critical length. Otherwise, the integral condition (4.48) is less restraining than the differential condition (4.46). For a typical UHPFRC, the initial slope C_2 of the stress-crack opening law is about 2.5-3.5 times the slope $f_{ct}^2/(2G_F)$ corresponding to a linear stress-crack opening relationship with the same fracture energy. The error in estimating the critical length required for stable crack growth using expression 4.48 is in the same range. As illustration, the maximal element length required for a stable tensile test according to Equality 4.46 gives $l_{cr} = 1 \text{ m}$, while condition 4.48 gives $l_{cr} = 2.86 \text{ m}$, with $G_F = 20 \text{ KJ/m}^2$, $f_{ct} = 9 \text{ MPa}$, and the initial slope of $C_2 = 6 \text{ MPa/mm}$ and $E^* = 6 \text{ GPa}$.

Finally, it is important to underline that the so-called *characteristic length*:

$$l_{ch} = \frac{E \cdot G_F}{f_{ct}^2} \quad (4.50)$$

frequently used to characterise the brittleness of a material [RILEM 2002] corresponds, in the case of a linear stress-crack opening law, to one half of the critical length previously introduced.

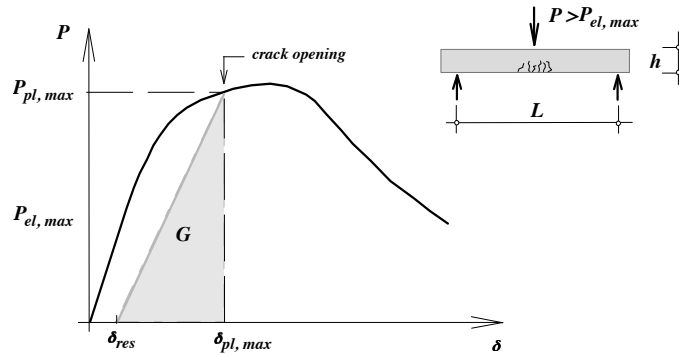
Condition for stable crack growth in bending

Let us now examine the stability of a fictitious crack in an element in bending (Figure 4.32 a). The more demanding stability criterion based on rates of energies (Equation 4.40) will be discussed during the definition of the analytical model for bending. In this section, only the integral stability condition, which is a minimal condition for stable crack growth, will be investigated. We consider a beam in three point bending and we assume that the beam has been loaded up to a certain load level P , when a discrete macrocrack starts to propagate. At this point, the total energy that can be released by the member in case of unloading (the shaded area in Figure 4.32 a) is:

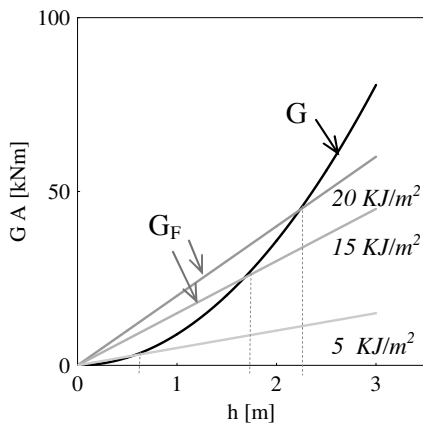
$$G = \frac{1}{2} P_{pl,max} (\delta_{pl,max} - \delta_{res}) \quad (4.51)$$

where $\delta_{pl,max}$ corresponds to the displacements of the load point for the force level prior to crack opening and δ_{res} is the residual displacement of the same point for zero force (Figure 4.32 a)). Both of these values can be calculated by taking into account the non-linear material behaviour of UHPFRC, using the equations developed in § 4.3.4 and in Appendix M1.

a)



b)



c)

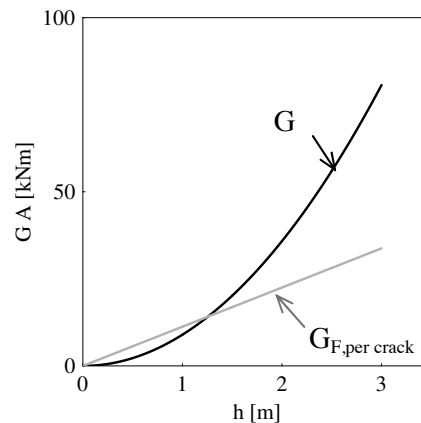


Figure 4.32: Stability of the UHPFRC element in bending: a) available energy in system at the onset of crack, and boundary conditions; b) instability points as function of element size, h , for various fracture energy values (5, 15 and 20 KJ/m^2); c) instability point assuming a crack shape for $G_F=16 KJ/m^2$

As a limit case, if the total energy defined by Equation 4.51 is higher than the fracture energy, the crack can propagate in an unstable way without work of the applied load. The instability points calculated with this approach are shown in Figure 4.32 b) as a function of elements size h . Elements slenderness is kept constant, $L/h = 10$, and several fracture energy values are assumed. Since the quantity of the strain energy that can be released increases with increase in element size, the fracture energy required in order to exhibit stable crack growth increases. However, it can be noted that for fracture energy values typical for UHPFRCs, stable crack propagation can be expected in thin elements, suggesting possible safe applications without additional ordinary reinforcement.

In bending, the crack propagates in length and the crack opening varies along the length of the crack. In order to give a simple estimation of the energy that can be consumed by a crack in bending, it is assumed that the crack propagates up to the entire height of the section and that the crack mouth opening displacement is equal to the maximal fictitious crack opening, $w_i \rightarrow w_{max}$, assuming the crack shape as defined in Equation 4.30. With these conditions, the energy required for crack opening, designated as $G_{F, per crack}$, can be calculated (Equation A 2.18) and the comparison with the strain energy that can be released is shown in Figure 4.32 c).

4.3.5.2.2 Application of energy balance approach to a UHPFRC element in bending;

Hypotheses of the model

Let us continue to observe the element in bending governed by a single load parameter, P (Figure 4.33). If the energy release rate at the onset of the macrocrack is lower than the corresponding fracture energy, that is if the Inequalities 4.39 and 4.40 are satisfied, a stable crack can grow in the element. If so, let us assume that the additional energy for crack growth is brought into the system by the increase in force. Consequently, the deformation of the system increases, with the macrocrack opening in the critical section, while the major part of the rest of the beam deforms in the same linear and non-linear way as if the crack were not present. (This can be seen by means of the numerical FEM model¹, Figure 4.39). Thus, the energy brought into the system is dissipated partly as deformational energy and partly as energy for crack opening.

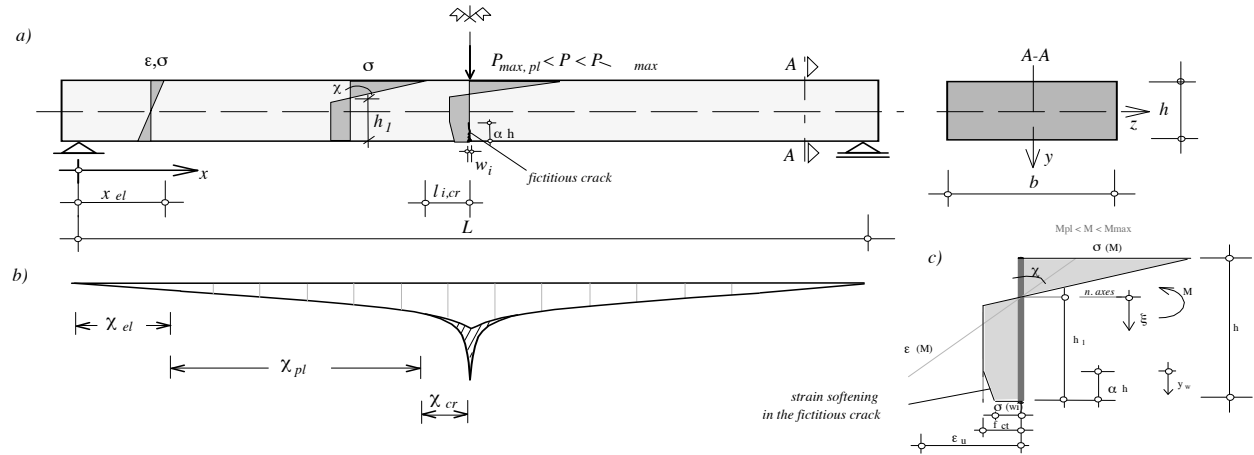


Figure 4.33: Case study: beam in three-point bending with a fictitious crack : a) system geometry and schematic presentation of regions exhibiting different stress states; b) distribution of curvature; c) stress distribution in cracked section

Additional hypotheses are introduced in order to relate the force and the deformation in the cracked system:

- if for the given force level $P_i = P + \Delta P$, $\Delta P > 0$, a crack propagates up to the length $\alpha_{ij} \cdot h$, the corresponding CMOD w_{ij} is calculated from the sectional equilibrium (Equations A.2.11);

¹ The hypothesis of the numerical FEM model are presented in Appendix M2: single macrocrack is modelled based on the FCM, and the surrounding material can exhibit plastic yielding in tension

consequently, the energy needed for fictitious crack growth, $G_{Fij}(\alpha_{ij} \cdot h, w_{ij})$, is quantified (Equation 4.63);

- the presence of the crack leads to a changed stress state in the vicinity of the crack, due to the local decrease in stress (Figures 4.34); this “disturbed” region is distributed around the fictitious crack, within a distance $2 l_{i,cr}$, which is proportional to crack length (Figure 4.39);
- the continuity of deformations in the disturbed region is assured by defining a continuous smooth function describing curvature (Equation 4.69, Figure 4.33 b)); this enables the total displacement, $\delta_{ij}(P_i, \alpha_{ij} \cdot h)$, of the system loaded with P_i , in the presence of a crack of length $\alpha_{ij} \cdot h$, to be calculated.

Based on the work of [Bazant, Becq-Giraudon 1999]¹ and [Bazant, Cedolin 1991], it is assumed that the displacement δ_i can be expressed as:

$$\delta_i(P_i) = \delta_{i0}(P_i) + \delta_{if}(P_i) \quad (4.52)$$

where $\delta_{i0}(P_i)$ is the displacement of the load point that would occur if no crack were present in the system (violating the condition of resistance), and the $\delta_{if}(P_i)$ is the additional displacement due to the fictitious crack opening while force is kept constant. The crack length $\alpha_i \cdot h$ corresponding to imposed force P_i is determined as a crack length $\alpha_{ij} \cdot h$ for which released energy G_{ij} is equal to fracture energy $G_{Fij}(\alpha_{ij} \cdot h, w_{ij})$, Figure 4.38 a) and b). The released energy is obtained based on the condition of minimization of potential energy for crack growth² (developed Equations 4.57 to 4.62).

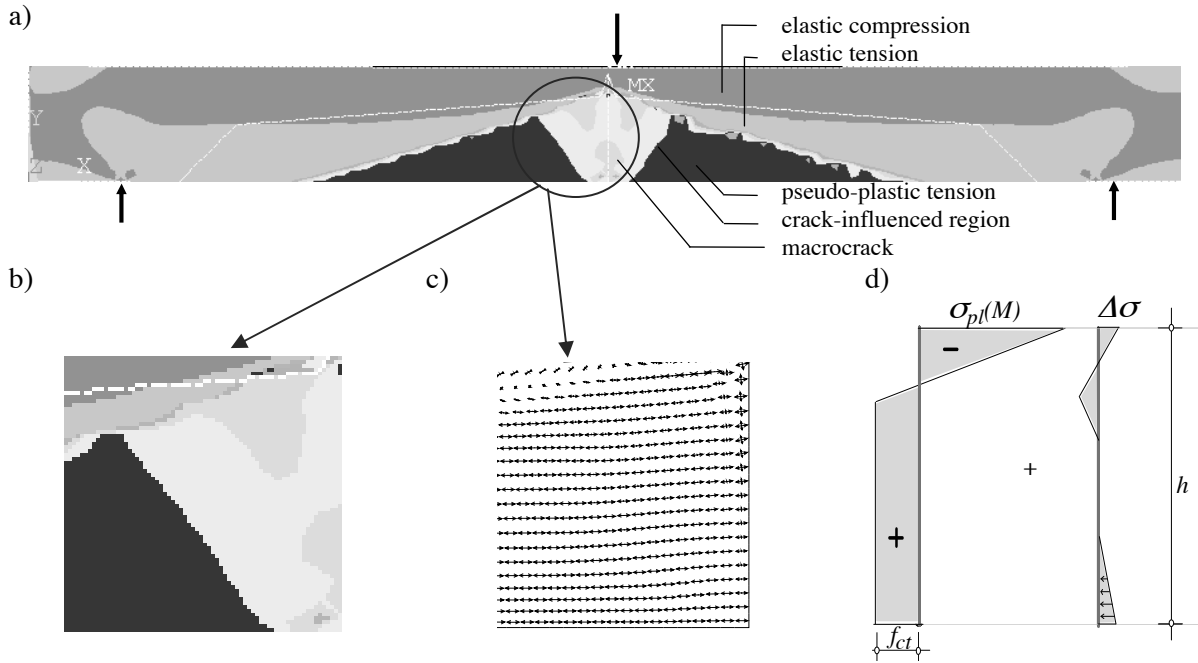


Figure 4.34: Beam with a fictitious crack at maximal force: a) normal stress distribution along the beam; b) disturbed field of normal stresses and c) of principal stresses close to the macrocrack; d) normal stresses in the elastic-pseudo plastic section and self-equilibrated stress variation ($\Delta\sigma$) due to fictitious crack opening

An interesting phenomenon concerning a fictitious crack opening in a UHPFRC element prior to peak force is noted: the energy liberated from the surrounding material due to local unloading can be virtually disregarded, owing to the fact that the crack opening up to peak load is very small (Figure 4.26 and 44.28) and the corresponding stress decrease is very limited (low slope of tensile softening curve). From the numeric analysis, it can be seen that the unloading region around the

¹ The energy released rate in this paper is related to stress intensity factor (SIF); for the FCM, the SIF loses its significance;

² In [Bazant, Li 1995] for the stability of a cohesive crack growth in a linear-elastic quasi-brittle material, an approach for obtaining crack opening by minimizing the complementary energy with respect to crack length is developed as a function of stress intensity factors

crack evolves in a way that can not be easily described analytically (Figure 4.34). However, following the hypothesis commonly accepted in the analysis of crack propagation in concrete [Bazant, Cedolin 1991] (Figure 4.35), the energy that can be released from the surrounding material can be expressed as a function of crack parameters (α and w_i), and element size (Equation 4.55).

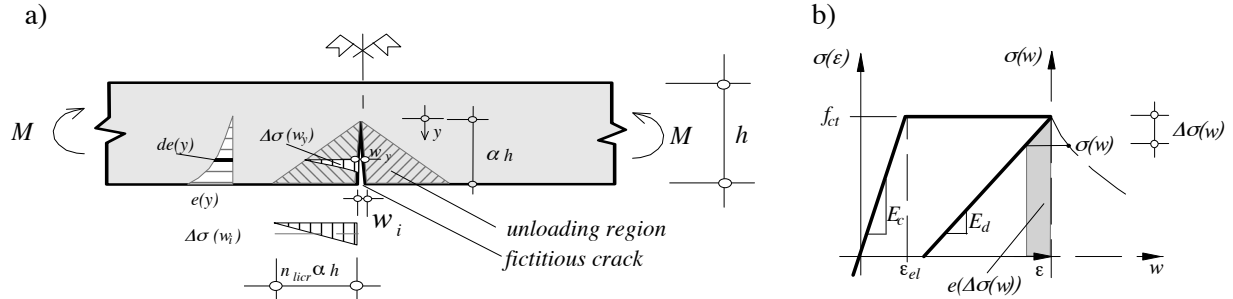


Figure 4.35: a) Assumptions regarding unloading region surrounding fictitious crack; b) portion of energy released by unloading

The stress decrease, $\Delta\sigma$, in the zone surrounding the crack causes the release of an amount of energy $e(\Delta\sigma(w))$ that can be estimated for a known unloading modulus of the material, E^* (Figure 4.35). For an elementary thickness dy along the height of the unloading region:

$$de(y) = \frac{1}{2} e[\Delta\sigma(w(y))] = \frac{1}{2} \frac{f_{ct} + f_{ct} - \Delta\sigma(w(y))}{2} \cdot \frac{\Delta\sigma(w(y))}{E^*}. \quad (4.53)$$

With a defined crack opening pattern (Equation 4.30) and considering the initial slope of the unloading stress-crack opening curve, C_2 , the previous expression becomes:

$$de(y) = \frac{1}{2} \cdot \left(f_{ct} - \frac{C_2}{2} \cdot \frac{w_i \cdot y}{\alpha \cdot h} \right) \cdot \frac{C_2}{E^*} \cdot \frac{w_i \cdot y}{\alpha \cdot h}. \quad (4.54)$$

Integrating this energy portion over the volume of the unloading region, the total energy E_{licr} that can be released from the surrounding material is

$$E_{licr} = 2 \cdot b \cdot \int_0^{\alpha \cdot h} de(y) \cdot n_{licr} \cdot \alpha \cdot h \cdot dy = b \cdot \frac{C_2}{E^*} \cdot w_i \cdot n_{li,cr} \cdot (\alpha \cdot h)^2 \cdot \left(\frac{f_{ct}}{3} - \frac{C_2}{8} \cdot w_i \right). \quad (4.55)$$

This value, as a function of crack opening and relative depth, is plotted in Figure 4.36 b), while the energy required to open a crack, G_{Fi} (Equation 4.67), as a function of the same parameters, is plotted in Figure 4.36 a). The ratio between these two quantities of energy, again as a function of crack length and opening is formulated as:

$$E_{licr} / G_{F,i} = \frac{C_2}{4 \cdot E^*} \cdot n_{li,cr} \cdot \alpha \cdot h \cdot \frac{(8 \cdot f_{ct} - 3 \cdot C_2 \cdot w_i)}{(3 \cdot f_{ct} - C_2 \cdot w_i)} \quad (4.56)$$

and it can be seen that for element heights of up to 100 mm , for typical UHPFRC material properties, this ratio is lower than 2-3 % (Figure 4.36 c), 4.37 a)). It is also interesting to observe that the portion of released energy due to stress decrease in the vicinity of the crack is more significant in quasibrittle materials in which the initial slope of the tensile softening branch is steeper, indicating lower fracture energy (Figure 4.37 b)).

Thus, for the fictitious crack opening in a UHPFRC prior to peak load, the portion of the energy released from the surrounding material can be disregarded. Moreover, in the case of more brittle materials, if simplified hypotheses concerning the shape of the unloading zone are made, the energetic contribution of this zone can be easily implemented in the analytical model under discussion.

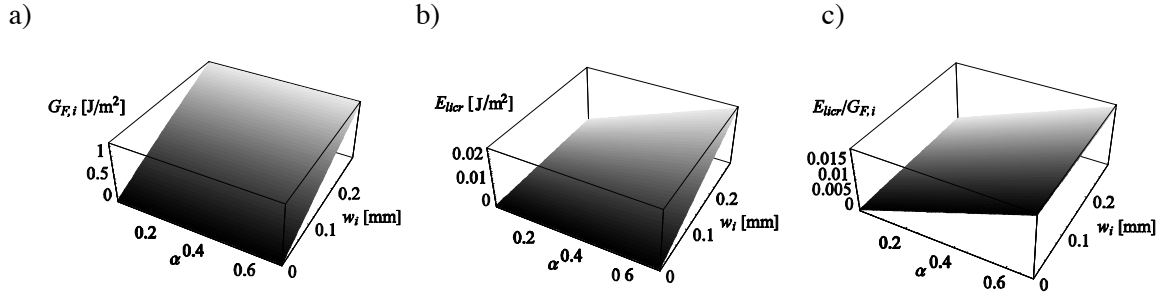


Figure 4.36: a) Energy consumed by fictitious crack, $G_{F,i}$, as a function of relative crack length, α , and crack opening, w_i ; b) energy that can be released from the surrounding material, E_{licr} ; c) ratio between E_{licr} and $G_{F,i}$ (beam depth $h=50$ mm)

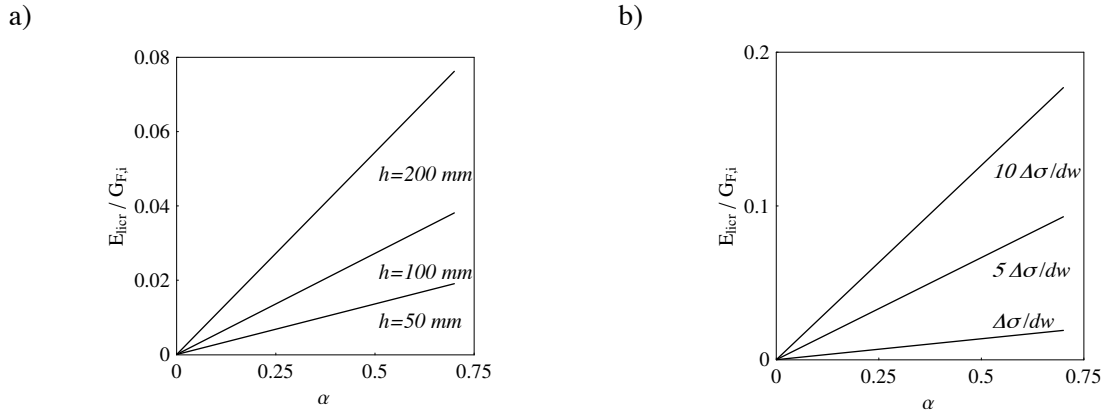


Figure 4.37: Ratio between E_{licr} and $G_{F,i}$: a) for a typical UHPFRC and various element heights; b) for a constant element height $h=50$ mm and variation in slope of tensile softening curve

Respecting the energy balance in the system, on condition that the potential energy for crack growth is minimised, it is obtained that

$$\frac{d\Pi_i}{b \cdot d\alpha \cdot h} = -G_{F_i} \quad (4.57)$$

where $\frac{d\Pi_i}{b \cdot d\alpha \cdot h}$ represents energy released rate G and can be obtained based on the previous hypothesis of the crack growing under constant force [Bazant, Becq-Giraudon 1999]:

$$\frac{d\Pi_i}{d\alpha \cdot h} = \frac{d(U_i - F_i)}{d\alpha \cdot h} \quad (4.58)$$

$$\frac{d\Pi_i}{d\alpha \cdot h} = \left. \frac{d(U_i)}{d\alpha \cdot h} \right|_{P=const} - \left. \frac{d(F_i)}{d\alpha \cdot h} \right|_{P=const} \quad (4.59)$$

In view of the fact that no additional strain energy is stored in the system with the increase in crack length under a constant force,

$$\frac{d\Pi_i}{d\alpha \cdot h} = - \left. \frac{d(F_i)}{d\alpha \cdot h} \right|_{P=const} = - \frac{Pd(\delta_i)}{d\alpha \cdot h} \quad (4.60)$$

the energy released for a crack of length $\alpha_i h$ in an equilibrated system is:

$$G(P_i, \alpha_{ij} \cdot h) = 2 \int_{L/2-l_{cr}(\alpha_i)}^{L/2} M(x) \cdot (\chi_{cr}(\alpha_i, P_i, x) - \chi_{pl}(P_i, x)) \cdot dx . \quad (4.61)$$

The energy equilibrium condition yields

$$G_{ij}(P_i, \alpha_{ij} \cdot h) == G_{Fij}(\alpha_{ij} \cdot h, w_{ij}) . \quad (4.62)$$

thus, for the given $P_i \leq P_{max}$, for every assumed crack length $\alpha_{ij} \cdot h$ there is a crack energy, $G_{Fij}(\alpha_{ij} \cdot h, w_{ij})$, and a corresponding energy $G_{ij}(P_i, \alpha_{ij} \cdot h)$ provided by the external load for propagation of the crack of length $\alpha_{ij} \cdot h$. A unique value of α_{ij} is found as the solution of the Equation 4.62, graphically presented in Figure 4.38 b).

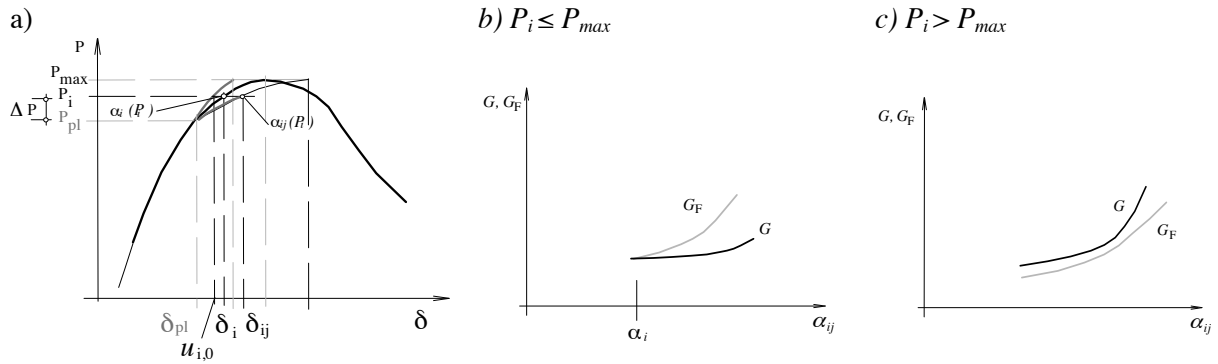


Figure 4.38: Equilibrium point as a function of assumed crack length, $\alpha_{ij} \cdot h$: a) possible force-displacement responses for different α_{ij} ; b) energy that can be released from the system, G_R , and energy that can be consumed by the crack, G_F , for a stable crack growth; c) as previous, for unstable crack growth in force-controlled loading

For a force level higher than the maximal force, the point of equilibrium can no longer be found, since the released energy always remains higher than the energy that can be consumed by a crack that is equilibrated with the given force (Figure 4.38 c)). The system becomes unstable under the force-controlled load.

4.3.5.2.3 Algorithm for resolution of the stated problem

Force control

Let us assume that for given force level $P_i = P + \Delta P_i$, $P \geq P_{pl,max}$, the crack propagates up to the length $\alpha_{ij} \cdot h$. There is a corresponding CMOD, w_{ij} , which satisfies the equilibrium of internal and external forces, obtained as a solution of equation

$$M(P, x_{cr}) = M(\alpha_{ij}, w_{ij}) \quad (4.63)$$

where $M(\alpha_{ij}, w_{ij})$ is given by Equation A 2.14 (Appendix M2). For given force level P_i an array of possible pairs $\{\alpha_{ij}, w_{ij}\}$ satisfying the equilibrium of force can be formed. It should be noted that Equation 4.63 has more than one root for w_{ij} , but there is only one rational solution in the range of w_{ij} covered by the equation $\sigma(w)$.

The energy needed for a crack of length $\alpha_{ij} \cdot h$ to open with CMOD w_{ij} , designated $G_{F,ij}$, can now be calculated for the stress distribution defined by the function $\sigma(w)$

$$G_F = \int_A \left(\int_0^w \sigma(w) dw \right) dA . \quad (4.64)$$

For a cross section of a constant width, $b=const$, and for a linear crack opening $w(y)$:

$$w(y) = \frac{w_{ij}}{\alpha_{ij} \cdot h} y, \quad (y = 0 \text{ at the crack tip, } y = \alpha_{ij} \cdot h \text{ at the crack mouth}) \quad (4.65)$$

G_F can be obtained as:

$$G_{F,ij} = b \int_0^{\alpha_{ij} h} \left(\int_0^{\frac{w_{ij} \cdot y}{\alpha_{ij} h}} \sigma(w) dw \right) dy. \quad (4.66)$$

With linear function $\sigma(w) = C_1 - C_2 w$,

$$G_{F,ij} = b \cdot \frac{C_1}{2} w_{ij} \alpha_{ij} h - b \cdot \frac{C_2}{6} w_{ij}^2 \alpha_{ij} h. \quad (4.67)$$

With another shape of $\sigma(w)$ relationship the expression for $G_{F,ij}$ can be found in Appendix M2.

Considering the beam, the increase in force, in the presence of a crack of length $\alpha_{ij} \cdot h$, leads to a new deformation state with a corresponding mid-span displacement δ_{ij} . In order to quantify the deformations, an additional assumption in this analysis concerns the description of the region influenced by the crack. Based on numerical simulations, it was seen that the length of the crack influenced region, $l_{i,cr}$, increases with crack propagation (Figure 4.39 b)), and that it can be assumed as a linear function of crack length:

$$l_{i,cr} = f(\alpha_i \cdot h) = n_{li,cr} \cdot \alpha_i \cdot h \quad (4.68)$$

with $n_{li,cr}$ in the range of $0.5-1$. Similar observations regarding the crack-influenced zone can be found in [Casanova 1996]. It is important remember that the region around the crack should not be confused with the crack process zone; as explained, the FCM hypotheses assume that the process zone is situated along the very line of the crack.

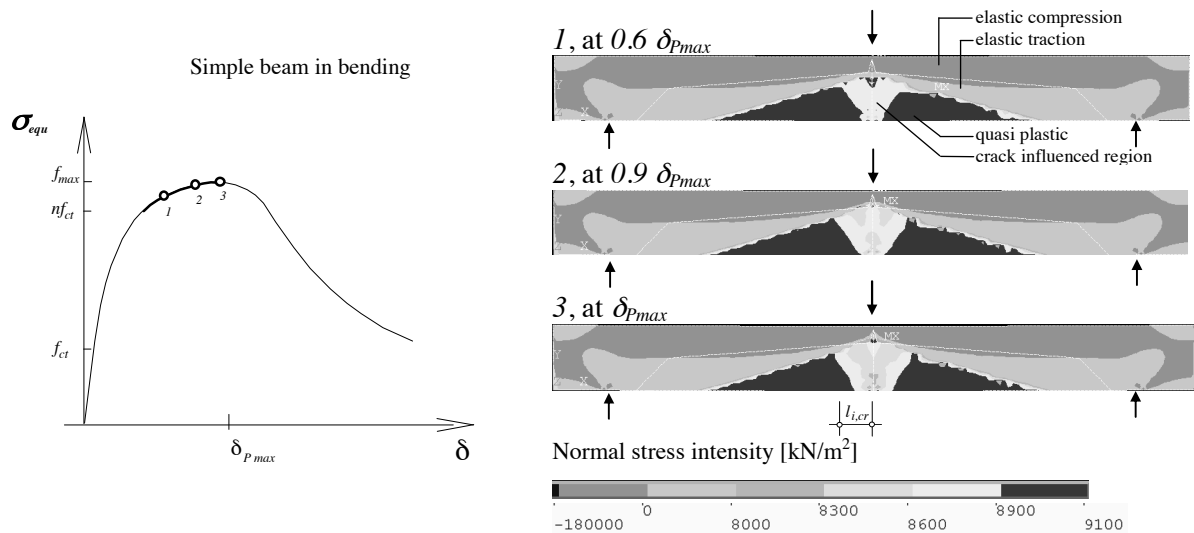


Figure 4.39: Stress regimes in a beam in bending, with plastic yielding in tension and crack opening: a) position of examined points on force-displacement diagram; b) propagation of region influenced by crack opening (regions of stress decrease)

Due to the change in stress field, influenced by the local stress decrease, defining the stress-strain relationship for the section in this region becomes less straightforward. However, in order to assure the continuity of deformations, the curvature in this region is assumed as being a parabolic function:

$$\chi_{cr} = a_{\chi}x^2 + b_{\chi}x + c_{\chi} \quad \forall L/2 - l_{i,cr} \leq x \leq L/2 \quad (4.69)$$

with a smooth connection with the curvature of a plastic section at $x = L/2 - l_{i,cr}$, and the value at $L/2$ corresponding to the curvature of the cracked section, $\chi_{cr,ij}$. Coefficients a_{χ} , b and c_{χ} , in Equation 4.69 are obtained by solving the following system of equations:

$$\begin{aligned} \chi_{cr}(L/2 - l_{i,cr}) &= \chi_{pl}(L/2 - l_{i,cr}) \\ \chi'_{cr}(L/2 - l_{i,cr}) &= \chi'_{pl}(L/2 - l_{i,cr}) \\ \chi_{cr}(L/2) &= \chi_{cr,ij} \end{aligned} \quad (4.70)$$

where $\chi_{cr,ij}$ is obtained for the imposed force and assumed crack length, from Equation A 2.11 (Appendix M2), and χ_{pl} is the function given by Equation 4.11. The expressions for coefficients a_{χ} , b and c_{χ} , are given in Appendix M2 (Equation A 2.23). Incorporating Equation 4.69 into Equation 4.61 available energy release rate, G , can be calculated for every α_{ij} .

Before maximal force is reached, there is a unique value for crack length, $\alpha_i h$, for which the released energy is equal to the energy consumed by the crack (the intersection of G and G_F , Figure 4.38 b), Equation 4.62). This also allows the displacement at any point of the element to be calculated. For the point of application of the force ($x=L/2$), displacement δ_i is calculated as:

$$\delta_{i,L/2} = 2 \cdot \int_0^{L/2} \chi(x) \cdot \bar{M}(x) \cdot dx = 2 \left[\int_0^{x_{el}} \frac{M(x)}{E_c I} \cdot \bar{M}(x) \cdot dx + \int_{x_{el}}^{L/2 - l_{i,cr}} \chi_{pl}(x) \cdot \bar{M}(x) \cdot dx + \int_{L/2 - l_{i,cr}}^{L/2} \chi_{cr}(x) \cdot \bar{M}(x) \cdot dx \right] \quad (4.71)$$

The algorithm of the procedure and the equations considered are given in Appendix M2.

Examples of obtained force-displacement curves are plotted in Figure 4.40 (black lines) against the numerically obtained curves (grey lines) using the FEM model¹ of the UHPFRC beam (Appendix M2). It can be seen that a very good prediction of the maximal load is obtained, and that the obtained deformations follow very well the trend of deformations obtained by the numerical simulation.

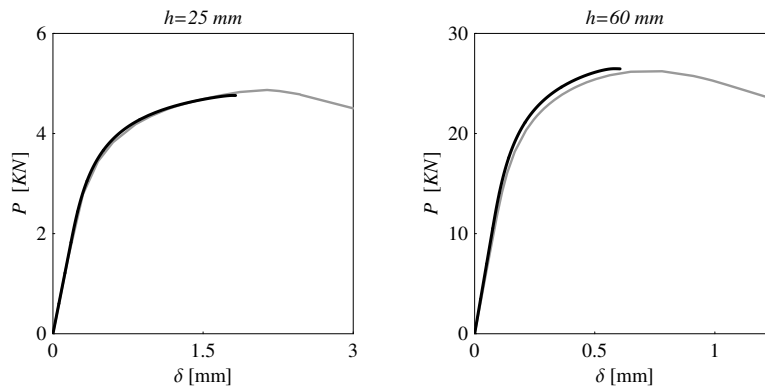


Figure 4.40: Prediction of maximal force with crack propagation governed by energy balance, for beams of different heights in three-point bending; beam geometry and material properties correspond to tested UHPFRC beams, and the value $l_{i,cr} = n_{li,cr} \alpha \cdot h = 0.75 \alpha \cdot h$ is used

¹ The hypothesis of the numerical FEM model are presented in Appendix M2

In order to obtain further points of force-displacement response for the element, the procedure must be performed under deformation-controlled loading.

Deformation control

Let us consider that imposing a deformation in the system is affine with imposing a curvature in the cracked section, $\chi_i, \chi_d > \chi_{pl,max}$. The imposed deformation is associated to a force level, P_i , as a function of a parameter describing the crack (w_i or α_i). As in the previous procedure, the solution for a crack parameter is found from the equilibrium of G and G_F . In case of decreasing force, the definition of the released energy function need to be changed. This is because the part of the beam outside the crack influenced region can no longer exhibit any increase in deformation, but actually starts to unload, providing the energy that can be consumed by the fictitious crack. The part of the beam that was in pseudo-plastic yielding undergoes inelastic unloading which can be evaluated using Equation 4.28, with maximal curvatures in the sections imposed by the maximal force, P_{max} . Any further increase in deformation is thus localised in the cracked section only (Figure 4.41 b)).

The total energy released for further propagation of the crack, after P_{max} was achieved, is schematically presented in Figure 4.41 a). Similar assumptions are made by [Pettersson 1980] for linear-elastic materials, and applied in the RILEM recommendations [Hillerborg 1985]; here the approach is extended here to non-linear materials:

$$G = \int_{\delta_{P,max}}^{\delta_i} P d\delta + \frac{P_{max} - P_i}{K_d} \cdot \frac{P_{max} + P_i}{2} \quad (4.72)$$

where K_d is the unloading stiffness of the microcracked beam that can be obtained using the procedure developed in Appendix M1. To calculate displacement of the element, the inelastic unloading should also be considered in the microcracked region:

$$\delta_{i,L/2} = 2 \cdot \int_0^{L/2} \chi(x) \cdot \bar{M}(x) \cdot dx = 2 \left[\int_0^{x_{el,P,max}} \frac{M(x)}{E_c I} \cdot \bar{M}(x) \cdot dx + \int_{x_{el,P,max}}^{L/2-l_{i,cr}} \chi_d(x) \cdot \bar{M}(x) \cdot dx + \int_{L/2-l_{i,cr}}^{L/2} \chi_{cr}(x) \cdot \bar{M}(x) \cdot dx \right] \quad (4.73)$$

The algorithm of the procedure and the equations considered are also given in Appendix M2.

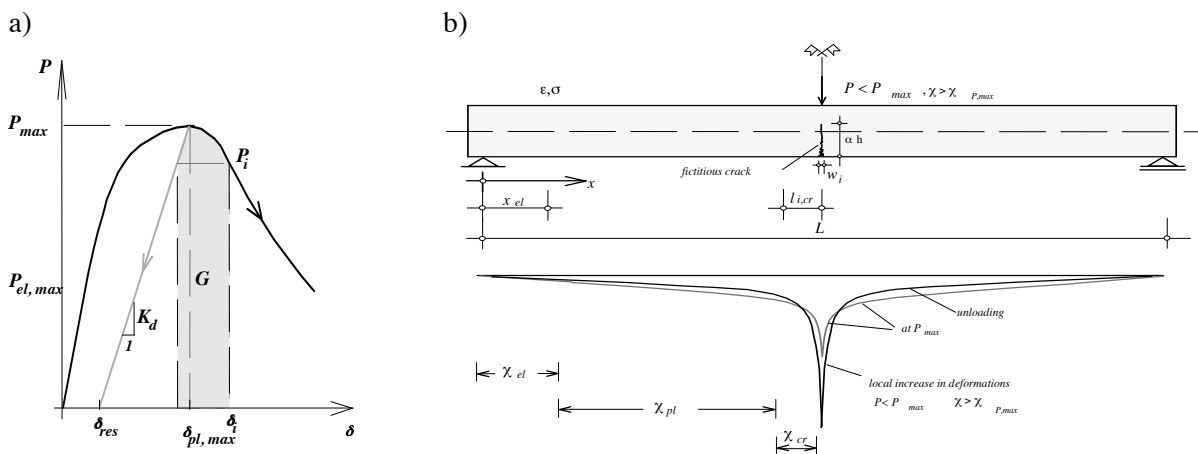


Figure 4.41: Softening of beam: a) energy released in softening; b) increase in deformations with decrease in global force: increase in deformations only locally, in the cracked region, and unloading of the rest of the beam

The deformation-controlled solution has two advantages: both pre and post-peak behaviour are using one single procedure, and the solutions are easily found since, for the given curvature, both G and G_F can be explicitly written as a function of w_i . The solution can be found without any other iterative procedure than the search for the root of the function $G(w_i) = G_F(w_i)$ for w_i .

The results of the deformation-controlled procedure in the form of force-displacement diagrams are shown in Figure 4.42 a) for beams of various heights. The results of the model (black lines) are plotted against numerical simulations (grey lines), using FEM analysis. The procedure gives the same results for the pre-peak behaviour as those obtained using the force-controlled algorithm, and it can be seen that a good prediction of the results in the descending part of the force-displacement curve is obtained. The results are also plotted as normalised values (Figure 4.42 b)), as load-point displacements over element height against the equivalent bending strength. It can be noted that elements of smaller height exhibit more ductile bending response, that will be further discussed in § 4.4.3.

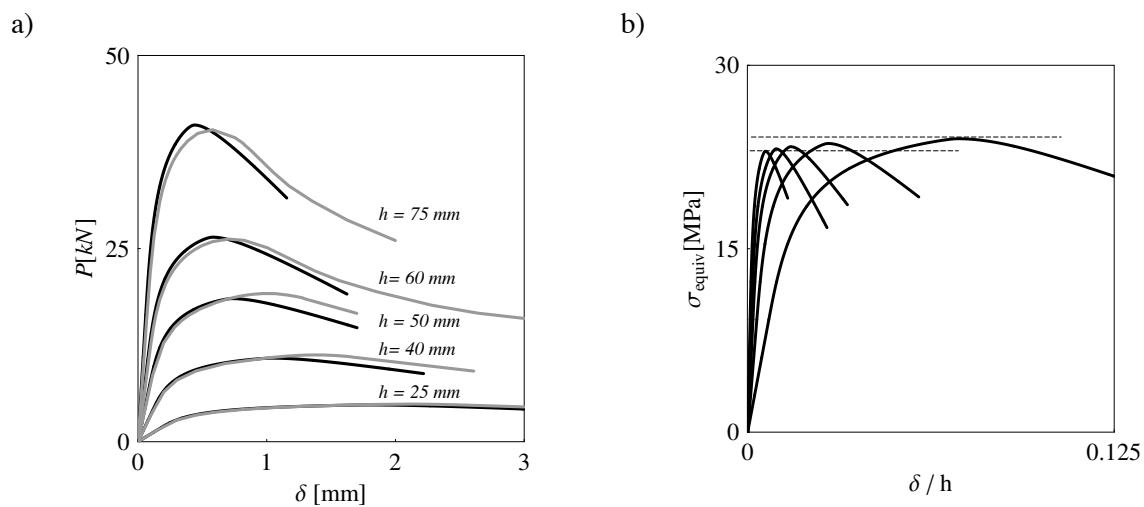


Figure 4.42: Force-displacement relationship according to model for beams of different heights ($h = 25-75$ mm); a) model (black lines) against numerically obtained results using FEM model (grey line); b) bending stress according to model against normalised mid-span displacement

Crack propagation can also be accurately described using the developed model. Figure 4.43 a) shows the development of crack opening as a function of crack propagation, α , for beams of different heights. The crack occupies a greater portion of the cross-section height in thinner beams. In all beams it can be seen that crack length tends to stabilise around a certain value, after which it is principally the crack opening that increases. Figure 4.43 b) shows the ratio between crack opening increase rate, w , for force/deformation increase, and crack length increase rate, αh . It can be seen that, at the beginning of crack propagation, the crack increases faster in length than in opening, while later the increase in opening becomes greater, which is in agreement with the experimental observations and the results of the numerical model.

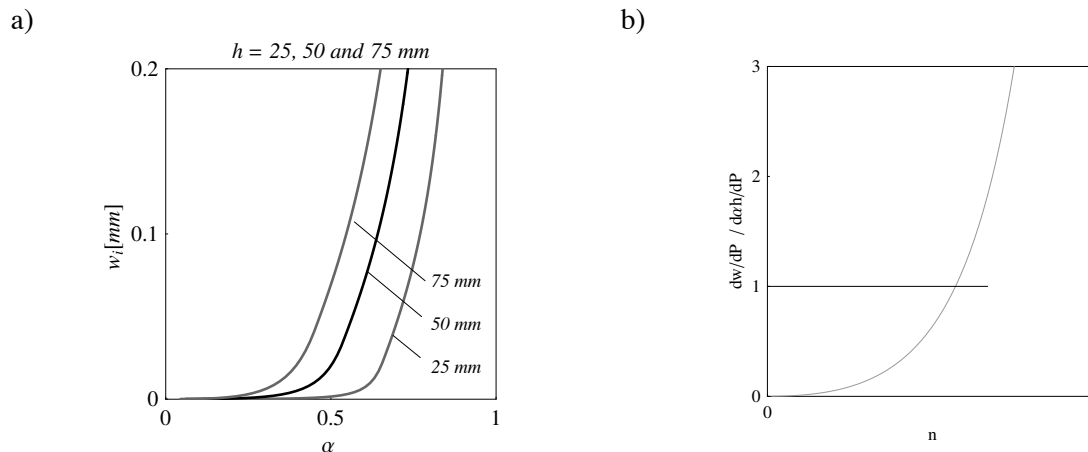


Figure 4.43: Development of macrocrack: a) crack opening versus crack length; b) increase in crack opening over increase in crack length: at the beginning of crack formation, the crack propagates faster than it opens

4.3.5.2.1 Discussion of the hypotheses

The value of the length of the crack-influenced region, l_{icr} , is a parameter that may be questioned with regard to the developed model. For this reason the influence of the length of the crack-influenced region $l_{icr} = n_{licr} \cdot \alpha \cdot h$ on the modelled force-displacement response is studied by varying the parameter n_{licr} within the range of possible values observed during numerical analysis (Figure 4.44 a)). It can be seen that the model is not highly sensitive to the variation of this parameter, as observed with some other models (Section 4.2), and the smaller values of n_{licr} slightly increase the resistance. The difference in terms of bending strength can be seen in Figure 4.44 b).

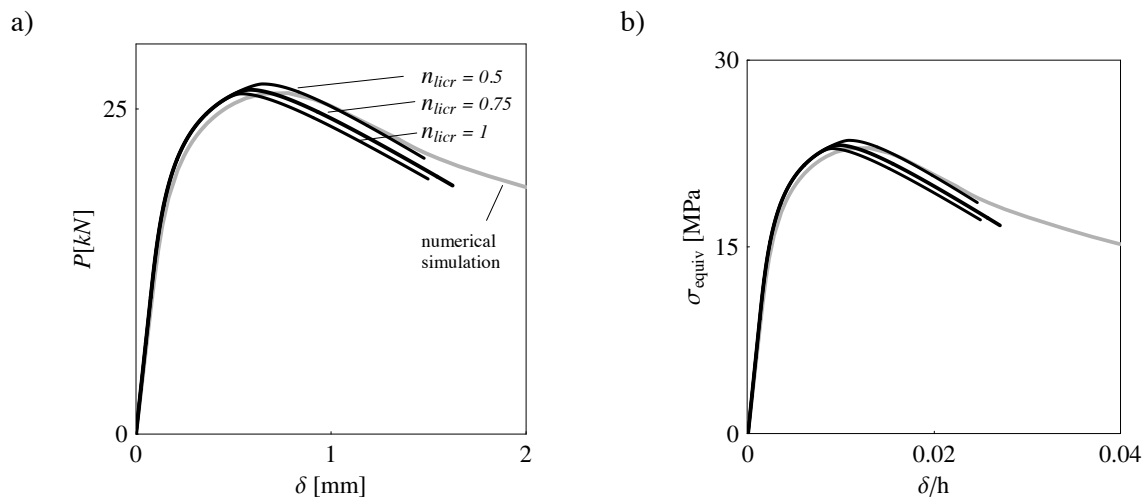


Figure 4.44: Influence of length of the crack-influenced zone, $l_{icr} = n_{licr} \alpha h$, on prediction of force-displacement response; diagrams are plotted against numerically obtained results

4.3.5.3 Simplified approach

A simplified relationship between the sectional forces and deformations can be obtained by introducing a parameter relating the curvature of the uncracked part of the section, χ , to the opening of the crack, w_i . This actually amounts to passing from the stress-crack opening relationship to the stress-strain relationship that defines the cracked zone. The crack opening is related to a “fictitious” plane deformation ε_{wi} that would be exhibited by the section with no discontinuity (Figure 4.46):

$$w_i = l_w \cdot \varepsilon_{w_i} \quad (4.74)$$

Parameter l_w is principally a size-dependent value, as assumed by many authors and demonstrated with the analytical model (Figure 4.46). It can be expressed as a function of section height, by introducing a parameter β :

$$w_i = \beta \cdot h \cdot \varepsilon_{w_i} = \beta \cdot h^2 \cdot \alpha \cdot \chi \quad (4.75)$$

and the crack opening can then be related to strain using the relationship:

$$\varepsilon_{cr} = \varepsilon_u + \frac{w_i}{\beta \cdot h} \quad (4.76)$$

The significance of fictitious strains ε_{w_i} and ε_{cr} in a cracked section is shown in Figure 4.45.

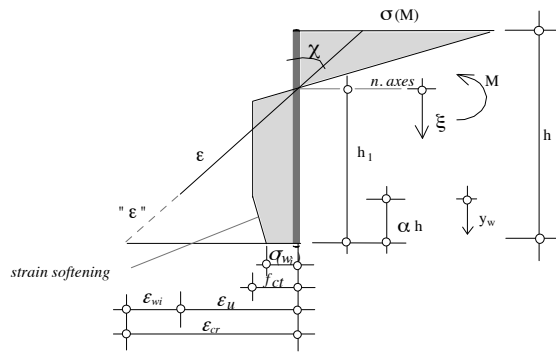


Figure 4.45: “Fictitious” strains, ε_{w_i} , and ε_{cr} , related to crack opening in cracked section in bending

The analytical model enables the value of parameter β to be quantified using Equation 4.75. This parameter is not a constant with the evolution of the crack, but yields to a certain value when the force yields to a peak force, Figure 4.46. The evolution of β as a function of crack opening is plotted for the sections of various heights in Figure 4.46. Obtained values for β give the values for l_w that are similar to values for the “equivalent specific length”, L_w , according to the Japanese recommendations [JSCE 2006], Equation 3.28. Values for L_w in [JSCE 2006] are obtained from numerical simulations, using the FEM analysis of a numerical model similar to the one developed in the present study. For thin elements, these obtained length values are lower than those proposed by the French recommendations [SETRA, AFGC 2002], see Section 3.3.2.7 of this thesis.

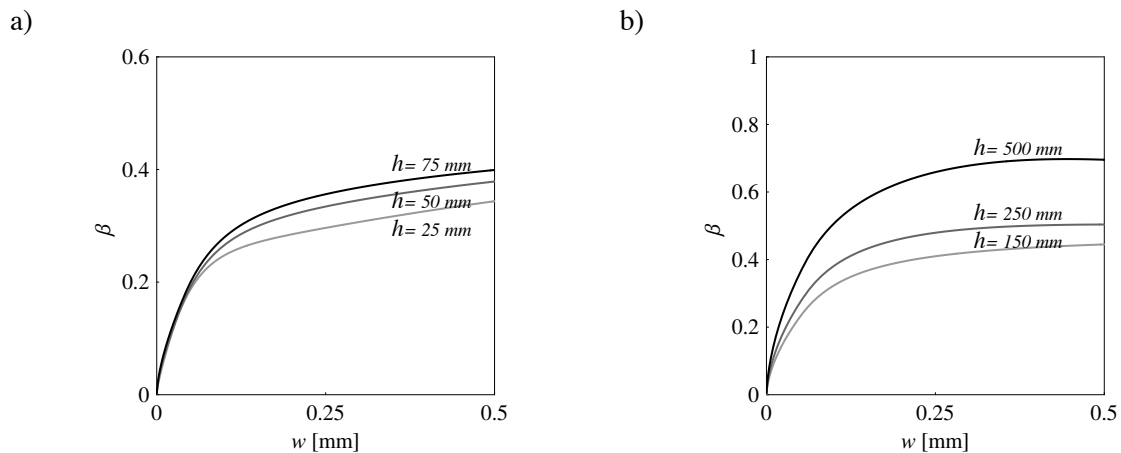


Figure 4.46: Parameter β obtained from analysis based on the proposed model, for sections of different heights: a) $h = 25-75 \text{ mm}$, b) $h = 150-500 \text{ mm}$

Once the value of parameter β is known, the analytical formulation of the proposed model allows a direct relationship between parameters describing the cracked section to be defined. This enables the moment-curvature relationship to be expressed using a closed form solution. Equations already developed for sectional equilibrium (Appendix M2) will be used. Substituting Equation 4.75 in one of the expressions relating w_i , α , and χ , (Equations A 2.8 to A 2.10) and solving it for α , the relationship $\alpha = \alpha(\chi)$ is obtained. For $w \in [0, w_1]$ and $\chi > 0$:

$$\alpha(\chi) = \frac{E_c f_{ct} + E_c^2 (-\varepsilon_u + h\chi) - \sqrt{E_c h (2E_c^2 f_{ct} \chi - C_2 \beta (f_{ct}^2 - 2E_c f_{ct} \varepsilon_u + E_c^2 (\varepsilon_u - h\chi)^2))}}{E_c h \chi (E_c + C_2 h \beta)} \quad (4.77)$$

Substituting Equation 4.77 in $M = M(\chi, \alpha)$,

$$M(\chi, \alpha) = b \frac{-f_{ct}^3 + E_c^3 (\varepsilon_u + 2h\chi) (\varepsilon_u + h\chi (\alpha - 1))^2 - E_c^2 f_{ct} (\varepsilon_u + h\alpha\chi) (3\varepsilon_u + h\alpha\chi) + E_c f_{ct}^2 (3\varepsilon_u + 2h\alpha\chi)}{6E_c^2 \chi^2} \quad (4.78)$$

the bending moment is expressed as a function of the curvature uniquely, $M = M(\chi)$.

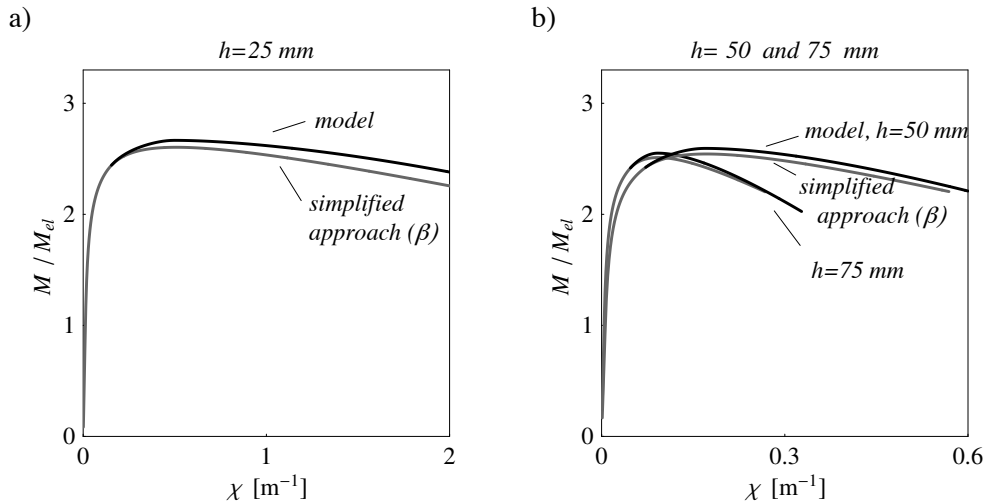


Figure 4.47: Moment-curvature relationships from the analytical model using $\alpha(w)$, (black line), and obtained relating the fictitious deformation and crack opening ($\alpha(w)$) transferred to $\alpha(\varepsilon)$ using parameter β , grey line)

The introduction of parameter β enables a unique relationship of bending moment and curvature in a cracked section to be formulated, which, for the simple functions of material laws, can be expressed in a closed form. The plausibility of the results obtained from the analytical model and by applying relationship 4.78 with a constant parameter β is shown by means of M - χ diagrams in Figure 4.47. The moment-curvature diagrams obtained by the analytical model are plotted as black lines, while the plots of the simplified model (Equation 4.78) are represented by grey lines. The results are compared for thin elements of different heights, using $\beta = \text{const} = 0.4$. It can be seen that the simplified approach enables the M - χ relationship to be followed very well.

It should be noted that for the small crack openings, characterising the resistant moment, the values of β are smaller than 0.4. Applying a higher value of β than that actually corresponding to peak force slightly decreases the resistance, but enables the integral M - χ curve to be followed more accurately, keeping the simulated values on the safety side (Figure 4.48).

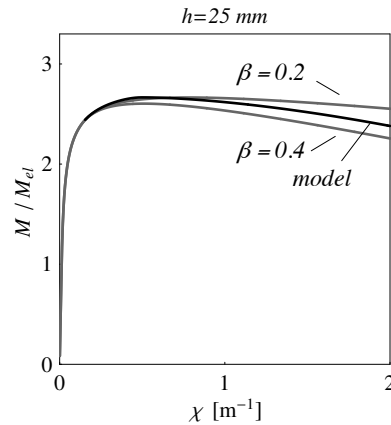


Figure 4.48: Influence of the choice of β constant value on the M - χ relationships

For a given set of material properties it is now possible to find the resisting moment from the equation

$$\frac{\partial M(\chi)}{\partial \chi} = 0 \Rightarrow \chi_{M_{\max}} \Rightarrow M_{\max} = M(\chi_{M_{\max}}) \quad (4.79)$$

It is also possible to find the deformational capacity i.e. χ of a section in softening regime, for a desired bending moment, M_i , as:

$$M(\chi_{M_i}) = M_i \Rightarrow \chi_{M_i} \quad (4.80)$$

which is a necessary piece of information when a certain rotation of the element has to be assured, typically in statically indeterminate systems (Chapters 5 and 6).

Force-displacement relationship

With the defined M - χ relationship of the cracked section (Equations 4.77 and 4.78), the deflections of the beam can be obtained using Equations 4.71 for the pre-peak phase and Equation 4.73 for the post-peak phase.

4.4 Application of the developed model

4.4.1 Validation of the model with experimental data: BSI® UHPFRC

The results of the model are compared with experimental results obtained in the test programme on thin beams made of BSI® UHPFRC, performed at the EPFL (Appendix T1). Beams of heights varying between 25 - 75 mm are tested in three point bending, with a constant span $L = 420$ mm. Some of the experimental results in terms of force - mid-span displacement are shown in Figure 4.49 a), together with results from the analytical model (black line) and numerical model (grey line). The results are obtained with material properties in tension based on results from uniaxial tensile test (§ 3.3.2.8). Experimentally achieved bending strengths are plotted in Figure 4.49 b) against element's height.

A significant dispersion in measured bending strengths, and in the force-displacement response in general, was also noted considering the elements of constant height, Figure 4.50 b). More remarkable scatter of the results is noted in the region of higher solicitations, characterised by macrocrack opening, while the non-linear response due to microcracking shows less dispersed results.

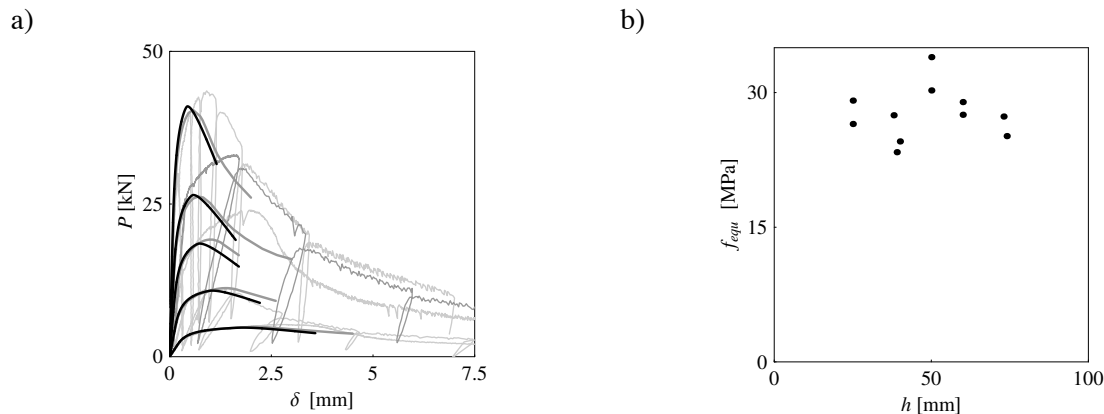


Figure 4.49: a) Measured and simulated force-mid-span deflection response for UHPFRC beams of different heights $h = 25-75$ mm; b) measured bending strength for beams of different heights

For the material with a pseudo-plastic phase up to $\varepsilon_u = 2.5$ ‰, the fictitious crack is assumed to start propagating at $\sigma_{equ} = n_{fct} f_{ct} = 2.4 f_{ct} = 21.6$ MPa (Figure 4.50, dashed line). A similar dispersion in results of bending test, applying similar materials, is reported by other researchers (e.g. [Reineck, Greiner 2004], [Graybeal 2006]).

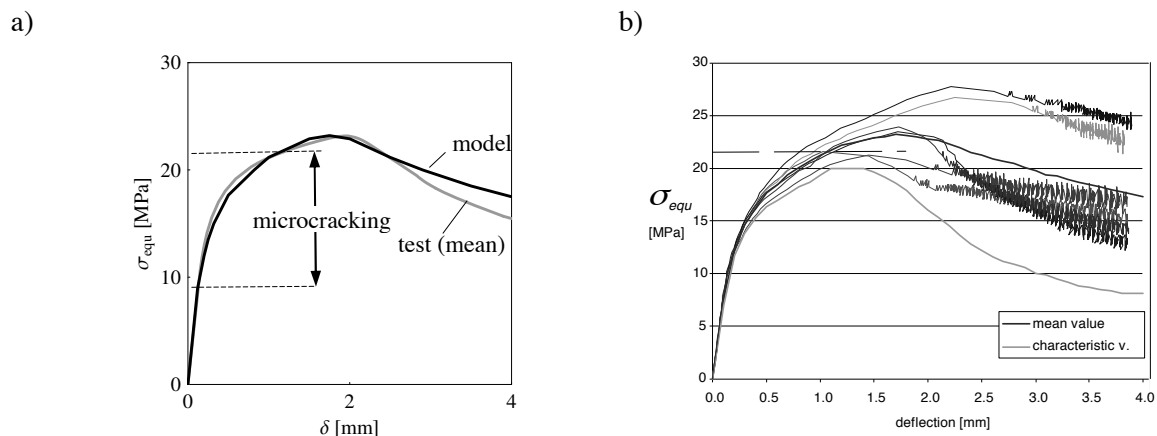


Figure 4.50: Beam in four-point bending: a) comparison of results of numerical model (black line) and the mean value of test results (grey line); b) test results on plates, $h=50$ mm, in four-point bending, with span $L=420$ mm [Simon 2006]; tensile resistance $f_{ct} = 9$ MPa and pseudo-plastic plateau in tension

The scatter in the results can be explained principally by the non-uniformity of the material resistance influenced by the effective fibre volume, which varies along the element. For the same reason, it can be expected that the bending response, modelled with a single crack opening, and the tensile material law obtained from uniaxial test (characterising the weakest section along a tie¹), will not precisely follow the behaviour of every tested sampler. However, a mean value is very well represented with the model using mentioned material properties (Figure 4.50 a)). The results of the bending response of five beams of constant height $h=50$ mm made of BSI (Figure 4.50) are obtained from the test performed at the LCPC. The experimental programme performed at EPFL included

¹ In uniaxial tension, there is a greater probability of localised deformation in the weakest section (due to element size), than in an element in bending where the maximal force concentrates in a smaller region.

elements of variable heights (Figure 4.49) but did not include more than three specimens of the same size, and the mean value given in Figure 4.50 is found more representative)

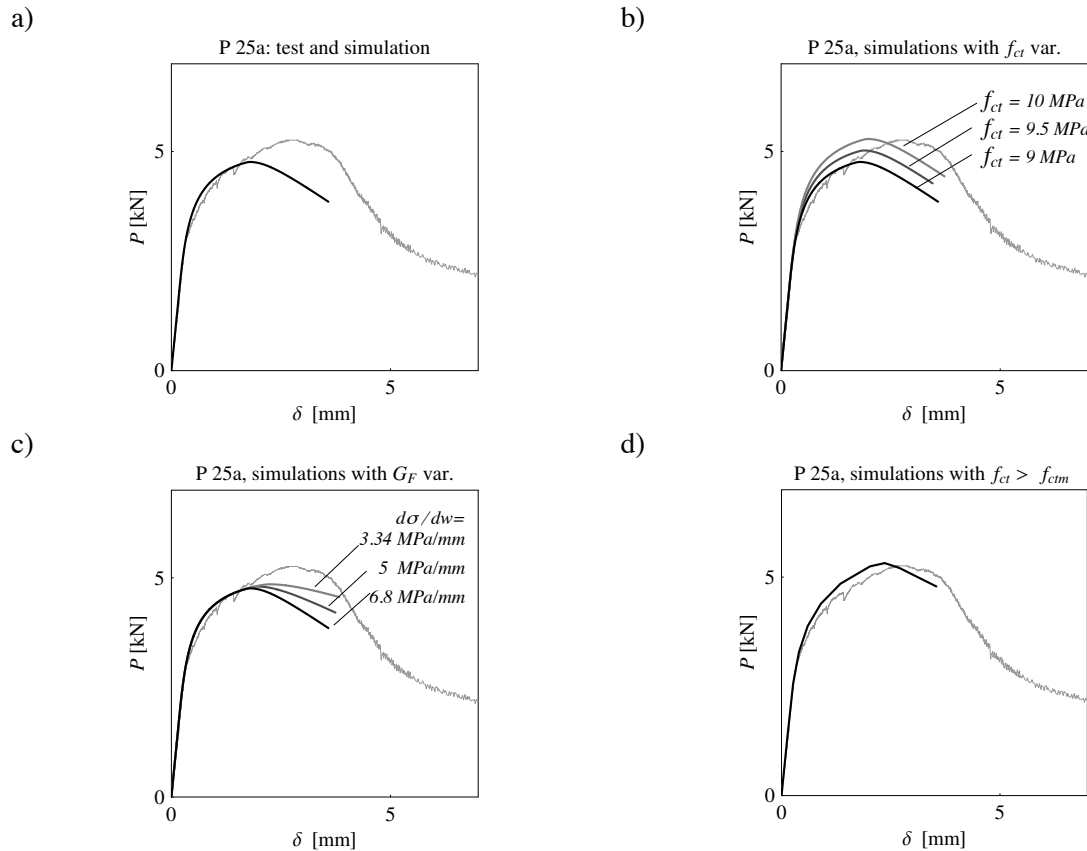


Figure 4.51: Simulated and measured response for a beam of $h = 25 \text{ mm}$: a) simulation with tensile material properties obtained from uniaxial tensile test; b) variation of tensile strengths, corresponding to a constant stress of pseudo-plastic plateau; c) variation of strain softening slope; d) simulation with strain hardening ($f_{ctm} = 9 \text{ MPa}$, $f_{ct} = 10 \text{ MPa}$)

Several phenomena characterising UHPFRC elements enable the scatter in measured bending response once the macrocrack starts to propagate to be explained, and can be demonstrated using the developed models (Figure 4.51 to 4.53):

- statistically, more resistant sections are present in the region of maximal solicitation, due to locally increased fibre effectiveness; consequently a crack starts to propagate in the most loaded section for a higher load level, as if a positive tensile hardening slope had developed; alternatively, due to the gradient of bending moment, a crack may start to propagate in an asymmetric section (Appendix T1);
- the crack pattern is irregular, dissipating more energy than the idealised linear crack; the tested beams had a relatively large width (200 mm), and the crack in some samples propagated along a very irregular line (Appendix T1); a longer crack line dissipates more energy, resulting in increased bending resistance;
- more than one macrocrack develops; similarly to the previous phenomenon, by dissipating more energy, more macrocracks enable a slight increase in resistance, and most of all a significant increase in deformations at peak-force; two or three macrocracks developing prior to peak-force were observed in some of the tested beams by means of photogrammetry analysis.

The simulations presented in Figures 4.51 to 4.53 demonstrate that a slight change in tensile material properties, respecting the range of possible tensile properties according to the tensile tests on notched ties for example (§ 3.3.2.8), enable the behaviour of some samples to be approached more accurately. In Figure 4.51 a), the modelled response is plotted against the experimental curve for a beam 25 mm thick. It can be seen that resistance is slightly underestimated, while deformations are

less accurately predicted. The same Figure b) shows the influence of increase in the constant-stress pseudo-plastic plateau, while in c) the influence of the decrease in the strain-softening slope, $d\sigma/dw$, is shown. It can be noted that the increased pseudo-plastic stress, obviously increasing the strength, overestimates stiffness in the pre-peak part, while the decreased softening slope (increased initial part of G_F) shows a tendency to increasing deformability. (According to uniaxial tensile test $d\sigma/dw = 6.8 \text{ MPa/mm}$, 5 MPa/mm is a possible value for UHPFRC, and 3.34 MPa/mm is a value that corresponds to a slope that would be obtained using a well accepted strain-softening curve given by Equation 3.33, with $\gamma = 4$.) Finally, assuming a tensile strain hardening with a slope rising from $f_{ctm} = 9 \text{ MPa}$ to $f_{ct} = 10 \text{ MPa}$, and maintaining the maximal strain prior to crack opening and the tensile softening slope, the measured curve is well simulated (Figure 4.51 d)).

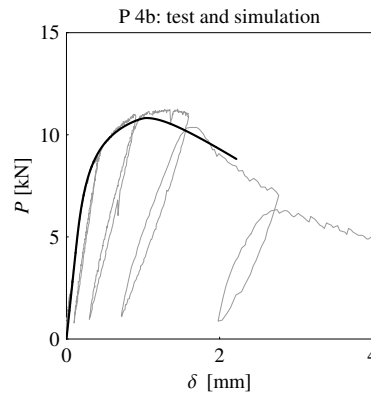


Figure 4.52: Simulated and measured response for a beam of $h = 38 \text{ mm}$ (nominal $h = 40 \text{ mm}$)

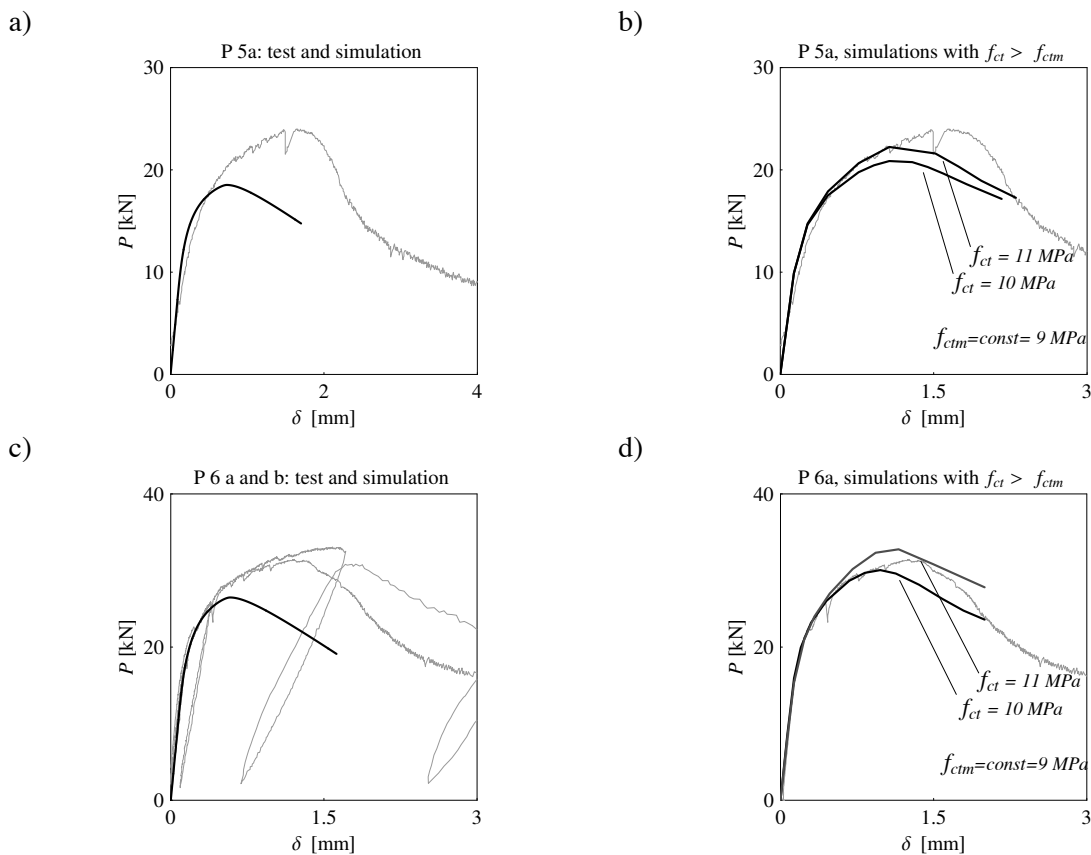


Figure 4.53: Simulated (black lines) and measured behaviour (grey lines) of beam of nominal height $h=50 \text{ mm}$

The behaviour of 38-mm high beam is well modelled with tensile behaviour obtained from uniaxial tensile test (Figure 4.52).

The behaviour of beams of thicknesses 50 and 60 mm is presented in Figure 4.53. Two very closely spaced macrocracks were observed in the sections close to mid-span, before P_{max} is attained, in the case of the beam of $h=50$ mm, explaining its higher strengths and deformability.

4.4.2 Validation of the model with experimental data: other materials

The model is validated for other materials both with and without tensile strain hardening. Two cases of strain hardening materials are studied:

- a material with a more pronounced tensile strength than that of the tested UHPFRC, and with a similar ultimate hardening strain;
- a material with a lower tensile strength and a more pronounced ultimate hardening strain.

An SFRC is studied as a material without tensile strain hardening but with a pronounced bending hardening, due to significant G_F

4.4.2.1 Application to materials with strain-hardening

Multi-scale fibre-reinforced concrete

A UHPFRC known as CEMTEC_{multiscale}©, mentioned in Section 3.2.3, [Rossi et al. 2005], is used here as an example of a strain hardening material with a high tensile strengths, in the range of 20 MPa, (Figure 4.54 a)), which is approximately two times greater than the tensile strength of the majority of UHPFRCs. The strain hardening slope is low, as is usual for UHPFRCs, with ultimate tensile strain $\epsilon_t = 2.5$ ‰. The compressive strength is $f_c = 220$ MPa and modulus of elasticity $E_c = 55$ GPa. More information on the material, data on tested elements and the numerical FEM modelling can be found in [Tailhan et al. 2003], [Parant 2003].

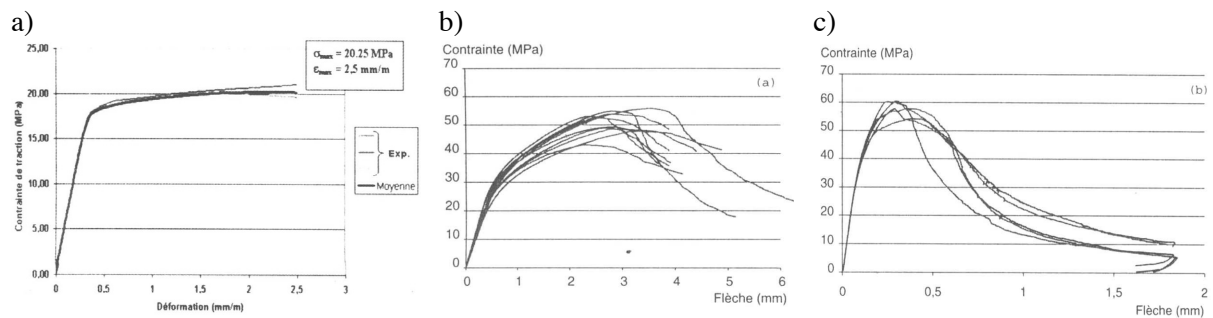


Figure 4.54: Measured data for multi-scale fibre-reinforced concrete CEMTEC_{multiscale}©: a) uniaxial stress-strain relationship in tension, b) bending stress-mid-span displacement curve of beams $h = 40$ mm in four-point bending test; c) bending stress-mid-span displacement curve of beams $h = 200$ mm in four-point bending test; Data from [Tailhan et al. 2003]

The simulation of element behaviour using the non-linear beam analysis developed in this thesis is shown in comparison to measured data in Figure 4.55. The analysed element is a beam of $40 \times 100 \times 600$ mm, subjected to four-point bending, with $3 \times 140 = 420$ mm of the span. Analysis is performed with the above-mentioned material properties, assuming various constant levels of pseudo-plastic tensile stress (18 -22 MPa).

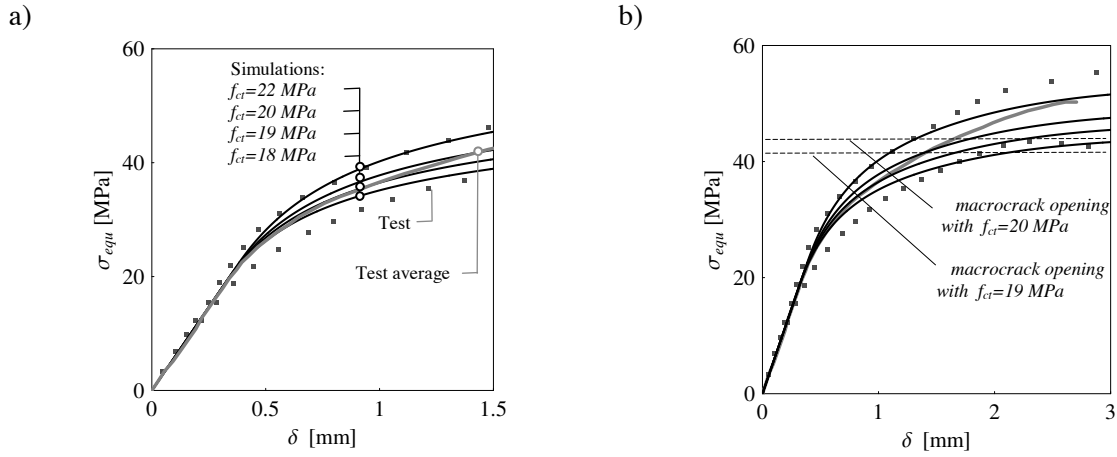


Figure 4.55: Simulated force-displacement curve (black line) for 40-mm thick beam with different levels of pseudo-plastic tensile stress, f_{ct} , and average measured curve (grey line): a) zoom in the region before localisation of deformation in the cracked section; b) position of the proposed design level at ULS (without safety factor) for different f_{ct}

It can be seen that both force and deformations are satisfactorily simulated with the proposed model. Maximal equivalent bending stress prior to crack localisation can be estimated using Equation 4.16:

$$\sigma_{equ}(M_{pl,max}) = f_{ct} \cdot \left(3 - \frac{2\sqrt{2}f_{ct}}{\sqrt{f_{ct}(E_c \varepsilon_u + \sqrt{f_{ct}(2E_c \varepsilon_u - f_{ct})})}} \right),$$

which, for tensile strength $f_{ct} = 19 \text{ MPa}$, results in $\sigma_{equ}(M_{pl,max}) = 2.14 f_{ct} = 40.7 \text{ MPa}$, or, for $f_{ct} = 20 \text{ MPa}$, $\sigma_{equ}(M_{pl,max}) = 2.12 f_{ct} = 42.5 \text{ MPa}$. Similar to the behaviour of BSI UHPFRC, measured bending strength, achieved with crack opening, is only slightly higher than the value $\sigma_{equ}(M_{pl,max})$, considering elements of heights of 40 – 200 mm (Figure 4.54 d) and c)). Moreover, the pseudo-plastic behaviour was considered as the representative material behaviour according to authors [Tailhan et al. 2003], and it was used to model numerically the complete pre-peak behaviour, allowing an increased length of the quasi-plastic plateau.

Engineered cementitious composite

Engineered cementitious composites (ECC) are cementitious fibre-reinforced materials characterised by a very pronounced tensile strain before strain softening occurs. In this paragraph, the behaviour of elements made of an ECC presented in [Kunieda et al. 2002] is simulated. Material characteristics in tension are given in Figure 4.56 a) and b), with tensile strength equal to 4.8 MPa, $\varepsilon_u = 3.5\%$ and $E_c = 23.3 \text{ GPa}$.

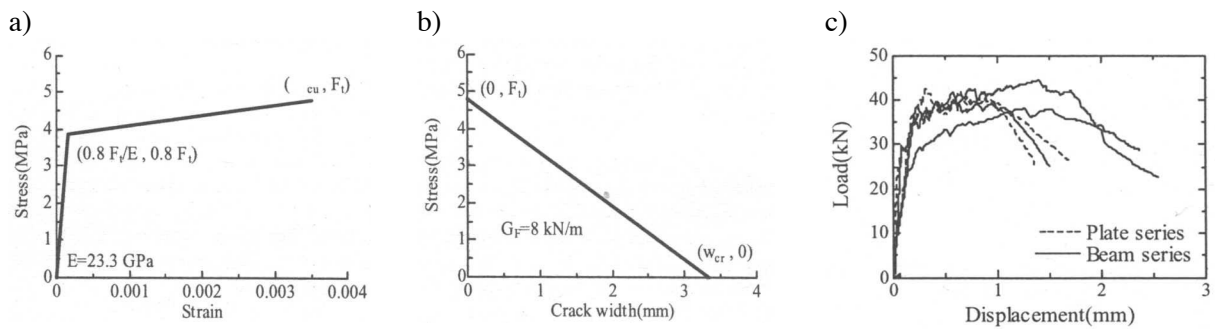


Figure 4.56: Data for ECC: a) uniaxial stress-strain relationship in tension, elastic and hardening region; b) stress-crack opening relationship; c) Force-mid-span displacement of tested beams and plates, $h = 100 \text{ mm}$; from [Kunieda et al. 2002]

The model is applied to elements of various sizes corresponding to the geometry of tested samples, tabulated in the mentioned literature source. Examples of the modelling of element behaviour in four-point bending are plotted in Figure 4.57. The beam of dimensions $100 \times 100 \times 400 \text{ mm}$, height, width and length, subjected to forces introduced with a span of $3 \times 100 = 300 \text{ mm}$, is simulated using the analytical model (Figure 4.57 a)), assuming various levels of constant pseudo-plastic tensile plateau. In the same Figure b) the same element is modelled using strain hardening slope as defined in Figure 4.56 a), and the predicted response of a triple-height element (300 mm) is also shown.

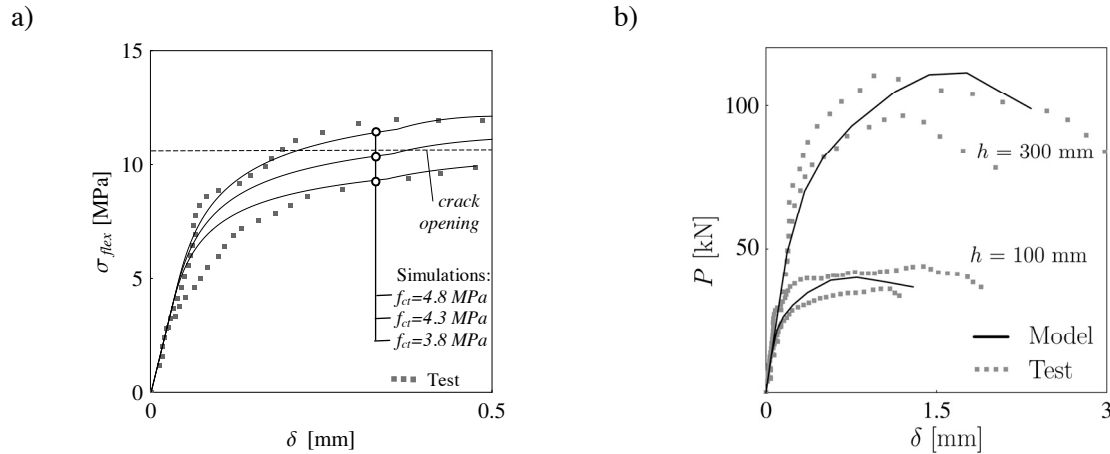


Figure 4.57: Simulated force-displacement curves (black lines) and lower and upper limits of measured response: a) beam in four-point bending, $h = 100 \text{ mm}$, modelled assuming different levels of constant pseudo-plastic stress, f_{ct} ; b) beams in four-point bending, $h = 100$ and 300 mm , modelled using strain hardening

Even in the case of more pronounced strain hardening deformations, the model can be seen to predict well the response, and strain hardening dominates in achieving bending strengths, with only a slight additional increase in bending stress with crack opening. With a tensile strength of 4.8 MPa and an elastic tensile stress $0.8 \cdot 4.8 = 3.8 \text{ MPa}$, for an average pseudo-plastic strain $f_{ct} = 4.3 \text{ MPa}$, the macrocrack can be assumed to start propagating at $\sigma_{equ}(M_{pl, max}) = 2.43 f_{ct} = 10.5 \text{ MPa}$, according to Equation 4.16 (dashed line in Figure 4.57a)). The bending stress is increased for a lower percentage with the macrocrack opening in comparison to materials with lower ϵ_u .

4.4.2.2 Application to materials without strain hardening

Results of the developed model are compared with the results of other models for bending in the presence of a fictitious crack, published in [RILEM 2002], and some of them presented in §4.2. The studied element is a beam subjected to three-point bending, with a constant cross-section ($150 \times 150 \text{ mm}$), with a span $L = 500 \text{ mm}$. Tensile behaviour is modelled as linear elastic, with $f_t = 3 \text{ MPa}$ and the initial strain softening curve has a slope of 30 MPa/mm up to to $w = 0.05 \text{ mm}$ and zero stress at $w_c = 10 \text{ mm}$: The modulus of elasticity is $E_c = 35 \text{ GPa}$.

The comparison of predictions of various models is presented in Figure 4.58 a), and the comparison of an average prediction and the model developed in the present study are plotted in Figure 4.58 b), as gray and black line respectively. It can be concluded that the model enables also good prediction of bending response of quasi-brittle materials without hardening plateau.

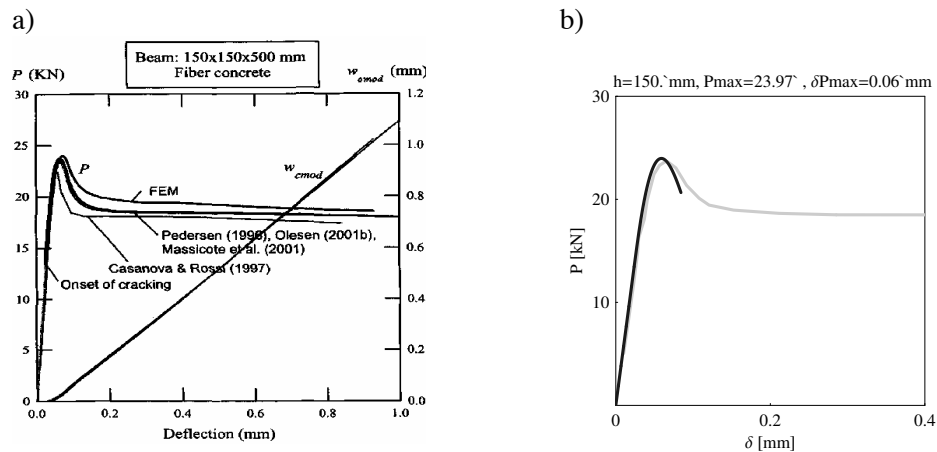


Figure 4.58: Bending response of SFRC: a) prediction of various models reported in [RILEM 2002]; b) comparison of the average prediction by the models presented in a), grey line, and the model developed in the present study (black line)

4.4.3 Size effect of UHPFRC elements in bending

In the previous section, the proposed analytical model was validated by a number of test results on beams made of different cementitious materials. In this section, the model will be used firstly to compare the bending behaviour of UHPFRC and FRC as a function of the element thickness. A parametric study will then be carried out to assess the influence of variations in the UHPFRC tensile behaviour on bending response. The relative influence of the tensile pseudo-plastic plateau and softening on the size effect in bending will be demonstrated.

4.4.3.1 Size effect on bending strength and ductility for UHPFRC and FRC

It is well known that both unreinforced ordinary concrete and fibre reinforced concrete are sensitive to size effect in bending, i.e. bending strength and ductility decrease as element thickness increases. This behaviour is typical of quasi-brittle materials with tensile behaviour characterised by a softening stress-crack opening relationship that directly follows the linear-elastic uncracked stage. For UHPFRC, cracking of the matrix is followed by a pseudo-plastic tensile plateau with relatively low stress increases and the development of high strain deformations; moreover, the post-peak softening behaviour is significantly more ductile than in ordinary and fibre reinforced concrete.

In this section, the influence of the pseudo-plastic plateau and the softening behaviour of UHPFRC on size effect in bending will be studied by comparing the behaviour of UHPFRC elements to the behaviour of FRC elements as a function of their thickness. The case of a beam in three-point bending will be considered: the slenderness of the beam is kept constant, with a span to depth ratio L/h of 8. Beams depth is varied from 25 to 500 mm to investigate size effect in a range of thicknesses of interest for structural applications. To help distinguish the influence of the pseudo-plastic plateau and the softening behaviour, three different materials are considered:

- the BSI®, UHPFRC used in tests carried out during this research (Figure 4.59 a));
- a hypothetical material with the same elastic and softening behaviour as the UHPFRC, but without the pseudo-plastic plateau;
- an ordinary FRC with a Young's modulus of 30 GPa, a tensile strength of 3 MPa and $F=d\sigma/dw$ equal to 20 MPa/mm (Figure 4.59 b)).

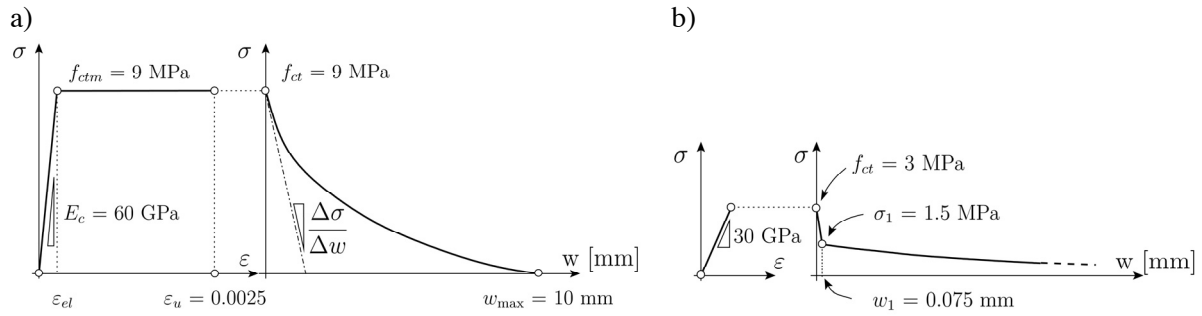


Figure 4.59: Tensile behaviour of: a) BSI; b) FRC

The results of the analysis are plotted in Figure 4.60 as equivalent bending stress versus nominal deflection, defined as the ratio between the deflection δ at mid-span of the beam and its value δ_{el} at cracking of the matrix. Comparing the peaks of the different curves, it can be noted that for UHPFRC (Figure 4.60 a)) the equivalent bending strength depends only slightly on the size of the elements, whereas for FRC (Figure 4.60 c)) the size effect on the bending strength of the member is more significant. Figure 4.60 also shows that the ductility of members strongly depends on their size: thick elements reach bending strength for smaller nominal deflections and show a shorter and much steeper post-peak behaviour than thin members.

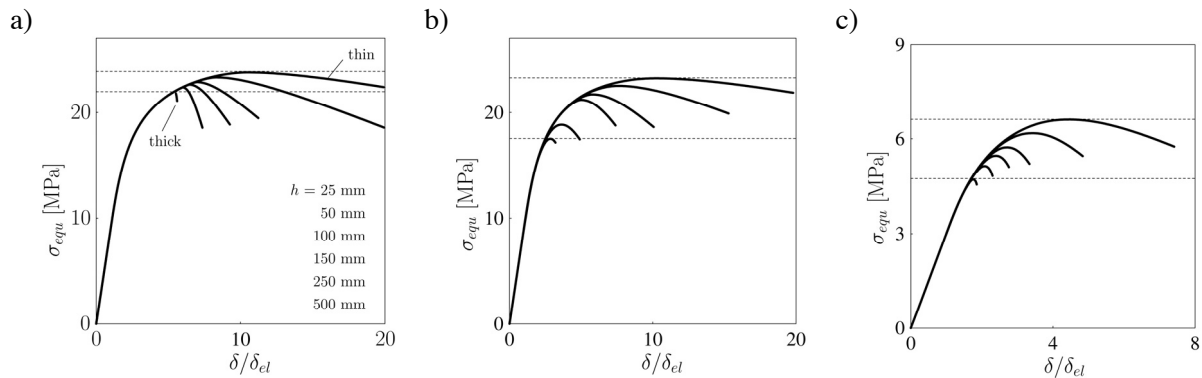


Figure 4.60: Bending behaviour of beams made of: a) UHPFRC with pseudo-plastic phase; b) UHPFRC without pseudo-plastic phase; c) FRC

Ductility also depends on the mechanical properties of the materials, as can be seen by comparing the nominal deflection at peak for UHPFRC ($\delta/\delta_{el} = 6 - 11$) and FRC ($\delta/\delta_{el} = 1 - 5$). However, for all considered materials the size effect on ductility is qualitatively similar. It is also interesting to note that, for the material with the same softening as UHPFRC but without the pseudo-plastic plateau, the behaviour is similar to that of UHPFRC in thin members (25 to 150 mm), with limited size effect on strength. On the other hand, it is similar to that of ordinary FRC in thicker elements, for which size effect becomes more pronounced (Figure 4.60 b), 4.61 a)).

In Figure 4.61 a), the results of the simulations are plotted for the different materials as the ratio between the equivalent bending strength and the tensile strength of the material versus element thickness. The upper value on the vertical axis ($f_{equ} / f_{ct} = 3$) corresponds to a perfectly-plastic behaviour in tension. The results are also given for an ordinary concrete that, for significant sizes, can be considered the limiting case of an elastic-perfectly brittle material ($\sigma_{equ} / f_{ct} \rightarrow 1$). This graph clearly shows that for UHPFRC size effect is less significant than for FRC and OC. Figure 4.61 b) shows the experimental results of tests carried out at the EPFL on UHPFRC beams of thicknesses ranging from 25 to 75 mm: based on test results in this range, no conclusions concerning size effect on bending strength can be drawn. As already suggested by Bazant and Cedolin [Bazant, Cedolin

1991] in the case of very slender ordinary concrete members, size effect in thin UHPFRC elements can be disregarded since it has less influence than the scatter of test results. Figure 4.61 c) shows experimental and analytical results for ECC members of thicknesses up to 300 mm [Kunieda et al. 2002], and similar results were also obtained by [Rossi et al. 2005] for CEMTEC_{multiscale} with thicknesses up to 200 mm (§4.4.2.1), confirming the validity of the predictions of negligible size effect, obtained with the proposed model.

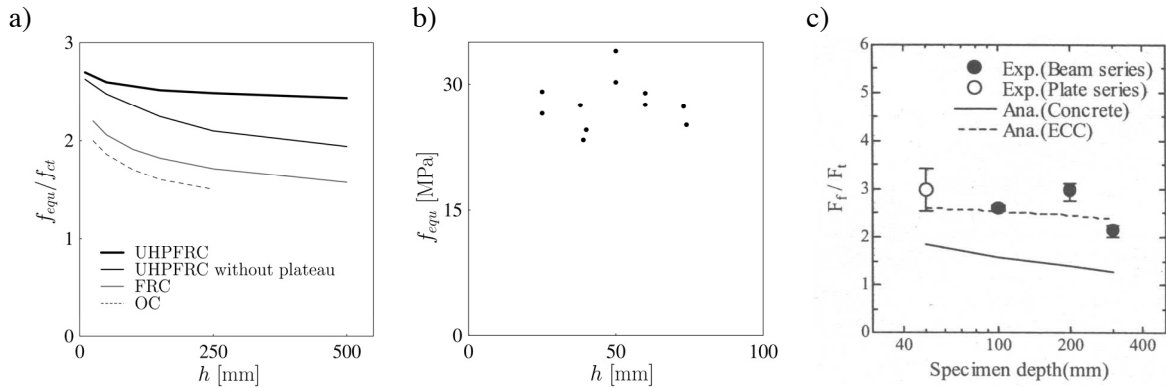


Figure 4.61: a) Theoretical size effect for UHPFRC, UHPFRC without pseudo-plastic plateau, FRC and OC; b) experimental size effect on bending strength for UHPFRC beam made of BSI; c) experimental and analytical results for ECC [Kunieda et al. 2002]

The limited influence of size effect on the bending strength of UHPFRC can be explained by the fact that most of the bending strength is activated during the development of the pseudo-plastic phase in concrete, whose behaviour is size-independent (Figure 4.62 a). Analytically, it was shown that for a typical UHPFRC with $\epsilon_{fct} = 2 - 3 \%$ the equivalent bending stress attained before the beginning of tension softening is between 2.2 - 2.5 times the tensile strength, f_{ct} . The additional limited increase in strength develops in the course of a local tension softening (Figure 4.62 b)), which is size-dependent.

In addition to the strains developed prior to tension softening, the slope of the stress-crack opening law also plays a major role. For instance, when considering a material with the same softening as a UHPFRC, it was shown in that size effect on the strength of thin elements is considerably reduced even without a pseudo-plastic phase (Figure 4.60 b)). This can be understood with the help of Figure 4.62 c): if the slope of the descending branch is small, the stress distribution in the tensile zone is similar to that obtained with a pseudo-plastic behaviour in tension (Figure 4.62 a)). Consequently, for thin elements a pseudo-plastic behaviour or a strain softening with a small slope lead to similar results regarding size effect.

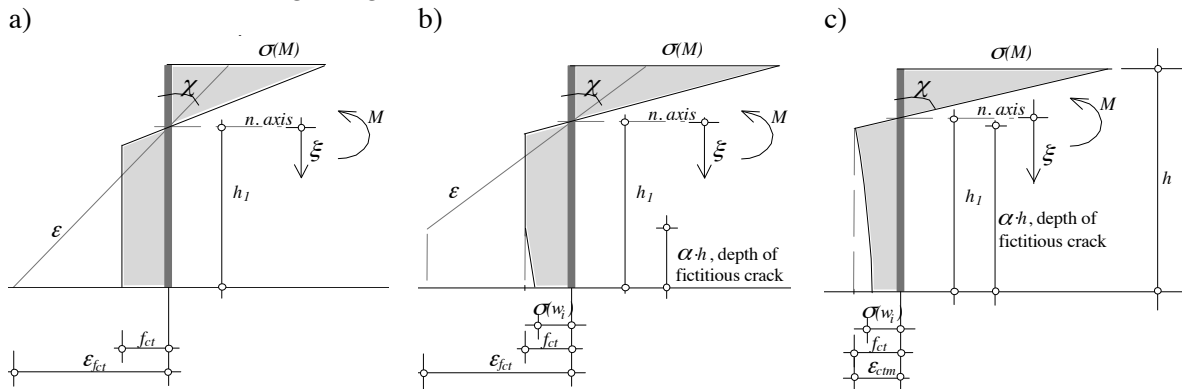


Figure 4.62: Stress distribution in the section developing fictitious crack: a) development of pseudo-plastic phase in tension; b) local softening due to opening of fictitious crack (with part of the height of section in pseudo-plastic phase); c) softening due to opening of fictitious crack without pseudo-plastic phase in tension

For modelling and design purposes, however, the two phenomena differ. With a dominant pseudo-plastic behaviour, the sectional and structural responses can be modelled using a continuum approach based on stress-strain relationships [Tailhan et al. 2003]. When softening behaviour dominates however, strain localisation develops and models based on fracture mechanics theories have to be used.

4.4.3.2 Influence of pseudo-plastic phase and tension softening on bending behaviour

To better understand the relative importance of the effect of the pseudo-plastic phase and softening behaviour of a material on the strength and ductility of a member, a parametric analysis is performed. The strain ϵ_{fct} prior to tension softening and the initial slope of the stress-crack opening law are the main parameters used for this study. The choice of the latter parameter is justified since, for most structural applications, bending strength is reached with small crack openings and thus the initial slope of the stress crack opening relationship is more significant than the value of the fracture energy G_F . The parametric study is performed based on the same tensile behavior as shown in Figure 4.59. The values of ϵ_{fct} and the initial softening slope are varied according to Figure 4.63. The values chosen for the softening slope $F=d\sigma/dw$ are: 3.3 MPa/mm, 6.8 MPa/mm (representing the UHPFRC used in this study) and 20 MPa/mm, which reasonably approximates the initial slope for an ordinary FRC.

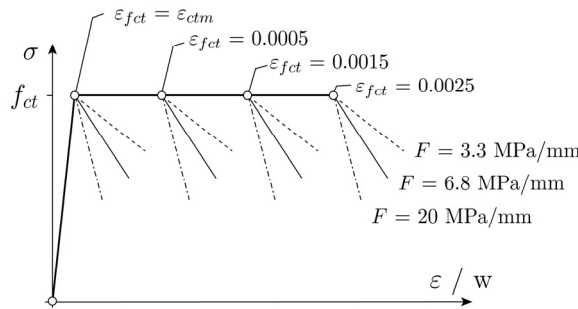


Figure 4.63: Variation in material properties in tension: strain ϵ_{fct} at end of pseudo-plastic phase and initial slope of stress-crack opening law

Figure 4.64 shows the results of the analysis for the element thicknesses varying from 25 to 500 mm. The influence of ϵ_{fct} while the tension softening slope is constant is shown in Figure 4.64 a). It can be clearly noted that size effect on bending strength is very limited for a pseudo-plastic plateau with strains up to 2.5‰ (black line). The same applies for $\epsilon_{fct} = 1.5\text{‰}$, whereas for smaller values of ϵ_{fct} size effect is more pronounced.

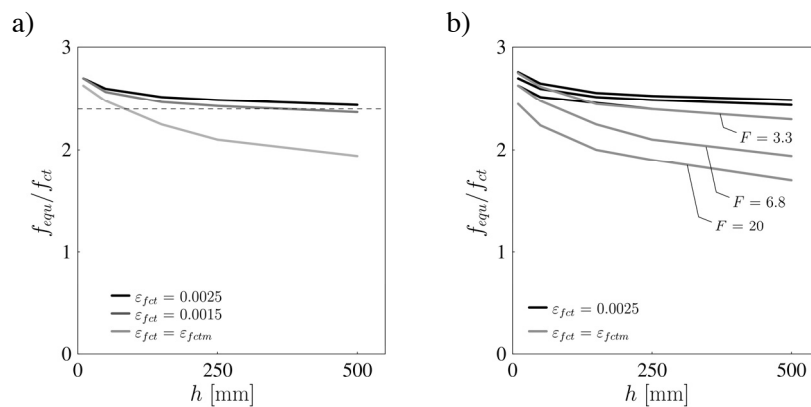


Figure 4.64: Influence of pseudo-plastic plateau and strain softening slope on the bending response: a) influence of ϵ_{fct} on size effect, with constant F ; b) Influence of F on size effect, for $\epsilon_{fct} = 2.5\text{‰}$ (solid lines) and $\epsilon_{fct} = \epsilon_{el}$ (grey lines)

However, if the tensile softening slope is small, the bending strength of elements without a softening plateau (Figure 4.64 b), grey line with $F = 3.3 \text{ MPa/mm}$) is similar to that of elements with a pseudo-plastic plateau (black lines). For small values of ε_{fc} (grey lines) variations in the softening slope have a significant influence on bending strength, while for greater value of ε_{fc} (black curves) the contribution of the softening slope to bending strength is less significant. Softening slope plays however important role in providing element's ductility.

4.5 Conclusions

4.5.1 Developed analytical model

An analytical model describing the non-linear inelastic bending response of a UHPFRC member has been developed. The model takes into account the multi-microcracking phase, modelled as pseudo-plastic tensile yielding, and a localised macrocrack, modelled using the hypothesis of the fictitious crack model. The problem is reduced to monodimensional expressions.

The analytical expressions developed in this work allow the non-linear relationship between the forces and deformations of a beam to be expressed in a closed form before propagation of the macrocrack. Good agreement is shown with experimental data for elements with a strain hardening of zero or low slope, covering the range of typical UHPFRC tensile behaviour. Expressions for the prediction of stiffness decrease caused by microcracking damage are also developed, showing good agreement with experimental results.

Expressions describing bending behaviour in the presence of a fictitious crack are obtained by introducing an additional condition based on energy equilibrium. The results are in good agreement with experimental data and with the prediction of a numerical finite element (FEM) model. Good agreement is also shown with the predictions of other models for materials without strain hardening. For practical applications, an explicit formulation of the force-deformation relationship is developed by introducing a parameter relating sectional deformations and crack opening. This simplified approach also provides satisfactory results.

The advantage of the proposed approach is that the non-linear force-displacement relationship and ultimate loads for bending failure mode are more easily obtained than with time-consuming solutions for FEM models.

4.5.2 Behaviour and design of UHPFRC in bending

The bending behaviour of a UHPFRC member is characterised by multi-microcracking (causing tensile strain hardening) and macrocrack propagation.

For a UHPFRC element in bending, tensile strain hardening is the principal source of the increase in the element's bending strength. For typical material properties, with tensile deformations ranging up to 2.5 ‰, the bending resistance achieved due to strain hardening is approximately 2.4 times the tensile strength. This contribution is size-independent as long as sufficient compressive strength is provided and compression softening is avoided, as is the case for members in pure bending.

The propagation of the macrocrack, characterised by tensile softening, makes a minor contribution to bending strength (up to roughly 10%), but plays an important role in providing ductility in bending, as a function of element size. According to experimental and theoretical results, bending strengths are attained for small macrocrack openings.

Finally, the existence of the multi-microcracking and fictitious crack propagation in UHPFRC result in a less pronounced size-effect on strength in comparison to other FRCs, due to tensile strain hardening (with positive or zero slope); this is also demonstrated experimentally. The size effect on ductility is however evident, even in the small range of variation of element height.

A parametric study was performed to investigate the size effect of UHPFRC members in bending, and identify the principal parameters influencing size effect. The results were compared to those obtained for members made of FRC and OC. On this basis, the following conclusions are drawn:

- in a range of thicknesses of interest for structural applications (25 to 500 mm), size effect on bending strength is limited for a typical UHPFRC, characterized by a pseudo-plastic behaviour in tension with a deformation capacity of 2 to 3 %;
- for very thin members (25 to 75 mm) it is demonstrated that size effect on bending strength is practically negligible;
- in the presence of a significant pseudo-plastic behaviour, the influence of post-peak tension softening on bending strength is not very significant, since most of the bending strength is developed while the concrete is in the pseudo-plastic tensile phase. The post-peak tensile behaviour is however relevant to the ductility in bending;
- in the case of a limited or non-existent pseudo-plastic phase, the bending response of UHPFRC elements is similar to that of ordinary FRC. However, if the tensile softening slope is low, thin members can exhibit a rather ductile behaviour and a limited size effect, even if there is no pseudo-plastic phase.

5. Application of the theory of plasticity in the design of statically indeterminate UHPFRC beams

The non-linear bending behaviour of statically indeterminate UHPFRC beams without ordinary reinforcement is studied in this chapter. A procedure for simulating the bending response in the presence of pseudo-plastic tensile yielding and the propagation of fictitious cracks is developed. Based on the results of this static analysis, the possibility of applying the theory of plasticity in predicting the load-bearing capacity of UHPFRC elements is investigated.

5.1 Introduction

Statically indeterminate beams or elements whose behaviour can be represented using a beam model (Figure 5.1) are common structural elements, and for this reason it is important to study their behaviour and provide easily applicable theories for assessing their resistances.

Thin UHPFRC beams without ordinary reinforcement exhibit pronounced deformations while maintaining a sufficiently high portion of the resisting moment, as shown by the previous analysis (Chapter 4). Owing to multi-microcracking and the propagation of the fictitious crack characterised by a low tensile softening slope, UHPFRC allows the development of a high degree of ductility in thin bending members, and the question arises as to whether it is possible – and if so, to what extent - to apply the theory of plasticity in the design of UHPFRC members. The application of the theory of plasticity is nowadays well accepted in the ultimate design of RC structures, since it provides good results and, at the same time, allows simple formulation of the final expressions. The required ductility in RC members is provided by the reinforcement in tension and the concrete in compression; in UHPFRC elements, the particular tensile properties of the material are the source of ductility. Since the tensile behaviour of UHPFRC is characterised by cracking, the element size and material fracture properties (h and G_F) have a significant influence on the possibility of developing a plastic response in a member.

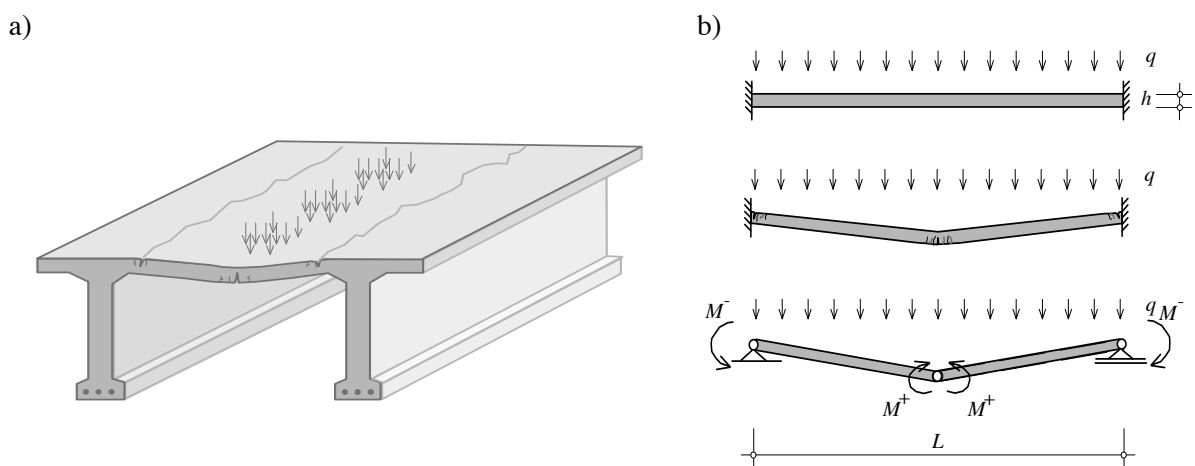


Figure 5.1: Statically indeterminate elements: a) thin UHPFRC slab failing in bending; b) clamped beam failing in bending and the corresponding failure mechanism (developed plastic hinges)

5.2 Theory of plasticity in design of concrete structures

The interest in the application of the theory of plasticity in structural design is mostly due to its practical aspects: if the hypotheses of the theory are respected, failure loads are found easily and accurately.

The background to the theory may be found in the first mathematical studies of stress and strains in plastically deformed solids, especially metals, and in works on yielding conditions (Coulomb 1773, Rankine 1853, Tresca 1864, Saint-Venant 1870), [Hill 1998]. Two schools were dominant in the development of the theory: the Russian (Gvozdev, Kachanov), and the German (Prandtl, Nadai, Lévy, and later Prager, Drucker). The purpose of the method is to predict the load which leads to the failure of the entire structure. For this purpose, the formulation of two theorems of limit analysis represented an important step towards the practical use of the theory of plasticity as a design tool.

Originally developed basically for metals, the theory was successfully extended to reinforced concrete structures: recognising the plasticity in RC members, and adapting the concept of plastic yielding to concrete, made the plastic approach a viable design method. According to [Nielsen 1999], the first traces of the application of the principles of plasticity in design of RC structures can be found in Danish codes as far back as the beginning of the 20th century. Nowadays, the theory of plasticity is suggested for limit analysis in the design of RC structures by many authors [Chen 1982], [Muttoni et al. 1997], [Nielsen 1999], [Alvarez et al. 2000], and also by current structural design codes [SIA 2003b], [Eurocode 2004].

5.2.1 Fundamentals of the theory of plasticity applied to concrete

Yielding criteria

The first step in the application of the theory of plasticity at the structural level is the definition of plastic yielding criteria for materials. Plasticity in RC structures is related to a certain ductility of concrete in compression that enables the reinforcement ductility in tension to be exploited. Therefore the yielding behaviour of both materials must be considered. The simplest and, in the analytical formulations, the most widely used hypothesis is to model the behaviour of concrete in compression and reinforcement in tension in accordance with rigid-perfectly-plastic laws (Figure 5.2 a)). Based on this assumption, the yield condition for a structural member failing in bending can be expressed with a rigid-perfectly-plastic moment-curvature relationship [Muttoni et al. 1997] (Figure 5.2 b)).

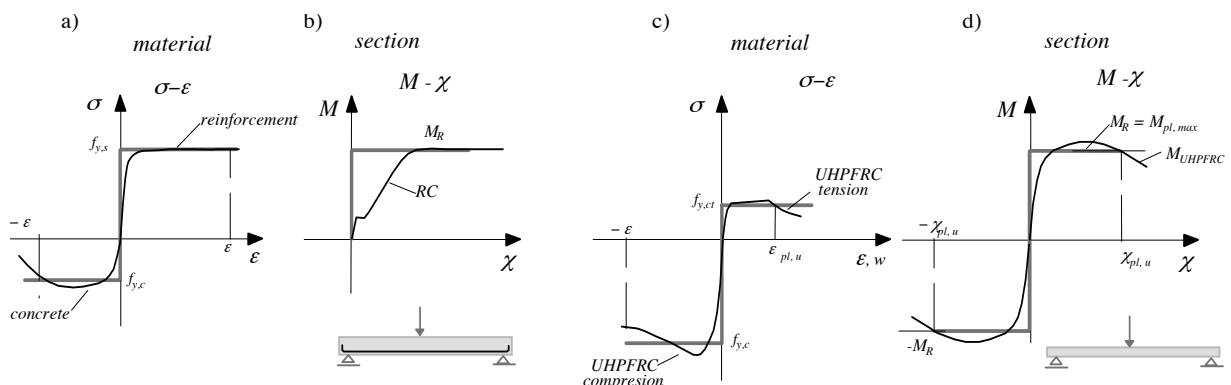


Figure 5.2: Uniaxial behaviour of ordinary concrete, reinforcement, UHPFRC, and behaviour of RC and UHPFRC elements in bending; corresponding idealised rigid-perfectly-plastic behaviours are plotted as grey lines

A rigid-perfectly-plastic material in a uniaxial state of stress is characterised by the yielding condition $I(\sigma)=0$. For f_y being a yielding stress e.g. the same in tension and in compression, for $|\sigma| = f_y$ any strain increment $d\varepsilon$ in the load direction is admissible, while no deformations are associated to $|\sigma| < f_y$ and $I(\sigma) > 0$ is an inadmissible state. For points where the yielding condition is respected, stress and strain variations are related by the normality flow rule:

$$d\varepsilon = d\lambda \cdot \frac{\partial I}{\partial \sigma}, \quad (5.1)$$

where $d\lambda$ is a positive scalar proportionality factor, which is nonzero if plastic deformations occur.

According to the above, it can be concluded to what extent the representation of concrete compressive behaviour as a rigid-perfectly-plastic behaviour is a simplification: the deformations in the concrete are not of a real plastic nature, but result from a progressive microstructure failure with aggregate interlock effect; however, for monotonically increasing strains, the amount of energy spent for concrete deformation is similar to that for idealised perfectly-plastic deformation (surfaces below $\sigma(\varepsilon)$ curves, Figure 5.2 a)). The hypothesis of rigid-perfectly-plastic behaviour of RC structures is thus an important simplification of the reality, but it relies on consistent scientific bases, and is well accepted in current codes of practice [SIA 2003b], [Eurocode 2004].

To extend the rigid-perfectly-plastic model to UHPFRC without ordinary reinforcement, the yielding properties of the material need to be considered in both compression and tension. The compressive behaviour can be regarded in a similar manner to the case of ordinary concrete (OC), with the difference that the “ductility” in UHPFRC is provided by the fibres. Behaviour in tension, exhibiting high deformations with a slow or no variation in stress, strongly resembles a plastic behaviour, as already discussed (Figure 5.2 c)). Finally, with regard to the moment-curvature relationship, modelled with real material properties, it can be noted that, especially for thin elements, it is characterised by a plateau (Figure 5.6), similar to that of an RC section, which extends up to a certain deformation with an almost constant moment-bearing capacity (Figure 5.2 d)). These observations indicate that the bending behaviour of thin UHPFRC members could be described using the theory of plasticity. It must be remembered, however, that the physical background of this moment-curvature relationship differs from that of an RC member: in the case of UHPFRC members, ductility is provided by progressive crack opening while fibres allow a significant stress-bearing capacity to be maintained, and the compressive deformations exhibited around the peak load only slightly exceed elastic deformations; in RC, however, ductility is achieved due to the plastic yielding of the reinforcing bars in tension, followed by significant compressive deformations in the concrete. In the first case, the size effect on ductility is much more pronounced than in RC structures. Moreover, there is a significant difference in the ductility capacity that can be achieved in UHPFRC and RC structures.

Limit analysis theorems

In addition to yield conditions, limit analysis is used to determine the load-carrying capacity of a structural element, avoiding complex calculations that take into account the progressive yielding that occurs in reality. The limit analysis is based on limit analysis theorems [Nielsen 1999]:

- the lower-bound theorem: the structure will not collapse or will be just at the point of collapse if the load is of such magnitude that it is possible to find a *statically admissible* stress distribution equilibrated with the applied load and characterised by stresses below or at yield;
- the upper-bound theorem: the structure will collapse if there is a *kinematically compatible* displacement field of plastic deformations for which the rate at which the external forces perform work exceeds the rate of internal work dissipation.

The coincident static and kinematic solution is easily developed for structures of a low static indeterminacy, e.g. by using the plastic hinge approach for beams and frames, where the position of plastic hinges coincides with points of maximal moments. In order to determine the value of the ultimate load according to the upper bound theorem, a sufficient number of plastic hinges to allow a structure to become a mechanism is required. In statically redundant systems, a kinematically

compatible collapse mechanism can only be developed if more than one hinge exists at the same time, meaning that the first plastic hinges to form should have sufficient deformational capacity to allow other hinges to form, thus avoiding a sudden brittle failure. Energy principles (principle of virtual work / virtual displacement) are often applied to determine the failure load, e.g. if an equilibrated system is subjected to a virtual displacement, the sum of the external and internal work, A_i and A_e respectively, is equal to zero. Assuming that the deformations are concentrated in plastic hinges (coherent with the theory of plasticity), for a one-dimensional system the principle of virtual work can be expressed by the following relationship:

$$\sum_{i=1}^n M_i \theta_i = \int_0^L q(x) \cdot w_j(x) dx, \quad (5.2)$$

where M_i represents the plastic moment of a plastic hinge i and θ_i represents its rotation and $q(x)$ is a function of ultimate load, performing work on displacements along the element, $w_i(x)$.

Applicability of the theory of plasticity

Practically, the theory of plasticity can be applied on the assumption that materials are sufficiently ductile to sustain large deformations, while the deformations of the structure must be sufficiently small for the second-order effects to be disregarded. The following conditions must be met in a plastic solution:

- equilibrium conditions (static equations)
- compatibility (kinematic equations) and
- plastic moment (comprising constitutive law).

While the equilibrium conditions remain the same as in the elastic analysis, the compatibility conditions differ significantly, due to the fact that the formation of a plastic hinge causes a discontinuity. However, the failure load of a structure can be easily predicted by applying the principle of virtual work (Equation 5.2) for example.

5.3 Non-linear analysis of statically indeterminate beams in bending

5.3.1 Analysis approach

To study the behaviour of a statically indeterminate member up to bending failure, the analysis must take into account the progressive change in stiffness due to multi-microcracking and the propagation of fictitious cracks at the most loaded sections.

A change in stiffness along a statically indeterminate member (e.g. Figure 5.3 a)) leads to a change in the distribution of internal forces in relation to the distribution under the initial (e.g. constant) stiffness (Figure 5.3 b)). Consequently, previously less loaded parts of the member start to progressively assume higher portions of the applied load. The force redistribution phenomenon generally has a favourable effect on structural behaviour, if the required sectional capacities are available. In this section, the capacity of UHPFRC members to redistribute forces will be addressed; the aim is to determine whether the plastic-like bending behaviour observed on thin statically determinate UHPFRC beams allows a sufficient redistribution of internal forces to occur and plastic behaviour in a statically indeterminate system to be achieved. The practical conclusion provides the answer to whether the theory of plasticity can be applied in the designing of UHPFRC elements.

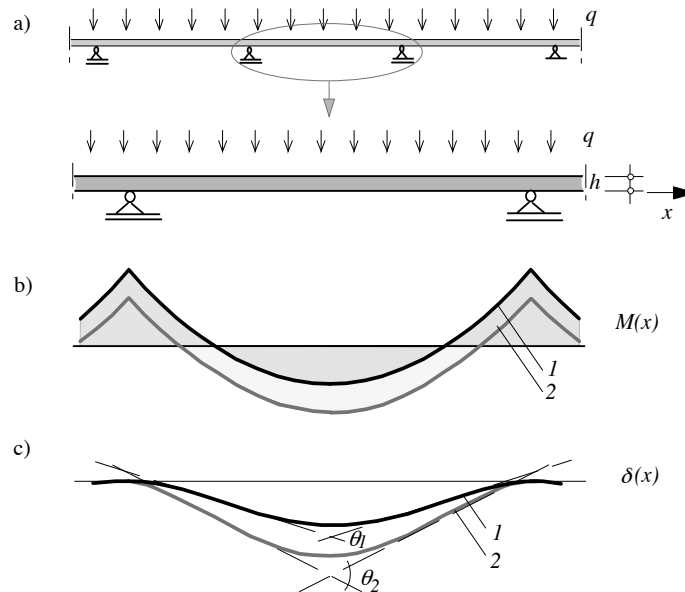


Figure 5.3: a) Statically indeterminate system under load ; b) possibility of redistribution of internal forces (bending moments); c) relative increase in rotation; in b) and c) case 1 corresponds to constant stiffness distribution along member length, and case 2 corresponds to decreased stiffness in support region

The study is performed on beams with a constant cross-section along the length, with two clamped edges, under a symmetric uniformly distributed load (Figure 5.4). The hypotheses of the beam theory detailed in Chapter 4 are also assumed in this analysis.

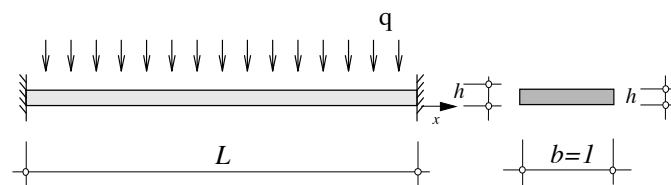


Figure 5.4: Boundary conditions of case study: clamped beam subjected to uniformly distributed load.

The beam is analysed under monotonically increasing deformation. Up to the moment when the maximal elastic deformation level, $\delta_{el,max}$, is attained (Figure 5.7) all sections have the same initial bending stiffness. The corresponding load level is q_{el} . For $\delta > \delta_{el,max}$ the material in the most loaded sections starts to exhibit pseudo-plastic tensile behaviour. This causes a progressive change in the stiffness of the sections and distribution of moment changes as a function of stiffness. The latter is based on the moment-curvature relationship, $M(\chi)$. For a given section and material law, the $M(\chi)$ relationship is established based on the equations developed in § 4.3.5. The characteristic points of this curve (Figure 5.5) are:

- maximal elastic moment $M_{el,max}$ and corresponding curvature $\chi_{el,max}$,
- maximal plastic moment $M_{pl,max}$ and corresponding curvature $\chi_{pl,max}$,
- resisting moment M_{max} and corresponding curvature χ_{Mmax} ; this point characterises only the section with the macrocrack,
- curvature $\chi_{pl,u}$ in the softening region, for which the bending moment is equal to $M_{pl,max}$ (designated curvature at failure, characterising only the section with the macrocrack).

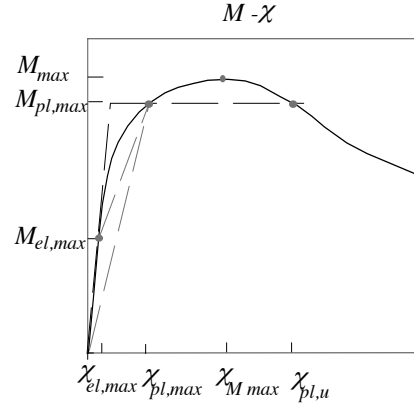


Figure 5.5: Characteristic points of moment-curvature diagram (solid curve) and idealised moment-curvature relationships (dashed line)

For an imposed deformation in the member, the corresponding non-linear state of stresses (internal forces) is found based on the algorithm below.

5.3.2 Algorithm for the simulation of non-linear load-displacement behaviour

For a symmetric load and symmetric material and geometric characteristics of the beam with respect to the mid-span, if the moment at the clamped edge, M_s , is known, the internal forces at any point of the beam can be determined from the equilibrium conditions. The moment function along the length of the element is:

$$M(x) = M_s + \frac{qL}{2}x - \frac{qx^2}{2}. \quad (5.3)$$

Disregarding the contribution of shear deformations, the work of internal and external forces, A_i and A_e respectively, can be calculated as:

$$A_i = \int_0^L \chi(M(x)) \cdot M(x) \cdot dx \quad (5.4)$$

$$A_e = \int_0^L w(x) \cdot q(x) \cdot dx = q \int_0^L w(x) \cdot dx = q \int_0^L \left(\int_x^L \int_x \chi(M(x)) \cdot dx dx \right) \cdot dx, \quad (5.5)$$

since

$$q(x) = \text{const} = q, \quad (5.6)$$

and

$$w(x) = \iint_x \chi(x) \cdot dx \cdot dx + C_1 \cdot x + C_2 = \iint_x \chi(M(x)) \cdot dx \cdot dx, \quad (5.7)$$

respecting the given boundary conditions, i.e.

$$w(x=0) = 0 \Rightarrow C_2 = 0, \quad (5.8)$$

$$w'(x=0) = 0 \Rightarrow C_1 = 0. \quad (5.9)$$

For an imposed deformation in the element the corresponding load level can be found from the energy conservation principle: the work of internal forces must be equal to the work of externally applied forces,

$$A_i = A_e . \quad (5.10)$$

The curvature of the section at the clamped edge is chosen as the governing degree of freedom to control the deformation of the beam. The algorithm for the calculation of the force-displacement response is then based on the following steps:

- for an imposed curvature at the clamped edge, χ_i , the corresponding bending moment is defined based on the moment-curvature relationship, $M_s = M(\chi_i)$, (§ 4.3.5);
- a corresponding load level q_i is assumed (e.g. using the relationship between the load found for χ_{i-1} and the load causing the same $M_s(\chi_{i-1})$ if stiffness were constant);
- if $A_{i,i}(\chi_i, q_i) = A_{e,i}(\chi_i, q_i)$, calculated using Equations 5.4 and 5.5, the solution is found. Otherwise, a new load value q_i is sought until the Relationship 5.10 is satisfied.

Both the moment-curvature, $M(\chi_i)$, and its inverse function, $\chi(M)$, are required in Equations 5.4 and 5.5. To express curvature as a continuous function of moment, two regimes must be distinguished:

- before the first macrocrack opens, while $\chi_i \leq \chi_{pl,max}$, thus $M_s \leq M_{pl,max}$, $\chi(M(x)) = \chi(x)$ function, defined in a closed form (Equation 4.11), characterises the sections along the length;
- for $\chi_i > \chi_{pl,max}$, the $M(\chi_i)$ relationship (Equation 4.78) characterises only the macrocracked section and the curvature function in the crack-surrounding region is represented by an approximating function, as defined in § 4.3.5 (Equations 4.69 and 4.70), while the rest of the beam is characterised by $\chi(x)$ (Equation 4.14) as long as the load continues to increase.

It is possible to integrate the defined curvature functions using the close form solutions. However, since the considered functions are monotonic, standard numerical integration procedures are found more appropriate for the calculation of internal and external work (right sides of Equations 5.4 and 5.5). The numerical integration is particularly convenient for the double integration of the curvature (Equation 5.7) to obtain the displacement function along the length of the beam, $w(x)$:

$$w(x_k) \approx \frac{\Delta x^2}{2} \sum_{i=0}^{n_{sk}} \left(\sum_{j=0}^{i-1} (\chi(x_{j-1}) + \chi(x_j)) + \frac{\chi(x_{i-1}) + \chi(x_i)}{2} \right) \quad (5.11)$$

for a small Δx , with $n_{xj} = \frac{x_j}{\Delta x}$, $x_i = i \cdot \Delta x$, $x_j = j \cdot \Delta x$.

Similarly, the integral in Equation 5.5 can be replaced by the sum:

$$\int_0^{x_k} w(x) \cdot dx \approx \sum_{l=0}^{n_{sk}} \frac{w(x_{l-1}) + w(x_l)}{2} \cdot \Delta x, \quad n_{sk} = \frac{x_k}{\Delta x}, x_i = i \cdot \Delta x, x_j = j \cdot \Delta x, x_l = l \cdot \Delta x \quad (5.12)$$

$$\int_0^{x_k} w(x) \cdot dx \approx \frac{\Delta x^3}{2} \sum_{l=0}^{n_{sk}} \left(\sum_{j=0}^{l-1} \left(\sum_{i=0}^{j-1} (\chi(x_{i-1}) + \chi(x_i)) + \frac{\chi(x_{j-1}) + \chi(x_j)}{2} \right) + \frac{\sum_{i=0}^{l-1} (\chi(x_{i-1}) + \chi(x_i)) + \frac{\chi(x_{l-1}) + \chi(x_l)}{2}}{2} \right) \quad (5.13)$$

5.3.3 Results of analysis

The static system with the boundary conditions presented in Figure 5.4 is analysed based on the procedure developed in Section 5.3.2. The characteristic points of the force-displacement and moment-curvature diagrams of the sections at the support and in the mid-span are presented qualitatively in Figure 5.7. The state of deformations along the element will be discussed based on the example of a beam of a rectangular cross-section of 50-mm height, a unit width, and the same length as the statically determinate beams studied in Chapter 4, $L=0.42\text{ m}$. The analysis is also performed for the beams of various heights, maintaining the same span-to-depth ratio. The moment-curvature relationship for the section of $h=50\text{ mm}$ made of UHPFRC (Table 3.3) is plotted in Figure 5.6. This relationship characterises both the positive and negative bending moments.

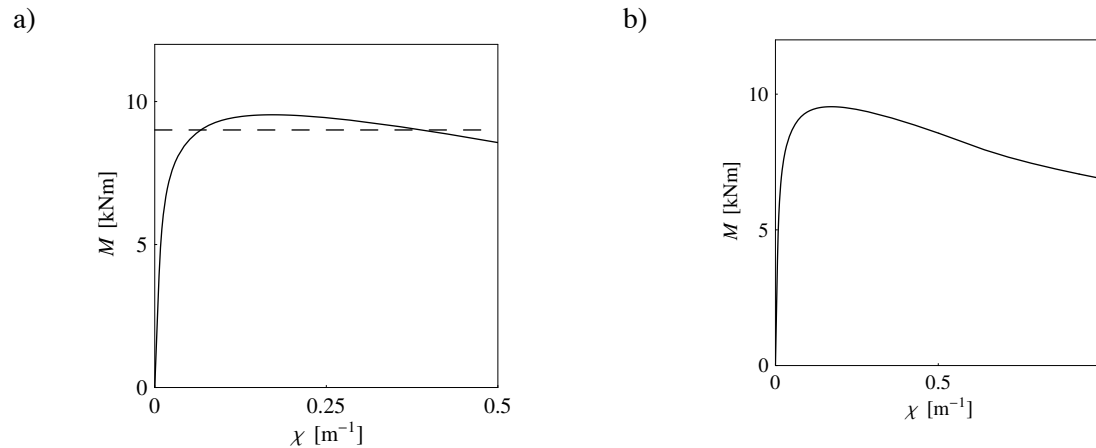


Figure 5.6: Moment-curvature relationship of UHPFRC section of height $h = 50\text{ mm}$ and unit width, used in case study; a) relevant region with level of moment at macrocrack opening (dashed line); b) entire curve up to $\chi = 1\text{ m}^{-1}$

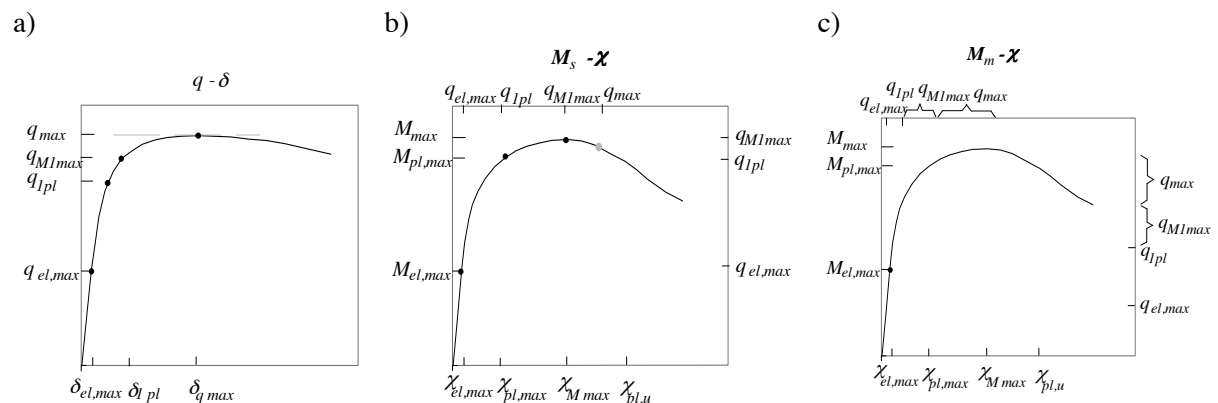


Figure 5.7: a) Force-mid-span displacement relationship for clamped beam and characteristic points; b) moment-curvature relationship of section at clamped edge ($M < 0$, $\chi < 0$); c) moment-curvature relationship of mid-span section

The following regimes are distinguished in the beam response (Figure 5.7 a)):

- 1) Linear-elastic regime up to $q = q_{el, max}$, $q_{el, max}$ being the load at which the maximal elastic moment is reached at the clamped end:

$$|M_s| = |M_{el,max}| \Rightarrow q_{el, max} = 12 \cdot |M_{el,max}| / L^2. \quad (5.14)$$

- 2) Non-linear behaviour up to load q_{1pl} for which the maximal pseudo-plastic moment is reached at the clamped edge, $|M_s| = |M_{pl,max}|$. The pseudo-plastic tensile yielding in the region of negative moment (clamped edge) influences the behaviour in this regime, and the maximal load level achieved can be defined as

$$q_{1pl} = k_l \cdot I_2 \cdot |M_{pl,max}| / L^2, \quad k_l > 1. \quad (5.15)$$

The coefficient k_l (for the given material and boundary conditions $k_l \approx 1.1$) shows that the increase in maximal negative moment $|M_s|$ is lower than in the elastic regime, since the corresponding curvature increases (stiffness decreases) with a higher gradient than in the elastic regime (Figures 5.6 and 5.8 a)). Consequently the moment at the mid-span section increases with a higher gradient, $M_m = M_s + qL^2/8$, (Figure 5.8 d)). When $|M_s| = |M_{pl,max}|$ the sections in the mid-span are also in pseudo-plastic yielding in tension. The regions of the beam in pseudo-plastic yielding can be distinguished in Figure 5.8 c), where the ratio of actual to elastic curvatures is plotted along the beam length. This diagram remains the same for various section heights, if slenderness is maintained. The concentration of curvature (i.e. deformation) at the clamped edge is similar in its effects to that of the formation of a plastic hinge (Figure 5.8 a) and c)), as already seen during the non-linear response of statically determinate systems (§ 4.3.4). This phase ends with the beginning of macrocrack propagation in the section at the clamped edge.

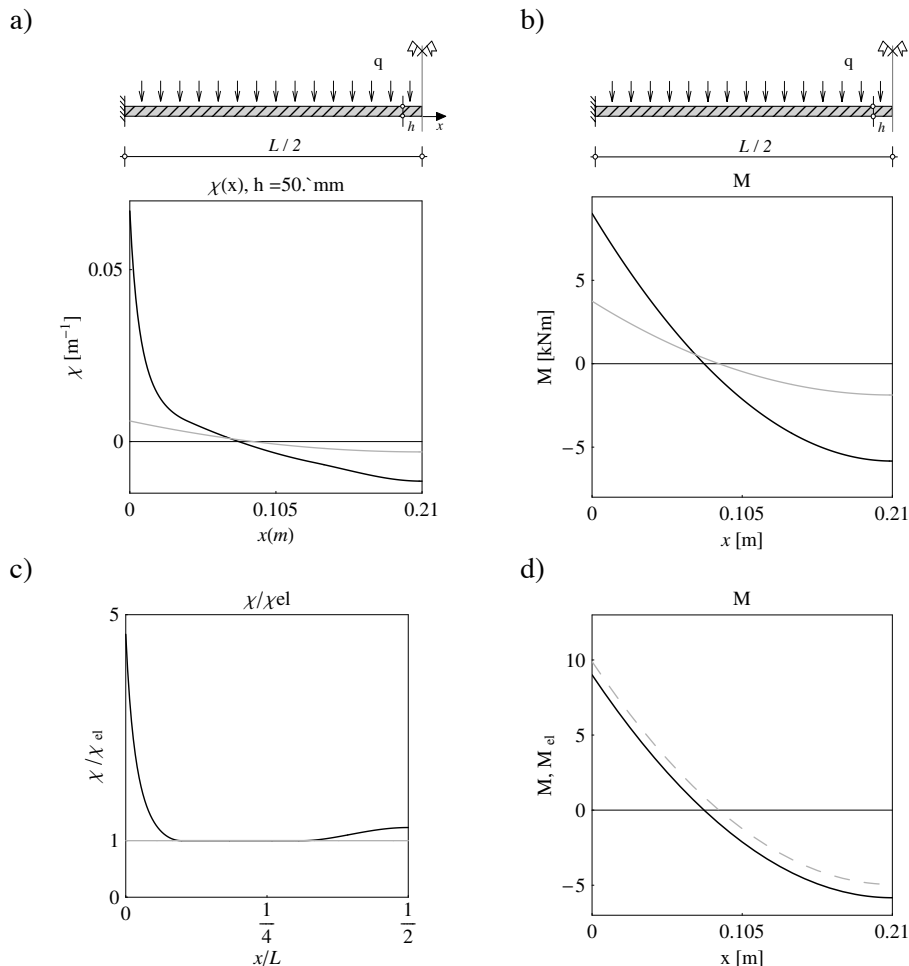


Figure 5.8: a) and b) distribution of curvature and bending moment along half the length of beam for $q = q_{el,max}$ (grey lines) and $q = q_{1pl}$ (black lines); c) ratio of curvature $\chi(M(x))$ to elastic curvature $\chi_{el}(M(x)) = M(x)/EI$ for $q = q_{1pl}$; d) $M(x)$ and $M_{el}(x) = -qL/12 + qL/2 x - qx^2/2$ for $q = q_{1pl}$

- 3) A non-linear part characterised by the propagation of a fictitious crack at the clamped edge is first studied up to $q = q_{M1max}$, q_{M1max} being the load value for which the maximal moment is reached at the clamped edge, $|M_s| = |M_{max}|$. (A symmetric behaviour is implicit, meaning that a fictitious crack starts to propagate at the second clamped edge simultaneously.) During this phase a more pronounced concentration of the curvature in the vicinity of the macrocrack occurs (Figure 5.9 a) and c)). With an increase in deformations in this regime, the load increases more slowly than in the previous phase (Figure 5.11); the bending moment at mid-span increases with a higher gradient (Figure 5.9 b)), enlarging the zone in pseudo-plastic yielding (Figure 5.9 c)). The maximal moment at the support $|M_s| = |M_{max}|$ is reached for the load level q_{M1max} ,

$$q_{M1max} = k_2 \cdot 12 \cdot M_{max} / L^2, \text{ with } k_2 > k_1 > 1, \quad (5.16)$$

with $k_2 = 1.13$ in the case study for $h = 50 \text{ mm}$. Since the M_{max} and the curvature for which it is attained are size-dependent values, as discussed in Chapter 4, the value of k_2 and the moment and deformations in the mid-span sections are also functions of section height. For this reason the graphic c) in Figure 5.9 is influenced not only by material properties and span-to-depth ratio, as in the previous regimes, but also by element size.

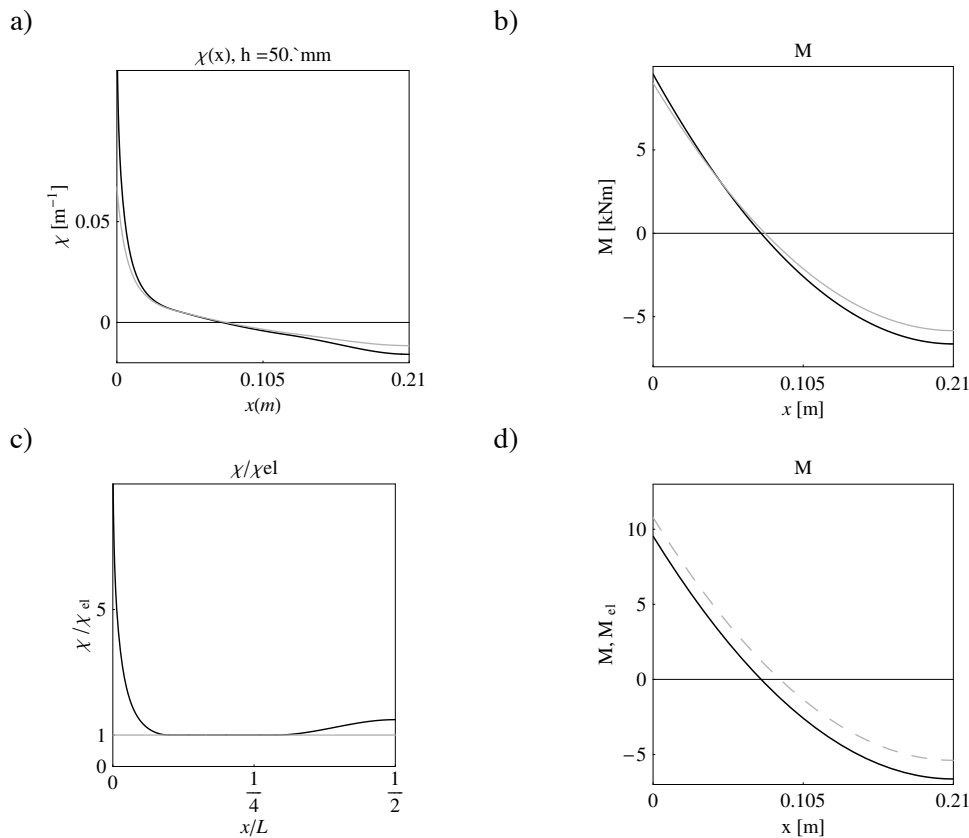


Figure 5.9: a) and b) distribution of curvature and bending moment along length of beam for $q = q_{1pl}$ (grey lines) and $q = q_{M1max}$ (black lines); c) ratio of curvature $\chi(M(x))$ to elastic curvature for $q = q_{M1max}$; d) $M(x)$ and $M_{el}(x)$ for $q = q_{M1max}$

- 4) Non-linear regime up to failure ($q = q_{max}$) is characterised by an increase in curvature at the clamped edge with a decrease in the corresponding bending moment $|M_s| < |M_{max}|$, while the load q can still increase

$$q_{max} \geq q_{1pl} \cdot \quad (5.17)$$

This phenomenon is already studied in RC and prestressed concrete structures, known as softening hinge, where the crushing of concrete in compression also contributes the softening [Muttoni 1990], [Bazant 2003]. The structural behaviour in this regime is strongly influenced by the gradient of the decrease in M_s which is influenced by element size and the fracture toughness of the material. For elements of small height the curvature at the clamped edge increases considerably in this regime, with a very small decrease in bending moment M_s (Figures 5.6 and 5.10). Consequently a significant moment redistribution occurs, the M_m and deformations at mid-span (Figure 5.10) continuously increase with an increasing q and the values of the two moments become more equal. If the section at the clamped edge can increase deformations with only a low decrease in M_s , the pseudo-plastic moment $M_{pl,max}$ can be reached in the mid-span while $|M_s| > |M_{pl,max}|$. In this case the deformations increases at an almost constant load rate, and the behaviour resembles that of a plastic beam (Figure 5.11).

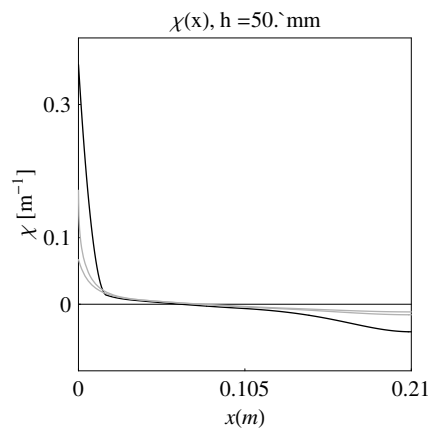


Figure 5.10: Distribution of curvature along beam ($h = 50 \text{ mm}$) when maximal load is reached ($q = q_{max}$, black line) and that from previous phases ($q = q_{M1max}$ and $q = q_{1pl}$, grey lines)

- 5) A further increase in deformations ($\delta > \delta_{q_{max}}$) is followed by a decrease in load. It is interesting to note that, in the case of beams of small height, the moment at the mid-span can continue to increase even if the load decreases because stiffness decreases faster at the clamped edge, and for a slow q decrease, the stiffer mid-span sections sustain higher moments.

The complete behaviour of the studied UHPFRC clamped beam in terms of force-displacement is shown in Figure 5.11 a). It can be seen that non-linear behaviour is dominant, and that the first non-linear part of the curve, up to the point when the maximal pseudo-plastic moment is reached at the clamped edge ($q = q_{1pl}$), deviates slightly from the linear behaviour (Figure 5.11 b)), while further deformations, governed by the fictitious crack opening, become more pronounced and, as will be shown in § 5.5, influenced by element size.

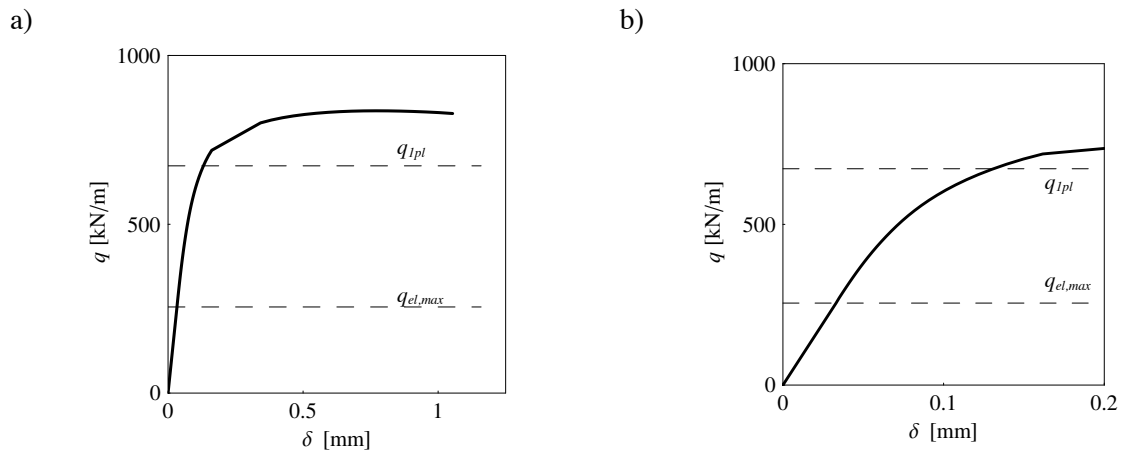


Figure 5.11: Force-displacement relationship of clamped beam $h=50\text{mm}$, $b=1$, $L=420\text{ mm}$, with levels of maximal elastic load, $q_{el, max}$, and maximal load prior to crack opening at clamped edges, q_{lpt} ; b) zoom of plot a) on region prior to first macrocrack opening

The progressive redistribution of internal forces as a function of load increase is shown in Figure 5.12. The graph is plotted as the ratio of the absolute value of moment at the support, $|M_s|$, to the moment in the mid-span, M_m . When this ratio yields 1 before q_{max} is achieved, plastic-like behaviour can be exhibited. In the same graph it can be seen that the redistribution occurring due to multi-microcracking in a typical UHPFRC is not sufficient to cause $|M_s| = M_m$, but for elements of a small height this can occur with propagation of the macrocrack.

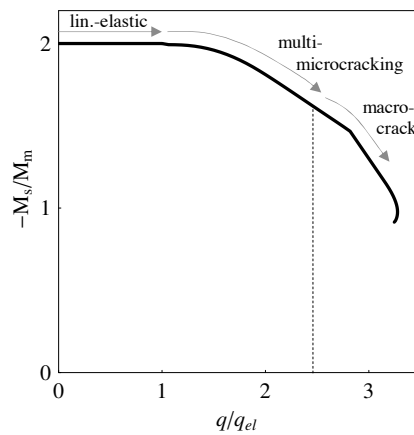


Figure 5.12: Redistribution of bending moments caused by change in stiffness due to multi-microcracking and fictitious crack opening; moment at clamped edge M_s over moment in mid-span, M_m , with relative load increase q/q_{el}

The increase in curvature for the section at the clamped edge and the mid-span section is plotted against the load level in Figure 5.13. It can be noted that the behaviour in the region close to the peak load is characterised by a significant increase in both curvatures, a small load variation, which is compatible with previous observations on the force-displacement relationship, and indicates the plastic-like behaviour in elements of small height.

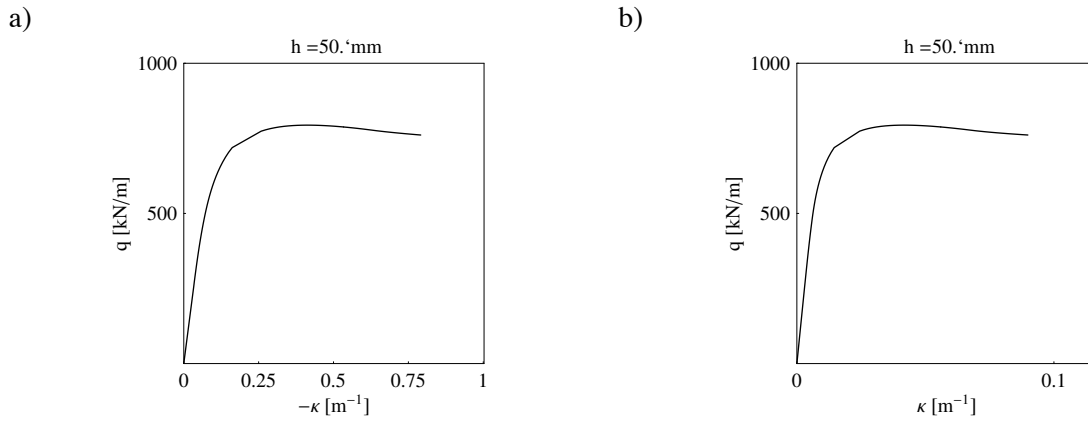


Figure 5.13: Development of curvature with load increase: a) curvature at support, b) curvature at mid-span section

5.4 Plastic solutions for a clamped beam

Instead of calculating the progressive failure of a member (Figure 5.15 a) and b)), as in the previous non-linear analysis, the theorems of limit analysis can be used to determine the load-carrying capacity of sufficiently ductile materials (§ 5.2). It is assumed that a rigid-perfectly-plastic moment-curvature relationship characterises the sectional behaviour of the studied element (Figure 5.14).

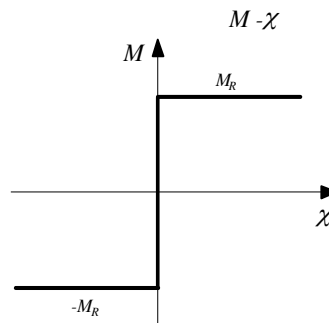


Figure 5.14: Idealised moment-curvature relationship corresponding to rigid-perfectly plastic behaviour

Limit analysis solutions

1) A statically admissible solution according to the theorem of the lower bound enables a lower limit of the failure load, q_{lb} , to be determined. For the given moment-curvature relationship characterising the element (Figures 5.14 and 5.5, dashed line), a statically admissible stress state can be assumed as being the one which is equilibrated with the applied load and never violates the yield condition i.e. $|M(x)| \leq M_R$ (Figure 5.15 c)). With the bending moment at the clamped edges $|M_s| = |M_R|$ and the resistant moment M_R attained at the mid-span section, $M_m = M_R$, a lower limit of the failure load is found as:

$$q_{lb} = 16 \cdot M_R / L^2 . \quad (5.18)$$

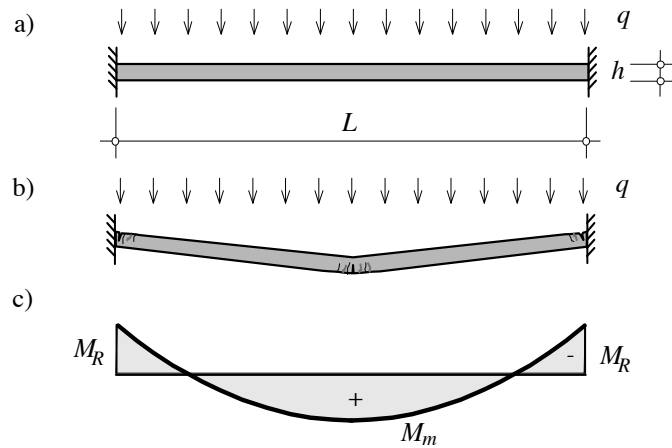


Figure 5.15: Clamped beam in bending: a) boundary conditions; b) non-linear deformations; c) assumed statically admissible moment field

2) A kinematically admissible solution according to the theorem of the upper bound can be found by applying the principle of virtual work on a kinematically admissible mechanism (Figure 5.16 b)). Respecting the definition of internal A_i and external A_e work,

$$A_i = \sum_{j=1}^n M_j \theta_j \quad (5.19)$$

$$A_e = \int_0^L q(x) \cdot w(x) dx \quad (5.20)$$

where A_i is the total energy dissipation in the plastic hinges and A_e is the work of externally applied forces, with $|M_R^-| = M_R^+$, and $q(x) = \text{const}$, for the assumed mechanism shown in Figure 5.16 b) and for the imposed virtual displacement $\delta = l$, it follows:

$$A_i = A_e \Leftrightarrow 4M_{pl} \theta = q_{ub} \cdot 2 \frac{L}{2} \cdot \frac{\delta}{2} \quad (5.21)$$

$$q_{ub} = 16 \cdot \frac{M_{pl, \max}}{L^2} . \quad (5.22)$$

Based on Equations 5.18 and 5.22 it can be noted that, for a perfectly plastic behaviour, the lower and the upper bound solution are equal, and henceforth referred to as the plastic solution.

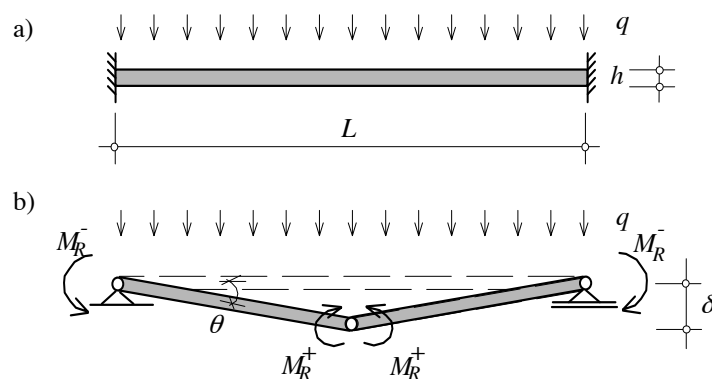


Figure 5.16: Clamped beam in bending: a) boundary conditions; b) assumed kinematically admissible mechanism

Plastic solution for UHPFRC: plastic moment

The concept of plastic yielding associated to UHPFRC elements in bending is mentioned in § 5.2. The source of ductility in a UHPFRC is related to material tensile properties which, being governed by cracking, cause the ductility to be influenced by material fracture properties and element size. The corresponding moment-curvature relationship will then also be dependent on these two parameters. As demonstrated in the previous analysis of bending members (Chapter 4), due to the presence of the multi-microcracking, element size has a limited influence on resistance, whereas the deformational capacity is strongly affected by element size.

The greatest increase in deformations in a UHPFRC element in bending is related to macrocrack propagation, while the corresponding bending stresses remain almost constant (Figure 5.17). For this reason the moment corresponding to the maximal moment before propagation of the macrocrack starts, $M_{pl,max}$, is assumed to represent the resistant plastic moment of a UHPFRC section:

$$M_R = M_{pl,max} \cdot \quad (5.23)$$

The value of $M_{pl,max}$ can be calculated from the material properties and geometry of the section (§ 4.3.4). For a rectangular cross-section

$$M_{pl,max} = n_{f_{ct}} \cdot f_{ct} \cdot \frac{bh^2}{6} \quad (5.24)$$

where $n_{f_{ct}}$ represents the ratio of the maximal bending stress achieved prior to crack localisation to tensile strength, f_{ct} , defined by Equation 4.17,

$$n_{f_{ct}} = \left(3 - \frac{2\sqrt{2}f_{ct}}{\sqrt{f_{ct}(E_c \varepsilon_u + \sqrt{f_{ct}(2E_c \varepsilon_u - f_{ct})})}} \right)$$

It should be remembered that the $n_{f_{ct}} \cdot f_{ct}$, the bending resistance achieved before the macrocrack starts to develop, is shown to be a size-independent, and thus the $n_{f_{ct}}$ is a function of material properties only.

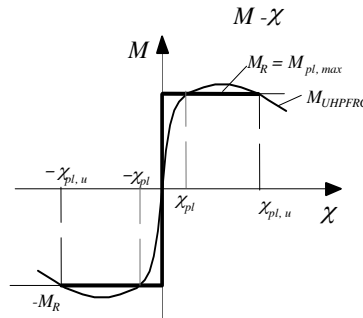


Figure 5.17: Comparison of moment-curvature response of a UHPFRC section and moment-curvature response of an idealised rigid-perfectly-plastic material

As seen in the analysis of statically indeterminate systems, the deformational capacity of the plastic hinges is the other relevant parameter that affects the development of a failure mechanism (e.g. Figure 5.16) and determines whether the behaviour of a UHPFRC element will approach a plastic behaviour. Using Equations 4.79 and 4.80, the maximal curvature $\chi_{pl,u}$ (Figure 5.17) characterised by the condition

$$\forall \chi, \chi_{pl,ini} \leq \chi \leq \chi_{pl,u} \Rightarrow M(\chi) \geq M(\chi_{pl,ini}) \quad (5.25)$$

can be defined for a section of a given height. The $\chi_{pl,ini}$ is the curvature characterising the beginning of plastic moment $M_{pl,max}$ (Figure 5.17). As mentioned, the value of the $\chi_{pl,u}$, designated curvature at failure, is strongly affected by element size (Figure 5.20). The value of this curvature is directly related to the deformational capacity of the plastic hinge.

During formation of the kinematic mechanism the value of $\chi_{pl,u}$ must not be exceeded if plastic behaviour is to be developed (Equation 5.25). In this case, limit analysis can be used to determine the failure load.

Plastic solution for UHPFRC: failure load

For the observed boundary conditions (Figure 5.16), the failure load obtained based on the lower- and upper-bound theorems (Equations 5.18 and 5.22), designated q_{pl} , with Relationships 5.23 and 5.24, can be expressed as a linear function of maximal elastic load, using parameter n_{fct} , as:

$$q_{pl} = \frac{4}{3} \cdot n_{fct} \cdot q_{el} \tag{5.26}$$

since

$$q_{pl} = 16 \cdot \frac{M_{pl}}{L^2} = 6 \cdot \frac{n_f \cdot M_{el}}{L^2} = \frac{16}{L^2} \cdot n_f \cdot \frac{q_{el} \cdot L^2}{12} . \tag{5.27}$$

For the UHPFRC used in this study $n_{fct} = 2.4$ (§ 4.3.4), and for the given static systems

$$q_{pl} = 3.2 \cdot q_{el} . \tag{5.28}$$

The obtained plastic solution for failure load can now be compared to the failure load obtained by non-linear analysis.

5.5 Comparison of results: non-linear and plastic analysis

UHPFRC beams of various heights are analysed using the algorithm presented in Section 5.3.2 and their response in terms of force-displacement relationship is compared to the plastic solution (Equation 5.28). Before presenting these results, the load-bearing capacity of the clamped beam studied in Section 5.3 (Figure 5.18, black line) is compared to the failure load obtained according to the plastic solution (grey line).

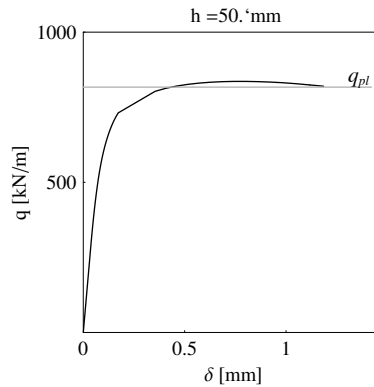


Figure 5.18: Force-displacement curve of UHPFRC beam of $h=50 \text{ mm}$ and failure load obtained using plastic analysis (grey line)

As indicated in Figure 5.18, the maximal load predicted for a beam of small height by the non-linear static analysis is slightly higher than the failure load predicted by the plastic analysis. This may be considered a solution that does not comply with the hypotheses of the theory of plasticity, since it implies that a higher value for the resistant moment, M_R , than the assumed plastic moment is achieved. However, this must not be interpreted as a violation of the yield condition, since the difference is due to the assumption made for the plastic moment value $M_R = M_{pl, max}$, (Equation 5.23), while in the non-linear analysis $M_{max} > M_{pl, max}$ occurs and, as will also be seen for other elements of small height, $q_{max} > q_{pl}$ can be obtained.

Beam height, h , is varied in the range of 10 to 250 mm, while span-to-depth ratio is kept constant, corresponding to the slenderness of the first case study $L/h=0.42/0.05=8.4$. The boundary conditions are also maintained (Figure 5.4).

The results are presented in Figure 5.19. In Figure 5.19 a) obtained load values q are normalised with the value of maximal elastic load $q_{el, max}$ and plotted against the mid-span displacement normalised by element height (δ/h). The corresponding level of plastic failure load, q_{pl} , is also indicated. In the same Figure b) the results are plotted as the redistribution of bending moments (ratio of support moment to moment at mid-span, $|M_s|/M_m$) against the normalised load value ($q/q_{el, max}$). In Figure c) the difference between the failure load predicted by the non-linear analysis and the plastic failure load is shown as a function of element height.

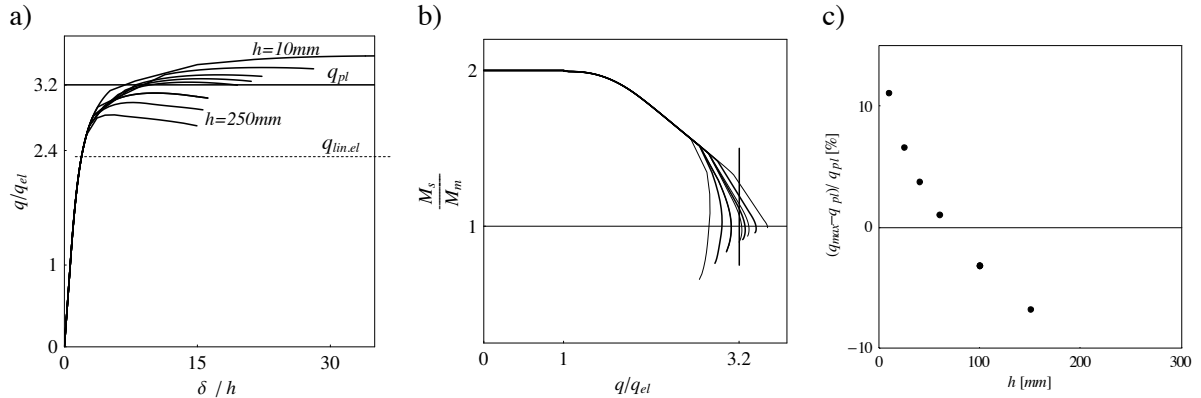


Figure 5.19: Bending response of elements of various heights ($h=10, 25, 40, 50, 60, 100, 150, 250$ mm, $L/h = const$): a) normalised force-displacement relationships; b) moment redistribution as function of load increase; c) maximal load from non-linear static analysis against plastic failure load

It can be noted that, for the given material properties, the elements of smaller height exceed the plastic load predicted by Equation 5.28 with $M_R = M_{pl, max}$. In the case of elements of $h > 100$ mm, the lower bound of failure load is not attained. These results are explained by the different deformational capacity of elements of different heights: in Figure 5.20 a) normalised moment-curvature relationships are plotted for the different element heights and the significant difference in capacity to increase curvature during macrocrack propagation can be noted. The intersection of the normalised M - χ curves with the horizontal line ($M/M_{el} = n_{fcr} = 2.4$ for the given UHPFRC) represents the position of the curvature $\chi_{pl,u}$, after which moment decreases below value of M_R . Very thin elements (e.g. $h=25$ and 50 mm) exhibit a significant increase in χ with almost no change in moment-bearing capacity, while for thicker elements (e.g. $h=150$ mm), the moment born by the section quickly decreases with an increase in χ . This results in a more pronounced redistribution of internal forces in thin elements, leading also to a more pronounced influence of size effect on bearing capacity (Figure 5.19 a)) than in the case of statically determinate elements. This is mainly because the effect of size on bending strength is limited, whereas it is more pronounced on ductility (Figure 5.20 a)) which influences the bending resistance of statically indeterminate members. This phenomenon restrains the application of the theory of plasticity to elements of small size. With the proposed concept of the plastic moment in UHPFRC elements (Figure 5.17, Equation 5.23), the failure loads for elements thicker than 100 mm overestimate the ultimate loads obtained by non-linear static analysis.

As already mentioned (Chapter 4), the curvature $\chi_{pl,u}$ for which the moment starts to decrease, being a plasticity-relevant parameter for UHPFRC, is also a function of the fracture properties of the material, namely of the tensile softening relationship slope ($d\sigma/dw$). The influence of this parameter on the increase in $\chi_{pl,u}$ is shown in Figure 5.20 b) for the case of a beam of $h=100$ mm: a lower tensile softening slope increases the capacity of a cracked section to deform, and the M - χ

relationship approaches the $M-\chi$ relationship of a thinner section. Thus, the enhanced fracture properties of the material lead to a more ductile behaviour, making it possible to reach the predicted plastic failure with thicker members. In the same manner, a higher tensile softening slope approaches a brittle behaviour, with a faster post-peak decrease in load-bearing capacity and reduced possibility for developing plastic behaviour at the element level.

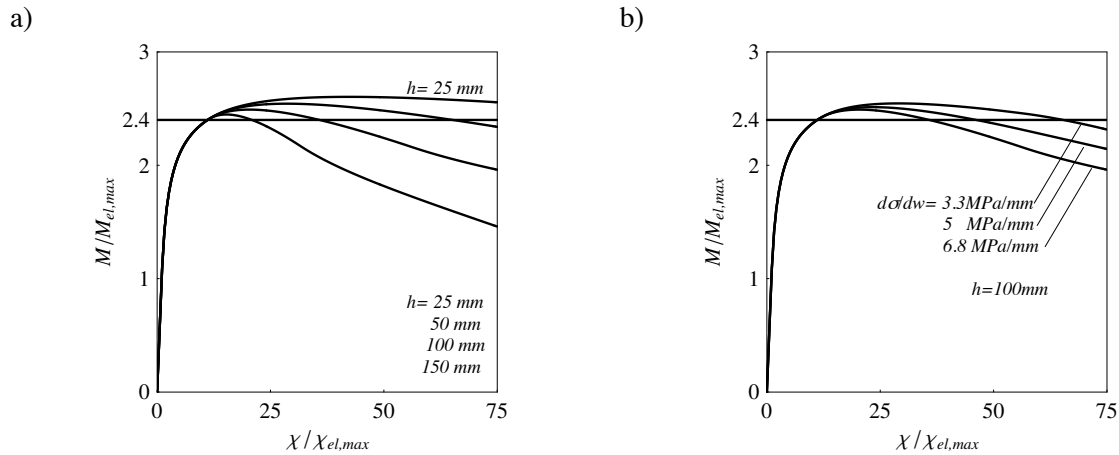


Figure 5.20: Curvatures characterising UHPFRC sections with a macrocrack: a) influence of variation of element size on ductility; b) influence of variation of initial slope of stress-crack opening curve on ductility

The presented study is performed using the initial slope of the stress-crack opening curve of 6.8 MPa/mm , based on the data from uniaxial tests on the unnotched specimens. This value may be considered slightly conservative for bending, as already seen in the analysis on simple beams where bending behaviour, modelled with these tensile properties, never led to overestimation of bending strength. Consequently, the simulated behaviour of statically indeterminate members can be accepted as being on the safety side for the elements made of BSI.

Regarding the influence of span-to-depth ratio, L/h , it should be mentioned that a slight loss of ductility is observed for an increase in L/h . However, for the L/h ratio range of interest for structural application, the results shown in Figure 5.19 can be considered representative.

In addition, it can be noted that the resistance of thicker elements (e.g. $h > 100\text{ mm}$, Figure 5.19 a)), though not reaching ultimate load predicted by the plastic analysis, can however exceed the maximal linear-elastic load, (slightly higher than $n_{fcr} \cdot q_{el} = 2.4q_{el}$). This signifies that the load can continue to increase in the system while the moment borne by the clamped edge $|M_s|$ decreases, and the mid-span moment M_m increases. Eventually the value of $|M_s|$ and M_m can become equal. Thus, a lower-bound plastic solution can be satisfied by assuming a value of resistant plastic moment $M_{R'}$ smaller than $M_R = M_{pl,max}$ (Figure 5.21). However, due to the lack of more precise definition for $M_{R'}$, non-linear analysis must be used to assess the ultimate load-bearing capacity of thicker elements.

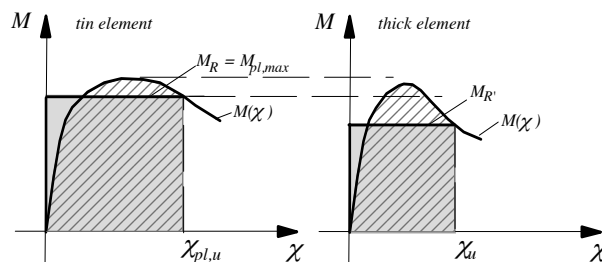


Figure 5.21: Alternative condition determining resistant plastic moment, based on required χ_u

The conclusions on the plastic behaviour of UHPFRC elements will be extended to slabs, as elements with a higher degree static redundancy, for which the experimental evidence is also presented (Chapter 6).

5.6 Compressive membrane action

In the above analysis the effect of membrane (arching) action was deliberately disregarded. The membrane effect was observed at the beginning of RC slab construction as a phenomenon allowing slabs with laterally restrained displacements (Figure 5.22) to carry higher loads than those predicted by plate theory. The effect was theoretically recognised by Ockleston [Ockleston 1958] and much theoretical and experimental work followed. The effect was also experimentally observed in frame structures [Beeby, Fathibitaraf 2001].

According to current publications, this membrane action was not studied in UHPFRC elements. However, regarding the physical mechanism of bending resistance development, the same effect as in RC elements may be assumed to develop. Due to the specific tensile deformations, the neutral axis, initially at the section centroid, moves towards the compressive zone (Chapter 4); this is followed by the displacements and causes the element's tendency to extend middle surface, which, being restrained, introduces the compressive force (Figure 5.22). Thus, the ultimate load in restrained systems is not carried by bending forces only, but also by the introduced arching action. Since the effect enhances element-bearing capacity, the fact to disregard it in models for predicting bending resistance leads to the results that are considered to be on the safety side.

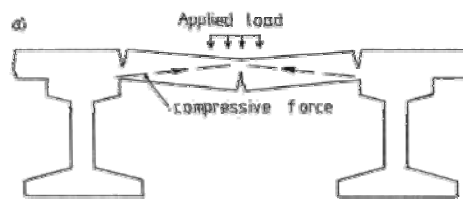


Figure 5.22: Schematic representation of compressive membrane (arching) action [Cope, Clark 1984]

5.7 Conclusion

The behaviour of statically indeterminate beams made of UHPFRC without ordinary reinforcement is studied in this section. An analytical approach is developed to simulate the non-linear response of UHPFRC beams subjected to bending up to failure, and by analysing elements of various heights, the following conclusions may be drawn:

- ductile tensile behaviour of UHPFRC allows redistribution of internal forces in statically indeterminate elements, leading to increase in load-bearing capacity;
- the load-bearing capacity of statically indeterminate members is more sensitive to size effect than the bending resistance of statically determinate elements. Thinner statically indeterminate elements can sustain higher loads. This is because non-linear bending behaviour in statically indeterminate elements is influenced by ductility, which, for UHPFRC elements, is significantly influenced by element size. The ductility, being more pronounced for thinner elements, allows a more significant redistribution of internal forces to occur, increasing load-bearing capacity;
- since the material fracture properties, primarily the slope of the tensile softening law, influence the ductility of UHPFRC members, their effect on the bending resistance of statically indeterminate members can be considered equivalent to that of the size: a decreased

slope of the initial part of the tensile softening law increases the load-bearing capacity of the element.

The possibility of the application of the theory of plasticity in the design of UHPFRC members is investigated, based on an introduced concept of plasticity in UHPFRC elements. The results from the non-linear static analysis are compared to plastic solutions, leading to the following conclusions:

- if the resistant plastic moment of a section is defined as the moment prior to the start of macrocrack propagation, i.e. before the tension strain softening is exhibited, the theory of plasticity can be applied to predict failure loads for thin elements (e.g. $h < 100 \text{ mm}$ for the elements made of BSI). The plastic-like behaviour is due to the ability of thin elements to allow a sufficient redistribution of internal forces without loss of load-bearing capacities; in terms of plastic behaviour: the deformational capacity of the first hinges developed in thin elements is sufficient to allow the formation of other hinges that compose the mechanism;
- unlike the deformations of a rigid-perfectly-plastic hinge, the deformations of a UHPFRC hinge are limited as a function of element size and material fracture properties, and as a consequence the theory of plasticity, using the proposed level of plastic moment, is not applicable to thick elements;
- straight forward prediction of failure load for thin elements based on the theory of plasticity is an important advantage to non-linear static analysis, in particular for practical design.

6. Bending and punching behaviour of thin UHPFRC slabs

The behaviour of thin UHPFRC slabs without ordinary reinforcement is studied in this chapter. Both bending and punching failure are investigated. An analytical procedure is developed for simulating the non-linear bending response of slabs in symmetric boundary conditions. The results are compared with experimental results obtained during a test programme performed at EPFL, and results from other researchers. The possibility of the application of the theory of plasticity in the design of thin UHPFRC slabs is discussed.

6.1 Thin UHPFRC slabs as structural elements

This study focuses on the behaviour of thin slabs as an element of ribbed deck slab, which represent a concept for an advanced application of UHPFRC in bridge design (Figure 6.1 b)). As concluded from the previous analyses, due to ductility in tension, UHPFRC elements can provide high bending resistance even without ordinary reinforcement (Chapter 4). Furthermore, in Chapter 5 it was demonstrated that the ductility of thin elements is sufficient to allow plastic behaviour to develop in statically indeterminate systems, leading to increased load-bearing capacity. Thus, thin slabs, as static systems with a higher level of redundancy, are postulated as elements that enable the material properties offered by UHPFRC to be used to better advantage. The low bending stiffness of the thin slabs is compensated by the stiffness of the ribs (Figure 6.1), which at the same time limit the span of the thin slabs, resulting in a final structural system with a significantly decreased material volume. The bending resistance of these systems is generally provided by prestressing reinforcement.

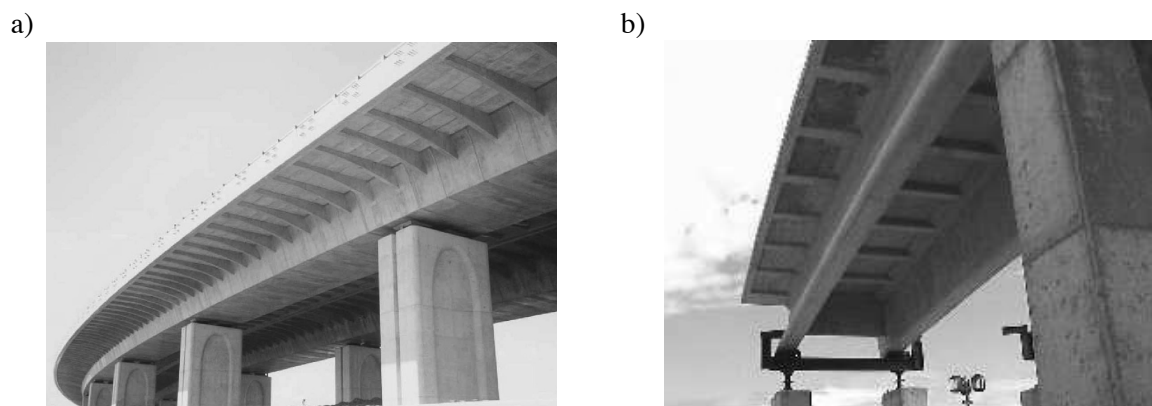


Figure 6.1: Thin slab between ribs: a) Furukawa Viaduct, Japan; prefabricated concrete bridge, 1999-2002 [JSCE 2003] ; b) UHPFRC slab of Seonyu footbridge in Seoul (‘Bridge of peace’), 2002, picture from from [Ductal 2007]

The concept of lightening a structure by combining thin slabs and shells with ribs was introduced for RC structures by Nervi (ribbed shells of Orvieto hangars, constructed in 1935, [Nervi 1997]). In the case of UHPFRC, this concept becomes more interesting since ordinary reinforcement is no longer required, thus there is less casting work involved, and the material strength and durability mean that element size can be significantly reduced. Moreover, the particular advantage of these UHPFRC elements lies in the possibility of applying a precasting procedure which, combined with decreased element weight, results in rapid and easy construction. Thin UHPFRC slabs are already in use in bridge design, principally as prestressed elements [Graybeal, Hartmann 2005] and mostly in footbridges (Chapter 7). A pilot project involving UHPFRC ribbed deck slabs is being conducted at the LCPC, within the framework of the MIKTI project [Toutlemonde et al. 2005], [Toutlemonde et

al. 2007]. These slabs are designed as part of a composite road bridge structure, 12 m width and spanning $90 + 130 + 90\text{ m}$.

Both analytical and experimental studies are conducted in the course of this thesis to assess the load-bearing capacity of thin slabs. The final aim, as in the previous chapter, is to provide a simple theory that allows the resistance of these elements to be predicted. Two possible failure modes of thin slabs are investigated: bending and punching-shear failure (Figure 6.2). Bending behaviour and design possibilities are discussed in Section 6.2, while the punching-shear behaviour is presented in Section 6.3.

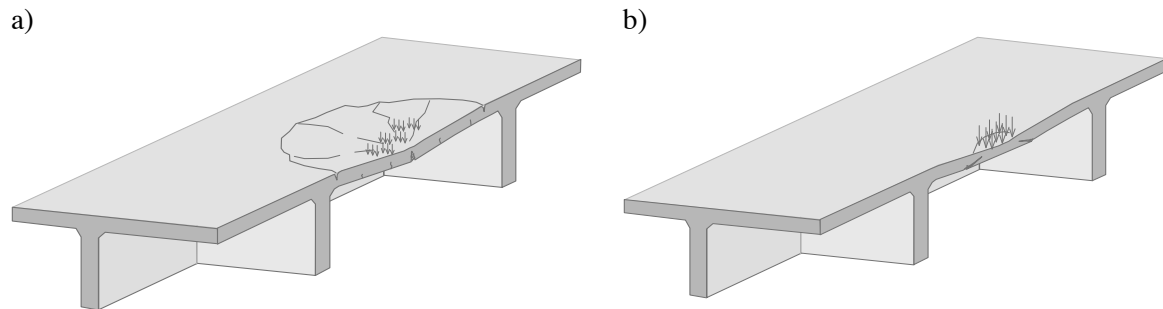


Figure 6.2: Schematic presentation of failure modes of thin slab between ribs: a) flexural deformations and macrocracking; b) punching-shear failure

6.2 Bending behaviour of UHPFRC slabs

The bending response of thin UHPFRC slabs is characterised by a pronounced non-linear behaviour due to multi-microcracking and the propagation of macrocracks at failure (Figure 6.2 a)). An analytical procedure is developed, enabling the non-linear behaviour due to pseudo-plastic tensile yielding to be taken into account in predicting the bending response of a slab under symmetric boundary conditions. Bending behaviour is also important in the analysis of punching-shear (Figure 6.2 b)), since the slab deformations, which interact with punching-shear failure, depend on the flexural characteristics of the slab, as in the case of reinforced concrete structures [Muttoni, Fernández Ruiz 2008].

During the experiments on thin slabs subjected to a central point load (Figure 6.9 and Appendix T1) it was observed that the pattern of failure lines (macrocrack) was similar to that in plastic-like elements, such as RC slabs. This suggests that a plastic-like behaviour can develop in UHPFRC slab without ordinary reinforcement, which is consistent with the conclusions drawn in Chapter 5. Thus, the question of the applicability of the theory of plasticity is extended to UHPFRC slabs.

Only a few theoretical and experimental works dealing with the behaviour of UHPFRC slabs have been published. Some experimental data can be found in [Harris 2004]. An attempt to model the pre-peak bending response of UHPFRC slab using finite element method is presented in [Fairbairn et al. 2005]. Considering the behaviour of SFRC slabs, an approach to predicting ultimate loads based on moment capacity can be found in [Mudhafar 1980], and numerical modelling of SFRC slabs-on-ground, based on non-linear fracture mechanics, is presented in [Meda A, Plizzari 2004].

6.2.1 Bending theory of thin plates

The procedure developed for the analysis of slabs taking into account material non-linearity is based on the hypotheses of the classic theory of thin plate bending.

Hypotheses of the elastic theory of thin plates

The principle assumptions in the development of the force-deformation relationship are reviewed in this section, while more details concerning the classic theory of the bending of thin plates can be found in the literature [Timoshenko, Woinowsky-Krieger 1959].

For a slab in the x - y plane, the out-of-plane displacement of the slab's middle plane is an equation of a continuous surface, δ , expressed, e.g. in Cartesian coordinates, as

$$\delta = \delta(x, y). \tag{6.1}$$

In the case of linear-elastic material behaviour, this displacement is governed by the classic plate equation:

$$\nabla^2 D \nabla^2 \delta = p(x, y) \tag{6.2}$$

with p being the load acting on the slab surface in the direction of δ , and D being the flexural rigidity of the plate (Equation 6.8).

The equation for thin plate with small deflections, $\delta \ll h$ (h being the slab thickness), is derived from kinematic, constitutive and equilibrium equations, based on the following hypotheses:

- in-plane deformations of the middle plane are disregarded;
- normals¹ on the middle plane remain straight, unstretched, and normal during deformation (assumptions of Kirchhoff).

The assumption of plane sectional deformations enables the displacement field to be expressed as a function of displacements of the slab's middle surface, δ , and the curvatures of the middle surface in two orthogonal directions x and y , $1/r_x$ and $1/r_y$ respectively, can be derived. The assumptions of straight and unstretched normals allow the shear strain in z direction to be disregarded, and thus the influence of shear forces on deformations is not taken into account².

Non-linear analysis of UHPFRC slab

The analysis of bending behaviour will be performed for a circular slab in axisymmetric boundary conditions (Figure 6.3), which coincides with boundary conditions of the experimentally studied elements (§ 6.2.4). The notations and sign conventions used in the analysis are shown in Figure 6.3.

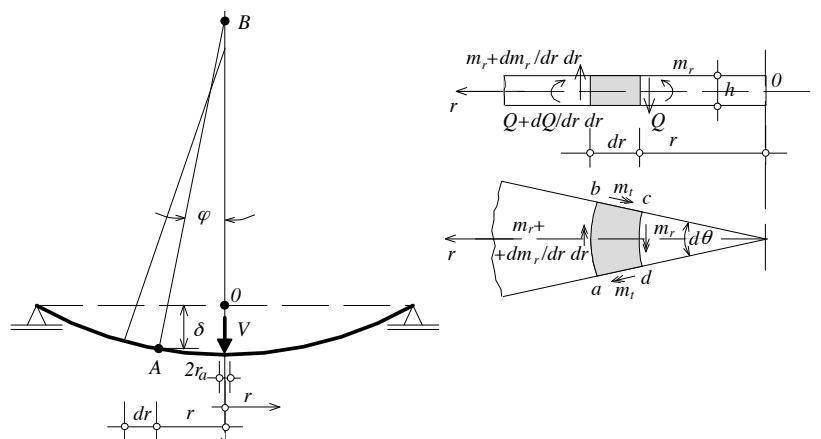


Figure 6.3: Circular slab in axisymmetric bending: notations, axes orientations and equilibrium of a slab element, adapted from [Timoshenko, Woinowsky-Krieger 1959]

¹ Points lying initially on a normal-to-the middle plane remain points in a normal-to-the middle surface after deformation

² This hypothesis is acceptable for slender elements

For a circular slab of constant thickness h , with boundary conditions and the loads that are symmetric with respect to the axis passing perpendicular to the plane of the slab and through the centre of the slab, all points at the same distance from the centre, r , have the same displacement, δ . This signifies that the slope at all points A on the same perimeter r (Figure 6.3) is the same and, in the case of small displacements, the curvature of the mid-plane, $1/r_r$, can be expressed as:

$$\chi_r = \frac{1}{r_r} = -\frac{\partial^2 \delta}{\partial r^2} = \frac{\partial \varphi}{\partial r}, \quad (6.3)$$

as shown in Figure 6.3. The minus sign preceding the second displacement derivative is used because the curvature is considered positive if it is convex downward, whereas if deflection $\delta(x, y)$ is convex downward, the second derivative $d^2 \delta/dx^2$ is negative.

For the symmetric shape of the middle plane it can be concluded that the curvature $1/r_r$ is one of the principal curvatures of the surface at the point A , and the second curvature, $1/r_t$, is perpendicular to plane r - z , passing through the normal AB (Figure 6.3). It can thus be stated that the radius of the second curvature is the AB and can be calculated as

$$\chi_t = \frac{1}{r_t} = -\frac{1}{r} \frac{\partial \delta}{\partial r} = \frac{\varphi}{r}. \quad (6.4)$$

The plane deformation hypothesis enables the deformations in the radial and tangential directions to be defined:

$$\varepsilon_r = \frac{z}{r_r} = \chi_r \cdot z, \quad \varepsilon_t = \frac{z}{r_t} = \chi_t \cdot z. \quad (6.5)$$

Linear-elastic material behaviour

The relationships between forces and deformations for a linear-elastic material behaviour are well known [Timoshenko, Woinowsky-Krieger 1959]:

$$\begin{aligned} m_r &= \int_{-h/2}^{h/2} \sigma_r \cdot z \cdot dz, \text{ with } \sigma_r = \frac{E}{1-\nu^2} (\varepsilon_r + \nu \cdot \varepsilon_t) \Rightarrow \\ m_r &= \frac{E}{1-\nu^2} \int_{-h/2}^{h/2} (\chi_r \cdot z + \nu \cdot \chi_t \cdot z) dz = D \cdot (\chi_r + \nu \cdot \chi_t), \end{aligned} \quad (6.6)$$

and, in a similar manner,

$$m_t = \frac{E}{1-\nu^2} \int_{-h/2}^{h/2} (\chi_t \cdot z + \nu \cdot \chi_r \cdot z) dz = D \cdot (\chi_t + \nu \cdot \chi_r), \quad (6.7)$$

where m_r is the moment per unit length acting along the circular section of the slab, m_t is the moment per unit length acting along a radial section (Figure 6.3), and D is the flexural stiffness of the slab in the linear-elastic regime:

$$D = \frac{E}{1-\nu^2} \frac{h^3}{12}. \quad (6.8)$$

Incorporating Relationships 6.3 and 6.4 into 6.6 and 6.7, with δ being a function of r only, gives the following:

$$m_r = -D \cdot \left(\frac{d^2 \delta}{dr^2} + \frac{\nu}{r} \frac{d\delta}{dr} \right) = D \cdot \left(\frac{d\varphi}{dr} + \frac{\nu}{r} \varphi \right)$$

$$m_t = -D \cdot \left(\frac{1}{r} \frac{d\delta}{dr} + \nu \frac{d^2 \delta}{dr^2} \right) = D \cdot \left(\frac{\varphi}{r} + \nu \frac{d\varphi}{dr} \right). \quad (6.9)$$

Non-linear material behaviour

The relationships between deformations and forces for the part of the beam exhibiting microcracking are no longer straightforward. In the beam analysis, it was shown that good correlation with test data is obtained when microcracking is represented by pseudo-plastic stress distribution and strain distribution based on the hypothesis of plane section deformations. Thus, the plane sectional deformations will also be assumed in this analysis, and Equations 6.5 are valid. Further, let us assume that, for the known curvatures of the mid-plane χ_r and χ_t , the deformations corresponding to normal stress can be estimated as a function of the linear combination of the two curvatures, $\chi_r + \nu \chi_t$, which for the moment remain uncertain in the microcracked region. This enables the position of the displaced neutral surface to be found from the normal force equilibrium, as in the equations developed in Appendix M1,

$$h_1 = h + \frac{f_{ct} \cdot (1-\nu^2)}{E_c (\chi_r + \nu \cdot \chi_t)} - \frac{\sqrt{2} \sqrt{f_{ct} \cdot (1-\nu^2)} \sqrt{h}}{\sqrt{E_c} \sqrt{\chi_r + \nu \cdot \chi_t}}. \quad (6.10)$$

The relationship between the couple of orthogonal curvatures and the bending moment in one direction can then be established as:

$$\chi_r + \nu \cdot \chi_t = \frac{8 f_{ct}^3 h^3 (1-\nu^2)}{9 E_c (f_{ct} h^2 - 2m_r)^2} \quad \text{for } m_{el,max} \leq m_r \leq m_{pl,max}, \quad (6.11)$$

and the moments expressed in polar coordinates as functions of the linear combination of curvatures are then obtained as:

$$m_r = \frac{f_{ct} h^2}{2} - \frac{\sqrt{2} \sqrt{(1-\nu^2)} f_{ct}^{3/2} h^{3/2}}{3 \sqrt{E_c} \sqrt{\chi_r + \nu \cdot \chi_t}}$$

$$m_t = \frac{f_{ct} h^2}{2} - \frac{\sqrt{2} \sqrt{(1-\nu^2)} f_{ct}^{3/2} h^{3/2}}{3 \sqrt{E_c} \sqrt{\chi_t + \nu \cdot \chi_r}}. \quad (6.12)$$

Based on Relationships 6.4 and 6.5, the moments are related to the displacement function as:

$$m_r = \frac{f_{ct} h^2}{2} - \frac{\sqrt{2} \sqrt{(1-\nu^2)} f_{ct}^{3/2} h^{3/2}}{3 \sqrt{E_c} \sqrt{-\frac{d^2 \delta}{dr^2} - \frac{\nu}{r} \frac{d\delta}{dr}}} = \frac{f_{ct} h^2}{2} - \frac{\sqrt{2} \sqrt{(1-\nu^2)} f_{ct}^{3/2} h^{3/2}}{3 \sqrt{E_c} \sqrt{\frac{d\varphi}{dr} + \frac{\nu}{r} \varphi}}$$

$$m_r = \frac{f_{ct} h^2}{2} - \frac{\sqrt{2} \sqrt{(1-\nu^2)} f_{ct}^{3/2} h^{3/2}}{3 \sqrt{E_c} \sqrt{-\frac{1}{r} \frac{d\delta}{dr} - \nu \frac{d^2 \delta}{dr^2}}} = \frac{f_{ct} h^2}{2} - \frac{\sqrt{2} \sqrt{(1-\nu^2)} f_{ct}^{3/2} h^{3/2}}{3 \sqrt{E_c} \sqrt{\left(\frac{\varphi}{r} + \nu \frac{d\varphi}{dr} \right)}}. \quad (6.13)$$

It should be noted that for $\nu \rightarrow 0$ Equations 6.10 to 6.13 obtain the same form as the equations developed in Chapter 4 for beam analysis.

Equilibrium of a slab element

The unknowns in Equations 6.9 and 6.13 are either the displacement or rotation function, and these can be obtained from the equilibrium equations of a finite element (Figure 6.3). The finite element is chosen as element *abcd* shown in Figure 6.3, so that the sections *ab* and *dc* are parts of the circle with a centre corresponding to the centre of the slab, with the same differential angle $d\theta$ and differing diameters for dr , with both $d\theta$ and dr yielding zero.

Bending moments acting on sections *ab* and *dc* are

$$m_t r d\theta \quad (6.14)$$

and

$$\left(m_r + \frac{dm_r}{dr} dr \right) \cdot (r + dr) \cdot d\theta . \quad (6.15)$$

Shear forces acting on sections *ab* and *dc* are

$$Q r d\theta \quad (6.16)$$

and

$$\left(Q + \frac{dQ}{dr} dr \right) \cdot (r + dr) \cdot d\theta . \quad (6.17)$$

The difference in shear forces is negligible for a finite element, and the shear forces create a moment in the *rz* plane that is equal to

$$Q r d\theta dr \quad (6.18)$$

Moments acting on sections *ad* and *bc*, $m_t dr$, are equal and give the resulting moment in the *rz* plane

$$m_t dr d\theta \quad (6.19)$$

and the shear forces in sections *ad* and *bc* are cancelled due to symmetry.

The equilibrium of the moments in the *rz* plane gives the following equation

$$\left(m_r + \frac{dm_r}{dr} dr \right) \cdot (r + dr) \cdot d\theta - m_r \cdot r \cdot d\theta - m_t \cdot dr \cdot d\theta + Q \cdot r \cdot d\theta \cdot dr = 0 , \quad (6.20)$$

which can be simplified by disregarding the infinitesimally small terms of higher order, resulting in

$$m_r + \frac{dm_r}{dr} \cdot r - m_t + Q \cdot r = 0 . \quad (6.21)$$

Slab equation for linear-elastic material behaviour

Substituting the moment values for the linear-elastic regime given by Equations 6.9 in Equation 6.21, the equilibrium equation governing the behaviour of the slab is obtained:

$$\frac{d^3 \delta}{dr^3} + \frac{1}{r} \frac{d^2 \delta}{dr^2} - \frac{1}{r^2} \frac{d\delta}{dr} = \frac{Q}{D} . \quad (6.22)$$

For simple boundary conditions, the solution of the third-order differential Equation 6.22 can be found in a closed form. Let us consider a slab subjected to central point load V and simply supported at the perimeter r_b (Figure 6.5). The fixed point of the slab is assumed to be the central point, while the linear support at the perimeter r_b is free to displace vertically. The three necessary boundary conditions are

$$\delta(0)=0, \delta'(0)=0, m_r(r_b)=0, \quad (6.23)$$

or, to avoid the singularity point at $r = 0$, assuming that the point load is introduced over a rigid surface of a small radius r_a , as shown in Figure 6.5,

$$\delta(r_a)=0, \delta'(r_a)=0, m_r(r_b)=0. \quad (6.24)$$

These boundary conditions enable the differential Equation 6.22 to be solved. With

$$Q(r)=V/(2\pi r), \quad (6.25)$$

for the first set of boundary conditions ($r_a \rightarrow 0$) the solution is

$$\delta(r,V)=\frac{r^2V\left(3+\nu-2(1+\nu)\cdot\text{Log}\left(\frac{r}{r_b}\right)\right)}{16D\pi(1+\nu)}. \quad (6.26)$$

For the second set of boundary conditions ($r_a \neq 0$):

$$\delta(r,V)=\frac{V\cdot K_\delta}{16D\pi\left(1+\nu+(\nu-1)\cdot\left(\frac{r_a}{r_b}\right)^2\right)} \quad (6.27)$$

where

$$\begin{aligned} K_\delta = & -4r_a^2 \cdot (1+\nu) \cdot \text{Log}(r_a)^2 - 2 \cdot \text{Log}(r) \cdot \left(2 \cdot r_a^2 + r^2 \cdot \left(1 - \frac{r_a^2 \cdot (\nu-1)}{r_b^2} + \nu \right) - 2 \cdot r_a^2 \cdot (1+\nu) \cdot \text{Log}\left(\frac{r_a}{r_b}\right) \right) - \\ & - (r-r_a) \cdot (r-r_b) \cdot \left(-3 + \frac{r_a^2 \cdot (\nu-1)}{r_b^2} - \nu - 2 \cdot (1+\nu) \cdot \text{Log}(r_b) \right) + \\ & + \frac{2 \cdot r_a^2 \cdot \text{Log}(r_a)}{r_b^2} \cdot \left(r^2 \cdot (1-\nu) + r_b^2 \cdot (3+\nu) + 2 \cdot r_b^2 \cdot (1+\nu) \cdot \text{Log}(r_b) \right). \end{aligned}$$

The derivation of the obtained displacement function enables the curvatures and moments to be expressed as functions of radius and applied force. For comparison with non-linear behaviour, the relationships for a linear-elastic material are plotted in Figure 6.4 for the two boundary conditions: the curves for boundary conditions 6.23 ($r_a = 0$), are plotted as black lines, and those for boundary conditions 6.24 ($r_a = 0.04 r_b$), are plotted as grey lines.

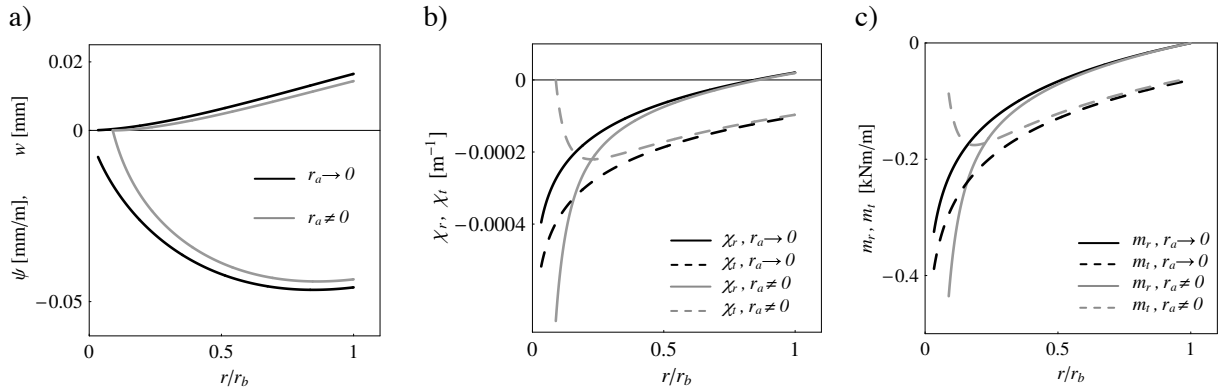


Figure 6.4: Slab in bending, distributions along the radius: a) rotations and displacements; b) radial and tangential curvature; c) radial and tangential bending moments; (radial: solid lines, tangential: dashed lines; conditions $r_a \neq 0$: grey lines)

The plots in Figure 6.4 a) show the distribution of the displacement and rotation along the radius, indicating hardly any change in the maximal displacement as a result of the difference between the two boundary conditions if $r_a \ll r_b$. However, a significant difference in curvature, and consequently

moment values, can be noted in the region close to load introduction (Figure 6.4 b) and c)). For the points distant from the load-point, this difference no longer exists, and for both boundary conditions the value of the tangential moment predominates (dashed lines).

The correct estimation of the value of maximal local deformation or maximal moment attained is however important for the taking into account of non-linear behaviour and identification of the beginning of macrocrack opening in the UHPFRC element. The sensitivity of these values to boundary conditions in the region of force introduction should thus not be disregarded. For a more realistic representation, the point load introduction zone may be considered as a surface of a certain perimeter. An example is shown in Figure 6.5, where the point load is represented as a uniformly distributed load, acting over a surface of radius r_c in the middle-plane. The loading conditions change, as will be explained (Equations 6.36 and 6.37), and the solution for these conditions, using numerical analysis (§ 6.2.3), is presented in Figure 6.7.

It must also be remembered that the point-load introduction zone is characterised by a pronounced triaxial state of stress, and the hypotheses of classic plate theory do not allow this phenomenon to be taken into account. For this reason, the representation of slab behaviour is accurate only at a certain distance from point-load introduction. (The point load clearly indicates a load of sufficient intensity to create a non-negligible triaxial stress state.)

Slab equation for non-linear material behaviour

For non-linear material behaviour, substituting the developed relationships for moments (Equations 6.13) in Equation 6.21, the equilibrium relationship gives:

$$\frac{A_m}{\sqrt{-\frac{1}{r} \cdot \frac{d\delta}{dr} - \nu \cdot \frac{d^2\delta}{dr^2}}} + \frac{A_m \cdot \left(\frac{\nu}{r^2} \cdot \frac{d\delta}{dr} - \frac{\nu}{r^2} \cdot \frac{d^2\delta}{dr^2} - \frac{d^3\delta}{dr^3} \right)}{2 \cdot \sqrt{\left(-\frac{d^2\delta}{dr^2} - \frac{\nu}{r} \cdot \frac{d\delta}{dr} \right)^3}} \cdot r - \frac{A_m}{\sqrt{-\frac{d^2\delta}{dr^2} - \frac{\nu}{r} \cdot \frac{d\delta}{dr}}} + Q \cdot r = 0 \quad (6.28)$$

where

$$A_m = \frac{\sqrt{2} \sqrt{(1-\nu^2)} f_{ct}^{3/2} h^{3/2}}{3\sqrt{E_c}} \quad (6.29)$$

The solution of differential Equation 6.28, even for simple boundary conditions, must be found numerically. An additional problem concerning the bending of UHPFRC slabs is that, during loading, both elements exhibiting linear-elastic behaviour (described by equilibrium Equation 6.22), and elements exhibiting pseudo-plastic tensile yielding (equilibrium Equation 6.28) are present. To obtain the force-displacement response of a UHPFRC slab, an incremental procedure is developed (§ 6.2.3).

6.2.2 Finite difference approach for non-linear behaviour of UHPFRC slabs

A procedure enabling the solution of Equation 6.21 to be found taking into account both linear (Equation 6.22) and non-linear material properties (Equation 6.28) is presented in this section. This procedure is developed based on finite difference analysis, and the solution is found by an incremental calculation. A similar procedure applied to reinforced concrete can be found in [Guandalini 2005]. The relationships concerning the equilibrium of a slab element presented in the previous chapter remain valid.

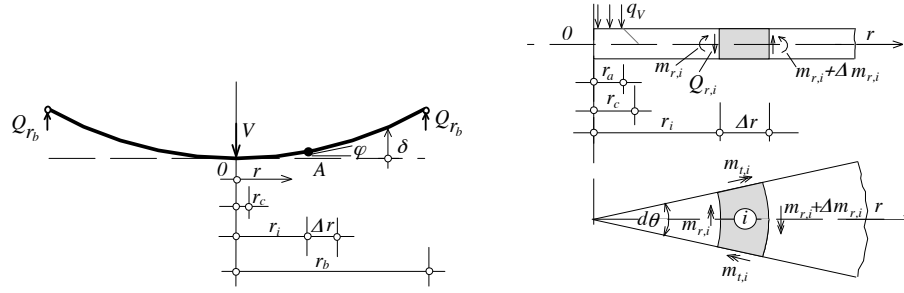


Figure 6.5: Boundary conditions of a circular slab and observed finite element

Let us consider a differential element of the slab (Figure 6.3). If

$$\frac{dm_r}{dr} dr = \Delta m_r, \quad (6.30)$$

the radial moments at the perimeter $r=r_i$ and $r=r_{i+1}=r_i+dr$ contouring the element i (Figure 6.5) are related as:

$$m_{r,i+1} = m_{r,i} + \Delta m_{r,i}. \quad (6.31)$$

The forces equilibrating the element i are shown in Figure 6.5. From the equilibrium of moments acting on the element, similar to that developed in Equation 6.20, disregarding the small values of higher order and with $dr = \Delta r$, the increase in radial moment, $\Delta m_{r,i}$ is obtained as:

$$\Delta m_{r,i} = \frac{-m_{r,i} + m_{r,i} - Q_i \cdot r + q(r_q - r_i)(r_i + \frac{\Delta r}{2})}{\frac{r_i}{\Delta r} + 1}. \quad (6.32)$$

The boundary conditions of the observed slab are

$$\delta(r_a) = 0 \quad (6.33)$$

$$\delta'(r_a) = \varphi(r_a) = 0 \quad (6.34)$$

$$m_r(r_b) = 0 \quad (6.35)$$

where $r_a \rightarrow 0$.

Loading conditions (Figure 6.5) are

$$q = q_V = \frac{V}{r_c^2 \pi} \quad \forall r_i \leq r_c \quad (6.36)$$

$$q = 0 \quad \forall r_c < r_i \leq r_b \quad (6.37)$$

where r_c is the radius of the surface over which the load, acting on the slab surface within a perimeter b , is introduced in the mid-plane, $r_c = (b+h)/2$ (Figure 6.5).

The shear force Q is defined by Equation 6.25 as a function of the acting point load V and radius r_i , valid for $r_i > r_c$, whereas for the region of the load introduction

$$Q(r) = q_V r / 2 \quad \forall r_i < r_c. \quad (6.38)$$

The incremental calculation starts at the point $r=r_a$ for which the boundary conditions are known. Equations 6.33 and 6.34 thus become the initial conditions for the procedure. The intensity of radial moment at the point r_a , $m_{r,i}(r_a)$, is then assumed. This assumption can be based, for example, on the linear-elastic solution, which in this case, for $r \rightarrow 0$ gives

$$m_{r,ini}(r_a) = \frac{V(1+\nu)(\text{Log}(r_a) - \text{Log}(r_b))}{4\pi} \quad (6.39)$$

The radial curvature, $\chi_{r,i}$, corresponding to moment $m_{r,i}$ can be determined if the curvature in the tangential direction, $\chi_{t,i}$, is known. Solving Equations 6.6 and 6.12 for χ_r , the following relationships are obtained

$$\chi_{r,i} = \frac{m_{r,i}}{D} - \nu \cdot \chi_{t,i} \quad \forall m_{r,i} \leq m_{el,max} \quad (6.40)$$

$$\chi_{r,i} = \frac{8 \cdot f_{ct}^3 \cdot h^3 \cdot (1 - \nu^2)}{9 \cdot E_c \cdot (f_{ct} \cdot h^2 - 2 \cdot m_{r,i})^2} - \nu \cdot \chi_{t,i} \quad \forall m_{r,i} > m_{el,max} \quad (6.41)$$

The curvature in the tangential direction, $\chi_{t,i}$ can be assumed from the geometry of the bent element (Equation 6.4), and the $\chi_{t,i}$ for element i is calculated in the middle of the element, at $r_i + \Delta r/2$, as

$$\chi_{t,i} = \frac{\varphi_{r,i} + \Delta\varphi_{r,i}}{r_i + \frac{\Delta r}{2}} \approx \frac{\varphi_{r,i} + \chi_{r,i} \cdot \frac{\Delta r}{2}}{r_i + \frac{\Delta r}{2}} \quad (6.42)$$

Substituting Equation 6.42 in Equation 6.40 or 6.41, curvature $\chi_{r,i}$ is obtained, and further, curvature $\chi_{t,i}$ (Equation 6.42) and the moment in the tangential direction is determined, using Equations 6.7 or 6.12, depending on whether the elastic or microcracking phase is attained.

The increment of the radial moment (Equation 6.32) can then be calculated, and the procedure can continue for the following element, $i+1$, with $m_{r,i+1} = m_{r,i} + \Delta m_{r,i}$ and $\Delta m_{r,i+1}$ being the increment of the radial moment to be found by applying the same steps as for the $\Delta m_{r,i}$.

Finally, for $r = r_b$, the obtained radial moment must satisfy the boundary condition $m_r(r_b) = 0$ (Equation 6.35). If this equality is not respected, a new hypothesis concerning the initial value of the radial moment at the starting point $m_r(r_a)$ is made and the procedure is repeated until Equation 6.35 is satisfied for the given load V .

6.2.3 Results of the non-linear analysis

The reliability of the results obtained using the developed finite difference procedure in comparison to the known analytical solution (Equation 6.26) is first shown for the linear-elastic domain (Figure 6.6).

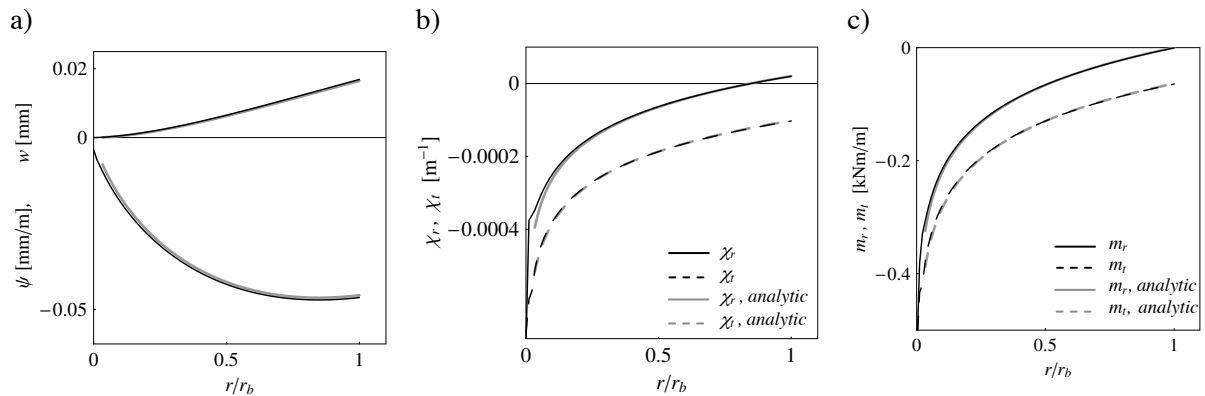


Figure 6.6: Comparison of analytical (grey lines) and finite difference-based solution (black lines) for thin slab in bending; distributions along radius: a) radial and tangential curvatures; b) radial and tangential bending moments; c) rotations and displacements

The results are plotted for boundary conditions $r_a \rightarrow 0$ (Equations 6.23), with slab thickness $h=50 \text{ mm}$, $r_b=0.45 \text{ m}$, and material properties corresponding to the elastic properties of the UHPFRC used in this thesis (Table 3.3). The Poisson's ratio is assumed as $\nu=0.2$, in accordance with French recommendations [SETRA, AFGC 2002], Article 1.6. The results (Figures 6.4 to 6.7) are plotted for unit force V , and will be used to compare elastic predictions of slab behaviour to non-linear analysis. It can be seen that the incremental procedure (black lines in Figure 6.6) and analytical solution (grey lines) give identical results for all considered forces and deformations, allowing the procedure to be extended to non-linear material behaviour.

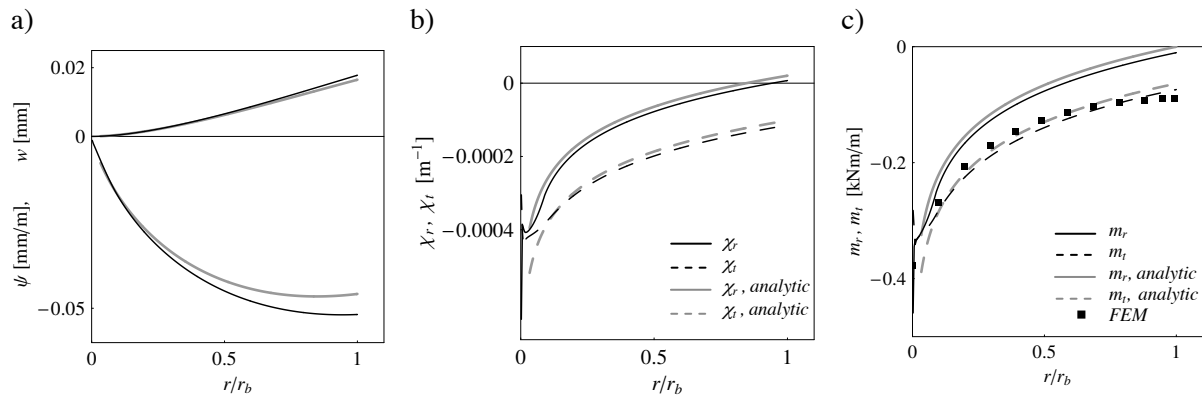


Figure 6.7: Behaviour of slab in bending considering different load introduction conditions: a) displacements and rotations along radius; b) radial and tangential curvatures; c) radial and tangential bending moments and numerical solution for tangential moment from FEM analysis (dots); black lines: numerical results for load uniformly introduced over a surface of perimeter r_c , ($r_c \approx 0.07r_b$); grey lines: analytical results for point-load introduction, $r_c = r_a = 0$

The results of the finite difference approach are also plotted for the boundary conditions corresponding to the force introduction over a surface of a radius r_c , as shown in Figure 6.5. No analytical solution is developed for these boundary conditions, but the results of finite difference approach (black lines in Figure 6.7) are plotted against the analytic solution for boundary conditions corresponding to point-load introduction, $r_c = r_a = 0$ (Equations 6.23, shown by grey lines in Figure 6.7). The plots in Figure 6.7 compare the displacements, rotations, moments and curvatures along the radius. The solutions are practically identical in the region of a principally biaxial state of stress, and the problem of the singularity point is avoided for $r_c \neq 0$. In Figure 6.7 c) the values for tangential moments obtained from a numerical finite element (FEM) model are also plotted (dark dots) against the analytical and the results of the finite difference procedure, also showing good plausibility. The point load in FEM models was introduced like a distributed load over a surface of a radius r_c .

Response of a UHPFRC slab in non-linear domain

The analysis is performed for the same case study (UHPFRC slab of 50 mm thickness, $r_b = 0.45 \text{ m}$) subjected to a central point load causing microcracking to occur. The results are plotted for load level $V = 30 \text{ kN} \approx 1/2 V_{max,m}$ (Figure 6.8 a) to c) and for $V = 55 \text{ kN} \approx 0.9 V_{max,m}$ (Figure 6.8 d) to e)), $V_{max,m}$ being the mean value of the experimentally obtained ultimate load (Table 6.1). The moment-curvature relationship for a slab element of unit width is plotted in Figure 6.10, based on the hypothesis presented in Chapter 4 and using the same UHPFRC material laws for BSI as in the previous analysis (Chapter 4 and 5). Numerical values are given in Table 6.1.

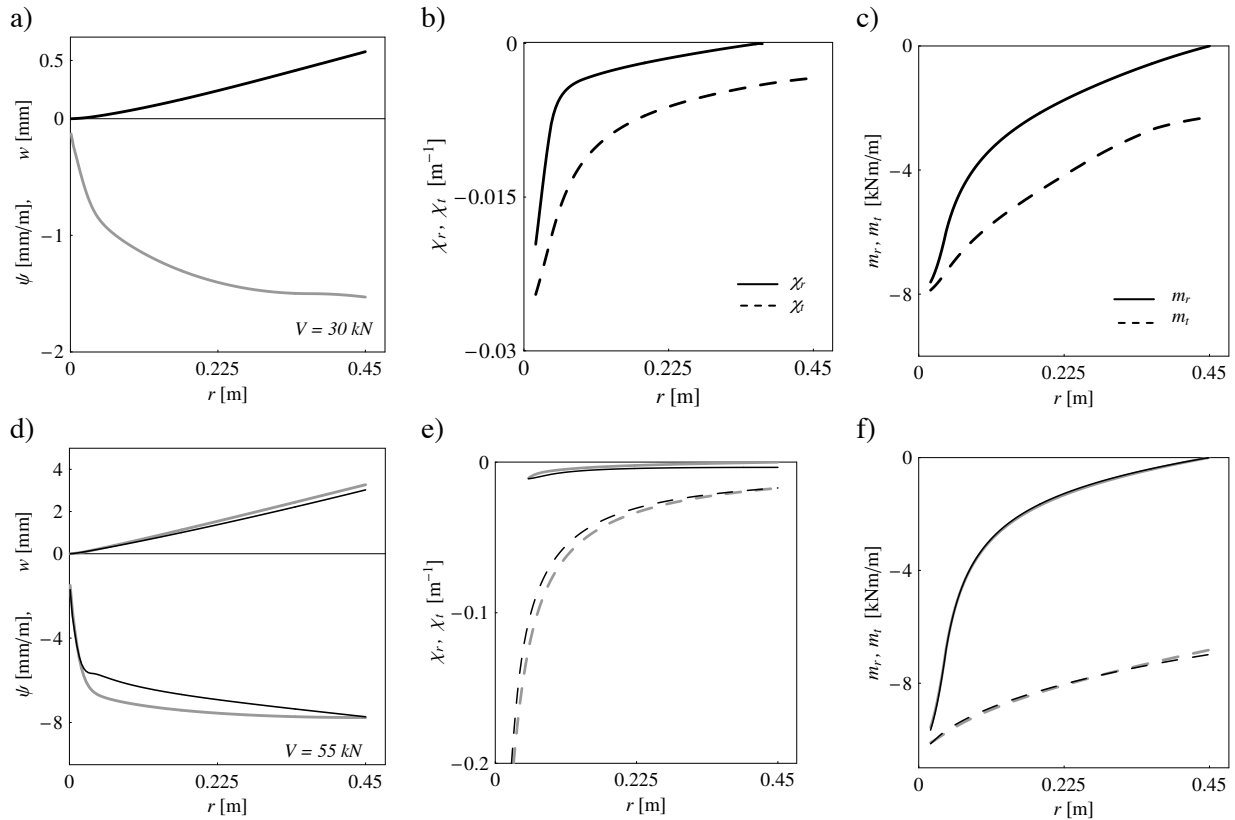


Figure 6.8: Simulated behaviour of a UHPFRC slab, at different load levels: a) to c) $V=30\text{ kN}$, d) to f) $V=55\text{ kN}$; a) and d) displacements and rotations; b) and e) radial and tangential curvatures; c) and f) radial and tangential bending moments (tangential values plotted as dashed lines)

It is interesting to note that, according to the linear-elastic analysis, for the load level $V=30\text{ kN}$ the beginning of macrocrack propagation is attained ($m_t = m_{pl,max} = 9\text{ kNm/m}$), and, according to the same analysis, the failure will occur for $V=31\text{ kN}$ ($m_t = m_{max} = 9.54\text{ kNm/m}$, Table 6.1). According to the non-linear analysis, however, the moment corresponding to the beginning of the macrocrack opening is still not reached for $V=30\text{ kN}$ (Figure 6.8 c)), which also corresponds to the experimental data. This is clearly the result of the decrease in stiffness due to the development of pseudo-plastic tensile yielding, leading to force redistribution and less loading of the central (microcracked) region. Finally, the experimentally attained ultimate load is double that of the ultimate load predicted by the linear-elastic analysis, indicating considerable ductility of the element.

The aspects of the non-linear behaviour are clearly apparent for the load level $V=30\text{ kN}$, e.g. by considering the ratio of radial to tangential moment, although the force-displacement response deviates only slightly from the linear-elastic response at $V=30\text{ kN}$ (Figure 6.11 c) and d)). In Figure 6.8 b) and c) it can be seen that the tangential curvature and moment (dashed lines) increase much faster than the radial curvature and moment (solid lines) in comparison to the elastic regime (e.g. Figure 6.7). This difference obviously applies to regions where pseudo-plastic tensile yielding occurs (for smaller values of r).

This difference becomes more pronounced with further increases in load, as seen in Figure 6.8 e) and f), where the distributions of radial and tangential moments and curvatures are plotted for load level $V=55\text{ kN}$. This load level corresponds to approximately 90% of the experimental failure load, and, as will be shown (§ 6.2.6), it is close to the failure load predicted by plastic analysis, with resistant plastic moment $m_R = m_{pl,max}$. In these figures it can be noted that the tangential curvature and tangential moment become much more significant than the corresponding radial values, indicating the localisation of tangential deformations, eventually causing the macrocrack opening along the radius (Figure 6.14 a)). In Figure 6.8 f) the maximal tangential moment value attains the level corresponding to macrocrack opening, $m_{pl,max}$, and the maximal slab deflection increases more

significantly (Figure 6.8 d)): comparing values in Figure a) and d) it can be concluded that if the force is doubled, deformations increase approximately fivefold.

It is important to note that, if the curvatures in the radial and tangential directions for the microcracked elements are not related as assumed in Equations 6.41 and 6.12, obtaining χ_r from the kinematic conditions taking into account the influence from the radial direction (Equation 6.42), suffices to provide the relationship between the deformations in two directions if the elements are sufficiently small.

6.2.4 Comparison of theoretical and experimental results

Thin UHPFRC slabs of various heights ($h = 40 - 60 \text{ mm}$) and of square shape of 900 mm side length were studied experimentally (Figure 6.9, and also Appendix T1). The slabs were tested to bending failure with the boundary conditions consisting of 8 radial point supports (Figures 6.9 and 6.14), symmetrically placed at the perimeter $r_b=450 \text{ mm}$, and a centrally introduced point load, displacement -controlled, acting over a contact surface of $30 \times 30 \text{ mm}$. The displacements are measured in the central and 12 symmetric points (Appendix T1).



Figure 6.9: Thin UHPFRC slab without ordinary reinforcement subjected to bending test under point load

The chosen disposition of the supports represents the boundary conditions as in the case of a continuous line support at the perimeter r_b . This can easily be concluded by analysing the slab with the two variants of support conditions using any standard finite element package. Thus, the analysis procedure developed in Section 6.2.3 can be applied to simulate the behaviour of tested specimens. A slight difference from axisymmetric behaviour exists due to the rectangular geometry of the slab, causing that the bending stiffness is higher in diagonal direction.

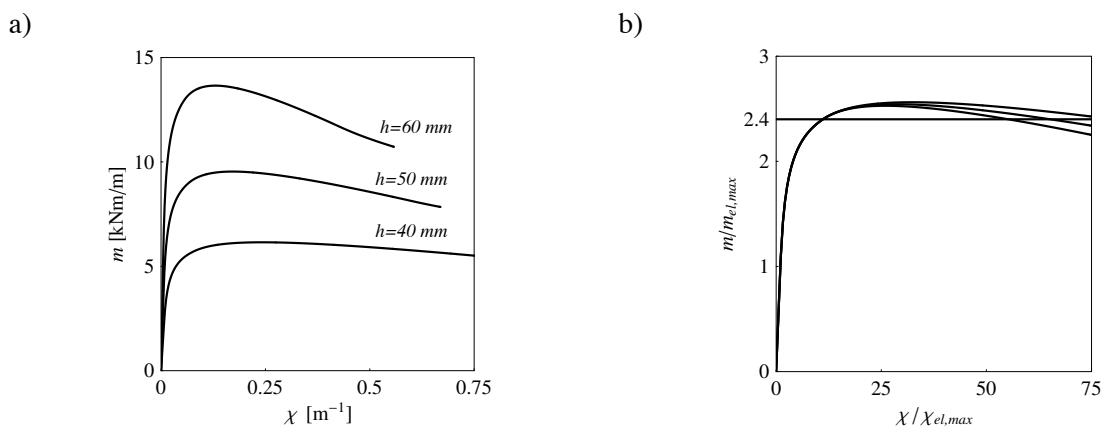


Figure 6.10: Moment-curvature relationships for slab elements of heights corresponding to tested UHPFRC slabs ($h=40-60 \text{ mm}$): a) $M-\chi$ for a section of unit width; b) normalised $M-\chi$ relationships plotted in diagram a)

Theoretical moment-curvature relationships for the elements of unit width and height corresponding to the thickness of the tested slabs are plotted in Figure 6.10, with the level of the beginning of macrocrack opening indicated ($m/m_{el,max}=2.4$).

By performing the algorithm for non-linear slab analysis while increasing the force in the system, $V=V+dV$, the response of a slab, e.g. force-mid-span displacement, is obtained. The results of this analysis for slabs of 40, 50 and 60 mm thickness are plotted against the measured data in Figure 6.11. The thick black curves in Figure 6.11 represent the simulated force-displacement response, and the straight grey lines represent the linear-elastic response. For each figure on the right, the zoom on the non-linear part before the peak force is plotted on the left.

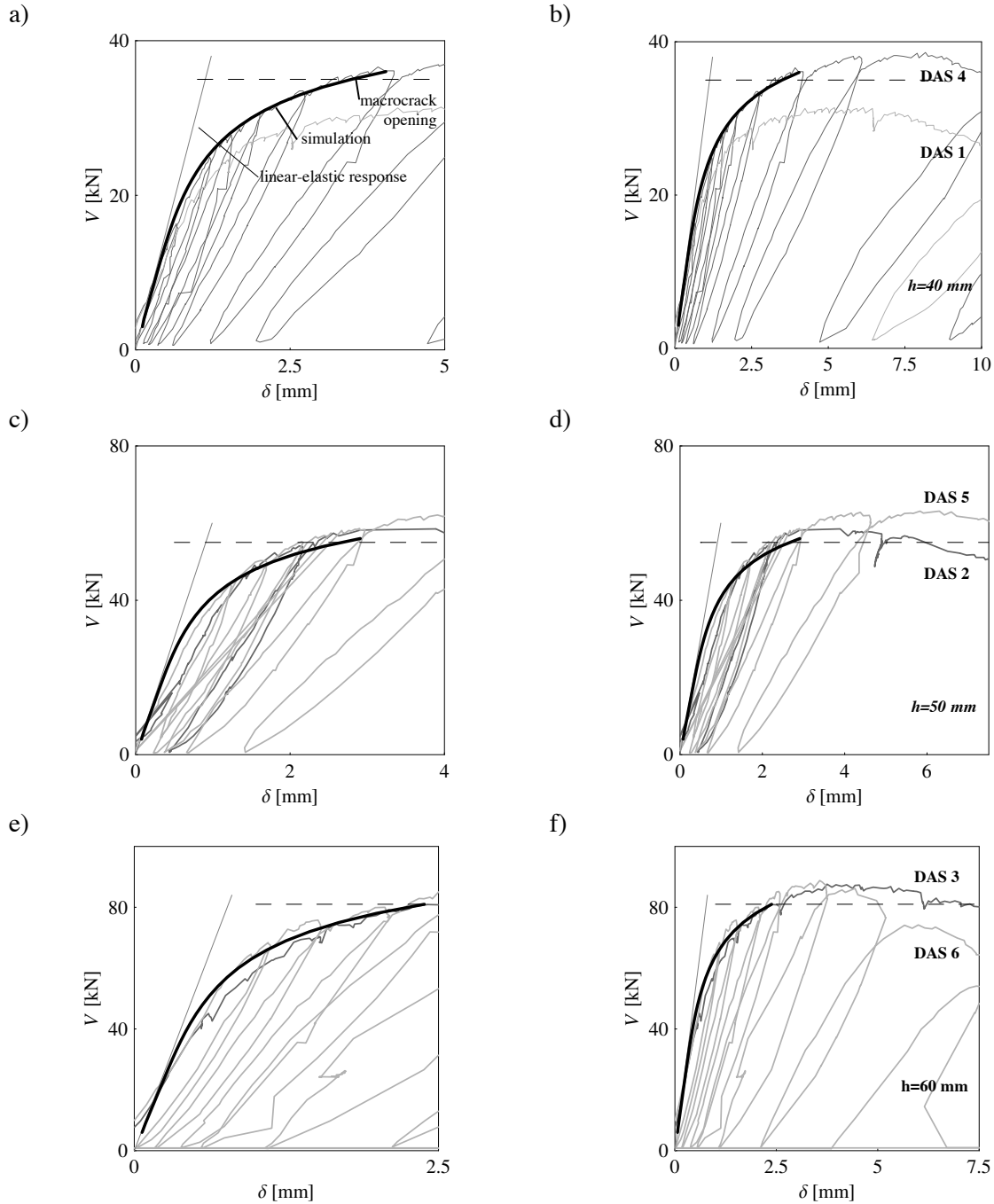


Figure 6.11: Measured and simulated force-displacement response of thin UHPFRC slabs subjected to central point load: a) and b) $h=40$ mm; c) and d) $h=50$ mm; e) and f) $h=60$ mm

Based on the good agreement of experimental and analytical results (Figure 6.11), it can be concluded that the non-linear behaviour of UHPFRC slabs prior to peak-load, can be well predicted using the analysis that takes into account material non-linearity due to multi-microcracking. This tensile behaviour is modelled by pseudo-plastic stress-strain relationship, as in the previous beam analysis. A more significant increase in deformations for a low force increase characterises all samples when the load approaches its ultimate value, which coincides with the maximal tangential moment approaching the level of macrocrack opening (Figures 6.8 and 6.10). The analytically obtained load levels for which the value of maximal moment corresponds to the beginning of macrocrack propagation are plotted as dashed lines in Figure 6.11. With the localisation of deformations in the radial macrocracks, the proposed algorithm, based on homogeneous material properties, can no longer be applied. The behaviour approaches the behaviour of rigid blocks rotating between the discrete macrocracks, and, as observed experimentally, the force remains almost constant while the deformations increase significantly. The black dots in Figure 6.12 represent experimentally obtained displacements along the radius of the slab for various load levels. It can be seen that for load levels approaching the ultimate load ($V=55 \text{ kN}$ for the 50 mm thick slab) the deformations become more concentrated in the centre. The same results are obtained from the developed non-linear analysis (Figure 6.12, solid black lines).

Beyond the level of deformations corresponding to macrocrack opening, deformations continue to increase with a very slight change in force level, indicating that the crack opening allows a plastic-like behaviour to develop. Following these observations, the possibility to predict ultimate load for thin UHPFRC slabs based on the theory of plasticity will be studied.

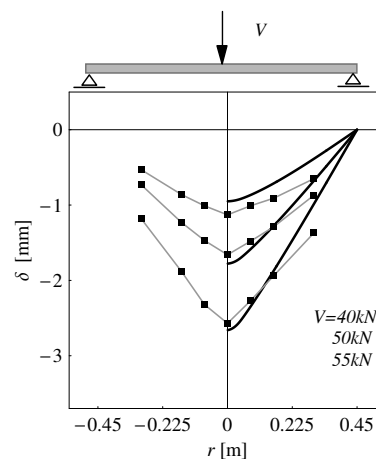


Figure 6.12: Measured and simulated displacements along the slab radius (see Appendix T1) for three load levels: $V=40$, 50 and 55 kN , for the 50 mm thick slab; measured data are indicated as black dots, simulated data are plotted for one half only (solid black line)

6.2.5 Theory of plasticity in design of thin UHPFRC slabs

The principal assumptions of the theory of plasticity and its application to concrete and UHPFRC structures are discussed in Chapter 5. The theory of plasticity has found a practical application in the design of reinforced concrete slabs since the yield lines method was developed by Ingerslev, as far back as 1921 [Nielsen 1999]. The theory was further elaborated by Johansen. The yield line method enables the upper bound solution (§ 5.2.1) for a ductile element with axisymmetric boundary and load conditions to be found in an easy and accurate manner.

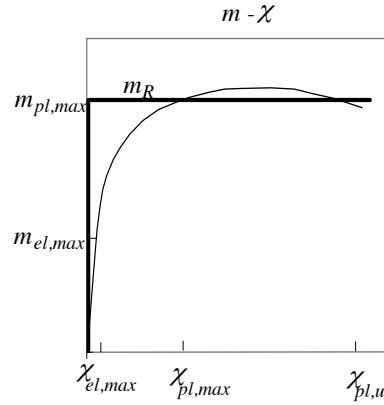


Figure 6.13: Moment-curvature relationship for a UHPFRC element (thin line) and idealised rigid-perfectly plastic moment (thick line)

The assumptions used for the definition of the resistant plastic moment of UHPFRC element, presented in Chapter 5, are also respected in the present analysis (Figure 6.13): the plastic moment coincides with the beginning of macrocrack propagation, $m_R = m_{pl,max}$, and can be defined using Equation 5.24,

$$m_R = n_{fct} \cdot f_{ct} \frac{bh^2}{6}$$

with $b=1$ (unit width), and n_{fct} defined in Equation 4.17 as

$$n_{fct} = \left(3 - \frac{2\sqrt{2}f_{ct}}{\sqrt{f_{ct}(E_c \varepsilon_u + \sqrt{f_{ct}(2E_c \varepsilon_u - f_{ct})})}} \right)$$

An upper bound solution for a slab can be found by applying the virtual displacements (§ 5.2.1) for the assumed yield line pattern forming a failure mechanism, resulting in the following relationship:

$$\iint_A q \cdot \delta(x, y) dx dy = \sum_i (\vec{m}_i \cdot s_i) \cdot \vec{\theta}_i \quad (6.43)$$

where q is load function, δ is a slab displacement function (Equation 6.1), m_i is a resistant moment acting along the yield line of length s_i , and θ_i is the rotation of the corresponding rigid segment (Figure 6.14).

6.2.5.1 Failure mechanism in tested UHPFRC slabs

A failure mechanism of the tested UHPFRC slabs, supported at 8 radial points subjected to central point load (Figure 6.9), can be assumed as being a mechanism formed of four yield lines and four rigid blocks, as presented in Figures 6.14 a). A kinematically possible failure mechanism consisting of two symmetric rigid blocks is a mechanism that dissipates less energy and characterises less ductile materials. All the tested UHPFRC slabs failed with the development of four yield lines, with the typical crack pattern as shown in Figure 6.14 b).

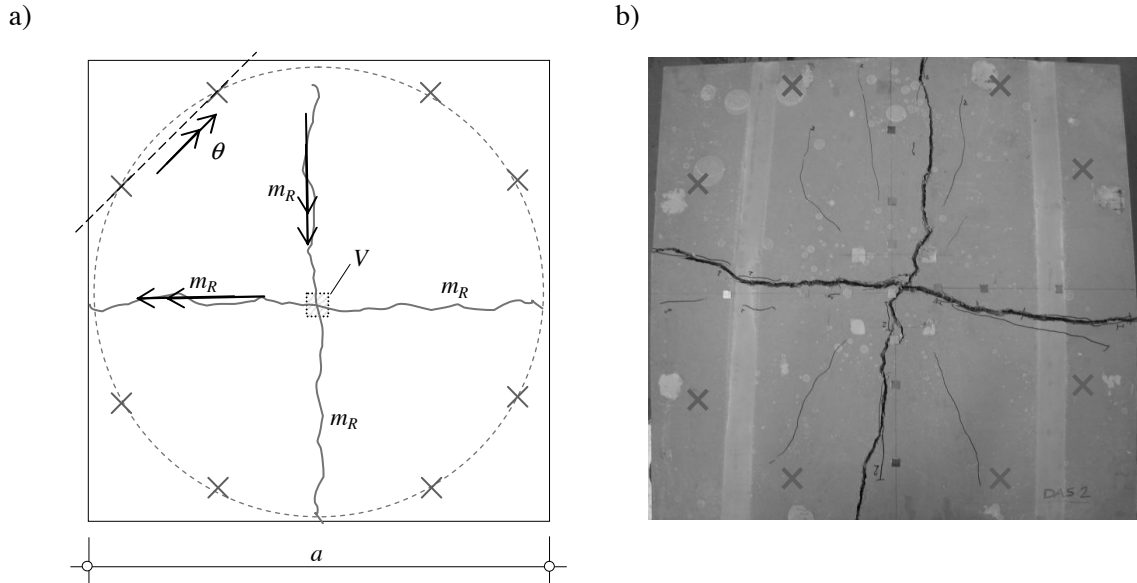


Figure 6.14: Crack pattern in UHPFRC slab and supports position (crosses): a) assumed crack pattern (yield lines); b) typical crack pattern in tested slabs

For the failure mechanism consisting of four symmetric rigid blocks rotating along indicated axes passing through two immediate support points (Figure 6.14 a)), the failure load can be calculated by applying Equation 6.43, whose left side gives

$$\iint_A \delta(x, y) dx dy = V \cdot \delta \quad (6.44)$$

with the concentrated force V being the only load, and the right side of Equation 6.43 yields

$$\sum_i (\vec{m}_i \cdot \vec{s}_i) \cdot \vec{\theta}_i = \sum_i s_i \cdot \left| \vec{m}_i \right| \cdot \left| \vec{\theta}_i \right| \cdot \cos(\vec{m}_i, \vec{\theta}_i) = 4 \cdot \left(2 \cdot \frac{a}{2} \cdot m_R \cdot \theta \cdot \cos\left(\frac{\pi}{4}\right) \right) \quad (6.45)$$

where m_R is the resistant plastic moment and a is the slab side length. The rotation of a rigid block is:

$$\theta = \frac{\delta}{r_{rb}} = \frac{\delta}{\frac{a}{2} \cdot \cos\left(\frac{\pi}{8}\right)} \quad (6.46)$$

Substituting Equations 6.44 and 6.45 in Equation 6.43, the failure load is obtained as a function of m_R :

$$V \cdot \delta = 4 \cdot \left(2 \cdot \frac{a}{2} \cdot m_R \cdot \theta \cdot \cos\left(\frac{\pi}{4}\right) \right) \quad (6.47)$$

$$V = 8 \cdot \frac{\cos\left(\frac{\pi}{4}\right)}{\cos\left(\frac{\pi}{8}\right)} \cdot m_R = 6.123 \cdot m_R \quad (6.48)$$

Incorporating the developed relationship for plastic moment, the failure load of a slab is formulated as

$$V = 6.123 \cdot n_{fct} \cdot f_{ct} \cdot \frac{h^2}{6}, \quad (6.49)$$

with $n_{fct}=2.4$ and $f_{ct}=9\text{ MPa}$ for the UHPFRC used in this study. It should be noted that, according to [Johansen 1972], in the case of point load and radial axysymmetric yield lines $V=2\pi m_R$, which gives practically the same result as Equation 6.48.

6.2.5.2 Comparison with experimental results

Applying Equation 6.48 or 6.49, failure loads for thin UHPFRC slabs of various heights are calculated, and the obtained values are plotted against measured values in Figure 6.15, while the numerical results are given in Table 6.1. Figure 6.15 a) shows examples of a complete force-displacement relationship for three of the six tested slabs ($h=40, 50$ and 60 mm), while in Figure 6.15 b) failure loads for all six slabs are plotted against the theoretical curve (Equation 6.49) predicting the ultimate failure load as a function of slab thickness. It can be noted that prediction of failure loads of thin slabs using plastic analysis, with the proposed limit of plastic moment, shows good agreement with actual failure loads.

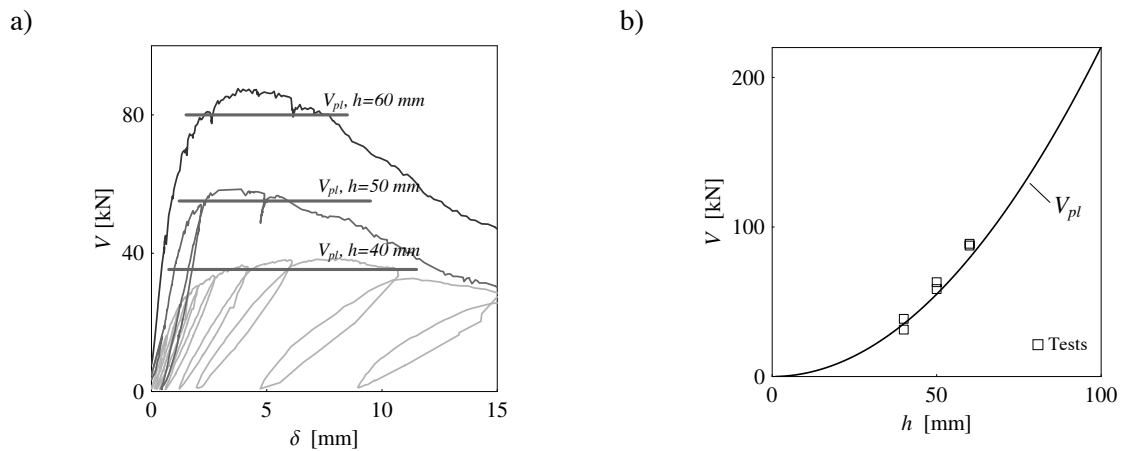


Figure 6.15: Failure load, V_{pl} , based on the plastic analysis with $m_R = m_{pl,max}$: a) V_{pl} against actual force-displacement response of thin UHPFRC slabs; b) V_{pl} as a function of slab thickness, and experimental failure loads (dots)

Table 6.1: UHPFRC slabs failing in bending: measured and predicted responses

specimen	nom. height	P_{max} measured	m_{max}	$m_{pl,max} = m_R$	No. cracks*	P_{el}^{**}	$P_{macrocrack,el.}$	$P_{max,el.}$	P_{pl}
	[mm]	[kN]	[kNm/m]	[kNm/m]		[kN]	[kN]		[kN]
DAS 1	40	31.4	6.15	5.76	4	7.7	18.5	19.8	35.3
DAS 4		38.6			4				
DAS 2	50	58.5	9.54	9	4	12.2	29.3	31	55.1
DAS 5		63.1			4				
DAS 3	60	87.6	13.64	13	4	18	43.2	45.3	79.6
DAS 6		88.8			4				

* Number of macrocracks emanating from the central load-point participating in the failure mechanism
 ** Elastic loads are obtained by considering average elastic moment, distributed along a distance $2(b/2+h)$, based on analytical or numerical analysis (Figure 6.7). $P_{macrocrack,el}$ is the force corresponding to $m_t = m_{pl,max}$, $P_{max,el}$ is the force corresponding to $m_t = m_{max}$, obtained by linear-elastic analysis, and P_{pl} is the failure load according to plastic analysis.

The prediction of failure load based on the yield line method is also shown against the actual failure load of thin UHPFRC slabs with clamped edges, tested at the Virginia Polytechnic Institute, USA [Harris 2004]. Slabs had various heights ($h = 50 - 70\text{ mm}$) and a square shape of 0.91 m side length. The material used in this study is Ductal UHPFRC, with properties similar to those of BSI, and more details can be found in [Harris 2004] and [Graybeal 2006]. The tested slabs developed the typical diagonal crack pattern in the central region of positive moment, while the crack pattern towards the supports was less regular. The same approach for defining the level of plastic moment was applied as

for BSI, with f_{ct} having a value between 7 and 9 MPa, $E_c=55\text{GPa}$, $f_c=220\text{MPa}$. For the yield lines shown in Figure 6.16 a), for $m_R^+ = m_R^- = m_R$, the upper bound solution yields $V=4\pi m_R$ [Johansen 1972]. With $f_{ct} = 9\text{MPa}$ the theoretical failure load slightly overestimates the actual failure load (Figure 6.16 b), black line), that can be explained either by the difference between the idealised and actual yield line patterns, particularly in the region of negative moment either by a smaller resistant moment, possibly influenced by element size. Theoretical prediction of failure load obtained with $f_{ct} = 7\text{MPa}$ shows better agreement with test results (Figure 6.16 b), grey line).

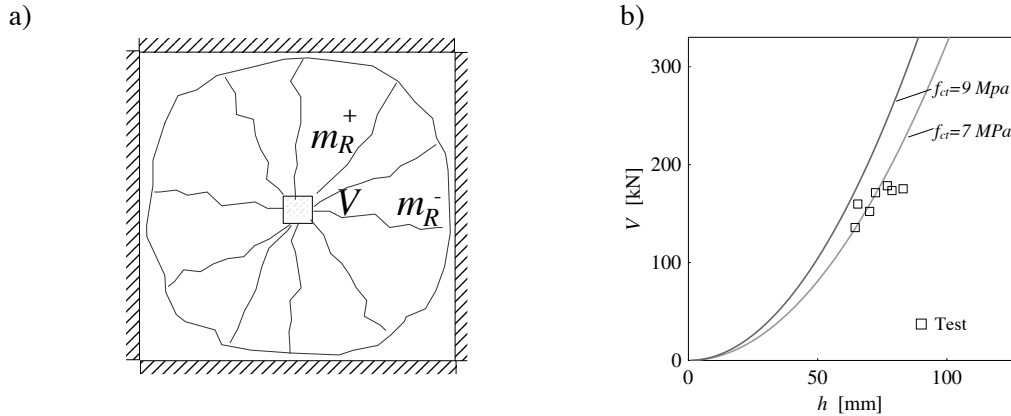


Figure 6.16: Bending failure of slab clamped at four sides subjected to central point load: a) yield line pattern; b) actual failure loads for slabs made of Ductal UHPFRC (dots) [Harris 2004], and predicted failure loads with $f_{ic}=9\text{MPa}$ and $f_{ic}=7\text{MPa}$

Restrained slabs made of BSI were tested to shear failure (§ 6.3), but one of the slabs, 50 mm thick, actually reached ultimate load in bending, at force $V=110\text{kN}$. For the assumed crack pattern shown in Figure 6.16 a) the theoretical failure load is $V=4\pi m_R=113\text{kN}$, thus very accurately predicting failure.

Based on the above considerations, plastic analysis can be applied in the prediction of ultimate bending failure loads of thin UHPFRC slabs, and load-bearing capacities can be predicted as a function of boundary conditions and element thickness.

6.2.6 Softening hinge in UHPFRC

The softening branch of the force-displacement relationship for the cracked slab can be simulated based on the softening hinge approach, as presented in [Marti et al. 1999] for steel-fibre reinforced concrete. This approach has actually been developed by Marti and co-authors in order to derive the tensile properties of SFRC from the measured force-displacement response, based on the rotation of rigid blocks between the crack lines and the softening moment-crack opening (moment-rotation) relationship. However, in the present study, the softening branch was not the main focus of interest.

6.2.7 Conclusions

Based on the finite difference approach, a procedure for simulating the non-linear bending response of thin slabs with axisymmetric boundary conditions is developed. The results show good agreement with the experimental results obtained for thin UHPFRC slabs. It must be noted however that, because of the hypothesis applied, this procedure does not allow failure modes other than bending to be identified.

The following conclusions concerning the behaviour of thin UHPFRC slabs can be drawn based on the obtained theoretical and experimental results:

- the pre-peak behaviour of UHPFRC slabs is well simulated by representing multi-microcracking as a homogeneous material behaviour, using the elastic-pseudo-plastic material law in tension;
- a major part of the load-bearing capacity of the slab is achieved with multi-microcracking behaviour; this is confirmed by the experiment, where cracks become visible for a force level close to maximal force;
- due to the system redundancy, the contribution of the tensile ductility of the material to the load-bearing capacity of slabs is much more significant than in statically determinate beams;
- when the capacity to develop microcracking is exhausted, deformations start to localise i.e. discrete macrocracks form. For the given boundary conditions, the dominant tangential deformations obtained by non-linear simulation are in agreement with experimentally observed macrocracks opening along the radius. Once macrocracks open, deformations of the rest of the element become negligible, and a rigid block mechanism starts to develop;
- finally, the ultimate load-bearing capacity of thin UHPFRC slabs without ordinary reinforcement can be well assessed based on the theory of plasticity, by applying the yield line method;
- comparison with test results shows that the proposal of choosing the bending moment at the beginning of macrocrack propagation as resistant plastic moment can be used to predict the slab's ultimate failure load;
- the applicability of the theory of plasticity is experimentally validated for thin elements, with dimensions of interest for the proposed structural concept. Due to the difference between a perfectly plastic hinge and the actual hinge in a UHPFRC element, characterised by a limited rotational capacity for the resistant moment level, the applicability of the theory of plasticity must be limited, as a function of element thickness and geometry. To that end, more thorough analytical and experimental verifications are required.

6.3 Punching shear strength of UHPFRC slabs

For the structural application of UHPFRC in road bridges, investigated in this study, the resistance to punching shear failure of thin slabs between the stiffening ribs (Figure 6.2) subjected to wheel load must be assured. Punching shear is a non-ductile failure mode, and has been studied in RC structures since the beginning of the 20th century as a problem initiated by the development of slabs on columns, dating back to 1906 in the USA (Turner, [Gasparini 2002]), and 1908 in Europe (Maillart, [Bill 1947], [Fürst, Marti 1997]). Greater efforts in both experimental and theoretical research in this field were made in the second half of the 20th century [Kinnunen, Nylander 1960]. Some physical relationships were observed, and more sound theories describing the punching phenomenon in RC slabs were further developed [Muttoni, Fernández Ruiz 2008], and also applied to punching shear as a failure mode of RC bridge decks subjected to the action of wheel load [Vaz Rodrigues 2007].

As to UHPFRC elements, resistance to a concentrated load action on slabs has not been extensively investigated. An experimental program was conducted at the Virginia Polytechnic Institute (VPI) on slabs made of Ductal UHPFRC [Harris 2004], and the results of punching shear tests on slabs made of both Ductal and BSI have recently been published in [Toutlemonde et al. 2007]. An attempt to cause punching shear failure in 30 mm thick UHPFRC slabs is reported in [Bunje, Fehling 2004], but all of the specimens failed in bending.

The experimental results of UHPFRC slabs tested at the EPFL, presented in Section 6.2, showed significant resistance to a locally introduced load without exhibiting punching failure. To assess punching resistance, a series of tests was performed on thin slabs with clamped edges (Figure 6.19). The specimen size, smaller than the size of slabs presented in [Harris 2004] and [Toutlemonde et al. 2007], led to smaller rotations attained at the peak force. This enabled the influence of structural properties (slab geometry and boundary conditions) on punching shear resistance to be identified.

6.3.1 Resistance models

Resistance to punching is related to shear resistance, which, in the case of UHPFRC, is influenced by the presence of fibres across the shear crack. Due to the lack of experimental and theoretical work on the punching shear failure of UHPFRC slabs without ordinary reinforcement, reflections on the physical background of the phenomenon will be based on knowledge acquired on the punching behaviour of RC structures and the shear behaviour of SFRC beams without stirrup reinforcement. The research in SFRC has shown that both fibres and structural parameters can influence shear resistance [Lim et al. 1987], [Narayanan, Darwish 1987], [Gustafsson, Noghabai 1999] etc.

Contribution of fibres to shear capacity

Casanova and Rossi ([Casanova 1996], [Casanova, Rossi 1997]) proposed an approach for taking the contribution of steel fibres to shear capacity into account. The model assumes the formation of a block mechanism in a beam of rectangular cross section with bending reinforcement (Figure 6.17). The contribution of fibres to shear resistance, V_f , is added to the concrete contribution, V_{Rd} , as a force transferred between crack faces for a certain crack mouth opening, w_m ,

$$V_f = \int_0^{0.9d\sqrt{2}} b \cdot \sigma\left(\frac{w_m}{0.9d\sqrt{2}}s\right) \cdot ds \frac{\sqrt{2}}{2} \quad (6.50)$$

resulting in

$$V_f = S \cdot \frac{1}{w_m} \cdot \int_0^{w_m} \sigma(w) \cdot dw, \quad (6.51)$$

where $\sigma(w)$ is the material stress-crack opening relationship, $S=0.9bd$ in the case of a beam of width b and d being the distance between the extreme compression fibre and the tensile reinforcement (Figure 6.17). To define the ultimate shear resistance, the maximal crack opening must be defined. Casanova proposes directly relating the crack opening to the longitudinal deformation of the reinforcement bar, ε_s , as $w_m = 0.9d\varepsilon_s$, and considering two cases: the elastic limit of the steel reinforcement and the limiting yielding deformation value of 1%.

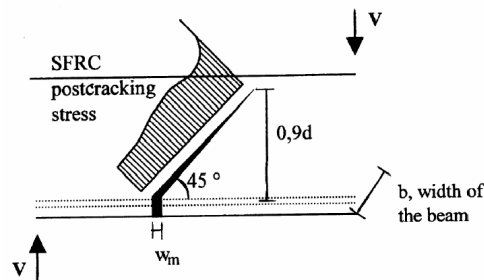


Figure 6.17: Shear crack in a rectangular SFRC beam [Casanova, Rossi 1997]

The fact that the limiting parameter for fibre contribution to shear strength is related to reinforcement properties means that this approach cannot be directly applied to UHPFRC without ordinary reinforcement bars. In addition, since crack propagation is influenced by structural properties, the limiting parameter w_m in the case of UHPFRC should be a function of element size and geometry. French recommendations for UHPFRC [SETRA, AFGC 2002] actually adopt this approach, by imposing a limit for w_m as a function of element thickness only.

To assess the punching shear resistances of UHPFRC elements, models that take into account both material and structural properties are thus required.

Critical shear crack

The critical shear crack model is a mechanical model describing the punching shear phenomenon in RC structures, presented in [Muttoni, Fernández Ruiz 2008]. The model relates punching shear strength to the opening of a critical shear crack, leading to the final formulation of a failure criterion based on slab rotation. In [Muttoni, Schwartz 19911] the width of the critical crack is assumed to be proportional to ψd (rotation multiplied by the beam’s static depth, Figure 6.18). The influence of aggregates on shear force bearing capacity is also taken into account, and the final formulation of the failure criterion is

$$\frac{V_R}{b_0 \cdot d \cdot \sqrt{f_c}} = \frac{3/4}{1 + 15 \frac{\psi \cdot d}{d_{g0} + d_g}}, \tag{6.52}$$

with V_R being the resistant punching shear force in [N], f_c compressive strength in [MPa], and d_g and d_{g0} the maximal and reference aggregate sizes in [mm], respectively, where $d_{g0}=16\text{ mm}$. The model predicts well the experimentally observed fact that the punching shear strength in RC structures decreases with increasing slab rotation, explained by the presence of the critical shear crack whose opening reduces the strength of the concrete compression strut.

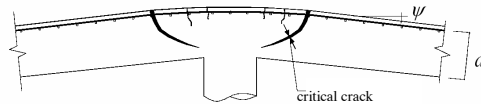


Figure 6.18: Critical shear crack in flat slab, adapted from [Guandalini 2005].

The same phenomenon may be assumed for FRCs, in addition to fibre action along the crack, providing a beneficial effect on shear resistance. The force transferred by the fibres decreases with the increase in crack opening, and the relationship between a critical crack opening and the element’s capacity to sustain punching shear also seems physically justifiable in the case of FRCs. The question arises as to what extent the theory is applicable in the prediction of shear resistance in UHPFRC elements without ordinary reinforcement. The discussion will be based on existing experimental data, briefly reviewed in the following section.

6.3.2 Punching shear resistance of thin slabs: experimental results

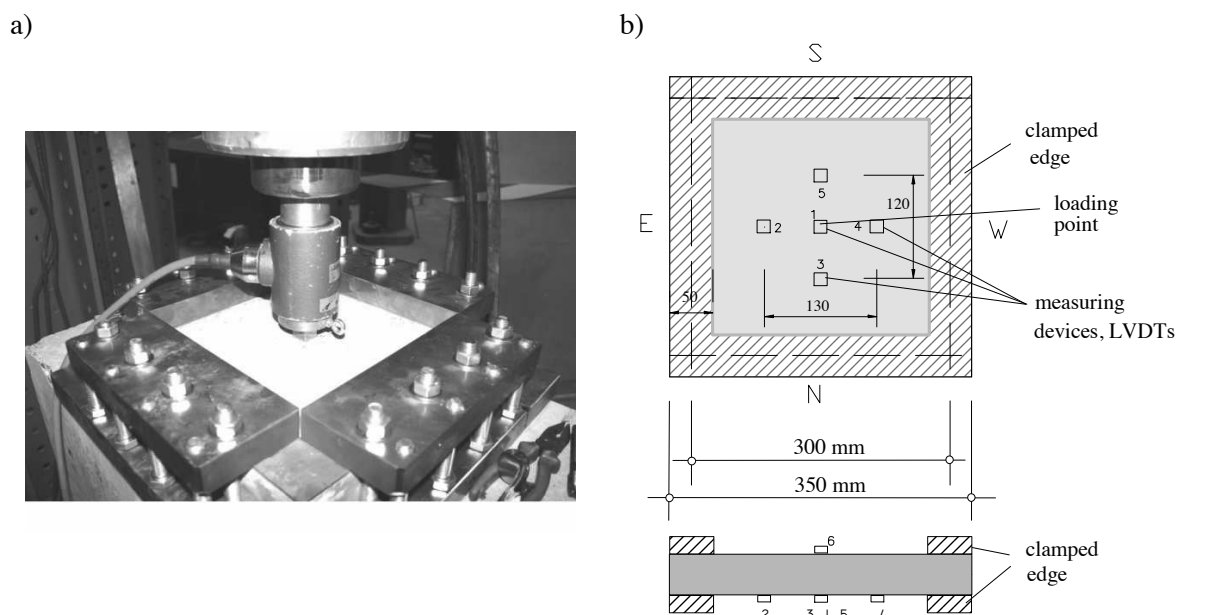


Figure 6.19: Punching shear test: a) test set-up; b) specimen geometry and position of measuring devices

Five UHPFRC slabs of thicknesses varying from 30 to 60 mm were tested at the EPFL Structural Laboratory. The slabs were of constant square shape, 350 mm side length, with restrained rotations along all four edges (Figure 6.19 a)) and the loading surface was 20 x 20 mm. The displacements were measured in the central and four symmetric points, as shown in Figure 6.19 b).

The force-central point deflection relationships are shown in Figure 6.20 and the related values are given in Table 6.2. Four of the five tested slabs failed in punching shear, whereas one slab, designated PP 50b, reached the maximal force in bending, and attained the punching shear failure for slightly increased deformation, in the post-peak phase. After the test, specimens were cut along two axes of symmetry in order to observe the shape of the punching surface: all the punching cones developed in a symmetrical way (Figure 6.20 c)). This could not have been concluded based on the crack pattern on the tensile side of the slab (Figure 6.20 b)), which could be associated to an asymmetric failure. Only one specimen (a 30 mm thick slab) is shown in Figure 6.20 b) and c), while the other specimens are documented in Appendix T1.

Resistance to punching shear is typically expressed by the average shear stress, v ,

$$v = V / (b_0 d), \quad (6.53)$$

V being the maximal load, d the distance between the extreme compression fibre and the tensile reinforcement and b_0 being the perimeter of the critical section. The perimeter of the critical section can be assumed to be based on the idealised punching surface. The majority of design codes ([SIA 2003b], [ACI 2005]) suggest that the crack should be assumed to form a 45-degree angle with respect to the slab surface, leading to the relationship $b_0 = 4 b_c + \pi d$ for a square surface of punching load introduction, with b_c being the side length.

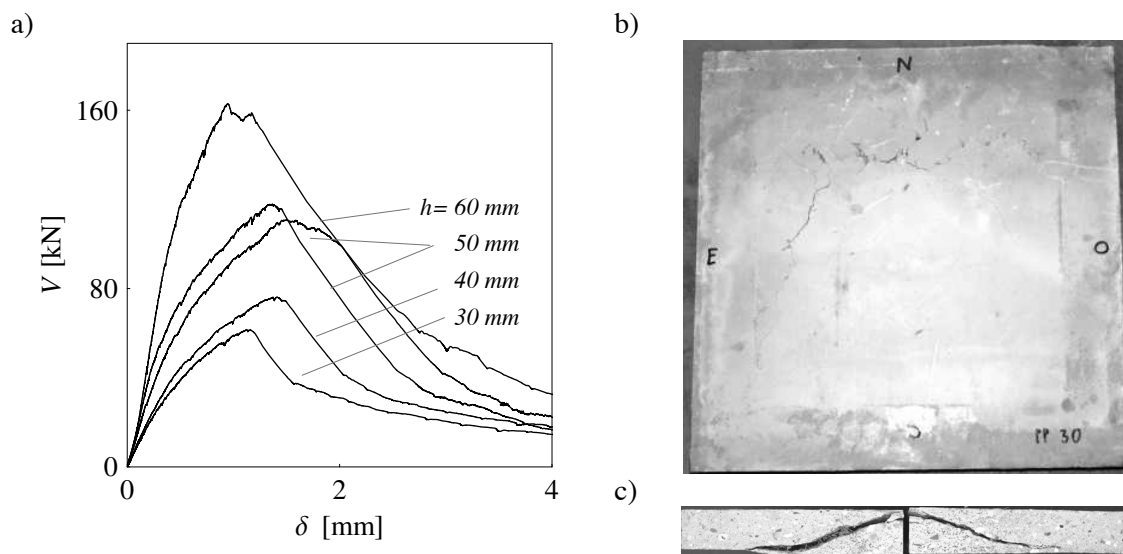


Figure 6.20: Results of punching shear tests of slabs made of BSI: a) force-mid-point displacement relationships; b) tensile face of a specimen; c) section through punching cone

Using Equation 6.53, the results of the test are plotted as a function of elements thickness in Figure 6.21. In the same figure, results from other authors are also shown:

- slabs made of Ductal [Harris 2004], tested at the VPI; the slabs were of square shape, with a side length 900 mm and clamped edges along all sides; thickness varied between 50 and 70 mm, and the punching shear surface also varied, between 25 and 50 mm (Table 6.3);

- slabs made of BSI and Ductal [Toutlemonde et al. 2007], tested at the LCPC; the slabs were part of a prototype ribbed deck slab, restrained by the ribs at a distance of 600 mm; the applied load simulated wheel load, using a reduced introduction surface, 190x260 mm with corners cut at 40 mm (Table 6.4). The ribbed slab was prestressed, with two T15S strands per rib in one direction and external cables in the perpendicular direction providing a compressive stress of 4 MPa.

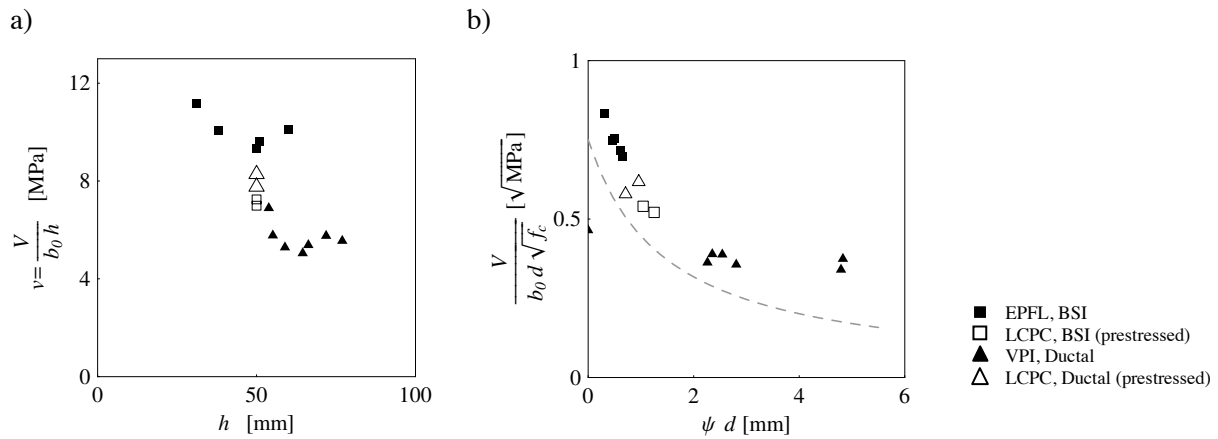


Figure 6.21: Punching shear resistance of UHPFRC slabs: a) average shear strength against element thickness; b) nominal strength against rotations times element depth, and failure criterion according to critical shear crack model for ordinary concrete structures

A certain dispersion of the achieved shear resistances can be noted based on the results of the above-mentioned tests (Figure 6.21 a)). Regarding only the resistances of the BSI slabs (filled squares), average shear strains vary only slightly, with a mean v value of 10 MPa. The highest resistance is attained in the thinnest specimen (11.1 MPa). However, the variation in element thicknesses is insufficient to clearly demonstrate its influence on shear strength. It is also interesting to note that a significant dispersion in shear strength exists between elements of the same thickness (e.g. $h=50\text{ mm}$) and made of similar materials, but with different geometries.

Tests at the VPI (filled triangles) were performed using a material with properties similar to those of BSI, as already mentioned in Section 6.2.5.2; however, significantly lower average shear strengths are attained. The resulting mean v value is 5.7 MPa.

The results for BSI slabs tested at the LCPC (voided squares in Figure 6.21 a)), show lower average shear strength than the specimens tested at the EPFL, whereas Ductal slabs tested at the LCPC (voided triangles) show higher resistance than slabs tested at the VPI. The difference between the shear strength of the BSI and that of the Ductal slabs tested at the LCPC is small (7.1 against 8 MPa mean v value). This suggests that the significant difference between the resistances of the BSI slabs tested at the EPFL and the Ductal slabs tested at the VPI is probably not due to a difference in material strengths.

Table 6.2: Results of punching shear tests on slabs made of BSI, performed at the EPFL

Specimen 350 x 350 x h	nominal h [mm]	actual h [mm]	b_c [mm]	actual P_{max} [kN]	$\delta_{P_{max}}$ [mm]
PP 30	30	31	20	61.51	1.13
PP 40a	40	38	20	76.167	1.37
PP 50a	50	51	20	117.74	1.37
PP 50b*	50	50	20	110.735	1.51
PP 60	60	60	20	162.842	0.95

* punching failure occurred after bending failure, at approx. $V=102\text{ kN}$ and $\delta=1.9\text{ mm}$; for a circular yield line pattern for a restrained slab [Johansen 1972] $V_{pl} = 4\pi m_R = 113\text{ kN}$ in the case of 50 mm thick slab;

Table 6.3: Results of punching shear tests on slabs made of Ductal, performed at the VPI

specimen	nominal h	actual h	b_c	actual P_{max}	$\delta_{P_{max}}$
Serie/test	[mm]	[mm]	[mm]	[kN]	[mm]
1/1	50.8 (2 in.)	55.12	38.1	103.64	18.39
1/2	50.8	58.93	50.8	120.99	20.22
1/3	50.8	53.85	25.4	100.52	No data
2/1	63.5 (2.5 in.)	66.29	50.8	146.78	14.48
2/3*	63.5	64.52	38.1	135.66	32.00
3/2	76.2 (3 in.)	71.88	38.1	156.57	15.24
3/3*	76.2	71.88	25.4	178.36	27.43

* punching failure occurred after bending failure: for specimen 2/3 punching failure occurred at approx. $V=115.648$ and $\delta=32$ mm; for the specimen 3/3 it occurred at approx. $V=146.78$ and $\delta=27.432$.

Table 6.4: Results of punching shear tests on slabs, performed at the LCPC

specimen	nominal h	b_c	actual P_{max}	$\delta_{P_{max}}$
	[mm]	[mm]	[kN]	[mm]
BSI	50	190, 260*	365	3
BSI	50	- / -	352	2.5
Ductal	50	- / -	417	2.4
Ductal	50	- / -	391	1.6

* the side dimensions of the steel plate for load introduction are 0.19 and 0.26 m with corners cut at 0.04m, giving a load-introduction surface perimeter of 0.85 m. With $h=d$, the accepted critical perimeter concept gives $b_0=1m$.

6.3.3 Relationship between slab rotation and punching shear strength

Based on the test results shown in Figure 6.21 a), it can be noted that specimens tested with the same boundary conditions and spans, with a slight variation in thicknesses, show a low dispersion in achieved resistances, whereas strengths change significantly with slab spans. This suggests that the parameters influencing shear strength are principally structural. For this reason, resistances are plotted in Figure 6.21 b) as a function of rotations, ψ , multiplied by element depth, d , and punching shear force is expressed as a nominal force $V/(b_0 d \sqrt{f_c})$. The results in Figure 6.21 b) are plotted with the rotation ψ outside the critical crack obtained based on the assumption of conical deformation of the slab outside the force introduction region [Muttoni, Fernández Ruiz 2008],

$$\psi = \delta_{P_{max}} / (r_b - b_c / 2), \quad (6.54)$$

where r_b is the radius of the slab. Compressive strengths of $f_c=180$ MPa and 220 MPa are used for BSI and Ductal respectively. For the slabs tested at the EPFL, $r_b=(0.3-0.05)/2$ m (Figure 6.19 b)), for those tested at the VPI $r_b=0.45$ m and for those tested at the LCPS $r_b=0.3$ m. The other values for the considered slabs are provided in Tables 6.2 to 6.4.

A correlation between nominal force and rotation similar to that observed for ordinary RC can be noted in Figure 6.21 b): the slabs tested at the VPI exhibited much higher deformations at failure, which may explain the reduced strength. (The specimens on the most right in Figure 6.21 b) are the specimens that actually failed in bending.)

Consequently, the critical shear crack theory as defined for RC is tested for applicability to UHPFRC without ordinary reinforcement: crack width remains proportional to ψd , aggregates are assumed to influence resistance as in an ordinary concrete, and thus $d_g=6$ mm and $d_{g0}=16$ mm are the values incorporated in Equation 6.52, and fibre action is disregarded. The criterion is plotted in Figure 6.21 b) against measured data, and the concordance of the results can be concluded. The criterion is also plotted in Figure 6.22 a) against the force- ψd relationship for slabs failing in punching (black lines) and bending (grey lines).

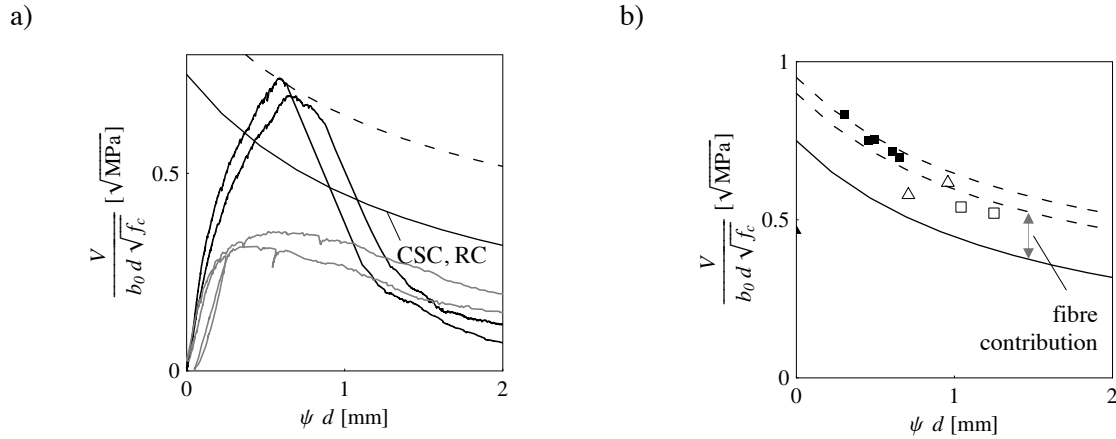


Figure 6.22: Critical shear crack criterion (CSC) as defined for RC, and possible adaptation for UHPFRC (dashed lines): a) in comparison to response of specimens that failed in punching (black lines) and bending (grey lines); b) in comparison to nominal resistance of specimens with low rotation

It must be emphasized that the critical shear crack theory has been validated for ordinary concretes, and the question arises as to whether the contribution of UHPC to shear strength is characterised by the same relationships. However, assuming its general validity, the difference between the prediction according to the critical shear crack theory and the actual V in UHPFRC elements can be associated to fibre action, V_f (Figure 6.22). Moreover, this contribution progressively decreases for increasing values of d , indicating that fibre contribution is influenced by structural parameters, i.e. depends on crack opening. In the following sections, the punching shear design method proposed in existing UHPFRC recommendations will be described (§ 6.3.4) and the dependency of fibre contribution on element size will be modelled by adapting the approach proposed by Casanova (§ 6.3.5).

6.3.4 Punching shear in UHPFRC design recommendations

In current recommendations for UHPFRC [SETRA, AFGC 2002], Article 2.3, ultimate shear strength V_u is given as the sum of concrete, V_{Rb} , reinforcement, V_a , and fibre contribution, V_f :

$$V_u = V_{Rb} + V_a + V_f, \quad (6.55)$$

with

$$V_f = \frac{S \cdot \sigma_p}{\gamma_{bf} \cdot \tan \beta_u}, \quad (6.56)$$

and σ_p being average residual tensile stress transferred by the crack, defined as

$$\sigma_p = \frac{1}{K} \cdot \frac{1}{w_{lim}} \cdot \int_0^{w_{lim}} \sigma(w) dw, \quad (6.57)$$

S being the area of fibre effect $S = 0.9 b_0 d = b_0 z$, β_u the angle of compression strut, assumed as $\pi/4$, K the fibre orientation coefficient for general effects and $\gamma_{bf}=1$ the partial safety factor for UHPFRC for ULS verifications. The crack opening is limited as $w_{lim} = \max(w_u, 0.3 \text{ mm})$, with $w_u = l_c \varepsilon_u$, and ε_u limited to 3 ‰ according to Article 6.3.313 of the recommendations. The characteristic length, l_c , is defined as $l_c = 2/3 h$ (§ 3.3.2.7). The latter limitation actually gives a constant value $w_{lim} = 0.3 \text{ mm}$ for all $h < 150 \text{ mm}$, signifying that size effect is not taken into account for this range of element thicknesses.

According to the French recommendations, the tensile hardening phase characterised by microcracking is represented by the stress-crack opening relationship. In the concept of the present thesis, only the tensile softening relationship is defined using stress-crack law. However, to apply the

French approach, it is sufficient to associate a crack opening to the ultimate strain, ε_u , characterising the material prior to the softening part: according to Relationship 3.27,

$$\varepsilon_u = \frac{w_i}{l_c} + \frac{f_{ct}}{E_c}$$

for a 50 mm thick section and $\varepsilon_u = 2.5 \text{‰}$, $w = 0.078 \text{ mm}$. According to [Jungwirth 2006], based on the microcrack spacing estimated as $\sqrt[3]{4} l_f$, crack opening at 2.5 ‰ is approx. 0.04 mm. Thus, the crack opening of 0.3 mm according to [SETRA, AFGC 2002] would correspond to the crack opening of 0.22 or 0.26 mm of crack in the softening branch defined for the UHPFRC used in the present study. On this basis, fibre contribution (Equation 6.57) is calculated as constant for all elements of heights smaller than 150 mm:

$$\sigma_p = \frac{1}{K} \cdot 8.44 \text{ MPa}$$

The integral of stress-crack opening law proposed in §3.3.2.8 is defined by Equation 3.39. According to Article 2.1 [SETRA, AFGC 2002] for local effects the orientation coefficient $K=1.75$ (for other than local effects $K=1.25$), but for thin plates, characterisation tests show that $K=1$. Both cases will be considered, leading to following nominal fibre contribution:

- for $K=1$, $V_f/(b_0 d \sqrt{f_c}) = 1/K \cdot 1/\gamma_{bf} \cdot 8.44/\sqrt{f_c} = 0.629/\gamma_{bf}$
- for $K=1.75$, $V_f/(b_0 d \sqrt{f_c}) = 0.35/\gamma_{bf}$

The contribution of concrete to shear resistance is defined as

$$V_{Rb} = \frac{1}{\gamma_E} \cdot \frac{0.21}{\gamma_b} k \sqrt{f_c} b_0 d \quad (6.58)$$

where the term γ_E is a safety coefficient such that $\gamma_E \gamma_b = 1.5$. For $f_c = 180 \text{ MPa}$, the concrete contribution is $V_{Rb} = 2.8 b_0 d / (\gamma_E \gamma_b)$. Without safety factors, $V_{Rb}/(b_0 d \sqrt{f_c}) = 0.21$. It should be noted that structural parameters are not taken into account in this part either.

The values of V_{Rb} and $V_u = V_{Rb} + V_f$ are plotted in Figure 6.23 a), without safety coefficients, and in b) with safety coefficients. It can be seen that fibre contribution with maximal crack opening 0.3 mm overestimates ultimate strengths for $K=1$, whereas for $K=1.75$ the ultimate strength for elements with small ψd is well predicted, although for higher ψd strength is still overestimated. It is clear however that the constant shear strength approach cannot satisfactorily reproduce the decreasing tendency of experimental data.

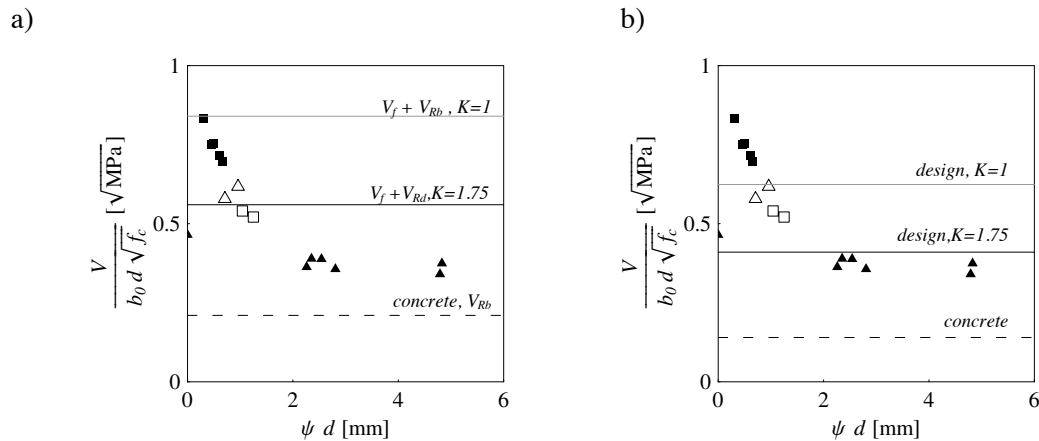


Figure 6.23: Shear strength according to [SETRA, AFGC 2002]: a) values without safety factors, for $K=1$ and $K=1.75$; b) values with safety factors, for $K=1$ and $K=1.75$

Based on the results presented in Figure 6.23, it can be concluded that a more accurate approach for predicting shear resistance is required, especially enabling size effect to be taken into account.

6.3.5 Fibre contribution to shear strength: a proposal

Fibre contribution to shear strength is related to maximal crack opening, as in the model proposed by Casanova (Equation 6.51). Maximal crack opening is, on the other hand, assumed as being a structure-related parameter, as proposed for ordinary concrete [Muttoni, Schwartz 1991]: assuming a constant rotation of the slab outside the critical shear crack (Figure 6.18), crack opening can be obtained from the kinematics of the rigid block mechanism. The critical crack opening is then directly related to rotation, as $w_{lim} \propto \psi d$. Assuming that the critical crack propagates up to $0.9 d$, $w_{lim} = \psi \cdot 0.9 d$ and fibre contribution (Equation 6.57) can be expressed as a function of structural parameters:

$$\frac{V_f}{b_0 \cdot d \cdot \sqrt{f_c}} = \frac{1}{K} \cdot \frac{1}{\psi \cdot d} \cdot \int_0^{\psi \cdot 0.9d} \sigma(w) dw \cdot \frac{1}{\sqrt{f_c}} \quad (6.59)$$

Figure 6.24 shows a comparison between fibre contribution to shear strength based on Equation 6.59 and test data for $K=1$ (solid lines) and $K=1.75$ (dashed lines). The curves are normalised with different compressive strength values: $f_c=180$ for BSI (black lines) and 220 MPa for Ductal (grey lines). The relationship shows the same tendency as the experimental data: fibre contribution to shear strength decreases for thicker elements or elements that attain higher rotations.

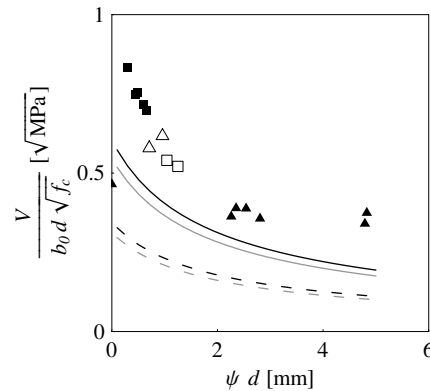


Figure 6.24: Fibre contribution to shear strength based on the proposed model; solid lines are plotted with $K=1$, dashed lines $K=1.75$; black lines $f_c=180$ (BSI), grey lines $f_c=220$ (Ductal)

Finally, the concrete contribution is added as a constant value, according to the French recommendations (Equation 6.58) and the resulting curves are plotted for $K=1$ in Figure 6.25 a), showing a remarkable improvement in prediction accuracy in comparison to that obtained for constant fibre contribution (Figure 6.23).

The nominal concrete contribution can also be assumed as being a size-dependent function, $v_{Rb} \left(\frac{1}{\psi \cdot d} \right)$, leading to a general expression for punching shear resistance

$$\frac{V}{b_0 \cdot d \cdot \sqrt{f_c}} = v_{Rb} \left(\frac{1}{\psi \cdot d} \right) + \frac{1}{K} \cdot \frac{1}{\psi \cdot d} \cdot \int_0^{\psi \cdot 0.9d} \sigma(w) dw \cdot \frac{1}{\sqrt{f_c}} \quad (6.60)$$

The curves obtained on the basis of Relationship 6.60 are plotted as solid lines in Figure 6.25 b), normalised for $f_c=180$ and 220 MPa , while the part corresponding to concrete contribution is plotted

as a dashed line. However, due to the lack of information on the behaviour of fibre-free UHPC as a function of ψ and d , the concrete contribution cannot be quantified on a rational basis.

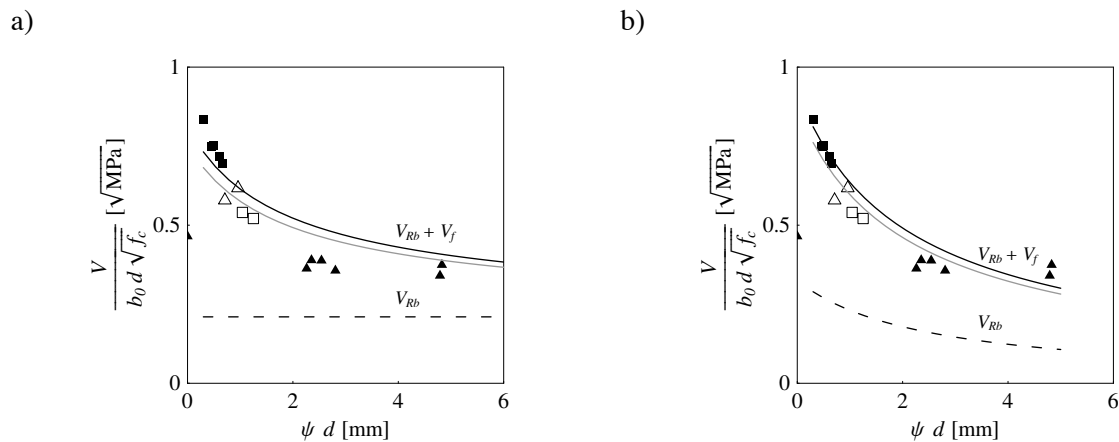


Figure 6.25: Punching shear strength of UHPFRC elements with fibre contribution related to element rotation and thickness: a) assuming constant concrete contribution (grey lines are normalised for 220MPa); b) assuming concrete contribution as a function of rotation and thickness

6.3.6 Practical aspects of size effect on punching shear strength

Although the actual participation of fibres and concrete in shear resistance still has to be more precisely quantified, the influence of structural parameters on shear strength is clearly shown in the proposed approach. Omitting size effect may lead to inaccurate estimations of shear resistance: for members thinner than 150 mm, the constant shear strength estimated according to the French recommendations may correctly predict the punching strength of one element (e.g. element *c* in Figure 6.26), whereas another may sustain higher shear strengths and fail in bending (element *b*), fail in punching shear for a higher level of shear strength (element *a*) or fail in punching before the predicted bending strength is attained (element *d*).

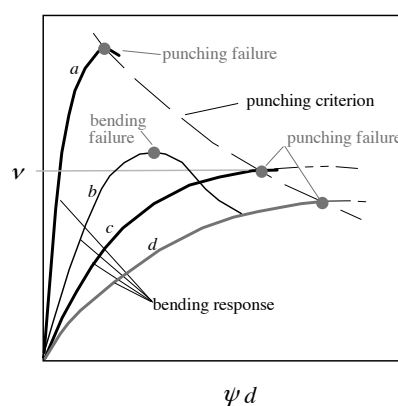


Figure 6.26: Size-dependent shear criterion (dashed line) and element response under concentrated load with indicated failures

Rotation ψ is related to slab stiffness, i.e. slabs with shorter spans or stiffer boundary conditions will generally develop smaller rotations than long-span slabs with less constrained boundary conditions. In the case of thin slabs (small d) with a stiff behaviour (small ψ), the constant shear strength approach (Equations 6.57 and 6.58) provides a conservative estimation of punching shear strength.

For more deformable and/or thicker elements, but still below 150 mm -thickness, however, constant shear strength approach overestimates the effective contribution of fibres to shear strength, leading to unsafe predictions. This is probably because in these cases the opening of the critical shear crack is higher than the limiting value of 0.3 mm proposed by the French recommendation for thicknesses smaller than 150 mm , and consequently the average stress borne by the fibres (Equation 6.57) decreases.

In the case of ordinary reinforced concrete, simple expressions exist to relate slab rotation to the applied load, enabling punching strength to be predicted as intersection point between the force-rotation curve and critical shear criterion. To obtain a general load-rotation relationship of an UHPFRC slab a non-linear analysis, such as the one developed in §6.2, must be used. However, the range of available test data, and in particular that obtained at the LCPC, well represents the geometry and boundary conditions of interest for the case of a ribbed slab, considered in this study, and the ultimate strength can be based on the experimental data. In tests carried out at the LCPC, the failure load applied on a surface of $0.26 \times 0.19\text{ m}$ was already 2-3 times the nominal wheel load prescribed by current codes of practice [Toutlemonde et al. 2007].

6.3.7 Conclusions

An analytical criterion for assessing the punching shear strength of UHPFRC members is proposed. It takes fibre contribution to shear strength and its dependency on element size and stiffness into account. Although current theoretical and experimental knowledge is still insufficient for a general model to be established, the predictions of the proposed approach are in good agreement with experimental results obtained in the framework of this research and by other authors.

On the basis of theoretical and experimental evidence the following conclusions may be drawn:

- fibre contribution to punching shear strength is a function of the opening w of the critical shear crack, which is a function of slab thickness and slab rotation outside the punching region ψ ;
- punching shear strength decreases for increasing slab thickness values;
- punching shear strength decreases for slabs that develop higher rotations ψ , i.e. long-span slabs or slabs with free boundary conditions;
- the influence of slab thickness, span and boundary condition should be taken into account to correctly evaluate punching shear strength;
- current design recommendations poorly estimate punching shear strength for element thicknesses lower than 150 mm , and may lead to unsafe predictions in the presence of significant critical crack openings;

With a view to the application of thin UHPFRC slabs in ribbed decks for road bridges:

- it is experimentally and theoretically demonstrated that significant shear stresses can be sustained by UHPFRC elements;
- analysed test results cover a range of sizes that is representative of possible structural applications in ribbed deck systems.

7. Structural application of UHPFRC

The structural application of UHPFRC to date is not very widespread, despite its obvious material advantages (Chapter 3) and its mechanical load-bearing potential in structural elements, as demonstrated by theoretical and experimental analysis (Chapters 4 and 5).

In this chapter the main advantages and drawbacks of UHPFRC for structural application and the domains in which its properties can be best exploited are briefly summarised. A state-of-the-art review of the structural applications of UHPFRC is presented with a particular focus on current structural concepts of UHPFRC in bridge design.

The case of a ribbed slab made of prestressed UHPFRC, identified as one of the most promising applications of UHPFRC in bridge design, is then considered in more detail. The slab design is based on the models developed in Chapters 4 to 6 and existing design recommendations. Finally, a discussion on optimal structural geometry is presented.

7.1 Advantages and limitations of UHPFRC for structural application

The most important advantages of UHPFRC for structural applications can be summarised as follows:

- mechanical strengths are greatly improved in relation to those of ordinary concrete;
- the use of ordinary reinforcement can be reduced and, in some cases, completely avoided due to the strength and ductility of UHPFRC in tension;
- hardened UHPFRC is a very dense material, resistant to chemical and physical aggression and consequently far more durable and stable in time than ordinary reinforced concrete;
- UHPFRC is generally self-placing and self-compacting.

Thanks to mechanical strengths, reduction of ordinary reinforcement, and matrix density, very thin and light members can be made of UHPFRC, with advantages from both a structural point of view (e.g. reduction of dead load) and an architectural point of view, since thin members can be freely shaped and sized to meet a wide range of functional and aesthetic requirements. The second point means that working time for shaping and placing ordinary reinforcement is greatly reduced and production speed increased, with valuable effects especially in the precast industry. Light precast members can be easily stored, moved and placed, resulting in faster construction phases and a reduction in construction site size [Graybeal, Hartmann 2005], [Resplendino, Bouteille 2006]. The dense matrix, resistant to environmental aggression, allows maintenance costs to be decreased [Denarié et al. 2005]. To summarise all the above advantages, the integral quantity of material, labour and invested time are reduced, also resulting in significantly decreased environmental impact when constructing with UHPFRC.

At the moment, however, certain technical aspects partly explain the limited use of UHPFRC in structures:

- the high price of the material, mainly due to the high portion of costly constituents (fibres, cement, admixtures) and the small-scale production;
- the sensitivity of the material to mixing procedure and mix proportions;
- the variability of mechanical properties as a function of casting conditions (formwork shape, paste flow).

It is interesting to note however that a study on cost effectiveness [Racky 2004], based on energy and raw material consumption and sustainability, shows the advantage of using UHPFRC rather than ordinary and high-strength concretes. The advantage is particularly significant when life cycle costs are considered.

The fact that, despite its outstanding properties, only a limited number of structures have been built using UHPFRC may also be related to designers' needs and habits and current knowledge on the subject:

- UHPFRC has not existed long enough, from a civil engineering point of view, to overcome the strong influence of traditional design concepts characterising common engineering practice;
- there is insufficient feedback from existing structures;
- design rules are lacking and partial recommendations have been published only recently.

7.2 Domains of application for UHPFRC

The current initial price and the technology required for UHPFRC can only be justified if its mechanical or other material properties are well exploited. For this reason, UHPFRC should not be considered an all-field alternative to ordinary concrete: successful applications should be sought in domains where OC barely meets specific design requirements. In accordance with the discussion in the previous paragraph, UHPFRC can be successfully used when durable and strong but light members are required, or in cases where a considerable liberty with regard to form is desirable. From this point of view UHPFRC can be an interesting alternative to structural steel.

Until now, UHPFRC has been used structurally mainly for:

- roof elements
- foot bridges
- road bridges
- protective elements in hydraulic or aggressive environments.

The majority of applications benefit from the lightness and strength of the structural elements (1-3, plus for structural repair), while some exploit mainly the material durability and resistance to aggressive environments in order to protect new or existing structures. Several applications primarily based on material compressive strength for columns or highly stressed details, e.g. prestressing anchorages, exist. UHPFRC has also been found suitable for architectural applications.

The first structural application of UHPFRC (1997-1998), and a good example of the use of UHPFRC in an aggressive environment, was the replacement of beams for the cooling towers of the Cattenom and Civaux nuclear power plants in France (Figure 7.1 a)). The prestressed UHPFRC beams had the shape of conventional concrete beams (Figure 7.1 a)), but with significantly reduced elements size, providing the required lightness and durability, [Resplendino 2004], [Acker, Behloul 2004].

The present study will deal in more detail with the application of UHPFRC in bridge design, but some of the other applications will be mentioned first as examples of the exploitation of material advantages.

Roofs

The most significant examples of the application of UHPFRC for roof elements are shown in Figure 7.1 b) to d). Figure 7.1 b) shows a roofing panels, 7.2 m long and 2.4 m wide, with a 13 mm thick slab, used for a storage silo in Joppa (2001, Illinois USA). The elements are designed to act as ribbed plates, supporting a two-storey mechanical penthouse placed on the top of the roof [Nowodworski, Rosiak 2002]. The main advantages of this solution are durability and economy in construction time (11 days in comparison to 35 days for steel roofs). The roof of the Millau Viaduct tollgate (2004, France) is one of the best known and most architecturally interesting applications of BSI (Figure 7.1 c)): the roof is made of precast curved multicellular thin-walled segments, assembled by prestressing and relying on steel columns [Resplendino 2004]. The entire structure is 98 m long and 28 m with, with a thickness of 0.2-0.85 m. The roof of the Shawnessy station at Calgary (2005, Canada) was made of 20 mm thick shell elements, using Ductal UHPFRC with polymeric fibres [Vicenzino, Culham 2005]. The latter solution was found economically competitive in relation to a metallic solution and more durable and architecturally attractive, especially because of the possibility

of casting the elements with metallic shapes, due to the plasticity of UHPCFRC. The production of the precast shells requires significant conceptual work in order to make casting of the curved thin elements possible in the presence of the early age shrinkage of UHPFRC. However, these elements are of interest for structural application since, as redundant systems, they allow the advantages of material ductility to be exploited without additional ordinary reinforcement and result in very small sectional dimensions.

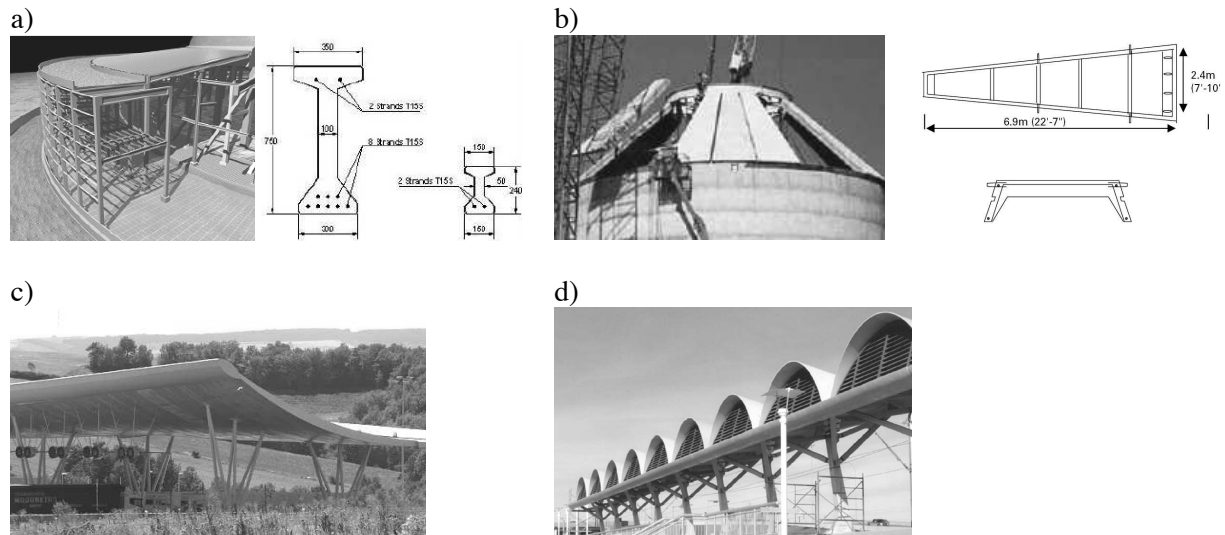


Figure 7.1: Application of UHPFRC: a) Cattenom nuclear power plant (1997-1998, France), with details of primary and secondary beam cross sections, [Acker, Behloul 2004]; b) roofing panels for silo (2001, Joppa, Illinois USA), with plan and cross section of element [Nowodworski, Rosiak 2002]; c) roof of Millau Viaduct tollgate (2004, France) [Dolo et al. 2005]; d) Shawnessy station (2005, Calgary, Canada), [Vicenzino, Culham 2005]

Footbridges

Footbridges certainly represent one of the most interesting applications for UHPFRC because of the importance of lightness and the architectural requirements usually involved in their conception. At present, UHPFRC beams of various cross section shapes and space truss footbridges have already been successfully realised (Figure 7.2).

The first UHPFRC footbridge was the Sherbrook footbridge (Figure 7.2 a)), constructed in 1997 in Canada. It is a 60 m long and 3.3 m wide longitudinally post-tensioned space truss bridge with no passive reinforcement, in which all structural elements of the superstructure (deck and truss members) are made of prestressed UHPFRC [Adeline, Cheyreyzy 1998], [Blais, Couture 1999]. This bridge represents an important example of attempting to exploit material compressive strength, also taking advantage of the increased strength of the concrete confined in the stainless steel tubes of strut members. The ties of the truss are prestressed. A deck slab only 30 mm thick resists local loads. Innovations in the detailing of precast members and anchorages [Ganz, Adeline 1997] also characterise this structure.

A space truss was also adopted for the more recent Gärtnerplatz footbridge in Kassel (2007, Germany) which has a total length of 133.2 m and a main span of 36 m (Figure 7.2 b)): the bridge deck and truss were constructed using a UHPFRC developed in Germany [Fehling et al. 2004]. The footbridge exhibits other interesting aspects, such as having glued connections between structural members.

Footbridges were also conceived in the form of prestressed simply supported beams, as in the case of the Sakata-Mirai footbridge (Figure 7.2 c)): conceptually simple, requiring a shorter construction

7. Structural application of UHPFRC

time than ordinary concrete or steel solutions, and much more durable, the Sakata-Mirai footbridge could be considered one of the most successful applications of UHPFRC in footbridge design. It is a box girder structure with hollow webs, 50 m span, 2.4 m deck width and variable height, made of Ductal UHPFRC. According to [Tanaka et al. 2002a], the structure's weight is approximately $\frac{1}{4}$ of the weight of an ordinary prestressed concrete girder (0.44 m^2 of concrete per meter of structure).

Another successful application of Ductal is found in the Seonyu footbridge in Seoul, known as Footbridge of Peace (Figure 7.2 d)), realized as a prestressed UHPFRC arch, 120 m span, consisting of one π -girder, 1.3 m high and 4.3 m wide [Behloul, Lee 2003]. The upper deck is 30 mm thick, transversally ribbed and prestressed. The structure is equipped with tuned mass dampers to avoid vibration problems.

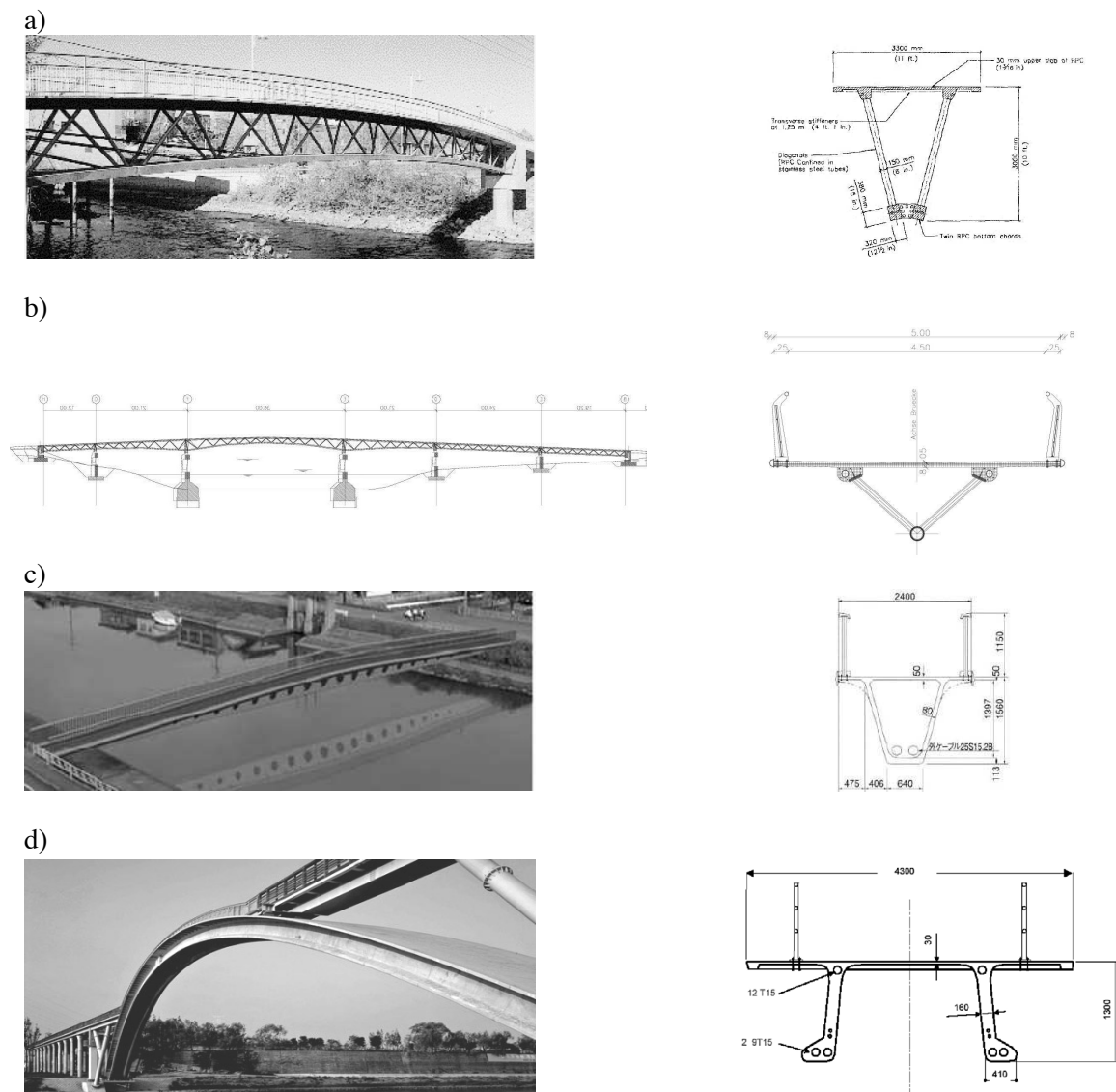


Figure 7.2: UHPFRC footbridges: a) Sherbrooke footbridge (1997, Canada); b) Gärtnerplatz footbridge (2007, Kassel, Germany); c) Sakata-Mirai footbridge (2002, Japan); d) Seonyu footbridge (2002, Seoul, Korea)

Columns in buildings

There are several significant advantages when UHPC is used for the construction of high-rise building columns [Cheyrezy et al. 1997], [Tue et al. 2004a], [Sugano et al. 2007], [Kimura et al. 2007] or in cases when thin columns are necessary to satisfy functional or architectural requirements. Compressive strength is not the only property of UHPC that offers advantages over other concretes: resistance to dynamic excitations [Kimura et al. 2007a], significantly decreased long-term deformations (§ 3.4.1), and fire resistance provided by the use of organic fibres (§ 3.4.4) are important properties required for column design.

A research project “UHPC hybrid structures”, conducted at Leipzig University [Tue et al. 2004] dealt with the development of hybrid compressive elements made with UHPC, providing high load-bearing capacity and adequate ductility owing to the use of steel tubes. This project also included comparative tests on HSC elements: the number of required sections of both concrete and steel can be reduced when UHPC is used, while ultimate loads and behaviour with respect to deformations remain the same as with HSC. UHPC columns are characterised by a high stiffness and only small plastic deformations observed during cyclic loading within the upper range of the service load.

It was shown [Foster 2001], [Foster, Attard 2001] that, by adding fibres, the cover spalling characterising high strength concrete in the presence of a high number of stirrups can be controlled. It was also experimentally shown that the addition of fibres can improve the strength and the stiffness of concrete-filled tubular columns [Campioni et al. 2002].

Reinforcement-free prestressing anchorage

The anchorage of prestressing tendons generates intense local compressive efforts as well as transversal tensile stresses in the concrete surrounding the anchorage detail. Usually, transversal reinforcement in the form of a steel spiral is provided in the anchorage zones to control transversal splitting cracks and confine the concrete, thus improving its strength and ductility. The placing of spirals limits the slenderness of the detail, constituting a disadvantage in light and slender UHPFRC structures. It was shown that UHPFRC and, to some extent, FRC can develop confining actions under localised compressive stress and that, thanks to its compressive strength and to the fibre confinement, the anchorage of prestressing cables can be realised without any transverse reinforcement. This technology was used in the Sherbrooke bridge [Ganz, Adeline 1997] where special micro-anchorage were developed, and later also in the Seonyu footbridge [Behloul, Lee 2003]. An experimental investigation of anchorage blocks made of UHPFRC, without any passive reinforcement is presented in [Toutlemonde et al. 2006].

7.2.1 Applications of UHPFRC in road bridges

Two different fields of application of UHPFRC in road bridges must be distinguished: the construction of new road bridges with the entire superstructure, or certain parts, made of UHPFRC, and the rehabilitation of existing road bridges by means of locally applied UHPFRC layers, or entire UHPFRC elements. This section mainly focuses on new structures and only some examples of UHPFRC use in bridge rehabilitation will be mentioned.

A fairly limited number of UHPFRC road bridges have been built up until now. Most of them are located in France, and significant research on the development of structural concepts for UHPFRC bridges is being carried out in the USA [Park et al. 2003], [Graybeal, Hartmann 2005], [Naaman, Chandrangsu 2004] and Canada [Braike et al. 2006]. Some applications also exist in Australia [Cavill, Chirgwin 2003] and Italy [Meda, Rosati 2003]. From a conceptual point of view, four solutions for UHPFRC structural elements have been proposed:

- π -shaped girders,
- I-shaped girders with ordinary concrete slab,
- box girders,
- composite bridges with steel beams as main girders and UHPFRC deck slab.

The most important properties of these UHPFRC bridges are summarised in Table 7.1. To compare the effectiveness of the applied structural concepts, the equivalent height h_{equiv} , which is the ratio of cross section area A_{uhpc} to deck width, is used. All the beams are precast and longitudinally prestressed. The box girder of the PS34 bridge over highway A51 in France is prestressed only externally.

Table 7.1: Main structural characteristics of UHPFRC road bridges

Structure	Bourg-lès-Valence, France	Road Bridge Virginia, USA	Shepherds Creek, Australia	Saint-Pierre-la-Cour France	PS34, bridge over A51, France	LCPC, Pilot project France
built in	2001	2004	2004	2005	2006	-
characteristic	5 π -shaped girders per span	2 π -shaped girders	16 I-shaped girders with RC slab	10 I-shaped girders with RC slab	mono-cellular box girder	ribbed deck slab on steel main girders
span, ℓ [m]	20.75, 22.75	21	15	19	47.4	90, 130
width [m]	12.2	4.8	20.8	12.6	4.4	12.2
ℓ/h	23, 25	25	25 (girder)	25 (girder)	30	17 ¹ 7.2 ²
h_{slab} [m]	0.15	0.076	-	-	0.12, 0.14 ³	0.05
web width [m]	0.11	0.064, 0.076	0.10	0.14	0.14	0.07-0.1 (ribs)
h_{equiv} [m]	0.25	0.17	0.08 (beams)	≈ 0.12 (beams)	0.28	0.14 (slab only)
material	BSI, 3% steel fibres	Ductal, 2% steel fibres	Ductal, 2% steel fibres	Ductal,	BCV, Vinci	BSI and Ductal

¹ slab's span-to-depth ratio between longitudinal beams

² span-to-depth ratio of slab's cantilever part

³ upper and lower slabs respectively

Road bridge at Bourg-lès-Valence, France: π -girder

This first road bridge made of UHPFRC was intended to serve as a reference and help establish design rules for further applications [Thibaux, Tanner 2002]. The bridge is composed of two statically determined spans of 22.75 and 20.75 m respectively (Figure 7.3 a)). The cross section consists of five precast π -shaped girders, 0.9 m high and 2.2 m wide, for a total deck width of 12.2 m. The bearing slab is made continuous in the longitudinal and transverse direction by cast-in-situ UHPFRC joints. Girders are prestressed with T15S prestressing strands (26 and 30 strands per girder of 20.75 and 22.75 m respectively). No transversal prestressing was applied in the deck and the bridge is completely free of passive reinforcement, except in the longitudinal and transversal joint areas.

a)



b)

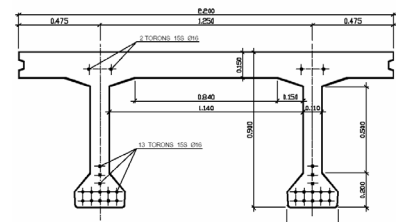


Figure 7.3: Bourg-lès-Valence road bridge: a) view on the two-span structure ; b) repetitive element of cross section (π -shaped prestressed beam [Thibaux, Tanner 2002])

The use of UHPFRC (BSI) resulted in 0.25 m equivalent height, which, according to the designers, reduced the dead weight of the structure by three times in comparison to optimised alternative solutions in OC ($h_{equiv} = 0.75$ m) or high-strength concrete ($h_{equiv} = 0.37$ m with $f_{ck} = 80$ MPa,

[Toutlemonde et al. 2002]). Upper deck and web thicknesses are 150 mm and 110 mm respectively. The contribution of the tensile strength of UHPFRC to resistant bending moment was not taken into account in the longitudinal direction but considered in the design of the unreinforced slab in the transversal direction [Thibaux, Tanner 2002].

Road bridge in Virginia, USA: π -girder

The first UHPFRC road bridge in the USA, built in 2004, was based on concept similar to that of the French bridge at Bourges-lès-Valence, but with far smaller dimensions (Table 7.1). The bridge is constructed in a single span of 21.3 m , consisting of two simply supported prestressed π -shaped girders, with a total deck width of 4.9 m . The material used is Ductal UHPFRC.

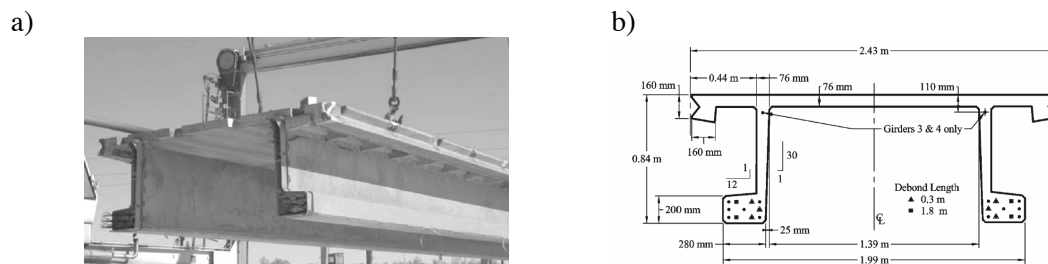


Figure 7.4: Road bridge in Virginia: a) placement of one of the two girders (π -shaped beam) b) details of main girder cross section [Graybeal, Hartmann 2005]

The girder geometry was the result of an in-depth study conducted at the Massachusetts Institute of Technology [Chuang, Ulm 2002], aimed at defining an optimal cross section shape that would withstand structural and environmental loads while at the same time reducing erection and overall construction time. The height of the girder is 0.84 m , with 76 mm of upper slab thickness and a 1.39 m distance between webs. The equivalent height of the girder is only 0.17 m . The optimised π -shaped girder was validated by laboratory testing at the FHWA's Turner-Fairbank Laboratory in Washington, DC. The UHPFRC solution was identified as being the most competitive solution for the long-term replacement of several road bridges [Keierleber et al. 2007], mainly due to the advantage of easy and rapid bridge construction.

Road bridges at Shepherds Creek, Australia, and Saint-Pierre-la-Cour, France: I-girder

A somewhat different concept to the previous two was developed by VSL and used with Ductal UHPFRC for two road bridges, one constructed in Australia in 2004 (Shepherds Creek bridge, Figure 7.5 a)), and one in France in 2005 (Saint-Pierre-la-Cour bridge, Figure 7.5 b)).

The structural system is based on multiple prestressed UHPFRC I-girders with 25 mm thick precast unreinforced UHPFRC plates placed between the main girders (Figure 7.5, details on the right), and fulfilling two functions: serving as formwork for the cast-in-situ upper slab, made of ordinary reinforced concrete, and protecting the superstructure from environmental aggressions during the life of the structure. The two bridges have single spans of 15 m and 19 m lengths respectively, with a total deck width of 20.8 m (Shepherds Creek bridge, 16 I-beams) and 12.6 m (Saint-Pierre-la-Cour bridge, 10 I-beams). The slenderness of the beams in both cases is $l/h=25$.

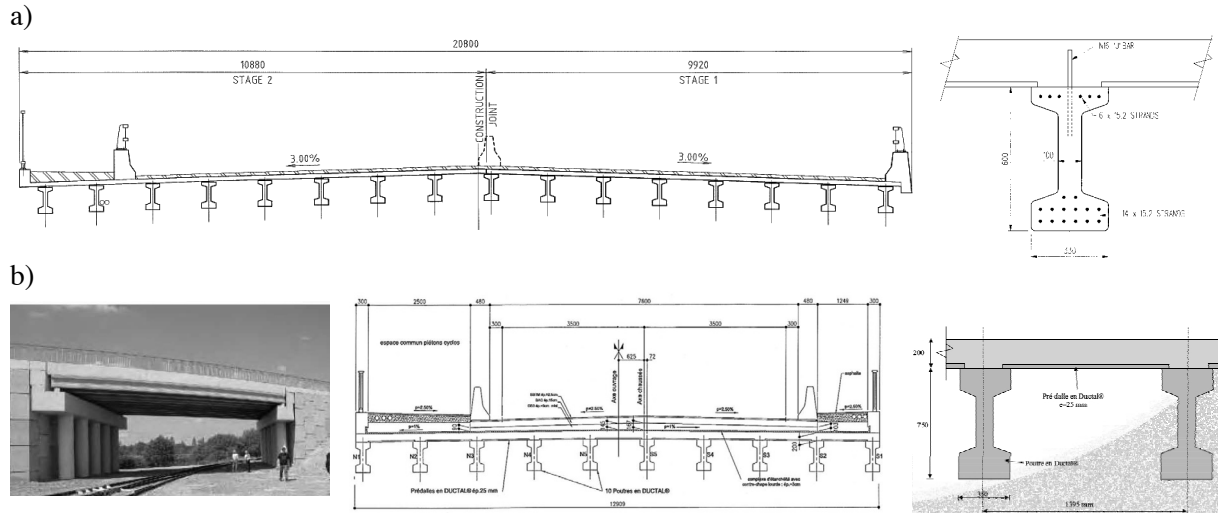


Figure 7.5: Road bridges with I-shaped UHPFRC girder and thin UHPFRC slabs used as formworks for ordinary RC slab: a) Shepherds Creek bridge: cross section and detail of I-girder and thin slab [Cavill, Chirgwin 2003]; b) Saint-Pierre-la-Cour bridge: view of structure and cross section [Resplendino, Bouteille 2006]

Bridge at La Chabotte, France: box girder

The PS34 bridge crossing highway A51 at La Chabotte, France is made of UHPFRC produced by Vinci, with mechanical properties similar to those of previously mentioned UHPFRCs. Unlike the previous road bridges, this structure has a smaller width, 3 m, but a significantly longer span of 47.4 m [Resplendino, Bouteille 2006]. The applied box girder concept (Figure 7.6 b)) allows more static height but limited material consumption and weight, as in the case of the Sakata Mirai footbridge. The bridge consists of precast segments, assembled in situ with glued joints and longitudinal external prestressing. The entire bridge was lifted and installed in one single operation. The segments were cast vertically with special hydromechanical and deformable formworks to allow early age shrinkage to develop without constraints. The bridge is free from passive longitudinal reinforcement. However, a certain amount of transversal reinforcement is provided in the lower slab in order to strengthen a section in which, during casting, opposing flows of fresh UHPCFR meet thus creating a possibly weaker joint. The thickness of the walled elements is 140 mm, and the equivalent height of the girder is 0.28 m for span-to-depth ratio $l/h=30$.



Figure 7.6: Bridge at La Chabotte, France, France: a) view of structure; b) cross section of bridge, [Resplendino, Bouteille 2006]

Ribbed deck slab

A concept of a composite plate-girder road bridge with UHPFRC ribbed deck supported by two longitudinal steel I-girders (Figure 7.7) is under investigation in the framework of the French National MIKTI project. Unlike existing UHPFRC road bridges, in this case UHPFRC is used for a structural element that transmits traffic loads to steel girders, and not to span the longitudinal bridge opening. The developed concept of the UHPFRC ribbed slab applies to a three-span bridge with a total length of 310 m, a main span of 130 m and a total deck width of 12.2 m. The solution has been

developed principally as an improved alternative to steel orthotropic decks [Toutlemonde et al. 2005]: the ribbed UHPFRC slab provides the advantages of both a concrete slab in terms of durability and stiffness, and those of an orthotropic steel plate in terms of lightness; problems related to the fatigue degradation of steel elements are avoided with the concrete solution.

The slab consists of prestressed precast segments, assembled in the bridge's longitudinal direction using cast-in-situ joints, and is additionally prestressed. This concept allows rapid construction. The thickness of the upper UHPFRC slab is designed to resist local bending and punching failure under concentrated wheel loading. Rib number and height are mainly calculated according to transversal bending strength and stiffness. The adopted solution with a 50 mm thick slab, regular rib spacing of 0.6 m, and constant rib height of 0.38 m (Figure 7.7 b)) results in an equivalent slab thickness of 0.14 m.

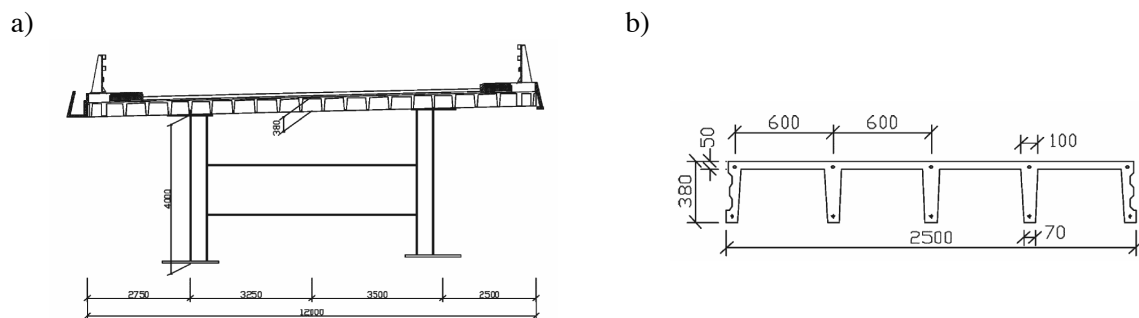


Figure 7.7: a) cross section of road bridge pilot project with UHPFRC ribbed deck slab; b) repetitive element of ribbed deck slab; [Toutlemonde et al. 2005]

7.2.1.1 Repair of existing bridge structure

The resistance of UHPFRC to chemical and physical attacks, as well as the possibility of casting it in very thin layers, make UHPFRC suitable for rehabilitation intervention on damaged or overexposed existing structures. Two additional advantages of this type of application are: the use of limited quantities of UHPFRC (reduced costs), and the very small additional load represented by thin layers, which is very important in existing structures with limited load-bearing capacity.

Kaag bridge deck repair with UHPC panels, Netherlands

Heavily reinforced UHPC precast panel elements were used to replace the wooden bridge decks of two movable bridges in the Netherlands [Kaptijn, Blom 2004]. The principal requirement was to keep the deck weight low: a solution using 45 mm thin panels, containing 5.6 % of mild reinforcement, with an only 9 mm concrete cover was adopted (Figure 7.8 a)). Panel dimension is increased along the joint line to 65 mm. The advantages of replacing the traditionally used wooden deck with the UHPC deck were sustainability and significantly decreased maintenance costs.

Rehabilitation and widening of bridge over the river Morge, Switzerland

Within the context of the European project SAMARIS (Sustainable and Advanced Materials for Road InfraStructure) UHPFRC was applied for the rehabilitation of a reinforced concrete bridge over the river Morge in Switzerland [Denarié et al. 2005]. This intervention represents the first application of this kind in bridges: the structure was widened by using ordinary RC beam and a UHPFRC precast element, and protected with a 30 mm thick UHPFRC layer (Figure 7.8 b)). The innovations implemented are based on the concept of making the construction process simpler and quicker by avoiding waterproofing membranes and concrete compacting by vibrating, while the superstructure zones exposed to environmental and mechanical loads are protected thanks to the material advantages of UHPFRC [Brühwiler et al. 2005]. The UHPFRC used in this rehabilitation was a type of CEMTEC_{multiscale}© (§ 3.2.3, [Rossi et al. 2005]) tailored at MCS-EPFL.

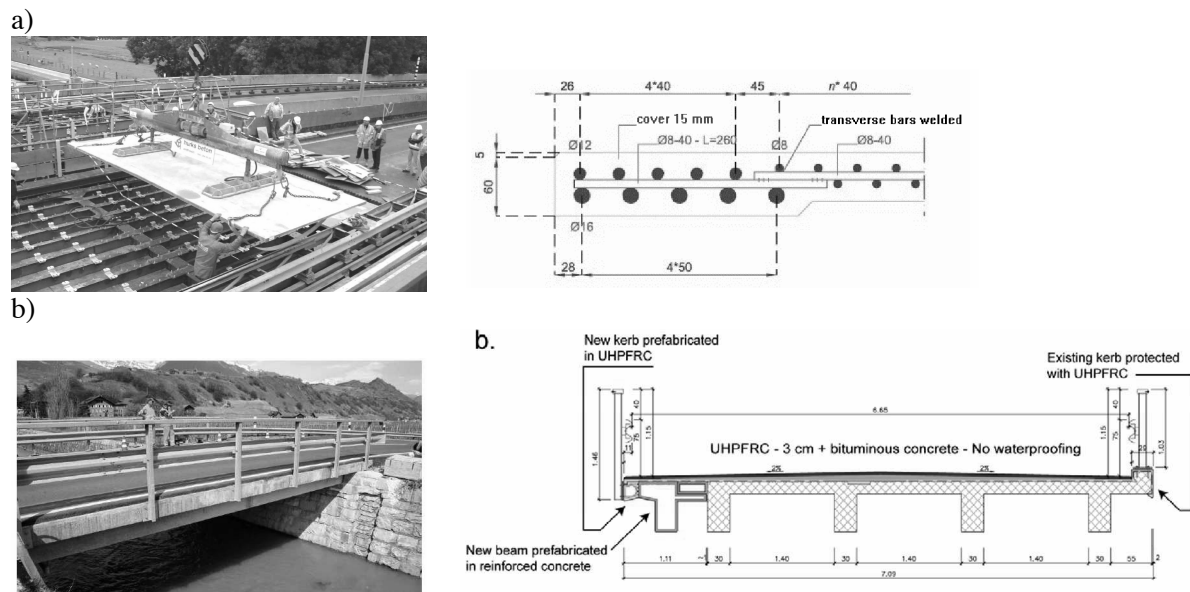


Figure 7.8: Rehabilitation of road bridges using UHPFRC: a) Kaag bridge (2002, Netherlands) and detail of deck panel cross section [Kaptijn, Blom 2004]; b) bridge over the river Morge (2004, Switzerland) with cross section of bridge after rehabilitation [Denarié et al. 2005]

Rehabilitation of columns of Valabres viaduct

The rehabilitation of the columns of the Valabres viaduct in France [Eiffage 2005] is an example of the use of UHPFRC's material properties for element strengthening and abrasion and shock protection. As in the previous rehabilitation example, UHPFRC allowed the simple execution of intervention work.

7.2.2 Conclusions on the application of UHPFRC in bridge design

Current UHPFRC bridge structures are designed to work in a conceptually similar way: the principal bending moment is borne mainly by the prestressing strands and UHPFRC in compression, the latter not being fully exploited. Shear strength and resistances to local loads are provided by UHPFRC's strength and ductility in tension, eradicating the need for ordinary reinforcement. In some cases, transversal moments are also borne only by the UHPFRC. UHPFRC members are generally precast and assembled in situ with dry or wet joints and prestressing. According to designers, all existing structures represent competitive variants in comparison to ordinary solutions, with the advantages of: reduction in ordinary reinforcement (speeding up production time), reduction of the weight of the superstructure, (with positive effects on the design of the supporting structure, but also on transport and placing), and improved durability.

However, considering the current initial costs of the material, in order to make UHPFRC structures competitive, their properties must be exploited to the maximum, requiring appropriate design methods and structural concepts based on material properties. In view of existing structural applications, some inductive conclusions concerning the potential of UHPFRC for application in bridge design can be drawn: UHPC is appropriate particularly when weight saving, rapid construction or resistance to highly aggressive environments are required.

7.3 Case study: design of a UHPFRC ribbed deck slab

Ribbed slab, as a structural concept for bridge deck slab enabling the advanced properties of UHPFRC to be fully exploited, is studied in this section. The ribbed slab is conceived as a light precast prestressed element that enables easy and rapid fabrication and construction.

The analysis and design of ribbed UHPFRC slab in this section are based on available experimental data (tests to failure for different failure modes), theoretical considerations presented in previous chapters, as well as available design recommendations. By performing the analysis for varying geometrical parameters of the slab, optimal dimensions and efficiency of the slab can be concluded.

7.3.1 Structural concept

Ribbed deck slab, as part of an advanced UHPFRC bridge system, enables the properties of the material to be fully exploited: thin slabs can provide sufficient resistance without ordinary reinforcement, and thin webs can sustain a relatively high prestressing force, due to material strengths. The ribs provide global stiffness to the deck slab, and limit the span of thin upper slabs. Thanks to the high material density and corrosion resistance, small concrete covers are sufficient. This leads to a structural element requiring very low material quantities.

For application in highway bridges, the required width of the driving surface, b_d (Figure 7.9a)), must be assured, while all other slab dimension (h , h_{ts} , b_r , Figure 7.9b)) are variables, defined to meet design requirements. A width of 12 m provides sufficient space for 2 highway lanes of 3.75 m [VSS 1992], and it will be a constant in the present study. This deck width also provides sufficient space for pedestrian lanes in the case of road bridges, with a reduced driving surface.

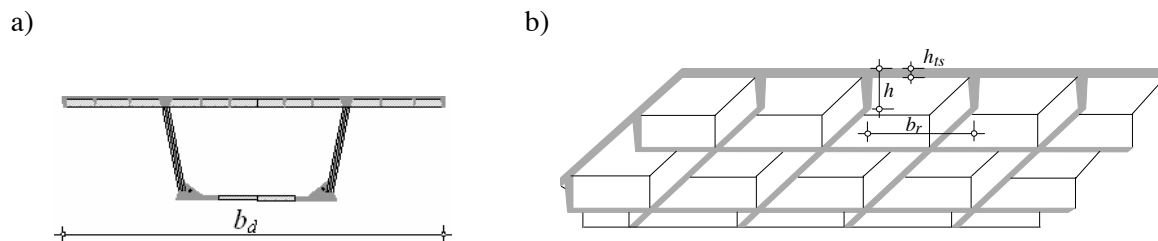


Figure 7.9: UHPFRC in bridge superstructure: a) ribbed-deck slab in complete bridge superstructure; b) zoom on ribbed slab and characteristic geometrical parameters

The concept of the rest of the superstructure is not detailed in the present work. For small spans, ribbed slabs solutions with different geometry can be considered [Sorelli et al. 2007], [Resplendino, Bouteille 2007], or beams with deeper longitudinal webs, as the π -girders optimised at the MIT, can be considered, [Chuang, Ulm 2002], Figure 7.4. For longer spans, possible solutions for the design of UHPFRC webs, maintaining the idea of light structures, are shown in Figure 7.10: the concept of corrugated webs (Figure 7.10 a)) may be applicable for UHPFRC, due to its high strengths and the possibility of casting in irregular forms; similarly, voided webs (Figure 7.10 b)) as applied for ordinary concrete (Figure 7.2 c)) and also for UHPFRC in pedestrian bridges, may be of interest. Both these concepts need external longitudinal prestressing. Another interesting structural application of UHPFRC in superstructures may be in thin shells below the bridge deck (Figure 7.10 c)), forming an integral superstructure, suitable for precast construction [Fanous et al. 1996].



Figure 7.10: Possible solutions for a light UHPFRC superstructure for higher spans: a) corrugated webs (as in the Altwipfergrund bridge, mixed design); b) voided webs – truss structures, Glacières and Sylans viaducts, 1988-89, France; c) shell-deck bridge [Fanous et al. 1996]

7.3.2 Design basis

7.3.2.1 Actions on the structure

Permanent and variable actions on the structure are considered based on the Swiss structural codes [SIA 2003] and the French recommendations for UHPFRC structures [SETRA, AFGC 2002].

Permanent actions

a) External loads

The self-weight of structural and non-structural elements and prestressing are the permanent actions considered in the present study. The self-weight of the bearing structure is a function of slab geometry, A_{uhpfrc} , and average weight per unit volume of UHPFRC, γ_{uhpfrc} . As already explained, slab dimensions vary during the analysis, whereas $\gamma_{uhpfrc} = 27.9 \text{ kN/m}^3$ (Table 3.3). The actions of non-structural elements are:

pavement self-weight, with thickness equal to 40 mm and weight $\gamma = 25 \text{ kN/m}^3$. This layer, much thinner than in conventional design ($80\text{-}90 \text{ mm}$ according to [OFROU 2002]), is acceptable for UHPFRC due to the much improved resistance to degradation and water penetration: in rehabilitation work on a bridge superstructure, [Denarié et al. 2005], a 40 mm thick bituminous concrete pavement was placed over a UHPFRC layer, without a waterproofing membrane.

guard rail self-weight: $\Delta g = 3.5 \text{ kN/m}$.

b) Prestressing

The adhesive prestressing is applied in the structural element via prestressing strands. The characteristic value of prestressing force, P_k , is considered at time $t \rightarrow \infty$, with prestressing losses due to shrinkage, creep and steel relaxation taken into account.

Variable actions

Road traffic is regarded as the only variable action in the present study. It is assumed as being in accordance to Articles 10.1 to 10.3 of [SIA 2003a]: Actions on Structures. The load model 1 of this standard is applied (Figure 7.11), comprising concentrated loads, $\alpha_{Qi} Q_{ki}$ and uniformly distributed loads, $\alpha_{qi} q_{ki}$. The axle load, $\alpha_{Qi} Q_{ki}$, is imposed on the structure over two square wheel surfaces (0.4 m side), and corresponds to values proposed by the Eurocode. The characteristic values of the loads are given in Figure 7.11. In the case of normal traffic load, $\alpha_{Qi} = \alpha_{qi} = 0.9$.

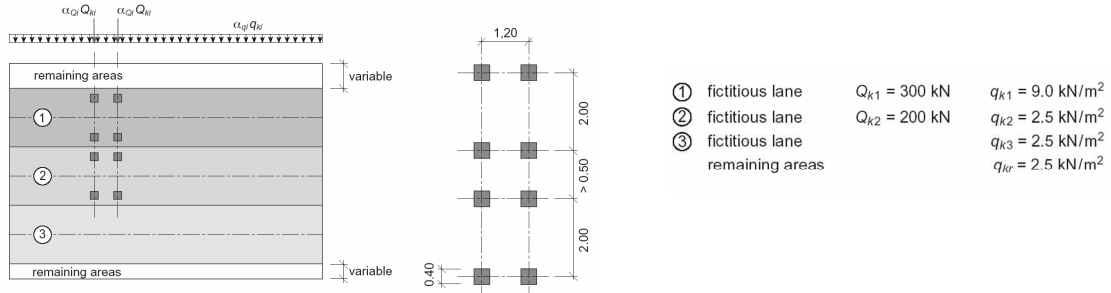


Figure 7.11: Traffic load “model 1” according to SIA [SIA 2003a]

7.3.2.2 Materials

UHPFRC

Material laws in compression and tension as defined in §3.3.1.4 and §3.3.2.8 are used. Partial safety factors for UHPFRC for fundamental combinations is $\gamma_b=1.3$, according to Article 2.1 of the French recommendations [SETRA, AFGC 2002]. The effect of placement method on strength values is considered using the reduction coefficient $1/K$, which can be determined for a structural element based on test results or references for similar works. According to Article 2.1 [SETRA, AFGC 2002], $K=1.25$ is applied for all loadings other than local effects, $K=1.75$ for local effects, and $K=1$ for thin plates.

Prestressing steel

Characteristics of the prestressing steel used in the study are given in Figure 7.12.

strands type		T15S
<i>characteristic</i>		
f_{pk}	[MPa]	1770
σ_p		$0.7 f_{pk}$
$f_{p0.1k}$	[MPa]	1520
f_{pd}		$f_{p0.1k} / 1.15$
ε_{uk}	[%]	≥ 3.5
E_p	[GPa]	195
ϕ_p	[mm]	15.7
A_p	[mm ²]	150
g_{pl}	[kg/m]	1.18

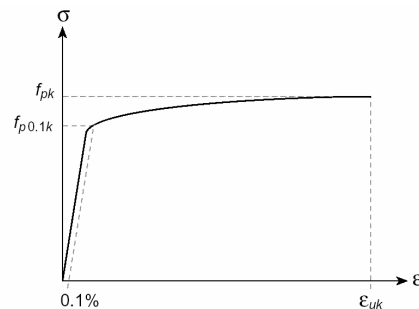


Figure 7.12: Characteristics of prestressing strands and typical stress-strain diagram for prestressing steel, [SIA 2003b]

Notations used in Figure 7.12: f_{pk} tensile strength, $f_{p0.1k}$ yielding strength, f_{pd} design value of yield strength, ε_{uk} ultimate strain, ϕ_p , A_p and g_{pl} strand diameter, cross section area and weight respectively.

7.3.2.3 Strength and design models

For a given design situation, design consists of verification of relevant limit states – ultimate limit states (ULS) and serviceability limit states (SLS). The partial factors are assumed in accordance with Swiss codes [SIA 2003] and the French recommendations for UHPFRC [SETRA, AFGC 2002]. The resistance of elements to various failure modes is determined in accordance to the recommendations for UHPFRC structures (§ 4.1) and the work presented in Chapter 4 to 6 of the present thesis. The applied models are recalled in § 7.3.3.

7.3.3 Design procedure

For a preliminary design, the initial problem is the choice of the governing criterion. Considering design at ULS, all potential modes of failure must be identified and design is performed in order to exclude them. Two kinds of failure modes are identified for the ribbed slab: local and global failures. Local failures comprise bending and punching-shear failure of thin slabs, while global failures are related to the loss of bending and shear resistance of prestressed T girders, representing a unit element of the ribbed slab. According to Article 6.3,3 [SETRA, AFGC 2002], the fundamental design assumptions for the analysis at the ULS are that plane sections remain plane and that concrete and prestressing reinforcement are not subjected to any relative slip. According to the same article, sectional strength is reached before the cracks are too wide. Design at SLS includes verification of stress states attained in structural elements, as well as deformations. The tested concept of light weight structure exposed to, in proportion, much higher variable loads, may exhibit the problems related to fatigue, and consequently, the possibility of occurrence of fatigue failure should also be verified. More data on fatigue performance of an UHPFRC ribbed slab are presented in [Toutlemonde et al. 2007a].

Structural model

Sectional forces, elastic deformations and displacements are calculated using a developed parametric 3D FEM model (Figure 7.13), using shell elements. The ribbed slab is treated as one-way slab, supported on two longitudinal bridge girders, assumed to be infinitely stiff. The one-way slab assumption is a correct model for most of the slab length, except in the vicinity of a support in transversal direction, e.g. diaphragms. The model is thus appropriate for the design of the slab in transversal direction, while no verifications in longitudinal bridge direction are performed in the present study.

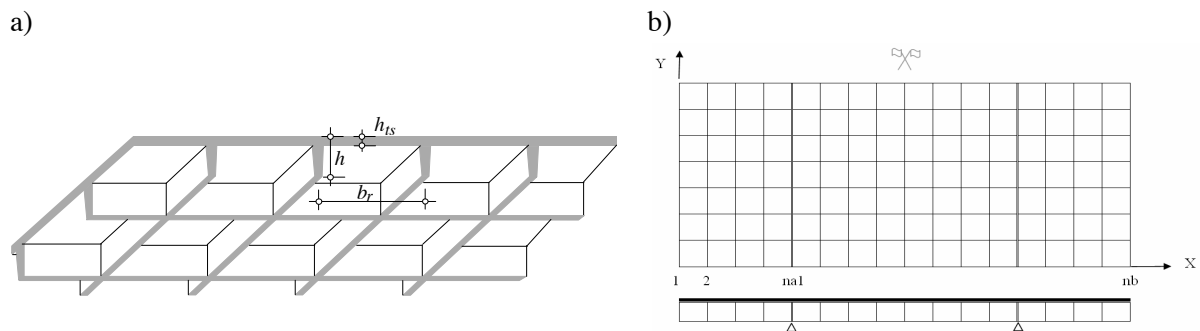


Figure 7.13: Parametric 3D model of the ribbed slab

For the design at SLS, the assumption is that, for service loads, the calculations based on linear elastic theory provide sufficient accuracy for sectional forces, and remain in accordance with everyday structural design approach. Even though forces distribution at ULS might differ from the result of a linear elastic calculation, the FEM model will be used to provide a preliminary estimation of global sectional forces.

7.3.4 Design for local failures

7.3.4.1 Bending failure of thin slabs

It is demonstrated in Chapter 6 that plastic analysis¹ using yield line method provides satisfactorily results for the prediction of failure loads of thin UHPFRC slabs, avoiding the non-linear analysis that is more demanding in terms of calculation. The design of thin slab element is thus performed assuming the resisting moment m_{Rd} equal to the maximal plastic moment, with partial safety factor for the material $\gamma_b=1.3$ (case of fundamental combinations) according to SETRA, part 2, 2.1, and $K=1$ for thin plates. The value of m_{Rd} can be directly calculated, omitting the effect of normal force due to prestressing, as explained in Chapter 6:

$$m_{Rd} = \frac{1}{\gamma_b \cdot K} \cdot n_{fct} \cdot \frac{h_{ts}^2}{6} f_{ct} \cdot \quad (7.1)$$

Based on the assumed yield line pattern (Figure 7.14 c)), and given disposition of the loads acting on the thin slab (Figure 7.14 a)), the required resistant moment can be expressed as a function of ultimate loads:

$$m_{Rd} \geq \frac{1}{16} \left(\frac{q_{rd} \cdot b_r^2}{3} + q_{Qd} \cdot a_Q^2 \left(1 - \frac{2 \cdot a_Q}{3 \cdot b_r} \right) \right). \quad (7.2)$$

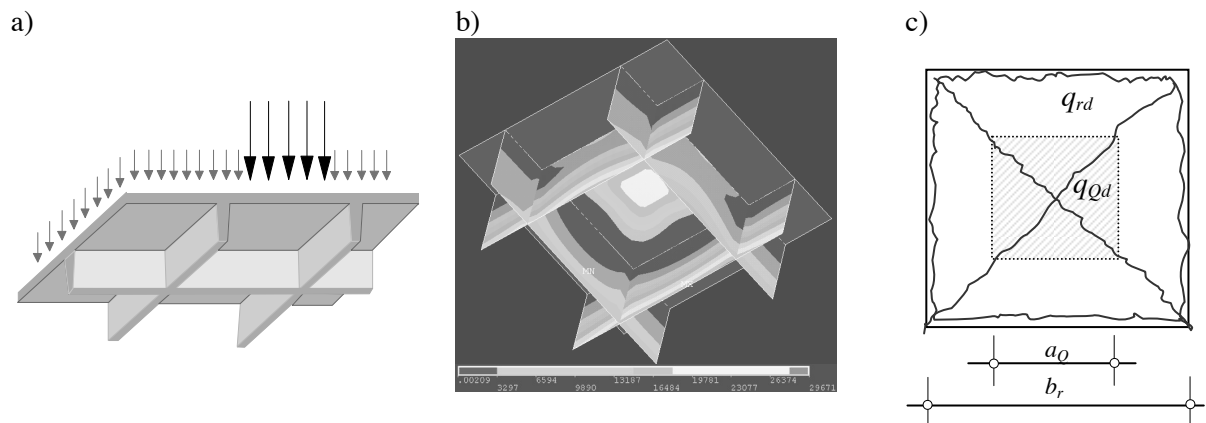


Figure 7.14: Thin slab between the ribs subjected to traffic load: a) loads on thin slab; b) numerical simulation of thin slab between the ribs; c) yield line pattern of thin slab

The loads in Equation 7.2 are:

- self-weights of the slab and the pavement, acting over the whole slab surface with $\gamma_G=1.35$;
- traffic load $\alpha_{Ql} Q_{kl} / 2 = 0.9 \cdot 150 = 135 \text{ kN}$, acting over a square surface of $0.4 \times 0.4 \text{ m}$ (q_{Qd} in Figure 7.14 c)) and $\alpha_{q1} q_{kl} / 2 = 0.9 \cdot 9 = 8.1 \text{ kN/m}^2$ acting on the rest of the slab surface; both loads are majored by $\gamma_Q=1.5$.

¹ According to Article 6.3.1 of [SETRA, AFGC 2002], the design involving plastic hinges is authorised only if passive of prestressing reinforcement is capable of withstanding bending moment, and the participation of fibres is overlooked. However, in Chapter 4 it is shown that, even if no tensile strain hardening phase is present, fracture properties of a typical UHPFRC enable sufficient elements ductility to be developed in thin elements, allowing the plastic analysis to be applied in predicting failure loads.

It can be easily seen that the permanent loads are smaller than 1% of the wheel load, and, for a practical estimation, they can also be disregarded.

Substituting value for m_R , given by the Equation 7.1, into Equation 7.2, minimal slab thickness, $h_{ts,min}$, can be calculated for the given design load as a function of slab geometry. In Figure 7.15 minimal slab thickness are plotted as a function of rib spacing, b_r .

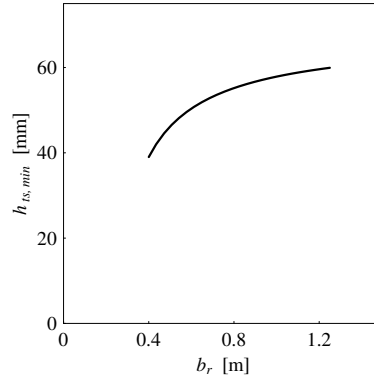


Figure 7.15: Minimal thickness of thin UHPFRC slab to resist bending failure under wheel load, as a function of rib spacing and resulting from ULS design based on the plastic analysis

For rib heights and spacing considered in this analysis, the results of the FEM analysis (Figure 7.14 b)) indicate that the system can be considered sufficiently stiff with respect to out-of-plane rib rotation, which allows to model the slab between the ribs as a clamped slab. As a consequence, a yield line pattern as shown in Figure 7.14 c) applies.

In addition, it should be noted that, for a moderated compressive normal force N , as induced by prestressing, the resistant bending moment is higher than the value of m_R given by Equation 7.1. According to [Greiner 2007], normal forces causing compressive stresses up to one third of UHPFRC compressive strength lead to an increase in resistant bending moment.

7.3.4.2 Punching failure of thin slabs

Based on the discussion presented in § 6.3, the limiting crack opening even for the elements of small thickness (smaller than 150 mm) in a deformable system seems to be higher than the suggested 0.3 mm [SETRA, AFGC 2002]. Consequently, for the design of elements with the boundary conditions of the studied slabs (thicknesses 30-80 mm, and side dimensions 400-1000 mm), ultimate punching shear resistance V_u is

$$V_{ud} = V_{Rbd} + V_{fd} \quad (7.3)$$

where

$$V_{Rbd} = \frac{1}{\gamma_E} \cdot \frac{0.21}{\gamma_b} k \cdot \sqrt{f_c} \cdot b_0 \cdot d = \frac{1}{1.5} \cdot 0.21 \cdot \sqrt{180} \cdot b_0 \cdot d = 1.88 \cdot b_0 \cdot d \quad (7.4)$$

and

$$V_{fd} = \frac{S \cdot \sigma_p}{\gamma_{bf} \cdot \tan \beta_u} \quad (7.5)$$

with

$$\sigma_p = \frac{1}{K} \cdot \frac{1}{w_{lim}} \cdot \int_0^{w_{lim}} \sigma(w) dw, \quad (7.6)$$

Two cases are considered: potentially less safe limit with $w_{lim}=1.5 \text{ mm}$ and $K=1$, and a case of a more rigid or thick slab with $w_{lim}=2 \text{ mm}$ and a conservative value of coefficient K , $K=1.75$. The inclination of punching surface against the horizontal plane is set to 45° . The integral of stress-crack opening law proposed in §3.3.2.8 is defined by Equation 3.31,

$$\int_w \sigma(w) \cdot dw = f_{ct} \cdot \frac{-\left(1 + \frac{w}{w_{n,w}}\right)^{-p} \cdot \left(w + w_{n,w} - w_{n,w} \left(1 + \frac{w}{w_{n,w}}\right)^p\right)}{p-1} \quad (7.7)$$

In the first case, $\sigma_p = 5.0 \text{ MPa}$, in the second case $\sigma_p = 4.44/K = 2.54 \text{ MPa}$, and thus

$$V_{ud} = 1.88 \cdot b_0 \cdot d + \frac{1}{1.3} 5.0 \cdot 0.9 \cdot b_0 \cdot d = 5.4 \cdot b_0 \cdot d \quad (7.8)$$

and

$$V_{ud} = 1.88 \cdot b_0 \cdot d + \frac{1}{1.3} 2.54 \cdot 0.9 \cdot b_0 \cdot d = 3.6 \cdot b_0 \cdot d. \quad (7.9)$$

For wheel load $\alpha_{Q1} Q_{k1} / 2 = 0.9 \cdot 150 = 135 \text{ kN}$, acting over a square surface of $0.4 \times 0.4 \text{ m}$ thus $b_0 = 1.6 + h \cdot \pi$ in [m], without considering the beneficial effect of asphalt pavement to load introduction on concrete surface. With partial load safety factor $\gamma_p = 1.5$, minimal slab thickness required according to the first case ($w_{lim} = 1.5 \text{ mm}$) is $h_{ts} = 25 \text{ mm}$, whereas, in the second case, $h_{ts} = 33 \text{ mm}$. Thus, slabs of thickness higher than 33 mm can be considered to satisfy the punching shear resistance. According to the previous section, bending strength of thin slabs will be determining for design at ULS (Figure 7.15).

7.3.5 Design for global failure

The representative element of the ribbed deck slab is a T-shaped beam consisting of a rib and a part of the upper thin slab, with a participating width b_{eff} (Figure 7.16).

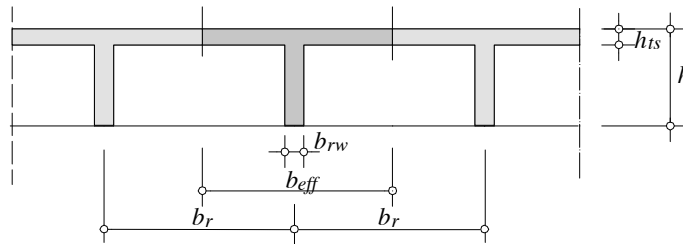


Figure 7.16: T-beam as a representative element of ribbed desk slab

According to the Swiss codes [SIA 2003b], the effective slab width (Figure 7.17 a)) is

$$b_{eff} = \sum b_{eff,i} + b_w \leq b, \quad (7.10)$$

where

$$b_{eff,i} = 0.2 \cdot b_i + 0.1 \cdot l_0 \leq 0.2 \cdot l_0, \quad (7.11)$$

and l_0 is distance between points of zero moments according to Figure 7.17 b). For the considered rib spacing ($0.4-1. \text{ m}$) and spans (spacing of the longitudinal bridge girders) higher than 4 m , the effective slab width i.e. the width of the upper flange of the T-shaped beam is equal to rib spacing, b_r .

$$\varepsilon_{cc}(t) = \varphi(t, t_0) \cdot \varepsilon_{c,el} \quad (7.12)$$

with creep coefficient $\varphi(t, t_0) = 0.2$ for thermally treated elements (§7.3.2.1) and

$$\varepsilon_{c,el} \approx \frac{\sigma_{p,0} \cdot A_p}{A_c \cdot E_c} \quad (7.13)$$

According to article 3.3.2.7 [SIA 2003b], prestressing losses due to strands relaxation, for $\sigma_{p,0} = 0.7 f_{pk}$, are estimated as $\Delta\sigma_{pr} / \sigma_{p,0} \approx 7\%$. Thus, total prestressing losses are

$$\Delta\sigma_p / \sigma_{p,0} = (\varepsilon_{cs} E_p + \varepsilon_{cc} E_p + \Delta\sigma_{pr}) / \sigma_{p,0} \quad (7.14)$$

For a minimal cross-section area, with closely spaced ribs and small rib height ($b_{eff}=0.4\text{ m}$ and $h=0.1\text{ m}$), $\Delta\sigma_p / \sigma_{p,0}=7.4\%$ with one strand per rib and $\Delta\sigma_p / \sigma_{p,0}=7.64\%$ with two strands per rib. For distant high ribs ($b_{eff}=1\text{ m}$ and $h=1\text{ m}$), $\Delta\sigma_p / \sigma_{p,0}=7.26\%$ with one strand per rib and $\Delta\sigma_p / \sigma_{p,0}=7.33\%$ with two strands per rib. In case when no thermal curing is provided, the value for $\varepsilon_{cs}(t)=500\mu\text{m/m}$ and $\varphi(t, t_0)=0.6$ result in an increase of losses, leading to $\Delta\sigma_p / \sigma_{p,0}=15.6\%$ for the smallest section. For further analysis, the prestressing losses are considered to be 10% of the initial prestressing force.

Design of bending resistance: case study

Two critical sections are considered: a section at the support (longitudinal bridge girder), designed for the maximal negative moment, and the mid-span section, designed for the maximal positive moment. As an example, positive and negative resistant bending moments of a UHPFRC T-shaped cross section with dimensions $h=0.4$, $b_r=0.6$, $b_{rw}=0.07$, $h_{st}=0.05$ (values similar to those of the ribbed deck slab presented in [Toutlemonde et al. 2005]) and without prestressing force are shown in Figure 7.19. It is interesting to notice that, due to material mechanical properties (tensile ductility in the first place), higher bending resistance is attained by the elements with a larger sectional surface subjected to tensile stresses, which is contrary to the concept of RC beams. The points corresponding to the end of the elastic phase, the beginning of local tensile softening, and the maximal bending moment are noted as A, B and C in Figure 7.19. It can be seen that in the beginning of the development of the pseudo-plastic phase in tension, significant increase in load-bearing capacity is achieved with a very slight decrease of the initial elastic stiffness, which is an important property at service states.

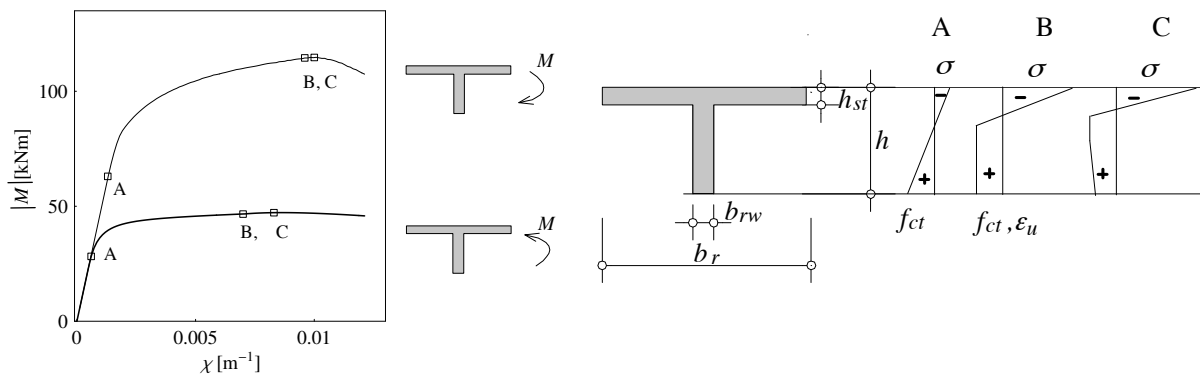


Figure 7.19: Simulated bending resistance of T-shaped cross section made of UHPFRC with neither ordinary nor prestressing reinforcement: positive bending moment (thick line), negative bending moment (thin line)

Prestressing strands are placed as shown in Figure 7.20 for sections subjected to negative and positive bending moment respectively. Concrete cover of 25 mm is assumed as sufficient and minimal rib width is fixed at 70 mm.

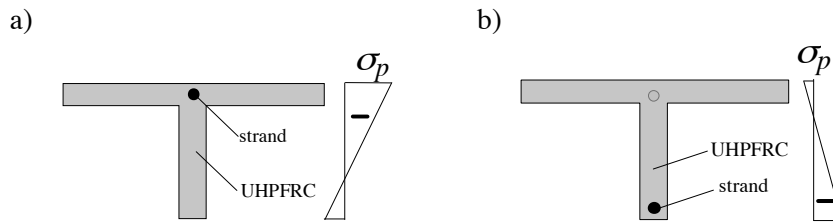


Figure 7.20: Position of prestressing strands in ribbed deck slab and distribution of prestressing stress, for the section subjected to: a) negative bending moment; b) positive bending moment

The contribution of the prestressing force to bending strength of a T-shaped beam is shown in Figure 7.21, using simulated moment-curvature relationship for the same beam geometry as in Figure 7.19. Figure 7.21 a) shows the response of the beam prestressed with one T15S strand, at $\sigma_p=0.7 f_{pk}$ and with prestressing losses of 10 % (black line), in comparison to the response obtained assuming an elastic-perfectly brittle behaviour for concrete in tension (dashed line), without prestressing strand (thin grey line) and with one prestressing strand T15S with no initial prestressing force (thick grey line). The relative contributions of strands and concrete in tension to ultimate moment, as well as the contribution of prestressing force to elements stiffness, clearly result from the plot. Figure b) shows the contribution of prestressing with variable number or disposition of strands: a section with no strand (thin grey line), with one strand in the lower part of the rib (black line) or with two strands with different positions, one at the lower part of the rib and one in the thin slab (thin black line, nearly coinciding with the response of the cross-section with one strand), or two strands in the lower part of the rib (thick grey line).

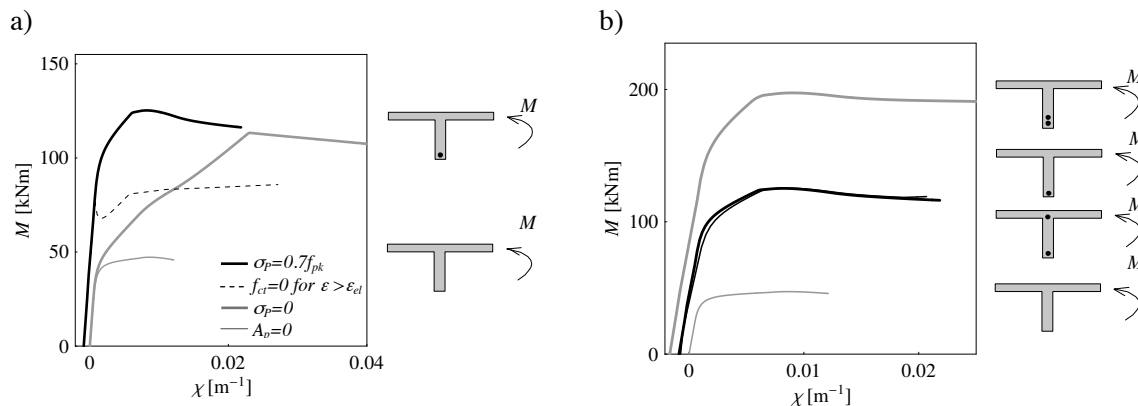


Figure 7.21: Simulated bending resistances of UHPFRC sections: contribution of prestressing strands, prestressing force and concrete tensile force

It must be noted that the maximal concrete compressive stresses remains very low, also in the case when two prestressing strands are used, and bending strength is governed by the capacity of prestressing strands and concrete in tension. This suggests that strands of higher yielding strength could be beneficial in these sections.

It is assumed that the design value of the resistant moment, M_{Rd} , corresponds to the beginning of yielding of prestressing reinforcement. Figure 7.22 shows a comparison between the nominal moment-curvature relationship (grey line) and the design moment-curvature relationship (black line) obtained with $K=1.25$, $\gamma_b=1.3$ and $\gamma_p=1.15$. The maximal nominal moment (M_R) and the design value of the resistant moment M_{Rd} are also indicated in the same plot. It is important to note that, in both cases, yielding of prestressing steel is attained before the tensile softening in concrete occurs, due to the pre-compression of concrete. As a consequence, the assumed definition of M_{Rd} is not influenced by the stress-crack opening relationship, neither for concrete nor for prestressing steel.

This do not always apply, when strands of higher strengths are used or in case of sections with a different geometry.

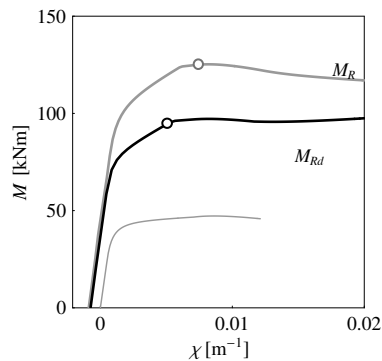


Figure 7.22: Design value of resistant bending moment (M_{Rd} , black line), in comparison to nominal resistant moment (M_R , grey line)

A variation of the slab thickness in the interval 40-60 mm (§ 7.3.4.1) changes insignificantly the value of M_{Rd} (for $h=100$ mm, $\Delta M_{Rd} = \pm 6$ % with respect to M_{Rd} for $h_{ts}=50$ mm, while for $h=800$ mm there is no change in M_{Rd}). Influence of variation of rib spacing b_r on M_{Rd} expressed per T-girder is also not significant (Figure 7.23 a)), however, when M_{Rd} is represented per unit slab with (Figure 7.23 b)) the influence of rib spacing on slab bearing capacity is obvious. Two cases of design values of resistant bending moments are presented in Figure 7.23: for rib height $h = 200$ mm (grey line) and $h = 400$ mm (black line), with one prestressing strand per rib. As expected, the most relevant geometric parameter for M_{Rd} is the depth of the rib, h . Differently from ordinary concrete, this is not only due to the increased level arm, but also to the increased contribution of the tensile force sustained by concrete and to the fact that a sufficient compressive strength is provided.

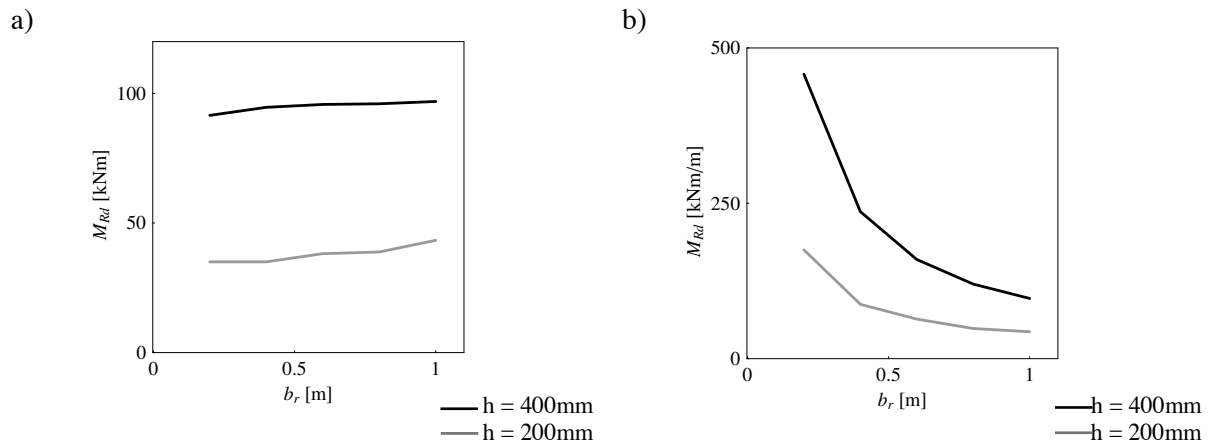


Figure 7.23: Influence of rib spacing on design value of the positive resistant bending moment: a) resistance per one T-girder; b) resistance per unit slab width.

Similar considerations apply to negative moment bending resistance, for which the results will be shown in the context of the following design step

Comparison of design and resistant moment values

Design values of bending moments due to dead and traffic load are obtained using the previously described 3D FEM model (§7.3.3). The number of ribs, n_b (Figure 7.24) is varied whereas the slab width is kept constant, $b_d=12$ m. The considered geometries consisted of 14 to 28 ribs, with the rib height 0.2 to 0.4 m, resulting in equivalent slab thickness, h_{equiv} in the range of 0.07-0.1 m for 0.2 m ribs and 0.1 to 0.15 m for 0.4 m high ribs. The length of the cantilever parts of the slabs varies in the

range of 2.3 to 3.5 m, as a function of rib spacing. For the same rib spacing, two different positions of the supports (main bridge girders, defined as a function of rib n_{a1} position in Figure 7.24) are considered. Examples of disposition of traffic wheel loads are presented in Figure 7.24 a): L1, causing maximal negative moment on the cantilever part and L2 causing maximal positive moment for the mid-span section; the rest of the traffic load is disposed according the model presented in Figure 7.11. An illustration of simulated response of the slab under wheel loads is shown in Figure 7.24 b).

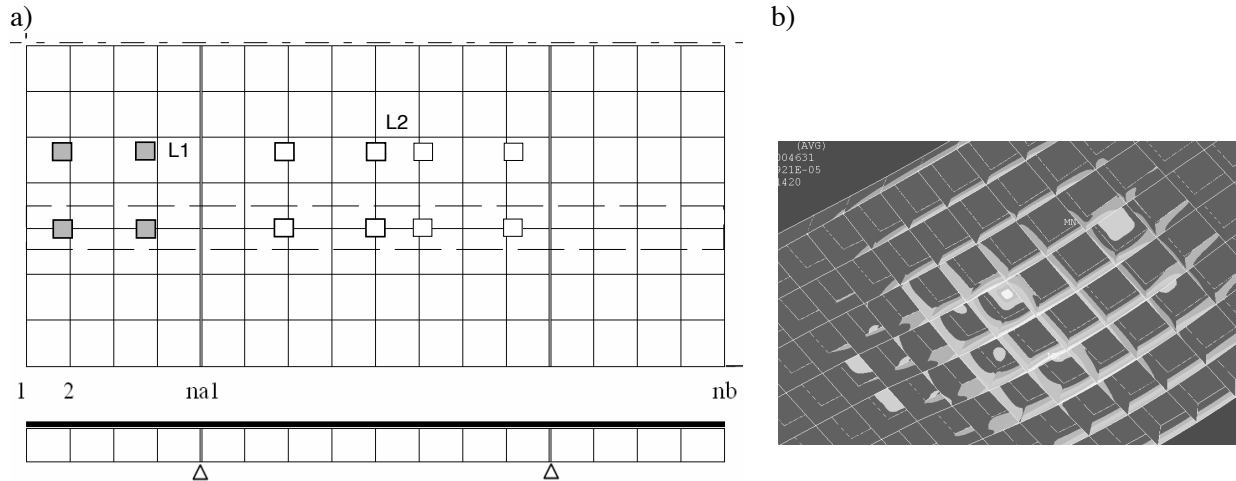


Figure 7.24: Numerical slab model: a) parametric definition of slab geometry and example of disposition of concentrated traffic loads L1 (grey squares) for maximal negative moment, L2 (voided squares) for maximal positive moment; b) view of a beam response – deformations obtained using 3D finite element model of ribbed deck slab

The results of the analysis for the slab with 0.4 m high ribs are presented in Figures 7.25 and 7.26. In Figure 7.25 design moment values (dots) issued from the calculation are compared with previously calculated design values of resistant moments (lines), for the mid-span section (Figure a)), and for the section at the support, (Figure b)). It can be noted that slabs with ribs height of 0.4 m and ribs spacing up to 0.7 m can be designed to sustain and transfer loads to the main girders. Presented design resistance moments are obtained with one strand T15S, thus, the small difference that exist between the design values can be overtaken by a slightly change in geometry or by application of prestressing strands of higher yielding strength. Thus further optimisations are possible, but the principal trends are well illustrated by the presented results. Slabs with ribs of smaller heights, on the contrary, are less appropriate to meet ULS design requirements for the given support disposition; for different support arrangements however, slabs with less deep ribs can represent attractive solutions.

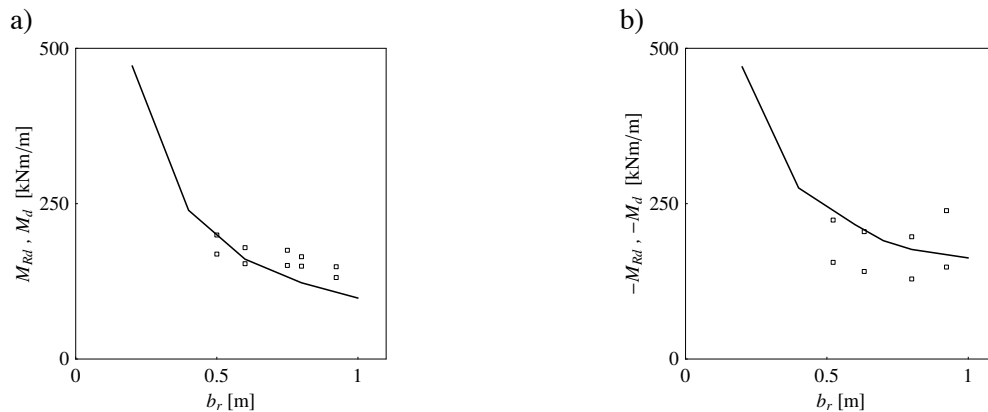


Figure 7.25: Resistant design moments (line) and design moments (dots) per unit slab with: a) in the mid-span; b) at the support

7.3.6 Serviceability states

Displacements under service loads, issued from the numerical simulation, are compared to admissible displacements, w_{admiss} , according to [SIA 2003b], and the results are presented in Figure 7.26. It can be seen that the design requirements are respected in the mid-span sections, while the displacements of cantilever of approx. 3 m do not meet minimal displacement requirements suggested by the recommendations. Maximal tensile stresses in thin slabs under service loads are verified using the results of the FEM model and adding the contribution of the prestressing force. Based on the results, prestressing force is indispensable in order to keep tensile stresses in service below the cracking level.

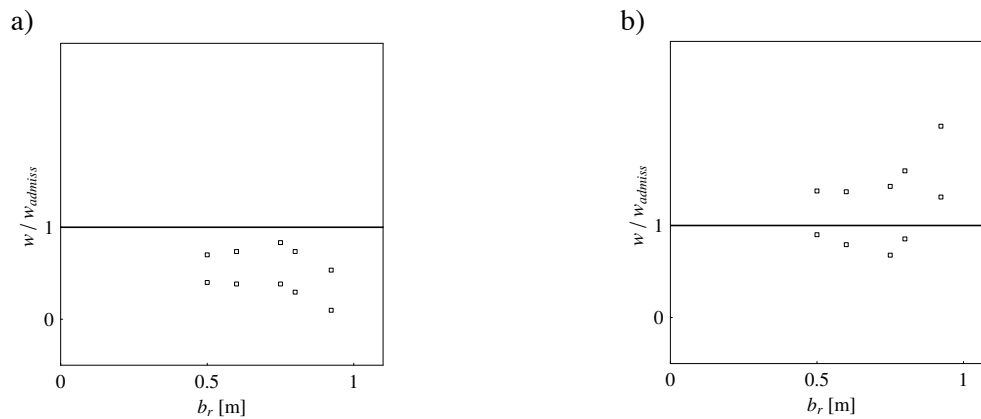


Figure 7.26: Comparison of slab displacements, w , and admissible displacements w_{admiss} according to [SIA 2003b]: a) mid-span displacements; b) displacements of the cantilever

7.3.7 Conclusions

A design case of structural application of UHPFRC is studied on the basis of existing design recommendations and the theoretical considerations presented in previous chapters. The same mechanical properties of the material as in the previous chapters are assumed and simplified hypothesis are made on the long term behaviour of UHPFRC. The study shows that thin-walled UHPFRC structural elements can be designed to satisfy ultimate limit states for road bridges. A concept of ribbed desk slab, with thin UHPFRC slabs and prestressed ribs is analysed: 40-60 mm thin UHPFRC slabs, with spans up to 1 m can sustain traffic load without ordinary reinforcement. With ribs of approximately 0.4 m height, 12 m wide slab supported on two longitudinal girders (main bridge girders) can be conceived to fulfil strength requirements for road bridges, resulting in 0.12-0.14 m of equivalent slab thickness, that is up to three times smaller slab thickness compared to ordinary reinforced concrete. More slender slabs could be designed for different support disposition, but problems related to serviceability limit states and to the shear strength of the ribs need to be more thoroughly considered. Further optimization of the geometry and of the exploitation of material properties seems possible, thus making the application of UHPFRC in ribbed desk slabs a promising field for future research.

8. Conclusions and prospects

Studies performed during this research contribute to better understand structural behaviour of ultra-high performance fibre-reinforced concrete (UHPFRC) and to reveal the possibilities for its application in bridge design. The research focuses primarily on bending behaviour of thin UHPFRC elements without ordinary reinforcement. Analytical and numerical models are developed to predict the non-linear bending response of beams and slabs governed by multi-microcracking and propagation of macrocrack. This allows the assessment of element behaviour at service states, the prediction of failure loads and the identification of the influence of material properties on bending response. It is demonstrated that the theory of plasticity can be applied to predict bending failure load for thin elements.

The theoretical study is supported by experimental research on beams and slabs. The UHPFRC used in the study is BSI, with 2.5 % in volume of 20-mm long fibres. It has mechanical properties of a typical UHPFRC, which allows the conclusions drawn in the framework of this research to apply in a more general way for UHPFRCs.

8.1 Conclusions of the research

Based on the theoretical and experimental parts of this research, relevant conclusions on element behaviour and on possibilities for modelling and design of UHPFRC members are presented.

Bending in simply supported UHPFRC beams

Testing and modelling

- a test series has been carried out on simply supported UHPFRC beams with thickness varying between 25 and 75 mm and tested in three-point bending;
- an analytical model describing the non linear behaviour of UHPFRC beams has been developed;
- a finite element model (FEM) describing the non linear behaviour of UHPFRC beams has been developed;
- the results of the analytical model are in good agreement with experimental data and with the prediction of the FEM model. Good agreement is also shown with test results from other authors on beams made of tensile strain hardening materials or materials without strain hardening phase;
- based on the comparison between theoretical and experimental results, multi-microcracking, causing tensile strain hardening with low stress increase, can be well modelled using pseudo-plastic material behaviour in tension for the thickness range of tested elements;
- explicit analytical expressions have been developed to describe the non-linear force-deformation response of a beam exhibiting multi-microcracking. Explicit expressions have also been developed to predict progressive reduction of the unloading-reloading stiffness caused by damage during microcracking;
- the propagation of a macrocrack, characterised by stress-crack opening relationship, can be simulated using the hypothesis of the fictitious crack model;
- a simplified formulation of the model is proposed to describe the bending behaviour in presence of macrocrack opening.

Behaviour of UHPFRC beams

According to the result of the analytical model and in agreement with experimental evidence, it is concluded that:

- the pre-peak behaviour and bending strength are mainly governed by multi-microcracking; for typical material properties, with tensile deformations ranging up to 2.5 ‰, the equivalent bending stress achieved due to strain hardening is approximately 2.4 times the tensile strength; this contribution is size-independent as long as sufficient compressive strength is provided and compression softening is avoided, as is the case of rectangular members in pure bending.
- the propagation of the macrocrack, characterised by tensile softening, provides a minor additional contribution to bending strength (up to roughly 10%), which is a size dependent value; bending strengths are attained for small macrocrack openings (smaller than 0.2 mm for the tested beams);
- in the case of thin beams, propagation of the macrocrack plays an important role in providing ductility at bending failure as well as post-peak toughness;
- from experimental observations, it must also be pointed out that more than one macrocrack can develop prior to peak-force, even though a gradient of moment existed;
- an important portion of the initial elastic structural stiffness of a beam is maintained for a load range that covers service conditions: for up to nearly 80% of the ultimate load, the residual stiffness equals more than 80% of the elastic one for specimens in three-point bending and approximately 60% for specimens under uniformly distributed load.

Influence of material properties and structural size on bending behaviour

The main results of a parametric study carried out using the analytical model can be summarized as follows:

- the size effect on bending strength is much less significant for UHPFRC than for other quasi-brittle materials: experimental results for thin members tested by the author (25 to 75 mm) confirm that size effect on bending strength is practically negligible; similar results are also reported by other authors for thicknesses up to 300 mm and for materials characterised by pronounced pseudo-plastic tensile deformations;
- the size effect on ductility is evident, even in a small range of variation of element thicknesses.
- even if the pseudo-plastic tensile phase is not pronounced, thin elements can develop a behaviour similar to that of elements with high pseudo-plastic tensile deformations, owing to the low stress decrease during tensile softening. As a consequence, if only force-displacement response of thin elements in bending is known, it is unreliable to characterise the material tensile hardening capacity by back analysis;
- in absence of pseudo-plastic tensile deformations, the behaviour of thick elements approaches that of typical quasi-brittle materials, with a pronounced size effect both on bending strength and ductility;
- the influence of the tension softening behaviour on bending strength is limited if the pseudo-plastic phase is pronounced, since most of the bending strength is developed while the concrete is in the pseudo-plastic tensile phase. The tensile softening is however important in providing ductility at failure and post-peak.

Statically indeterminate systems: beams and slabs

Numerical procedures have been developed to simulate the non-linear response of statically indeterminate UHPFRC beams and slabs subjected to bending. Firstly, the case of a clamped beam has been theoretically studied and the following conclusions are drawn:

- load carrying capacity of statically indeterminate members is positively affected by the ductility in bending of thin UHPFRC beams, which allow a significant redistribution of internal forces;
- load carrying capacity of statically indeterminate members is more sensitive to size effect than the bending strength of statically determinate elements. This is due to the fact that the load carrying capacity of a statically indeterminate system depends on the possibility to redistribute internal forces. Redistribution is strictly related to ductility in bending that, as demonstrated for simply supported beams, is controlled by the opening of a macrocrack and is thus much more affected by size effect.

A test series has been carried out on thin UHPFRC square slabs (40-60 mm thickness, 900 mm side length) supported on eight symmetrical points and subjected to central point load: all of the slabs failed in bending. The experimental behaviour was modelled using the same hypotheses for the behaviour of UHPFRC as the hypothesis used for modelling beam elements. The following conclusions are drawn:

- good agreement of experimental and theoretical results on pre-peak behaviour of UHPFRC slabs is shown; this confirms again that multi-microcracking can be well represented as a homogeneous material behaviour using an elastic-pseudo-plastic material law in tension;
- a major part of the load-bearing capacity of the slab is achieved with multi-microcracking behaviour; this is also confirmed by the experiment, during which cracks become visible only for a force level close to maximal force; it seems thus viable to predict the service response of a thin UHPFRC slab using elastic-plastic material tensile law and commercial FEM models;
- when the capacity to develop microcracking is exhausted, deformations start to localise i.e. discrete macrocracks form and a rigid block mechanism starts to develop. For the given boundary conditions, the non-linear simulation predicts dominant tangential deformations that are in agreement with experimentally observed macrocracks, opening along radii.

Application of the theory of plasticity in design of UHPFRC elements in bending

- A concept of plasticity for thin UHPFRC elements without ordinary reinforcement has been defined based on the bending response in statically determinate systems: the moment-curvature relationship during the first phase of macrocrack opening in thin elements is characterised by an almost constant moment with increasing curvatures. Thus, the moment level at the beginning of macrocrack propagation is assumed as plastic resistant moment, and a rigid-perfectly plastic moment-curvature relationship is defined with a limiting value for the curvature.

Based on this definition, the applicability of theory of plasticity in the design of statically indeterminate UHPFRC members has been thus evaluated:

- according to the results of the non-linear beam analysis, the applicability of the theory of plasticity to UHPFRC elements in bending depends on element size;
- with the proposed definition of plastic resistant moment, the theory of plasticity can be applied to predict failure loads for thin UHPFRC beams up to approximately $h < 100$ mm.

For thicker beams, the deformational capacity of the first developed plastic hinges may not be sufficient to allow the formation of other hinges and the development of a mechanism;

- the ultimate load-bearing capacity of thin UHPFRC slabs without ordinary reinforcement is well assessed based on the theory of plasticity, by applying the yield line method: for the investigated span and thickness range, the comparison with test results validates the proposed definition of plastic resistant moment.

Punching-shear in thin UHPFRC slabs

- A test series has been carried out on small square slabs (300 mm side length and 30-60 mm thickness) clamped on the edges and subjected to central point load on a 20x20 mm² surface;
- an analytical approach for assessing the punching shear strength of UHPFRC members has been proposed: fibre contribution to shear strength is taken into account as a function of element size and stiffness.

Although current theoretical and experimental knowledge is still insufficient for a general model to be established, the predictions of the proposed approach are in good agreement with the experimental results obtained in the framework of this research and by other authors. On the basis of theoretical and experimental evidence, the following conclusions can be drawn:

- significant shear stresses can be sustained by UHPFRC elements;
- fibre contribution to punching shear strength is a function of the opening of the critical shear crack, which is a function of slab thickness and slab bending stiffness at failure;
- punching shear strength decreases for increasing slab thickness;
- punching shear strength decreases for slabs that develop higher deformations, i.e. long-span slabs or slabs with free boundary conditions; thus, the influence of slab thickness, span and boundary condition should be taken into account to correctly evaluate punching shear strength;
- current design recommendations poorly estimate punching shear strength for element thicknesses lower than 150 mm, and may lead to unsafe predictions in the case of slabs with pronounced deformations;

Structural application of UHPFRC

A state of the art of existing structural application of UHPFRC has been made with specific attention to bridge design. It can be concluded that:

- current structural application of UHPFRC in bridge design often considers classical prestressed concrete shapes, sized with respect to increased material strengths. Principal bending solicitations are sustained in a manner similar as in ordinary concrete, with tensile forces being sustained by prestressing steel. However, savings in concrete quantity in the range of up to three times in comparison to ordinary concrete are achieved and shear reinforcement is usually completely avoided thank to the shear carrying capacity of the fibres;
- the concept of thin walled structures is particularly gainful for application of UHPFRC, since very thin elements can be conceived, providing local resistances, while a sufficient stiffness and global resistance are assured by the prestressed elements, resulting in significantly decreased weight.

The design and optimization of a ribbed deck slab against local and global failure in bending and punching shear is considered as a case study, showing that:

- thin slabs (40-60 mm) restrained by the ribs can safely resist both bending and punching-shear failure introduced by design wheel-load;
- depending on rib spacing and the span between principal girders i.e. slab supports, a ribbed slab with an equivalent height in the range of 110 to 140 mm can be designed for road bridge applications;
- for the design resistance level of prestressed elements coinciding with strand yielding, a high percentage of the initial element stiffness is maintained at service states;
- investigated ribbed deck allows significant material savings (up to three times), that could not be achieved with ordinary concrete.

8.2 Prospects for further research

UHPFRC being a relatively new building material, lot of subjects still need to be studied for a more rational structural application of UHPFRC. Larger experimental information should be provided both from laboratory tests and from monitoring of real structures behaviour. At the same time, phenomena influencing the structural response of UHPFRC must be theoretically analysed.

Unreinforced members in bending

- it has been demonstrated that the bending response of UHPFRC members can be satisfactorily modelled if the tensile behaviour in the multi-microcracking phase is considered as a homogeneous stress-strains relationship, independent of the size of the structure. However, existing recommendations suggest the multi-microcracking phase to be considered as size dependent, like the macrocracking phase. Further theoretical and experimental investigation should be carried out to allow the size-dependency of the multi-microcracking phase to be assessed.
- up to present, experimental research on beams without ordinary reinforcement mainly focused on very thin elements. In thin members, however, the influences of the microcracking and macrocracking phase on structural response can not be clearly separated. To gain a clearer information, future experimental investigation should consider also deeper beams (>200 mm);
- this would also give the opportunity to study size-effect on bending strength and ductility on a wider range of thicknesses and to provide upper limits for a safe application of UHPFRC elements without additional reinforcement or normal force.

Prestressed members in bending

- the interaction between fibres and prestressing reinforcement in carrying tensile forces after cracking should be studied in more detail: reinforcement is supposed to influence crack propagation as well as the crack pattern along a beam. As a consequence, existing design relationships between crack opening and equivalent tensile strain, developed for members without reinforcement, should be validated in the case of reinforced members;
- the effective importance of fibres contribution in tension should be evaluated as a function of sectional geometry and the amount of prestressing reinforcement;
- bond behaviour between reinforcement and concrete should be investigated in order to assess whether the bending response can be modelled by assuming homogeneous strains and no relative slip between concrete and steel, or the slip with strain localisation in reinforcement should be considered;
- the pre and post-peak compressive behaviour of UHPFRC should be better investigated to allow the ductility of prestressed beams to be predicted;

Design relevant aspects for beams in bending

- if the behaviour of a prestressed beam can be modelled with continuum mechanics (dominating multi-microcracking and no relative slip between reinforcement and concrete), simplified analytical expressions can be provided to predict the behaviour in service and estimate the load bearing capacity of prestressed beams;
- in cases where more refined models are needed and simplified analytical expressions can not be drawn, tabulated data on the bearing capacities of “standardised elements” could be provided as a support for designers. To that aim casting procedures assuring material quality must also be provided;
- service states requirements should more specifically be defined for UHPFRC; e.g. to what extent should multi-microcracking be allowed in service for prestressed and non-prestressed members;
- design prescription for UHPFRC should be associated with proper limits of applicability in terms of material properties, e.g. the slope of the tensile softening curve, and in terms of structural and geometrical properties, e.g. member size, type of prestressing.

Bending behaviour of slabs

- the slabs with larger spans, different boundary conditions and thickness should be investigated experimentally to study if the multi-microcracking develops in a similar manner and to assess the limits for the application of the theory of plasticity in presence of various kinematical mechanisms;
- failure mechanisms should be studied in order to quantify the interaction between the rotation capacity in bending and the geometry of the structure on the development of a plastic-like mechanism;
- the existence of a state of compression in the slab, as it might result from prestressing or from an arching effect in case of constrained boundary conditions, should result in an increase its load-bearing capacity.

Prospects for structural research

On the basis of the results of this work, structural systems made of thin walled UHPFRC elements, with or without prestressing, seem the most promising and feasible applications for UHPFRC in civil engineering. Further optimisations of slab systems seem to be a realistic possibility, both from the point of view of statics and construction. However, it needs to be remembered that particular care should be taken to casting procedure for UHPFRC elements, and further detailing, e.g. joint regions.

Some interesting conceptual approaches might be considered for future work:

- several UHPFRC road bridges have already been realised with box-girder or π -shaped girders and reinforcement-free upper decks. Up to present, quite thick upper decks have been realised in order to carry transversal bending moment: the concept of a transversally ribbed slab might represent an effective alternative solution;
- investigate possibility to exploit UHPFRC as a tensile-force bearing element, disposing a higher amount of concrete in tensile structural part, exhibiting deformations in the range of admissible ultimate tensile deformations prior to failure

It finally has to be considered that thin and light structures as those made possible by UHPFRC could face problems that are usually not associated with concrete but rather with steel structures. Thin walled elements loaded by in-plane compression, like webs or upper slabs in positive moment zones, could be affected by the risk of local instability. Serviceability limit states, in terms of maximal admissible deformation as well as vibration, and problems related to fatigue, might overcome other design requirements: and research effort should also concentrate on these domains.

Bibliographic references

- ACI , *Superplasticizers and Other Chemical Admixtures in Concrete*, SP-119, 665 pp., **1989**.
- ACI , *Building Code Requirements for Structural Concrete*, ACI American Concrete Institute, ACI 318-05, 430 p., USA, **2005**.
- Acker P. , *Why Does Ultrahigh-Performance Concrete (UHPC) Exhibit Such Low Shrinkage and Such Low Creep?*, ACI American Concrete Institute, Special Publication SP-220, pp. 141-154, **2004**.
- Acker P., Behloul M. , *Ductal Technology: a Large Spectrum of Properties, a Wide Range of Applications*, Proceedings of the International Symposium on Ultra High Performance Concrete, Kassel, pp. 11-23, **2004**.
- Acker P., *Swelling, shrinkage and creep: a mechanical approach to cement hydration*, Materials and Structures, Vol. 37, pp. 237-243, May, **2004**.
- Adeline R., Behloul M., Bernier G. , *Reactive powder concrete pretensioned beams*, Post-Tensioned Concrete Structures, FIP Symposium London, 25-27 September, Vol. 2, pp. 592-606, UK, **1996**.
- Adeline R., Cheyrezy M. , *La passerelle de Sherbrooke; premier ouvrage d'art en BPR*, XIIIe Congrès de la FIP, La technique française du béton, AFPC, p.343-347, France, **1998**.
- Akkaya Y., Shah S. P., Ankenman B. , *Effect of Fiber Dispersion on Multiple Cracking of Cement Composites*, Journal of Engineering Mechanics, Vol. 127, Issue 4, pp. 311-316 , April, **2001**.
- Aldea A., Shah S. P., Karr A. , *Permeability of cracked concrete* , Materials and Structures, Vol. 32, No. 5, pp. 370-376, **1999**.
- Alford N. McN., Groves G. W., Double D. D. , *Physical Properties of High Strength Cement Pastes*, Cement and Concrete Research, Vol. 12, pp. 349-358, **1982**.
- Alvarez M., *Einfluss des Verbundverhaltens auf das Verformungsvermögen von Stahlbeton*, IBK-Bericht, rapport de Thèse doctorale, 236, 182pp., Zurich, Switzerland, juillet, **1998**.
- Alvarez M., Köppel S., Marti P. , *Rotation capacity of reinforced concrete slabs*, ACI Structural Journal, Vol. 97, No. 2, pp. 235-242, **2000**.
- Anderson T. L. , *Fracture Mechanics, Fundamental and Applications*, CRC Press, USA, 688, **1995**.
- Apostolos F., Shah S. P. , *Prediction of Ultimate Behavior of Confined Columns Subjected to Large Deformations*, ACI Journal, Vol. 82, Issue 4, pp. 423-433, July-August, **1985**.
- Armelin HS, Bantia N. , *Predicting the flexural post-cracking performance of steel fiber reinforced concrete from the pullout of single fibers*, ACI Materials Journal, Vol. 94, No. 1, pp. 18–31, January, **1984**.
- Aveston J., Kelly A. , *Theory of Multiple Fracture of Fibrous Composites*, Journal of Materials Science, Vol. 8, pp. 352–362, **1973**.
- Aveston J., Cooper G., Kelly A. , *The Properties of Fibre Composites*, Proceedings National Physical Laboratory, IPC Scientific and Technical Press, pp. 15 - 24, Teddington, **1971**.
- Balaguru P., Gambarova P., Rosati G., Schumm C. , *Bond of reinforcing bars and prestressing tendons in HPRFRC matrices*, High Performance Fiber Reinforced Cement Composites 2 (HPRFRC 2), Edited by A. E. Naaman and H. W. Reinhardt, pp. 349-380, Ann Arbor, Michigan, USA, **1995**.

Barros J. A. O., Figueiras J. A. , *Flexural behavior of SFRC : testing and modeling*, ASCE Journal of Materials in Civil Engineering, Vol. 11, USA, November, **1999**.

Barros J. A. O., Gouveia A. V., Cruz P. J. S., Antunes J. A. B., Azevedo A. F. M. , *Design methods for steel fiber reinforced concrete industrial floors*, Third International Conference Construction Materials: Performance, Innovations and Structural Implications, Vancouver, **2005**.

Bartos P., *Review paper: bond in fiber reinforced cements and concretes*, The International Journal of Cement Composites and Lightweight Concrete, Vol. 3, No. 3, pp. 159-177, **1981**.

Bazant Z. P., *Scaling of Structural Strength*, Elsevier, 319, **2005**.

Bazant Z. P., Becq-Giraudon E. , *Effects of Size and Slenderness on Ductility of Fracturing Structures*, Journal of Engineering Mechanics, Vol. 125, No 3, March, **1999**.

Bazant Z. P., *Asymptotic Matching Analysis of Scaling of Structural Failure Due to Softening Hinges. I: Theory*, Journal of Engineering Mechanics, 641-650, June, **2003**.

Bazant Z. P., *Concrete fracture models: testing and practice*, Engineering Fracture Mechanics 69, pp. 165-205, **2002**.

Bazant Z. P., Cedolin L. , *Stability of structures - Elastic, Inelastic, Fracture, and Damage Theories*, **1991**.

Bazant Z. P., Oh B. , *Crack band theory for fracture of concrete*, Materials and Structures, Vol. 16, No. 93, pp 155-177, **1983**.

Bazant Z. P. , *Instability, ductility, and size effect in strain-softening concrete*, Journal of Engineering Mechanics, Vol. 102 (2), pp. 331–344, **1976**.

Bazant Z. P., Li Y-N. , *Stability of Cohesive Crack Model: Part I - Energy Principles*, Journal of Applied Mechanics, 62, pp. 959-964, December, **1995**.

Beeby A. W., Fathibitaraf F. , *Membrane effect in the reinforced concrete frames—a proposal for change in the design of frames structures*, Engineering Structures, Vol. 23, pp. 82–93, **2001**.

Behloul M., Lee K. C. , *Ductal® Seonyu footbridge*, Structural concrete, Journal of the fib, Vol. 4, Nr. 4, pp 195-201, December, **2003**.

Behloul M. , *Analyse et modélisation du comportement d'un matériau à matrice cimentaire fibrée à ultra hautes performances*, E.N.S. Cachan, Doctoral Thesis, 182 p., Cachan, France, December, **1996**.

Bendsoe M. P., *Optimization of Structural Topology, Shape, and Material*, Springer, Heidelberg, **1995**.

Benouaich D., Badoux M., Burdet O. , *Précontrainte extérieure des ponts*, Rapport OFROU, Mandat de recherche 94/98, VSS, 545, 81 p., Zürich, Switzerland, juin, **2000**.

Bill M., Maillart R. , *Robert Maillart*, Verlag für Architektur AG, p. 180, Switzerland, **1947**.

Blais P., Couture M., *Precast, Prestressed Pedestrian Bridge - World's First Reactive Powder Concrete Structure*, PCI Journal, pp 60-71, USA, September-October, **1999**.

Botsis J., *Fracture Mechanics, Lecture notes*, Ecole Polytechnique Fédérale de Lausanne, March, **2004**.

Bouteille S., Resplendino J., *Derniers développements dans l'utilisation des bétons fibrés ultra performants en France*, Actes des journées techniques organisées par l'Association Française de Génie Civil (AFGC):Performance, Durabilité, Esthétique, 19 p., Paris, France, **2005**.

- Brandt A. M.**, *On the optimisation of the fibre orientation in the cement based composite materials*, ACI SP-81, pp. 267-285, USA, **1985**.
- Brühwiler E., Denarié E., Habel K.**, *Ultra-High Performance Fibre Reinforced Concrete for advanced rehabilitation of bridges*, Proceedings Fib Symposium "Keep Concrete Attractive", Budapest, Hungary, Editors G. L. Balasz, A. Borosnyoi, pp. 951-956, Budapest, Hungary, **2005**.
- Bunje K., Fehling E.**, *About shear force and punching shear resistance of structural elements of Ultra High Performance Concrete*, Proceedings of the International Symposium on Ultra High Performance Concrete, pp. 401-411, Germany, **2004**.
- Campione G., La Mendola, L., Sanpaolesi L., Scibilia N., Zingone G.**, *Behavior of fiber reinforced concrete-filled tubular columns in compression*, Materials and Structures, Vol. 35, pp. 332-337, **2002**.
- Carpinteri A., Massabò R.**, *Continuous versus discontinuous bridged crack model for fiber-reinforced materials in flexure*, International Journal of Solids and Structures, Vol. 34 (18), pp.2312-2338, **1997**.
- Carreira D. J., Chu K. H.**, *Stress-strain relationship for plain concrete in compression*, ACI Journal, 82(72), pp 797-804, USA, **1985**.
- Casanova P., Rossi P.**, *Analysis and design of Steel Fiber Reinforced Concrete Beams*, ACI Structural Journal, 94 No. 5, pp 595-602, USA, September - October, **1997**.
- Casanova P.**, *Bétons renforcés de fibres métalliques*, Du matériau à la structure, Dissertation LMT, Cachan, **1996**.
- Casanova P., Rossi P.**, *Analysis of metallic fibre-reinforced concrete beams submitted to bending*, Materials and Structures, 29, 354-361, 07, **1996**.
- Cavill B., Chirgwin G.**, *The world first Reactive Powder Concrete road bridge at Shepherds Gully Creek, NSW*, 21th Biennial Conference of the Concrete Institute of Australia, Brisbane, 17-19 July, 11 pp., Brisbane, Australia, July, **2003**.
- CEB**, *High Performance Concrete - Recommended Extensions to the Model Code 90 - Research Needs*, CEB (Comité euro-international du béton), Thomas Telford Publishing, Bulletin d'information N°228, Lausanne, Switzerland, **1995**.
- CEB**, *CEB-FIP Model Code 1990*, Comité Euro-International du béton (CEB), Thomas Telford Publishing, 460p., London, UK, **1993**.
- Chamberlain B., Chiesl N., Day J.**, *Concrete, A Material for the New Stone Age*, Materials Technology Workshop, University of Illinois, Urbana-Champaign, 95, **1995**.
- Chen W. F.**, *Plasticity in reinforced concrete*, McGraw-Hill., 474 p., **1982**.
- Cheyrezy M., Adeline R., Behloul M.**, *Ultra-high strength concrete for high-rise building columns*, Multi-Purpose High-Rise Towers and Tall Buildings, Proceedings of the Third International Conference "Conquest of vertical space in the 21th century, organised by The Concrete Society, London, 7-10 Octobre, p. 237, Octobre, **1997**.
- Choi C.-K., Park H.-G., Wight J. K.**, *Shear Strength of Steel Fiber-Reinforced Concrete Beams without Web Reinforcement*, ACI Structural Journal, Vol. 104, No. 1, pp. 12-21, January-February, **2007**.
- Chuang E., Ulm F. J.**, *Ductility enhancement of high performance cementitious composites*, CEE Report R02-02, Department of Civil and Environmental Engineering, Massachusetts Institute of Technology, Cambridge, USA, July, **2002**.

Cope R. J., Clark L. A., *Concrete slabs - analysis and design*, Elsevier applied science publishers, 502 pp, London, UK, **1984**.

Cusson D., Paultre P., *Stress-strain model for confined high-strength concrete*, ASCE Journal of Structural Engineering, Vol. 121, pp. 468-477, USA, March, **1995**.

DAfStB, *State-of-the-art Report on Ultra-High-Performance Concrete - Concrete Technology and Design, draft 3*, Deutscher Ausschuss für Stahlbeton/German Association for Reinforced Concrete, Berlin, Germany, **2003**.

Denarié E., Brühwiler E., Znidaric A., Houst Y., Rohleder R., *Full scale application of UHPFRC for the rehabilitation of bridges - from the lab to the field. in European project 5th FWP / SAMARIS - Sustainable and Advanced Materials for Road Infrastructures*, SAMARIS D22, WP 14: HPRCC, <http://samaris.zag.si/>, 60 p., **2005**.

Denarié E., *Matériaux Cimentaires Avancés*, Notes de cours, MCS - ENAC, EPFL, Novembre, **2005**.

Dolo J.-M., Hajar Z., Simon A., Thibaux T., *Une coque mince en béton fibré ultra-performant pour la gare de péage*, Travaux, Vol. 816, pp. 77-80, France, **2005**.

Donza H., Cabrera O., Irassar E.F., *High-strength concrete with different fine aggregate*, Cement and Concrete Research, 32, No. 11, pp. 1755-1761, November, **2002**.

Ductal, Ductal®, URL : <http://www.ductal-lafarge.fr/wps/portal/Ductal>

Eiffage, BSI®/Céracem Références, Eiffage Travaux Publics, 2005, URL: <http://www.bsieiffage.com/>

Elliott K. S., Peaston C. H., Paine K. A., *Experimental and theoretical investigation of the shear resistance of steel fibre reinforced prestressed concrete X-beams - Part II: Theoretical analysis and comparison with experiments*, Materials and Structures, Vol. 35, pp. 528-535, November, **2002**.

Eurocode, *Eurocode 2: Design of concrete structures - Part 1-1: General rules and rules for buildings*, European Committee for Standardization (CEN), Brussels, **2004**.

Ezeldin A. S., Balaguru P. N., *Normal and high-strength fibre-reinforced concrete under compression*, Journal of Materials in Civil Engineering, Vol. 4, No. 4, pp. 415-429, November, **1992**.

Fairbairn E. M. R., Toledo Filho R. D., Formagini S., Rosa J. I., Battista R. C., *Experimental analysis and modeling of ultra high performance fiber reinforced concrete plates*, International Workshop on High Performance Fiber Reinforced Cementitious Composites, Honolulu (USA), May 23, 2005 - May 26, 2005, Honolulu, USA, 05, **2005**.

Fanella D. A., Naaman A. E., *Stress-Strain Properties of Fiber Reinforced Mortar in Compression*, ACI Journal, Proceedings, Vol. 82, No. 4, pp. 475-483, July-August, **1985**.

Fanous F. S., Klaiber F. W., Wassef W. G., *Service Load Test of 1:3 Scale Shell Bridge Model*, ASCE Journal of Structural Engineering, Vol. 122, No. 2, pp. 210-216, February, **1996**.

Fehling E., Bunje K., Leutbecher T., *Design relevant properties of hardened ultra high performance concrete*, Conference on High Performance Concrete (UHPC'04), University of Kassel, Germany, September 13-15 2004, 327-338, September, **2004**.

Fehling E., Schmidt M., Teichmann T., Bunje K., Bornemann R., Middendorf B., *Entwicklung, Dauerhaftigkeit und Berechnung - Ultrahochfester Beton (UHPC)*, Forschungsbericht DFG FE 497/1-1, Schriftenreihe Baustoff- und Massivbau, Band 1, p. 132, Kassel, **2005**.

- Fehling E., Schreiber W., Bunje K., Schmidt M.** , *Brücke aus Ultrahochfestem Beton in Kassel über die Fulda*, Bauingenieur, Vol. 79, pp 350-352, July-August, **2004**.
- Foster S. J., Attard M. M.** , *Strength and ductility of fiber-reinforced high-strength concrete columns*, ASCE Journal of Structural Engineering, Vol. 127, pp. 28-34, USA, **2001**.
- Foster S. J.**, *On Behavior of High-Strength Concrete Columns: Cover Spalling, Steel Fibres and Ductility*, ACI Structural Journal, Vol. 98 n° 4, pp. 583-589, **2001**.
- Fürst A., Marti P.** , *Robert Maillart's Design Approach for Flat Slabs*, ASCE Journal of Structural Engineering, Vol. 123, No. 8, pp. 1102-1110, August, **1997**.
- Ganz H. R., Adeline R.** , *Mini-anchorage for Reactive powder Concrete*, International Conference on New Technologies in Structural Engineering, Lisbon, Portugal, Lisbon, Portugal, July, **1997**.
- Gasparini D. A.**, *Contribution of C. A. P. Turner tot Development of Reinforced Concrete Flat Slabs 1905-1909*, ASCE Journal of Structural Engineering, Vol. 128, No. 10, pp. 1243-1252, USA, October, **2002**.
- Gopalaratnam V. S., Shah S. P.**, *Tensile failure of steel fiber-reinforced mortar*, Journal of Engineering Mechanics, Vol. 113, No. 5, pp. 635-652, USA, **1987**.
- Grabowski E., Gillott J. E.** , *Effect of replacement of silica flour with silica fume on engineering properties of oilwell cements at normal and elevated temperatures and pressures*, Cement and Concrete Research, Vol. 19, Issue 3, pp. 333-343, May, **1989**.
- Granger S., Loukili A., Pijaudier-Cabot G., Chanvillard G.** , *Experimental characterization of the self-healing of cracks in an ultra high performance cementitious material: Mechanical tests and acoustic emission analysis*, Cement and Concrete Research, Vol. 37 (4), pp. 519-527, **2007**.
- Graybeal B. A., Hartmann J. L.** , *Construction of an optimized UHPC vehicle bridge*, Seventh International Symposium on the utilization of High-Strength/High-Performance Concrete, ACI Special Publication SP-228, Vol. 2, pp. 1109-1118, Washington D.C., USA, June, **2005**.
- Graybeal B. A., Hartmann J. L.** , *Ultra-High Performance Concrete Material Properties*, Transportation Research Board Conference, November, **2003**.
- Graybeal B. A.**, *Material Property Characterization of Ultra-High Performance Concrete*, U.S. Department of Transportation, Federal Highway Administration, Report No. FHWA-HRT-06-103, 188 p., August, **2006**.
- Greiner S.** , *Tragverhalten von dünnen Bauteilen aus ultrahochfestem Faserfeinkornbeton*, Beton - und Stahlbetonbau, vol. 102, pp.154-162, Berlin, Germany, March, **2007**.
- Griffith A. A.**, *The phenomenon of rupture and flow in solids*, Phil. Trans. Roy. Soc. London A 221, pp. 163-198, **1921**.
- Guandalini S.**, *Poinçonnement symétrique des dalles en béton armé*, Thèse de doctorat, N. 3380 (2005), 289 pp., Lausanne, Switzerland, décembre, **2005**.
- Gustafsson J., Noghabai K.** , *Steel Fibers as Shear Reinforcement in high Strength Concrete Beams*, International journal of Nordic Concrete Research, Publication No. 22, Norsk Betongforening, Oslo, **1999**.
- Habel K.**, *Structural Behaviour of Elements Combining Ultra-High Performance Fibre-Reinforced Concretes (UHPRFC) and Concrete*, EPFL, Swiss Federal Institute of Technology, Doctoral Thesis, No. 3036, 196 p., Lausanne, Switzerland, July, **2004**.

Harris D. K., *Characterizations of Punching Shear Capacity Of Thin UHPC Plates*, Virginia Polytechnic Institute and State University, USA, December , **2004**.

Hearn N., Morley C. T., *Self-sealing property of concrete—Experimental evidence*, *Materials and Structures*, Vol. 30, No. 7, 404-411, August, **1997**.

Heinz D., Dehn F., Urbonas L., *Fire Resistance of Ultra High Performance Concrete (UHPC) - Testing of Laboratory Samples and Columns under Load*, International Symposium on Ultra High Performance Concrete, pp. 703-716, Kassel, Germany, September, **2004**.

Hill R., *The Mathematical Theory of Plasticity*, Oxford University Press, 368, England, **1998**.

Hillerborg A., Modéer M., Petersson P. , *Analysis of crack formation and crack growth in concrete by means of fracture mechanics and finite elements*, *Cement and Concrete Research*, vol. 6 n°6, pp. 773-781, Lund, Suède, **1976**.

Hillerborg A. , *The theoretical basis of a method to determine the fracture energy G_f of concrete* , *Materials and Structures*, RILEM Technical Committees, Springer Netherlands, Volume 18, Number 106, 291-296, July, **1985**.

Hillerborg A. , *Application of the fictitious crack model to different types of materials*, *International journal of Fracture*, Vol. 51, No. 2, pp. 95-102, Netherlands, **1991**.

Hillerborg A. , *Analysis of fracture by means of the fictitious crack model, particularly for fibre reinforced concrete* , *The International Journal of Cement Composites*, Vol. 2, No. 4, pp. 177-184 , November, **1980**.

Hsu L. S., Hsu T. T. C. , *Stress-strain behavior of steel-fiber high strength concrete under compression*, *ACI Materials Journal*, Vol. 91, No. 4, pp. 448-457, USA, July-August, **1994**.

Irwin G. R., *Onset of Fast Crack Propagation in High Strength Steel and Aluminium Alloys*, *Proceedings of the Sagamore Conference on Strength Limitations of Metals*, Syracuse University Press, Vol. 2, pp. 289-305, **1956**.

Johansen K.W., *Yield-line Theory*, Cement and Concrete Association, 181 p., **1962**.

Johansen K.W., *Yield-line formulae for slabs*, Cement and Concrete Association, **1972**.

JSCE , *Recommendations for Design of UHSFRC Structures*, Japan Society of Civil Engineers, **2004**.

JSCE , *Recommendations for Design and Construction of Ultra High Strength Concrete Structures, Draft*, Japan Society of Civil Engineers, September, **2006**.

JSCE , *Bridges in Japan*, **2003**.

Jungwirth J., Muttoni A. , *Versuche zum Tragverhalten von ultra hochfestem Beton - Kurzfassung* , *IS-BETON*, Bericht 00.02.R8, p. 27, Lausanne, **2005**.

Jungwirth J. , *Zum Tragverhalten von zugbeanspruchten Bauteilen aus Ultra-Hochleistungs-Faserbeton*, Thèse EPFL N°3429, pp. 214, Lausanne, **2006**.

Kabele P. , *Assessment of Structural Performance of Engineered Cementitious Composites by Computer Simulation*, A habilitation thesis, Czech Technical University in Prague, **2000**.

Kabele P., *Analytical modeling and fracture analysis of engineered cementitious composites*, Doctoral Thesis, The University of Tokyo, **1995**.

- Kabele P.**, *New Developments in Analytical Modeling of ECC's Structural Behavior*, Proceedings of the JCI International Workshop on Ductile Fiber Reinforced Cementitious Composites, Tokyo: Japan Concrete Institute, pp. 239-248, Japon, **2002**.
- Kamen A.**, *Comportement au jeune âge et différé d'un BFUP écrouissant sous les effets thermomécaniques*, rapport de Thèse doctorale, EPFL, **2007**.
- Kaptijn N., Blom J.**, *A new bridge deck for the Kaag bridges*, Proceedings of the International Symposium on Ultra High Performance Concrete, Kassel, pp. 49-57, Kassel, Germany, **2004**.
- Keierleber B., Bierwagen D., Fanous F., Phares B., Couture I.**, *Design of Buchana County, Iowa, bridge using Ultra High Performance Concrete and PI girders*, Proceedings of the 2007 Mid-Continent Transportation Research Symposium, 11 pp., USA, August, **2007**.
- Keller T., Schaumann E., Vallée T.**, *Flexural behavior of a hybrid FRP and lightweight concrete sandwich bridge deck*, Composites, Part A 38, pp. 879-889, **2007**.
- Kenel A.**, *Biegetragverhalten und Mindestbewehrung von Stahlbetonbauteilen*, ETH, Dissertation Nr 14874, 115 p., Zürich, Switzerland, December, **2002**.
- Kim Y. Y., Fischer G., Li V. C.**, *Performance of Bridge Deck Link Slabs Designed with Ductile Engineered Cementitious Composite*, ACI Structural Journal, Vol. 101, No. 6, pp. 792-801, November-December, **2004**.
- Kimura H., Ishikawa Y., Kambayashi A., Takatsu H.**, *Seismic behavior of 200 MPa Ultra-High-Strength Steel-Fiber reinforced concrete columns under varying axial load*, Journal of Advanced Concrete Technology, Vol. 5, No. 2, pp. 193-200, Japan, **2007**.
- Kimura H., Ueda T., Ohtake K., Kambayashi A.**, *Structural design of 80-story RC high-rise building using 200 MPa Ultra-High-Strength concrete*, Journal of Advanced Concrete Technology, Vol. 5, No. 2, pp. 181-192, Japan, **2007**.
- König G., Tue N. V., Zink M.**, *Hochleistungsbeton: Bemessung, Herstellung Und Anwendung*, Wiley-VCH, 429, **2001**.
- Kosa K., Naaman A. E.**, *Corrosion of Steel Fiber Reinforced Concrete*, ACI Materials Journal, Vol. 87, pp. 27-37, January, **1990**.
- Kullaa J.**, *Micromechanics of multiple cracking*, Journal of Materials Science, 33, pp. 4225-4234, **1998**.
- Kunieda M., Kamada T., Rokugo K.**, *Size Effects on Flexural Failure Behavior of ECC Members*, Proceedings of the JCI International Workshop on Ductile Fiber Reinforced Cementitious Composites (DFRCC) - Application and Evaluation (DRFCC-2002), Takayama, Japan, Oct. 2002, pp. 229-238, Japon, October, **2002**.
- Larrard F., Sedran T.**, *Optimisation of ultra-high-performance concrete by the use of a packing model*, Cement and Concrete Research, Vol. 24, 6, pp. 997-1008, **1994**.
- Larrard F., Sedran T.**, *Mixture-proportioning of high-performance concrete*, Cement and Concrete Research, Vol. 32, issue 11, pp. 1699-1704, November, **2002**.
- Li V. C.**, *From Micromechanics to Structural Engineering – The Design of Cementitious Composites for Civil Engineering Applications*, Journal of Structural Mechanics and Earthquake Engineering, JSCE, Vol. 10 n° 2, pp. 37-48, **1993**.
- Li V. C.**, *Postcrack Scaling Relations for Fiber Reinforced Cementitious Composites*, Journal of Materials in civil engineering, Vol. 4, Issue 1, pp. 41-57, **1992**.

- Li V. C., Wang Y., Backer S. ,** *A micromechanical model of tension softening and bridging toughening of short random fiber reinforced brittle matrix composites*, Journal of Mechanics and Physics of solids, vol. 39 (5), pp.607-625, **1991**.
- Li V. C., Fischer G. ,** *Reinforced ECC – An Evolution from Materials to Structures*, Proceedings of the 1st fib congress - Concrete Structures in the 21st Century, pp. 105 -122, Osaka, **2002**.
- Li V. C.,** *Integrated structures and materials design*, Materials and Structures, **2006**.
- Li V. C., Mihashi H., Wu H. C., Alwan J. M., Brincker R., Horii H., Leung C. K. Y., Maalej M., Sang H. ,** *Micromechanical models of mechanical response of HPFRCC*, Proceedings High Performance Fiber Reinforced Cement Composites 2. Edition, London, **1996**.
- Li V. C., Mishara D. K., Wu H. C. ,** *Matrix design for pseudo-strain-hardening fibre reinforced cementitious composites* , Materials and Structures, Volume 28, Number 10 , pp. 586-595, December, **1995**.
- Li V. C. ,** *A Simplified Micromechanical Model of Compressive Strength of Fiber-Reinforced Cementitious Composites*, Cement and Concrete Composites, 14, pp. 131 - 141, **1992**.
- Li V. C., Stang H., Krenchel H. ,** *Micromechanics of crack bridging in fiber-reinforced concrete*, Materials and Structures 26, pp. 486-494, **1993**.
- Lim T. Y., Paramasivan P., Lee S. L. ,** *Shear and Moment Capacity of Reinforced Steel Fibre Concrete Beams*, Magazine of Concrete Research, Vol. 39, No. 140, pp. 148-160, **1993**.
- Maalej M., Li V. C. ,** *Flexural strength of fiber cementitious composites*, ASCE Journal of Materials in Civil Engineering, Vol. 6, pp. 390, USA, August, **1994**.
- Maeder U., Lallemand–Gamboa I., Chaignon J., Lombard J. P. ,** *CERACEM a new high performance concrete : characterization and applications*, International Symposium on UHPC, pp. 67 - 76, Kassel, **2004**.
- Markovic I. ,** *High-Performance Hybrid-Fibre Concrete, Development and Utilisation*, PhD Thesis, DUP Science, Delft University Press, 211, Netherlands, January, **2006**.
- Marti P., Pfyl Th., Sigrist V., Ulaga T. ,** *Harmonized Test Procedures for Steel Fiber-Reinforced Concrete*, ACI Materials Journal, Vol. 96, No. 6, pp. 676-686, **1999**.
- Meda A, Plizzari G. ,** *New Design Approach for Steel Fiber-Reinforced Concrete Slabs-on-Ground Based on Fracture Mechanics*, ACI Structural Journal, 101, No.3, pp. 298-303, May-June, **2004**.
- Meda A, Rosati G. ,** *Design and construction of a bridge in very high performance fiber-reinforced concrete*, ASCE Journal of Bridge Engineering, Vol. 8, No.5, pp. 281-287, September-October, **2003**.
- Mehta P. K., Monteiro P. J. M. ,** *Concrete, Microstructure, Properties and Materials*, Mc Graw Hill, 650, **2005**.
- Menn C. ,** *Prestressed Concrete Bridges*, Birkhäuser Verlag AG , pp. 535, Basel, Switzerland, **1990**.
- Menn C.,** *Comparison of costs and material quantities for some new highway bridges in Switzerland*, Prestressed Concrete of Switzerland, pp. 41-48, Wildegg, Switzerland, **1982**.
- Mielenz R. C. ,** *History of chemical admixtures for concrete*, Concrete International, Vol. 6, Issue 4, p. 40-54. , April, **1984**.

- Kunieda M., Kamada T., Rokugo K.** , *Size Effects on Flexural Failure Behavior of ECC Members*, JCI International Workshop on Ductile Fiber Reinforced Cementitious Composites, Takayama, Japan, October, **2002**.
- Morrison J. K., Shah S. P., Jenq Y.-S.** , *Analysis of fiber debonding and pullout in composites*, ASCE Journal of Engineering Mechanics, Vol. 114, No. 2, pp. 277-294, USA, February, **1988**.
- Mudhafar A. G.** , *Moment Capacity of Steel Fiber Reinforced Small Concrete Slabs*, ACI Structural Journal, Vol. 77, No. 4, pp. 247-257, USA, July-August, **1980**.
- Mufti A. A., Newhook J. P.** , *Punching Shear Strength of Restrained Concrete Bridge Deck Slab*, ACI Structural Journal, Vol. 95, pp. 375-381, USA, July, **1998**.
- Muttoni A., Fernández Ruiz M.** , *Shear strength of members without transverse reinforcement as function of the critical shear crack width*, ACI Structural Journal, V. 105, No 2, pp. 163-172, Farmington Hills, USA, March-April, **2008**.
- Muttoni A.**, *Ponts avec un système statique innovant*, SIA D 0160, Progrès dans la conception des ouvrages en béton, pp. 33- 36, Zürich, Switzerland, **1999**.
- Muttoni A.** , *Die Anwendbarkeit der Plastizitätstheorie in der Bemessung von Stahlbeton*, ETH, Dissertation, 159 p., Zürich, Switzerland, May, **1989**.
- Muttoni A., Schwartz J., Thürlimann B.** , *Design of Concrete Structures with Stress Fields*, Birkhäuser Verlag, 143p., Basel, Switzerland, **1997**.
- Muttoni A., Schwartz J.** , *Behavior of Beams and Punching in Slabs without Shear Reinforcement*, IABSE Colloquium, Vol. 62, pp. 703-708, Stuttgart, Germany, **1991**.
- Muttoni A.**, *Die Anwendbarkeit der Plastizitätstheorie in der Bemessung von Stahlbeton*, Birkhäuser Verlag, Institut für Baustatik und Konstruktion ETH Zürich, 176, Basel, Switzerland, **1990**.
- Naaman A. E., Likhitrungsilp V., Parra-Montesinos G.** , *Punching shear response of high-performance fiber-reinforced cementitious composite slabs*, ACI Structural Journal, Vol. 104, No. 2, 170-179 , March-April, **2007**.
- Naaman A. E., Reinhardt H. W., Fritz C., Alwan J. M.** , *Non-linear analysis of RC beams using a SIFCON matrix*, Materials and Structures, vol. 26, pp. 522-531, **1993**.
- Naaman A. E.** , *Tensile strain-hardening FRC composites: Historical evolution since the 1960* , Advances in Construction Materials 2007, Springer Berlin Heidelberg, pp. 181-202, Stuttgart, Germany, **2007**.
- Naaman A. E., Breen J. E.** , *External Prestressing in Bridges*, ACI Special Publication SP-120, 458. p, **1990**.
- Naaman A. E., Reinhardt H. W.** , *Proposed classification of HPFRC composites based on their tensile response*, Materials and Structures, 39, pp. 547-555, **2006**.
- Naaman A. E., Nammur G. G., Alwan J. M., Najm H. S.** , *Fibre Pull-out and Bond Slip. I Analytical Study*, ASCE Journal of Structural Engineering, Vol. 117, No. 9, pp. 2769-2790, **1991**.
- Naaman A. E., Moavenzadeh F., McGarry F. J.** , *Probabilistic Analysis of Fiber-Reinforced Concrete*, Journal of the Engineering mechanics Division : Proceedings of the American Society of Civil Engineers, Vol. 100, Issue EM2, pp. 397-413, April, **1974**.
- Naaman A. E., Chandrangsu K.** , *Innovative bridge deck system using high performance fiber-reinforced cement composites*, ACI Structural Journal, Vol. 101, No. 1, pp. 57-64, January-February, **2004**.

Naaman A. E., Nammur G. G., Alwan J. M., Najm H. , *Fiber pullout and bond slip. II: Experimental validation*, ASCE Journal of Structural Engineering, Vol. 117, No. 9, pp. 2791-2800, September, **1991**.

Nammur G. G., Naaman A. E. , *Bond Stress Model for Fiber Reinforced Concrete Based on Bond Stress-Slip Relationship*, ACI Materials Journal, Vol. 86, No. 1, pp. 45-57, USA, January, **1989**.

Narayanan R., Darwish, I. Y. S. , *Shear in Prestressed Concrete Beams Containing Steel Fibers*, International Journal of Cement Composites and Lightweight Concrete, Vol. 9, No. 2, pp. 81-90, **1987**.

Narayanan R., Darwish, I. Y. S. , *Use of Steel Fibres as Shear Reinforcement*, ACI Structural Journal, Vol. 84, No. 3, pp. 216-227, May-June, **1987**.

Nervi P. L., *Savoir construire*, Editions du Linteau, Paris, 185 p., **1997**.

Nielsen C. V. , *Ultra high strength steel fibre reinforced concrete. Part I: Basic strength properties of Compresit matrix. Part II: Structural applications of Compresit*, Technical University of Denmark, Serie R, n. 323, Denmark, **1995**.

Nielsen M. P., *Limit analysis and concrete plasticity*, CRC Press, 908 p., Copenhagen, Denmark, **1999**.

Nowodvorski H., Rosiak K. , *Ultra-high performance concrete, with ductility. The world's first long-span roof in Ductal - The Joppa Clinker Dome Roof*, 2nd Material Specialty Conference of the Canadian Society for Civil Engineers, Montréal, Quebec, Canada, 5-8 June, 9 pp., Montréal, Canada, June, **2002**.

Ockleston A. J. , *Arching Action In Reinforced Concrete Slabs*, The Structural Engineer, 36, pp. 197-201, London, **1958**.

Okamura H., Ozawa K. , *Mix design for self-compacting concrete*, JSCE, 25, **1995**.

Olesen J. F., *Fictitious crack propagation in fiber reinforced concrete beams*, ASCE Journal of Engineering Mechanics, Vol. 127, No. 3, pp. 272-280, USA, March, **2001**.

Onsager L., *Ann. N.Y. Acad. Sci.* 51, 627 , **1949**.

Ouyang C., Shah S. P., Mura T., Chen J-C. , *Response of Quasi-Brittle Materials Reinforced by Short, Aligned Fibers*, Journal of Engineering Mechanics, 125, Issue 11, pp. 1268-1275 , November, **1999**.

Parant E. , *Mécanismes d'endommagement et comportements mécaniques d'un composite cimentaire fibré multi-échelles sous sollicitations sévères: fatigue, choc, corrosion*, Doctoral thesis, LCPC, 245 p., Paris, France, December, **2003**.

Park H., Chuang E., Ulm F.-J. , *Model-Based Optimization of Ultra High Performance Concrete Highway Bridge Girders*, Massachusetts Institute of Technology, Cambridge, USA, March, **2003**.

Pedersen, C., *New production processes, materials and calculation techniques for fiber reinforced concrete pipes*, PhD thesis, Department of Structural Engineering and Materials, Technical University of Denmark, Series R, No. 14, **1996**.

Pedrazzini A., Pedrazzini E. , *Three New Flaz River Bridges, Samedan, Switzerland*, fib-CH, Structural Concrete in Switzerland, The second fib-Congress, pp. 76-80, Naples, Italy, June, **2006**.

Pentala V., *Concrete and Sustainable Development*, ACI Materials Journal, Vol. 94, No. 5, pp. 409-416, September-October, **1997**.

- Petersson P.**, *Fracture Energy of Concrete: Practical Performance And Experimental Results*, Cement and Concrete Research, Vol. 10, No. 1, pp. 91-101, **1980**.
- Pfyl Th.**, *Tragverhalten von Stahlfaserbeton*, IBK-Bericht, PhD thesis, ETHZ (Swiss Federal Institute of Technology), Nr. 279, 140 p., Zürich, Switzerland, February, **2003**.
- Racky P.**, *Cost-effectiveness and sustainability of UHPC*, Proceedings of the International Symposium on Ultra High Performance Concrete, University of Kassel, pp. 797-805, Kassel, Germany, **2004**.
- Rapoport J., Aldea A., Shah S. P., Ankenman B., Karr A.**, *Permeability of cracked steel fiber-reinforced concrete*, ASCE Journal of Materials in Civil Engineering, Vol. 14, No. 4, pp. 355-358, USA, July-August, **2002**.
- Reda M. M., Shrive N. G., Gillott J. E.**, *Microstructural investigation of innovative UHPC*, Cement and Concrete Research, 29, pp. 323-329, **1999**.
- Redaelli D., Muttoni A.**, *Tensile Behaviour of reinforced ultra-high performance fiber reinforced concrete elements*, fib Symposium, Dubrovnik 2007, pp. 267-274, Dubrovnik, Croatia, May, **2007**.
- Redaelli D.**, *Testing of reinforced high performance fibre concrete members in tension*, Proceedings of the 6th Int. Ph.D. Symposium in Civil Engineering, Zurich 2006, 8 p., Zurich, Switzerland, August, **2006**.
- Reineck K.-H., Greiner S.**, *Entwurf und Konstruktion dichter Heisswasser-Wärmespeicher aus ultrahochfestem Faserfeinkornbeton*, Abschlussbericht BMU 0329606V, Institut für Leichtbau Entwerfen und Konstruieren, Universität Stuttgart, Germany, March, **2004**.
- Reineck K.-H., Greiner S.**, *Tests on ultra-high performance fibre reinforced concrete designing hot-water tanks and UHPFRC-shells*, International Symposium on UHPC, No.3, pp 361-374, Kassel, Germany, 08, **2004**.
- Resplendino J.**, *First recommendations for Ultra-High Performance Concretes and examples of applications*, Proceedings of the International Symposium on Ultra High Performance Concrete , pp. 79-89, Kassel, Germany, **2004**.
- Resplendino J., Bouteille S.**, *Construction de deux ponts routiers en béton fibré ultra performant (BFUP)*, Bulletin Ouvrages d'Art, SETRA - Service d'études techniques des routes et autoroutes, Vol. 53, pp. 2-11, France, November, **2006**.
- Resplendino J., Petitjean J.**, *Ultra-High-Performance Concrete : First Recommendations and Examples of Application*, The fifth International Symposium on High Performance Computing, 18 p., Tokio-Odaiba, Japan, october, **2003**.
- Resplendino J., Bouteille S.**, *Tabliers de ponts réalisés en béton fibré ultra performant (BFUP) et en matériau composite (fibre de verre)*, Actes des journées techniques organisées par l'Association Française de Génie Civil (AFGC): Le développement durable, une exigence d'innovation pour le génie civil, 15 p., Paris, France, mars, **2007**.
- Richard P., Cheyreyz M.**, *Composition of Reactive Powder Concretes*, Cement and Concrete Research, vol. 25, no. 7, pp 1501-1511, USA, October, **1995**.
- RILEM**, *RILEM TC 162-TDF: Test and Design Methods for Steel Fibre Reinforced Concrete*, Materials and Structures, Vol. 35, pp 262-278, June, **2002**.
- RILEM**, *Round-robin analysis of the RILEM TC 162-TDF beam-bending test: Part 1 -Test method evaluation*, Materials and Structures, 36, pp. 609-620, November , **2003**.

RILEM, *Round-robin analysis of the RILEM TC 162-TDF beam-bending test: Part 2 - Approximation of δ from CMOD response*, Materials and Structures, 36, pp. 621- 630, November, **2003**.

RILEM, Test and design methods for steel fibre reinforced concrete: σ - ϵ , design method, Materials and Structures 33(226): 75–81, **2000**.

Romualdi J. P., Mandel J.A. , *Tensile strength of concrete affected by uniformly distributed and closely spaced short lengths of wire reinforcement*, Journal of the American Concrete Institute, 61, No. 6, pp. 657-671, June, **1964**.

Rossi P. , *High Performance Multimodal Fiber Reinforced Cement Composites (HPMFRCC): The LCPC Experience*, ACI Materials Journal, 94, pp 478-483, Detroit, USA, November - December, **1997**.

Rossi P. , *Ultra-high performance fibre reinforced concretes (UHPFRC): an overview*, BEFIB'2000, Proceedings of the Fifth International RILEM Symposium on Fibre-Reinforced Concretes (FRC), Ed. by P. Rossi and G.Chanvillard, pp 87-100, Lyon, France, September, **2000**.

Rossi P., Arca A., Parant E., Fakhri P. , *Bending and compressive behaviors of a new cement composite*, Cement and Concrete Research, 35, pp.27-33, **2005**.

Rossi P., Acker P., Malier Y. , *Effect of steel fibres at two different stages: the material and the structure*, Materials and Structures, Vol. 20, pp 436-439, **1987**.

Roy D. M., Gouda G. R. , *High strength generation in cement pastes*, Cement and Concrete Research, Vol. 3, pp 807-820, **1973**.

Roy D. M., Gouda G. R., Bobrowsky A. , *Very high strength cement pastes prepared by hot pressing and other high pressure techniques*, Cement and Concrete Research, Vol. 2, pp 349-366, USA, **1972**.

Sargin M., Handa V. , *A general formulation for the stress-strain properties of concrete*, Solid Mechanics Division, University of Waterloo, Waterloo, Rep. No. 3, pp. 1-27, Canada, May, **1969**.

Sato Y., Van Mier J. G. M., Walraven J. C. , *Mechanical characteristics of multi-modal fiber reinforced cement based composites* , Fifth RILEM Symposium on Fibre-Reinforced Concretes , pp. 791-800, Lyon, France, September, **2000**.

Satoshi K., Hidemi N., Akira O. , *Influence of Aggregate Properties on High Strength Concrete*, Journal of Research of the Taiheiyō Cement Corporation, 146, pp. 21-32, Japan, **2004**.

Schmidt M., Fehling E., Geisenhanslüke C. , *Ultra High Performance Concrete (UHPC)*, International Symposium on Ultra High Performance Concrete, Kassel, **2004**.

Schmidt M., Fehling E. , *Ultra-High-Performance Concrete: Research, Development and Application in Europe* , Seventh International Symposium on the Utilization of High-Strength/High-Performance Concrete that was held in Washington, D.C., USA, June 20-24, 2005, pp.51-78, June, **2005**.

Scrivener K., *The Microstructure of Concrete*, Materials Science of Concrete I, Ed. by J. Skalny, American Ceramics Society, Westerville, OH, pp 127-161, USA, **1989**.

Scrivener K., *Advanced Cementitious Materials*, Lecture Notes, Ecole Polytechnique Fédérale de Lausanne, Switzerland, **2005**.

SETRA, AFGC, *Béton fibrés à ultra-hautes performances, (Ultra high performance fibre-reinforced concretes)*, recommandations provisoires, 152 p., France, Janvier, **2002**.

- Shah S. P.**, *Do Fibers Increase the Tensile Strength of Cement-Based Matrixes?*, ACI Materials Journal, 88, pp. 595-602, November-December, **1991**.
- Shah S. P., Naaman A. E., Moreno J.**, *Effect of confinement on the ductility of lightweight concrete*, International Journal of Cement Composites and Lightweight Concrete, Vol. 5, Issue 1, pp. 15-25, February, **1983**.
- SIA**, *SIA 262 - Construction en béton*, 94p., Zurich, Switzerland, **2003**.
- SIA**, *SIA 260 - Bases pour l'élaboration des projets de structures porteuses*, 44p., Zurich, Switzerland, **2003a**.
- SIA**, *SIA 261 - Actions sur les structures porteuses*, 114p., Zurich, Switzerland, **2003b**.
- Sigmund O.**, *A 99 line topology optimization code written in Matlab*, Structural and Multidisciplinary Optimization, 21, pp.120-127, **2001**.
- Simon A., Hajar Z., Lecointre D., Petitjean J.**, *Realization of two bridges with Ultra-High-Performance Fibre-Reinforced Concrete*, 6th International symposium on Utilization of High Strength / High Performance Concrete, Leipzig, Germany, 2002, pp. 753-768, June, **2002**.
- Simon A.**, *Plaques minces en BFUP, communication interne*, France, **2006**.
- Sorelli L., Davila R., De Jesus M., Ulm F.-J., Toutlemonde F.**, *Optimal Design of UHPC Highway Bridges Based on Crack Criteria*, The 5th international Conference on Concrete under Severe Conditions of Environment and Loading (CONSEC'07), pp. 1085-1092, **2007**.
- Spasojevic A.**, *Possibilities for Structural Improvements in the Design of Concrete Bridges*, Proceedings of the 6th Int. PhD Symposium in Civil Engineering, Zurich 2006, 8 p., Zurich, Switzerland, 8, **2006**.
- Stang H., Shah S. P.**, *Pullout problem : stress versus fracture mechanical approach*, Journal of Engineering Mechanics, 116, No. 10, 2136-2150, **1990**.
- Stang H., Li V. C.**, *Classification of Fibre Reinforced Cementitious Materials for Structural Applications*, 6th RILEM Symposium on fibre reinforced concrete (FRC), - BEFIB 2004, Varenna, Italy, pp. 197-218, September, **2004**.
- Stang H., Shah H. R.**, *Failure of Fibre-reinforced Composites by Pull-Out Fracture*, Journal of Materials Science, 21, pp.953-957, **1986**.
- Stang H., Li V. C., Krenchel H.**, *Design and Structural applications of stress-crack width relations in fibre reinforced concrete*, Materials and Structures, 28, 210-219, **1995**.
- Stang H., Olesen J. F.**, *On the interpretation of bending tests on FRC-materials*, Proceedings FRAMCOS-3, volume 1, Fracture Mechanics of Concrete Structures, (H. Mihashi and K. Rokugo, Editors) Aedificatio Publishers (D-79104 Freiburg, Germany) 511-520, **1998**.
- Stiel T., Karihaloo B., Fehling E.**, *Effects of Casting Direction on the Mechanical properties of CARDIFRC*, International Symposium on Ultra High Performance Concrete, pp.481-493, Kassel, Germany, September, **2004**.
- Sugano S., Kimura H., Shirai K.**, *Study of new RC structures using Ultra-High-Strength Fiber-Reinforced Concrete (UFC) - The challenge of applying 200 MPa UFC to Earthquake resistant building structures*, Journal of Advanced Concrete Technology, Vol. 5, No. 2, pp. 133-148, Japan, **2007**.
- Swamy R. N., Mangat P. S.**, *A theory for the flexural strength of steel fiber reinforced concrete*, Cement and Concrete Research, Vol. 3, Issue 4, pp. 413-427, May, **1974**.

Swamy R. N., Jones R., Chiam A. T. P. , *Influence of Steel Fibers on the Shear Resistance of Lightweight Concrete I-Beams*, ACI Structural Journal, Vol. 90, Issue 1, pp. 103-114, January-February, **1993**.

Tada H., Paris P. C., Irwin G. R. , *The Stress Analysis of Cracks Handbook*, Paris Productions Incorporated, St. Louis, Missouri, USA, December, **1985**.

Taerwe L., *Influence of Steel Fibers on Strain-Softening of High-Strength Concrete*, ACI Materials Journal, Vol. 89 (1), pp. 54-60, January, **1993**.

Taerwe L., Van Gysel A. , *Influence of steel fibers on design stress-strain curve for high-strength concrete*, ASCE Journal of Engineering Mechanics, Vol. 122, pp. 695-704, USA, Août, **1996**.

Tailhan J.-L., Rossi P., Parant E., Clément J.-L., Arca A. , *Comportement en traction uni-axial d'un composite cimentaire à écrouissage positif à partir d'une approche inverse, Caractérisation du comportement en traction uniaxiale*, Bulletin des Laboratoires des Ponts et Chaussées, LCPC, n° 248, pp 35-48, Paris, **2003**.

Tanaka Y., Musya H., Ootake A., Shimoyama Y., Kaneko O. , *Design and construction of Sakata-Mirai footbridge using Reactive Powder Concrete*, Proceedings of the 1st FIB Congress 2002: Concrete Structures in the 21st Century, Osaka, Japan, pp. 417-424, Osaka, Japan, **2002**.

Thibaux T., Tanner J. A. , *Constructions des premières ponts français en béton fibré à ultra haute performance*, Proceedings of the 1st fib congress - Concrete Structures in the 21st Century, pp. 139 - 144, Osaka, **2002**.

Thorenfeldt E., Tomaszewics A., Jensen J. J. , *Mechanical properties of high-strength concrete and application in design*, Proceeding on Utilisation of High Strength Concrete, Stavanger, Norway, **1987**.

Timoshenko S., Woinowsky-Krieger S. , *Theory of Plates and Shells*, McGraw-Hill., Second Edition, 580 p., **1959**.

Tjiptobroto P., Hansen W. , *Tensile Strain Hardening and Multiple Cracking in High-Performance Cement-Based Composites Containing Discontinuous Fibres*, ACI Materials Journal, Vol. 90, 1, pp. 16-25, January-February , **1993**.

Toutlemonde F., Légeron F., Brazillier D. , *Rational structural design using HPC in some typical bridge structures*, Proceedings 6th international symposium on utilization of high strength / high performance concrete, pp. 797-812, Leipzig, **2002**.

Toutlemonde F., Légeron F., Piquet A. , *Valorisation des bétons à hautes et très hautes performances dans les structures d'ouvrages d'art*, Bulletin des Laboratoires des Ponts et Chaussées, 246-247, pp. 57-72, **2003**.

Toutlemonde F., Boulay C., Sercombe J., Le Maou F., Renwez S., Adeline R. , *Characterization of Reactive Powder Concrete (RPC) in Direct Tension at Medium to High Loading rates*, 2nd International Conference on Concrete under Severe Conditions : Environment and Loading, CONSEC'98, vol. 2, pp. 887-896, Tromsø, Norvège, June, **1998**.

Toutlemonde F., Renaud J.-C., Lauvin L., Brisard S., Resplendino J. , *Local bending tests and punching failure of a ribbed UHPFRC bridge deck*, Fracture Mechanics of Concrete and Concrete Structures FraMCos, Editors A. Carpinteri, P. Gambarova, G. Ferro, G. Plizzari, Vol. 3, pp. 1481-1489, **2007**.

Toutlemonde F., Renaud J.-C., Lauvin L., Behloul M., Simon A., Vildaer S. , *Testing and analysing innovative design of UHPFRC anchor blocks for post-tensioning tendons*, Fracture

Mechanics of Concrete and Concrete Structures FraMCoS, Editors A. Carpinteri, P. Gambarova, G. Ferro, G. Plizzari, Vol. 2, pp. 1193-1201, **2007**.

Toutlemonde F., Lauvin L., Renaud J.-C., Kretz T., Brisard S. , *Fatigue Performance of an UHPFRC ribbed slab applied as a road bridge deck verified according to the Eurocodes*, Concrete under Severe Conditions : Environment & Loading, CONSEC'07, Editors F. Toutlemonde et al. , pp. 1191-1200, Tours, France, **2007**.

Toutlemonde F., Resplendino J., Sorelli L., Bouteille S., Brisard S. , *Innovative design of ultra high-performance fiber reinforced concrete ribbed slab: experimental validation and preliminary detailed analyses*, Seventh International Symposium on the utilization of High-Strength/High-Performance Concrete, ACI Special Publication SP-228, Vol. 2, pp. 1187-1205, USA, June, **2005**.

Tue N. V., Simesch G., Schneider H., Schmidt D. , *Bearing Capacity of Stub Columns made of NSC, HSC and UHPC confined by a Steel Tube*, Proceedings of the International Symposium on Ultra High Performance Concrete, University of Kassel, pp. 339-350, Kassel, Germany, September, **2004**.

Tue N. V., K uchler M., Schenck G., J rger R. , *Application of UHPC filled tubes in buildings and bridges*, Proceedings of the International Symposium on Ultra High Performance Concrete, University of Kassel, pp. 807-817, Kassel, Germany, **2004**.

Ulfkjaer J. P., Krenk S., Brincker R. , *Analytical model for fictitious crack propagation in concrete beams*, ASCE Journal of Engineering Mechanics, Vol. 121, pp. 7-14, USA, January, **1995**.

Ulm F.-J., Constantinides G., Heukamp H. , *Is concrete a poromechanics material? - A multiscale investigation of poroelastic properties*, Materials and Structures, Vol. 37 , pp. 43-58, January-February, **2004**.

Ulm F.-J. , *Ductility Enhancement of High Performance Cementitious Composites and Structures*, Department of Civil and Environmental Engineering, MIT, Cambridge, USA, July, **2002**.

USDOT , *High Performance Concrete Structural Designers' Guide*, U.S. Department of Transportation, Federal Highway Administration, March, **2005**.

Van Mier J. G. M., *High Performance Fibre Reinforced Concrete - Faserbewehrter Hochleistungsbeton*, Holcim Betontagung 2003, **2003**.

Van Mier J. G. M. , *Fracture Processes of Concrete - Assessment of Material Parameters for Fracture Models*, 448 p., Boca Raton, USA, **1997**.

Van Mier J. G. M., *Strain-softening of concrete in uniaxial compression - Report of the round robin test carried out by RILEM TC 148-SSC*, Materials and Structures, Vol. 30, pp. 195-209, May, **1997**.

Vaz Rodrigues R. , *Shear Strength of Reinforced Concrete Bridge Deck Slabs*, EPFL, PhD thesis, n  3739, 289 p., Lausanne, Switzerland, March, **2007**.

Vernet C., *Evolution chimique et propri t s m caniques des b tons*, Ecole th matique CNRS - ATILH: Physique, chimie et m canique des mat riaux cimentaires, La Colle-sur-Loup, Octobre, **2003**.

Vicenzino E., Culham G. , *First Use of UHPFRC in Thin Precast Concrete Roof Shell for Canadian LRT Station*, PCI Journal, pp.60-67, USA, 09, **2005**.

VSS, *Norme Suisse SN 640 201, Profil G om trique type – Dimensions de base et gabarit des usagers de la route*, VSS – Union des professionnels suisses de la route, Zurich, **1992**.

Walraven J. C., *Design with ultra high strength concrete: basics, potential and perspectives*, Proceedings of the International Symposium on Ultra High Performance Concrete , pp. 853-864, Kassel, Germany, **2004**.

Wittmann F. H. , *Crack formation and fracture energy of normal and high strength concrete*, Sadhana, India, Vol. 27, part 4, pp. 413 - 423, August, **2002**.

Yudofreund M., Odler I., Brunauer S. , *Hardened Portland Cement Pastes of Low Porosity, I. Materials and Experimental Methods*, Cement and Concrete Research, Vol. 2, No. 3, pp 313-330, USA, May, **1972**.

Yudofreund M., Hanna K. M., Skalny J., Odler I., Brunauer S. , *Hardened Portland Cement Pastes of Low Porosity, V. Compressive Strength*, Cement and Concrete Research, Vol. 2, pp 731-743, USA, **1972**.

List of Abbreviations

materials:

DSC	Densified Small particle Concrete
ECC	Engineered Cementitious Composites
FRC	Fibre Reinforced Concrete
HPC	High-Performance Concrete
HPFRC	High-Performance Fibre Reinforced Concrete
HPRC	High-Performance Reinforced Concrete
HSC	High-Strength Concrete
MDF	Macro Defect Free concretes
NSC	Normal Strength Concrete
RC	Reinforced Concrete
RPC	Reactive Powder Concrete
UHPC	Ultra-High Performance Concrete
UHPRC	Ultra-High Performance Fibre-Reinforced Concrete
CH	Calcium Hydroxide, portlandite, $Ca(OH)_2$
C-S-H	Calcium Silicate Hydrate, $3CaO \cdot 2SiO_2 \cdot 4H_2O$

mechanics:

CMO	Crack Mouth Opening
CMOD	Crack Mouth Opening Displacement
COD	Crack Opening Displacement
FCM	Fictitious Crack Model
FEM	Finite Element Method
FM	Fracture Mechanics
LEM	Linear Elastic Mechanic
SLS	Serviceability Limit State
ULS	Ultimate Limit State

institutions and projects:

AFGC	Association Française de Génie Civil
DAfStB	Deutscher Ausschuss für Stahlbeton / German Association for Reinforced Concrete
LCPLC	Laboratoire Central des Ponts et Chaussées
RILEM	Réunion Internationale des Laboratoires et Experts des Matériaux, systèmes de construction et ouvrages (The International Union of Laboratories and Experts in Construction Materials, Systems and Structures)
SIA	Swiss Society of Engineers and Architects
MIKTI	French national project on steel-concrete composite bridge innovation
NR2C	New Road Construction Concept
SAMARIS	Sustainable and Advanced MATERIALS for Road InfraSTRUCTure

List of Notations:

Capital Greek letters

Δ	variation
Δf	variable non-linear hinge length
Δl	length increase
Δl_{fo}	elongation corresponding to strain level ε_u
Δl_m	elongation of measurement base
ΔU_f	increase in fibre elastic strain energy
ΔU_{f-mc}	increase in fibre strain energy during first crack opening
ΔU_{f-mu}	increase in fibre strain energy during macrocracking
ΔU_{fr}	frictional energy, dissipated by matrix sliding over the fibres
ΔU_m	decrease in matrix strain energy
Π	potential energy

Small Greek letters

α	relative crack length (ratio of crack length to element thickness); fibre orientation factor used in stress-crack opening law
α_{Qi}	concentrated traffic load factor
α_{qi}	distributed traffic load factor
β	parameter relating crack opening and fictitious sectional deformation; parameter used in Carreira's concrete compressive law
γ	weight per unit volume; parameter used in stress-crack opening law
γ_{bf}	partial safety factor for UHPFRC
γ_c	partial safety factor for concrete
γ_G	partial safety factor for permanent load
γ_Q	partial safety factor for variable load
γ_{uhpfrc}	weight per unit volume of UHPFRC
δ	displacement; fibre pullout length
δ_{el}	maximal linear-elastic displacement
δ_i	arbitrary displacement
δ_{i0}	displacement of the element without crack or macrocrack
δ_{if}	additional displacement of the element due to crack or macrocrack opening
$\delta_{L/2}$	mid-span displacement
δ_p	crack opening corresponding to maximal crack-bridging stress
δ_{pmax}	displacement at maximal force
$\delta_{pl,max}$	displacement under maximal pseudo-plastic load
δ_{res}	residual displacement
δ_x	displacement at point x
ε	strain
ε_c	concrete compressive strain
ε_{c1}	concrete compressive strain at maximal stress
ε_{cc}	creep strain in concrete
ε_{cm}	strain in concrete matrix
ε_{cr}	“fictitious” strain related to crack mouth opening
ε_{cs}	shrinkage strain in concrete
ε_{el}	maximal elastic tensile strain
ε_{equ}	equivalent bending strain
$\varepsilon_{fct}, \varepsilon_u$	tensile strain attained at tensile strength, f_{ct} , before softening
ε_r	residual strain
ε_s	strain in reinforcement steel
ε_t	tensile strain
ε_{uk}	ultimate strain of prestressing cable
ε_{wi}	“fictitious” strain related to crack opening
ε_{sx}	strain in x direction
η	reduction factor for fibre volume fraction, V_f ; normalised compressive strain ($\varepsilon_c / \varepsilon_{c1}$)
η_i	relative density parameter (pseudodensity)
θ	rotation
ν	Poisson's ratio

ξ	ordinate in direction of y axis, with the origin at the neutral axis
ρ	radius
ρ_{xx}	radius of the beam's mid-plane
σ	normal stress
σ_l	stress at the point of slope change of the softening curve
σ_c	concrete compression stress
$\sigma_{c,pl}$	minimal compressive strength attained in bending at the end of pseudo-plastic phase
σ_{equ}	equivalent bending stress
σ_p	stress in prestressing strand; average residual tensile stress transferred by the crack
$\sigma_{p,0}$	initial stress in prestressing strand
$\sigma(w)$	stress-crack opening relationship
σ_{xx}	normal stress in x direction
τ	shear stress
τ_f	frictional stress at the matrix-fibre interface
ϕ	fibre orientation angle with respect to crack
ϕ_p	diameter of prestressing strand
χ	curvature at a section
χ_c, χ_{cr}	curvature at a cracked section
χ_{el}	elastic curvature at a section
$\chi_{el,max}$	curvature at a section at the beginning of pseudo-plastic tensile behaviour
χ_m	average curvature
χ_{pl}	curvature at a section with pseudo-plastic tensile behaviour
$\chi_{pl,max}$	curvature at a section at the end of pseudo-plastic tensile behaviour
$\chi_{pl,u}$	curvature at a cracked section in bending softening regime at $M=M_R$
χ_r	middle plane curvature in radial direction
χ_t	middle plane curvature in tangential direction
χ_{unload}	curvature during inelastic unloading
ψ	slab rotation
φ	rotation

Capital Roman letters

A	cross-section area
A_e	work of external forces
A_i	work of internal forces
A_p	cross-section area of prestressing strand
C	structural compliance
C_1	parameter of the bilinear stress-crack opening curve
C_2	initial slope of the stress-crack opening curve
CV	stress variation coefficient
D	diameter; flexural plate rigidity; parameter in Sargin's concrete compressive law
E	total energy; Young's modulus (modulus of elasticity)
E^*	modulus of elasticity at unloading of multi-microcracked concrete prior to softening
$E_{1,2}$	energy needed to grow the first microcrack sufficiently to reach the softening
E_c	concrete modulus of elasticity (initial tangential stiffness in uniaxial loading)
$E_{c,l}$	secant modulus of compressive stress-strain curve, corresponding to maximal stress
E_d	modulus of elasticity at unloading of multi-microcracked concrete
E_f	fibre modulus of elasticity
EI	elastic bending stiffness
E_i	energy needed for the formation of new microcrack
EI_d	unloading bending stiffness
EI_{sec}	secant bending stiffness
E_{licr}	total energy that can be released from the surrounding material
F	load vector; initial slope of the stress-crack opening relationship ($d\sigma/dw$)
G	energy release rate
G_F	fracture energy
$G_{F,II}$	fracture energy of the second failure mode, released during debonding at the fibre-matrix interface
$G_{F,m}$	matrix fracture energy
$I_{z,el}$	moment of inertia of elastic uncracked section
J	contour integral
K	global stiffness matrix ; fibre orientation coefficient
K_I	stress intensity factor for mode I

Notations

K_{σ}	damage governing variable
K_d	stiffness of microcracked beam
K_{el}	stiffness of elastic beam
K_{sec}	secant stiffness of microcracked beam
L	span length
L_{eq}	equivalent specific length
L_{moy}	average span length
M	bending moment
\overline{M}	unit moment function
$M_{el,max}$	maximal bending moment in elastic regime
M_m	moment at the mid-span of clamped beam
$M_{pl,max}$	maximal bending moment in pseudo-plastic regime
M_R	resistant bending moment
M_{Rd}	design value of resistant bending moment
M_s	moment at the clamped beam edge
N	normal force; number of elements
P	force
$P_{el,max}$	maximal force load sustained in linear-elastic regime
P_{max}	maximal force load
$P_{pl,max}$	maximal force load sustained in elastic-pseudo-plastic regime
Q	shear force acting on a slab section
Q_{ki}	axle (traffic) load, characteristic value
RI	fibre reinforcement index
S	area of fibre effect (contributing to shear strength)
U	displacement vector; strain energy
U_{db}	debonding energy (at matrix-fibre interface)
V	shear force; volume
V^*	volume of zero density
V_0	initial volume
V_{cr}	critical fibre volume fraction (minimal V_f required to enable multi-microcracking to occur)
V_{ef}	effective fibre volume fraction
V_f	fibre volume fraction (content of fibres by volume); shear force carried by fibres
V_m	matrix volume fraction ($1 - V_f$)
V_R	resistant shear force
V_{Rd}	shear force carried by concrete
V_u	ultimate shear strength
W_s	work required for creation of crack surface

Small Roman letters

a	crack length
a_{χ}	coefficient of the curvature function in crack disturbed region
b	cross-section width
b_0	perimeter of the critical punching-shear section
b_{χ}	coefficient of curvature function in crack disturbed region
b_{eff}	effective (participating) slab width
b_d	deck width
b_r	rib spacing
b_{rw}	rib width
c_{χ}	coefficient of the curvature function in crack disturbed region
d	effective beam depth
d_f	fibre diameter
d_g	maximal aggregate size
d_{g0}	reference aggregate size in critical shear crack criterion
e	amount of energy
f	coefficient of fibre inclination
f_c	concrete compressive strength
f_{ck}	concrete characteristic compressive strength
f_{cm}	concrete mean compressive strength
f_{ct}	concrete tensile strength
$f_{ct,m}$	matrix tensile strength
f_{equ}	equivalent bending strength
$f_{p0.1k}$	yielding strength of prestressing strand
f_{pd}	design yielding strength of prestressing strand
f_{pk}	strength of prestressing strand

$f_{s,f}$	fibre strength
f_y	yielding strength
g_{pl}	weight of prestressing strand per unit length
h	element height
h_l	neutral axis position in a section with pseudo-plastic yielding
$h_{l,d}$	neutral axis position in a section during inelastic unloading
h_{equiv}	equivalent height of concrete cross section
h_m	distance of measurement device from the specimen surface
h_{ts}	slab thickness
k	parameter used in concrete compressive curve proposed by Thorenfeldt et al.
k_0	initial stiffness of the elastic solid
k_i	local stiffness matrix
l	length
l_{bf}	debonding length of a single fibre
l_c	characteristic length, used to relate stress-crack opening to stress-strain tensile law
l_{ch}	characteristic length (function of material fracture and mechanical properties)
l_{cr}	critical length
$l_{i,cr}$	length of the disturbed region around the crack
l_f	fibre length
l_m	length of measurement base
l_w	length relating crack opening and fictitious plane deformation
m	bending moment per unit width
m_R	resistant plastic moment per unit width
m_r	bending moment in radial direction, per unit width
m_{Rd}	design value of resistant plastic moment per unit width
m_t	bending moment in tangential direction, per unit width
n_{ct}	ratio of compressive and tensile strength
n_{jct}	ratio of bending strength before tensile softening to tensile strength
$n_{li,cr}$	ratio of crack length and crack disturbed region
p	probability density function; parameter in stress-crack opening law
q	distributed force load
q_{lpl}	maximal distributed force load prior to opening of first macrocrack in statically indeterminate system
$q_{el,max}$	maximal distributed force load sustained in linear-elastic regime
q_{ki}	distributed traffic load, characteristic value
$q_{pl,max}$	maximal distributed force load sustained in elastic-pseudo-plastic regime
q_{M1max}	minimal q for which the resistant moment is reached in one section in statically indeterminate system
q_{max}	maximal distributed force load
r	radius; normalised crack opening
r_a	radius of load-introduction zone on the slab surface
r_b	radius of a circular slab
r_c	radius of load-introduction surface in middle plane
r_r	middle-plane radius in radial direction
r_t	middle-plane radius in tangential direction
r_x	middle-plane radius in x -direction
r_y	middle-plane radius in y -direction
s	non-linear hinge length
t	time
u	longitudinal displacement
u_i	local displacement vector
v	average shear stress; vertical displacement
w	crack opening; vertical displacement in topological optimisation procedure
w_0	initial vertical displacement in topological optimisation procedure
w_c	crack band width
w_{CMOD}	crack mouth opening displacement
w_{cr}	critical crack opening
w_i	arbitrary crack opening
w_{max}	maximal crack opening
$w_{n,w}$	parameter in stress-crack opening curve
x	axis in Cartesian coordinate system, along beam length
x_0	neutral axis position
x_{el}	length of linear-elastic region
y	axis in Cartesian coordinate system
y_{hel}	distance between outermost tensile fibre and section centroid
y_w	axis along crack length
z	axis in Cartesian coordinate system; position of fibre centroid with respect to crack face

Appendices : Table of contents

Appendix M1:

Behaviour of beam with pseudo-plastic tensile yielding	M1.1
M1.1 Problems involved	M1.1
M1.2 Section equilibrium	M1.1
M1.3 Elements behaviour	M1.3
M1.4 Inelastic unloading	M1.4

Appendix M2:

Behaviour of beam with a fictitious crack	M2.1
M2.1 Problems involved	M2.1
M2.2 Static equilibrium of the cracked section	M2.1
M2.3 Fracture energy of a crack in bending	M2.4
M2.4 Continuous curvature function	M2.5
M2.5 Algorithm for energy balance	M2.6
M2.6 FEM model	M2.8

Appendix T1:

Testing of thin UHPFRC elements	T1.1
T1.1 Problem statement and objectives	T1.1
T1.2 Testing program and preparation of the specimens	T1.2
T1.3 Thin beams in three-point bending	T1.3
T1.4 Thin slabs failing in bending	T1.18
T1.3 Thin slabs failing in punching shear	T1.28

Appendix M1:

Behaviour of beam with pseudo-plastic tensile yielding: equation development

M1.1 Problems involved

Increasing bending deformations beyond the maximal elastic level, UHPFRC member sustains microcracking that is modelled as pseudo-plastic behaviour. This behaviour causes asymmetrical distribution of stresses over section height (Figure A1.1). The applied criterion for plastic yielding in the developed equations is $\sigma_t = \sigma_{xx} = f_{ct}$. Development of analytical formulation of force-deformation relationships for a section and beam with pseudo-plastic yielding in tension is given in the present appendix. The inelastic behaviour of macrocracked region is considered in § 1.4.

M1.2 Section equilibrium in pseudo-plastic tensile yielding

From the equilibrium of the sectional forces, the force and deformation are uniquely related by the given constitutive relationships (§ 4.3.3).

$$\begin{aligned} \sum M &= 0 \Rightarrow M = M(\kappa, h_1), \\ \sum X &= 0 \Rightarrow h_1 = h_1(\kappa) \\ &\Rightarrow M = M(\kappa) \end{aligned}$$

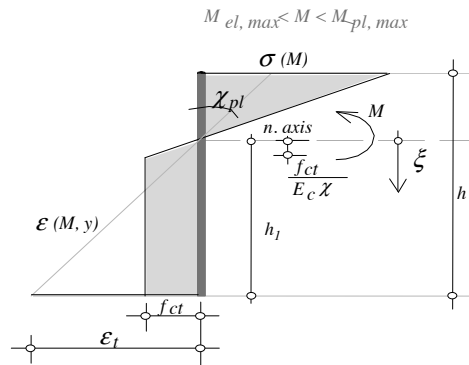


Figure A 1.1: Equilibrium equations describing the problem, and the distribution of stresses and strains for the section in pseudo-plastic yielding in traction

M1.2.1 Case of zero normal force, $N=0$

$$\sum M = 0 \Leftrightarrow M = \int_A \sigma_{xx} \xi dA = \int_0^{-(h-h_1)} \sigma_c(\varepsilon(\xi)) \xi b d\xi + \int_0^{h_1} \sigma_t(\varepsilon(\xi)) \xi b d\xi, \quad (A 1.1)$$

since for $b = const \Rightarrow dA = b d\xi$.

With $\varepsilon(\xi) = \chi \cdot \xi \Rightarrow$

$$M = M(\chi, h_1) = \frac{\chi(h-h_1)^2 E_c}{2} \cdot b \cdot \frac{2}{3} (h-h_1) + \frac{f_{ct}^2}{2E_c \chi} \cdot b \cdot \frac{2}{3} \frac{f_{ct}}{E_c \chi} + f_{ct} \left(h_1 - \frac{f_{ct}}{E_c \chi} \right) \cdot b \cdot \left(h_1 - \frac{1}{2} \left(h_1 - \frac{f_{ct}}{E_c \chi} \right) \right) \quad (A 1.2)$$

The position of neutral axes, h_1 , in function of χ is obtained as a solution of normal force equilibrium:

$$\begin{aligned} \Sigma X = 0 \Leftrightarrow N &= \int_A \sigma_{xx} dA = \int_0^{-(h-h_1)} \sigma_c(\varepsilon(\xi)) dy + \int_0^{h_1} \sigma_t(\varepsilon(\xi)) dy \\ &- \frac{\chi(h-h_1)^2 E_c}{2} + \frac{f_{ct}^2}{2E_c \chi} + f_{ct} \left(h_1 - \frac{f_{ct}}{E_c \chi} \right) = 0 \end{aligned} \quad (\text{A 1.3})$$

This equation has 2 solutions, but only the first presented one is physically acceptable:

$$\begin{aligned} h_{1,1}(\chi) &= h + \frac{f_{ct}}{E_c \chi} - \frac{\sqrt{2} \sqrt{f_{ct}} \sqrt{h}}{\sqrt{E_c} \sqrt{\chi}} \quad \text{and} \quad h_{1,2}(\chi) = h + \frac{f_{ct}}{E_c \chi} + \frac{\sqrt{2} \sqrt{f_{ct}} \sqrt{h}}{\sqrt{E_c} \sqrt{\chi}}, \quad h_{1,2} > h \quad (\text{A 1.4}) \\ &\Rightarrow h_1(\chi) = h_{1,1}(\chi) \quad \text{for} \quad \chi_{el,max} \leq \chi \leq \chi_{pl,max} \end{aligned}$$

The position of the neutral axis can also be expressed as a function of moment acting on the section:

$$h_1(M) = \frac{h}{2} \cdot \left(\frac{5}{4} - \frac{3M}{bf_{ct}h^2} + \left(\frac{3M}{bf_{ct}h^2} \right)^2 \right) \quad \text{for} \quad M_{el,max} \leq M \leq M_{pl,max} \quad (\text{A 1.5})$$

Incorporating equation A 1.4. in A 1.2 the moment is expressed as the function of the curvature, Equation 4.12 (Chapter 4). The curvature, χ , can be expressed in function of the moment, or as a function of tensile strain at the far most fibre of the section:

$$\chi(\varepsilon_t) = \frac{E_c^2 h \varepsilon_t + \sqrt{-E_c^2 f_{ct}^2 h^2 + 2E_c^3 f_{ct} h^2 \varepsilon_t}}{E_c^2 h^2} = \frac{E_c \varepsilon_t + \sqrt{-f_{ct}(f_{ct} - 2E_c \varepsilon_t)}}{E_c h} \quad \text{for} \quad \varepsilon_{el} \leq \varepsilon_t \leq \varepsilon_u \quad (\text{A 1.6})$$

Maximal bearing capacity before the localisation of the deformation i.e. tensile softening, is attained when the tensile strain at the far most fibre, ε_t , reaches the maximal ultimate tensile strain. ε_u . Maximal curvature of the section prior to crack opening, $\chi_{pl,max}$, is obtained as $\chi_{pl,max} = \chi(\varepsilon_u)$, for which the maximal moment before the crack opening, $M_{pl,max}$, is calculated (Equations 4.15).

Verifications of the equations:

The equations can be verified for the limiting case when pseudo-plastic behaviour yields to linear-elastic behaviour. As result, the known values of linear-elastic analysis are obtained:

$$\text{Lim}(h_{1,1})_{\chi \rightarrow \chi_{el}} = \text{Lim} \left(h + \frac{f_{ct}}{E_c \chi} - \frac{\sqrt{2} \sqrt{f_{ct}} \sqrt{h}}{\sqrt{E_c} \sqrt{\chi}} \right)_{\chi \rightarrow \frac{f_{ct}^2}{E_c h}} = \frac{h}{2}$$

$$\begin{aligned} \text{Lim}(\chi(\varepsilon_t))_{\varepsilon_t \rightarrow \varepsilon_{el}} &= \text{Lim}_{\varepsilon_t \rightarrow \frac{f_{ct}}{E_c}} \left(\frac{E_c \varepsilon_t + \sqrt{-f_{ct}(f_{ct} - 2E_c \varepsilon_t)}}{E_c h} \right) = \frac{2f_{ct}}{E_c h} \\ \text{Lim}(\chi(M))_{M \rightarrow M_{el}} &= \text{Lim}_{M \rightarrow f_{ct} \frac{bh^2}{6}} \left(\frac{8b^2 f_{ct}^3 h^3}{9E_c (bf_{ct} h^2 - 2M)^2} \right) = \frac{2f_{ct}}{E_c h} \\ \text{Lim}(h_{1,1})_{M \rightarrow M_{el}} &= \text{Lim}_{M \rightarrow f_{ct} \frac{bh^2}{6}} \left(\frac{h}{2} \cdot \left(\frac{5}{4} - \frac{3M}{bf_{ct} h^2} + \left(\frac{3M}{bf_{ct} h^2} \right)^2 \right) \right) = \frac{h}{2} \end{aligned}$$

M1.3 Elements behaviour

The relations given in Equations 4.10 to 4.15 enable description of non-linear response of the element subjected to arbitrary external load. Introducing moment as $M=M(P,x)$ in Equation 4.11, curvature is expressed as a continuous function over the length of the element for the part in quasi plastic yielding, while the relations for linear-elastic regime are well known. In the case of concentrated force acting in the mid-span of a beam, the following forms of considered functions are obtained:

$$\begin{aligned} M(P,x) &= \frac{P}{2} x \quad \forall x \leq \frac{L}{2} \Rightarrow \chi(M) = \chi(P,x) \\ \chi(P,x) &= \frac{P/2 \cdot x}{E_c bf_{ct} h^3 / 12} \quad \forall x \leq \frac{f_{ct}}{3bh^2 P} \\ \chi(P,x) &= \frac{8b^2 f_{ct}^3 h^3}{9E_c (bf_{ct} h^2 - P \cdot x)^2} \quad \forall \frac{f_{ct}}{3bh^2 P} < x < \frac{L}{2} \end{aligned} \quad (\text{A } 1.7)$$

Displacement at a point x due to load P is obtained from Equation 4.8, which, for the given symmetric load case, can be written as

$$\delta_x(P) = 2 \int_0^{L/2} \chi(x,P) \cdot \bar{M}(x) \cdot dx = 2 \left[\int_0^{x_{el}} \chi(x,P) \cdot \bar{M}(x) \cdot dx + \int_{x_{el}}^{L/2} \chi(x,P) \cdot \bar{M}(x) \cdot dx \right] \quad (\text{A } 1.8)$$

with

$$x_{el} = \frac{f_{ct} bh^2}{3P} \quad (\text{A } 1.9)$$

and with curvature defined in Equation A 1.7. The displacement of the load point is then obtained by integration of the left side of the equation

$$\delta_{L/2}(P) = 2 \left[\int_0^{x_{el}} \frac{P/2 \cdot x}{E_c bf_{ct} h^3 / 12} \cdot \frac{1}{2} \cdot x \cdot dx + \int_{x_{el}}^{L/2} \frac{8b^2 f_{ct}^3 h^3}{9E_c (bf_{ct} h^2 - P \cdot x)^2} \cdot \frac{1}{2} \cdot x \cdot dx \right]. \quad (\text{A } 1.10)$$

The solution for this load case is given in Equation 4.22.

M1.4 Inelastic unloading of microcracked beam

The phase of multi-microcracking in UHPFRC is modelled as a homogeneous plastic behaviour of the continuum (Chapter 3 and 4), and the term “pseudo-plastic” is used to distinguish the modelled behaviour from the real plastic behaviour, even if, for the monotonically increasing loading, the distinction can not be made. Pseudo-plastic behaviour in this model actually represents the process of matrix-fibre interaction during which a part of the energy that was brought for increase in element deformation is a non-recoverable energy (spent for cracking, interfacial processes), and consequently, the deformations can not be fully recovered as in the elastic behaviour, nor the complete pseudo-plastic deformation remains, as it would be the case in real plastic behaviour. This phenomenon is also observed experimentally, for the unloading path of the tested specimen in regime of microcracking, both in the uniaxial tension (Figure 3.20) and bending test (Figure A1.1).

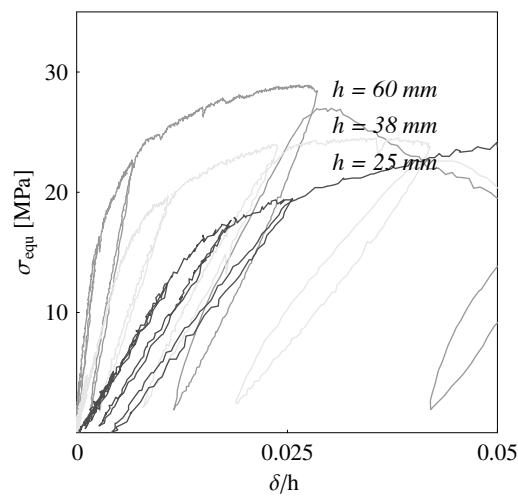


Figure A1.1: UHPFRC beams in three-point bending test with unloading cycles

The unloading curves of UHPFRC beams in bending test (Figure A1.1) show inelastic unloading, with a decreased constant stiffness. The reloading path shows the same stiffness as the unloading one, representing the actual stiffness of the element that has reached a certain level of microcracking (damage), as a function of maximal load. There is an interest to predict the real stiffness of the element with respect to its load history, especially since the elements, during service life, are likely to undergo microcracking.

In addition, the unloading stiffness provides the information on the system’s energy that can be recovered. In Figure A1.2. the difference between the surface below force-displacement curve ($\int P(d)d\delta$) and the strain energy that can be recovered from the body is schematically shown for an elastic and inelastic damaged body: in a damaged body only a part of the energy $\int P(d)d\delta$ is a recoverable energy U_{inel} . This represents the portion of the energy that can be released from the body at the beginning of opening of the fictitious crack, which is relevant for the stable crack growth (Chapter 4).

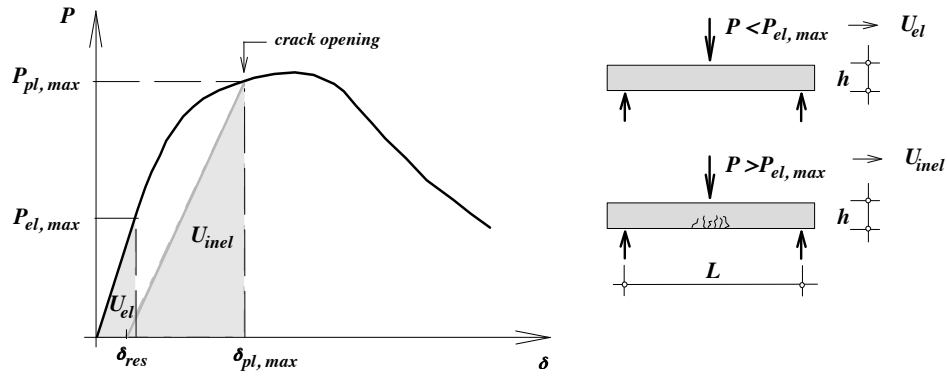


Figure A1.2: Recoverable strain energy of a beam in bending, for elastic deformation, U_{el} , and inelastic (damage) deformation, U_{inel} , with a residual deformation, δ_{res} .

M1.4.1 Inelastic (damaged) stiffness of a cross section

Let us observe a section loaded with a bending moment M_i , $M_{el,max} < M_i \leq M_{pl,max}$. For this section, distribution of stresses and strains (Figure A1.3 a)) is completely defined by Equations 4.4 and A 1.5. If the maximal bending moment ever sustained by the section is higher than the maximal elastic moment, the bending stiffness of the section at the unloading, EI_d , differs from the stiffness at loading, the secant bending stiffness EI_{sec} , and a residual deformation is maintained at complete unloading (Figure A1.2 b)). The aim of this section is to determine the stiffness of the section in unloading (Equation A1.28).

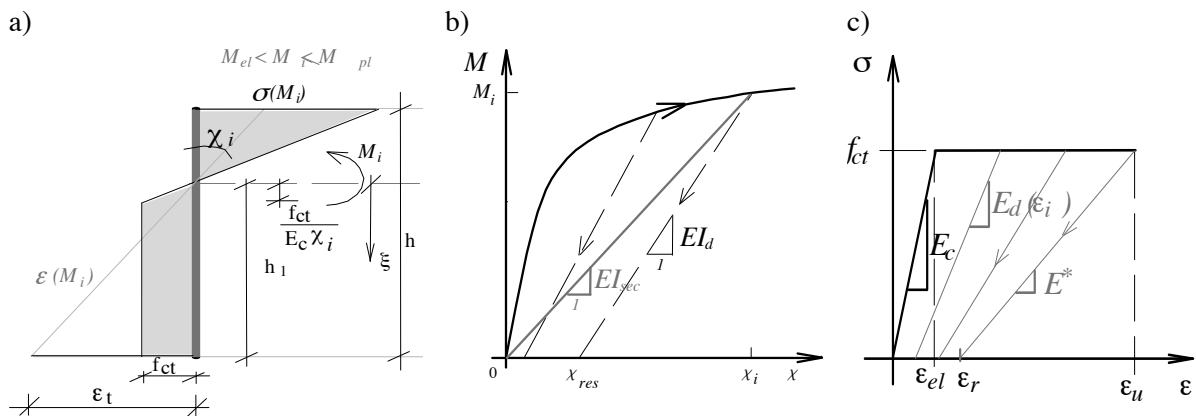


Figure A1.3: Force-deformations relationship UHPFRC element: a) distribution of stress and strain in the section in bending loading; b) moment-curvature relationship for loading and unloading of a beam; c) uniaxial stress-strain relationship for loading and unloading;

Uniaxial tension

It is experimentally observed in the uniaxial tensile test, that the value of modulus at unloading decreases with increase in maximal deformation reached in the specimen, $E_d = E_d(\epsilon)$, Figure A1.2 c). For the UHPFRC treated in this study, the value of modulus at unloading for the deformations prior to strain softening is determined to be $E_d(\epsilon_u) = E^* = 5.8 \text{ GPa}$ [Jungwirt 2006]. This is closely one tenth of the initial modulus of elasticity, E_c .

The unloading modulus in function of maximal previously reached deformation can be expressed using the following function

$$E_d(\varepsilon) = E_c \forall \varepsilon \leq \varepsilon_{el}$$

$$E_d(\varepsilon) = \frac{E^* \cdot (E_c \cdot \varepsilon_u - f_{ct})}{\varepsilon \cdot (E_c - E^*) + E^* \cdot \varepsilon_r} \forall \varepsilon_{el} < \varepsilon \leq \varepsilon_u \quad (A1.11)$$

where ε is maximal tensile strain ever attained in the section and ε_r is the residual deformation for unloading of the section that has reached maximal deformation $\varepsilon = \varepsilon_u$ (Figure A1.3 c))

$$\varepsilon_r = \varepsilon_u - \frac{f_{ct}}{E^*} \quad (A1.12)$$

The proposed expression for unloading modulus $E_d(\varepsilon)$, Equation A 1.11, respects the limit conditions:

$$\lim_{\varepsilon \rightarrow \frac{f_{ct}}{E_c}} E_d(\varepsilon) = E_c$$

$$\lim_{\varepsilon \rightarrow \varepsilon_u} E_d(\varepsilon) = E^* \quad (A 1.13)$$

For all other values of deformation between this limits, the value of E_d monotonically decreases from E_c to E^* , showing that, the more damaged the section is, the smaller the value of E_d will be and more residual deformation will appear.

Bending with zero normal force

If a section was subjected to bending moment M_i , $M_{el,max} < M_i \leq M_{pl,max}$, distribution of modulus of unloading over the depth of the section, E_d , can be related to deformations reached under bending moment M_i , Figure A1.4 c). Distribution of secant modulus, E_{sec} , is shown in Figure A1.3 b). It should be noted that, if the section's behaviour is modelled with the plastic yielding in tension, from the point of view of the Theory of plasticity, it is not correct to speak about a ratio between stress and strain, since the same stress corresponds to any strain in the region of plastic yielding. However, this relationship is assumed here in another context: $E_{sec} = f_{ct} / \varepsilon$.

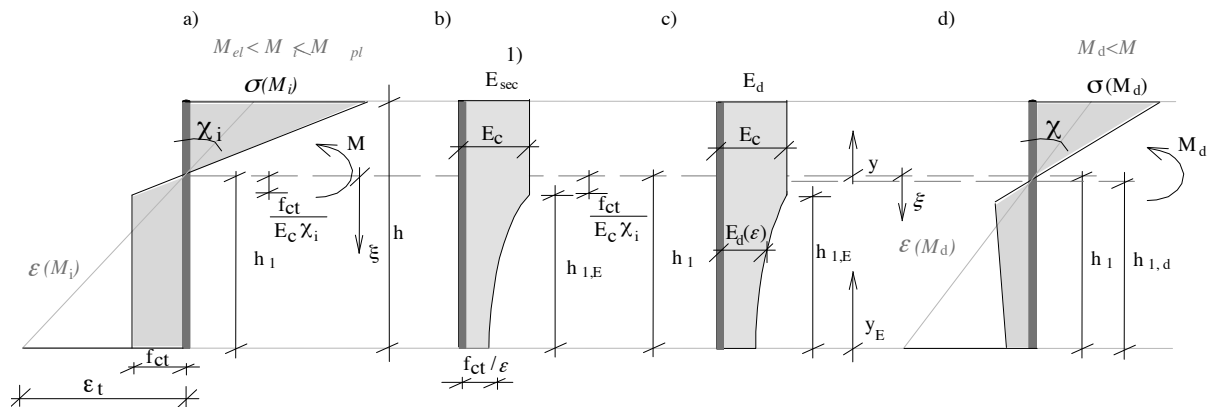


Figure A1.4: Section in loading and unloading: a) stress-strain distribution for loading; b) distribution of relation stress-strain for loading (secant modulus); ¹⁾ from the point of view of the Theory of plasticity, this relation is not correct in the zone of plastic yielding; c) distribution of stress-strain relationship for unloading ; d) stress distribution at unloading

The position of the neutral axis, h_1 , and the curvature ε_i for the given bending moment M_i determine the maximal deformation achieved at any point of the section, $\varepsilon(y)$. Modulus of unloading at every point is then a function of the maximal deformation reached.

If ε in Equation A 1.11 is introduced as a function of the curvature χ_i , the distribution of the unloading modulus is given with the following expression

$$E_d(\xi) = E_c \forall \xi < \frac{f_{ct}}{E_c \cdot \chi_i} \quad (A 1.14)$$

$$E_d(\xi) = \frac{E^* \cdot (E_c \cdot \varepsilon_u - f_{ct})}{\xi \cdot \chi_i \cdot (E_c - E^*) + E^* \cdot \varepsilon_r} \forall \xi \geq \frac{f_{ct}}{E_c \cdot \chi_i}$$

where the axis ξ is determined by the position of neutral line from the bottom of the section, h_1 ,

$$h_1(\chi_i) = h + \frac{f_{ct}}{E_c \chi_i} - \frac{\sqrt{2} \sqrt{f_{ct}} \sqrt{h}}{\sqrt{E_c} \sqrt{\chi_i}} \forall \chi_{el} \leq \chi_i \leq \chi_{pl,max} \quad (A 1.15)$$

The limit of the zone of inelastic unloading is noted as $h_{1,E}$, and is determined as

$$h_{1,E} = h_1 - \frac{f_{ct}}{E_c \cdot \chi_i} \quad (A 1.16)$$

The state of stresses over the section in unloading is governed by the unloading modulus. The stress at a point of a damaged section in unloading is then

$$\sigma_{xx}(\xi) = \sigma_i(\xi) - \Delta \varepsilon(\xi) \cdot E_d(\xi) = f_{ct} - (\varepsilon_i(\xi) - \varepsilon(\xi)) \cdot E_d(\xi) \quad \forall \frac{f_{ct}}{E_c \cdot \chi_i} < \xi < h_1(\chi_i)$$

$$\sigma_{xx}(\xi) = f_{ct} - (\chi_i \cdot \xi - \chi \cdot (\xi - \Delta h_1)) \cdot E_d(\xi) \quad \forall \frac{f_{ct}}{E_c \cdot \chi_i} < \xi < h_1(\chi_i) \quad (A 1.17)$$

where

$$\Delta h_1 = h_1 - h_{1,d} \quad (A 1.18)$$

is the difference in the position of the neutral axes. Stresses in the rest of the section remain proportional to initial modulus of elasticity, E_c .

New state of stresses is an equilibrated state, and the equilibrium of the normal force can be written

$$\int_A \sigma_{xx}(\xi) \cdot dA = 0 \Leftrightarrow \int_{h_1}^{h_1-h_{1,E}} (f_{ct} - (\chi_i \cdot \xi - \chi \cdot (\xi - h_1 + h_{1,d})) \cdot E_d(\xi)) \cdot d\xi + \int_{h_1-h_{1,E}}^{h_1-h} E_c \cdot \chi \cdot (\xi - h_1 + h_{1,d}) d\xi = 0 \quad (A 1.19)$$

The position of neutral axes and the moment-curvature relationship can be found by solving Equation A 1.19 for $h_{1,d}$.

$$h_{1,d} = \frac{(-f_{ct}^2 / E_c + 4 \cdot f_{ct} \cdot h_1 \cdot \chi_i - E_c \cdot (h - 3 \cdot h_1) \cdot (h - h_1) \chi_i^2) + 2 \cdot (1 - \chi_i / \chi) \cdot (E_c \cdot h_1 \cdot \chi_i - f_{ct}) \cdot \varepsilon_{rf} + 2 \cdot \chi_i \cdot (f_{ct} - K_1 \cdot (f_{ct} + E_c \cdot \varepsilon_{rf})) + E_c \cdot (h - h_1) \cdot \chi_i}{K_1 \cdot (\varepsilon_{rf} \cdot \chi - (\varepsilon_{rf} + h_1 \cdot \chi) \cdot \chi_i) \cdot (f_{ct} + E_c \cdot \varepsilon_{rf}) + \chi \cdot \chi_i \cdot (f_{ct} - K_1 \cdot (f_{ct} + E_c \cdot \varepsilon_{rf})) + E_c \cdot (h - h_1) \cdot \chi_i} \quad (A 1.20)$$

where

$$K_1 = \ln\left(\frac{f_{ct}}{E_c} + \varepsilon_{rf}\right) - \ln(\varepsilon_{rf} + h_1 \cdot \chi_i) \quad (\text{A } 1.21)$$

$$\varepsilon_{rf} = \frac{E^* \cdot \varepsilon_r}{E_c - E^*} \quad (\text{A } 1.22)$$

It can be shown that

$$\text{Lim}(h_{1d})_{\chi \rightarrow \chi_i} \Rightarrow h_{1,d} \rightarrow h_1 \quad (\text{A } 1.23)$$

Bending moment at unloading, M_d , is then obtained by the integration of normal stress

$$M_d = \int_A \sigma_{xx}(y) \cdot y \cdot dA \quad (\text{A } 1.24)$$

For a more convenient form of the expressions, the following approach is used: Let us consider the curvature of the section χ as an imposed unloading curvature, χ_d , as shown in Figure A 1.5. The decrease in force, ΔM , for decrease in curvature $\Delta\chi = \chi_d$, can then be calculated from the decrease in stress due to unloading modulus, distributed over the depth of the section according to Equation A 1.14.

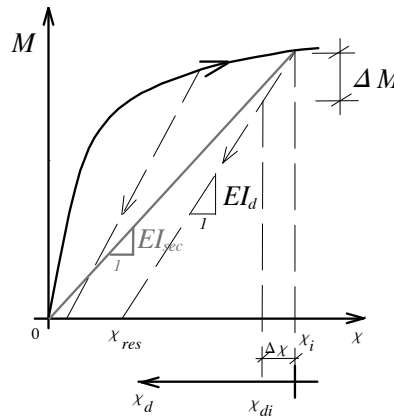


Figure A1.5: Curvature at unloading

Thus, for an χ_d , the decrease in moment can be calculated as

$$\Delta M_d = \int_A \Delta \sigma_{xx}(y) \cdot y \cdot dA = b \cdot \int_y E_d(y) \cdot \varepsilon(y) \cdot y \cdot dy = b \cdot \int_{h_{1,d}}^{h_{1,d}-h} E_d(\xi) \cdot \chi_d \cdot \xi^2 d\xi = \chi_d \cdot b \cdot \int_{h_{1,d}}^{h_{1,d}-h} E_d(\xi) \cdot \xi^2 d\xi = \chi_d \cdot EI_d \quad (\text{A } 1.25)$$

$$EI_d = b \cdot \int_{h_{1,d}}^{h_{1,d}-h} E_d(\xi) \cdot \xi^2 d\xi \quad (\text{A } 1.26)$$

Unloading stiffness, EI_d , is constant for all χ_d , and for

$$\text{Lim}(\Delta M_d)_{\chi_d \rightarrow 0} \Rightarrow \chi \rightarrow \chi_i \Rightarrow h_{1,d} \rightarrow h_1 \quad (\text{A 1.27})$$

according to Equation A1.23; the unloading stiffness of the section can be calculated as

$$\begin{aligned} EI_d &= b \cdot \int_{h_1}^{h_1-h} E_d(\xi) \cdot \xi^2 d\xi = b \cdot \left(\int_{h_1}^{h_1-h_{1,E}} E_d(\xi) \cdot \xi^2 d\xi + \int_{h_1-h_{1,E}}^{h_1-h} E_d(\xi) \cdot \xi^2 d\xi \right) = \\ &= EI_d(\chi_i) = b \cdot \left(\int_{h_1}^{h_1-h_{1,E}} \frac{E^* \cdot (E_c \cdot \varepsilon_u - f_{ct})}{\xi \cdot \chi_i \cdot (E_c - E^*) + E^* \cdot \varepsilon_r} \cdot \xi^2 d\xi + \int_{h_1-h_{1,E}}^{h_1-h} E_c \cdot \xi^2 d\xi \right) = \\ &= b \cdot \left(\frac{(f_{ct} + \sigma_{rf}) \cdot (E_c \cdot h_1 \cdot \chi_i - f_{ct}) \cdot (f_{ct} - 2 \cdot E_c \cdot \varepsilon_{rf} + E_c \cdot h_1 \cdot \chi_i) - 2 \cdot E_c^2 \cdot \varepsilon_{rf}^2 \cdot K_1}{2 \cdot E_c^2 \cdot \chi_i^3} + \frac{1}{3} \cdot E_c \cdot \left((h - h_1)^3 + \frac{f_{ct}^3}{E_c^3 \cdot \chi_i^3} \right) \right) \end{aligned} \quad (\text{A 1.28})$$

with h_1 given with Equation A1.15, K_1 with Equation A1.21, and σ_{rf} being

$$\sigma_{rf} = E_c \cdot \varepsilon_{rf} \quad (\text{A 1.29})$$

where ε_{rf} is given with Equation A1.22.

Thus for every previously achieved maximal deformation in the section, as a function of χ_i , the unloading stiffness can be calculated, Figure A1.7. Since χ_i can be expressed as the continuous function over x for a known distribution of $M(x)$ the distribution of unloading stiffness becomes also a continuous function over x .

Residual curvature

We consider now the other limit of Equation A1.25

$$\text{Lim}(\Delta M_d)_{\chi_d \rightarrow (\chi_i - \chi_{res})} \Rightarrow \Delta M_d = M_i \quad (\text{A 1.30})$$

Since EI_d , is constant for χ_d Equation A1.25 for the previous limit condition yields to

$$M_i = (\chi_i - \chi_{res}) \cdot EI_d \quad (\text{A 1.31})$$

and the residual curvature, χ_{res} , can be calculated as

$$\chi_{res} = \chi_i - \frac{M_i}{EI_d(\chi_i)} \quad (\text{A 1.32})$$

The residual curvature in function of maximal curvature of the section is plotted in Figure A1.6.

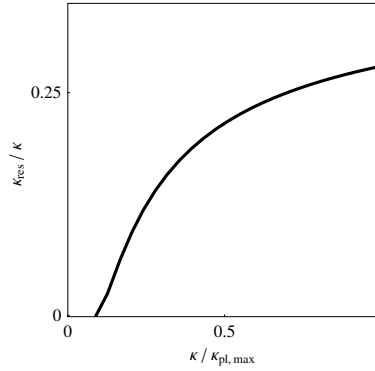


Figure A1.6: Residual curvature of the unloaded section

Secant Stiffness

In the case of inelastic unloading with the unloading modulus equal to the secant modulus, $E_d = E_{sec}$, with no residual deformation remaining, unloading stiffness of the section can be calculated using Equation A 1.26, replacing the distribution of E_d with the distribution of secant modulus (Figure A1.3b)). For the limit case when $\chi \rightarrow \chi_i$ the unloading secant stiffness becomes

$$EI_{d,sec} = b \cdot \left(\int_{h_1}^{h_1-h_{1,E}} \frac{f_{ct}}{\xi \cdot \chi_i} \cdot \xi^2 d\xi + \int_{h_1-h_{1,E}}^{h_1-h} E_c \cdot \xi^2 d\xi \right) = b \cdot \left(\frac{f_{ct}}{2 \cdot \chi_i} \left(h_1^2 - \frac{f_{ct}^2}{E_c^2 \cdot \chi_i^2} \right) + \frac{1}{3} \cdot E_c \cdot \left((h-h_1)^3 + \frac{f_{ct}^3}{E_c^3 \cdot \chi_i^3} \right) \right)$$

$$EI_{d,sec} = b \cdot \left(\frac{f_{ct} h_1^2}{2 \cdot \chi_i} - \frac{f_{ct}}{2 \cdot \chi_i} \frac{f_{ct}^2}{E_c^2 \cdot \chi_i^2} + \frac{1}{3} \cdot E_c \cdot \left(-\frac{f_{ct}}{E_c \chi_i} + \frac{\sqrt{2} \sqrt{f_{ct}} \sqrt{h}}{\sqrt{E_c} \sqrt{\chi_i}} \right)^3 + \frac{f_{ct}^3}{E_c^3 \cdot \chi_i^3} \right) \quad (A 1.33)$$

which, introducing h_l given by Equation (A 1.15) yields to

$$EI_{sec} = b \cdot \left(\frac{f_{ct} \cdot h^2}{2 \cdot \chi_i} - \frac{\sqrt{2} \cdot f_{ct}^{3/2} \cdot h^{3/2}}{3 \cdot \sqrt{E_c} \cdot \chi_i^{3/2}} \right) \quad (A 1.34)$$

On the other hand, secant stiffness can be calculated as the ratio of moment and the corresponding curvature, M_i / χ_i , where M_i is given by Equation 4.13:

$$M(\chi_i) = b \left(\frac{f_{ct} h^2}{2} - \frac{\sqrt{2} f_{ct}^{3/2} h^{3/2}}{3 \sqrt{E_c} \sqrt{\chi_i}} \right) \quad \text{for } \chi_{el,max} \leq \chi_i \leq \chi_{pl,max}$$

$$\Rightarrow EI_{sec} = b \left(\frac{f_{ct} \cdot h^2}{2 \cdot \chi_i} - \frac{\sqrt{2} \cdot f_{ct}^{3/2} \cdot h^{3/2}}{3 \cdot \sqrt{E_c} \cdot \chi_i^{3/2}} \right) \quad , \quad (A 1.35)$$

The expression A 1.34 is used here as a control of the approach applied in development of Equation A1.28, since the identity is demonstrated using another approach, Equation A1.35.

However, Equation A1.34 is useful as a general control of the arbitrary value of unloading stiffness, EI_d , which needs to be the value higher than EI_{sec} for the same M_i or χ_i .

M1.4.2 Comparison of sectional bending stiffness

The initial bending stiffness, EI , unloading, EI_d , and secant bending stiffness, EI_{sec} , for a rectangular cross section are plotted in Figure A1.7. Values are normalised by the value of the initial bending stiffness, which is in this case

$$EI = E_c \cdot \frac{b \cdot h^3}{12}. \quad (\text{A 1.36})$$

The material data correspond to data for the UHPRFC treated in this study (Chapter 3). The curves in Figure A1.7 are plotted against the maximal curvature reached in the section χ , normalised by the value of the maximal curvature that can be taken by the section before the fictitious crack opening, $\chi_{pl,max}$.

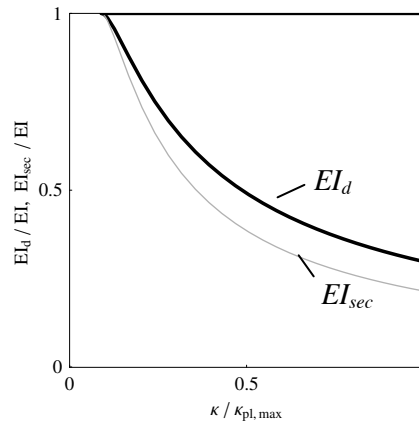


Figure A1.7: Normalised unloading bending stiffness in function of maximal deformation attend

For the microcracked section prior to crack opening, $\chi \rightarrow \chi_{pl,max}$, the following can be stated based on the given equations:

- the unloading bending stiffness of the section is approximately $1/3$ of the initial bending stiffness (0.298 for the given material)
- the secant stiffness of the section is approximately $1/5$ of the initial bending stiffness of the section (0.215 for the given material)
- the unloading stiffness of the section is app. 40% higher than the secant stiffness (39% for the given material)

M1.4.3 Inelastic unloading of a damaged beam before crack opening

In this section, the intention is to model the unloading behaviour of a microcracked element in bending, based on the previously developed relationship, and to compare it with measured data.

For the known distribution of curvature over the length of the element, the displacement at any point can be calculated from Equation 4.3 or 4.8, as already mentioned in § 4.3.3, or Appendix M1. Let us calculate the displacement at any point of the element as

$$\delta(q, x) = \int_0^L \chi(M(x, q)) \cdot \bar{M} \cdot dx \quad (\text{A 1.37})$$

The observed beam is symmetric, subjected to central point load P (Figure 1.8). If the beam was previously loaded up to the force level P_i , inducing bending moments higher than the maximal elastic moment, $M_{el,max}$, the following expression governs unloading and reloading displacement

$$\delta(P, P_i) = 2 \left[\int_0^{x_{el}} \frac{M(x, P)}{E_c I} \cdot \bar{M}(x) dx + \int_{x_{el}}^{L/2} \chi_{unload}(x, P, P_i) \cdot \bar{M}(x) dx \right] \quad (A 1.38)$$

where x_{el} is the limit of the elastic unloading over the length of the beam (Figure A 1.8), obtained as the solution of the equation $M(x, P_i) = M_{el,max}$, where $M(x, P)$ is the function of the moment bending moment over the length of the element, x , due to load P ; for the given boundary conditions

$$x_{el} = \frac{M_{el,max} \cdot 2}{P_i} \quad (A 1.39)$$

χ_{unload} is the unloading curvature at the force P , for previous maximal force P_i , and can be expressed using the residual curvature and unloading stiffness (Figure A 1.5). By introducing the unite force moment function for the displacement at the mid-span, $\bar{M}(x) = \frac{1}{2} \cdot x$, Equation A 1.38 becomes

$$\delta_{L/2}(P, P_i) = 2 \left[\int_0^{x_{el}} \frac{M(x, P)}{E_c I} \cdot \frac{1}{2} \cdot x dx + \int_{x_{el}}^{L/2} \left(\chi_{res}(x, P_i) + \frac{M(x, P)}{EI_d(x, P_i)} \right) \cdot \frac{1}{2} \cdot x dx \right] \quad (A 1.40)$$

where the functions for EI_d and χ_{res} , given as functions of χ_i , Equation A 1.28 and A 1.32, are now expressed as functions of x and P_i , maintaining the influence of maximal curvature reached at the section at the position x in the following way:

$$\chi_{res}(x, P_i) = \chi_{pl}(M(x, P_i)) - \frac{M(x, P_i)}{EI_d(\chi_{pl}(M(x, P_i)))} \quad (A 1.41)$$

$$EI_d(\chi_i) = EI_d(\chi_{pl}(M(x, P_i))) \quad (A 1.42)$$

with

$$\chi_{pl}(M) = \frac{8b^2 f_{ct}^3 h^3}{9E_c (bf_{ct} h^2 - 2M)^2} \quad \forall M_{el,max} \leq M \leq M_{pl,max} \quad (A 1.43)$$

as developed in Annex M1.

It is obvious that the Equation A1.40 respect the limit condition:

$$\lim(\delta(P, P_i))_{P_i \rightarrow P_{el}} = \delta_{el} \quad (1.44)$$

The integral on the right side of Equation A 1.40 can be easily obtained numerically with any standard integration method, since the functions involved are smooth. The array developed in Chapter 5 can be applied with appropriate boundary conditions.

$$w(x_k) \approx \frac{\Delta x^2}{2} \sum_{i=0}^{n_{xk}} \left(\sum_{j=0}^{i-1} (\chi(x_{j-1}) + \chi(x_j)) + \frac{\chi(x_{i-1}) + \chi(x_i)}{2} \right) + C1$$

for small Δx , with $n_{xj} = \frac{x_j}{\Delta x}$, $x_i = i \cdot \Delta x$.

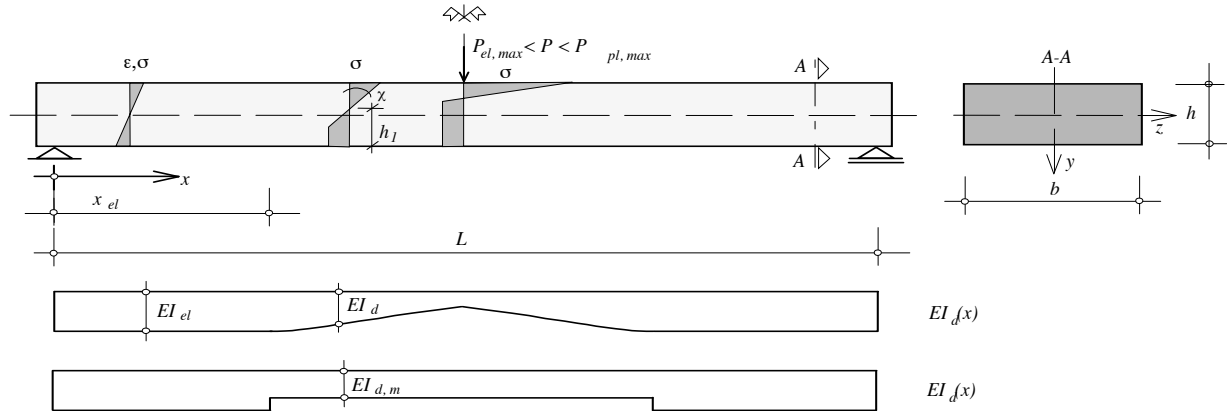


Figure A 1.8: Geometry of the beam in unloading and distribution of unloading stiffness

Equation A 1.40 is plotted in Figure A1.9 against the measured data for the beams of different depth and for the unloading beginning at different force level. The plausibility of the results indicate that:

- the developed analysis can be reliably used for simulation of elements behaviour,
- the applied material models for tensile behaviour (both in loading and unloading) enables correct simulation of elements behaviour.

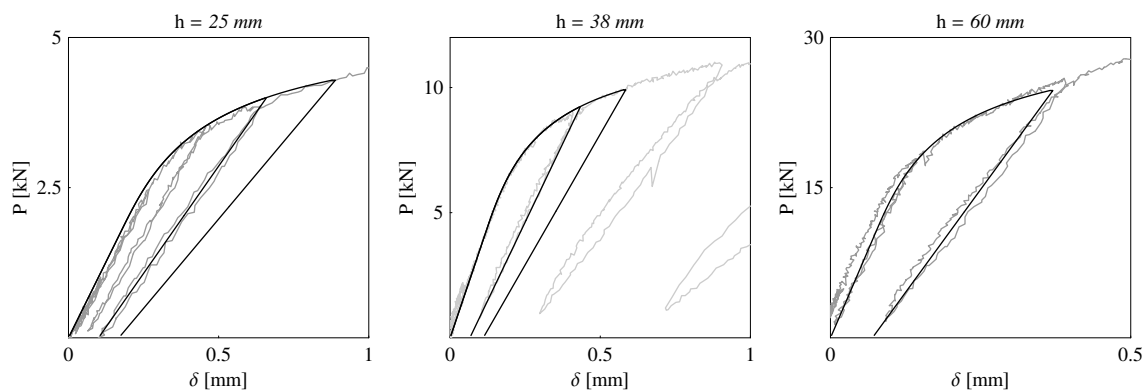


Figure A 1.9: Comparison of simulated unloading and measured data

It should be point out that, during this analysis, it was primarily insisted on term “unloading”; The exposed procedure, however, refers also to reloading, and the same expression (Equation A 1.40) can be used to simulate the loading path of the previously damaged member (Figure A 1.9).

Integral of the residual curvatures (Equation A1.32) gives the residual deformation of the member.

M1.4.4 Comparison of elements bending stiffness

Comparison of elastic, secant and damaged bending stiffness of a beam is shown in Figure A 1.10. Figure A1.10 a) shows schematically the inelastic force-displacement relationship of a beam and the mentioned stiffness; Figure A 1.10 b) shows the calculated values for the unloading stiffness, K_d , and secant stiffness, K_{sec} , normalised by the elastic stiffness, K_{el} , considering the following values:

$$K_i = \frac{dP}{d\delta} \quad (\text{A 1.45})$$

$$K_{el} = \frac{dP}{d\delta} \quad \forall P \leq P_{el} \Rightarrow K_{el} = \frac{48 \cdot EI}{L^3} \quad (\text{for three-point bending}) \quad (\text{A 1.46})$$

$$K_{sec} = \frac{P_i}{\delta(P_i)} \quad (A 1.47)$$

where $\delta(P_i)$ can be calculated according to Equation 4.30, and

$$K_d = \frac{dP}{d\delta_{unloading}} \quad (A 1.48)$$

where $\delta_{unloading}$ is calculated using Equation A 1.40.

For $P_i = P_{pl, max}$, unloading stiffness is approximately 60 % of the initial elastic stiffness (for the given material and boundary conditions $K_d=0.59 K_{el}$). It should be noted, however, that for e.g. $P_i = 0.8 P_{pl, max}$, the unloading stiffness is almost 85 % of the initial stiffness, and for the smaller values of P_i it approaches fast the initial one, K_{el} . Additionally, it can be noted that, in particular in the region of smaller maximal force, P_i , the difference of values of K_d , K_{sec} is becoming less significant, which is of practical consequence for the design, since the value for K_{sec} can be obtained much easier, Equation A 1.47.

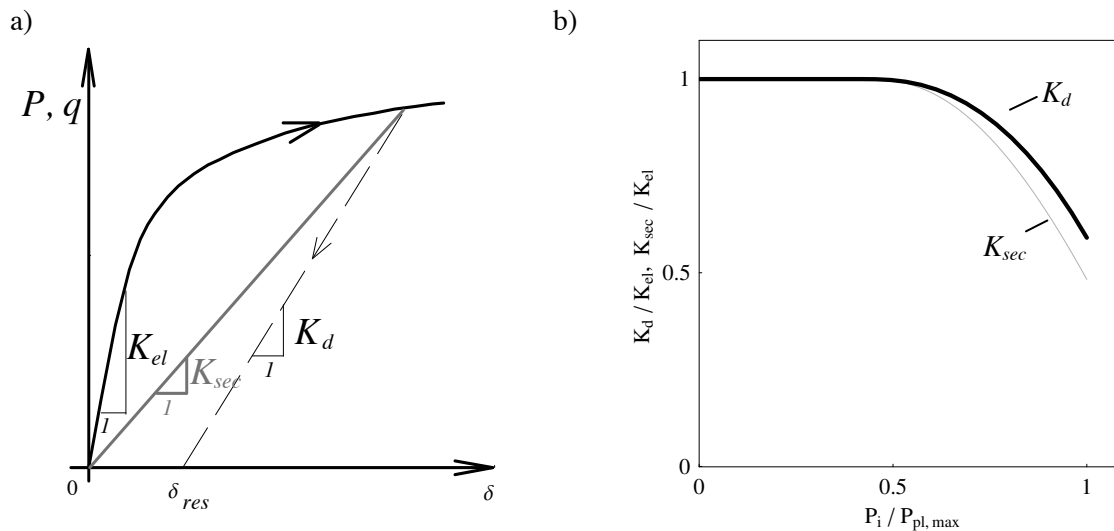


Figure A 1.10: Elastic, K_{el} , secant, K_{sec} , and unloading damaged stiffness, K_d , of a beam: a) Notations in force-displacement diagram; b) Calculated loss of stiffness of a beam in three-point bending; Stiffness are normalised with the elastic stiffness, and the force is normalised with the maximal force attained prior to crack opening.

The ratios plotted in Figure A1.10 b) are maintained for any slenderness of the element. However, changing other boundary conditions, as the load case for example, the loss in stiffness changes.

For uniformly distributed load q , it is observed that the unloading and secant stiffness decrease much faster than in the case of the concentrated point load (Figure A 1.11 b)). This is due to the gradient of the moment function, $M(x,P)$, implying that, under uniformly distributed load, the zone of the member in the micro-cracked phase is larger than in the case of concentrated load for the same maximal moment.

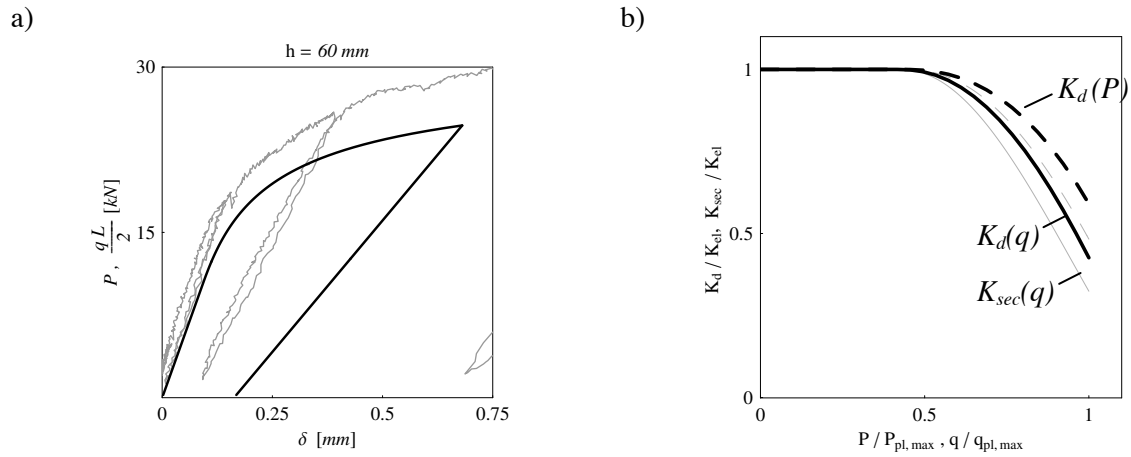


Figure A 1.11: Comparison of bending response of a beam under uniformly distributed, q , and concentrated load, P :

- a) Simulated force-displacement response under q (plotted as $qL/2$) and measured response under P ;
 b) Calculated loss of stiffness (normalised with the corresponding elastic stiffness), where $K_d(q)$ and $K_{sec}(q)$ are the unloading and secant stiffness of beam under uniformly distributed load

Simulations for uniformly distributed load are performed using in the same approach as developed in Section 1.4, simply by introducing appropriate moment function, $M(x, q)$. The elastic bending stiffness changes as well:

$$K_{el}(q) = \frac{dq}{d\delta} \quad \forall q \leq q_{el} \Rightarrow K_{el}(q) = \frac{384 \cdot EI}{5 \cdot L^4} \quad (1.49)$$

The values plotted in Figure A 1.11 b) are of importance for prediction of elements stiffness at the service state, thus for the design. Considering that the level of service load is in the range of app. 60 % of ultimate failure load:

- not important overestimation of deformations is obtained by using secant elements stiffness,
- not high decrease in stiffness appears under service loads, implying that not significant redistribution takes place at SLS in statically indeterminate system, and consequently an elastic analysis can be accepted.

Appendix M2:

Behaviour of beam with fictitious crack: equation development

M2.1 Problems involved and content

Increasing the deformations beyond the level when ultimate pseudo-plastic strain ε_u is reached in the most loaded section, a fictitious crack is assumed to start to propagate. The equilibrium of sectional forces has an infinite number of solutions in the cracked section, and the unique equilibrated solution is found considering the cracked element. This appendix contains the development of the equations applied in the development of equilibrated solution for an element in bending. The algorithms for developed procedures are given in Section 2.5.

M2.2 Static equilibrium of cracked section with regions in pseudo -plastic yielding in tension

The parameters describing state of deformation and stresses of the cracked section with the regions in pseudo-plastic yielding are schematically presented in Figure A 2.1 b). The curvature of the non-cracked part of the section is $\chi > \chi_{pl,max}$, and the fictitious - macrocrack is characterised by length, αh , and the crack mouth opening, w_i . In order to establish the equilibrium of sectional forces, the hypothesis given in Chapter 4. are applied. The expressions are developed for $N=0$.

a) b)

$$\sum M == 0 \Rightarrow M = M(\kappa, h_1, \alpha, w_i),$$

$$\text{with } w = w(w_i, \alpha) \wedge h_1 = h_1(\kappa, \alpha)$$

$$\Rightarrow M = M(\kappa, \alpha, w_i),$$

$$\sum X == 0 \Rightarrow w_i = w_i(\kappa, \alpha)$$

$$\vee \alpha = \alpha(\kappa, w_i)$$

$$\vee \kappa = \kappa(\alpha, w_i),$$

$$\Rightarrow M = M(\kappa, \alpha)$$

$$\vee M = M(\kappa, w_i)$$

$$\vee M = M(\alpha, w_i)$$

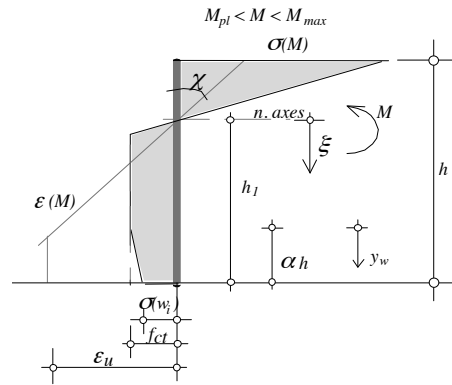


Figure A 2.1: Section with pseudo-plastic yielding and a fictitious crack: a) equilibrium conditions; b) stress distribution and notations

M2.2.1 Equilibrium of bending moment

The equation of the equilibrium of bending moment, written with respect to the neutral axes, with $dA=b \cdot d\xi$ for $b=const$, is

$$\Sigma M = 0 \Leftrightarrow M = \int_A \sigma_{xx} \xi dA = \int_0^{-(h-h_1)} \sigma_c(\varepsilon(\xi)) \xi d\xi - \int_0^{h_1-ah} \sigma_t(\varepsilon(\xi)) \xi d\xi - \int_0^{ah} \sigma_w(w(y_w)) (h_1 - y_w) dy_w \quad (A 2.1)$$

If a multi linear law for stress-crack openings, $\sigma_w(w)$, is applied:

$$\begin{aligned} \sigma_w(w) &= C_1 - C_2 w = f_{ct} - \frac{f_{ct} - \sigma_{w1}}{w_1} w \quad \forall 0 \leq w \leq w_1 \\ \sigma_w(w) &= C_3 - C_4 w = \sigma_{w1} - \frac{\sigma_{w1} - \sigma_{w2}}{w_2 - w_1} (w - w_1) \quad \forall w_1 \leq w \leq w_2, \quad C_3 = \sigma_{w1} + \frac{\sigma_{w1} - \sigma_{w2}}{w_2 - w_1} w_1, C_4 = \frac{\sigma_{w1} - \sigma_{w2}}{w_2 - w_1}, \\ &\text{etc.} \end{aligned} \quad (A 2.2)$$

for the crack openings $w \in [0, w_1]$, Equation A. 2.1 gives

$$\begin{aligned} M = M(\chi, h_1, \alpha, w_i) &= \frac{\chi(h-h_1)^2 E_c}{2} \cdot b \cdot \frac{2}{3} (h-h_1) + \frac{f_{ct}^2}{2E_c \chi} \cdot b \cdot \frac{2}{3} \frac{f_{ct}}{E_c \chi} + f_{ct} \left(h_1 - \frac{f_{ct}}{E_c \chi} \right) \cdot b \cdot \left(h_1 - \frac{1}{2} \left(h_1 - \frac{f_{ct}}{E_c \chi} \right) \right) - \\ &- \frac{ah(f_{ct} - \sigma_w(w_i))}{2} \cdot b \cdot \left(h_1 - \frac{1}{3} ah \right) \end{aligned} \quad (A 2.3)$$

and, similar, for the crack openings $w \in [w_1, w_2]$, Equation A 2.1 gives

$$\begin{aligned} M = M(\chi, h_1, \alpha, w_i) &= \frac{\chi(h-h_1)^2 E_c}{2} \cdot b \cdot \frac{2}{3} (h-h_1) + \frac{f_{ct}^2}{2E_c \chi} \cdot b \cdot \frac{2}{3} \frac{f_{ct}}{E_c \chi} + f_{ct} \left(\frac{\varepsilon_u}{\chi} - \frac{f_{ct}}{E_c \chi} \right) \cdot b \cdot \frac{1}{2} \left(\frac{\varepsilon_u}{\chi} + \frac{f_{ct}}{E_c \chi} \right) + \\ &+ \frac{(f_{ct} + \sigma_{w1})}{2} \cdot \frac{ahw_1}{w_i} \cdot b \cdot \left(\frac{\varepsilon_u}{\chi} + \frac{ahw_1}{w_i} \cdot \frac{f_{ct} + 2\sigma_{w1}}{3(f_{ct} + \sigma_{w1})} \right) + \sigma_{w1} \left(ah - \frac{ahw_1}{w_i} \right) \cdot b \cdot \left(h_1 - \frac{1}{2} \left(ah - \frac{ahw_1}{w_i} \right) \right) - \\ &- (\sigma_{w1} - \sigma_w(w_i)) \left(ah - \frac{ahw_1}{w_i} \right) \frac{1}{2} \cdot b \cdot \left(h_1 - \frac{1}{3} \left(ah - \frac{ahw_1}{w_i} \right) \right) \end{aligned} \quad (A 2.4)$$

The hypotheses on plane deformations in the non-cracked part and the hypothesis that the macrocrack propagates when the strain at the crack tip reaches ε_u , give the following relationships:

$$h_1 = h_1(\chi, \alpha) = \frac{\varepsilon_u}{\chi} + \alpha \cdot h \quad \forall \quad \alpha = \alpha(\chi, h_1) = \frac{h_1}{h} - \frac{\varepsilon_u}{\chi h} \quad (A 2.5)$$

Introducing e.g. the first of the relationships A 2.5 in the equations A 2.3 and A 2.4, bending moment is obtained as a function of three parameters,

$$\begin{aligned} M &= M(\chi, \alpha, w_i) = \\ &= \frac{b}{6 \cdot E_c^2 \cdot \chi^2} \left(-f_{ct}^3 + 3 \cdot E_c^2 \cdot f_{ct} \cdot (\varepsilon_u + h \cdot \alpha \cdot \chi)^2 \right) - \\ &- \frac{b}{6 \cdot E_c^2 \cdot \chi^2} \cdot E_c^2 \cdot \left(2 \cdot E_c \cdot (\varepsilon_u + h \cdot (\alpha - 1) \cdot \chi)^3 + C_2 \cdot h \cdot w_i \cdot \alpha \cdot \chi \cdot (3 \cdot \varepsilon_u + 2 \cdot h \cdot \alpha \cdot \chi) \right) \end{aligned} \quad (A 2.6)$$

M2.2.2 Equilibrium of normal force

The equilibrium of the normal force provides the following relation for $w \in [0, w_1]$

$$\begin{aligned} \Sigma X == 0 \Leftrightarrow & - \int_0^{-(h-h_1)} \sigma_c(\varepsilon(\xi)) dy = \int_0^{h_1-ct} \sigma_t(\varepsilon(\xi)) dy + \int_0^{ct} \sigma_w(w(y)) dy \Leftrightarrow \\ & \frac{f_{ct}^2}{2E_c \chi} + f_{ct} \left(h_1 - \frac{f_{ct}}{E_c \chi} \right) - \frac{ct(h-f_{ct}-\sigma_w(w_i))}{2} - \frac{\chi(h-h_1)^2 E_c}{2} = 0 \end{aligned} \quad (A 2.7)$$

With relationship A2.5, the previous equation can be solved for w_i , α or χ . A unique solution exists for $w_i = w_i(\alpha, \chi)$ while two solutions exists for α and χ , but only one physically acceptable. Only the development of the equations for $w \in [0, w_1]$ is presented.

$$w_i(\alpha, \chi) = - \frac{f_{ct}^2 + E_c^2(\varepsilon_u + h\chi(\alpha-1))^2 - 2E_c f_{ct}(\varepsilon_u + h\alpha\chi)}{C_2 E_c h \alpha \chi} \quad (A 2.8)$$

$$\alpha(w_i, \chi) = - \frac{1}{2E_c h \chi} \left(C_2 w_i - 2f_{ct} + 2E_c \varepsilon_u - 2E_c h \chi + \sqrt{C_2 w_i (-4f_{ct} + C_2 w_i + 4E_c \varepsilon_u) + 4E_c h \chi (2f_{ct} - C_2 w_i)} \right) \quad (A 2.9)$$

$$\chi(\alpha, w_i) = - \frac{1}{2E_c h (\alpha-1)^2} \left(-2f_{ct} \alpha + C_2 w_i \alpha + 2E_c (\alpha-1) \varepsilon_u + \sqrt{C_2 w_i \alpha - 2f_{ct} \sqrt{2f_{ct} (1-2\alpha) + C_2 w_i \alpha} + 4E_c \varepsilon (\alpha-1)} \right) \quad (A 2.10)$$

M2.2.3 Bending moment as a function of two parameters

Incorporating one of the previous relationships (Equation A 2.8 to A2.10) in the expression for bending moment, Equation A 2.6, the moment is obtained as a function of two variables:

$$M = M(\chi, \alpha) \vee M = M(\chi, w_i) \vee M = M(w_i, \alpha)$$

Moment-curvature relationship for known α is defined with

$$\begin{aligned} M(\chi, \alpha) = & \frac{b}{6 \cdot E_c^2 \cdot \chi^2} \left(-f_{ct}^3 + E_c^3 \cdot (\varepsilon_u + 2 \cdot h \cdot \chi) \cdot (\varepsilon_u + h \cdot (\alpha-1) \cdot \chi)^2 + E_c \cdot f_{ct}^2 (3 \cdot \varepsilon_u + 2 \cdot h \cdot \alpha \cdot \chi) \right) - \\ & - \frac{b}{6 \cdot E_c^2 \cdot \chi^2} \left(E_c^2 \cdot f_{ct} \cdot (\varepsilon_u + h \cdot \alpha \cdot \chi) \cdot (3 \cdot \varepsilon_u + h \cdot \alpha \cdot \chi) \right) \end{aligned} \quad (A 2.11)$$

Moment-curvature relationship for known crack opening is defined with

$$\begin{aligned}
 M(\chi, w_i) &= \frac{b}{12 \cdot E_c^2 \cdot \chi^2} \left(-C_2 \cdot w_i \cdot (f_{ct} - E_c \cdot \varepsilon_u) \cdot (A - 2 \cdot f_{ct} + C_2 \cdot w_i + 2 \cdot E_c \cdot \varepsilon_u) \right) + \\
 &+ \frac{b}{12 \cdot E_c^2 \cdot \chi^2} \left(2 \cdot E_c \cdot h \cdot (A \cdot (C_2 \cdot w_i - f_{ct}) + C_2 \cdot w_i \cdot (C_2 \cdot w_i - 2 \cdot f_{ct} + E_c \cdot \varepsilon_u)) \cdot \chi \right) + \\
 &+ \frac{b}{12 \cdot E_c^2 \cdot \chi^2} \left(2 \cdot E_c^2 \cdot h^2 \cdot (3 \cdot f_{ct} - 2 \cdot C_2 \cdot w_i) \cdot \chi^2 \right)
 \end{aligned} \tag{A 2.12}$$

where

$$A = \sqrt{C_2 \cdot w_i (C_2 \cdot w_i - 4 \cdot f_{ct} + 4 \cdot E_c \cdot \varepsilon_u) + 4 \cdot E_c \cdot h \cdot (2 \cdot f_{ct} - C_2 \cdot w_i) \cdot \chi} \quad . \tag{A 2.13}$$

Bending moment in function of crack parameters (length and CMO) is defined with

$$\begin{aligned}
 M(\alpha, w_i) &= \frac{b \cdot h^2}{12 \cdot (f_{ct} - E_c \cdot \varepsilon_u)} \left(2 \cdot f_{ct}^2 - 2 \cdot f_{ct} \cdot (B - C_2 \cdot w_i \cdot (\alpha - 1) \cdot \alpha + 3 \cdot E_c \cdot \varepsilon_u) \right) + \\
 &+ \frac{b \cdot h^2}{12 \cdot (f_{ct} - E_c \cdot \varepsilon_u)} \left(C_2 \cdot w_i \cdot \alpha \cdot (B - C_2 \cdot w_i \cdot \alpha - 2 \cdot E_c \cdot (\alpha - 3) \cdot \varepsilon_u) \right)
 \end{aligned} \tag{A 2.14}$$

where

$$B = \sqrt{C_2 \cdot w_i \cdot \alpha - 2 \cdot f_{ct}} \cdot \sqrt{f_{ct} \cdot (2 - 4 \cdot \alpha) + C_2 \cdot w_i \cdot \alpha + 4 \cdot E_c \cdot (\alpha - 1) \cdot \varepsilon_u} \quad . \tag{A 2.15}$$

M2.3 Fracture energy of crack in bending

The energy needed to open a fictitious crack of length $\alpha_i \cdot h$ and width b , up to a crack mouth opening of w_i , noted as $G_{F,i}$, can be calculated for the known stress distribution in function of crack opening $\alpha(w)$, and the known geometry of the crack (Equation 4.30) as

$$G_{F,i} = \int_{b \cdot \alpha_i \cdot h} \left(\int_0^w \sigma(w) dw \right) dA \quad . \tag{A 2.16}$$

Developed expression for $G_{F,i}$ when the stress-crack opening relationship is linear is given in Chapter 4, Equation 4.67. For stress-crack opening given by the function

$$\sigma(w) = f_{ct} \frac{1}{\left(1 + \frac{w}{w_{n,w}} \right)^p} \tag{A 2.17}$$

it is obtained:

$$G_{F,i} = b \cdot \frac{f_{ct} \cdot \alpha \cdot h \cdot \left((2 - p) \cdot w_i \cdot w_{n,w} + w_{n,w}^2 - (w_i + w_{n,w})^2 \cdot (1 + w_i)^{-p} \right)}{(2 - 3 \cdot p + p^2) \cdot w_i} \quad . \tag{A 2.18}$$

M2.4 Continuous curvature in the zone disturbed by the fictitious crack opening

The curvature in the region disturbed by the macrocrack is assumed as a parabolic function:

$$\chi_{cr}(x) = a_{\chi}x^2 + b_{\chi}x + c_{\chi} \quad \forall L/2 - l_{i,cr} \leq x \leq L/2 \quad (\text{A 2.19})$$

with the smooth change at $x = L/2 - l_{i,cr}$, and the value at $L/2$ corresponding to the curvature of the cracked section, χ . The coefficients in Equation A 2.19 are obtained by solving the following system of equations:

$$\begin{aligned} \chi_{cr}(L/2 - l_{i,cr}) &= \chi_{pl}(L/2 - l_{i,cr}) \\ \chi'_{cr}(L/2 - l_{i,cr}) &= \chi'_{pl}(L/2 - l_{i,cr}) \\ \chi_{cr}(L/2) &= \chi_{cr,ij} \end{aligned} \quad (\text{A 2.20})$$

With introduced notation:

$$\begin{aligned} A_{\chi} &= \chi_{pl}(L/2 - l_{i,cr}) \\ B_{\chi} &= \chi'_{pl}(L/2 - l_{i,cr}) \\ C_{\chi} &= \chi_{cr,ij} \end{aligned} \quad (\text{A 2.21})$$

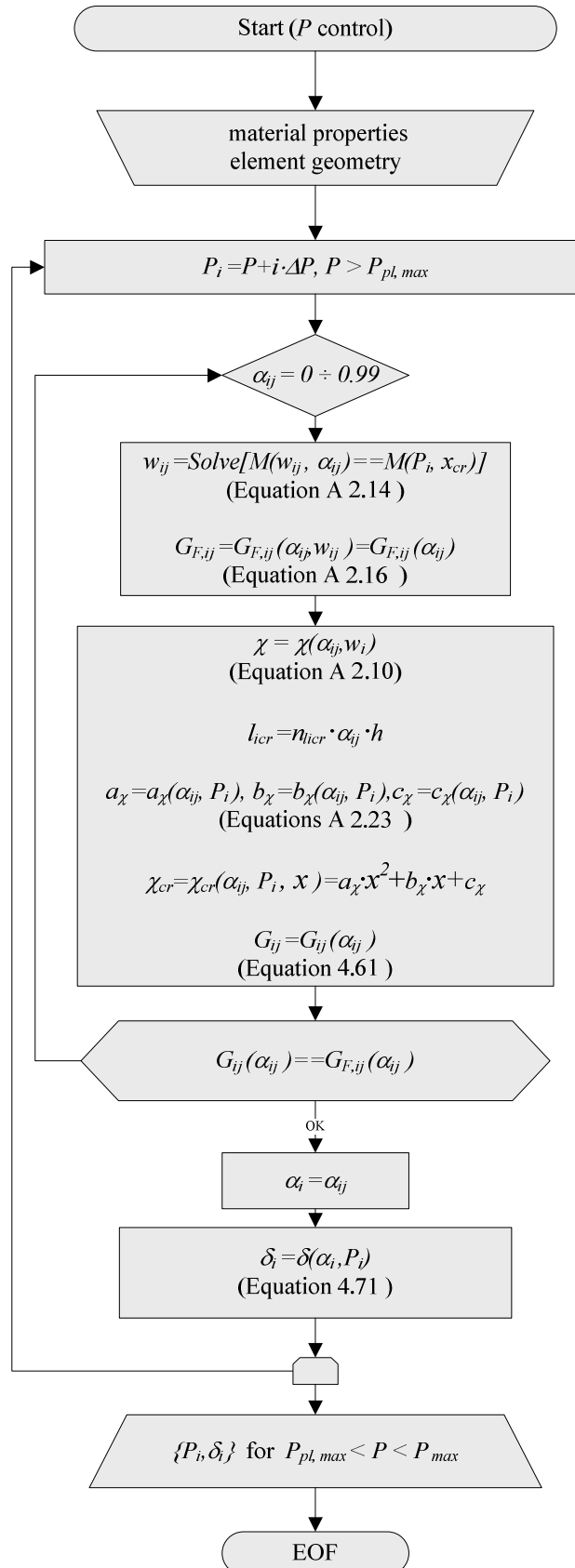
where all of the values on the right side are defined, system of equations A 2.20 can be written as

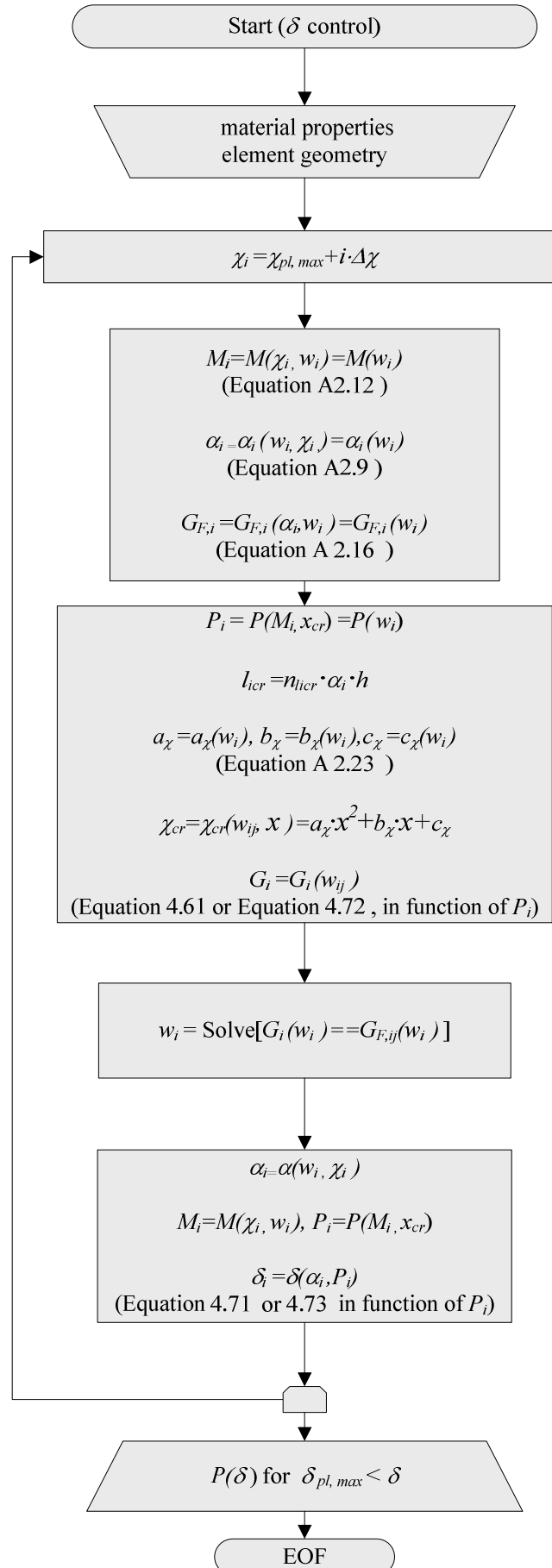
$$\begin{aligned} (a_{\chi}x^2 + b_{\chi}x + c_{\chi})_{x \rightarrow L/2 - l_{i,cr}} &= A_{\chi} \\ (2a_{\chi}x + b_{\chi})_{x \rightarrow L/2 - l_{i,cr}} &= B_{\chi} \\ (a_{\chi}x^2 + b_{\chi}x + c_{\chi})_{x \rightarrow L/2} &= C_{\chi} \end{aligned} \quad (\text{A 2.22})$$

and the solution of the system for the coefficients a_{χ} , b_{χ} , c_{χ} , is the following:

$$\begin{aligned} a_{\chi} &= -\frac{A_{\chi} + B_{\chi} \cdot l_{i,cr} - C_{\chi}}{l_{i,cr}^2} \\ b_{\chi} &= \frac{A_{\chi} \cdot (L - 2 \cdot l_{i,cr}) + B_{\chi} \cdot (L - l_{i,cr}) \cdot l_{i,cr} - C_{\chi} \cdot (L - 2 \cdot l_{i,cr})}{l_{i,cr}^2} \\ c_{\chi} &= \frac{-A_{\chi} \cdot (L - 4 \cdot l_{i,cr}) \cdot L + (L - 2 \cdot l_{i,cr}) \cdot (C_{\chi} \cdot (L - 2 \cdot l_{i,cr}) - B_{\chi} \cdot L \cdot l_{i,cr})}{4 \cdot l_{i,cr}^2} \end{aligned} \quad (\text{A 2.23})$$

M2.5 Algorithm for energy balance: force and displacement control





M2.6 FEM model

A numerical finite element (FEM) model for analysing the response of UHPFRC beams in bending was also developed in this study. The hypotheses of this model are the same as the hypotheses used for the development of the analytical model:

- the macrocrack is modelled according to the assumptions of the fictitious crack model: the crack shape is modelled as linear, and the transfer of stresses over the crack faces is simulated by internodal forces, using non-linear spring elements; the macrocrack coincides with the mid-span section of the beam in symmetric boundary conditions;
- the material surrounding the macrocrack is modelled as linear-elastic in compression and elastic-plastic in tension, enabling pseudo-plastic or strain hardening behaviour to be simulated.

Software package ANSYS is used for processing the model. Elements and material models used are:

- element type PLANE82 for the beam, with linear elastic or plastic (bilinear hardening) material properties;
- element type COMBIN39 for non-linear springs, with $F - \delta$ relationships defined based on the material $\sigma - \varepsilon$ and $\sigma - w$ relationship characterising tensile softening.

As long as the stress state in an element is such that the direction of first principal stresses in the region of the macrocrack is close to the direction of springs ($\sigma_1 \approx \sigma_x$), this model can be used for prediction of the response of beams made of quasi-brittle materials.

Appendix T1:

Testing of thin UHPFRC elements

T.1 Problem statement and objectives

This testing program is developed to provide more information on the behaviour and on the load bearing capacity of thin UHPFRC slabs without ordinary reinforcement. The type and geometry of tested elements were chosen to be representative of upper slabs in ribbed structural members conceived to resist traffic loads (Figure T.1). In the case of two way ribbed slabs, failure of the upper slab is a local bending or punching shear mechanisms (Figure T.1 a)), whereas in one-way ribbed systems (e.g. π -shaped girders) the occurrence of a bending failure might also give rise to a global failure mechanism (Figure T.1 b)). Most of existing experimental research on UHPFRC structural elements is oriented towards bending and shear behaviour of beams, whereas available experimental data on bending and punching shear failure of thin slabs are lacking.

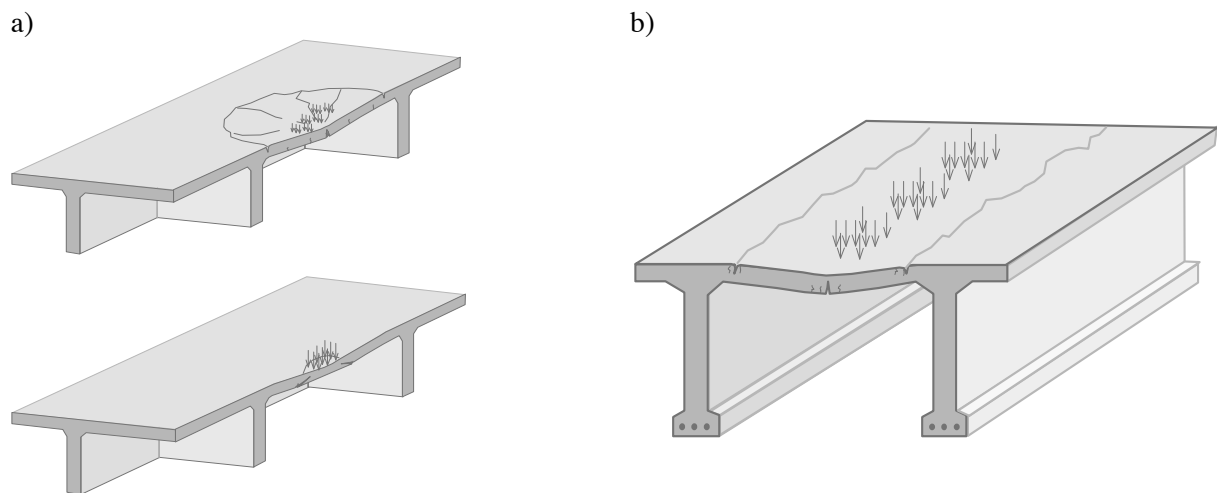


Figure T.1: Examples of structures with thin UHPFRC slabs and slab failure modes: a) two-way ribbed slab with flexural and punching shear failure of thin slab; b) π -shaped girder and transversal flexural failure of thin slab.

Possible modes of failure and corresponding ultimate resistance of thin slabs without ordinary reinforcement are the principal interest of the experimental analysis. Beams in three-point bending were also tested to provide basic information on the bending behaviour of statically determinate systems. The influence of elements size on structural response was also investigated by testing beams and slabs with variable thickness. Data obtained by this test program allowed to verify the validity of structural models developed in this thesis.

T.2 Testing program and preparation of the specimens

A total of 21 specimens were tested, Figure T.2:

- six 900 x 900 mm slabs, with thickness varying from 40 to 60 mm
- four 350 x 350 mm slabs, with thickness varying from 30 to 60 mm
- 11 500 x 200 mm beams, with thickness varying from 25 to 75 mm

All of the elements were tested up to failure. Different test set-ups were conceived in order to achieve the desired modes of failure (Figure T.2). Beams were tested in three-point bending, while slabs were tested under central-point load. Beside the geometry, the boundary conditions of the two series of slabs also changed. Within a particular test series, the test parameter is the elements thickness.

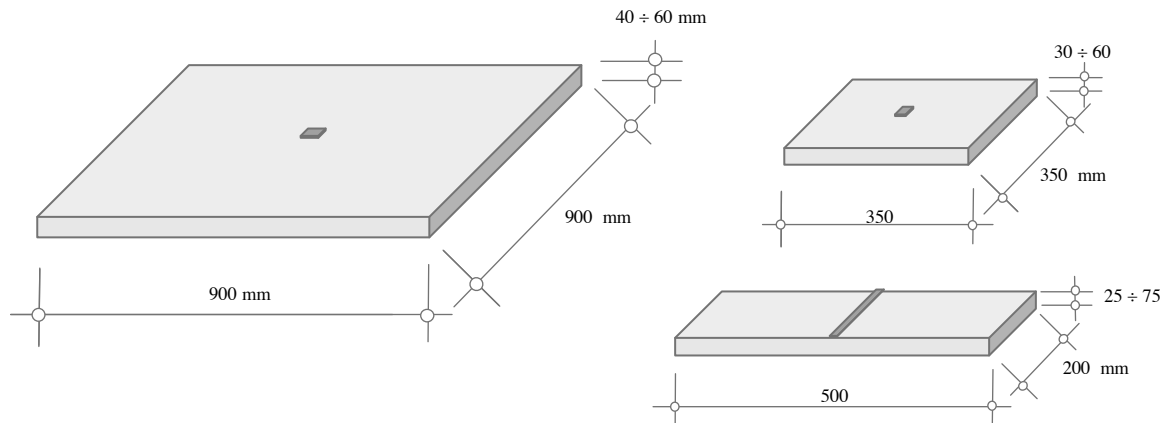


Figure T.2: Geometry of tested specimens: a) slabs tested in bending failure under point load; b) slabs tested in punching shear failure; c) beams (plates) tested in three-point bending.

Specimens were cast and tested at the Structural Concrete Laboratory of the EPFL. All of the elements were made of the same concrete, BSI®, without any conventional reinforcement. The composition of the material is given in § 3.2.3, while the mechanical behaviour in compression and in tension is described in § 3.3.1. and § 3.3.2 respectively.

Mixing and casting procedure

The components of concrete (pre-mixed powder and aggregates, water, admixtures and fibres) were mixed according to the procedure prescribed for BSI®. Mixing time is 12 minutes, of which 3 minutes with fibres. A sufficiently powerful mixer and a rigorous proportioning of components are indispensable to achieve good mechanical properties as well as workability of fresh concrete.

Fresh concrete was cast in wooden formworks, previously impregnated with oil. The material is self-compacting, and easily sets in formworks without need of vibrating. The pouring method was conceived in order to minimize undesired preferential orientations of the fibres. No thermal treatment is needed for the used UHPFCR. However, like for ordinary concrete, a curing product was applied on the surface of concrete immediately after casting and the formworks were coated with plastic sheets to prevent surface desiccation at early age. Elements were demoulded after approximately 24 h then stored in water until testing day.

The amount of the material produced with a single batch being limited by the capacity of the mixer, not all of the samples were produced with exactly the same concrete. For each batch of concrete, quality control tests were performed. Slump flow of the fresh concrete was controlled as a first indicator of quality of the produced material. Three cubes of dimensions $a = 100 \text{ mm}$ and three prisms with dimensions $70 \times 70 \times 280 \text{ mm}$ were cast for every batch for quality control tests on the hardened material. Cubes were subjected to compressive strength test, performed at the Laboratory of Construction Materials of the EPFL. The same laboratory also performed tests for the modulus of Elasticity. Prisms were tested in three point bending (displacement controlled test with span $l_s = 190 \text{ mm}$) to indirectly check the tensile properties of the material. These tests were performed at the Structural Concrete Laboratory of the EPFL. The results of quality control tests are presented, for every batch, in Tables T.2, T.4 and T.6.

T.3 Thin beams in three point bending

The geometry and boundary conditions of the specimens are given in Figure T.3. The thickness h varies between 25 and 75 mm, while the span and the width are kept constant.

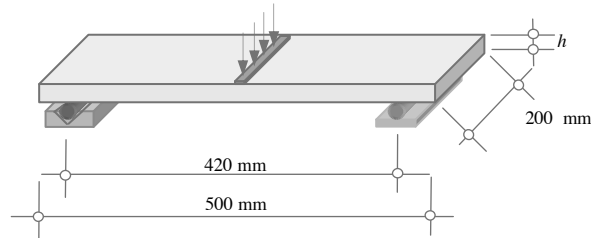


Figure T.3: Geometry and boundary conditions of beams

T.3.1 Test setup and instrumentation

Tests are carried out by controlling the displacement of the actuator of the test machine, with a loading speed ranging between $v = 0.002 \text{ mm/s}$ and $v = 0.008 \text{ mm/s}$ as a function of elements size and loading phase (pre or post-peak). Beams were instrumented with Linear Variable Differential Transformer (LVDTs) and marked with points for photogrammetric analysis, Figure T.4. The LVDT that measures the vertical displacement at mid-span is designated as LVDT_01 (Figure T.5 a)). Two other LVDTs measure the horizontal elongation on the tensile side of the beam, between points symmetrically placed with respect to the load point (Figure T.5 b) and Figure T.6)).

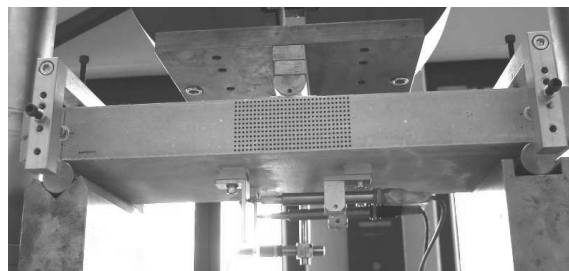
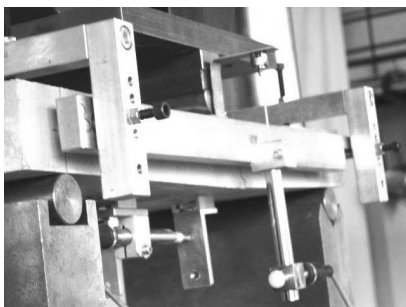


Figure T.4: Test setup and instrumentations: LVDTs and points for photogrammetric measures.

a)



b)



Figure T.5: Measuring devices: a) LVDT_01, measuring vertical displacement; b) LVDT_02 and LVDT_03 measuring horizontal elongations

As already mentioned (Chapter 4), the elongations measured on the tensile side of the beam must be corrected to take into account the rotation of the beam at points where the measuring devices are fixed.

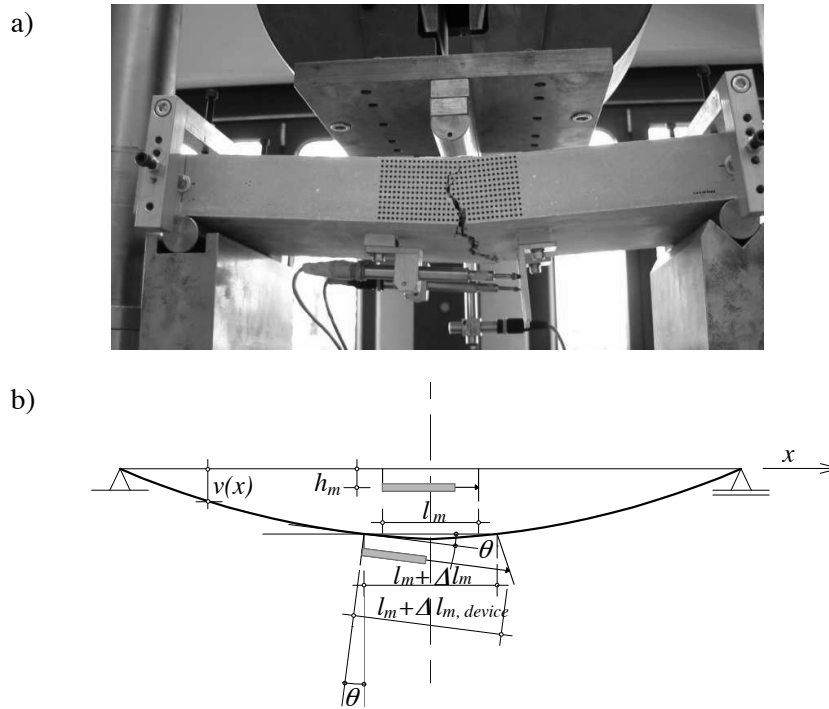


Figure T.6: LVDTs for horizontal elongations : a) view of the device position; b) effect of the rotation on the measured elongation.

Applied force and the vertical displacement of the actuator are measured by the sensors of the test machine. The results obtained with photogrammetry are not discussed in detail in this Appendix. Post-processing of photogrammetric images of the beams allowed useful information such as position, number and propagation of cracks to be obtained.

T.3.2 Principal results

Most of the beams were tested under monotonically increasing displacement, but some specimens were subjected to loading and unloading cycles. Tests results are summarized in Table T.1, while more detailed information e.g. measured force-displacement curves, crack patterns etc, are given in §1.3.3-1.3.12. The results of tests for quality control are given in Table T.2: as it can be observed, the average values from bending tests on prisms are similar for the two batches, allowing the results of all the beams to be directly compared.

Table T.1: Summary of test results: UHPFRC beams

Specimen	Date of casting	Date of testing	Material	Slump flow [cm]	$f_{c,m}$ * [MPa]	Measured height [mm]	P_{max} [kN]	No. of cracks**	remark
P 25a	16.05.06.	13.07.06	G27	68.7	187	24.5	5.31	1	
P 25b	16.05.06.	19.07.06	G27	68.7	187	25.5	5.83	3	
P 25c	16.05.06.	not tested	G27	68.7	187	-	-	-	
P 4a	16.05.06.	12.07.06	G27	68.7	187	38.9	-	-	pre- cracked, at 11KN
P 4b	16.05.06.	20.07.06	G27	68.7	187	38.1	11.27	2	
P 4c	16.05.06.	13.07.06	G27	68.7	187	40.2	13.96	1	
P 5a	19.05.06.	12.07.06	G29	68.0	153	50.0	23.96	2	
P 5b	19.05.06.	not tested	G29	68.0	153	-	-	-	
P 5c	19.05.06.	19.07.06	G29	68.0	153	50.05	26.53	3	
P 6a	16.05.06.	19.07.06	G27	68.7	187	59.9	32.93	3	more fibres
P 6b	16.05.06.	13.07.06	G27	68.7	187	59.1	-	-	more fibres
P 6c	16.05.06.	not tested	G27	68.7	187	-	-	-	more fibres
P 7.5a	19.05.06.	18.07.06	G29	68.0	153	73.7	43.37	-	
P 7.5b	19.05.06.	14.07.06	G29	68.0	153	73.2	-	-	pre- cracked, at 42KN
P 7.5c	19.05.06.	not tested	G29	68.0	153	-	-	-	

* mean value of compressive strength obtained on specimens for quality control (table below)

** number of macrocracks observed prior to P_{max}

Table T.2: Test results of material quality control

Material	Date of casting	Slump flow [cm]	Cubes	Date of test	f_c [MPa]	Modulus of elasticity [GPa]	Prisms	Date of test	P_{crack} [kN]	P_{max} [kN]
G27	16.05.06	68.7	G27A	20.07.06	175		G27A	25.07.06	32	33.8
			G27B	20.07.06	183		G27B	25.07.06	31	40.57
			G27C	20.07.06	203		G27C	25.07.06	32	44.8
			mean		187		mean			39.7
G29	19.05.06	68.0	G29A*	21.07.06	226*	61.50	G29A	25.07.06	33	39.2
			G29Ab*		200.2					
			G29B	20.07.06	143.5	G29B	25.07.06	30	41.02	
			G29C	20.07.06	163	G29C	25.07.06	30	41.75	
			mean		(153)	60.25	mean		40.6	

* specimens tested for modulus of elasticity; corresponding compressive strength in this case are obtained from $\varnothing 50$ mm and $h = 100$ mm cylinders, drilled from cubes with $a = 100$ mm

T.3.3 Beam P 25a, $h = 24.5$ mm

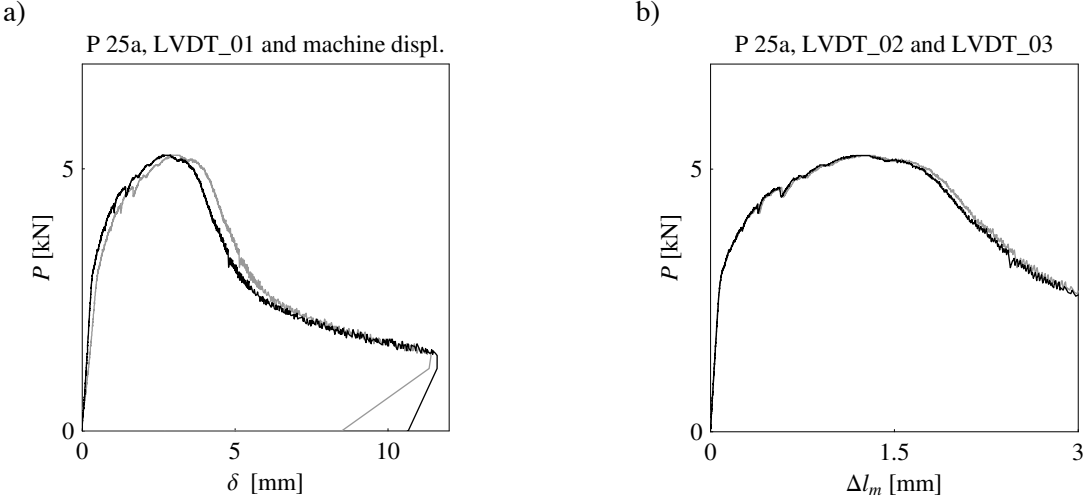


Figure T.7: Beam P 25a: a) force-vertical displacement measured at mid-span by LVDT_01 (black line) and force-vertical displacement of the actuator (grey line); b) force-elongation at tensile side measured by LVDT_02 (black line) and LVDT_03 (grey line).

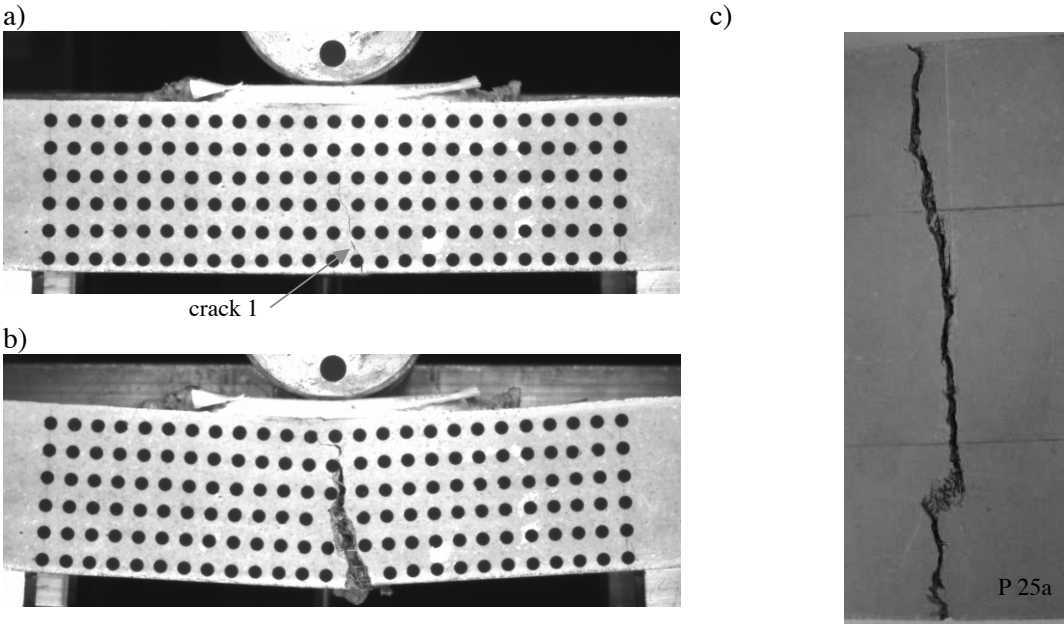


Figure T.8: Cracking of the beam: a) crack at P_{max} and b) crack at failure, observed by photogrammetry analysis; c) crack pattern on tensile beam side.

T.3.4 Beam P25 $b, h=25.5$ mm

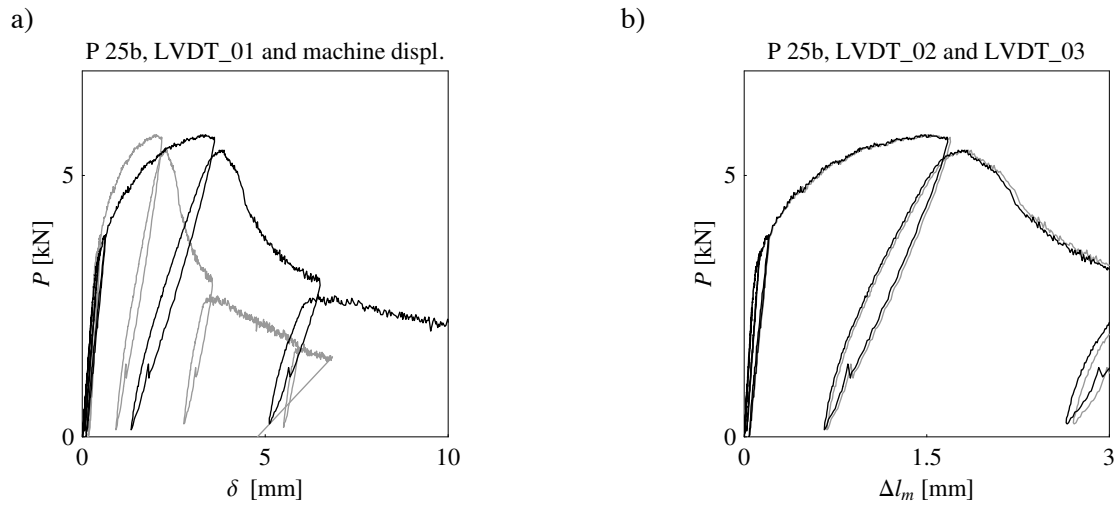


Figure T.9: Beam P 25b: a) force-vertical displacement measured at mid-span by LVDT_01 (black line) and force-vertical displacement of the actuator (grey line); b) force-elongation at tensile side measured by LVDT_02 (black line) and LVDT_03 (grey line).

During this test, a problem probably occurred with the LVDT_01, which unexpectedly recorded higher displacements than the sensor of the testing machine. A comparison with the results obtained for beam P 25a also indicates that the values measured by LVDT_01 probably overestimate the effective displacement.

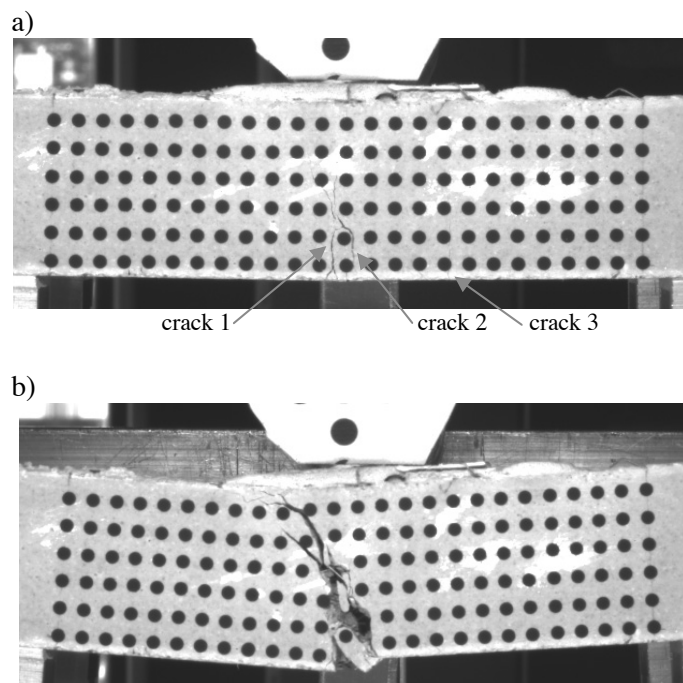
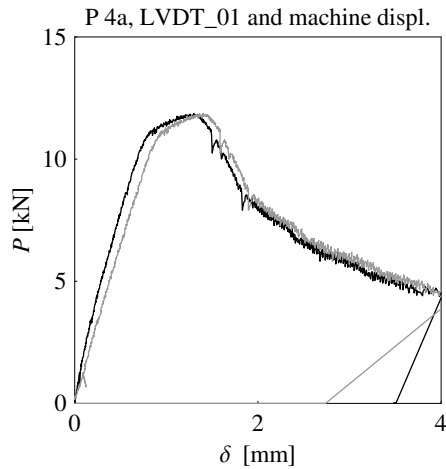


Figure T.10: Cracking of the beam observed by photogrammetry analysis: a) cracks at P_{max} , b) crack at failure.

T.3.5 Beam P 4a, $h = 38.9$ mm

a)



b)

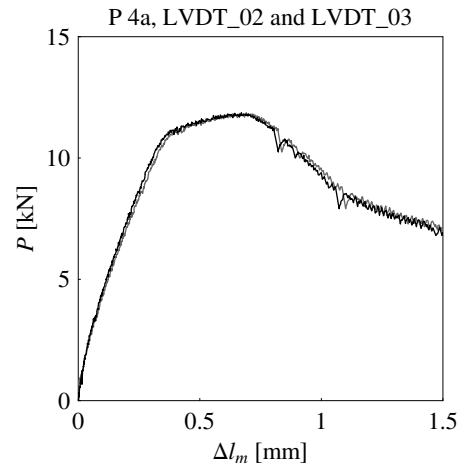


Figure T.11: Beam P 4a: a) force-vertical displacement measured at mid-span by LVDT_01 (black line) and force-displacement of the actuator (grey line); b) force-elongation at tensile side measured by LVDT_02 (black line) and LVDT_03 (grey line).

The beam was pre-cracked during the positioning of the loading device, with a force of approximately $11 \div 12$ kN. It can be observed that up to approximately this force level, the force-displacement response is linear, with the actual stiffness of the microcracked element, as explained in Chapter 4. Photogrammetric monitoring of this beam was not performed.

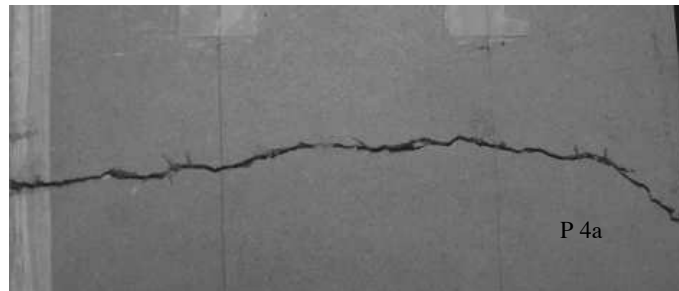


Figure T.12: Crack pattern on tensile beam side.

T.3.6 Beam P 4b, $h = 38.1$ mm

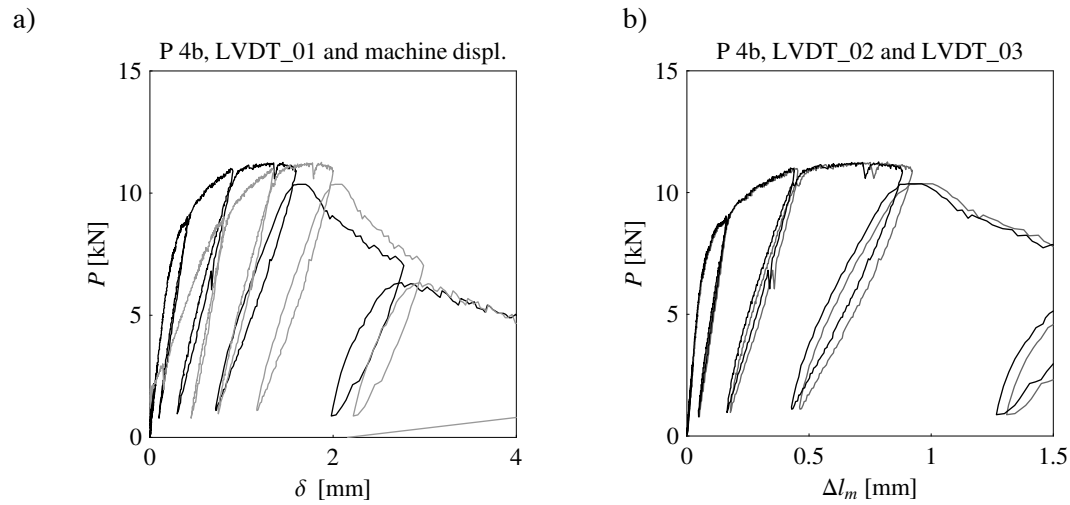


Figure T.13: Beam P 4b: a) force-vertical displacement measured at mid-span by LVDT_01 (black line) and force-displacement of the actuator (grey line); b) force-elongation at tensile side measured by LVDT_02 (black line) and LVDT_03 (grey line).

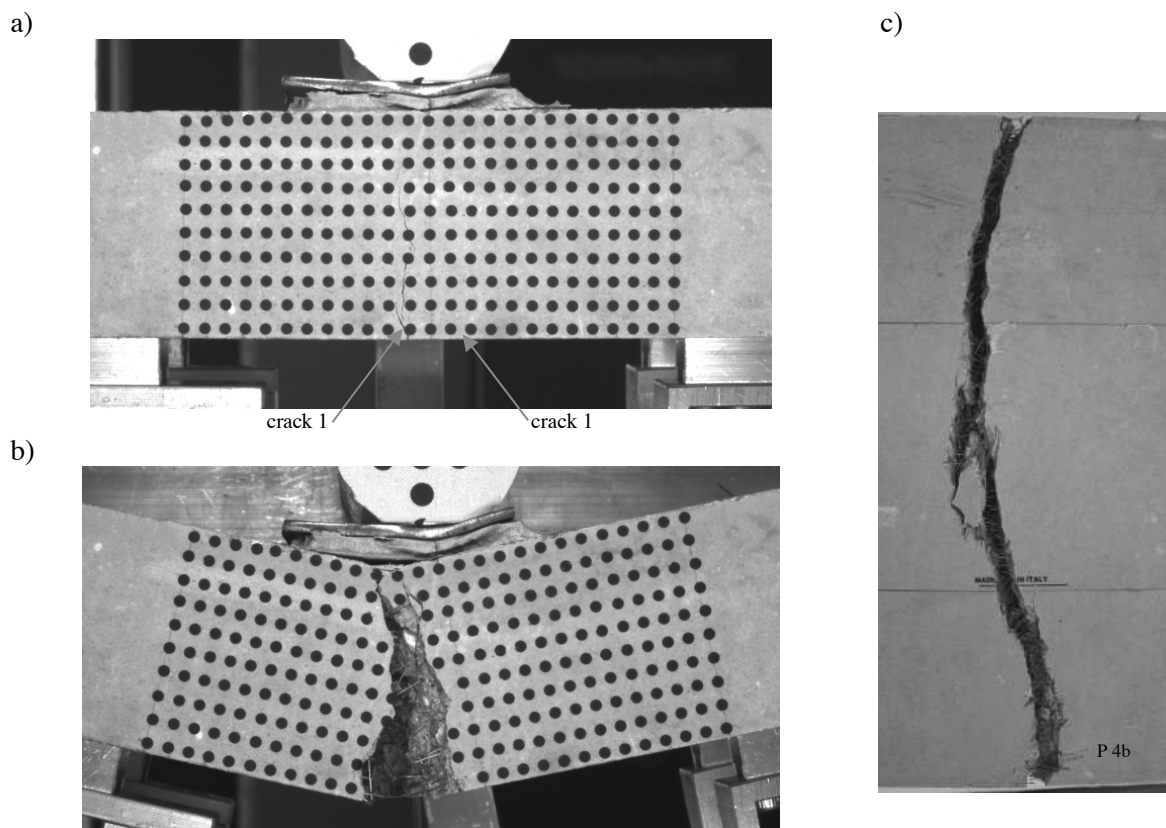


Figure T.14: Cracking of the beam: a) cracks at P_{max} and b) crack at failure, observed by photogrammetry analysis; c) crack pattern on tensile beam side.

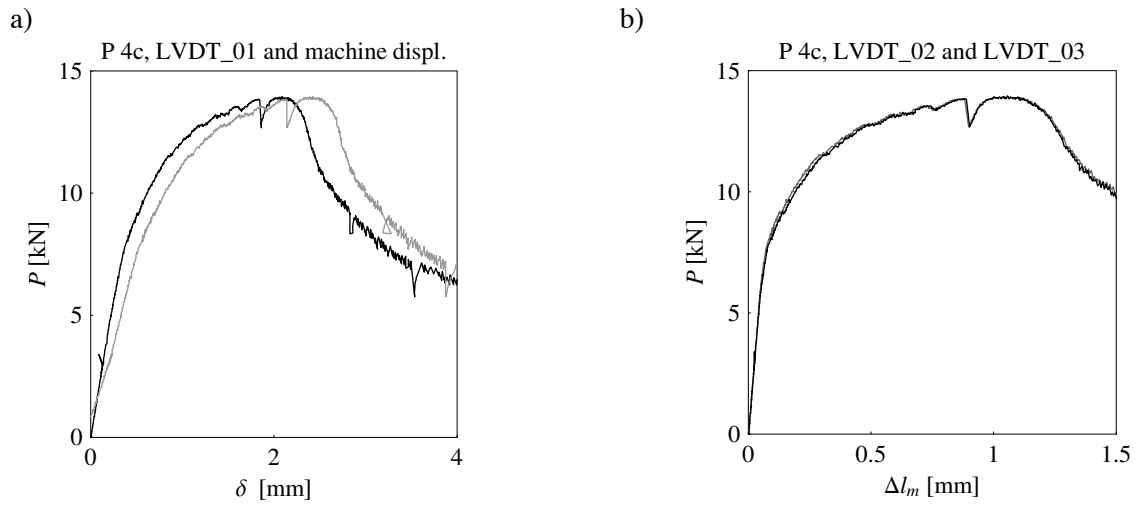
T.3.7 Beam P 4c, $h=40.2$ mm

Figure T.15: Beam P 4c: a) force-vertical displacement measured at mid-span by LVDT_01 (black line) and force-displacement of the actuator (grey line); b) force-elongation at tensile side measured by LVDT_02 (black line) and LVDT_03 (grey line).

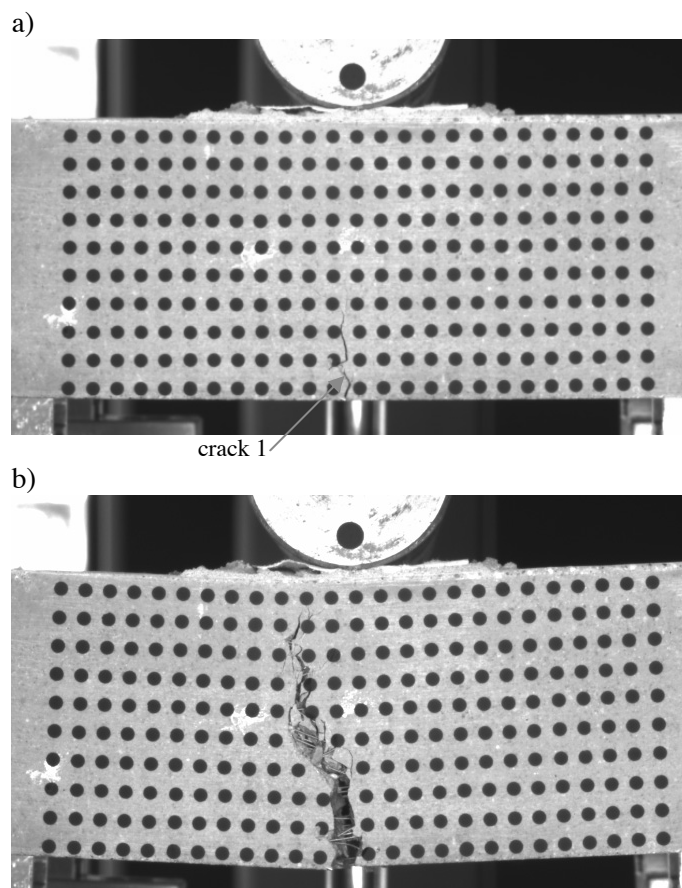


Figure T.16: Cracking of the beam observed by photogrammetry analysis: a) crack at P_{max} , b) crack at failure.

T.3.8 Beam P 5a, $h=50$ mm

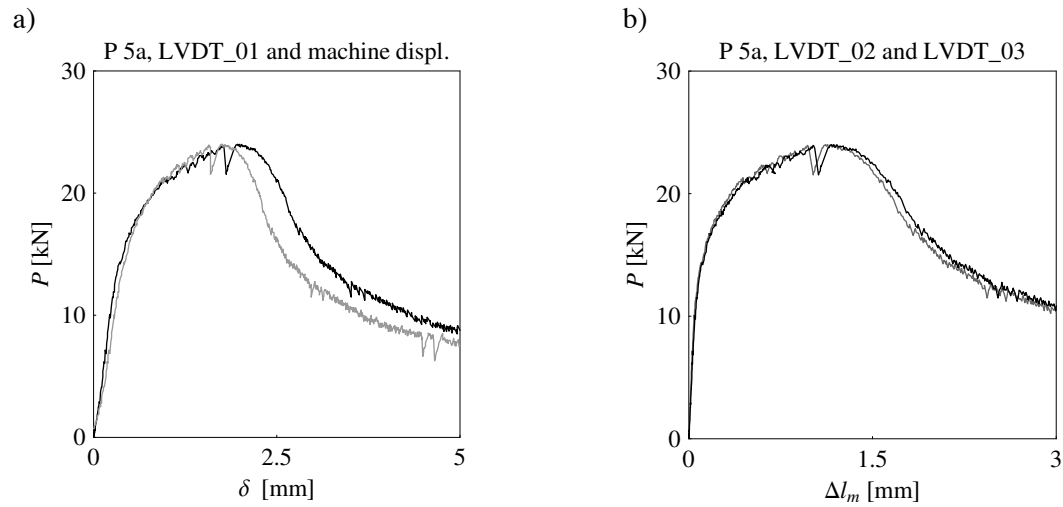


Figure T.17: Beam P 5a: a) force-vertical displacement measured at mid-span by LVDT_01 (black line) and force-displacement of the actuator (grey line); b) force-elongation at tensile side measured by LVDT_02 (black line) and LVDT_03 (grey line).

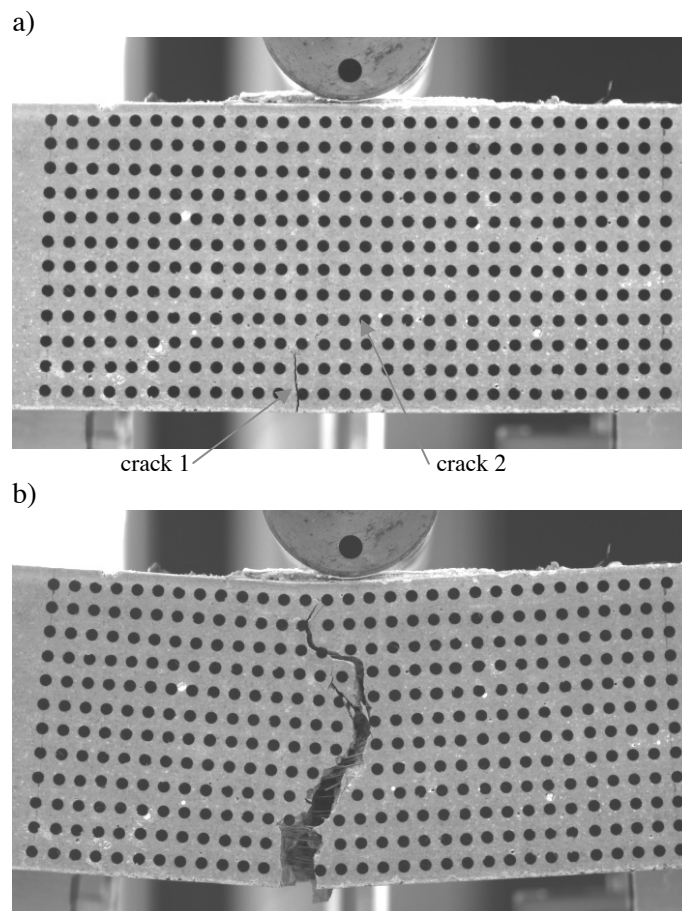


Figure T.18: Cracking of the beam observed by photogrammetry analysis: a) cracks at P_{max} , b) crack at failure.

T.3.9 Beam P 5c, $h=50.5$ mm

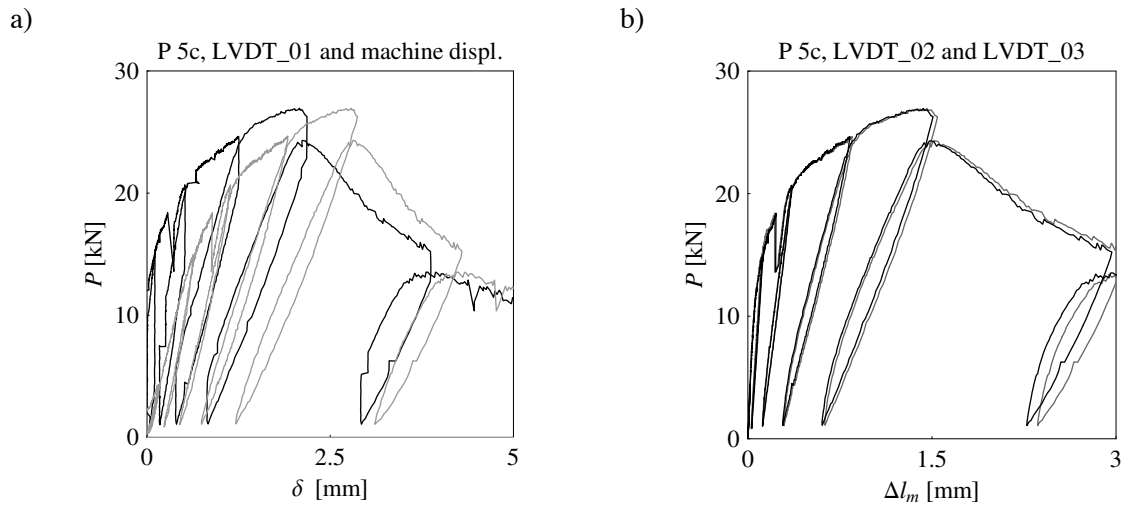


Figure T.19: Beam P 5c: a) force-vertical displacement measured at mid-span by LVDT_01 (black line) and force-displacement of the actuator (grey line); b) force-elongation at tensile side measured by LVDT_02 (black line) and LVDT_03 (grey line).

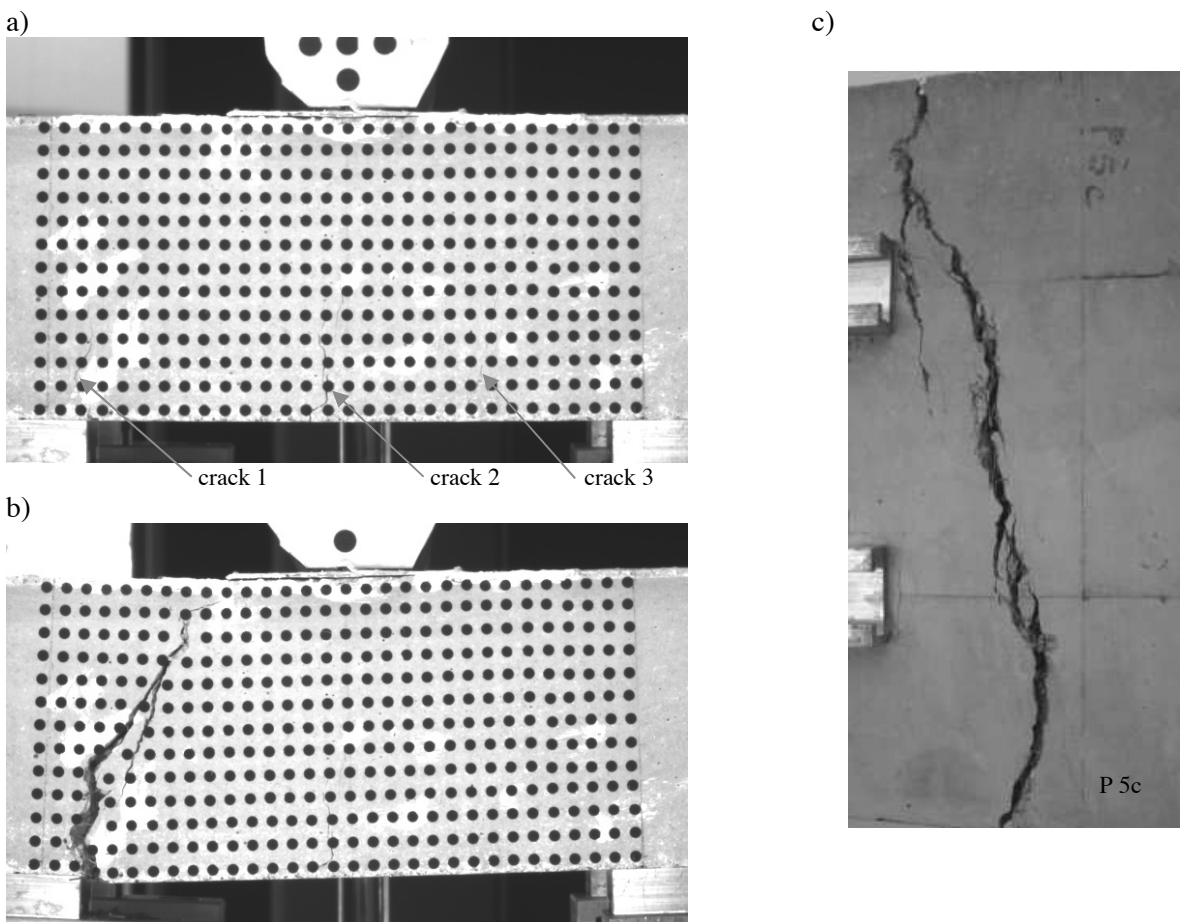


Figure T.20: Cracking of the beam: a) cracks at P_{max} and b) cracks at failure, observed by photogrammetry analysis; c) crack pattern on tensile beam side.

T.3.10 Beam P 6a, $h=59.9$ mm

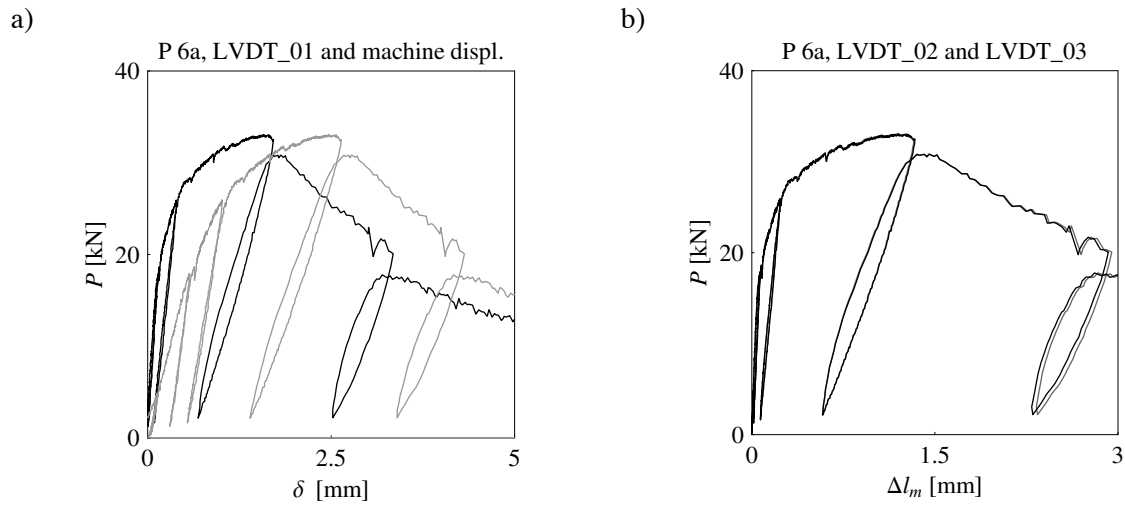


Figure T.21: Beam P 6a: a) force-vertical displacement measured at mid-span by LVDT_01 (black line) and force-displacement of the actuator (grey line); b) force-elongation at tensile side measured by LVDT_02 (black line) and LVDT_03 (grey line).

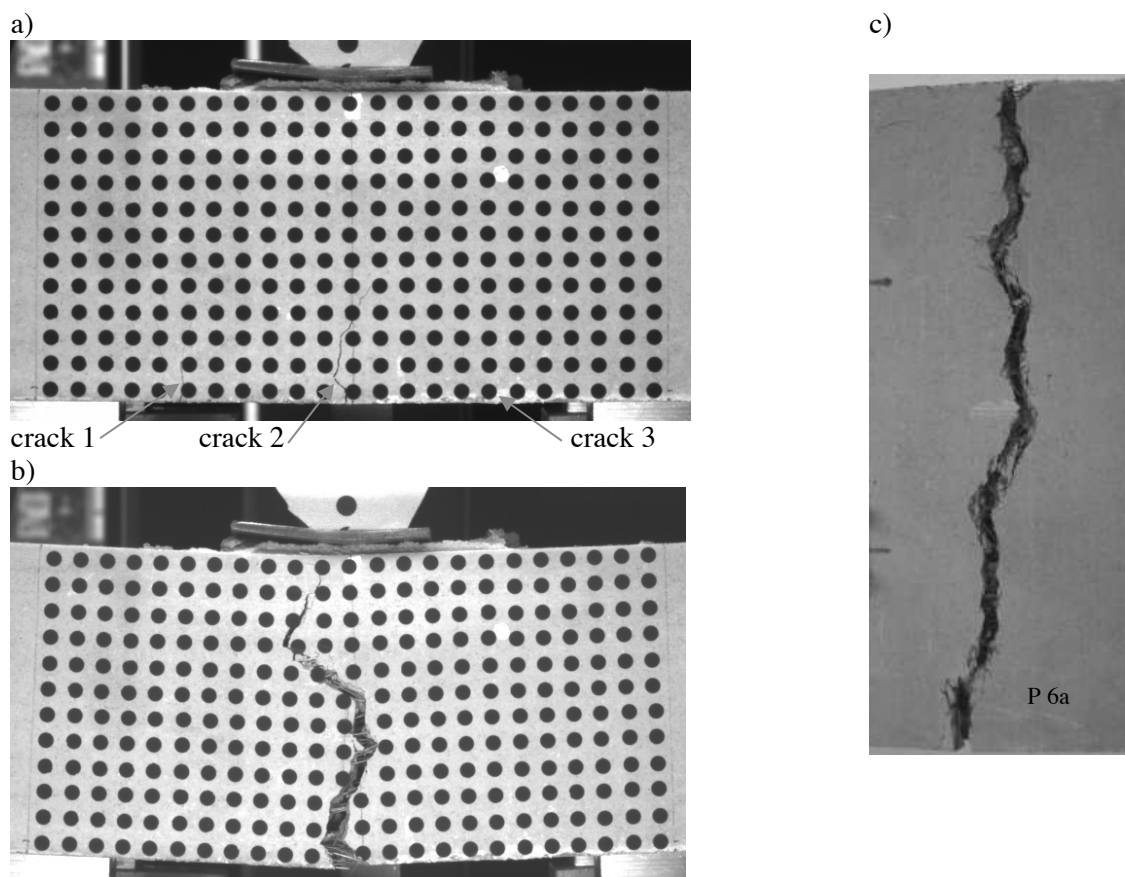


Figure T.22: Cracking of the beam: a) cracks at P_{max} and b) crack at failure, observed by photogrammetry analysis; c) crack pattern on tensile beam side.

T.3.11 Beam P 6b, $h=59.1$ mm

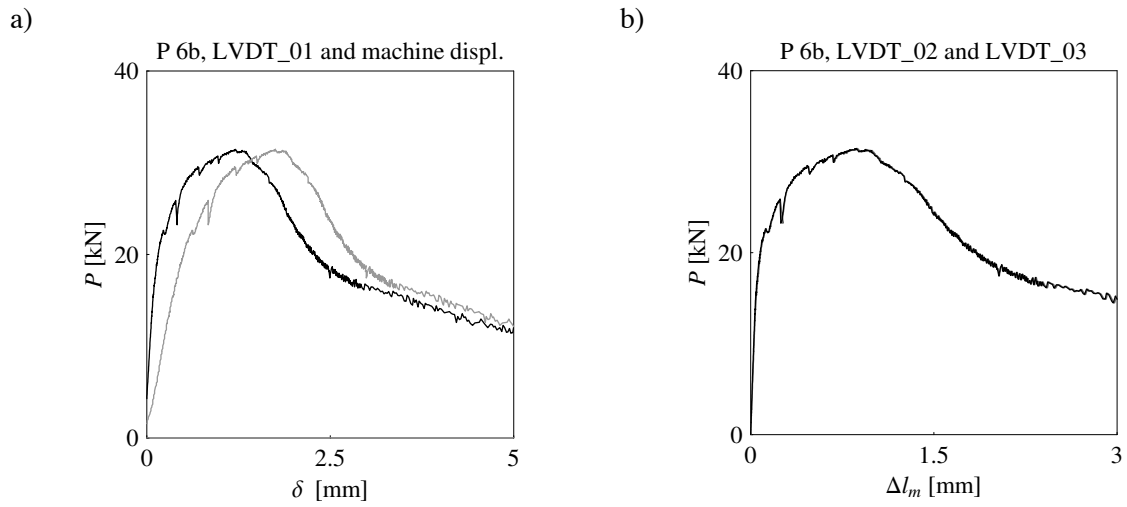


Figure T.23: Beam P 6b: a) force-vertical displacement measured at mid-span by LVDT_01 (black line) and force-displacement of the actuator (grey line); b) force-elongation at tensile side measured by LVDT_02 (black line) and LVDT_03 (grey line).

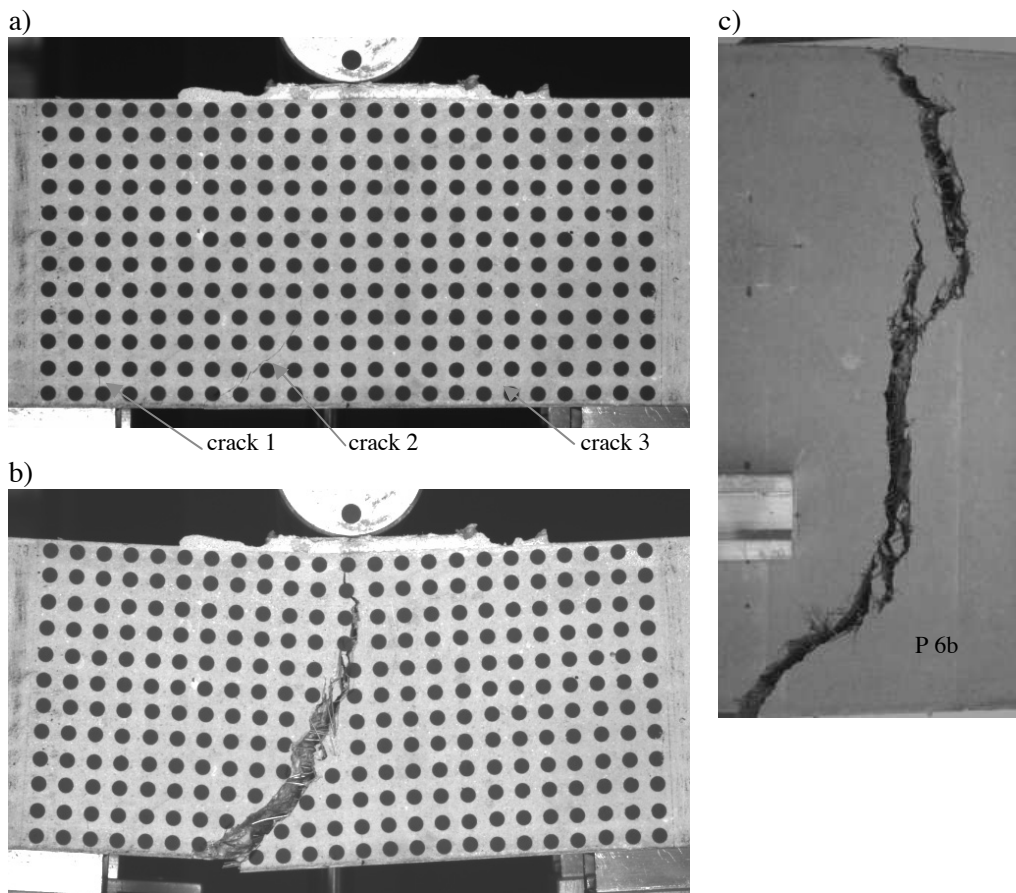


Figure T.24: Cracking of the beam: a) crack at P_{max} and b) crack at failure, observed by photogrammetry analysis; c) crack pattern on tensile beam side.

T.3.12 Beam P 75a, $h=73.7$ mm

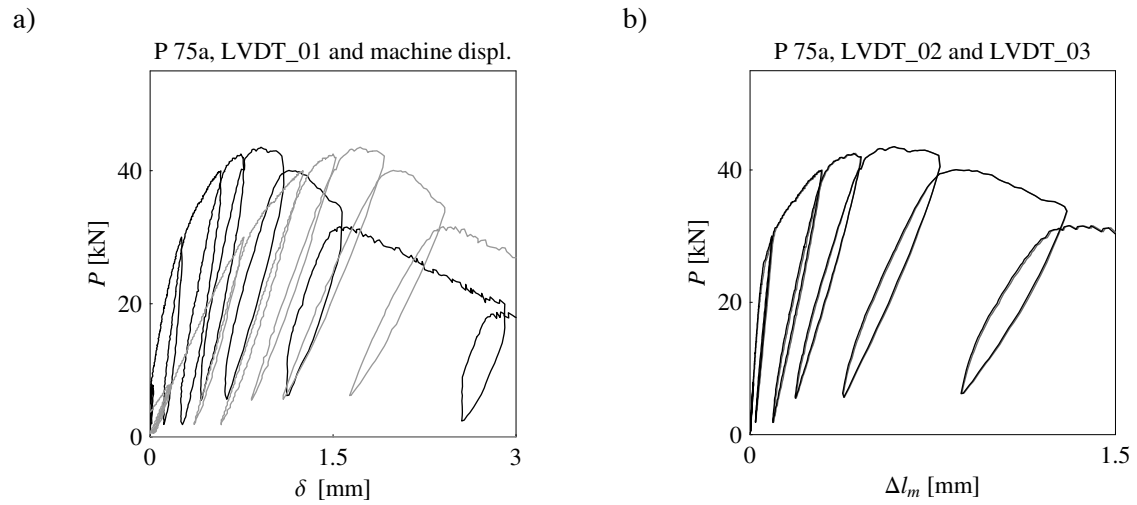


Figure T.25: Beam P 75a: a) force-vertical displacement measured at mid-span by LVDT_01 (black line) and force-displacement of the actuator (grey line); b) force-elongation at tensile side measured by LVDT_02 (black line) and LVDT_03 (grey line).

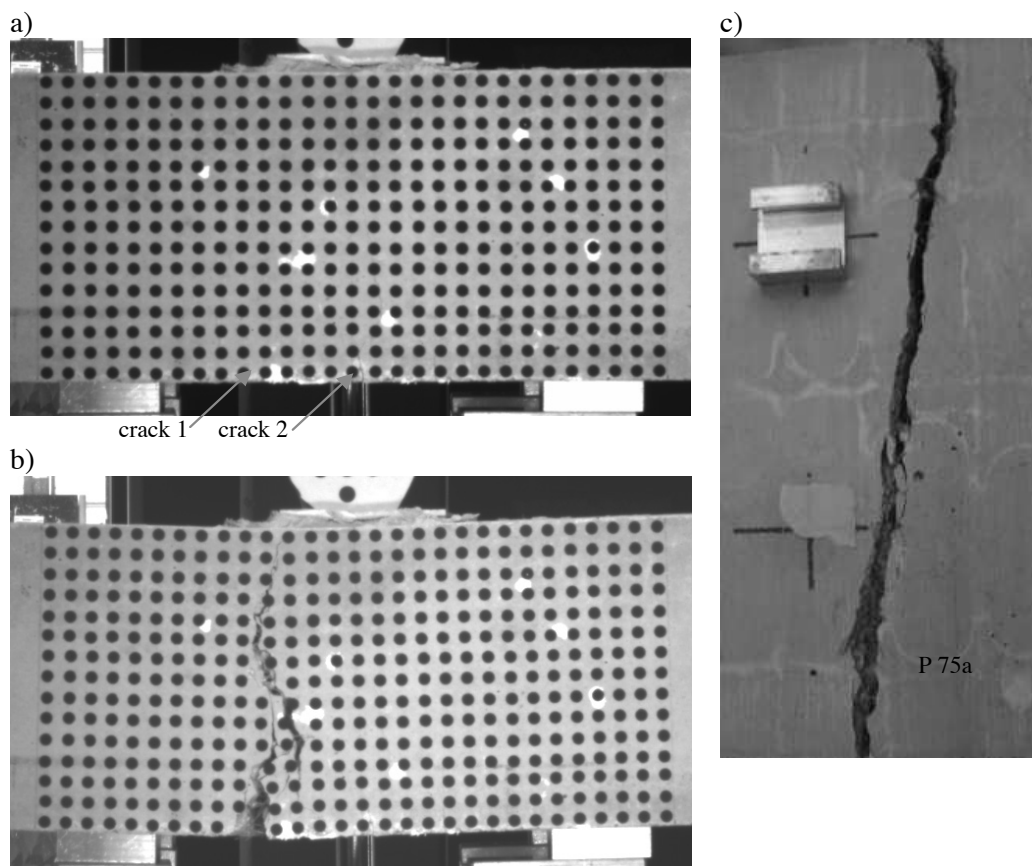


Figure T.26: Cracking of the beam: a) cracks at P_{max} and b) crack at failure, observed by photogrammetry analysis; c) crack pattern on tensile beam side.

T.3.13 Beam P 75b, $h=73.2$ mm

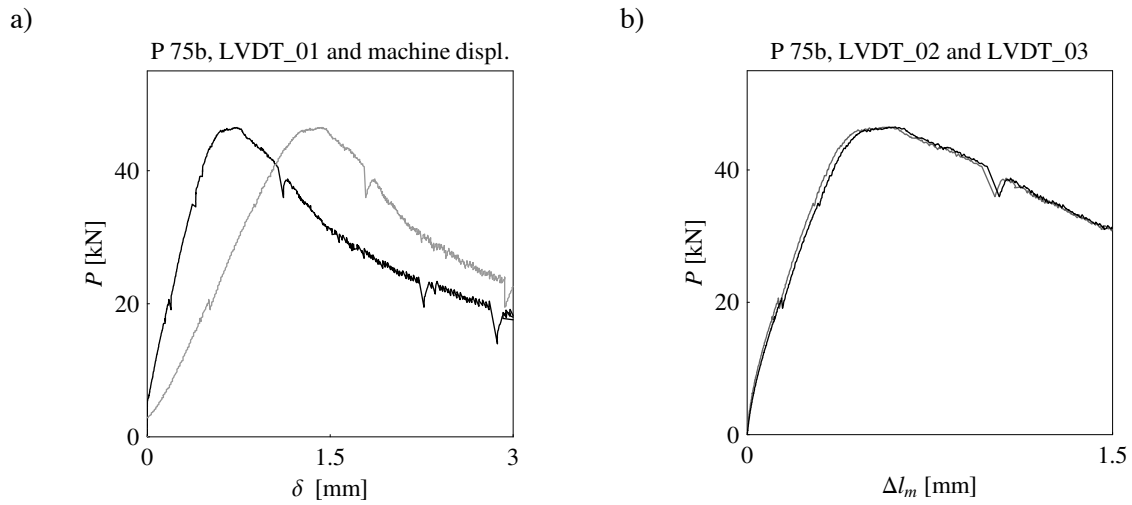


Figure T.27: Beam P 75b: a) force-vertical displacement measured mid-span by LVDT_01 (black line) and force-displacement of the actuator (grey line); b) force-elongation at tensile side measured by LVDT_02 (black line) and LVDT_03 (grey line).

This beam was pre-cracked with the force of approx. 42 KN.

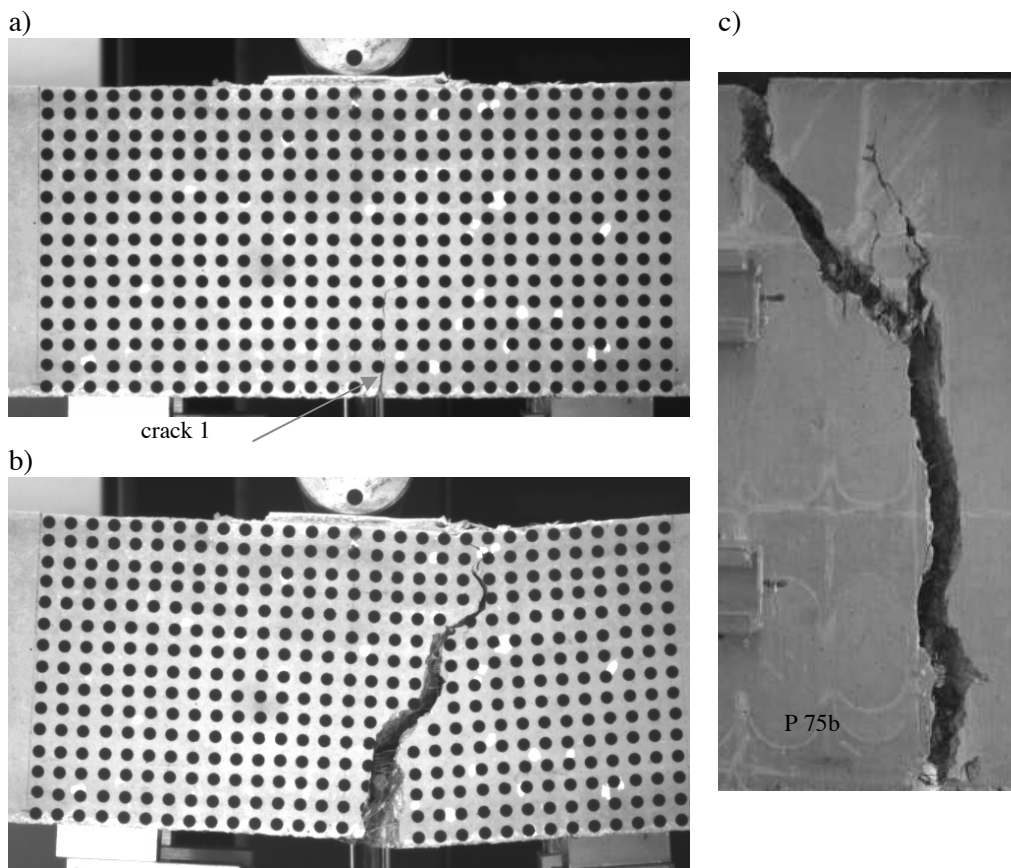


Figure T.28: Cracking of the beam: a) crack at P_{max} and b) crack at failure, observed by photogrammetry analysis; c) crack pattern on tensile beam side.

T.3.14 Summary of force-displacement responses

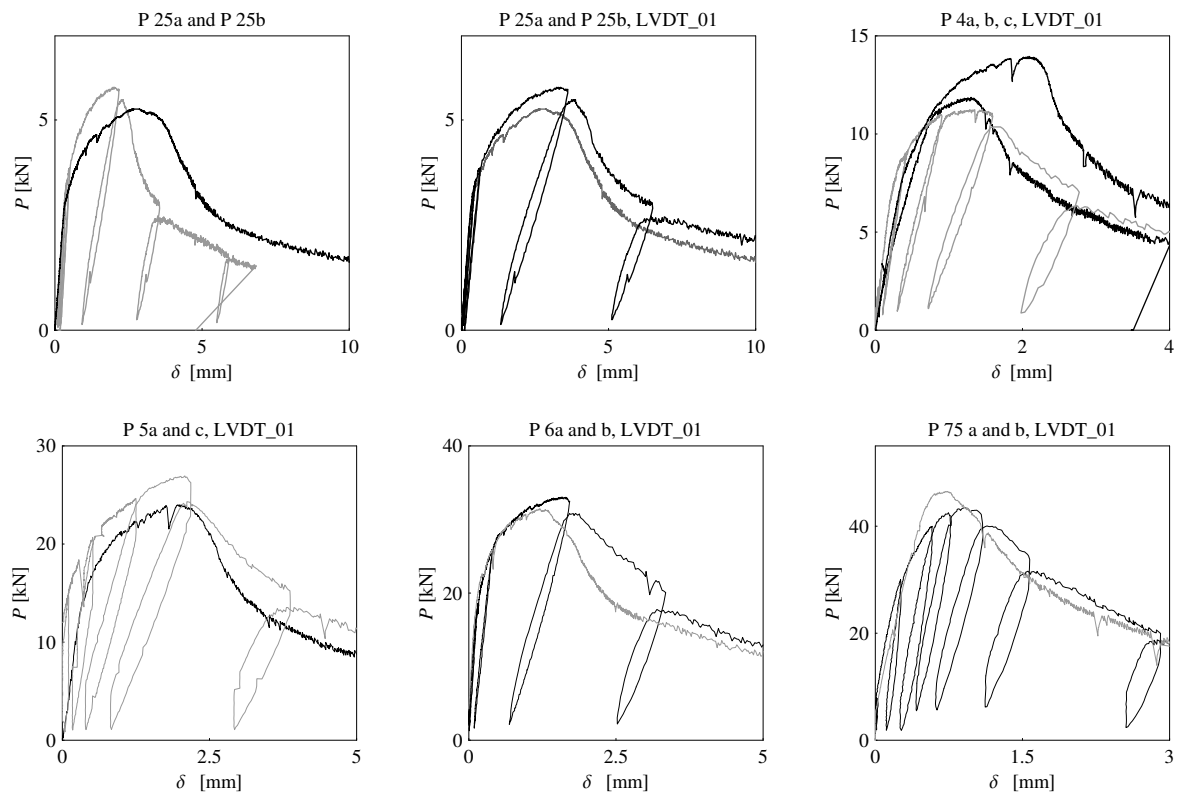


Figure T.29: Force-displacement of tested beams: comparison of the responses for beams of the same height.

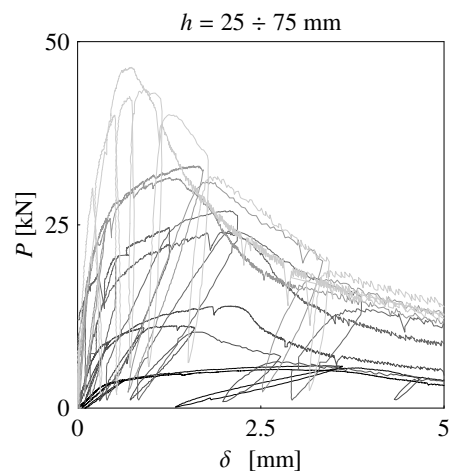


Figure T.30: Comparison of force-displacement response of all tested beams

T.4 Thin slabs failing in bending

The dimensions of the slabs are chosen in accordance to theoretical considerations on possible minimal thicknesses that could be applied in road bridge design, while the spans are chosen as an upper limit, representing a more flexible system. Axisymmetric boundary conditions and central load-point (Figure T. T.31) were chosen to allow easy interpretation of results.

T.4.1 Test setup and instrumentation

Slabs were supported on eight points, disposed symmetrically on the largest interior slab radius (Figure T.31). Load is introduced over a small square surface of 30x30 mm by controlling the displacement of the actuator.

Displacements and deformations are measured using Linear Variable Differential Transformers (LVDTs). LVDTs designated LVDT_01 to LVDT_12 are used to measure vertical displacements (Figure T.31 and TT.32): the mid-span vertical displacement is measured by LVDT_08, while the rest of the measurement points is disposed symmetrically with respect to boundary conditions (Figure T.31 b)). LVDT_16 to LVDT_19 are used to measure the horizontal displacement on the tensile slab side, close to the central point (Figure T.31 b) and T T.32b).

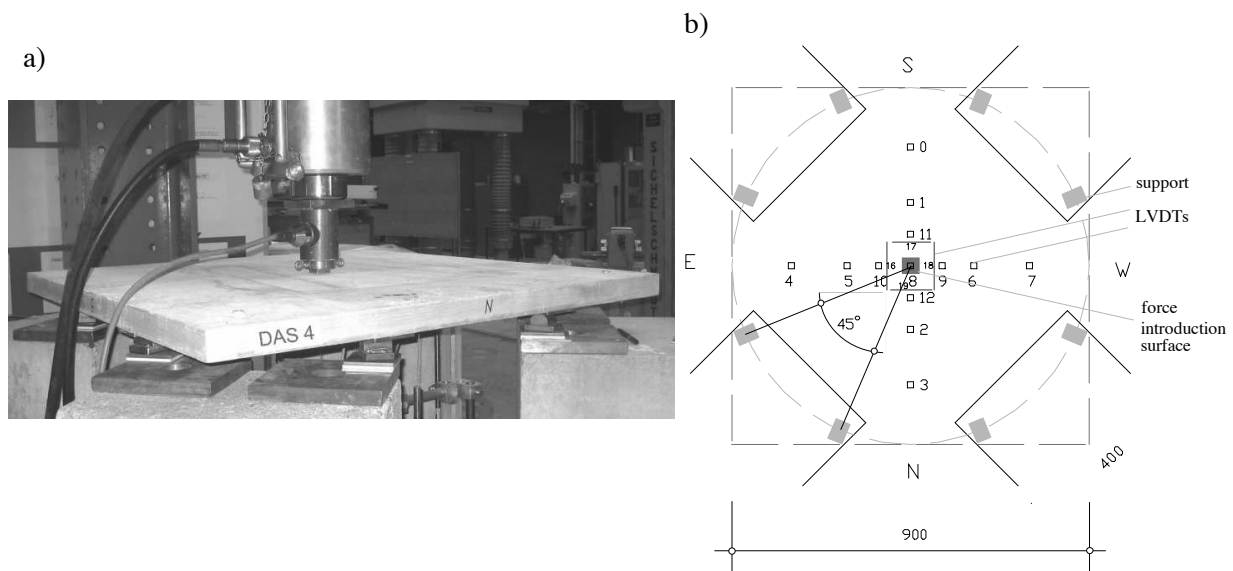


Figure T.31: a) test setup; jack for displacement controlled test under central point loading; b) position of supports and measuring points

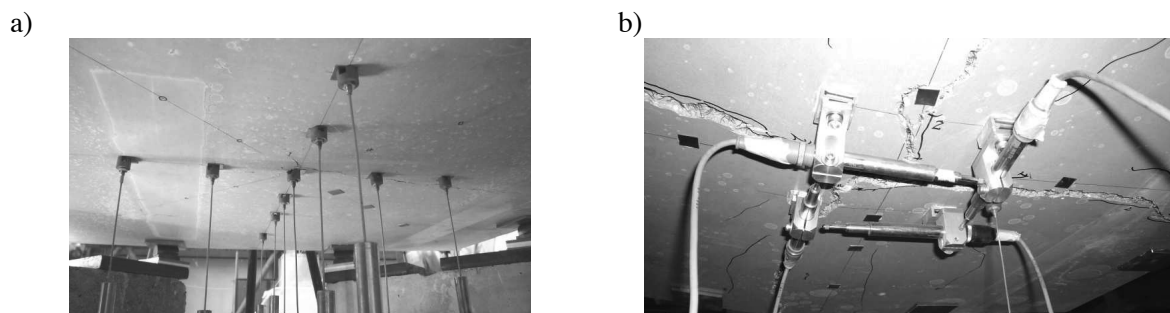


Figure T.32: Measuring devices: LVDTs for vertical displacements and horizontal elongation

T.4.2 Principal results

All tested slabs failed in bending. The failure crack pattern was similar for all slabs, consisting of four axisymmetric yield lines, coinciding with the direction of smallest stiffness (directions E-W and N-S in Figure T.31 b)). Test results for slabs and for quality control tests are summarized in Tables T.3 and T.4.

Table T.3: Summary of test results: UHPFRC slabs, flexural failure

Sample	Date of casting	Date of testing	Material	Slump flow [cm]	$f_{c,m}$ * [MPa]	Nominal height [mm]	P_{max} [kN]	δ [mm]	No of cracks**
DAS 1	04.05.2006	06.06.2006	G19	62.3	188.5	40	31.4	5.14	4
DAS 4	12.05.2006	09.06.2006	G24	70	181.0	40	38.6	8.37	4
DAS 2	09.05.2006	06.06.2006	G22	62	198.8	50	58.5	4.09	4
DAS 5	12.05.2006	09.06.2006	G25	67	185.8	50	63.1	5.88	4
DAS 3	12.05.2006	09.06.2006	G26	68	178.3	60	87.6	4.0	4
DAS 6	16.05.2006	13.06.2006	G28	70	155.8	60	88.8	3.82	4

* mean value of compressive strength obtained on specimens for quality control (table below); values of modulus of elasticity accepted according to tests on G29 samples, $E_{c,m} = 60.25 \text{ GPa}$

** number of cracks in failure mechanism

Table T.4: Test results of material quality control

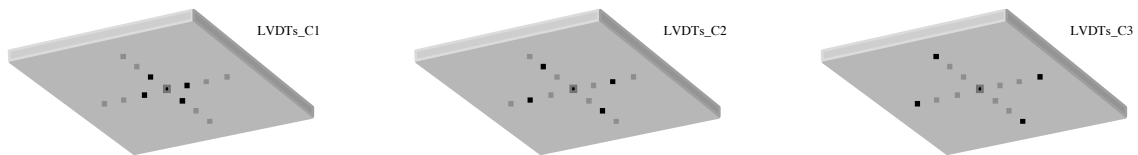
Material	Date of casting	Slump flow [cm]	Cubes	Date of test	f_c [MPa]	Prisms	Date of test	P_{crack} [kN]	P_{max} [kN]
G19	04.05.06	62.3	G19A	02.06.06	185	G19A	06.06.06	32	40
			G19B	02.06.06	202.5	G19b	06.06.06	33	37
			G19C	02.06.06	178	G19c	06.06.06	30	47
			mean		188.5	mean			41.3
G22	09.05.06	62	G22A	07.06.06	180	G22A	06.06.06	28	40.76
			G22B	07.06.06	203	G22B	06.06.06	28	38.84
			G22C	07.06.06	213.5	G22C	06.06.06	24	28
			mean		198.8	mean			35.7
G24	12.05.06	70	G24A	13.06.06	180.5	G24A	09.06.06	32	32.23
			G24B		183.5	G24B	09.06.06	32	32
			G24C		179.0	G24C	09.06.06	28	35
			mean		181.0	mean			33.1
G25	12.05.06	67	G25A	13.06.06	185	G25A	09.06.06	29.7	29.7
			G25B	13.06.06	188	G25B	09.06.06	30	30
			G25C	13.06.06	184.5	G25C	09.06.06	28	28
			mean		185.8	mean			29.2
G26	12.05.06	68	G26A	13.06.06	169	G26A	09.06.06	28	31
			G26B	13.06.06	184.5	G26B	09.06.06	27	28.2
			G26C	13.06.06	181.5	G26C	09.06.06	29	33.6
			mean		178.3	mean			30.8
G28	16.05.06	70	G28A	14.06.06	162	G28A	13.06.06	30	30
			G28B	14.06.06	155.5	G28B	13.06.06	29	31
			G28C	14.06.06	150	G28C	13.06.06	30	30.7
			mean		155.8	mean			30.6

Result presentation

Force-vertical displacements and crack pattern at failure

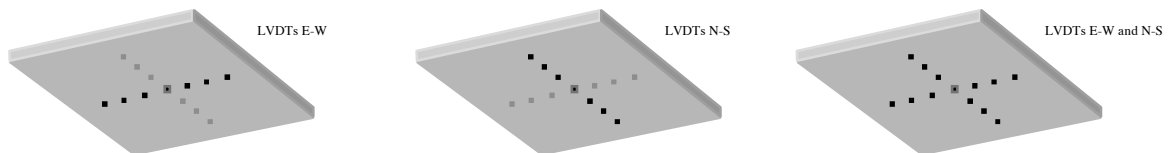
Sensors having the same distance from the central load-point are grouped in the same plot. Force versus central-point displacement is first shown, than a view of the slab at failure, than three more plots that respectively group:

- sensors at a distance $C1 = 80$ mm : LVDT_10, LVDT_12, LVDT_9, LVDT_11
- sensors at a distance $C2 = 160$ mm : LVDT_5, LVDT_2, LVDT_6, LVDT_1
- sensors at a distance $C1 = 300$ mm : LVDT_4, LVDT_3, LVDT_7, LVDT_0



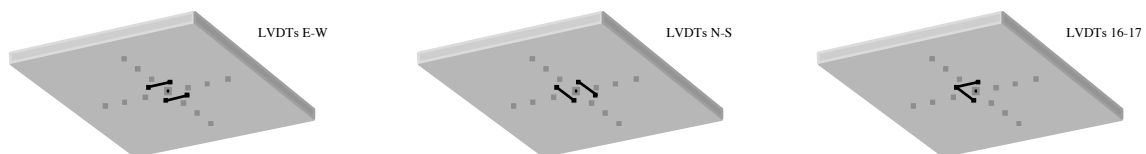
Deformed shape

The deformation of the slab at different load levels (at peak load and at 0.2, 0.4, 0.6, 0.8 of peak load) is plotted in three diagrams, according to the schema below:

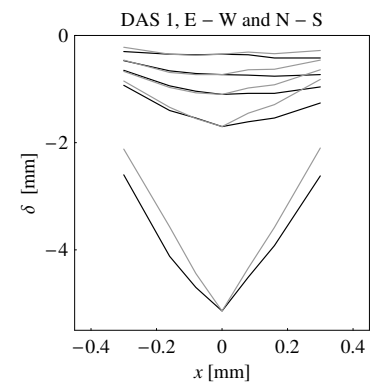
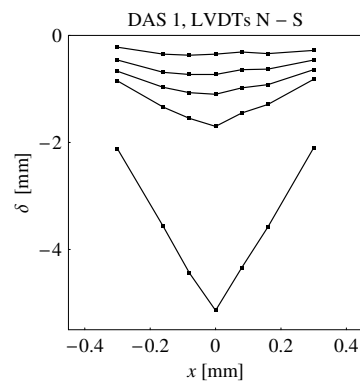
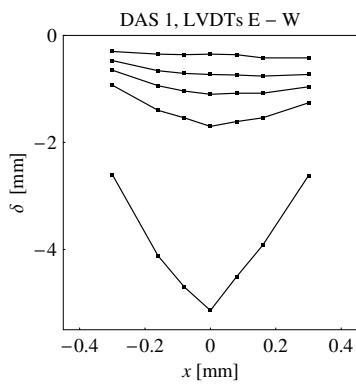
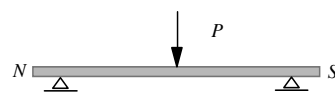
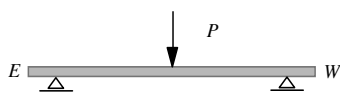
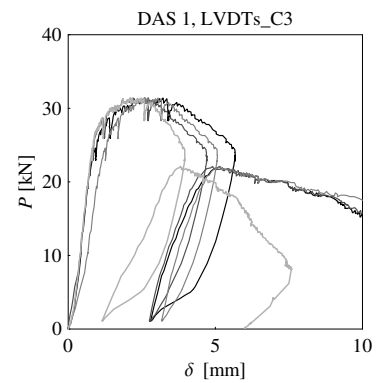
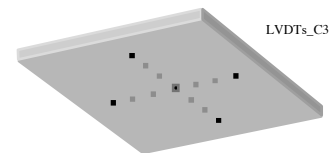
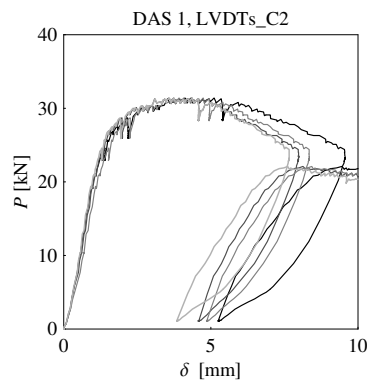
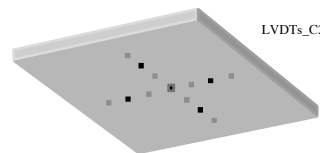
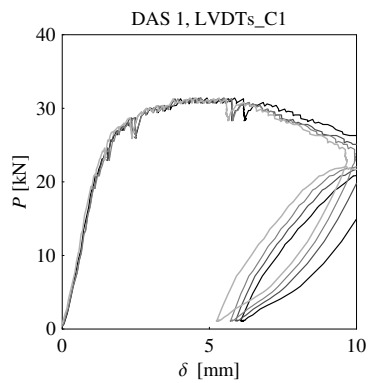
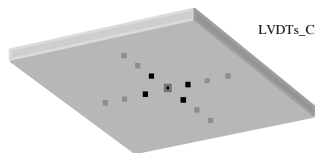
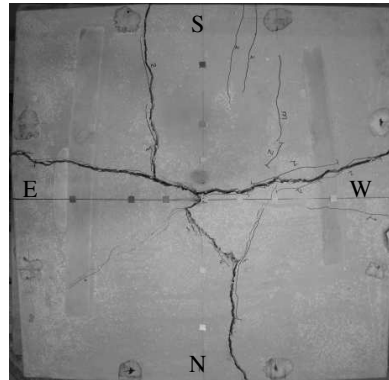
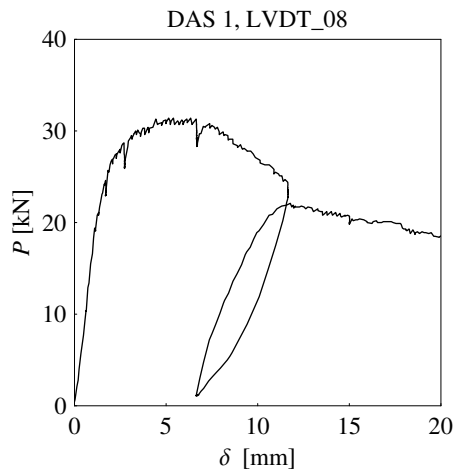


Horizontal elongations

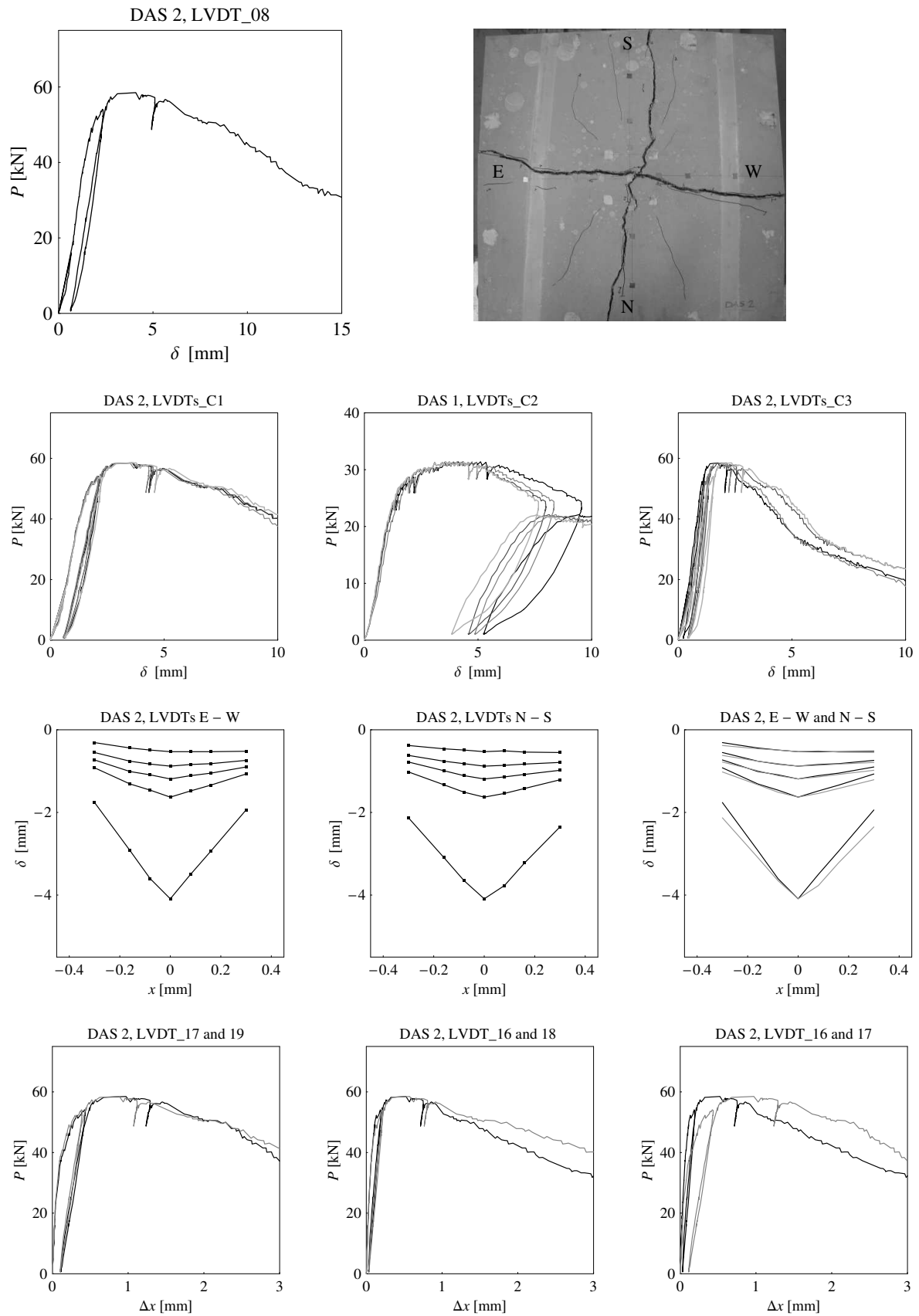
For slab DAS 1, sensors LVDT_16 to LVDT_19 were not used. For the other slabs, three more plots present the horizontal elongations measured by LVDT_16 to LVDT_19, according to the schema below:



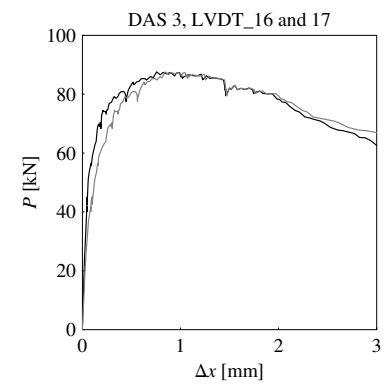
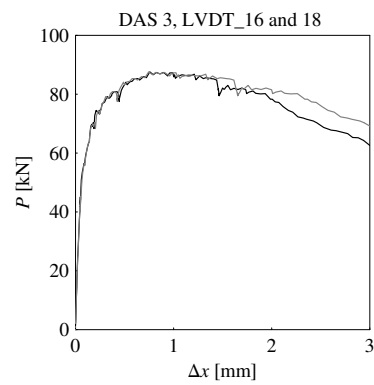
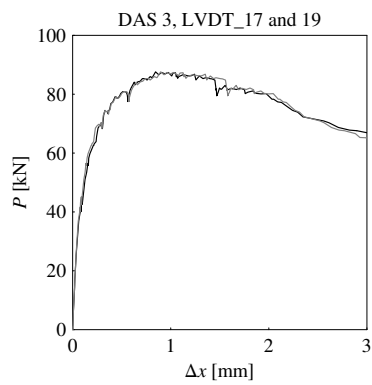
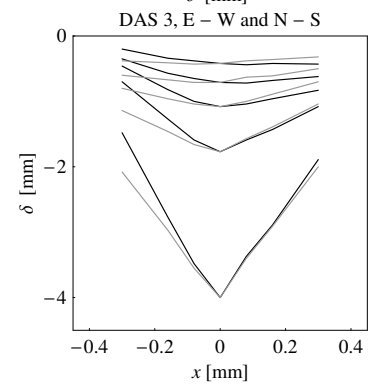
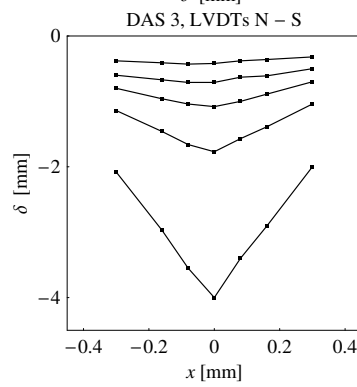
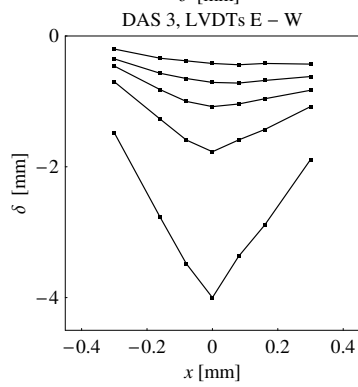
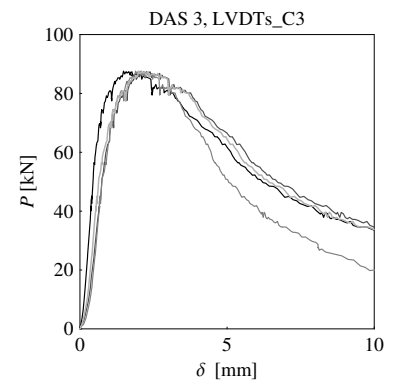
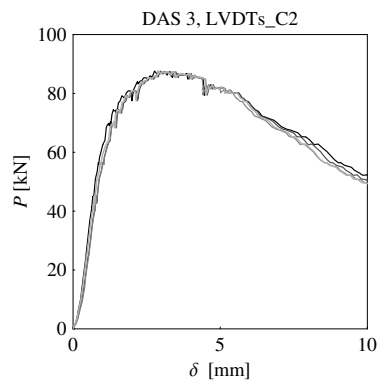
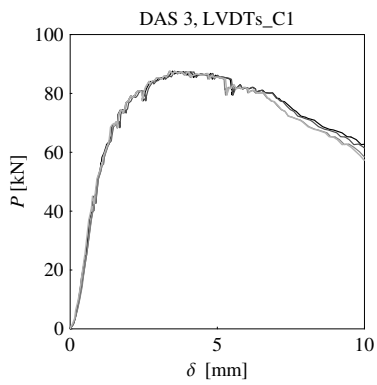
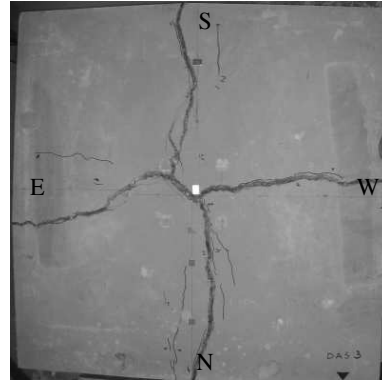
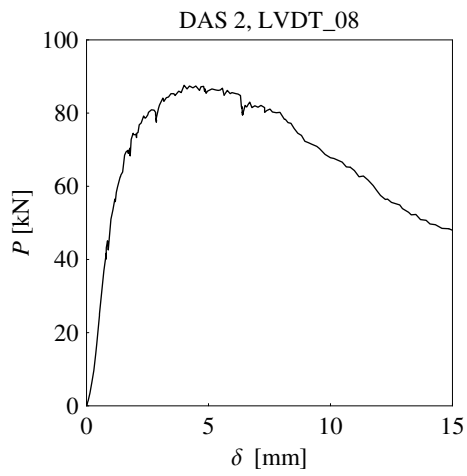
T.4.3 DAS 1, $h = 40$ mm



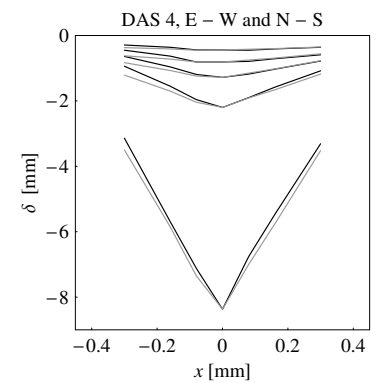
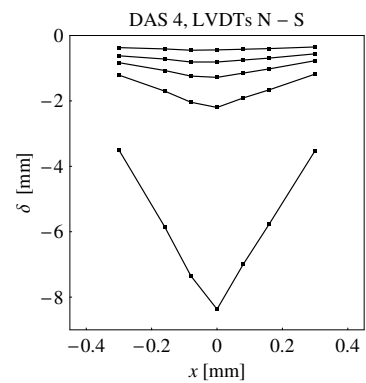
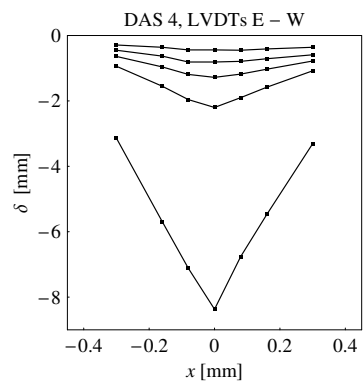
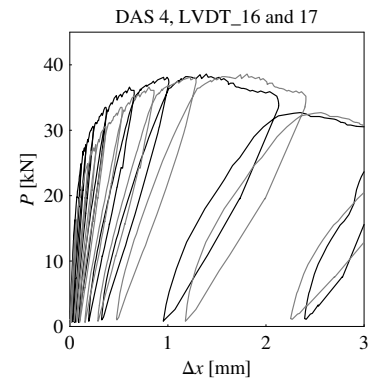
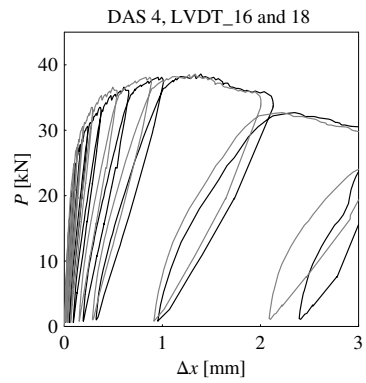
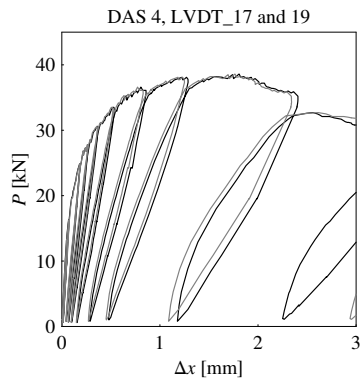
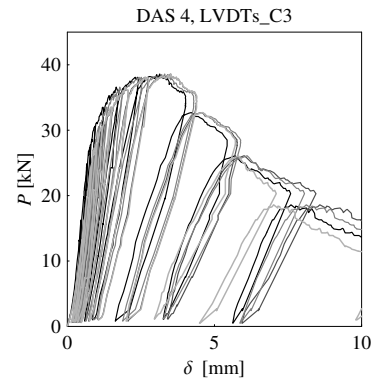
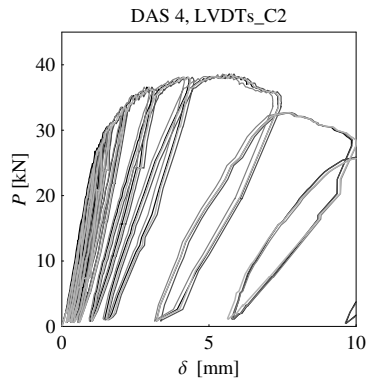
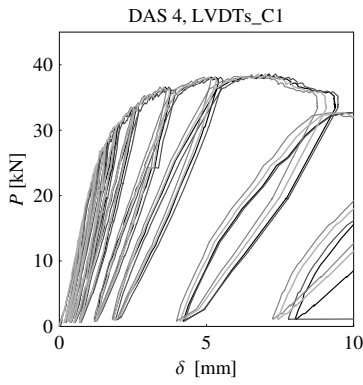
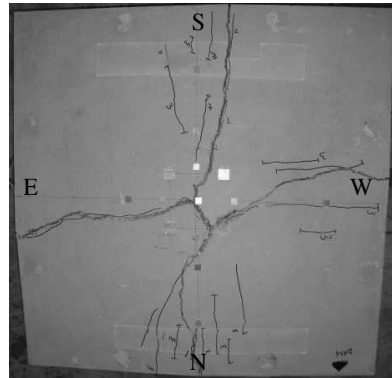
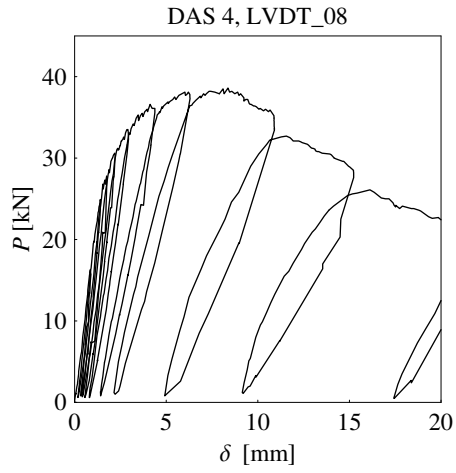
T.4.4 DAS 2, $h=50$ mm



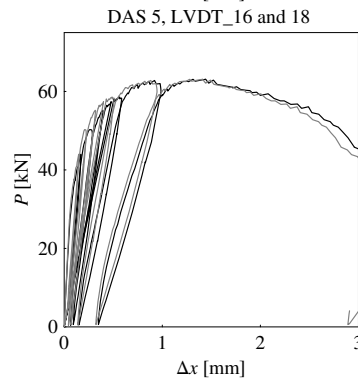
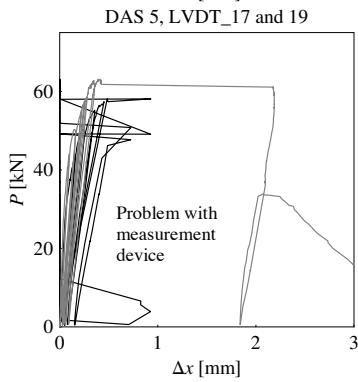
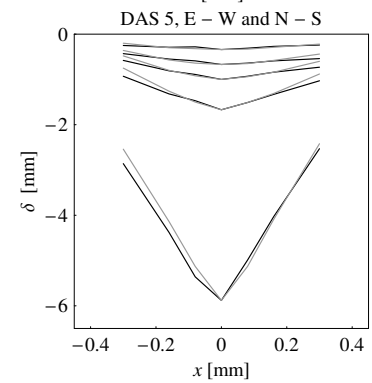
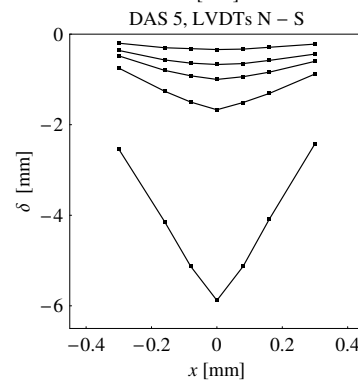
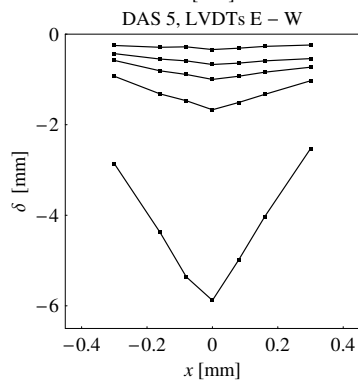
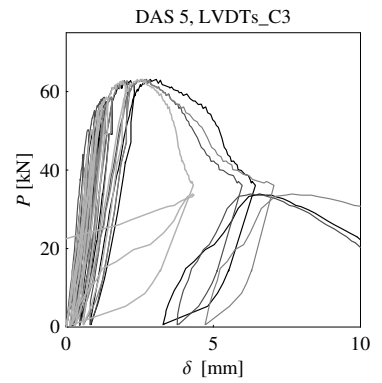
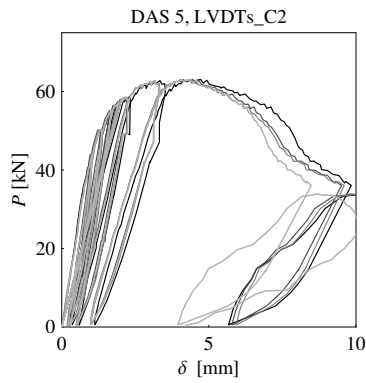
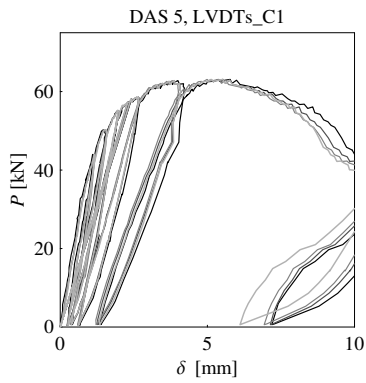
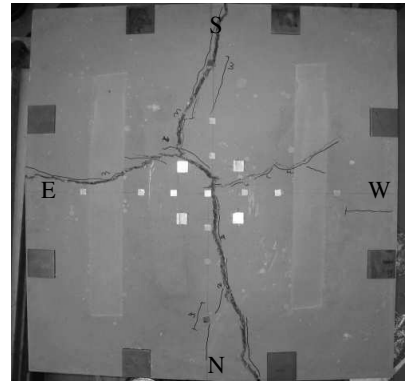
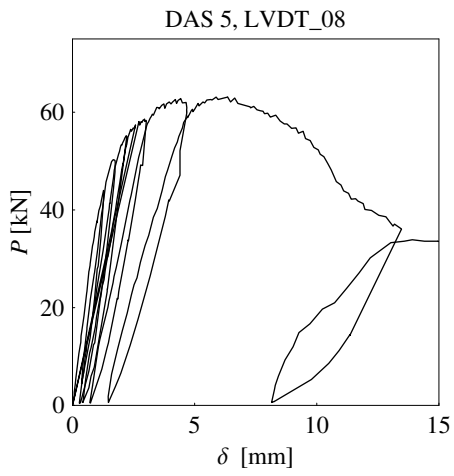
T.4.5 DAS 3, $h=60$ mm



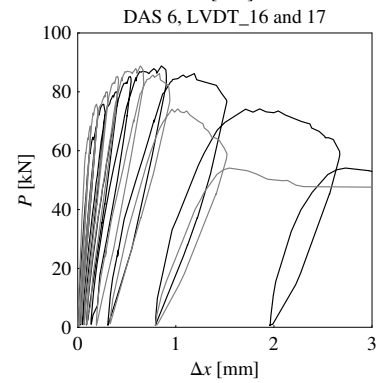
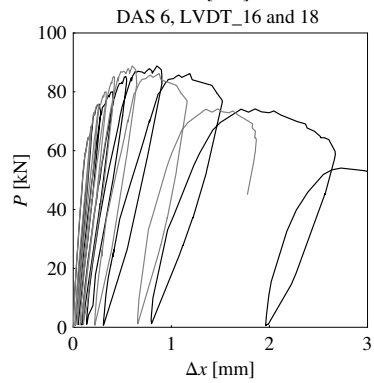
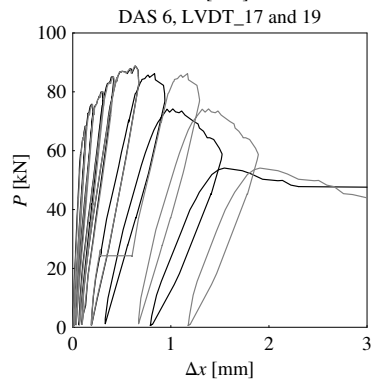
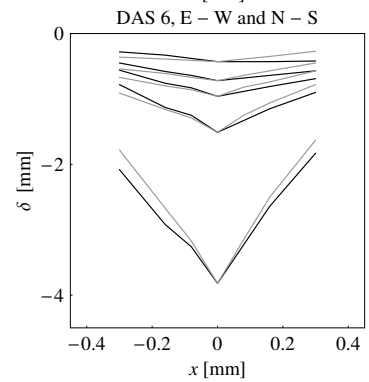
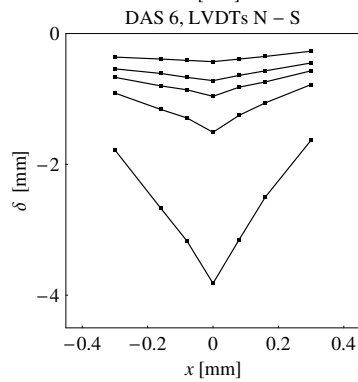
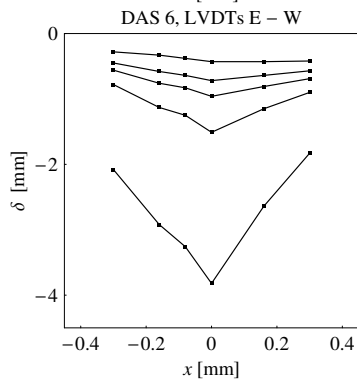
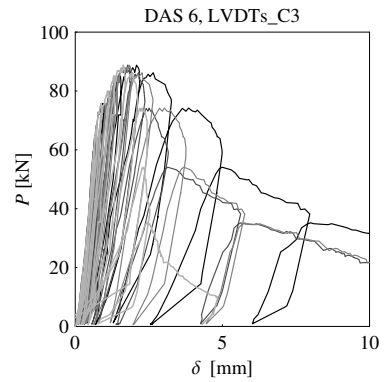
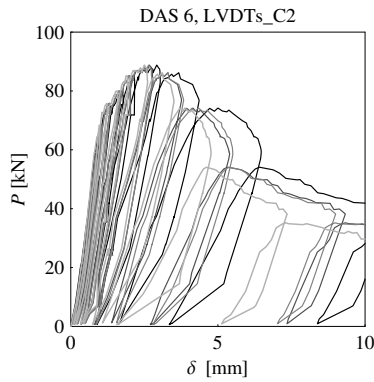
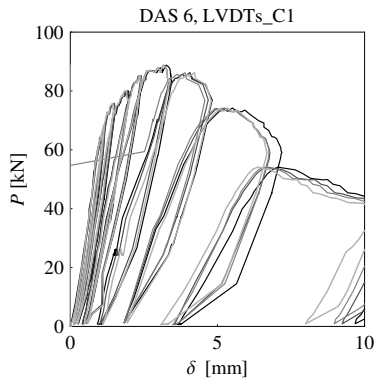
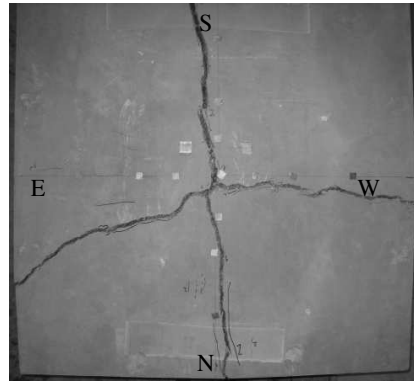
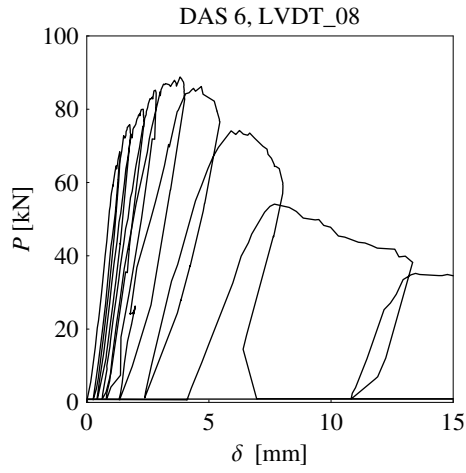
T.4.6 DAS 4, $h=40$ mm



T.4.7 DAS 5, $h=50$ mm



T.4.8 DAS 6, $h=60$ mm



T.4.9 Summary of force-mid-span displacement responses

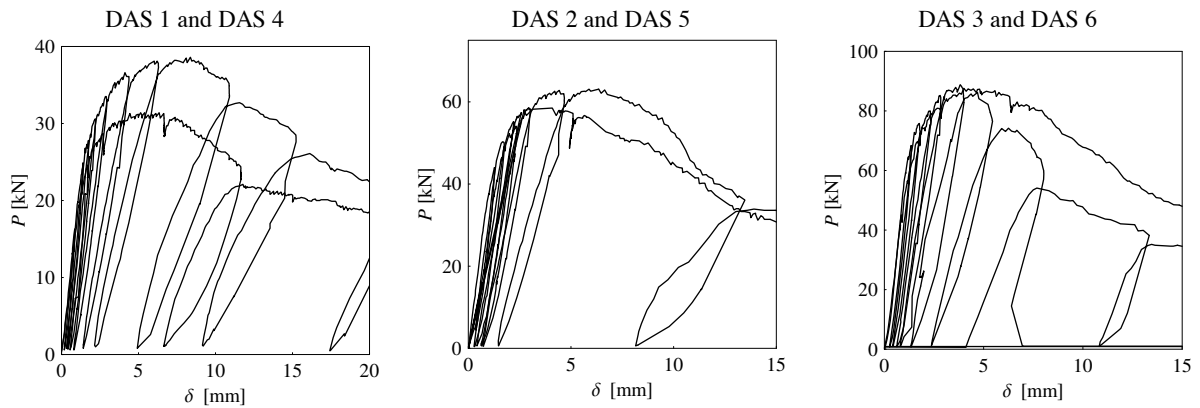


Figure T.33: Comparison of force-mid-span displacements response of slabs of the same thickness

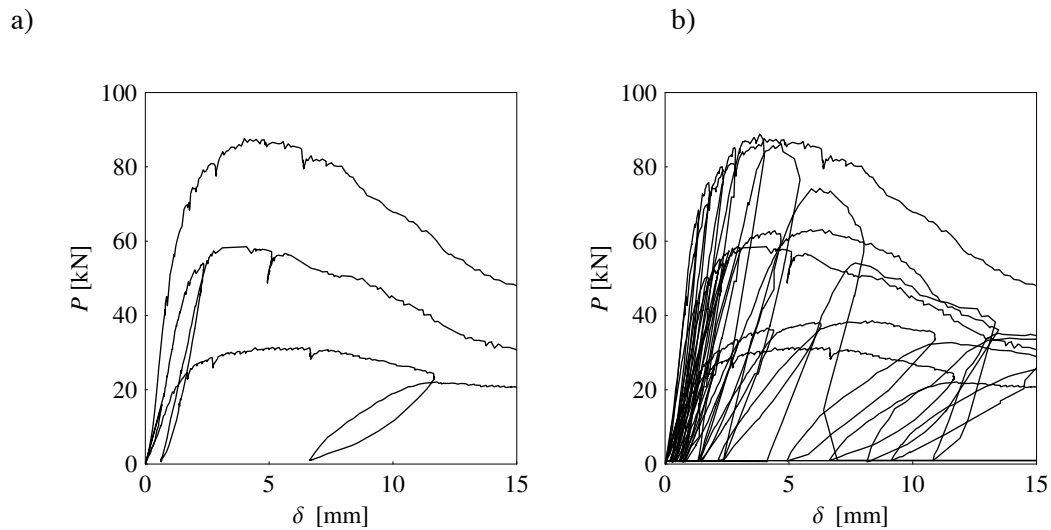


Figure T.34: Comparison of force-mid-span displacements response of slabs: a) DAS 1-DAS 3 , $h=40-60$ mm; b) DAS 1-DA6 3, $h=40-60$ mm.

T.5 Thin slabs failing in punching shear

The aim of this test series is to assess the punching shear resistances of thin slabs with thicknesses interesting for structural application of UHPFRC. The thicknesses were thus chosen based on the same reasons as in the case of slabs failing in bending. A smaller span and boundary conditions that allow bending strength to be increased were chosen to enable punching-shear failure to be reached before bending failure.

T.5.1 Test setup and measuring devices

To increase bending strength of tested specimens, slabs were clamped along all four sides, as shown in Figure T.35. Tests are displacement controlled, with load introduced over a surface of 20x20 mm (Figure T.36). Vertical displacements were measured with LVDTs at five points on the tensile side of the slabs.

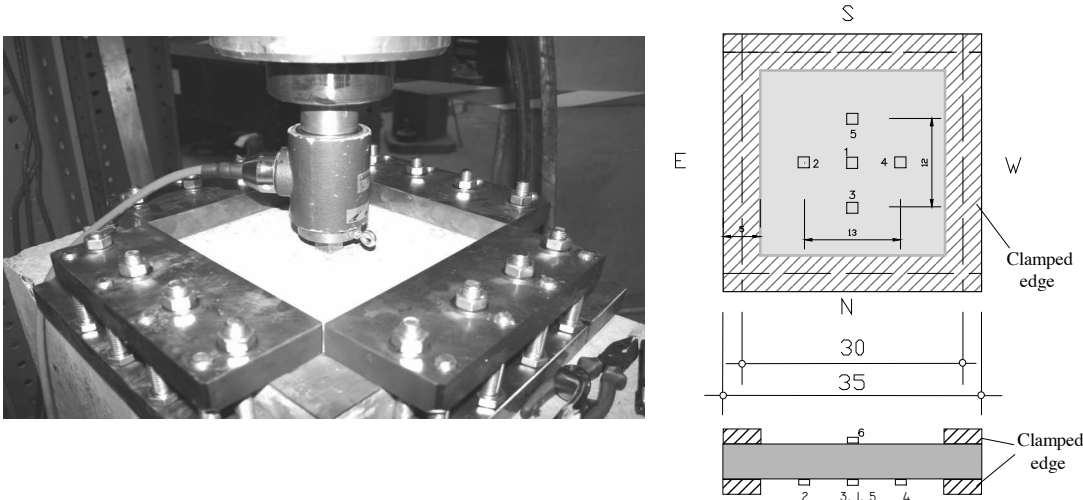


Figure T.35: Test setup, supports position and position of measuring points



Figure T.36: Load introducing surface, 20x20 mm

T.5.2 Principal results

Test results on thin slabs and on quality control specimens are summarized in Tables T.5 and T.6. Force versus load-point displacement for all the slabs are compared in Figure T.37, while more detailed information on each test is provided in the following paragraphs.

Table T.5: Summary of test results: UHPFRC slabs, punching shear failure

Specimen	Date of casting	Date of testing	Material	Slump flow [cm]	$f_{c,m}$ [MPa]	Nominal height [mm]	Actual thickness [mm]	V_{max} [kN]	$\delta_{V,max}$ [mm]
PP 30	29.08.06	10.10.06	G33	63	175.2	30	31	61.51	1.13
PP 40	29.08.06	26.09.06	G33	63	175.2	40	38	76.17	1.37
PP 50a	29.08.06	25.09.06	G33	63	175.2	50	51	117.74	1.37
PP 50b	29.08.06	26.09.06	G33	63	175.2	50	50	110.74**	1.51
PP 60	29.08.06	26.09.06	G33	63	175.2	60	60	162.84	0.95

* mean value of compressive strength obtained on specimens for quality control (table below); values of modulus of elasticity accepted according to tests on G29 samples, $E_{c,m} = 60.25 \text{ GPa}$

** punching failure occurred for $\delta = 1.9 \text{ mm}$ and $V = 102 \text{ kN}$.

Table T.6: Test results of material quality control

Material	Date of casting	Slump flow [cm]	Cubes	Date of test	f_c [MPa]	Prisms	Date of test	P_{crack} [kN]	P_{max} [kN]
G33	29.08.06	63	G33A	25.09.06	181.5	G33A	27.09.06	32	52
			G33B	02.06.06	170	G33B	27.09.06	36	45
			G33C	02.06.06	174				
			mean		175.2	Mean		34	48.5

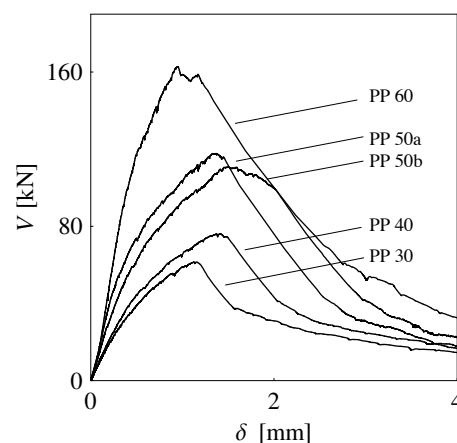


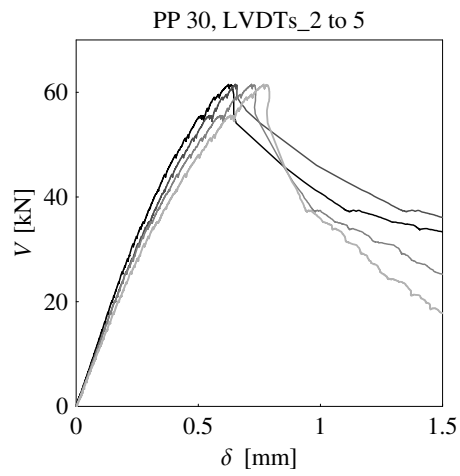
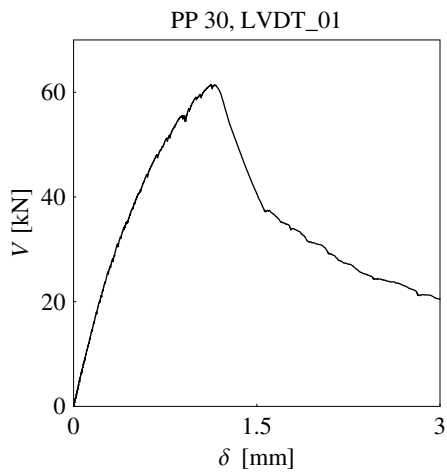
Figure T.37: Force – load-point displacement curve of slabs failing in punching shear

T.5.3 Result presentation

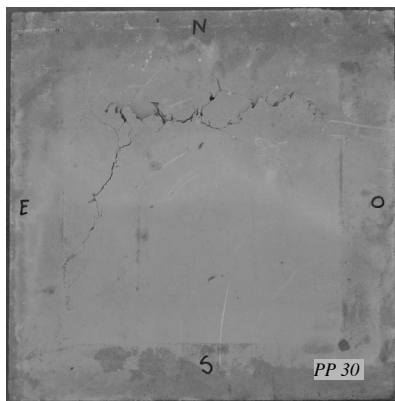
Results are presented separately for each tested slab (§1.5.4 to §1.5.8) in the following order:

- force versus load-point displacement (LVDT_01) curve;
- force-displacement curves measured at distances 65 and 60 mm from the load-point, plotted in the same figure (LVDTs_2 to 5, the first plotted as black and the last as most lightest grey line);
- a view of the tensile slab surface at failure and sections through the slab central point in directions north-south (N-S) and east-west (E-W), i.e. showing the form of the punching cone;
- figures illustrating deformations of the slab in the two monitored direction (E-W and N-S) for various load levels: V_{max} , and $0.2, 0.4, 0.6, 0.8 \cdot V_{max}$. In E-W direction these curve are obtained with measurements of LVDT_2, LVDT_21 and LVDT_4, while in N-S direction they are obtained with measurements of LVDT_3, LVDT_21 and LVDT_5. Deformations in E-W and N-S directions are finally compared (N-S direction plotted as grey lines) to check the symmetry of deformations.

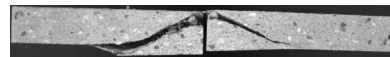
T.5.4 PP 30, $h=31$ mm



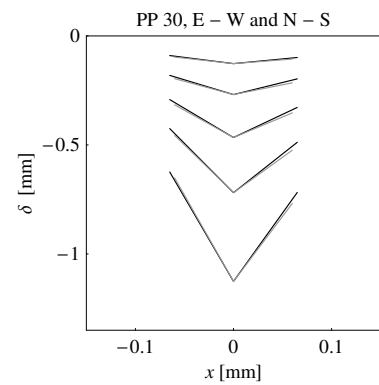
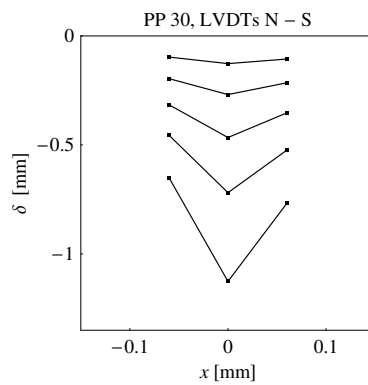
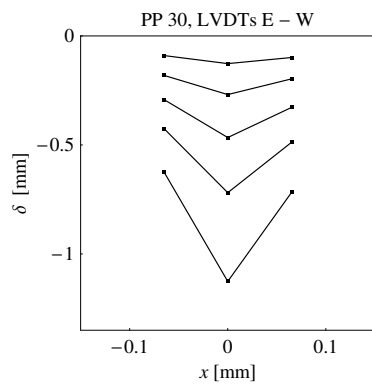
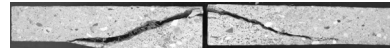
tensile slab surface



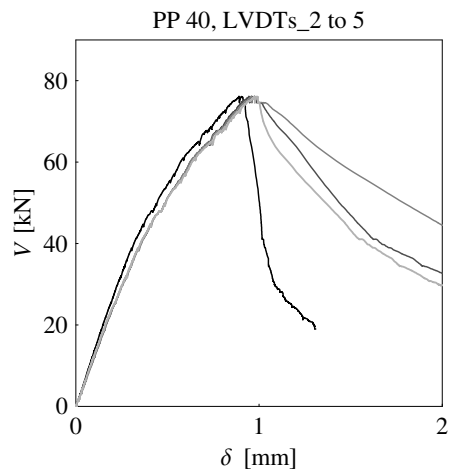
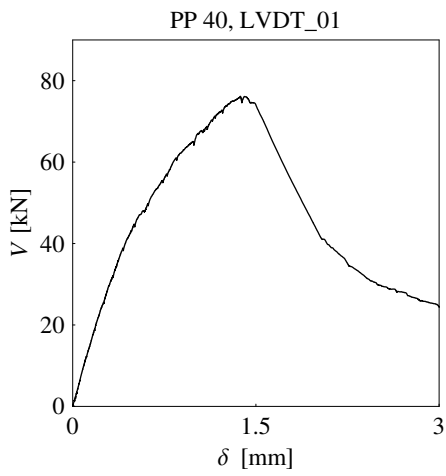
section in N-S direction



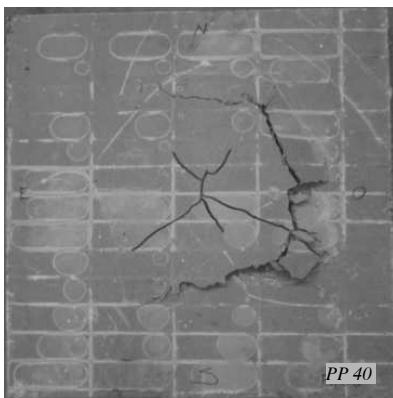
section in E-W direction



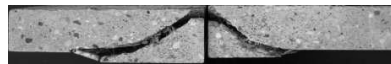
T.5.5 PP 40, $h=38$ mm



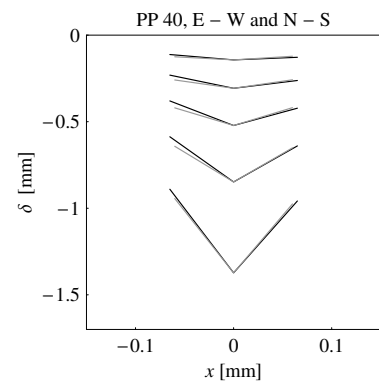
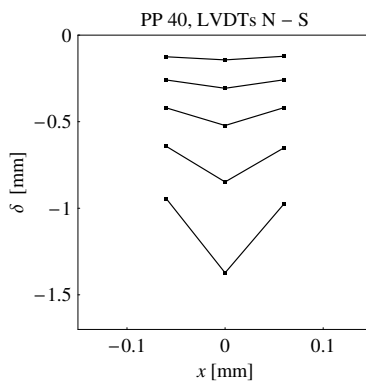
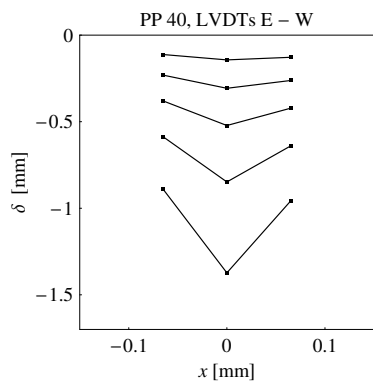
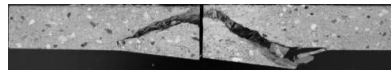
tensile slab surface



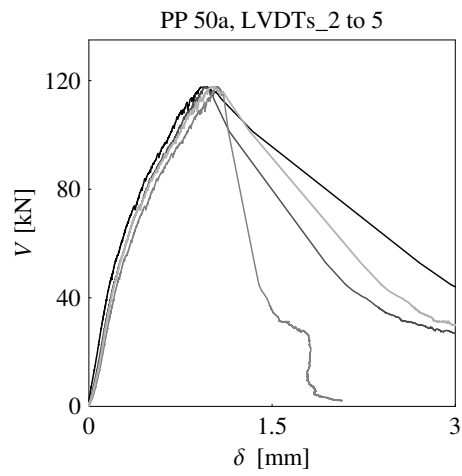
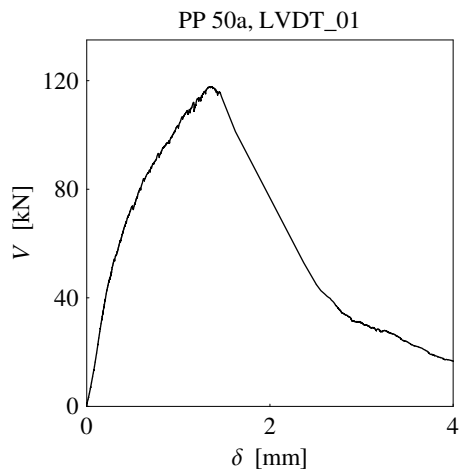
section in N-S direction



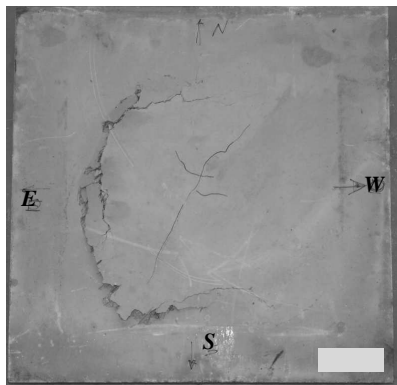
section in E-W direction



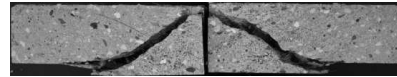
T.5.6 PP 50a, $h=51$ mm



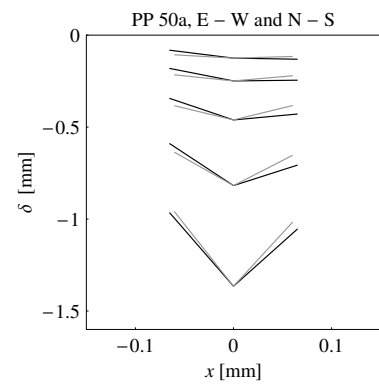
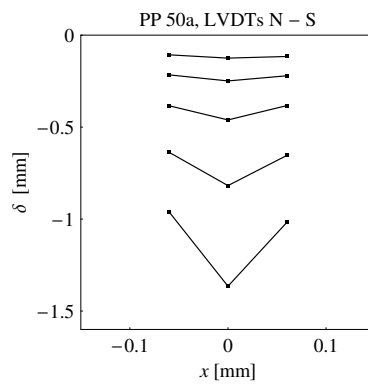
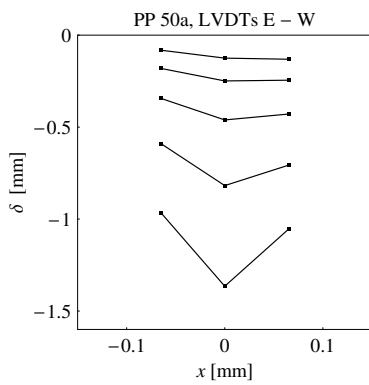
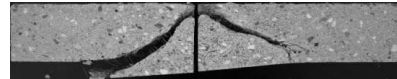
tensile slab surface



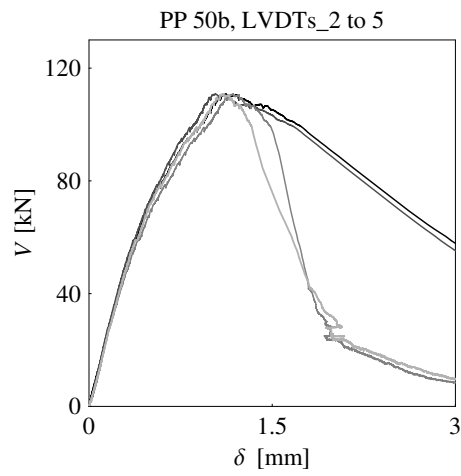
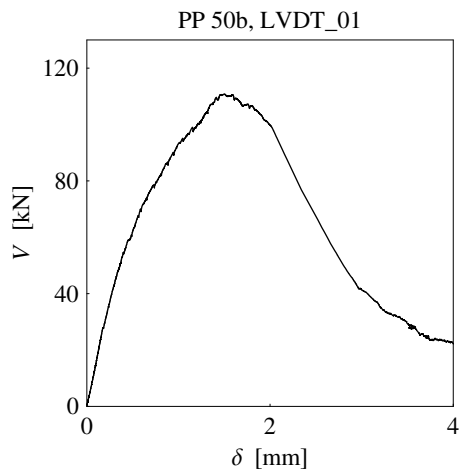
section in N-S direction



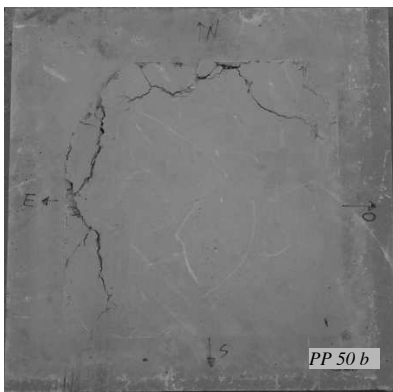
section in E-W direction



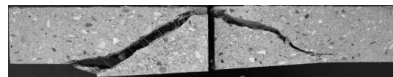
T.5.7 PP 50b, $h=50$ mm



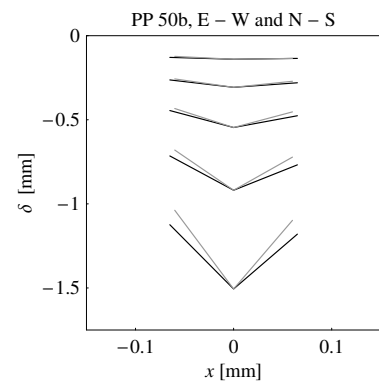
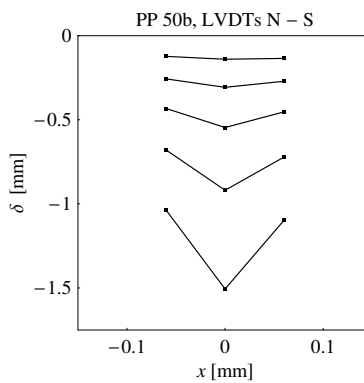
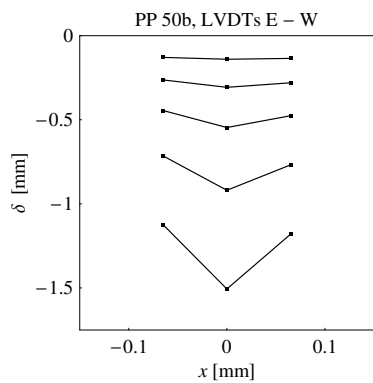
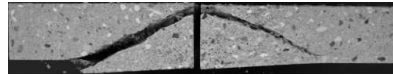
tensile slab surface



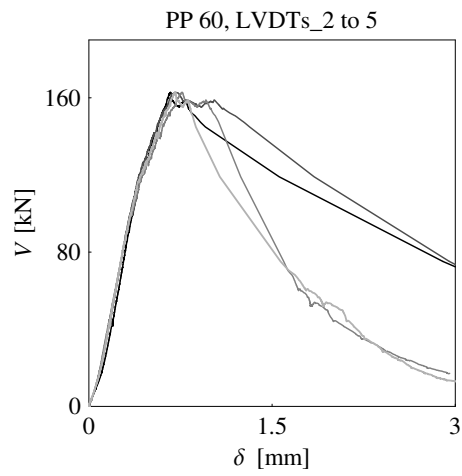
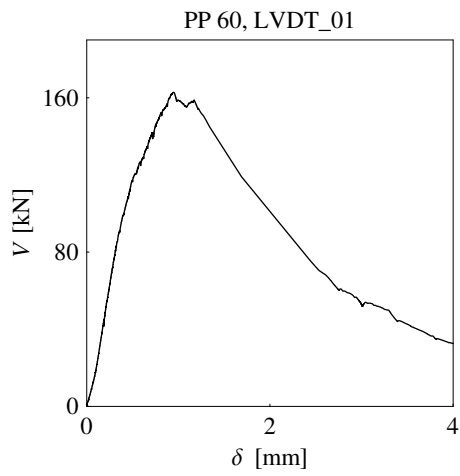
section in N-S direction



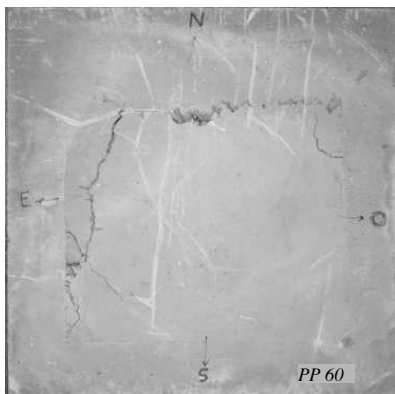
section in E-W direction



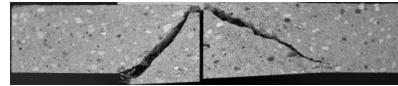
T.5.8 PP 60, $h=60$ mm



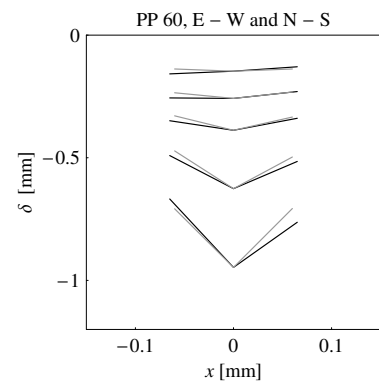
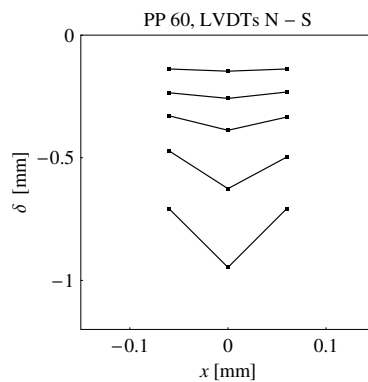
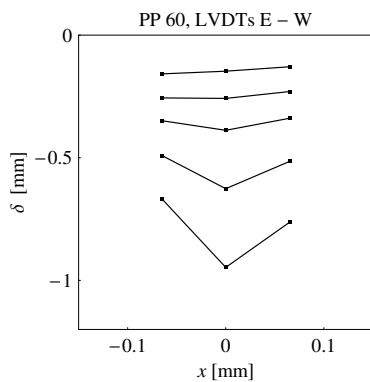
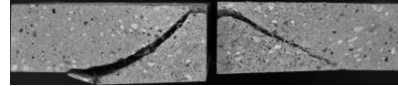
tensile slab surface



section in N-S direction



section in E-W direction



Curriculum vitae

Personal information

name	Ana Spasojevic
place of birth	Niš, Serbia
date of birth	13th August 1976
nationality	Serbian
e-mail	ana.spasojevic@epfl.ch

Education

2003 – to date	PhD Student at IS-Béton – EPFL, Lausanne, Switzerland
2001	Graduated at the Department of Structural Engineering, Faculty of Civil Engineering and Architecture, University of Niš. Graduated in Concrete bridges, with grade 10/10, and with an average grade during studies 9.77 (10). Final thesis on: “ <i>Design of a cable stayed footbridge, with a prestressed concrete deck</i> ”.
1995-2001	Graduate studies at the University of Niš, Faculty of Civil Engineering and Architecture, Department of Structural Engineering.
1995	Graduate Secondary school, "Bora Stankovic" Niš, group for Mathematics and Natural Sciences (“summa cum laude” award).

Work experience

2003 – to date	IS-Béton – EPFL, Lausanne, Switzerland. PhD student, teaching assistant for the courses: “Structures”, “Concrete Structures”, “Concrete Bridge Design”.
2001 – 2003	Faculty of Civil Engineering and Architecture, University of Niš. Research and teaching assistant in: "Structural Analyses I", "Structural Analyses II", "Structural Informatics".

Awards

2003	One-year fellowship for doctoral studies, Structural program at the EPFL
2002	First prize for the best Diploma Work at the Workshop for Young Engineers of East Europe, organised by DAAD (Deutscher Akademischer Austausch Dienst)
2002	Award for the best graduate from the Faculty of Civil Engineering and Architecture, University of Nis
2001	Charter and Scholarship from the Fund of Royal Court Karadjordjevic, for the University year 2001/2002, in the field of civil engineering

Publications

Spasojevic A., Redaelli D., Fernández Ruiz M., Muttoni A., “*Influence of Tensile Properties of UHPFRC on Size Effect in Bending*”, Second International Symposium on Ultra-High Performance Concrete, Kassel, 2008, pp. 303 - 310

Spasojevic A. , *Possibilities for Structural Improvements in the Design of Concrete Bridges*, Proceedings of the 6th Int. Ph.D. Symposium in Civil Engineering, Zurich 2006, 146, Zurich, Suisse, 8, 2006.

Spasojevic A. “*Konkursno idejno resenje mosta preko reke Nišave na bulevaru Medijana u Nišu – prvonagrađjeni rad*”, “*First awarded contest solution of a road bridge over Nišava river*”, Proceeding of the Symposium, JDGK, Yugoslav Society of Civil Engineers, September 2004.

A. Spasojevic, Dj. Djordjevic, “*Some Relevant Aspects of Footbridge Vibrations*”, Facta Universitatis, Series: Architecture and Civil Engineering, Vol.2, No.4, 2002, pp. 281-289.